ELECTROCHEMICAL IMPEDANCE

Analysis and Interpretation

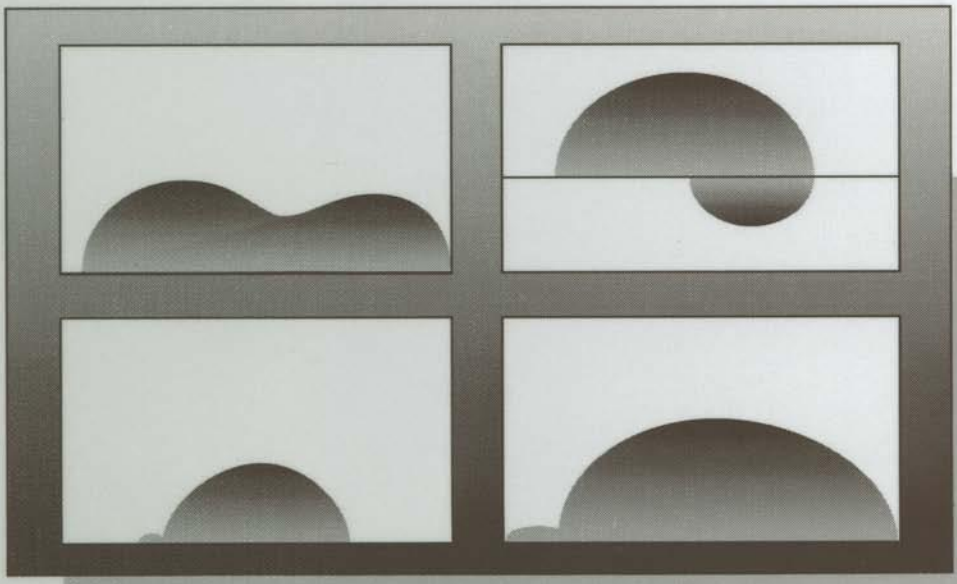

Scully/Silverman/Kendig editors

STP 1188 ASTM

STP 1188

Electrochemical Impedance: Analysis and Interpretation

John R. Scully, David C. Silverman, and Martin W. Kendig, Editors

ASTM Publication Code Number (PCN):
04-011880-27

ASTM
1916 Race Street
Philadelphia, PA 19103

Library of Congress Cataloging-in-Publication Data

Electrochemical impedance : analysis and interpretation / John R. Scully, David C. Silverman, and Martin W. Kendig, editors.
(STP ; 1188)
"ASTM publication code number (PCN) : 04-011880-27."
Includes bibliographical references and indexes.
ISBN 0-8031-1861-9
1. Corrosion and anti-corrosives. 2. Electric resistance—Data processing. 3. Electrochemical analysis—Data processing. I. Scully, John R., 1958- . II. Silverman, David C., 1947- III. Kendig, Martin W. IV. Series: ASTM special technical publication ; 1188.
TA418.74.E43 1993
620.1'1223—dc20 92-42059
CIP

Peer Review Policy

Each paper published in this volume was evaluated by three peer reviewers. The authors addressed all of the reviewers' comments to the satisfaction of both the technical editor(s) and the ASTM Committee on Publications.

The quality of the papers in this publication reflects not only the obvious efforts of the authors and the technical editor(s), but also the work of these peer reviewers. The ASTM Committee on Publications acknowledges with appreciation their dedication and contribution to time and effort on behalf of ASTM.

Printed in Fredericksburg, VA
March 1993

Foreword

This publication, *Electrochemical Impedance: Analysis and Interpretation,* contains papers presented at the symposium of the same name, held in San Diego, CA on 4–5 November 1991. The symposium was sponsored by ASTM Committee G-1 on Corrosion of Metals. John R. Scully, University of Virginia, Center for Electrochemical Science and Engineering, David C. Silverman, Monsanto, and Martin W. Kendig, Rockwell International Science Center, presided as symposium chairmen and are editors of the resulting publication.

Contents

Overview 1

MODELING AND CORROSION PROCESSES

Impedance Spectra Calculated from Model Polarization Curves—U. BERTOCCI AND R. E. RICKER 9

Discussion 22

Specific Aspects of Impedance Measurements in Low Conductivity Media—S. CHECHIRLIAN, M. KEDDAM, AND H. TAKENOUTI 23

Analysis of EIS Data for Common Corrosion Processes—F. MANSFELD, H. SHIH, H. GREENE, AND C. H. TSAI 37

Analyzing Simulated Electrochemical Impedance Spectroscopy Results by the Systematic Permutation of Data Points—P. R. ROBERGE 54

The Effect of Parasitic Conduction Pathways on EIS Measurements in Low Conductivity Media—K. C. STEWART, D. G. KOLMAN, AND S. R. TAYLOR 73

The Characterization of the Coarsening of Dealloyed Layers by EIS and Its Correlation with Stress-Corrosion Cracking—R. G. KELLY, A. J. YOUNG, AND R. C. NEWMAN 94

APPLICATIONS OF KRAMERS-KRONIG TRANSFORMATIONS

Application of the Kramers-Kronig Relations in Electrochemical Impedance Spectroscopy—P. AGARWAL, M. E. ORAZEM, AND L. H. GARCIA-RUBIO 115

Kramers-Kronig Transformation in Relation to the Interface Regulating Device—C. GABRIELLI, M. KEDDAM, AND H. TAKENOUTI 140

Validation of Experimental Data from High Impedance Systems Using the Kramers-Kronig Transforms—B. J. DOUGHERTY AND S. I. SMEDLEY 154

CORROSION AND INHIBITION

The Impedance Response of Film-Covered Metals—S. TURGOOSE AND R. A. COTTIS 173

Corrosion Prediction from Circuit Models Application to Evaluation of Corrosion Inhibitors—D. C. SILVERMAN 192

Use of Electrochemical Noise in the Study of Inhibitor Systems: Part I—The Effect of Silicate Polymerization on the Inhibition of Aluminum—S. T. HIROZAWA AND D. E. TURCOTTE 205

The Influence of Corrosion Product Film Formation on the Corrosion of Copper-Nickel Alloys in Aqueous NaCl—H. HACK AND H. PICKERING 220

Discussion 236

Interpreting Electrochemical Impedance Spectra from Segmented Electrode Arrangements—A. N. ROTHWELL, J. L. DAWSON, D. A. EDEN, AND J. W. PALMER 237

Discussion 251

CORROSION OF ALUMINUM

Evolution of Electrochemical Impedance During Sealing of Porous Anodic Films on Aluminum—J. L. DAWSON, G. E. THOMPSON, AND M. B. H. AHMADUN 255

Discussion 275

Characterization of the Corrosion of Aluminum Thin Films Using Electrochemical Impedance Methods—J. R. SCULLY 276

Detection and Monitoring of Localized Corrosion by EIS—F. MANSFELD, Y. WANG, S. H. LIN, H. XIAO, AND H. SHIH 297

Potentiodynamic Polarization and Electrochemical Impedance Spectroscopy for the Statistical Process Control of Aluminum Anodizing—P. R. ROBERGE, E. HALLIOP, AND S. YOUSRI 313

Equivalent Circuit Modeling of Aluminum/Polymer Laminates Using Electrochemical Impedance Spectroscopy—G. R. T. SCHUELLER AND S. R. TAYLOR 328

Discussion 343

CORROSION OF STEEL IN SOIL AND CONCRETE

Electrochemical Impedance of a Buried Large Structure—S. SUDO AND S. HARUYAMA 347

Calculation of Extended Counter Electrode Polarization Effects on the Electrochemical Impedance Response of Steel in Concrete—S. C. KRANC AND A. A. SAGÜÉS 365

Discussion 383

Electrochemical Impedance and Harmonic Analysis Measurements on Steel in Concrete—M. I. JAFAR, J. L. DAWSON, AND D. G. JOHN 384

COATINGS ON METALS

Electrochemical Impedance of Coated Metal Undergoing Loss of Adhesion—M. W. KENDIG, S. JEANJAQUET, AND J. LUMSDEN 407

Analyzing and Interpreting Electrochemical Impedance Spectroscopy Data from Internally Coated Steel Aerosol Containers—W. S. TAIT, K. A. HANDRICH, S. W. TAIT, AND J. W. MARTIN 428

Study of Protection Mechanisms of Zinc-Rich Paints by Electrochemical Impedance Spectroscopy—S. FELIU, JR., R. BARAJAS, J. M. BASTIDAS, M. MORCILLO, AND S. FELIU 438

Evaluation of High-Performance Protective Coatings by Electrochemical Impedance and Chronoamperometry—R. D. GRANATA AND K. J. KOVALESKI 450

Discussion 462

Improved Coatings Testing and Evaluation Using Electrochemical Impedance Spectroscopy—P. KAMARCHIK 463

Author Index 475

Subject Index 477

Overview

Over the past quarter century electrochemical impedance has blossomed into a major corrosion measurement technology. Its usage has grown to include applications ranging from fundamental studies of corrosion mechanisms and material properties to very applied studies of quality control and routine corrosion engineering. Today, computer controlled "user friendly"systems are available from several manufacturers. This has made data acquisition a routine procedure, whereas only a decade ago users were confronted with the need to develop their own data acquisition systems. However, diagnostic tools for evaluating the validity of the data, procedures for developing a fundamental understanding of the results and their relationship to the process being studied, and knowledge of the limits of practical application to real world systems are still under active investigation. This Special Technical Publication has been published as a result of the 1991 symposium entitled Electrochemical Impedance: Analysis and Interpretation held in San Diego, California. The goal of the symposium was to provide a clear picture of the current state of the art in interpretation and analysis of electrochemical impedance data. The symposium was a natural extension of the efforts within ASTM Subcommittee G.01.11 on Electrochemical Corrosion Testing and Task Group G.01.11.06 on Electrochemical Impedance to provide standardized methodologies for using this technology and reporting the results. Both of these groups are part of ASTM Committee G.01 on Corrosion of Metals.

The collection of twenty-seven papers published in this volume has been grouped into six major categories that very closely characterize the major areas of research and engineering application of Electrochemical Impedance Techniques in corrosion. These areas are: corrosion process characterization and modeling, applications of Kramers-Kronig transformations for evaluating the validity of data, corrosion and its inhibition by either corrosion products or specially added inhibitors, corrosion of aluminum and aluminum alloys, corrosion of steel in soils and concrete, and evaluation of coatings on metal substrates. The papers range from theoretical modeling to practical applications. The effort has been made to include many of the recognized contributors in this field. A careful reading of the papers should provide a broad overview of the plethora of information available and the important questions being asked about this technology.

Modeling and Corrosion Processes

Corrosion characterization and modeling impacts virtually all applications of this technology. The papers in this section should provide methodologies that would be useful in a number of areas. Modeling has tended to encompass use of electrical equivalent circuit models, the elements of which are used to represent physical processes. Bertocci and Ricker take the opposite approach and attempt to calculate polarization scans and impedance spectra from basic kinetic equations including the metal reaction, oxygen reduction, and hydrogen evolution as a function of pH. This approach, while a long way from being generally implemented, would circumvent the ambiguities that can occur when using passive linear circuit analogues. Low-conductivity fluids are difficult media in which to conduct electrochemical studies. Chechirlian, Keddam, and Takenouti discuss an equivalent circuit which might be used to help to eliminate artificial relaxation processes that

occur when generating impedance spectra in low-conductivity media. Mansfeld, Shih, Greene, and Tsai attempt to tailor software packages to specific corrosion phenomena. Their paper presents a number of results that show that such tailoring can lead to good fits with the data and interesting insights into the corrosion phenomena. Roberge presents an alternative to modeling by a number of equivalent circuits. His method in which he projects the center of a semicircle from a series of permutations of three points on the spectra is suggested to provide a rich source of information concerning the corrosion processes. High-frequency artifacts are often present when generating impedance spectra. Stewart, Kolman, and Taylor discuss the factors that may contribute to the occurrence of such artifacts and propose a model that can reproduce spectra for a set of measuring resistors using a particular make of potentiostat. New applications of electrochemical impedance techniques are continually being reported. The paper by Kelly, Young, and Newman reports an application of the impedance technique to study the development of porosity due to dealloying of silver as well as gold surface diffusion in solid solution silver-gold alloys.

Applications of Kramers-Kronig Transformations

"Are my spectra valid?" is a question continually asked. Kramers-Kronig Transformations provide a way of assuring that the impedance spectra truly reflect the corrosion process and are not affected by phenomena such as too large of an amplitude or the system not being at steady state. In their paper, Agarwal, Orazem, and Garcia-Rubio introduce the concept of a measurement model as a tool for identifying possible frequency-dependent errors in the data. They show that the measurement model can be used to determine that the spectra are consistent with the Kramers-Kronig transformations without having to explicitly integrate the transforms. Impedance spectra are sometimes generated in a potential region in which a small increase in potential results in a decrease in current, a negative resistance. Gabrielli, Keddam, and Takenouti provide evidence and suggest how Kramers-Kronig transforms can be used to check validity under these circumstances. Lastly, Dougherty and Smedley provide an application of the use of Kramers-Kronig transformations to show the validity of impedance spectra generated in aluminum-methanol-water systems. Their results show an ability to discern when the requirements of linearity, stability, and causality are violated.

Corrosion and Inhibition

Corrosion of metals can be affected by corrosion products, corrosion inhibitors, or other constituents in the fluid that are either adsorbed onto the surface or become incorporated in the three-dimensional surface region. Electrochemical impedance has been an important tool for studying the electrochemistry of this interaction. However, relating the spectra to actual physical phenomena can be difficult. Turgoose and Cottis start from first principles to construct the impedance spectra. They create a generalized equivalent circuit in which all elements are defined and constrained by physical, chemical, or electrochemical processes. They show that this generalized circuit can account for many of the features observed in the spectra from film-covered electrodes. However, such an approach cannot be implemented on a routine basis in poorly characterized systems. Silverman takes an alternative approach of using simple circuits to extract corrosion-related parameters on a routine basis from the spectra of steel in near neutral uninhibited and inhibited water. He shows that by careful use of the circuit models, practical estimates of corrosion rates and practical insights into the corrosion mechanism can be obtained. Also under the category

of inhibitors, Hirozawa and Turcotte show that electrochemical noise and electrochemical impedance techniques can be combined to give interesting insights into corrosion inhibition of aluminum. They show that elimination or reduction of electrochemical noise may indicate improvement in the protectiveness of the oxide film. Product films can also affect corrosion as in the case of helping to protect copper-nickel alloys in seawater. Hack and Pickering use electrochemical impedance to shed light on the reason that such films are protective. They report that oxygen reduction which affects corrosion of these alloys is itself controlled by diffusion through the outer product layer. Lastly, steel corrosion in aqueous systems can be a function of whether the steel is base metal, weld metal, or lies in the heat-affected zone. Rothwell, Dawson, Eden, and Palmer discuss an electrode and instrumentation that is proposed to allow the generation of impedance measurements on single electrodes while they are effectively galvanically coupled as in the real situation. In this way, base and weld metal can be studied separately under coupled conditions.

Corrosion of Aluminum

Corrosion and protection of aluminum alloys is an area of tremendous technological interest given the increased application of this material over the last 30 years. Electrochemical impedance has expanded both the depth and breadth of corrosion and protection information that can be acquired. Dawson, Thompson, and Ahmadun survey the literature on electrical equivalent circuit models useful for interpreting the impedance behavior of anodized aluminum. Circuit parameters are then used to monitor detailed changes in anodized film hydration and barrier properties. Mansfeld, Wang, Lin, Xiao, and Shih describe electrical equivalent circuit models and experimental data fitting procedures for detecting and monitoring pitting corrosion. They emphasize the utility of the technique for studying stable pitting phenomena under freely corroding conditions at open circuit potentials that are above the pitting potential. Scully extends the application of impedance techniques to aluminum thin films of one micrometer thicknesses or less. The nondestructive nature of the method is one of the key advantages of the technique in these applications. Passivity, salt film formation, and localized corrosion of aluminum in hydrofluoric acid solutions are characterized. Roberge, Halliop, and Yousri discuss EIS and polarization techniques as replacements for the long-term salt spray exposure method. They seek to advance electrochemical impedance as a tool for routinely monitoring anodized film quality or anodizing baths, or both. Schueller and Taylor discuss a novel application of EIS. The aim of their paper is the detection of delamination between an aluminum alloy/polymer laminate. The approach is technologically significant as a possible nondestructive tool for characterizing damage in adhesively bonded components. An equivalent circuit model was proposed using transmission line circuitry which describes the impedance spectra of edge exposed laminates. Model laminates with known rectangular defects were analyzed and compared with the circuit model.

Corrosion of Steel in Concrete or Soil

Advancement in the understanding of corrosion of metals in soils and concrete has been frustrated, in part, because traditional electrochemical polarization methods fail to compensate for the high resistance of the soil or concrete. Impedance methods are able to overcome this obstacle as well as provide a nondestructive tool and, hence, represent an opportunity to advance current understandings. Sudo and Haruyama model the impedance spectra of a two-electrode cell consisting of a buried metallic structure and a small nonpolarizable disk counter electrode at the soil surface. Their results show that care is required

in assuming that the low-frequency complex plane impedance intercept with the real axis is always inversely proportional to the corrosion rate. Kranc and Sagüés investigate surface counter electrode placement and current distribution effects for a model reinforced concrete geometry containing both corroding and passive reinforcing steel. Predicted impedance spectra yield apparent polarization resistances which underestimated the corrosion current mainly due to current distribution effects. Finally, Jafar, Dawson, and John discuss the application of harmonic analysis for evaluation of corrosion rates as well as Tafel parameters in the case of laboratory concrete samples containing reinforcing steel. Their paper highlights the advantages of harmonic analysis as an extension of impedance techniques for rapid assessment of corrosion rates.

Coatings on Metals

Impedance techniques continue to develop as a tool for rapidly assessing the performance of organic coatings on metals. The papers presented in this section demonstrate that while the applicability of the technique to various coatings continues to expand, its versatility is not without bounds. Kendig, Jeanjaquet, and Lumsden discuss the theoretical limits of various impedance parameters including the "breakpoint frequency" for estimation of coating delamination. The application described includes adhesion loss adjacent to a macroscopic defect on a fusion bonded epoxy coated pipe steel. Their analysis shows that the low-frequency impedance of such macroscopic delaminations may become insensitive to the depth of the delaminated zone for certain combinations of solution resistance and interfacial impedance associated with the delaminated region. The paper points to possible limitations of certain impedance parameters in detecting coating delaminations. Tait, Handrich, Tait, and Martin apply the impedance technique to internally coated steel aerosol containers. One theme of their paper concerns estimation of the fraction of containers from a total population that will ultimately experience failure. This estimation is based on the statistical treatment of a range of impedance results (due to a range of defects) obtained from a subset of the total population of containers. Feliu, Jr., Barajas, Bastidas, Morcillo, and Feliu report on the use of impedance methods to characterize zinc-rich organic paints. Both the impedance spectra and the protection mechanisms of these coatings differ from those of barrier coatings. The paper focuses on analysis of impedance data for the case of cathodically protected steel substrates resulting from the interconnected zinc particles. This phenomenon is distinguished from the barrier properties of the organic coating by exploiting the differences in the frequency range over which each is effectively probed. Granata and Kovaleski report on their efforts to use impedance as well as chronoamperometry techniques as coating evaluation tools for high-performance fusion-bonded coatings, marine service epoxy, and polyimide used in electronics. Kamarchik applies the impedance approach to automotive and electrodeposited coatings and to container interior coatings for beverage and food end-uses. Impedance provides indication of changes in coating performance long before visual changes were observed using more traditional exposure tests such as continuous salt fog.

Summary

The papers presented in this book should provide the reader with a broad overview of the present state of the art concerning analysis and interpretation of electrochemical impedance spectra. Armed with the information provided in this book, the reader should be better equipped to explore the frontiers of this technology as well as apply it to

corrosion science and engineering. The symposium chairmen gratefully acknowledge the efforts of the authors and ASTM personnel in the preparation of this book.

John R. Scully
University of Virginia
Center for Electrochemical Science
and Engineering
Charlottesville, VA 22903

David C. Silverman
Monsanto
St. Louis, MO 63167

Martin W. Kendig
Rockwell International Science Center
Thousand Oaks, CA 91360

Modeling and Corrosion Processes

Ugo Bertocci[1] *and Richard E. Ricker*[1]

Impedance Spectra Calculated from Model Polarization Curves

REFERENCE: Bertocci, U. and Ricker, R. E., **"Impedance Spectra Calculated from Model Polarization Curves,"** *Electrochemical Impedance: Analysis and Interpretation, ASTM STP 1188,* J. R. Scully, D. C. Silverman, and M. W. Kendig, Eds., American Society for Testing and Materials, Philadelphia, 1993, pp. 9–22.

ABSTRACT: Once steady state polarization curves have been calculated from a model based on a description of the kinetics of the electrode processes, all the necessary elements for computing the impedance spectra at any potential within the range used for the polarization curves are available. This paper described the basic equations necessary for this purpose, and develops, as an example of interest in corrosion studies, the case in which both oxygen reduction and hydrogen evolution occur as cathodic processes. The effect of changes of pH at the metal surface are examined, and comparisons between calculated curves and experimental data are presented.

KEYWORDS: polarization curve, impedance spectra, electrode kinetics, charge transfer kinetics, cathodic reactions, anodic reactions, modeling, corrosion

Nomenclature

subscript a = quantities relative to anodic electrode reaction (7)
subscript b = value taken in the bulk of the electrolyte
subscript h = quantities relative to electrode reaction (5)
subscript n = generic chemical species involved in a reaction
subscript o = value taken at the electrode/solution interface
subscript s = quantities relative to electrode reaction (3)
subscript z = zero-frequency limit
D = diffusion coefficient
D_{H} = diffusion coefficient for H^+
D_{OH} = diffusion coefficient for OH^-
D_s = diffusion coefficient for O_2 dissolved in the electrolyte
e^- = electron
E = electrode potential
F = Faraday constant
i = current density
$j = \sqrt{-1}$
k = rate constant
K_W = ionic product of water
R = gas constant
T = absolute temperature

[1]Corrosion Group, Materials Science and Engineering Laboratory, National Institute of Standards and Technology, U.S. Department of Commerce, Gaithersburg, MD 20899.

(O_2), (H^+), (OH^-), (M^{++}) = concentrations of the species described by the chemical symbol in parenthesis
α = symmetry factor
δ = diffusion layer thickness
ν = frequency
ω = circular frequency

For the purpose of analyzing corrosion data, polarization curve modeling combined with curve fitting can give great insight into the electrochemical processes that determine the corrosion rate of a metal/solution system.

Electrochemical impedance spectroscopy (EIS) is also used for studying corrosion processes and, for the interpretation of the results, modeling programs based on the combination of passive circuit elements are often used. What is not generally recognized is that once the polarization curves have been calculated by the modeling algorithms, all the necessary elements for computing the impedance spectra at any potential within the range used for the polarization curves are available. Therefore, as an extension of the polarization modeling programs, it is possible to generate impedance plots at potentials positive and negative with respect to the corrosion potential, which, moreover, are the logical consequence of the assumptions made for the calculation of the polarization curves. The model impedance plots so generated can be employed to explore the effect of the electrode potential on the ac response, as well as of changing quantities such as reactant concentrations and diffusion layer thickness. Comparison with experimental data at different potentials can be used to verify the validity of the hypotheses made as to the reaction mechanisms governing the corrosion process.

In some cases, while the fitting of the polarization curves is good, discrepancies between calculated and experimental impedance plots may be observed. These discrepancies are the consequence of the fact that impedance data give more information about the electrode kinetics than steady state polarization curves [*1*], so that, when found, they indicate that the kinetics are more complicated than postulated, and one will have to judge if the differences will be significant for practical corrosion cases.

This paper describes the mathematics involved in the modeling, gives some examples of the results of the calculations, and shows a few comparisons between model curves and experimental results.

Mathematical Treatment

The calculation of steady state polarization curves requires the solution of a set of simultaneous equations that describe the charge transfer kinetics of the electrode reactions postulated to occur, as well as the material transport of the reacting species in the diffusion layer. If homogeneous reactions take place, they must also be taken into account; many of these homogeneous reactions, among which an important one is the ionic dissociation of water, can be considered fast enough to be always at equilibrium, so that the mathematical treatment is simplified. We will not describe further the general treatment, since it can be found in textbooks [*2*], examples have been shown in a previous paper [*3*], and because it will be given in greater detail in the example treated in the following section.

As a result of solving the system of equations, for every value of the electrode potential E, the current densities for all electrode reactions and the concentrations of all reacting species at the electrode surface can be obtained. From these, the impedance spectrum can be calculated by differentiating the current-potential relationships under the assumption of

small perturbations [4]. Similarly, a relationship between perturbations of the current and of the concentrations of the electroactive species at the electrode can be obtained. The electrode admittance Y, that is the derivative of the total current with respect to the electrode potential, is then the sum of the admittances for the various electrode reactions that take place on the electrode.

From the equations relating current densities and reactant concentrations at the interface, the so-called Warburg impedances are obtained. The functions of the circular frequency $\omega = 2\pi\nu$, for a diffusion layer of thickness δ, have the form [5]

$$f_n(\omega) = \frac{1}{\sqrt{2\omega D_n}}\left[\tanh\left(\delta\sqrt{\frac{j\omega}{D_n}}\right) - j\tanh\left(\delta\sqrt{\frac{j\omega}{D_n}}\right)\right] \quad (1)$$

where the index n indicates an electroactive species in solution. These formulae allow the computation of the impedance spectrum, at equilibrium or at any other potential.

When the frequency tends to zero, the hyperbolic tangent becomes equal to its argument, giving

$$\lim_{\omega\to 0} f_n(\omega) = \frac{1}{\sqrt{2\omega D_n}}\left(\delta\sqrt{\frac{j\omega}{D_n}} - j\delta\sqrt{\frac{j\omega}{D_n}}\right) = \frac{\delta}{D_n} \quad (2)$$

If Eq 2 is used instead of Eq 1, the imaginary part of the electrode admittance goes to zero, and the zero-frequency electrode impedance can be computed.

For the purpose of illustrating this approach to modeling, we will give an example that retains some of the complications that are of interest to corrosion researchers, but is still quite simple and general. Effects due to adsorption or the formation of surface films were not considered, and therefore they will not appear in the impedance spectra. This is a drastic limitation of the present formulation of our model, which was deliberately accepted in order not to complicate the treatment in such a way as to make it unwieldy. The consequences of this simplified treatment will often be evident at the lowest frequencies, and an example will be shown in one of the following sections. The usefulness of this approach to modeling, however, should not be unduly impaired by the fact that it will not account for all complications that may appear in practice.

A Modeling Example

Polarization Curves

As is often the case for corroding metals, the cathodic reactions to be considered are oxygen reduction and hydrogen evolution. These reactions have been extensively studied and give rise to an extraordinarily complicated set of electrode reactions [6]. There are indications that the reaction order of oxygen depends on the metal [7], and some of the studies concerning O_2 reduction on oxides [8] point to relatively high Tafel slopes. Here, however, the following simplifications will be employed:

(1) Only the cathodic partial reactions will be considered. The justification is that in most corrosion cases, the system is so far from equilibrium that the back-reaction can be neglected.

(2) For the oxygen reduction reaction, no intermediates, such as H_2O_2, will be considered. The overall reaction is written as

$$O_2 + 4H^+ + 4e^- = 2H_2O \tag{3}$$

and the charge transfer kinetics are described by the equation

$$i_s = -4k_sF(O_2)_o(H^+)_o \exp\left(-\frac{\alpha_s FE}{RT}\right) \tag{4}$$

where the subscript s refers to Reaction 3. The effect of the oxygen and hydrogen ion concentration on the rate is considered to be of first order, and a one-electron rate-determining step is assumed.

(3) The hydrogen evolution reaction is written as

$$2H^+ + 2e^- = H_2 \tag{5}$$

and the charge transfer kinetics are given by

$$i_h = -k_hF(H^+)_o \exp\left(-\frac{\alpha_h FE}{RT}\right) \tag{6}$$

The subscript h refers to Reaction 5.

(4) The only anodic reaction considered is the oxidation of a metal M, according to the reaction

$$M = M^{++} + 2e^- \tag{7}$$

with the charge transfer kinetics given by

$$i_a = 2k_aF \exp\left(\frac{\alpha_a FE}{RT}\right) \tag{8}$$

The rate-determining step is assumed to involve one electron. To keep the treatment simple, no hydrolysis of the metal ions or formation of solid corrosion products is considered. Also in this case, the back-reaction is neglected, under the assumption that the corroding metal is far from equilibrium.

(5) In order to determine the concentration of dissolved oxygen $(O_2)_o$ and of hydrogen ions $(H^+)_o$ at the interface, transport in the diffusion layer of thickness δ has to be considered, and the composition of the bulk solution must be known. Since Reaction 7 going cathodically is not considered, the concentration of metal ions in solution and at the interface can be disregarded. However, if one wishes to calculate the metal concentration at the electrode surface in order to estimate the likelihood of oxide or hydroxide precipitation, this can be easily done.

For the description of transport in the diffusion layer, the following two equations must be considered

$$i_s = -4FD_s \frac{d(O_2)}{dx} \tag{9}$$

where D_s is the diffusion coefficient of dissolved oxygen, and

$$i_s + i_h = -FD_H \frac{d(H^+)}{dx} + FD_{OH} \frac{d(OH^-)}{dx} \tag{10}$$

Since the concentrations of H^+ and OH^- are always in equilibrium with each other, linked by the ionic product of water

$$[H^+][OH^-] = K_W \tag{11}$$

the OH^- concentration can be eliminated, and Eq 10 can be written in the form

$$i_s + i_h = -F\left(D_H + \frac{D_{OH}K_W}{(H^+)^2}\right)\frac{d(H^+)}{dx} \tag{12}$$

where the apparently variable diffusion coefficient for H^+ takes care of the fact that in neutral or alkaline solutions, transport of the charges is carried out in part or mostly by OH^- ions moving in direction opposite to the gradient of H^+ ions.

For the integration of Eq 9, the assumption of a constant concentration gradient is reasonable, giving

$$i_s = \frac{4FD_s}{\delta}[(O_2)_o - (O_2)_b] \tag{13}$$

but integration of Eq 12 for the computation of $(H^+)_o$ gives an equation that contains the unknown current densities i_s and i_h. Substituting for i_s and i_h gives a third degree equation in $(H^+)_o$

$$A(H^+)_o^3 + B(H^+)_o^2 + C(H^+)_o - D = 0 \tag{14}$$

where

$$A = (H^+)_b k_s \Phi(k_h\Phi + G_H),$$
$$B = [(H^+)_b^2 k_s G_H - k_s K_W G_{OH} - (H^+)_b k_h G_s - 4(H^+)_b(O_2)_b k_s G_s]\Phi - (H^+)_b G_h G_s,$$
$$C = (H^+)_b k_s K_W G_{OH}\Phi + (H^+)_b^2 G_s G_H - K_W G_{OH} G_s, \text{ and}$$
$$D = (H^+)_b K_W G_{OH} G_s.$$

In these expressions the symbols G_s, G_H and G_{OH} represent the ratios D_s/δ, D_H/δ, and D_{OH}/δ, which are to be substituted with frequency-dependent terms in the formulae for the calculation of the impedance spectra. Φ represents the electrode potential dependent term

$$\Phi = \exp\left(-\frac{\alpha FE}{RT}\right)$$

which is the same for all electrode reactions, since in this example all symmetry factors α are taken as 0.5.

For the calculation of the polarization curves, for every value of E, the system formed by Eqs 4, 6, 8, 13, and 14 must be solved. If the metal concentration at the electrode interface is desired, once i_a is obtained, the equation

$$(M^{++})_o = (M^{++})_b + \frac{\delta i_a}{2FD_M} \tag{15}$$

is solved.

Figure 1 shows the calculated current-potential curves for a hypothetical metal immersed in an aerated, weakly acidic solution (pH = 1). The anodic rate constant is chosen as small, so that the corrosion rate is not limited by oxygen transport. On the cathodic side, the limiting current for oxygen reduction is clearly visible, followed at lower potentials by hydrogen evolution. At even lower potentials (below −800 mV) another limiting current begins to appear due to the rapid rise in pH of the solution in contact with the metal. Figure 2, which gives the concentrations of O_2 and H^+ at the metal surface, helps in clarifying the significance of the curves in Fig. 1: the first cathodic limiting current is associated with the fall in O_2 concentration, which affects Eq 4, while the second is caused by the fall in H^+ concentration, which affects Eqs 4 and 6.

Keeping all other parameters constant, but in a less acidic solution (pH = 4), the curves in Fig. 3 show a case where the pH change at the interface occurs before oxygen is depleted, generating a first current arrest. The interpretation of the E/I curves would be rather difficult without knowledge of the concentrations at the interface, shown in Fig. 4. Of course, these calculations span a very wide acidity range at the electrode surface, and one should be aware that in these conditions the kinetics of the reactions might be fundamentally different at different pH's, invalidating the starting hypotheses used for the computations.

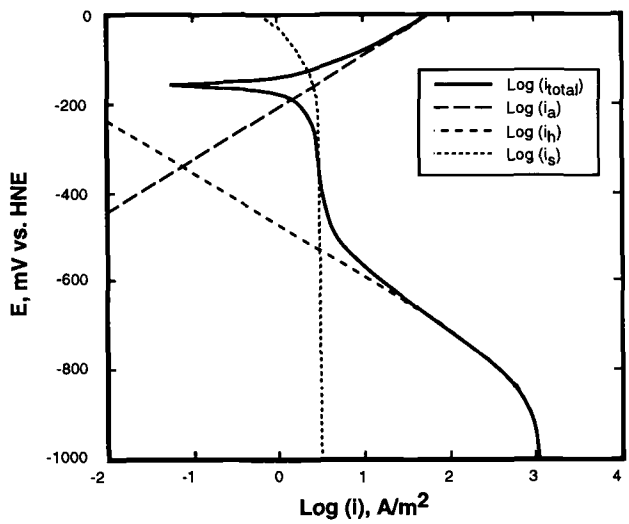

FIG. 1—*Current/Potential Curve. Solution concentrations:* $(O_2)_b = 2 \times 10^{-4}$ *mol/L, pH* = *1.* δ = *0.025 mm. Kinetic parameters:* $K_a = 3 \times 10^{-10}$, $K_s = 0.1$, $K_h = 10^{-11}$ *m/s.*

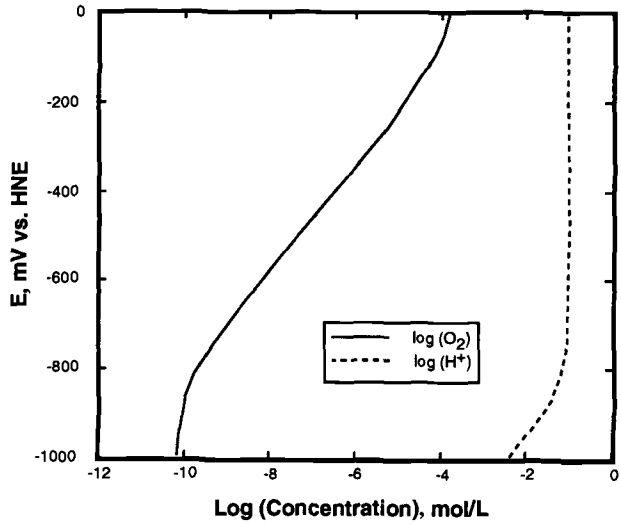

FIG. 2—*Concentrations at the electrode as a function of the electrode potential. Same conditions as in Fig. 1.*

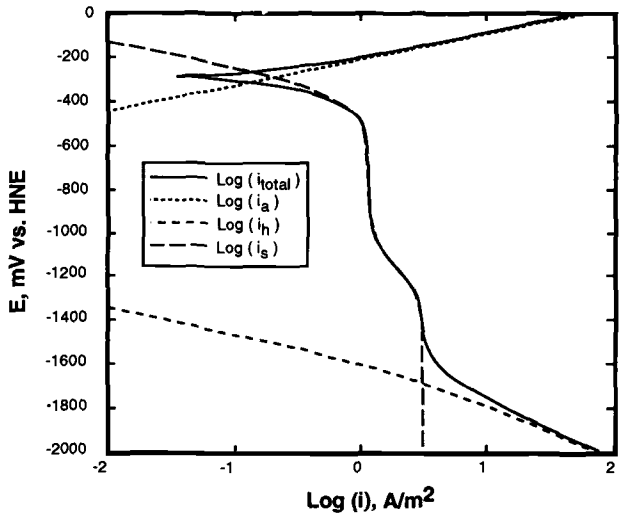

FIG. 3—*Current/Potential Curve. Same conditions as in Fig. 1, except pH = 4.*

In Fig. 5 the zero-frequency electrode resistance is shown, together with the resistances of the two cathodic reactions. Since the two reactions occur in parallel, the smaller of the two resistances determines the total resistance.

For a comparison with experimental data, Fig. 6 shows the results of slow potentiodynamic scans on a Ti electrode in an acidified (pH = 1) Na_2SO_4 solution, under moderate stirring and in an oxygen atmosphere, together with a model curve calculated keeping the concentrations and transport conditions close to the experimental values, and choosing as rate constants the values that give the best fit. Both oxygen reduction and

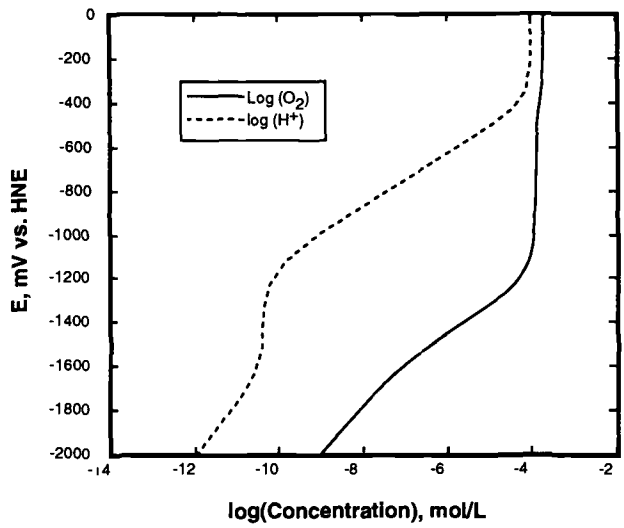

FIG. 4—*Concentrations at the electrode as a function of the electrode potential. Same conditions as in Fig. 3.*

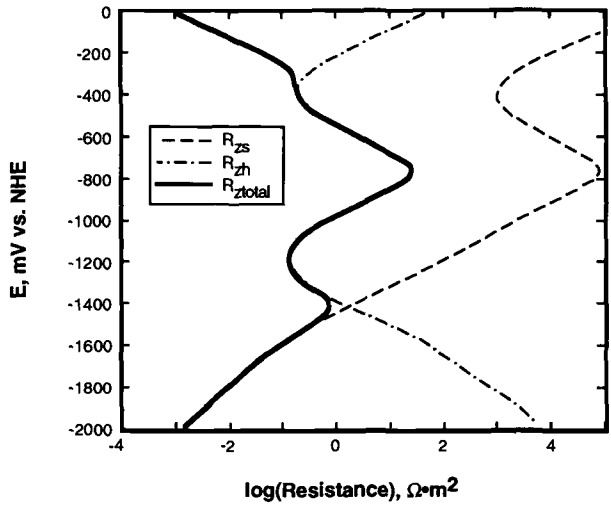

FIG. 5—*Zero-frequency resistances as a function of the electrode potential. Same conditions as in Fig. 3.*

hydrogen evolution can be seen, since no metal corrosion would occur in the potential range shown. The similarity is satisfactory; the interpretation that the slope increase at the lowest potentials is due to incipient alkalinization at the interface is supported by the calculations on the model system shown in Fig. 7. The ohmic drop error in the experimental data has already been subtracted.

Once the current-potential curves are calculated, at any potential the current densities for all reactions, as well as the concentrations of the reacting species at the electrode, are

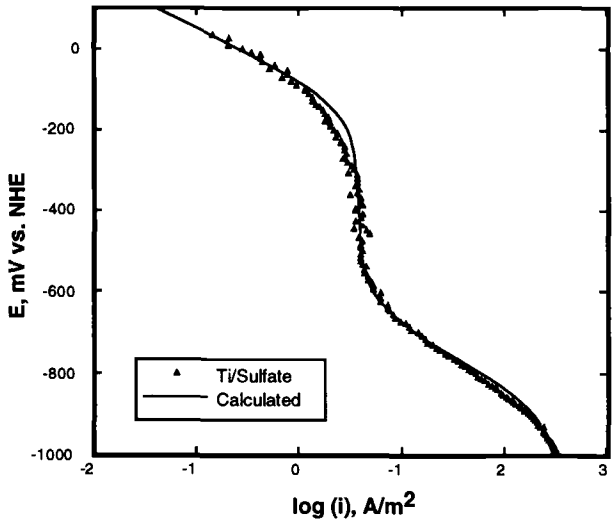

FIG. 6—*Comparison between current/potential curves measured on a Ti electrode in acidified Na_2SO_4, pH = 1, under O_2 atmosphere and calculated for pH = 1, $(O_2)_b = 9 \times 10^{-4}$ mol/L, $\delta = 0.09$ mm, $K_s = 0.08$, $K_h = 1.2 \times 10^{-12}$ m/s.*

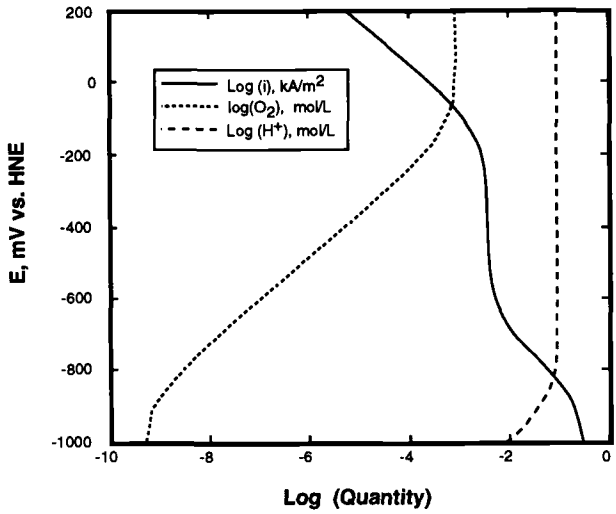

FIG. 7—*Cathodic current and concentrations at the electrode as a function of the electrode potential calculated with the parameters given in Fig. 6.*

known. For the calculation of the impedance spectra at any potential, therefore, one has to differentiate the expression for the total current, as well as Eqs 13 and 14, which link the perturbations of the oxygen and hydrogen ion concentrations to those of the currents and of the potential, under the effect of a small sinusoidal voltage signal.

Differentiating the partial currents (Eqs 8, 4, and 6), one obtains, respectively,

$$di_a = \frac{\alpha F i_a}{RT} dE \tag{16}$$

$$di_s = \frac{\alpha_s F i_s}{RT} dE + \frac{i_s}{(O_2)_o} d(O_2) + \frac{i_s}{(H^+)_o} d(H^+) \tag{17}$$

and

$$di_h = \frac{\alpha F i_h}{RT} dE + \frac{i_h}{(H^+)_o} d(H^+) \tag{18}$$

and from Eq 13

$$di_s = \frac{4FD_s}{\delta} d(O_2) \tag{19}$$

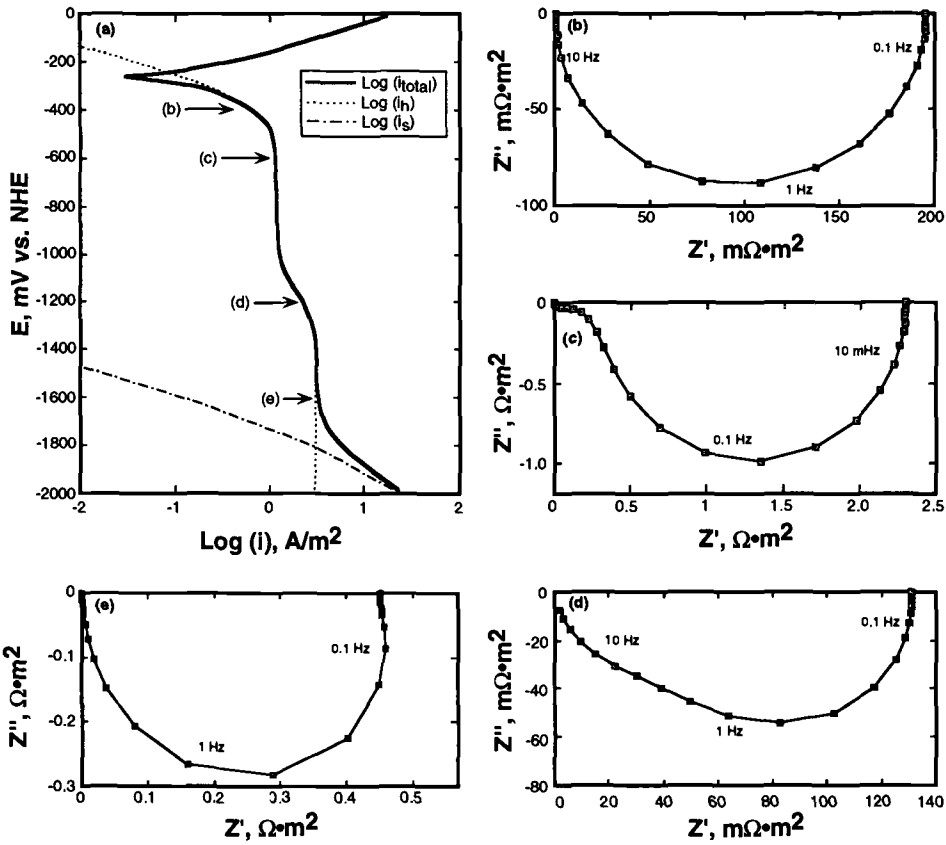

FIG. 8—*Nyquist impedance plots for system giving the current/potential curve shown. Conditions:* $(O_2)_b = 2.10^{-4}$ *mol/L, pH = 4,* $\delta = 0.025$ *mm. Kinetic parameters:* $K_a = 3 \times 10^{-10}$, $K_s = 0.1$, $K_h = 10^{-11}$ *m/s.* $R_{sol} = 0.5$ *m*$\Omega \cdot m^2$, $C_{dl} = 0.5$ *F/*m^2.

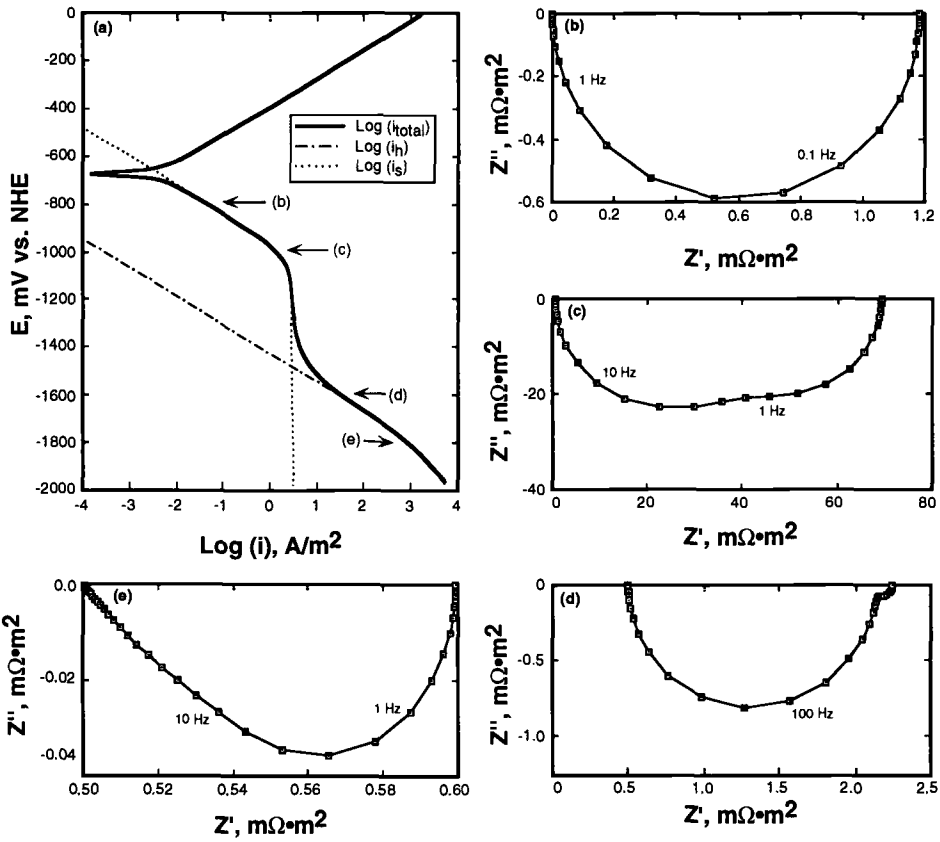

FIG. 9—*Nyquist impedance plots for system giving the current/potential curve shown. Conditions:* $(O_2)_b = 2.10^{-4}$ *mol/L, pH = 13,* $\delta = 0.025$ *mm. Kinetic parameters:* $K_a = 3 \times 10^{-10}$, $K_s = 0.1$, $K_h = 10^{-11}$ *m/s.* $R_{sol} = 0.5$ *mΩ·m²,* $C_{dl} = 0.5$ *F/m².*

while the expression for the $d(H^+)$, obtained from Eq 14, is

$$d(H^+) = \frac{F\alpha([2C_1\Phi + C_2]H^+)_o^2 + 3C_3(H^+)_o + C_5)(H^+)_o\Phi}{RT(2[C_3\Phi + C_4] + C_5\Phi + 3[C_1\Phi + C_2]H^+)_o\Phi + C_6)} dE \qquad (20)$$

In this expression the quantities C are frequency dependent because they contain the terms G_s, G_H, and G_{OH}, which, in order to obtain the impedance spectra, must be substituted with the appropriate expressions derived from Eq 1.

While the admittance for the anodic reaction Y_a is real and immediately derived from Eq 16, the admittances Y_s and Y_h are obtained from Eqs 17 and 18, eliminating $d(O_2)$ and $d(H^+)$ by introducing Eqs 19 and 20, and are complicated, frequency-dependent, and complex quantities.

Summing Y_a, Y_s, and Y_h gives the total electrode admittance, and, in order to simulate the experimental behavior of a galvanic cell, a capacitative branch depending on the double layer capacitance C_{dl} has to be included as well. A solution resistance R_{sol} can also be added in series to the electrode impedance.

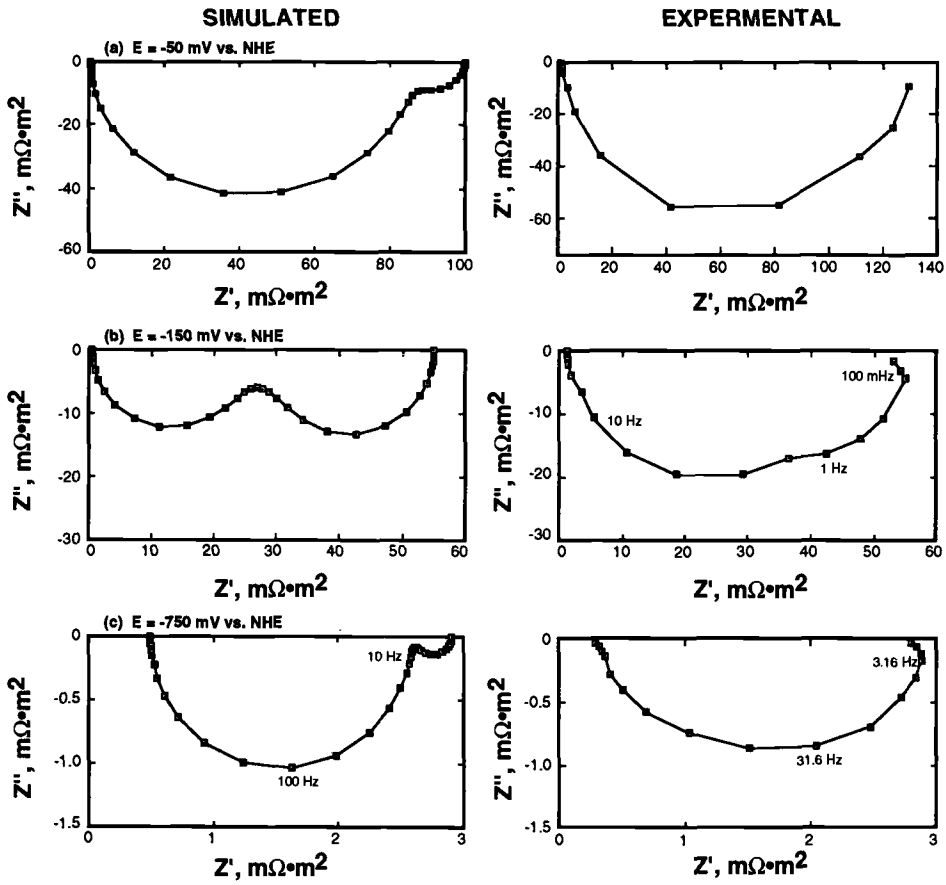

FIG. 10—*Comparison between Nyquist plots obtained on Ti electrode in acidified Na_2SO_4, and impedance spectra calculated with the same parameters as in Fig. 6.* R_{sol} = *0.5* $m\Omega \cdot m^2$, C_{dl} = *0.7* F/m^2.

As examples of the results, Figs. 8 and 9 show side by side the E/I curves and Nyquist plots obtained at various potentials for the case of a weakly acidic (pH = 4) and of an alkaline (pH = 13) solution. The rate constant for the anodic reaction has been chosen so that corrosion is under anodic control, and the impedance spectra shown emphasize the cathodic behavior of the system.

Employing the modeling example in acidic solution shown in Fig. 6, chosen so as to match the experimental polarization curve, the comparison can be extended to the impedance spectra taken on the same electrode at various potentials. Since the impedance in the potential range where the current is diffusion-limited (approximately from −200 to −600 mV versus NHE) is very difficult to measure at low frequencies because of the noise caused by fluctuations in stirring, the examples shown in Fig. 10 are taken where either oxygen is not transport-limited or hydrogen evolution is already occurring. There is a qualitative similarity between model and experimental curves: in particular, the separation between charge transfer and transport semicircles of Fig. 10*b* appears in both experimental and model plots.

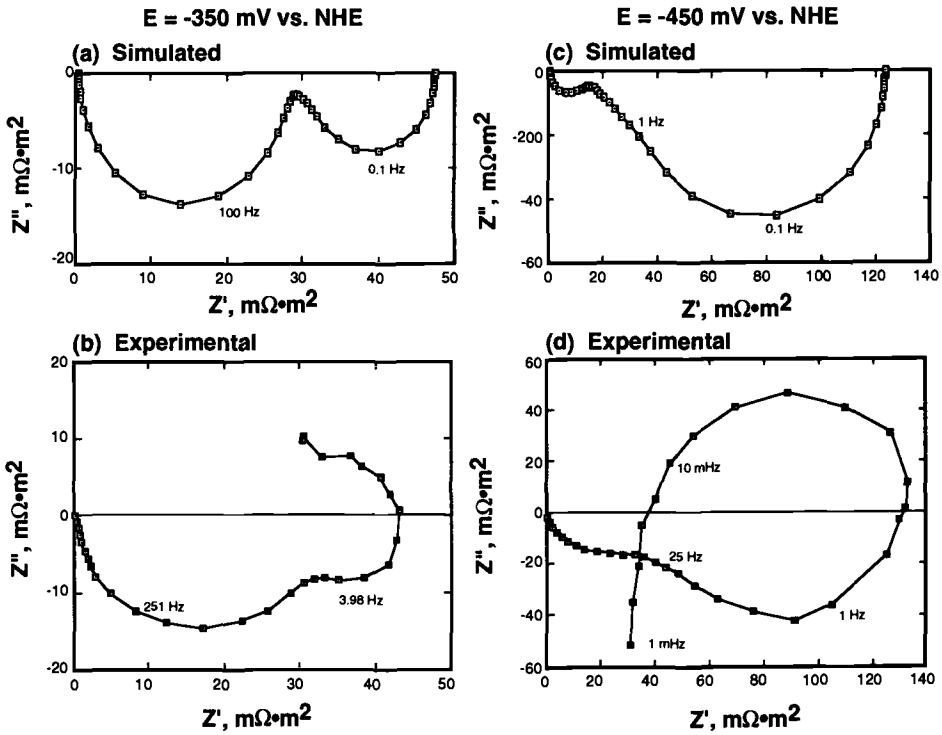

FIG. 11—*Comparison between Nyquist plots obtained on brass electrode in acidified Na_2SO_4, and impedance spectra calculated for pH = 1, $(O_2)_b = 7 \times 10^{-4}$ mol/L, $\delta = 0.06$ mm, $K_s = 0.03$, $K_h = 3 \times 10^{-12}$ m/s. $R_{sol} = 0.5$ mΩ·m², $C_{dl} = 0.04$ F/m².*

On the other hand, as seen in Fig. 11, the comparison between model spectra and experimental data taken on a brass rotating disk electrode in the same solution shows that, although there is fair matching in the higher frequency range, where charge transfer and diffusional transport predominate, there are large differences at low frequency, indicating that the reaction mechanism on the brass electrode is more complicated than that used for the modeling.

Conclusions

Impedance spectra generated from the same electrochemical models which give current-potential curves have the advantage of having a built-in physical meaning over models based on passive element circuits. Therefore, the effect of changing the numerical values of the quantities involved in the calculations, such as reactant concentrations, stirring, and electrochemical rate constants, can be easily examined and compared with the experimental results. Of particular value is the possibility, with this modeling method, of studying the effect of performing the impedance measurements at potentials other than the corrosion or equilibrium potential.

A few examples of comparison between model data and experimental curves have been presented; when the agreement is good in the polarization curves, but not in all frequency ranges in the impedance spectra, it is very likely that the electrochemical model employed

neglects some reaction paths, which may or may not be important for the evaluation of the corrosion properties of the material under study.

In the present paper, scant attention has been given to the anodic side of the corrosion reactions, which is only sketchily described. That such a simple model can still be useful is encouraging. However, the challenge ahead is to develop a more realistic model of the anodic processes, which can still be sufficiently general in application.

References

[1] Keddam, M., Mattos, O. R., and Takenouti, H., *Journal of the Electrochemical Society*, Vol. 128, 1981, p. 257.
[2] K. J. Vetter, *Elektrochemische Kinetik*, Springer, Berlin, 1961.
[3] Bertocci, U. and Ricker, R. E., in *Computer Modeling in Corrosion, ASTM STP 1154*, R. S. Munn, Ed., American Society of Testing and Materials, Philadelphia, 1992, pp. 143–161.
[4] Gerischer, H., *Zeitschrift für physikalische Chemie*, N. F. 1, 1954, p. 278.
[5] Schuhmann, D., *Comptes Réndus de l'Academie des Sciences, Paris*, Vol. 262C, 1966, p. 624. Sluyters-Rehbach, M. and Sluyters, J. H., *Electroanalytical Chemistry*, A. Bard, Ed., Vol. 4, M. Dekker, New York, 1970, p. 1.
[6] Hoare, J. P., *Encyclopedia of the Electrochemistry of the Elements*, A. Bard, Ed., Vol. 2, M. Dekker, New York, 1974, p. 192. Tarasevich, M. R., Sadkowski, A., and Yeager, E. *Comprehensive Treatise on Electrochemistry*, Vol. 7, Plenum Press, New York, 1983, p. 301.
[7] Fabjan, C., Kazemi, M. R., and Neckel, A., *Berichte der Bunsengesellschaft für Physikalische Chemie*, Vol. 84, 1980, p. 1026.
[8] Bertocci, U., Cohen, M. I., Mullen, J. L., and Negas, T., "Electrocatalysis on Non-Metallic Surfaces," NBS Special Publ. 455, 1976, p. 313.

DISCUSSION

H. Takenouti[1] *(written discussion)*—Fitting the polarization curve adequately is a rather easy task and can be done even on different reaction models for the same polarization curve. On the contrary, fitting the impedance data is quite difficult. Therefore, there is no evidence that one can calculate the electrode impedance from the polarization data alone.

U. Bertocci and R. E. Ricker (authors' closure)—We agree that complete modeling of impedance data requires, in general, more information than modeling polarization curves, and we have pointed this out in the paper. However, we believe that the approach to modeling that we have presented is nevertheless useful and informative, since it can show what the effect is of changing real physical parameters on the impedance spectra.

[1]UPR15 DU CNRS, Physique des Liquides et Electrochimie, 75252 Paris Cedex 05, France.

Serge Chechirlian,[1] *Michel Keddam,*[2] *and Hisasi Takenouti*[2]

Specific Aspects of Impedance Measurements in Low Conductivity Media

REFERENCE: Chechirlian, S., Keddam, M., and Takenouti, H., **"Specific Aspects of Impedance Measurements in Low Conductivity Media,"** *Electrochemical Impedance: Analysis and Interpretation, ASTM STP 1188,* J. R. Scully, D. C. Silverman, and M. W. Kendig, Eds., American Society for Testing and Materials, Philadelphia, 1993, pp. 23–36.

ABSTRACT: Impedance measurements in the high frequency range, namely $f > 1$ kHz, often exhibit one or several loops irrelevant to the electrode process. For low conductivity media, encountered in corrosion studies such as in natural waters or in organic solvents, these relaxations also appear at a lower frequency range. This may lead to a possible misinterpretation of data by mistaking them for faradaic relaxation phenomena. The influences of the solution resistivity, the position of the Luggin capillary tip, and the nature of reference electrode were extensively studied. The corrosion of austenitic stainless steel in acetic acid was used as a model system. The conductivity of acid was changed by varying the water content. The reference electrode was either Ag/AgCl or the tip of a platinum wire embedded in a glass capillary. The results allowed us to propose an equivalent electrical circuit. The circuit is described as a capacity divider bridge (due to the stray capacitances between reference/working and reference/counter electrodes) and by the electrolyte resistance inside the capillary tip. The numerical simulations fit the experimental data well.

KEYWORDS: electrode impedance, acetic acid, low conductivity media, electrolyte resistance, potential distribution, Luggin capillary, equivalent electrical circuit

Electrode impedance method is now largely used in corrosion studies. The field of application extends towards systems whose impedance measurements themselves are increasingly difficult. The corrosion in a fairly weak conductive medium is one of the typical examples. Unfortunately, the identification of different contributions in the measured impedance often becomes difficult when measured in an extremely low conductive medium. For instance, the high frequency limit of the electrode impedance may no longer allow one to determine the electrolyte resistance. The relaxation time constants linked with the electrolyte cell or with the regulating device were reported by many authors [*1–6*]. However, a study completely devoted to the particular aspect of extremely low-conductivity medium for impedance measurements and more generally for nonsteady state techniques is fairly rare [*6*].

The aim of this paper is to collect experimental data with different parameters intervening in the impedance measurements in a three-electrode cell. Particularly, the influence of the bulk solution resistivity, the internal resistance of reference electrode, and the distance of Luggin capillary tip from the electrode surface will be examined. Then, an electrical equivalent circuit which suitably accounts for the experimental data will be devised. Before discussing the impedance measurements themselves, the dc potential distribution inside the electrolyte cell that allows one to evaluate the electrolyte resistance will be determined and discussed.

[1]Research engineer, Centre de Recherche, Rhône Poulenc, 69151 Décines, France.
[2]Directeur de recherche, CNRS, Physique des Liquides et Électrochimie, Laboratorie de l'Université P&M Curie, 75252 Paris, Cedex 05, France.

Theory

To evaluate the electrolyte resistance associated with a disk electrode, Newman calculated the potential distribution of the ideal geometry cell, i.e., a hemispherical cell [7]. The disk working electrode is set at the center of the sphere. The counter electrode is located at the hemispherical wall at an infinite distance. If there is no overpotential at the disk electrode, then whole applied potential corresponds to the ohmic drop in the electrolyte. Therefore, the potential distribution inside the electrolyzing cell is completely determined by the solution resistivity (ρ) and the disk electrode radius (r_0). This situation is named the primary current or potential distribution.

The electrode potential is set at zero at the working electrode, Φ_0 at the counter electrode, then the local potential Φ can be expressed in the elliptical coordinate system (ξ, η) by

$$\frac{\Phi}{\Phi_0} = \left(\frac{2}{\pi}\right) \tan^{-1}(\xi) \tag{1}$$

The cylindrical coordinate system (x, r) is linked with the elliptical system through

$$x = r_0 \times \xi \times \eta \tag{2}$$

$$r = r_0 \sqrt{(1 + \xi^2)(1 - \eta^2)} \tag{3}$$

At the axis of the hemisphere, i.e., $r = 0$, one can derive from Eq 3, $\eta = 1$ then

$$\frac{\Phi}{\Phi_0} = \left(\frac{2}{\pi}\right) \tan^{-1}\left(\frac{x}{r_0}\right) \qquad \text{for } r = 0 \tag{4}$$

Similarly, at the electrode plane, i.e., $x = 0$ and outside the disk, one calculates from Eq 2 that $\eta = 0$. Then Eq 1 is expressed in the cylindrical coordinates by

$$\frac{\Phi}{\Phi_0} = \left(\frac{2}{\pi}\right) \tan^{-1}\left\{\sqrt{\left(\frac{r}{r_0}\right)^2 - 1}\right\} \qquad \text{for } x = 0 \tag{5}$$

From the potential gradient at the disk surface, Newman calculated the local current density then the overall disk current I_{tot}. The expression of the electrolyte resistance R_e is then obtained by

$$R_e = \frac{\Phi_0}{I_{tot}} = \frac{\rho}{4r_0} \tag{6}$$

If the Luggin capillary is used to determine the electrode potential, and the reference tip is located on the axis ($r = 0$), then the electrolyte resistance can be calculated by Φ instead of Φ_0 in Eq 6 (see also Eq 4).

Experimental

As previously indicated, the electrolyte resistance can be lowered by using a Luggin capillary. We are therefore particularly interested in the influence of the following experimental conditions for impedance measurements:

TABLE 1—*Chemical composition of working electrode material (%).*

C	Si	Mn	Ni	Cr	Mo	W	Cu	S	P
0.057	0.46	1.55	11.19	16.95	2.04	0.03	0.25	0.002	0.026

(1) The solution resistivity (ρ).
(2) The internal resistance of reference electrode including the series resistance of Luggin capillary.
(3) The distance of the reference tip from the disk surface.

Electrolytes

The solution resistivity was modified by adding water to a pure acetic acid (special order to the Société des Solvants): 20% acid for $\rho \approx 10$ kΩ·cm and 99.5% acid for $\rho \approx 5$ MΩ·cm. These solutions were used without any supporting electrolyte. The electrolytes were maintained at 25°C under Ar atmosphere.

Electrolyzing Cell

A 68-mm-diameter cylindrical glass cell contained approximately 260 ml of solution. The counter electrode was a platinum gauze covering the bottom and the side walls of the cell. The working electrode, made of an austenitic stainless steel (chemical composition of which is displayed in Table 1), was a disk of 5.6 mm in radius tightly flush mounted to a P.T.F.E. rotating disk holder (10 mm in radius). The surface area of the working electrode was thus 1 cm^2. This electrode was dipped in the solution by 40 mm. All runs were made in the 900 to 1000 r/min range.

Reference Electrodes

Three types of reference electrodes were used: (1) Ag/AgCl in anhydrous acetic acid in saturated LiCl equipped with a Luggin capillary. This capillary was filled with 0.1 M $LiClO_4$. The capillary tip was filled with asbestos fibers to reduce the solution leakage. (2) The cross section of Pt wire embedded in a glass capillary. The reference tip was sharpened into a pencil form to minimize the screening effect. Often the use of a Pt wire linked to the reference electrode through a capacitor is recommended. This allows one to reduce the reference electrode impedance and improve the impedance measurements in high frequencies. Our Pt electrode was not connected to the other reference electrode thus the dc potential was not stable enough to perform the impedance measurements below 1 Hz. (3) Saturated Hg/Hg_2SO_4 reference.

Regulating Device

A commercial potentiostat (Solartron EI 1186) was coupled with a transfer function analyzer (Solartron FRA 1250) for impedance measurements. The experimental setup was monitored by a personal computer (Apple IIe).

Results

To evaluate the potential distribution inside the electrolyzing cell, we derived a model experiment considering only the vertical section of the electrolyzing cell [*8*]. The part

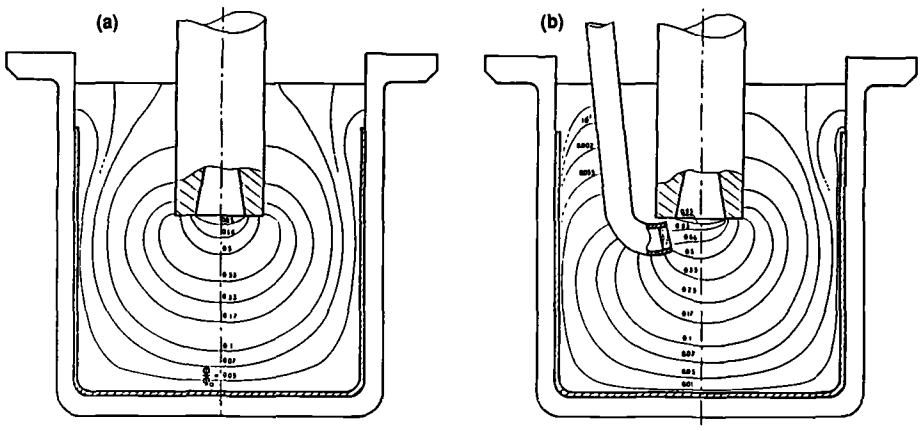

FIG. 1—*Two-dimensional potential distribution realized on a graphite paper* (a) *without and* (b) *with the electrode reference tip.*

corresponding to the electrolyte was materialized by a graphite paper. A conducting silver glue replaced the counter and the working electrodes. A 30 V dc voltage was applied between these two electrodes. Equipotential curves were then plotted by a metallic point and a digital voltmeter. Figure 1*a* illustrates the results with dimensionless potential scale. In this experiment, the working electrode was polarized at 1. From this figure we can see the equipotential curve depicts an ellipse near the working electrode. On the other hand, one half of the ohmic drop is located at $\frac{x}{r_0} < 0.7$.

Figure 1*b* illustrates the case where a reference electrode was introduced in the cell. From this figure one can see that the presence of this electrode does not deeply disturb the potential distribution. With this cell configuration about 30% of the ohmic drop was located between the reference tip and working electrode.

In Fig. 2, the results of this two-dimensional cell are compared with those deduced from Eq 4 and that experimentally determined in the real cell. These curves are similar in shape but a real quantitative difference can be noticed. As for the two-dimensional cell, the local current density should be quite different from the real three-dimensional cell. The divergence between the real cell and the calculated results may be attributable to cell geometry. This is why we carried out another experiment with a cell geometry closer to the ideal.

The working electrode was a 5-mm-diameter iron disk (Johnson-Matthey). The electrode face just touched the surface of 1 N H_2SO_4 electrolyte. The electrode was polarized at 30 mA, i.e., 0.15 A/cm^2 by the galvanostat to satisfy the conditions of the primary potential distribution. The dc potential at $x = 0$, was measured by means of a saturated Hg/Hg_2SO_4 reference electrode connected through a Luggin capillary. The results are illustrated in Fig. 3 with the reduced potential scale. The theoretical curve calculated using Eq 5 is indicated by a solid line whereas dots are the experimental data. On the disk surface, measured data showed values close to 0.1 instead of 0 as expected. This difference is most likely due to the fact that the capillary tip could not completely approach the disk surface, and also, when very close to it, some screening effect may have occurred. For the potential distribution outside the disk, experiments agree fairly well with the theory. Consequently, Newman's expression can be suitably used to evaluate the electrolyte resistance provided that the cell configuration is similar enough to the Newman ideal

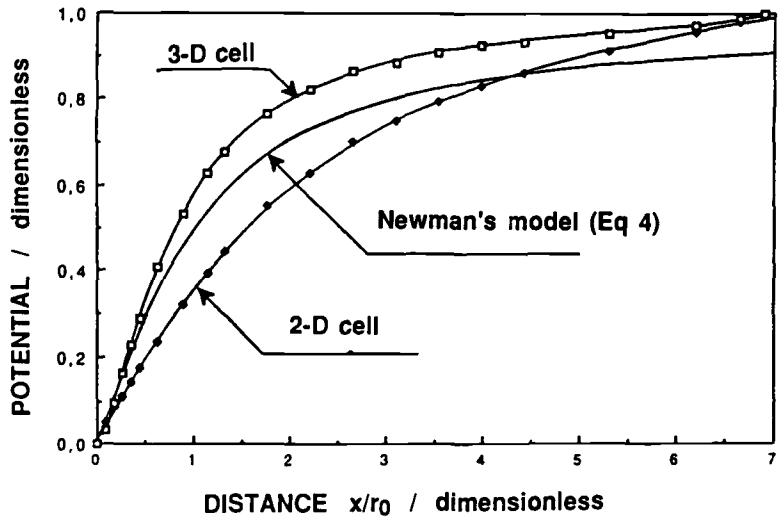

FIG. 2—*The comparison of the potential distributions with respect to the position of reference tip according to the electrode axis.*

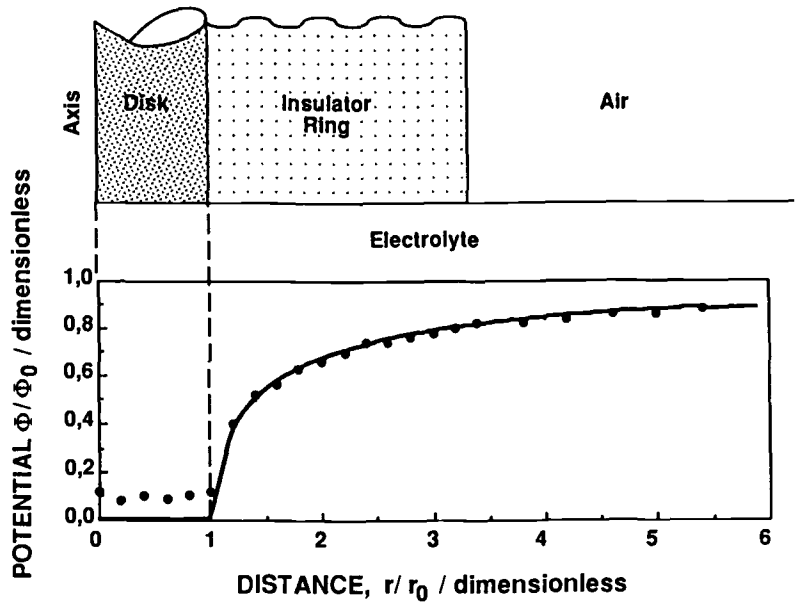

FIG. 3—*The potential distribution at x = 0. Iron disk (Johnson-Mattey, ∅ = 5 mm) in 1 N H_2SO_4. Disk rotation speed = 900 r/min.*

form. Now, we are able to identify the electrolyte resistance in the experimental impedance data.

Impedance diagrams from the working electrode rotated in the solution of 80% acetic acid (HAc) with the Pt reference electrode at various distances from the specimen are displayed in Fig. 4*a*. One may consider that these measurements correspond to the more favorable case, both the electrolyte resistivity and the impedance of reference electrode are relatively small. For the distance of the reference tip from the disk surface $x \geq 1.5$ mm the impedance diagram shows a capacitive loop for frequencies higher than 100 Hz and a capacitive branch for lower frequencies. This is a very common feature of impedance diagrams for slowly corroding metals when obtained in a moderately conductive medium, i.e., $10 < \rho < 1$ kΩ·cm with a reference electrode having a sintered glass liquid junction. The use of a Pt wire linked to the reference electrode through a capacitor often eliminates this high-frequency parasitic loop as previously stated.

Therefore, the low-frequency capacitive branch is relevant to the working electrode. Table 2 summarizes the resistance determined by the extrapolation of this branch towards the high-frequency limit for different values of x. The experimental values agree reasonably with the calculated value according to Eqs 4 and 6. We calculated also the capacitance equal to approximately 30 μF/cm² from the low-frequency branch. This value is also reasonable for the double layer capacitance of a stainless steel surface. From the high-frequency loop, one can determine a parallel capacitance equal to 3 nF.

When the reference tip is set close to the disk surface ($x \leq 1$ mm) one observes an inductive loop in an intermediate frequency range. The appearance of two relaxation time constants seems to be a general feature of the spurious electrode impedance.

Figure 4*b* shows the impedance diagram obtained with Ag/AgCl reference electrode having Luggin capillary tip. For frequencies lower than 100 Hz, the electrode behavior is similar to that determined with the Pt reference electrode. The resistance determined by

TABLE 2—*Electrolyte resistance and the position of reference tip for different solutions with different reference electrodes.*

Solution	Reference	x(mm)	ξ	R (kΩ)[a]	Re (kΩ)[b]
80% HAc ρ = 10 kΩcm	Platinum	0	0	0	0
		0.5	0.089	0.4	0.25
		1.5	0.268	1.00	0.75
		3.0	0.535	1.60	1.40
	Ag/AgCl	0	0	0	0
		1.0	0.179	0.57	0.50
		1.5	0.268	0.84	0.74
		2.5	0.357	1.30	1.19
		5.0	0.893	1.94	2.00
99.5% HAc ρ = 5 MΩcm	Platinum	0	0	0	0
		1.0	0.179	180	250
		2.0	0.357	750	480
		3.0	0.535	1160	690
	Ag/AgCl	0	0	0	0
		0.5	0.089	300	200
		1.0	0.179	450	250
		2.5	0.446	560	590

[a]Experimental value.
[b]Calculated by Eqs 4 and 6.

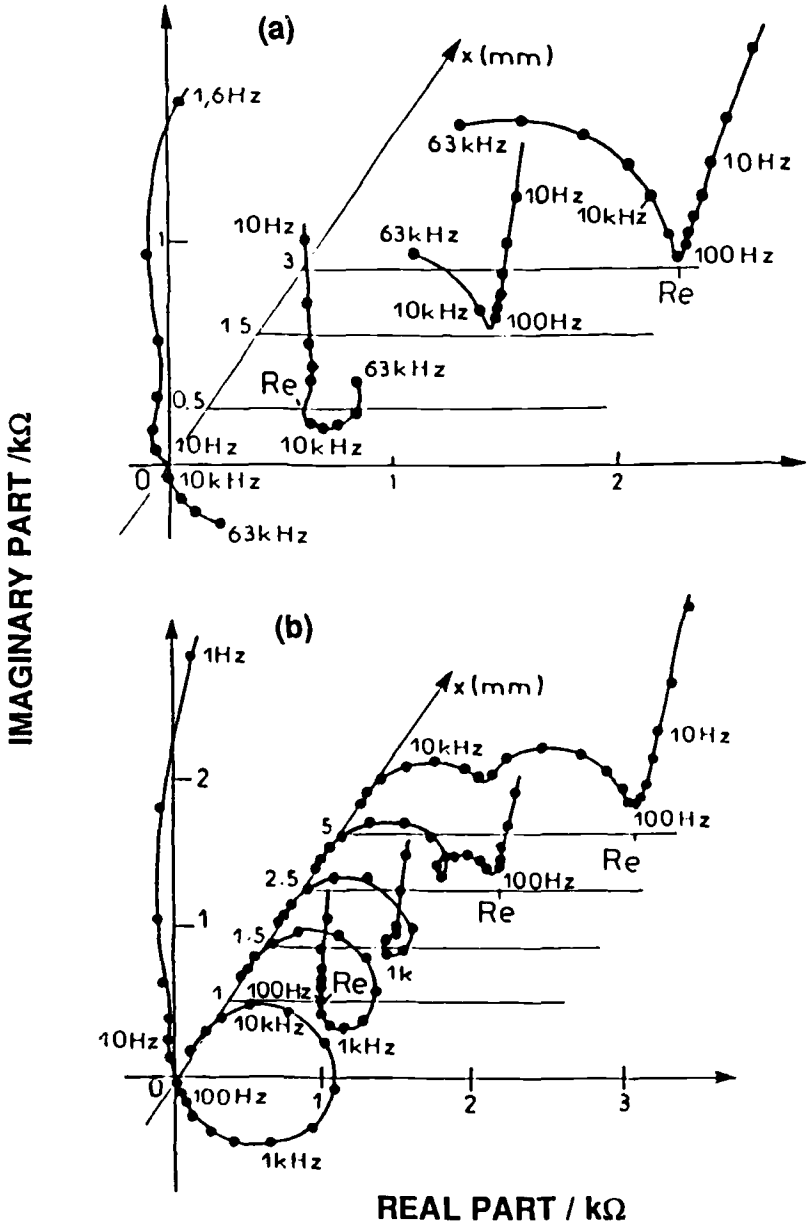

FIG. 4—*Experimental Impedance diagrams. Stainless steel disk electrode (∅ = 11,2 mm) in 80% HAc, 25°C, Disk rotation speed = 1000 r/min.* (a) *with Pt reference electrode* (b) *with Luggin capillary connected to Ag/AgCl reference.*

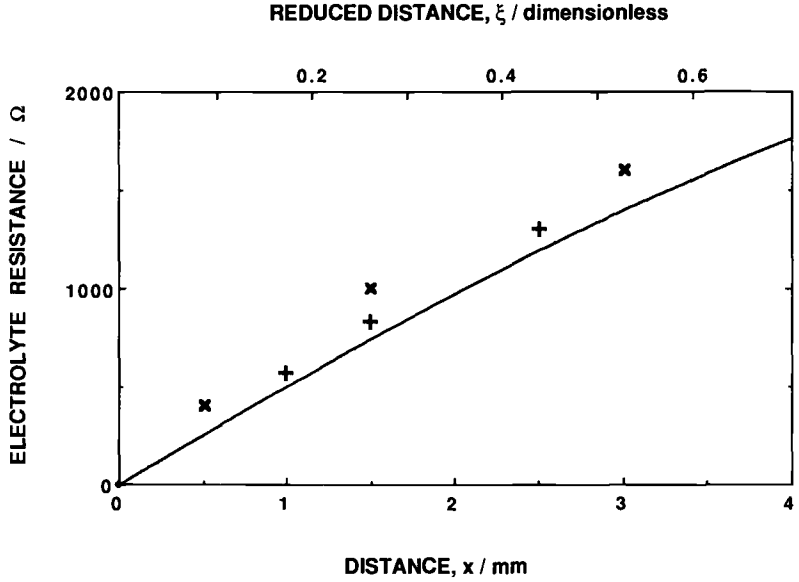

FIG. 5—*Comparison of experimental and calculated electrolyte resistance with respect to the reference tip position* X, *80% HAc,* ρ = *10 kΩ·cm,* (x) *Pt tip,* (+) *Ag/AgCl reference electrode.*

the extrapolation of low capacitive loop can be identified to the electrolyte resistance as can be verified in Table 2. Figure 5 showed a comparison between the experimental electrolyte resistance and the calculated one for two reference electrode system. Experimental electrolyte resistance is slightly higher than theoretical value. This discrepancy may be explained by the fact that the capillary tip positions could not be determined with enough accuracy. The capacitance determined on this branch also remains about 30 μF/cm^2 in agreement with the Pt reference electrode results. However, two capacitive loops can be clearly seen for $x \geq 2.5$ mm. The medium-frequency loop transforms into an inductive loop when the capillary tip approaches to the disk surface. The characteristic frequency of this intermediate frequency loop remains the same and equal to approximately 1 kHz. The high-frequency capacitive loop is less sensitive to the position of capillary tip. The impedance can be represented by a resistor of 1.1 kΩ in parallel with a capacitor of 16 nF whatever the value of x.

A similar feature can be observed for the solution having a higher resistivity (Fig. 6). Impedance diagrams obtained with Pt reference electrode (Fig. 6*a*) are very similar to those of Fig. 4*b* though the solution resistivity is 500 times greater. In this solution, even at the frequency as low as 1 Hz, the impedance relevant to the working electrode cannot be observed. All impedance diagrams illustrated in Fig. 6 are essentially experimental artifacts. The extrapolation of these diagrams towards low-frequency limit is nevertheless identified as the electrolyte resistance as can be concluded from the results displayed in Table 2. Figure 7 illustrates the comparison between experimental and theoretical value of the electrolyte resistance. Though the discrepancy between these two data are significantly great compared with the results displayed in Fig. 5, it can be attributed to a rather poor reproducibility of the solution resistivity for a very anhydrous solution.

As a conclusion of this experimental section, we can assert that one can identify the

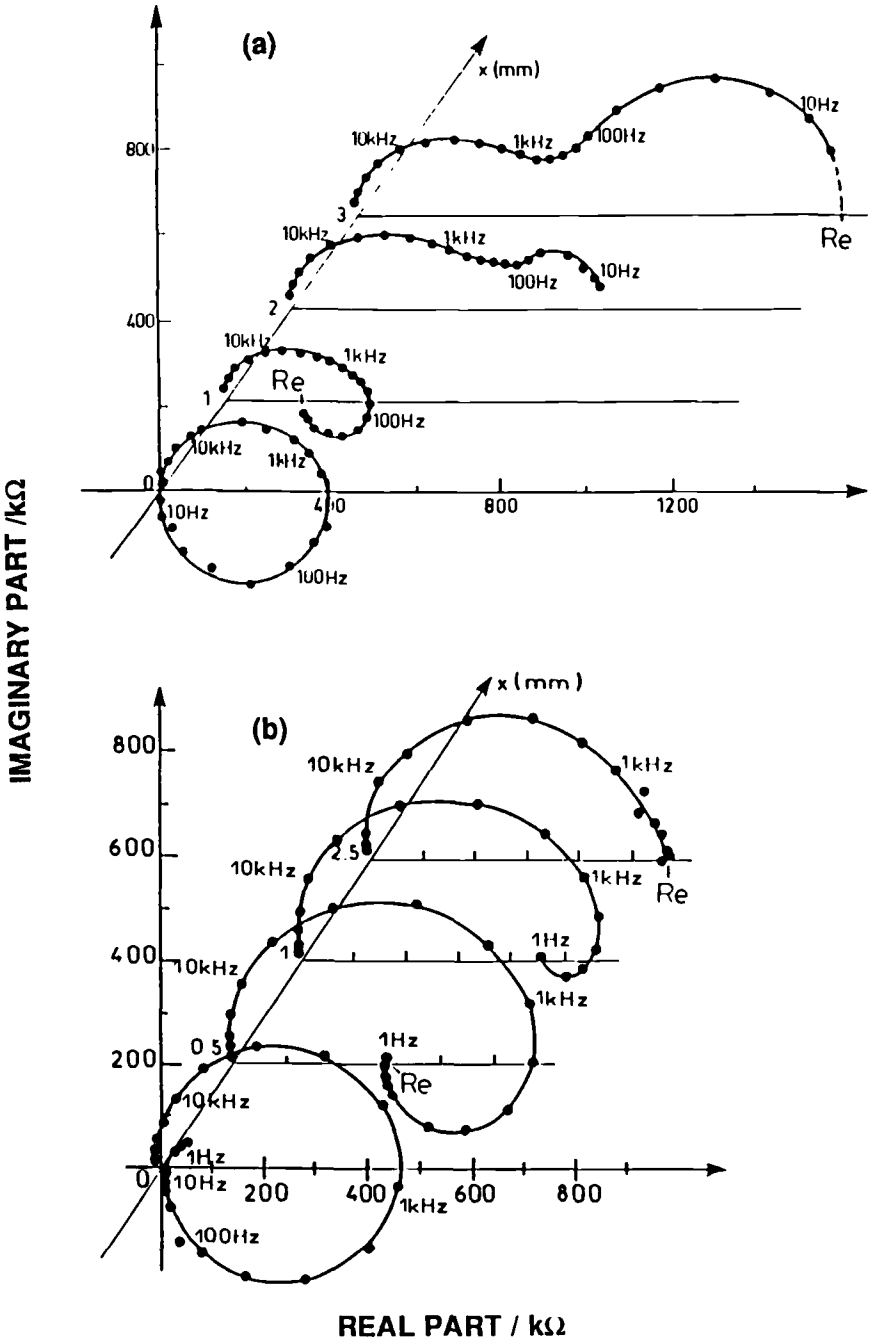

FIG. 6—*Experimental impedance diagrams. Stainless steel disk electrode (∅ = 11,2 mm) in 99.5% HAc, 25°C,* (a) *with Pt reference electrode* (b) *with Luggin capillary connected to Ag/AgCl reference.*

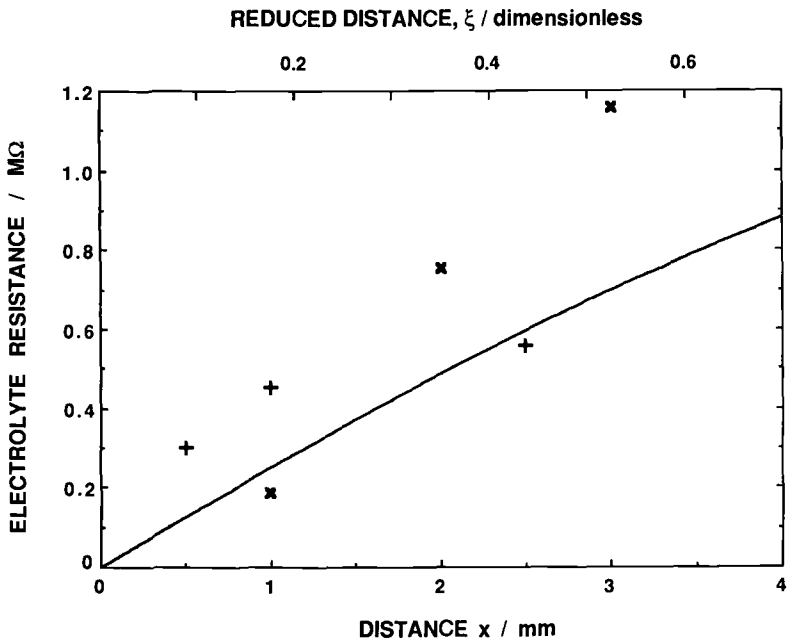

FIG. 7—*Comparison of experimental and calculated electrolyte resistance with respect to the reference tip position* x, *99.5% HAc,* ρ = *5 MΩ·cm.* (X) *Pt tip,* (+) *Ag/AgCl reference electrode.*

electrolyte resistance from the measured impedance as demonstrated by comparing the measured value to that calculated using Eqs 4 and 6. Concerning the high-frequency capacitive loop, both its diameter and the characteristic frequency are dependent upon the solution resistivity. However, both the characteristic frequency and the diameter of this loop are essentially independent of the position of reference tip for a given solution. In the intermediate frequency range, the impedance can be seen as capacitive or as inductive. The transformation of one behavior to the other depends on the solution resistivity.

Modeling

Based on the aforementioned conclusion, an equivalent electrical circuit describing the results is devised (Fig. 8). The electrical network is somewhat more complicated than that proposed by Cahan et al. [*2*]. The physical origins attributed for each element are described in the figure caption and some justifications are given in the following paragraphs. In Fig. 8 no inductance is used although such a characteristic was observed experimentally. This is explained by the transfer function due to a capacitive divider C_1–C_2 and the overall current [*3*]. The measured impedance Z_{mes} can be expressed by

$$Z_{mes} = \frac{V_C}{I} \tag{7}$$

where V_C is the potential at the point C (Fig. 8). This potential was derived by using the Kirchhoff's theory for three points: A, B, and C marked on the figure. The results of

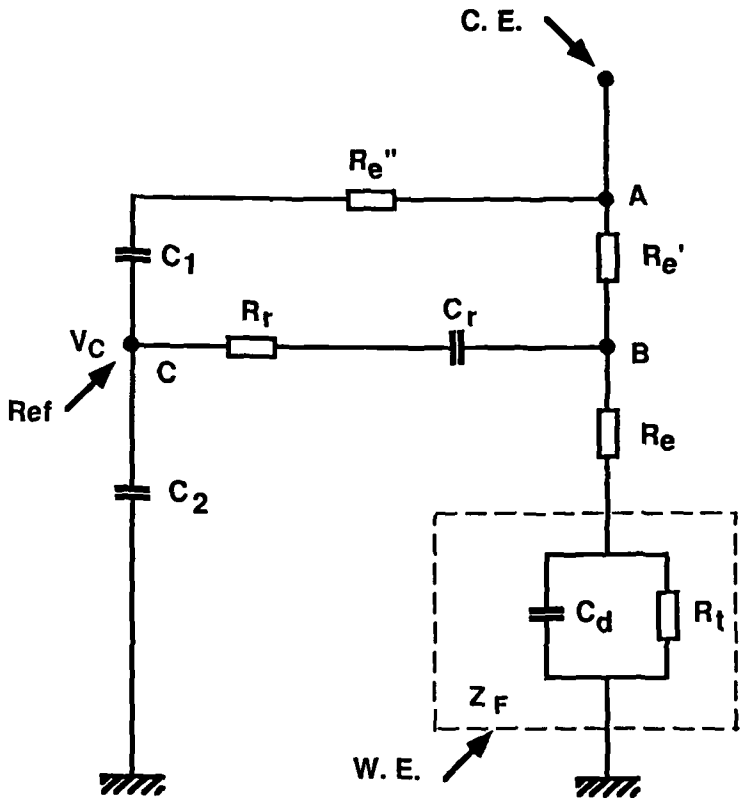

FIG. 8—*Electrical equivalent circuit.* $C_d - R_t$*: Impedance of working electrode.* R_e*: Electrolyte resistance between working electrode and reference tip.* R'_e*: Electrolyte resistance between counter electrode and reference tip.* $R_e + R'_e$ *is equal to that calculated by Eq 8.* $C_l - R''_e$*: Coupling between reference and counter electrodes.* $C_r - R_r$*: Impedance of reference electrode including Luggin capillary.* C_1*: Stray capacitance between reference and working electrodes.* C_2*: Input capacitance of regulating device.*

simulation calculations are shown in Figs. 9 and 10, respectively, for 80% and 99.5% acetic acid and for Pt and Ag/AgCl reference electrodes. The position of the reference tip x is simulated by varying the value of R_e whereas R_{tot} ($= R_e + R'_e$) remains constant. For R_e, the experimental value was used instead of calculated one and displayed in Table 2 because the accuracy of the distance x and of the solution resistivity for an anhydrous acid were poor.

Using the value in Table 3, R_{tot} was calculated by Eq 8 and then corrected for the wall position with $x = 6.07$ i.e., $\Phi/\Phi_0 = 0.90$. R_r is identified as the electrolyte resistance between working electrode and Pt tip or that of Luggin capillary tip. Equation 6 applied to the Pt tip is indeed close to 0.2 MΩ for 80% acid. Similarly, for 99.5% acid, the electrolyte resistance associated with the Luggin capillary tip was close to 100 MΩ. This resistance is high enough compared with the resistance inside the capillary tip for Ag/AgCl reference electrode. This resistance is actually evaluated to be 1.8 MΩ with the capillary geometry (80 mm in length and 2 mm in inner diameter) and the resistivity of the filling solution (7 kΩ·cm). If the dielectric capacitance of the glass wall used for Pt electrode or Luggin

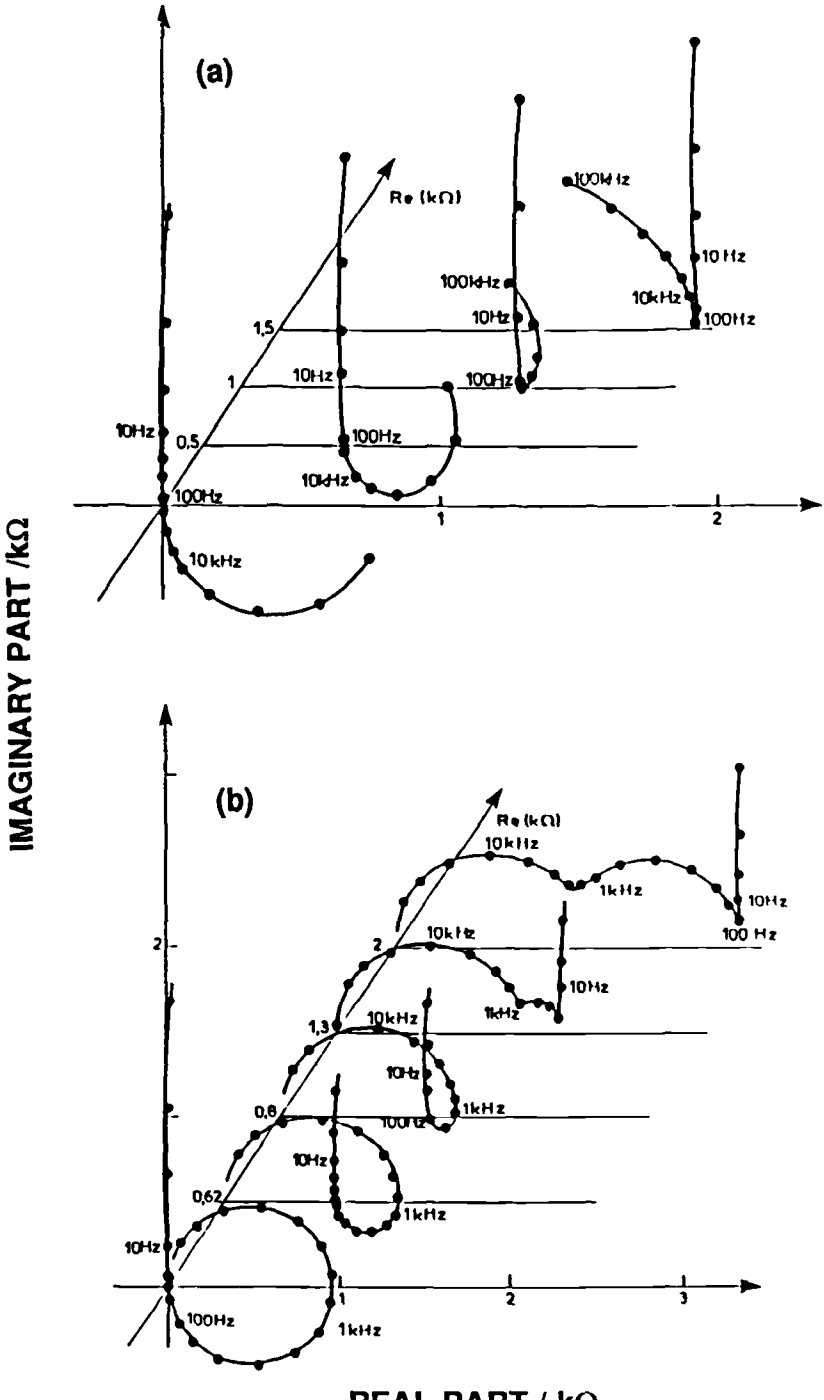

FIG. 9—*Calculated impedance diagrams for 80% acetic acid. Numerical values for the equivalent circuit (Fig. 8) are given in Table 3.* (a) *Pt tip electrode* (b) *Ag/AgCl/Luggin capillary.*

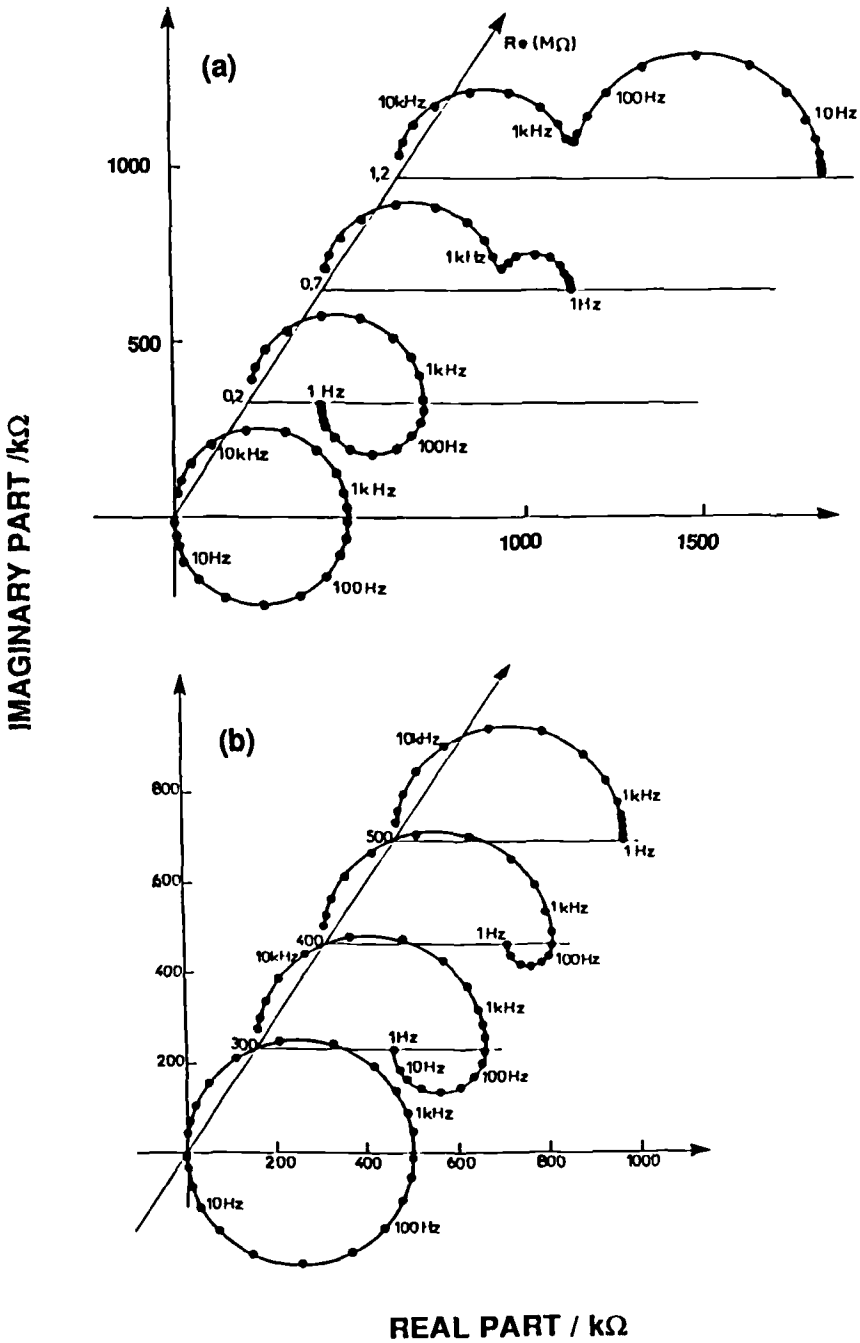

FIG. 10—*Calculated impedance diagrams for 99.5% acetic acid. Numerical values for the equivalent circuit (Fig. 8) are given in Table 3.* (a) *Pt tip electrode* (b) *Ag/AgCl/Luggin capillary.*

TABLE 3—*Numerical values used in simulation calculations.*

Solution	Ref Elec.	R_{tot}	R''_e/Ω	R_f/Ω	R_f/Ω	C_d/F	C_1/F	C_2/F	C_f/F
80% HAc	Pt	4 kΩ	0.2 M	0.2 M	0.1 M	30 μ	10 p	30 p	0.1 μ
	Ag/AgCl	4 kΩ	2 M	2 M	0.1 M	30 μ	10 p	30 p	—
99.5%	Pt	2 MΩ	2 M	0.1 G	0.1 M	30 μ	10 p	30 p	0.1 μ
HAc	Ag/AgCl	2 MΩ	2 M	0.1 G	0.1 M	30 μ	10 p	30 p	—

capillary is taken into account, then one evaluates a capacitance of about a few tens pF. This value is in good agreement with C_1. R''_e may be considered as the resistance coupling the capillary wall and the counter electrode, though there is no clear relationship with the solution resistivity. C_2 is a reasonable value for the parasitic capacitance of potentiostat circuit. C_f for platinum electrode is also in an excellent agreement with the double layer capacitance of the exposed Pt surface. For Ag/AgCl reference electrode, the contribution of the capacitance was neglected. All parameters used in the simulation calculations ascertain therefore the reliability of the equivalent circuit proposed in this paper.

Conclusion

The use of impedance measurements particularly for corrosion studies in extremely resistive medium is increasing. We verified first that the potential distribution inside the electrochemical cell can be adequately expressed by the model proposed by Newman. Therefore, we are able to calculate the value of the high electrolyte resistance in the real system. Consequently, from measured impedance it is possible to identify and isolate the electrolyte resistance. At higher frequencies, two spurious time constants are observed experimentally. The proposed equivalent electrical circuit accounted for the experimental artifacts and the physical reality of each element of the circuit was identified.

References

[1] Bewick, A., Fleischmann, M., and Liler, M., *Electrochimica Acta,* Vol. 1, 1959, p. 83.
[2] Cahan, B. D., Nagy, Z., and Genshaw, A., *Journal of the Electrochemical Society,* Vol. 119, 1972, p. 64.
[3] Gohr, H., Mimik, M., and Schiller, C. A., *Journal of Electroanalytical Chemistry,* Vol. 18, 1984, p. 273.
[4] Savova-Stoynov, B. and Stoynov, Z. B., *Journal of Applied Electrochemistry,* Vol. 17, 1987, p. 1150.
[5] De Souza, J. P., Mattos, O. R., Sathler, L., and Takenouti, H., *Corrosion Science,* Vol. 27, 1987, p. 1351.
[6] Chechirlian, S., Eichner, P., Keddam, M., Takenouti, H., and Mazille, H., *Electrochimica Acta,* Vol. 35, 1990, p. 1553.
[7] Newman, J., *Journal of the Electrochemical Society,* Vol. 113, 1966, p. 501.
[8] Chechirlian, S., "Contribution to the Electrochemical Study of Corrosion in Low Conductive Media: Application to the Study of Austenic Stainless Steel in Concentrated Acetic Acid Solutions," Ph.D. Thesis (89 ISAL 0014), Institut National des Sciences Appliquées de Lyon, March 1989.

Florian Mansfeld,[1] *Hong Shih,*[1] *Harold Greene,*[1] *and C. H. (Raymond) Tsai*[1]

Analysis of EIS Data for Common Corrosion Processes

REFERENCE: Mansfeld, F., Shih, H., Greene, H., and Tsai, C. H., "**Analysis of EIS Data for Common Corrosion Processes,**" *Electrochemical Impedance: Analysis and Interpretation, ASTM STP 1188,* J. R. Scully, D. C. Silverman, and M. W. Kendig, Eds., American Society for Testing and Materials, Philadelphia, 1993, pp. 37–53.

ABSTRACT: The software program ANALEIS with its modules, BASICS, COATFIT, PITFIT, and ANODAL can be used for the simulation and analysis of EIS data for simple corrosion systems. The advantage of ANALEIS is the optimization of the data analysis for each particular corrosion system based on the characteristics of its equivalent circuit. BASICS is used for systems that are under charge transfer or mass transport control or show an inductive loop. COATFIT addresses the case of the impedance behavior of polymer-coated metals. PITFIT can be used to analyze impedance data obtained for localized corrosion of aluminum alloys. Data for anodized and sealed aluminum alloys can be analyzed with ANODAL. Examples are given for the simulation and analysis of impedance data for these corrosion systems.

KEYWORDS: electrochemical impedance spectroscopy (EIS), charge transfer control, mass transport control, polymer coatings, pitting, anodized aluminum, software, simulation, analysis

While there is no doubt that EIS has become a very powerful tool for the analysis of corrosion processes, it has also become evident that corrosion scientists and engineers sometimes find the experimental data quite confusing. Often it is stated that despite the fact that EIS has produced interesting results, its use has not been pursued further because of the "complexity of the data analysis." These observations point to the need of software which can be applied to the analysis of EIS data. In most cases, such software consists of a general program which can be used for a large number of equivalent circuits (EC). This approach provides the user with the possibility to perform simulation and analysis for a large number of ECs, but it has the disadvantage that for such a large variety of ECs the analysis procedure cannot be optimized. In most cases an initial input of the fit parameters is necessary and the analysis is only possible if the initial guesses are close to the actual values.

The approach taken by the authors for the analysis of experimental EIS data is quite different. Based on the experience obtained in experimental applications of EIS and the results reported in the literature [*1*], it is clear that there are several corrosion processes for which the use of EIS has been proven successful by a number of researchers. While in general the transfer function for a given system should be derived from the kinetics of the

[1]Professor, research assistant professor, and graduate students, respectively, Department of Materials Science and Engineering, Corrosion and Environmental Effects Laboratory, University of Southern California, Los Angeles, CA 90089-0241.

partial reactions involved in the corrosion process [*1,2*], it has become apparent that for simple systems such as polymer-coated metals, anodized aluminum, and corrosion inhibitors ECs can be developed based on the physical and chemical properties of the system under study [*1*]. As discussed in a recent review [*1*], most investigators agree on the model for the impedance for these cases as expressed by the appropriate EC. Different analysis modules have been developed for each of these cases with the goal of providing an optimized analysis routine without the need of initial input parameters. These modules are part of the software package ANALEIS which is a software library for the simulation and analysis of EIS data. BASICS is part of ANALEIS and addresses the simplest cases of corrosion systems. Other modules are devoted to the analysis of EIS data for polymer-coated metals (COATFIT), anodized aluminum (ANODAL), and localized corrosion of aluminum alloys (PITFIT).

This paper will discuss the models used for the simulation and analysis of EIS data, give examples for the analysis procedure used in each module, and present fit results for a typical case of each corrosion system. A general description of the approach used in ANALEIS for the analysis of impedance spectra is given in the Appendix.

Simulation and Analysis of EIS Data

Charge Transfer Control

Simple corrosion systems, which are entirely under charge transfer control, and the cases of uniform corrosion on homogeneous surfaces can be described by the simple EC in Fig. 1. This EC allows the establishment of correlations between electrochemical system parameters and characteristic impedance elements [*3*]. In Fig. 1, C_{dl} is the capacitance of the electrode surface and R_p is the polarization resistance which is inversely proportional to the corrosion current density (cd) i_{corr}. All ohmic resistances in the system under study such as the electrolyte resistance, cable resistances, etc. are contained in R_s.

The impedance modulus $Z(j\omega)$ for the EC in Fig. 1 can be expressed as a function of frequency $f = \omega/2\pi$ as

$$Z(j\omega) = R_s + R_p/(1 + j\omega C_{dl}R_p) \tag{1}$$

The values of R_s and R_p can be determined from the high (Eq 2) and low (Eq 3) frequency limits of the measured impedance spectra, respectively

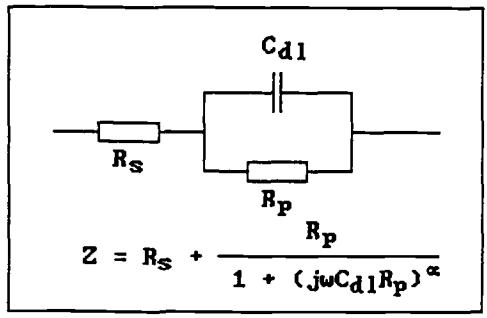

FIG. 1—*Equivalent circuit (EC) for a simple corrosion system under charge transfer control.*

$$R_s = \lim_{f \to \infty} |Z| \tag{2}$$

and

$$R_s + R_p = \lim_{f \to 0} |Z| \tag{3}$$

Various approaches to determine the experimental value of C_{dl} will be described in the following subsection.

Corrosion systems which are in agreement with the simple EC in Fig. 1 can be analyzed with BASICS. Since the general approach taken in BASICS has been discussed in detail elsewhere [4], only a short description will be given in the following.

Complex Plane Plots and Analysis by Cirfit—A number of different methods are presently used for displaying the experimentally determined complex impedance $Z(j\omega) = Z' + jZ''$ [1]. In a complex plane plot of $-Z''$ versus Z', a semicircle is obtained with a radius of $R_p/2$. The values of R_s and R_p can be determined from the intercept of the semicircle on the real axis according to Eqs 2 and 3. The capacitance C_{dl} can be obtained from the frequency f_{max} of the maximum of the imaginary impedance Z'' and R_p

$$C_{dl} = (2\pi f_{max} R_p)^{-1} \tag{4}$$

In most reported cases impedance data obtained at the corrosion potential E_{corr} have the shape of depressed semicircles with the center of the circle below the real axis. Mansfeld and Kendig et al. [5–8] have accounted for such deviations from the ideal behavior (Eq 1) by introducing an exponent α which leads to

$$Z(j\omega) = R_s + R_p/(1 + (j\omega C_{dl} R_p)^{\alpha}) \tag{5}$$

with $0 < \alpha \leq 1$.

It is important to recognize that the use of the exponent α in Eq 5 is only a formal description of the experimental data and that the physical meaning of α is not clear.

The determination of the experimental values of R_s, R_p, and C_{dl} is greatly facilitated by the application of numerical fitting procedures such as the computer program CIRFIT which was first developed by Kendig et al. [9] for the evaluation of complex plane plots. Cirfit is an improved version of CIRFIT. The advantages of Cirfit become apparent when a complete semicircle cannot be determined in the measured frequency range, the experimental data show scatter, or when deviations from the ideal behavior occur.

Bode-plots and Bodefit—One disadvantage of the display of experimental data in complex plane plots is the fact that the dependence of the impedance on the frequency of the applied signal is not directly shown [10]. Therefore, Bode-plots are recommended for the display of EIS data. In Bode-plots, $\log |Z|$ and the phase angle are plotted versus $\log f$. One advantage of such Bode-plots is the possibility to detect the regions that are dominated by resistive elements such as R_s and R_p in which a slope of zero is observed and regions dominated by capacitive elements for which a slope of -1 is observed in the ideal case.

The elements of the EC in Fig. 1 can be determined from the high- and low-frequency regions of Bode-plots according to Eqs 2 and 3. The capacitance can be calculated from the impedance at $f = 1/2\pi$, since at this frequency $\log |Z| = -\log C_{dl}$ for $\alpha = 1$. The analysis of Bode-plots is facilitated and made more accurate by the use of the program

Bodefit. One of the advantages of Bodefit is the possibility to determine R_p even if a clear dc limit does not occur in the measured frequency range which allows calculation of R_p according to Eq 3.

The Integration Method and Intfit—For systems with high values of R_p it is often not possible to collect sufficient data points in the frequency range that can be used in realistic times for carrying out the experiment. Many corrosion systems are not stable due to changes in the corrosion kinetics with time that can cause changes in the numerical values of the elements of the EC in Fig. 1 during the time which is needed to carry out the measurement in the mHz region. Kendig and Mansfeld [*11*] have therefore proposed the integration method which has the advantage that only the data in the frequency region above f_{max} (Eq 4) need to be recorded. As in all applications of analysis routines, the user has to make sure that the data to be analyzed agree with the model on which the analysis is based such as the simple model shown in Fig. 1 or its modification in Eq 5. The integration method is based on one of the elements in the Kramers-Kronig relationships [*12,13*] which assumes a symmetric dependence of Z'' with respect to f_{max}. According to Eq 6, R_p can be determined from a plot of $-Z''$ versus log f

$$R_p = (9.2/\pi) \int_{\infty}^{f\max} Z''(f)\, d \log f \tag{6}$$

The capacitance C_{dl} and the value of α can also be obtained with the integration method according to

$$C_{dl} = (2\pi f_{max} R_p)^{-1} \tag{7}$$

$$\alpha = (4/\pi) \arctan (2\, Z''_{max}/R_p) \tag{8}$$

where Z''_{max} is the imaginary part of the impedance at f_{max}.

One of the main advantages of the integration method is the independence of the $-Z''$ versus log f plot of value of R_s [*14*]. Therefore, the integration method becomes most valuable for those systems for which R_s approaches or even exceeds R_p. In these cases the

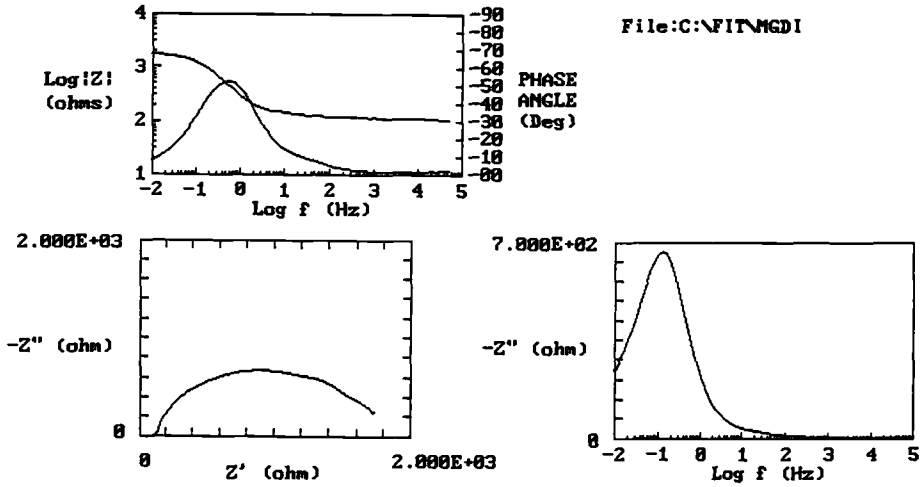

FIG. 2—*Impedance plots for MgAZ31 exposed to distilled water.*

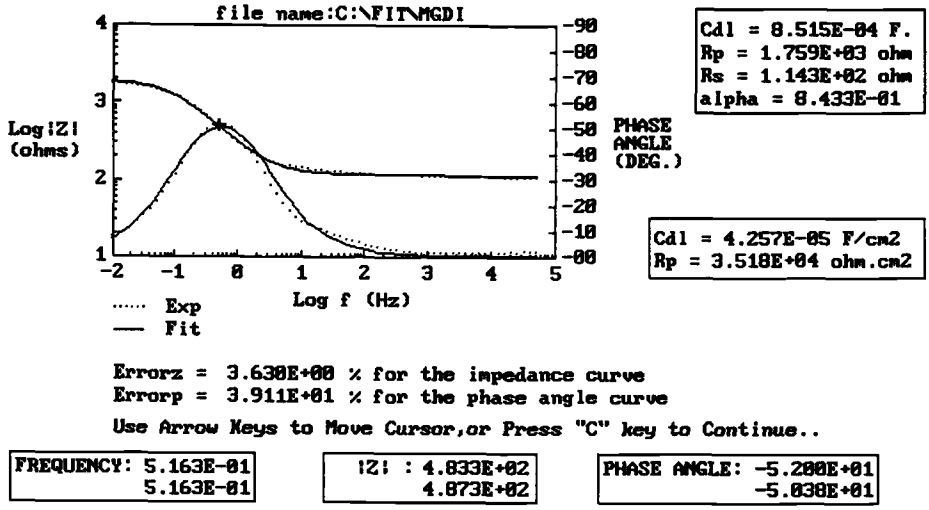

FIG. 3—*Results of the analysis of the data in Fig. 2 with Bodefit.*

use of Bode-plots for the analysis of the EIS data would not be very useful since the spectra would be dominated by R_s.

Figures 2 through 5 serve as examples for the application of BASICS in the analysis of experimental EIS data. The experimental data shown in Fig. 2 were obtained for MgAZ31 in distilled water. These data are plotted as Bode-plots (Fig. 3), complex plane plots (Fig. 4), and in the format which is used for integration method (Fig. 5).

Figure 3 shows the experimental and fitted data as Bode-plots. In addition, the fit parameters C_{dl}, R_p, R_s, and α obtained with Bodefit are shown. Both C_{dl} and R_p are also reported after normalization to the electrode area. The errors of the impedance modulus

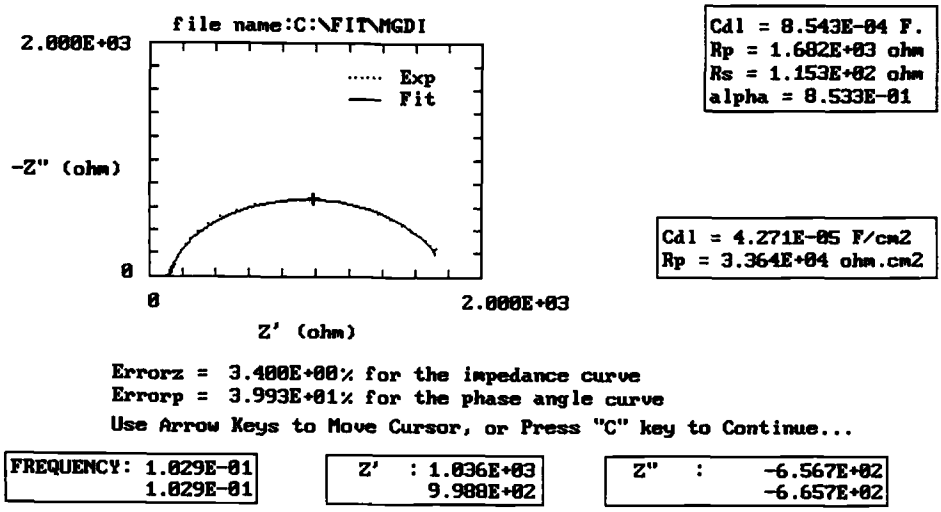

FIG. 4—*Results of the analysis of the data in Fig. 2 with Cirfit.*

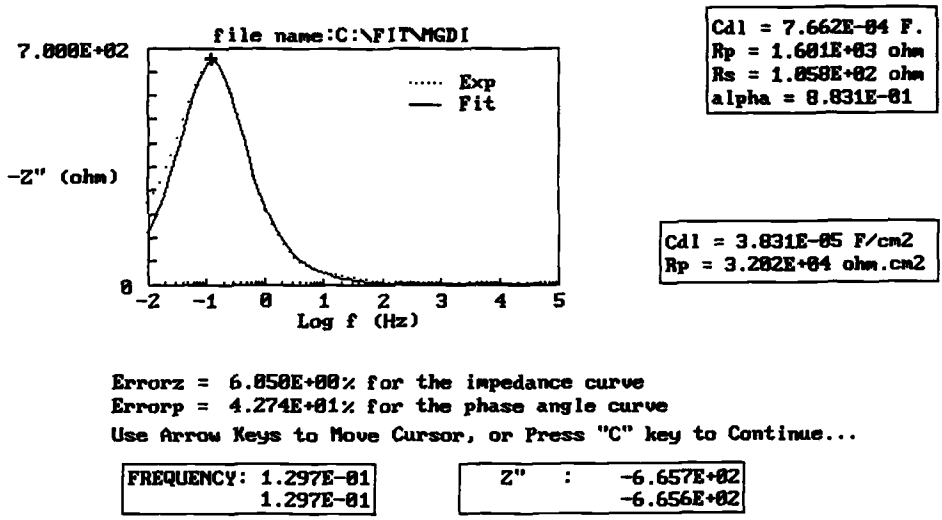

FIG. 5—*Results of the analysis of the data in Fig. 2 with Intfit.*

("Errorz") and phase angle ("Errorp") [*4*] are also given. In Fig. 4 the results of the analysis with Cirfit are presented, while Fig. 5 gives the results of the data analysis with Intfit. Close agreement of the fit parameters obtained with the three different analysis methods is observed. In the analysis with BASICS demonstrated here, it is not necessary to enter initial values for the fit parameters. Only information concerning R_s and the electrode area has to be entered. The use of Intfit often leads to an answer in the shortest time since only integration of the $Z'' - \log f$ curve and simple calculations (Eqs 6 through 8) are required.

Mass Transport Control

One of the basic reaction schemes in electrochemistry is described by the Randles-circuit shown in Fig. 6 which describes the response of a single-step charge transfer process with diffusion of reactants or products, or both, to the interface [*15,16*]. The Warburg impedance W is given by

$$W = \sigma\omega^{-1/2}(1 - j) \tag{9}$$

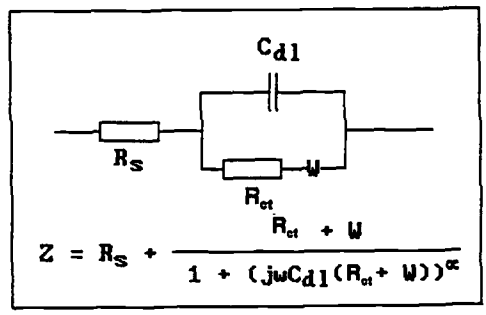

FIG. 6—*Randles-circuit.*

where σ is the Warburg coefficient. The charge transfer resistance R_{ct} is usually defined as the impedance at low frequencies extrapolated to $Z'' = 0$ [*17*].

Figure 7*a* gives a typical complex plane plot for the EC in Fig. 6, while Fig. 7*b* shows the corresponding Bode-plots. Figure 7*c* is a so-called Randles-plot in which Z' is plotted versus $\omega^{-1/2}$. According to Eq 9, the Warburg coefficient σ can be determined from the slope of the straight line in a Randles-plot. Spectra as those shown in Figs. 7*a–c* can be simulated as well as analyzed with the appropriate routines in BASICS.

Experimental data agreeing with the Randles-circuit (Fig. 6) are presented in Fig. 8 for a 70Cu-30Ni alloy which had been exposed for two weeks to a seawater medium containing a copper-tolerant microorganism [*18*]. The analysis of these data with the analysis program Warfit, which is part of BASICS, is shown in Fig. 9 for the experimental and fitted data in a complex plane plot. The fit parameters R_s, R_{ct}, C_{dl}, σ, and α are also displayed. It will be noted that the analysis of the experimental data was possible despite the fact that few data points had been collected in the low-frequency region, where the mass transport process can be clearly recognized.

Polymer-Coated Metals

Impedance spectra for polymer-coated metals exposed to (corrosive) electrolytes can be analyzed with the software module COATFIT which is based on the EC shown in Fig. 10*a*. In this EC, C_C is the capacitance of the coating which depends on its dielectric constant ϵ and its thickness d

$$C_C = \epsilon\epsilon_0 A/d \tag{10}$$

R_{po} has been called the "pore resistance" by Mansfeld and Kendig [*19–21*], who considered it to be due to the formation of ionically conducting paths in the polymer. R_p is the polarization resistance of the area at the polymer/coating interface at which corrosion occurs and C_{dl} is the corresponding capacitance. An increase of C_C with exposure time can

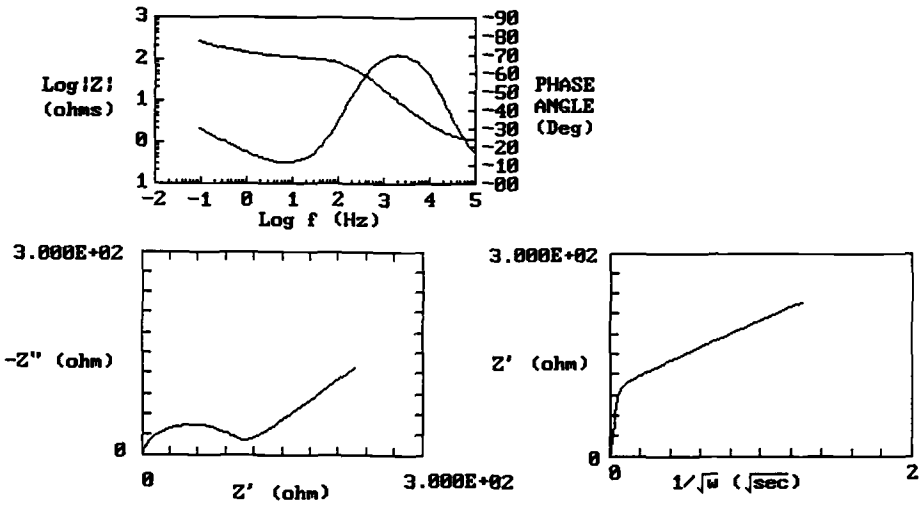

FIG. 7—*Bode-plots* (a), *Complex plane plot* (b) *and Randles-plot* (c) *for Randles circuit (Fig. 6).*

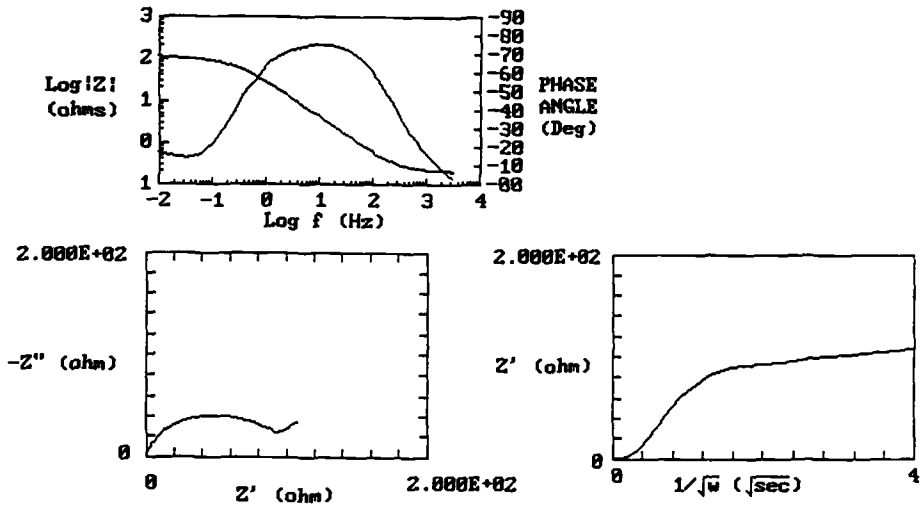

FIG. 8—*Impedance plots for 70Cu-30Ni after exposure to seawater medium.*

be related to water uptake by the coating [*22*]. The rate at which R_{po} decreases with increasing exposure time has been used by Mansfeld and Kendig [*19–21*] to rank the efficiency of different pretreatment procedures for steel in providing corrosion protection by a polybutadiene coating. The changes of C_{dl} can be used to estimate the corroding or delaminated area A_{corr} [*23*] and to calculate the specific polarization resistance R_{po}^{0} ($\Omega \cdot cm^2$) from which an estimate of the corrosion rate of the delaminated area can be made. Figure 10*b* shows the results of the analysis of an impedance spectrum of polymer-coated Mg AZ31 that had been exposed to 0.5 N NaCl. The experimental and the fitted impedance spectra are superimposed in Fig. 10*b*. Also shown are the fit parameters C_C, C_{dl}, R_{po}, R_p, R_s, α_1, and α_2. A_{corr} is calculated as $A_{corr} = C_{dl}/C_{dl}^{0}$, where $C_{dl}^{0} = 20\ \mu F/cm^2$. The delamina-

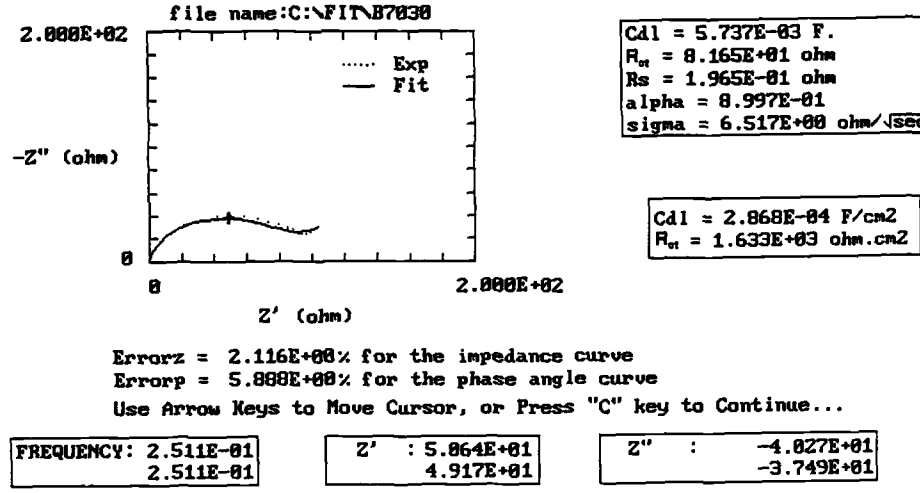

FIG. 9—*Results of the analysis of the data in Fig. 8 with Warfit.*

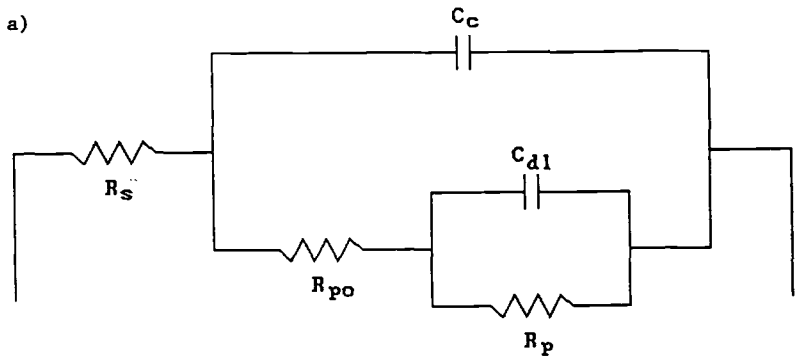

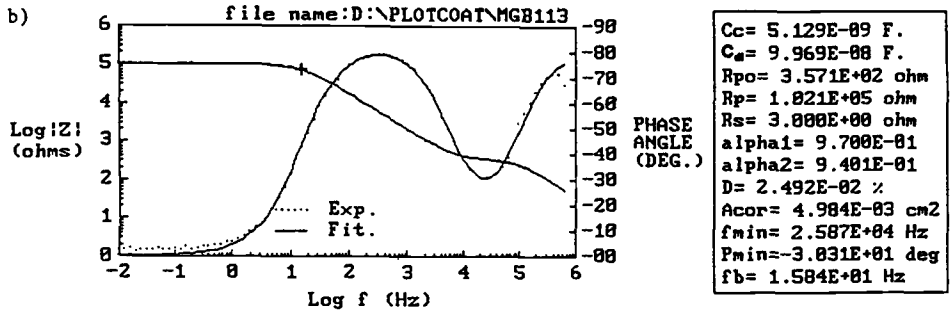

FIG. 10—*EC for polymer-coated metals exposed to corrosive environments* (a) *and comparison of an experimental impedance spectrum for polymer-coated MgAZ31 exposed to 0.5 N NaCl with a spectrum based on the fit parameters shown in the insert* (b).

tion ratio D is calculated as $D = A_{corr}/A$, where A is the total exposed area of the polymer-coated metal. The parameters f_b (the breakpoint frequency), P_{min} (the minimum of the phase angle in the high-frequency region, Fig. 10*b*), and f_{min}, (the corresponding frequency, Fig. 10*b*), are also listed in the insert of Fig. 10*b*. As shown elsewhere [*24,25*], these parameters are useful indicators of coating delamination and corrosion at the metal/coating interface which can be determined directly from the experimental data without the need for a quantitative analysis of the spectrum.

COATFIT provides the possibility of assessing the quality of the fit of the experimental data to the EC in Fig. 10*a* through the use of the deviation plots for the phase angle (in degree) or the impedance modulus $|Z|$ (in %), or both. The deviation for each of the experimental data points is plotted as a function of log f. If the measured data agree with the assumed EC, only random variations due to scatter of the experimental data are observed. If the measured data do not agree with the assumed EC, a systematic trend—

usually a sinusoidal variation—is observed. The deviation plots allow elimination of data points which show excessive scatter, and a repeat of the fit procedure after such data have been removed. Figures 11*a* and *b* show deviation plots for the spectrum in Fig. 10*b*. Since no systematic errors are observed, it can be assumed that the experimental data for the polymer-coated Mg agree with the EC in Fig. 10*a*. Removal of data points which exceed a deviation of 5° in the phase angle plot (Fig. 11*a*) or 4% in the impedance module plot (Fig. 11*b*) did not significantly increase the quality of the fit.

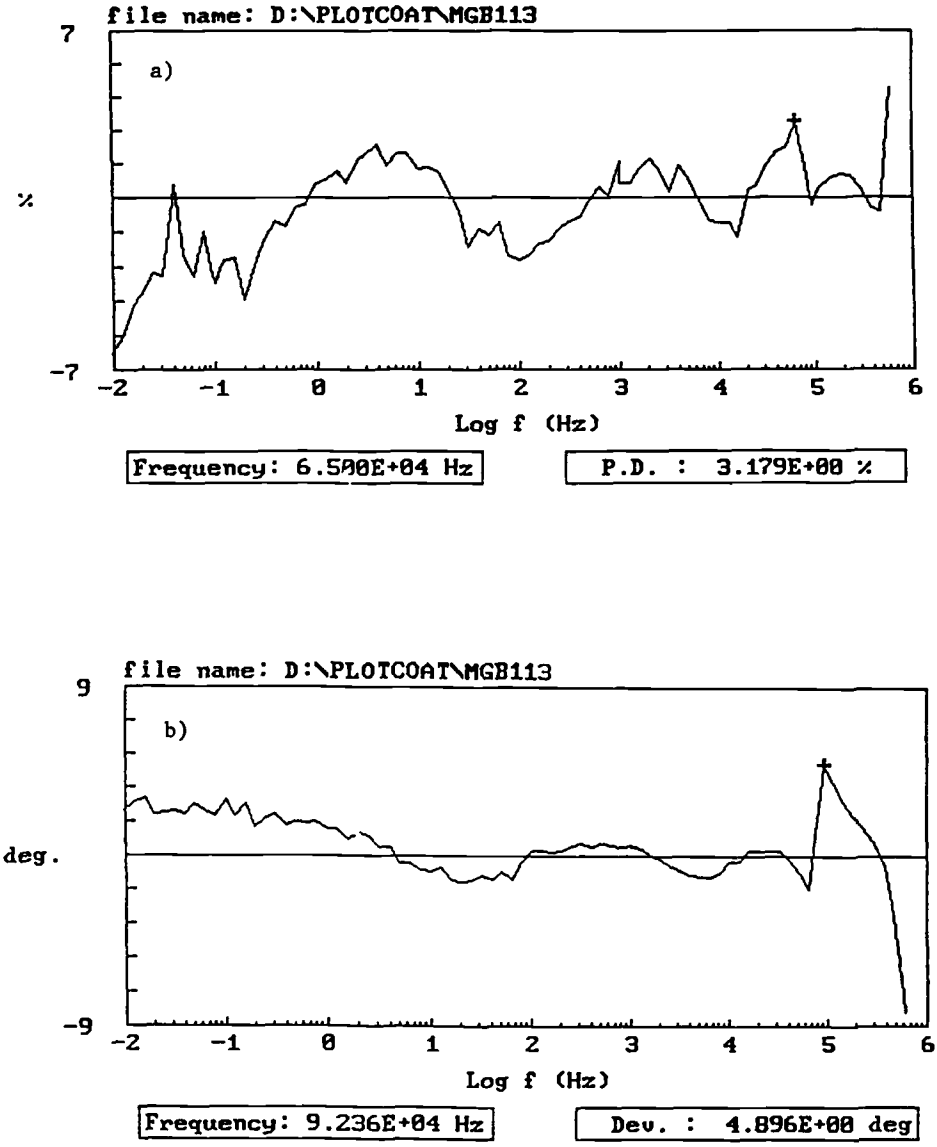

FIG. 11—*Deviation plots for the phase angle* (a) *and impedance modulus* |Z|(b) *for the experimental data in Fig. 10b.*

Anodized Aluminum

Impedance spectra for anodized aluminum alloys can be analyzed with the module ANODAL. The analysis is based on the EC in Fig. 12*a*, where C_p is the capacitance of the outer porous layer, R_p is the resistance of the sealed pores, R_b is the resistance, and C_b is the capacitance of the inner barrier layer [*26–29*]. Analysis of impedance spectra for a large number of anodized and sealed aluminum alloys has shown that the spectra fall into a very narrow scatter band if the same anodizing and sealing procedure is followed. EIS has therefore been recommended as a quality control test for anodized and sealed aluminum alloys [*27*]. It should be noted that for unsealed or dichromate sealed samples, R_p is very low. Therefore, C_p does not appear in the measured spectrum in these two cases [*29*].

Figure 12*b* shows the results of a fit of experimental data for sulfuric-acid-anodized (SAA) and hot-water-sealed (HWS) Al 6061 which had been exposed to 0.5 N NaCl. Good agreement between the measured and the fitted spectra is observed at the highest and lowest frequencies. However, significant deviations occur in the frequency range between 1000 and 0.1 Hz. These deviations become especially obvious in the frequency dependence of the phase angle, where a large difference between the experimental and fitted data is found for the phase angle minimum at about 10 Hz. It seems clear therefore that the EC in Fig. 12*a*, which has been used by the majority of investigators [*24–26*], has to be modified to include a transmission line impedance $Z_{po} = K(j\omega)^n$ (Fig. 13*a*). Excellent

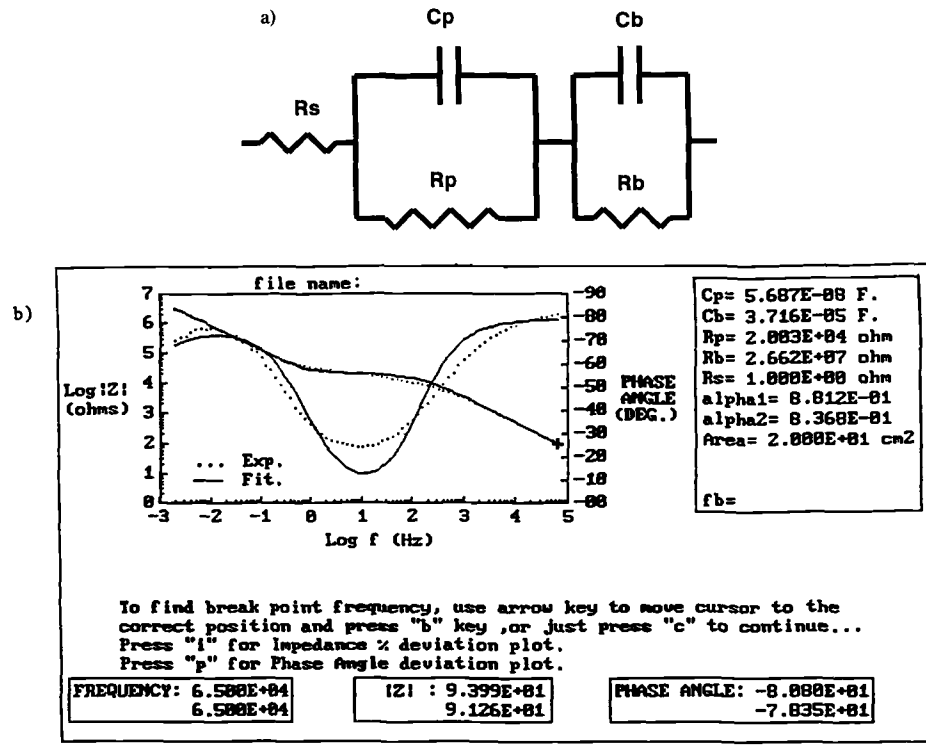

FIG. 12—*EC for anodized Al alloys* (a) *and comparison of experimental data for Al 6061 (sulfuric-acid-anodized (SAA) and hot-water-sealed (HWS)) obtained in 0.5 N NaCl with data obtained by a fit to the EC in* a (b).

agreement between the experimental data for Al 6061 (SAA + HWS) and the fitted data has been observed when the EC in Fig. 13*a* was used (Fig. 13*b*). The small statistical fluctuations in the deviation plots confirm the validity of the modified EC in Fig. 13*a* for this case. From the fitted values of C_b and C_{po} in Fig. 13*b* the barrier layer thickness was calculated as 250 Å using $\epsilon = 10$ and the porous layer thickness as 20 μm for $\epsilon = 55$ [*28*]. The calculated thickness of the barrier layer agrees very well with the value of 234 Å determined from the anodizing voltage of 17 V and the relationship given by Tajima (14 Å/V [*30*]). The thickness of the porous layer was measured directly in the SEM using a cross-section of the anodized specimen. A value of 20 to 21 μm was obtained.

An application of EIS for the analysis of the influence of different processing parameters on the properties of the anodized layer is shown in Fig. 14, where R_p is plotted as a function of exposure time to 0.5 N NaCl for Al 6061 (SAA) which was unsealed or hot water sealed for time periods between 30 and 75 min. For the unsealed sample, R_p was very low, but increased by a factor of 100 during exposure for 60 days. Apparently the pores were sealed to some extent as a result of the corrosion process. Sealing for 30 min gave low values of R_p; however, for sealing times between 40 and 75 min, very similar and high R_p values exceeding 10^4 Ω ($A = 20$ cm^2) independent of exposure time were observed.

Localized Corrosion of Aluminum

Mansfeld and co-workers have observed that the impedance spectra for aluminum alloys and Al-based metal matrix composites show characteristic changes when pits initiate and

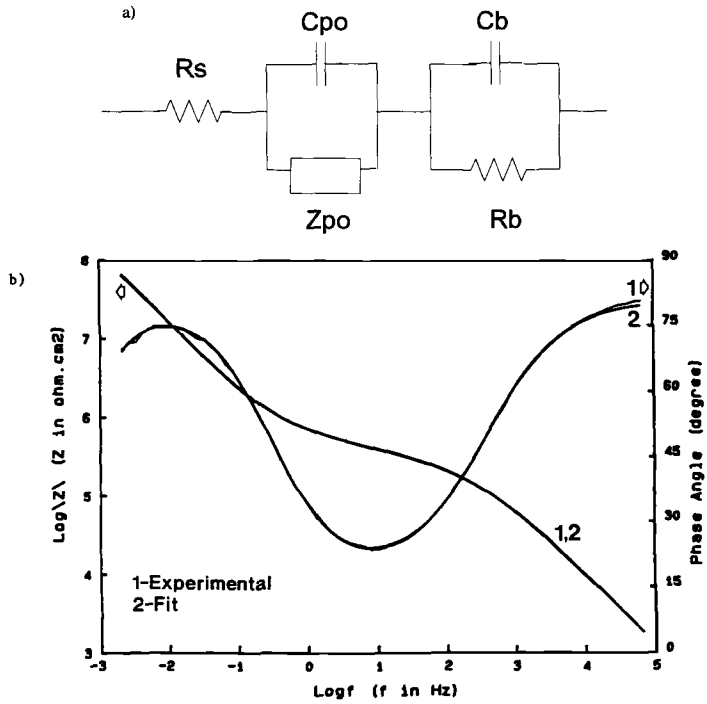

FIG. 13—*Modified EC for anodized Al alloys* (a) *and results of the fit of the experimental data for Al 6061 (SAA + HWS) in Fig. 12*b *to the EC in* a (b).

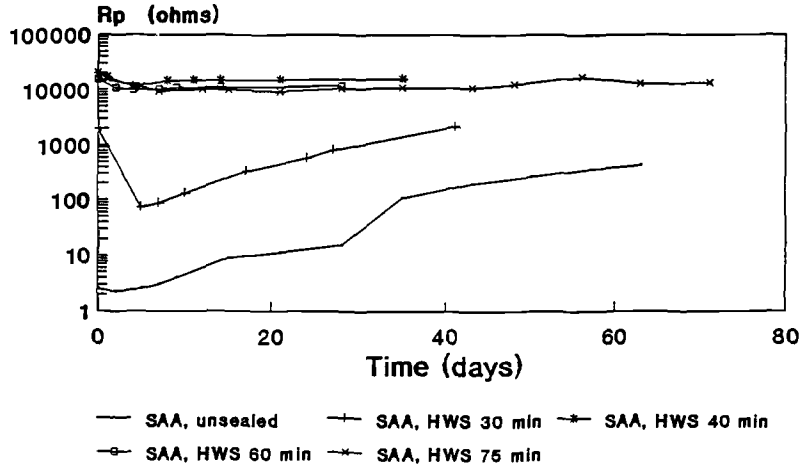

FIG. 14—*Time dependence of* R_p *for Al 6061 (SAA + HWS) with different sealing times.*

grow [*31–35*]. The experimental impedance spectra for these materials can be explained by the EC in Fig. 15, where R_p and C_p are the polarization resistance and capacitance, respectively, of the passive surface; R_{pit} and C_{pit} are the corresponding values for the growing pits; and $W = KF^{-1}(j\omega)^n$ is a transmission line impedance. F is the area fraction at which pits have initiated. The pitting model in Fig. 15 is explained in more detail in another paper in this symposium, which also presents a detailed discussion of the fit procedure and examples for the results of this procedure [*36*]. Figure 16 gives a comparison of experimental data and fitted data and lists the numerical values of the fit data. C_t corresponds to $C_t = C_p(1 - F) + FC_{pit}$, which for small values of F simplifies to $C_t = C_p + FC_{pit}$. Since it is not possible to obtain F separately with the PITFIT program, only the values of R_{pit}/F and K/F result from the analysis of the experimental spectra. The procedure to obtain R_{pit}, K, and F separately has been described elsewhere [*36*]. As a result of the final analysis it has been possible to determine pit growth rates based on the

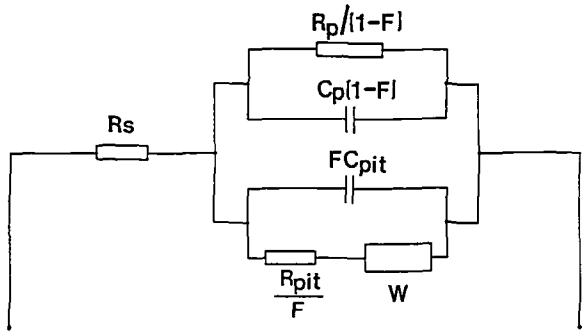

$$0 \leq F \leq 1, \qquad W=(K/F)(j\omega)^n$$

FIG. 15—*EC for the impedance of Al alloys for which pits have initiated.*

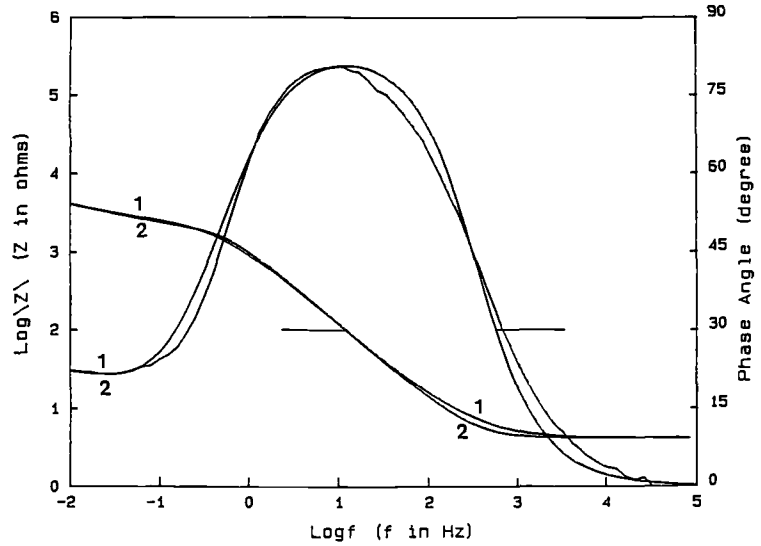

FIG. 16—*Comparison of experimental and fitted EIS data for Al 6061 after 24 h exposure to 0.5 N NaCl: curve 1—experimental data, curve 2—fitted data for* R_s = *4.2* Ω, R_p = *1.42* 10^4 Ω, C_t = *175* μF, R_{pit}/F = *2.43* 10^3 Ω, K/F = *541* Ω *(rad/s)*$^{-n}$, n = -0.59.

value of R^o_{pit} normalized to the area of the growing pit $A_{pit} = 2FA$. For Al 7075-T6 which had been passivated in 1000 ppm $CeCl_3$ for 7 days [*27,28*], the time dependence of the pit growth rate has been determined as (Fig. 17)

$$\log (1/R^o_{pit}) = a + b \log (t - t_o) = -3.00 - 0.99 \log (t - t_o) \tag{11}$$

where t_o = 21 days is the time at which pits initiated as indicated by the changes in the EIS data. These results can be expressed as [*36*]:

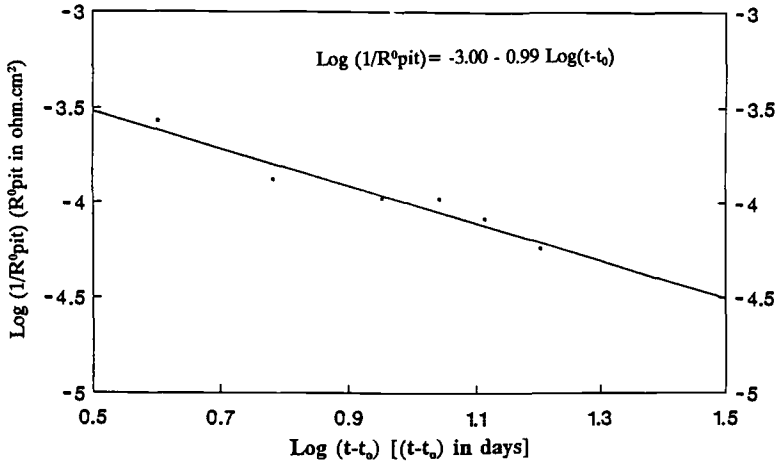

FIG. 17—*Time dependence of the polarization resistance of pits* R^o_{pit} *for Al 7075-T6 (passivated in* $CeCl_3$*) during exposure to 0.5 N NaCl.*

$$d\,r/dt = a'/(t - t_o) \tag{12}$$

which suggests that the radius r of a hemispherical pit increases logarithmically with time

$$r = c \log (t - t_o) \tag{13}$$

Summary and Conclusions

The software program ANALEIS with its modules BASICS, COATFIT, PITFIT, and ANODAL can be used for the simulation and analysis of EIS data for simple corrosion systems. The advantage of ANALEIS is the optimization of the data analysis for each particular corrosion system based on the characteristics of its equivalent circuit. BASICS is used for systems that are under charge transfer or mass transport control or show an inductive loop. COATFIT addresses the case of the impedance behavior of polymer-coated metals. Data for anodized and sealed aluminum alloys can be analyzed with ANODAL. A new model for the impedance of anodized Al is proposed. PITFIT can be used to analyze impedance data obtained for localized corrosion of aluminum alloys. The quality of each fit is judged using deviation plots which can also be used to eliminate data points with excessive scatter.

APPENDIX

In the software package ANALEIS, a number of different methods have been used for the data analysis in order to obtain the best fit of the experimental impedance spectra to the particular equivalent circuit which is applicable for the particular system under investigation. In each module of ANALEIS a different strategy is used to obtain the best possible fit. In other software [*37,38*] nonlinear list square methods are used; however, this approach requires fairly accurate initial guesses of the fit parameters in order to initiate the fit process. For complicated spectra, for which it is difficult to obtain accurate initial guesses, the fit procedure sometimes cannot be performed.

In order to avoid this problem, a computer-aided search is used in ANALEIS to determine the initial fit parameters [*39,40*]. Estimates of these parameters can be obtained in different frequency regions of the spectra by mathematical calculations. This method has been used to replace random input of initial parameters; however, it requires a certain understanding of the experimental impedance spectra. For example, in the module BASICS, R_s can be estimated from the high-frequency region, C_{dl} and α from the capacitive region, and R_p from the low-frequency region. In the COATFIT module, the initial values of R_s, C_c, R_{po}, and α_1 can be obtained from the high-frequency region and the impedance at the minimum of the phase angle, while initial values for C_{dl}, α_2, and R_p are obtained from the low-frequency region of the spectra. For the PITFIT module, R_{pit}, K, and n are obtained after deconvolution in the low-frequency region which is dominated by the transmission line impedance. A similar approach is used for the analysis of EIS data for anodized aluminum with the ANODAL module.

After determination of the initial fit parameters as previously described, the quality of the fit is improved using different mathematical methods [*41–51*] such as the Monte Carlo method [*41,44*], the nonlinear least square method [*41–45,48*], the Newton-Raphson approach [*41–45,48*] to solve the Jacobian matrix, regression analysis of a fourth-order polynomial equation [*46,47*], deconvolution [*41,45*], linear programming [*50,51*], and the

nonequal space Simplex rule. A detailed description of the mathematical procedures used in ANALEIS is beyond the scope of this paper. The best fit has the minimum accumulation of the total impedance error at all frequencies. In certain cases, minimization of the difference between the experimental and fitted values of the phase angle is used to obtain the best fit, since the phase angle is a very sensitive indicator of the quality of the fit.

References

[1] Mansfeld, F. and Lorenz, W. J., "Electrochemical Impedance Spectroscopy—Applications in Corrosion Science and Technology," in *Techniques for Characterization of Electrodes and Electrochemical Processes*, R. Varma and J. R. Selman, Eds., John Wiley and Sons, New York, 1991, p. 581.

[2] Bertocci, U. and Ricker, R. E., "Impedance Spectra Calculated from Model Polarization Curves," *Electrochemical Impedance: Analysis and Interpretation, ASTM STP 1188*, J. R. Scully, D. C. Silverman, and M. W. Kendig, Eds., American Society for Testing and Materials, Philadelphia, 1993 (this publication).

[3] Mansfeld, F., *Corrosion*, Vol. 37, 1981, p. 301.

[4] Mansfeld, F., Tsai, C. H., and Shih, H., "Software for the Simulation and Analysis of EIS-Data," *Computer Modeling in Corrosion, ASTM STP 1154*, R. S. Munn, Ed., American Society of Testing and Materials, Philadelphia, 1992.

[5] Mansfeld, F., Kendig, M. W., and Lorenz, W. J., *Journal of the Electrochemical Society*, Vol. 132, 1985, p. 290.

[6] Mansfeld, F. and Kendig, M. W., *Werkst. Korros.* Vol. 34, 1983, p. 397.

[7] Mansfeld, F. and Kendig, M. W., *Proceedings, 6th European Symposium Corrosion Inhibitors*, Ferrara, Italy, 1985.

[8] Mansfeld, F., Kendig, M. W., Allen, A. F., and Lorenz, W. J., *Proceedings, 9th International Conference on Metallic Corrosion*, Toronto, Canada, Vol. 1, 1984, p. 368.

[9] Kendig, M. W., Meyer, E. M., Lindberg, G., and Mansfeld, F., *Corrosion*, Vol. 23, 1983, p. 1007.

[10] Mansfeld, F., *Corrosion*, Vol. 44, 1988, p. 558.

[11] Kendig, M. W. and Mansfeld, F., *Corrosion*, Vol. 39, 1983, p. 466.

[12] van Meirhaeghe, R. L., Dutoit, E. C., Cardon, F., and Gomes, W. P., *Electrochimica Acta*, Vol. 21, 1976, p. 39.

[13] Macdonald, D. D. and Urquidi, M., *Journal of the Electrochemical Society*, Vol. 132, 1985, p. 2316.

[14] Mansfeld, F., Chen, Y. C., and Shih, H., in *The Measurement and Correction of Electrolyte Resistance in Electrochemical Tests, ASTM STP 1056*, L. L. Scribner and S. R. Taylor, Eds., American Society for Testing and Materials, Philadelphia, 1990, p.95.

[15] Ross Macdonald, J., "Impedance Spectroscopy—Emphasizing Solid Materials and Systems," John Wiley and Sons, New York, *Interscience*, Chap. 2, 1987.

[16] Gabrielli, C., "Identification of Electrochemical Processes by Frequency Response Analysis," Solartron–Schlumberger, 1980.

[17] Epelboin, I., Keddam, M., and Takenouti, H., *Journal of Applied Electrochemistry*, Vol. 2, 1982, p. 71.

[18] Little, B., Wagner, P., and Mansfeld, F., "An Electrochemical Evaluation of Biofilms and Calcareous Deposits Formed in Natural Seawater," *Proceedings, International Congress on Microbiologically Induced Corrosion*, Knoxville, TN, October 1990, pp. 5–9.

[19] Mansfeld, F., Kendig, M., and Tsai, S., *Corrosion*, Vol. 38, 1982, p. 478.

[20] Kendig, M., Mansfeld, F., and Tsai, S., *Corrosion Science*, Vol. 23, 1983, p. 317.

[21] Mansfeld, F. and Kendig, M., *Laboratory Corrosion Tests and Standards, ASTM STP 866*, G. S. Haynes and R. Baboian, Eds., 1985, p. 122.

[22] Brasher, D. M. and Kingsbury, A. H., *Journal of Applied Chemistry*, Vol. 4, 1954, p. 62.

[23] Titz, J., Wagner, G. H., Spaehn, H., Ebert, M., Juettner, K., and Lorenz, W. J., *Corrosion*, Vol. 46, 1990, p. 221.

[24] Mansfeld, F., Tsai, C. H., and Shih, H., "Proceedings, Symposium on Advances in Corrosion Protection by Organic Coatings," *The Electrochemical Society Proceedings*, Vol. 89, No. 13, 1989, p. 228.

[25] Mansfeld, F. and Tsai, C. H., *Corrosion*, Vol. 47, 1992, p. 958.

[26] Hitzig, J., Juettner, K., Lorenz, W. J., and Paatsch, W., *Corrosion Science,* Vol. 24, 1984, p. 945.
[27] Mansfeld, F. and Kendig, M. W., *Corrosion,* Vol. 41, 1985, p. 490.
[28] Hitzig, J., Juettner, K., Lorenz, W. J., and Paatsch, W., *Journal of the Electrochemical Society,* Vol. 133, 1986, p. 887.
[29] Mansfeld, F. and Kendig, M. W., *Journal of the Electrochemical Society,* Vol. 135, 1988, p. 828.
[30] Tajima, T. S., in *Advances in Corrosion Science and Technology,* Vol. 1, Plenum Press, New York, 1970, p. 227.
[31] Mansfeld, F., Lin, S., Kim, S., and Shih, H., *Corrosion Science,* Vol. 27, 1987, p. 997.
[32] Mansfeld, F. and Shih, H., *Journal of the Electrochemical Society,* Vol. 135, 1988, p. 332.
[33] Mansfeld, F., Lin, S., Kim, S., and Shih, H., *Electrochimica Acta,* Vol. 34, 1989, p. 1123.
[34] Mansfeld, F., Lin, S., Kim, S., and Shih, H., *Materials Science Forum,* Vols. 44 & 45, 1989, p. 83.
[35] Mansfeld, F., Lin, S., Kim, S., and Shih, H., *Journal of the Electrochemical Society,* Vol. 137, 1990, p. 78.
[36] Mansfeld, F., Wang, Y., Lin, S. H., Xiao, H., and Shih, H., "Detection and Monitoring of Localized Corrosion with EIS," *Electrochemical Impedance: Analysis and Interpretation, ASTM STP 1188,* J. R. Scully, D. C. Silverman, and M. W. Kendig, Eds., American Society for Testing and Materials, Philadelphia, 1993 (this publication).
[37] Macdonald, J. R., "Impedance Spectroscopy: Old Problems and New Developments," *Electrochimica Acta,* Vol. 35, 1990, p. 1483.
[38] Boukamp, B. A., *Equivalent Circuit Users Manual,* 1988/1989.
[39] Shih, H. and Mansfeld, F., *Corrosion Science,* Vol. 29, 1989, p. 1235.
[40] Shih, H. and Mansfeld, F., *Corrosion,* Vol. 45, 1989, p. 615.
[41] Korn, G. A. and Korn, T. M., *Mathematical Handbook for Scientists and Engineers,* 2nd ed., McGraw-Hill Book Co., New York, 1968.
[42] Burden, R. L., Faires, J. D., and Reynolds, A. C., *Numerical Analysis,* 2nd ed., Prindle, Weber & Schmidt, Boston, 1981.
[43] Jansson, P. A., *Deconvolution with Application in Spectroscopy,* Academic Press, 1984.
[44] Dahlquist, G. and Bjorck, A., *Numerical Methods,* translated by N. Anderson, Prentice-Hall, Englewood Cliffs, NJ, 1974.
[45] Hogg, R. V. and Tanis, E. A., *Probability and Statistical Inference,* Macmillan Publishing Co., New York, 1983.
[46] Neter, J., Wasserman, W., and Kutner, M. H., *Applied Linear Statistical Models,* IRWIN Inc., IL, 1985.
[47] Draper, N. R. and Swith, H., *Applied Regression Analysis,* 2nd ed., John Wiley and Sons, New York, 1981.
[48] Vlach, J. and Singhal, K., *Computer Methods for Circuit Analysis and Design,* Van Nostrand Reinhold Co., New York, 1983.
[49] Kahaner, D., Moler, C., and Nash, S., *Numerical Methods and Software,* Prentice-Hall, Englewood Cliffs, NJ, 1977.
[50] Gass, S. I., *Linear Programming,* 2nd ed., McGraw-Hill, New York, 1964.
[51] Dantzig, G. B., *Linear Programming and Extensions,* Prentice-Hall, Englewood Cliffs, NJ, 1961.

Pierre R. Roberge[1]

Analyzing Simulated Electrochemical Impedance Spectroscopy Results by the Systematic Permutation of Data Points

REFERENCE: Roberge, P. R., **"Analyzing Simulated Electrochemical Impedance Spectroscopy Results by the Systematic Permutation of Data Points,"** *Electrochemical Impedance: Analysis and Interpretation, ASTM STP 1188,* J. R. Scully, D. C. Silverman, and M. W. Kendig, Eds., American Society for Testing and Materials, Philadelphia, 1993, pp. 54–72.

ABSTRACT: While electrochemical impedance spectroscopy (EIS) can be a rapid and accurate method for measuring corrosion rates, the difficulties in interpreting EIS data points have overshadowed the numerous advantages offered by this technique. Since the charge transfer conductance across a corroding interface is proportional to the corrosion rate, it is the prime parameter sought by all electrochemical techniques. The simplest model representing such an interface must also include a capacitance that describes the capacitive charge acceptance of any metallic surface exposed to an electrolyte. The validation of this RC equivalent circuit model can be achieved by permuting the three data points selected to project the center of a circle in a Nyquist representation. This paper reviews some of the applications of the permutation technique that have been recently published and indicate how some of the apparent limitations of the technique can serve to reveal important information on the mechanistic behavior of a corroding interface. These studies of various alloys exposed to aqueous environments indicate that the non-adherence of the EIS measurements to a perfect RC model is a rich source of information concerning the types of corrosion processes occurring on a metallic surface.

KEYWORDS: electrochemical impedance spectroscopy (EIS), interface modeling, permutation technique, corrosion monitoring

Electrochemical impedance spectroscopy (EIS) has been successfully applied to the study of corrosion systems for over twenty years [*1*]. Since Epelboin and co-workers [*2*] published their early work on the system iron-H_2SO_4-propargylic acid, impedance techniques have found increasing applications in corrosion research because of the possibility of obtaining information on the chemical mechanisms involved. An imporant advantage of EIS over other laboratory techniques is the possibility of using very small amplitude signals without disturbing the properties being measured. Another major quality of EIS is the possibility of working in low or variable conductivity environments. EIS has thus been successfully applied to study the corrosion of iron and carbon steel in neutral waters [*3–6*] or deoxygenated formic acid [*7*].

But even with many fundamental advantages over other electrochemical techniques, EIS remains difficult to use for field corrosion monitoring [*8*]. The time required to obtain a full impedance diagram imposes a serious limitation to the technique when the specimens

[1]Associate professor, Department of Chemistry and Chemical Engineering, Royal Military College, Kingston, Ontario, Canada, K7K 5L0.

under study are modified relatively rapidly. The difficulties interpreting ac impedance data [*9*] is another obstacle that has overshadowed the application of EIS to field situations [*8*].

Geometric Extrapolation

In order to overcome these difficulties, a method was developed that consisted of finding the geometric center of an arc formed by three successive data points on a complex impedance diagram [*10*]. The three experimental data points, *a*, *b*, and *c* (Fig. 1), with their corresponding coordinates (x_1, y_1), (x_2, y_2), (x_3, y_3), are linked by the segments *ab* and *bc* with calculated points (x_4, y_4) and (x_5, y_5) as centers. From the slopes of the perpendicular lines to the segments *ab* and *bc* which can be calculated using Eqs 1 and 2, it is possible to find the intercepts y_6 and y_7 (Eq 3) with the *Y* axis made by the perpendicular lines passing through (x_4, y_4) and (x_5, y_5), respectively.

$$\text{slope 1} = \frac{y_2 - y_1}{x_2 - x_1} \tag{1a}$$

$$\text{slope 2} = \frac{y_3 - y_2}{x_3 - x_2} \tag{1b}$$

$$\text{slope 3} = \tan(\text{inv tan slope 1} + 90°) \tag{2a}$$

$$\text{slope 4} = \tan(\text{inv tan slope 2} + 90°) \tag{2b}$$

$$y_6 = y_4 - \text{slope 3} \times x_4 \tag{3a}$$

$$y_7 = y_5 - \text{slope 4} \times x_5 \tag{3b}$$

By merging Eqs 3a and 3b it is possible to find (Eq 4) the intercept (x_8, y_8) which also corresponds to the center of a semicircle made by the original data points used for these calculations, i.e., (x_1, y_1), (x_2, y_2) and (x_3, y_3). If an impedance diagram had a slightly

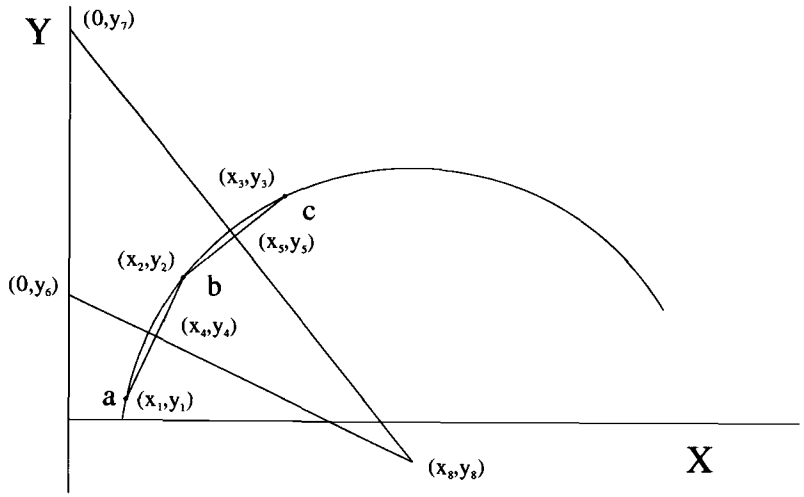

FIG. 1—*Geometric method used to extrapolate the center of a depressed semicircle.*

depressed semicircular shape, the projected centers would be found in the fourth quadrant.

$$x_8 = \frac{y_7 - y_6}{\text{slope } 3 - \text{slope } 4} \tag{4a}$$

$$y_8 = y_6 - \text{slope } 3 \times x_8 \tag{4b}$$

The analysis of EIS measurements was further developed by systematically permuting the data points involved in the projection of centers. This mathematical treatment is schematically illustrated in Fig. 2 where one can see how one central point can be combined with three pairs of adjacent points to generate three discrete projected centers. By repeating the symmetrical combinations of three points that are possible for a certain number of data points (frequencies), a population of centers (Fig. 3) can be generated that can serve to calculate an average center position. It then becomes possible to estimate with a certain degree of confidence the impedance parameters behind the apparent RC behavior illustrated in Fig. 4: (1) the arc diameter (or R_p), (2) the angle of tilt or depression angle made with the abscissa, and (3) the solution resistance R_s (high frequency intercept of the circle with the abscissa).

While in general a fairly good agreement can be achieved between corrosion rates estimated from polarization resistance and direct mass loss measurements or solution analyses [*9,11*], the data analysis of EIS results has often revealed the presence of an angle of tilt [*9,11–13*]. It is a common practice to introduce an empirical factor to express this reality through the mathematical fitting procedures used by many authors. The empirical factor would then appear as an exponent β, also often expressed as $(1 - \alpha)$, with a value between 0 and 1, which would be added to the imaginary component of an impedance frequency (ω) response $Z(\omega)$ (Eq 5).

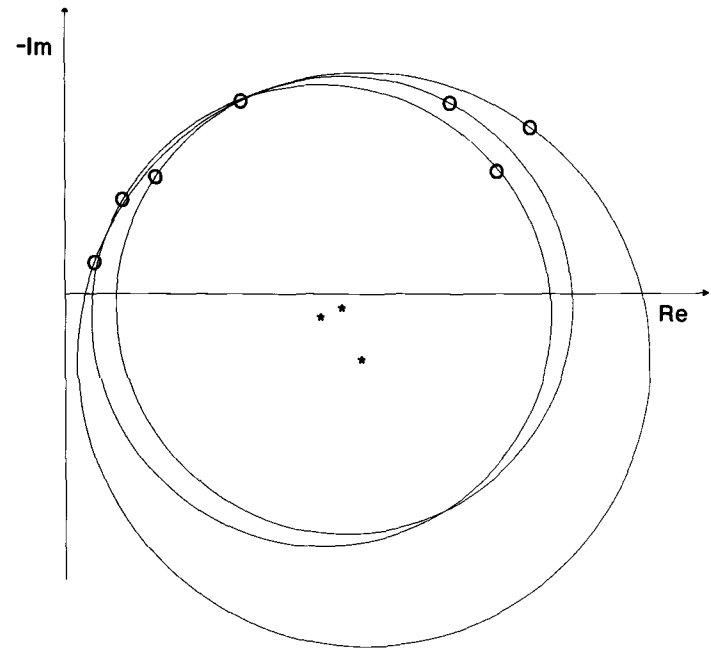

FIG. 2—*Schematic representation of the permutation technique—one central data point is combined with pairs of data points to draw circles and estimate centers.*

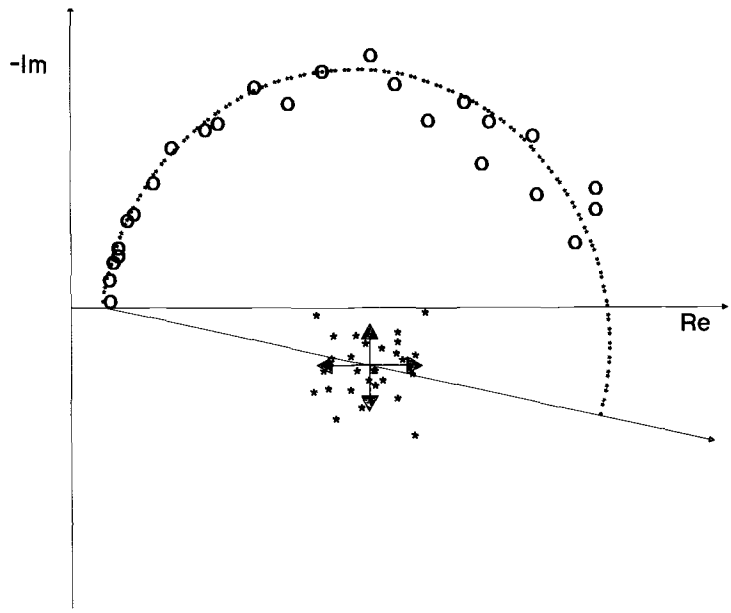

FIG. 3—*Schematic representation of the permutation technique—the population of projected centers can serve to calculate a mean value and its associated standard deviation.*

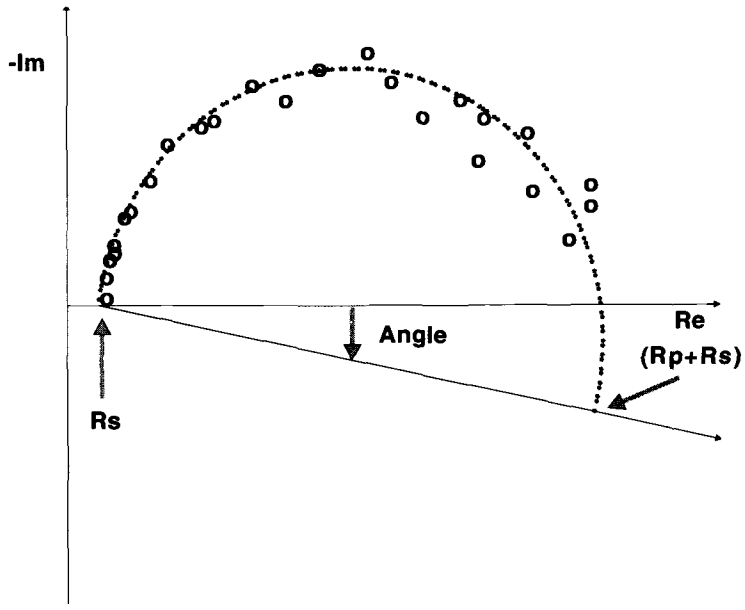

FIG. 4—*Schematic representation of the permutation technique—the three main parameters calculated with the technique, the solution resistance (R_s), the depression angle, and the polarization resistance (R_p).*

$$Z(\omega) = R_s + \frac{R_p}{1 + (j\omega R_p C_{dl})^{\beta}} \tag{5}$$

The constant phase element (CPE) corresponding to this empirical factor has often been associated with dispersion effects [*14–16*] which, in the case of a corroding metal, have been attributed to microscopic roughening of the surface [*17–20*].

Once the calculations are performed it is also possible to estimate the double layer capacitance (C_{dl}) from the high frequency portion of the original data. The geometric analysis of EIS data has been applied to the analysis of results obtained with a multitude of alloys and systems in various testing conditions. Copper and copper-nickel alloys were tested for their resistance to sea water erosion corrosion. These measurements were done in laboratory and testing rig conditions [*21,22*].

Carbon steel specimens were used in a laboratory environment when EIS was applied to a study of the efficiency of inorganic and organic inhibitors for the control of corrosion induced by typical corrodents found in oil and gas process waters (NaCl, H_2S) [*23–26*]. The experiments with carbon steel were pursued in field conditions with commercial probes and industrial partners [*27*].

Various aluminum and aluminum-lithium alloys have also been recently characterized by using EIS and this analytical technique. These tests were all performed in a laboratory environment simulating either exposure to sea water [*28*] or during an effort to replace the ASTM Test Method of Salt Spray (Fog) Testing (B117) of anodized aluminum with an accelerated electrochemical technique [*29*]. In general, by simplifying both the instrumental and analytical complexities involved in performing EIS measurements, it was possible to apply the EIS technique to practical problems where *in-situ* monitoring techniques are needed. EIS has been proven to be applicable to a broad variety of problems, ranging from low conductivity environments, to very difficult erosion corrosion conditions.

Additionally, it was found that EIS measurements can be a very rich source of on-line information for systems where corrosion is a problem. The statistical data analysis performed by permuting the EIS data points to generate the resistance to polarization and its associated corrosion resistance can also reveal some interesting characteristics of an interfacial behavior. The variable depression angle of projected arc centers from the real axis of Nyquist plots seems to be closely related to the microscopic transformation of the surface profile. During the study of carbon steel resistance to localized corrosion induced by adding inhibitors it was found that there is a good agreement between measured pit depths and this calculated depression angle [*30*], indicating that indeed such a parameter could be a good indicator of pitting corrosion attack.

Equivalent Circuits

The important features that contribute to the impedance response of a metal/electrolyte interface can be modeled using an equivalent circuit. The geometric extrapolation technique is based on the assumption that the simplest such circuit prevails (Fig. 5*a*). It is often difficult to explain a complex physical system with such a crude simplification; more realistic models have been developed to better fit both the physical nature of an interface and the results obtained with EIS [*11,31–36*].

While such a practice has made EIS an important tool for fundamental studies of interfacial behavior, it might have discouraged more adventurous and widespread uses of the technique. Such an inhibition is probably historical since all electrochemical measurement methods have to be applied with caution to the evaluation of corrosion rates [*9,37*].

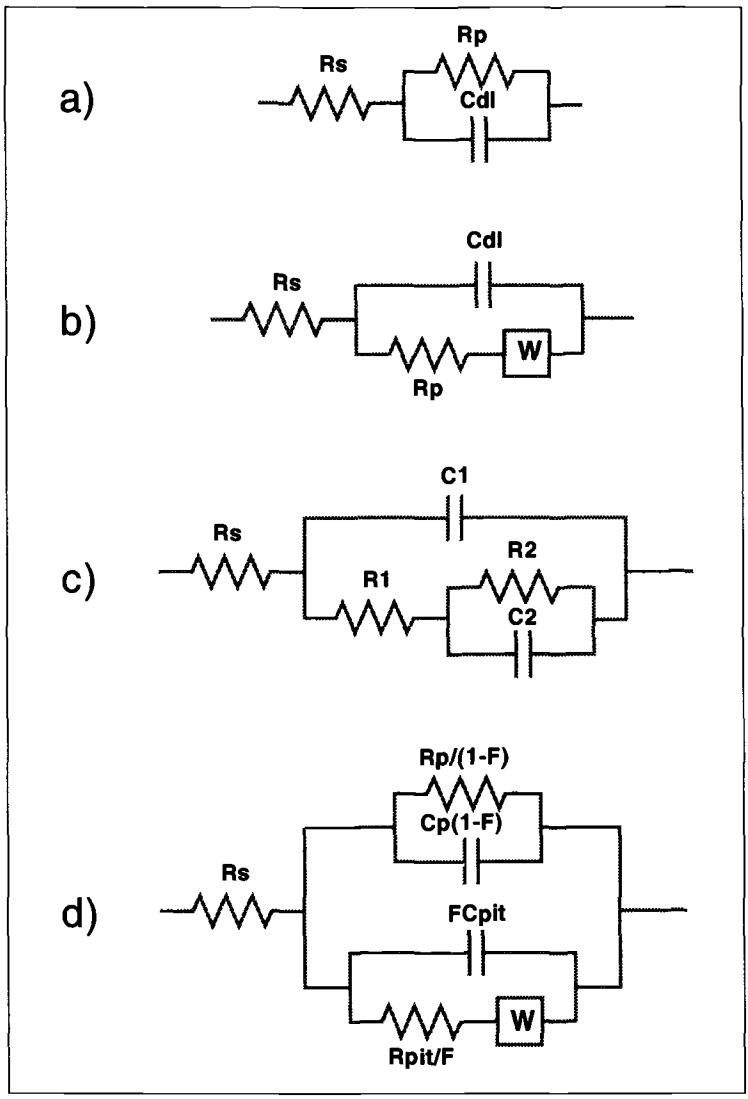

FIG. 5—*Equivalent circuit models considered:* (a) *simplest representation of an electrochemical interface,* (b) *representation of the impedance of coated materials* [38,41], (c) *of one relaxation time constant with extended diffusion* [38,42] *and* (d) *of the impedance of pitting processes of aluminum-based materials* [38,40].

The distance taken by the linear polarization techniques over any other electrochemical technique for monitoring corrosion of real systems [*38,39*] can only be explained by the instrumental simplicity of the technique itself.

Since the geometric extrapolation technique has made it possible to use the EIS technique in very perturbed environments while removing the requirement of a specialized operator, it became important to justify the results of analysis obtained with various systems. Additionally, it became increasingly obvious that empirical parameters such as

the angle of tilt observed and adopted by most researchers in the field to explain the divergence between practical results and data synthesized with equivalent circuits were far more significant for corrosion monitoring than one might be led to believe by surveying modern literature.

The patterns created by the permutation of data points used in the geometric extrapolation technique have thus become a tool in themselves since they have a tendency to exaggerate the differences between the simplest RC model assumed by the technique and the complex reality of some measurements.

Analyzed Experimental Results

Erosion Corrosion of Cu-Ni Alloys

Figures 6 and 7 represent typical EIS results obtained with cylinders made of 70-30 Cu-Ni alloys. Rotating the prepassivated alloys seemed to temporarily cause a decrease of the polarization resistance of these alloys but the polarization resistance eventually reverted to initial values after a few hours of rest. While the results obtained before and during rotation with the 70-30 Cu-Ni alloyed with Nb (Fig. 6) seemed to fit relatively well the RC model assumed by the geometrical extrapolation method, the projection of centers from results obtained with the 70-30 Cu-Ni alloyed with chromium (Fig. 7) created linear patterns of projected centers that indicated a departure from such a simple model. Such a behavior was reproduced for many specimens machined out of the same cast specimens.

The dispersion of projected centers observed with the 70-30 Cu-Ni (Nb) alloy after the erosion period (Fig. 6*c*) eventually disappeared and focused patterns such as those of Fig. 6*a* were obtained again. The dispersion in this case was attributed to the non-equilibrium state of the interface. The extremely long recuperation time for the process (a few days) was thought to be indicative of the solid state nature of the rearrangements in progress.

The microscopic examination of 70-30 Cu-Ni specimens after a few weeks of exposure to saline environment revealed that the addition of 2% chromium to create a higher strength alloy had also created the spontaneous susceptibility of this alloy to suffer a localized intergranular form of corrosion attack. The depression angle which seemed to prevail for all the measurements obtained with these alloys also seemed to be higher ($\approx$35°) for results obtained with the chromium-modified alloy.

Inhibition of Carbon Steel Corrosion

The cylindrical mild steel specimens used in these studies were exposed to various aqueous environments in preparation of field tests for the evaluation of corrosion inhibitor efficiency in industrial oil and gas environments. The EIS results illustrated in Fig. 8 were obtained with C-steel specimens exposed to a deaerated solution of sodium-molybdate, a common inorganic passivator, before adding a strong depassivator (NaCl) and air. The projection of centers from the experimental data points is also characterized by a relatively large angle of tilt which sometimes reaches values close to 45° (Fig. 8*b*). An interesting correlation was found during this study between the summation of depression angles and either the average pit depth or deepest pit depth measured after exposures that lasted up to 80 days (Fig. 9) [*30*].

Such a relation between the depression angle of projected arc centers from the real axis and the microscopic transformation of surface profiles (Fig. 10) during localized corrosion could form the basis for a rapid detection of the most vicious types of corrosion attack.

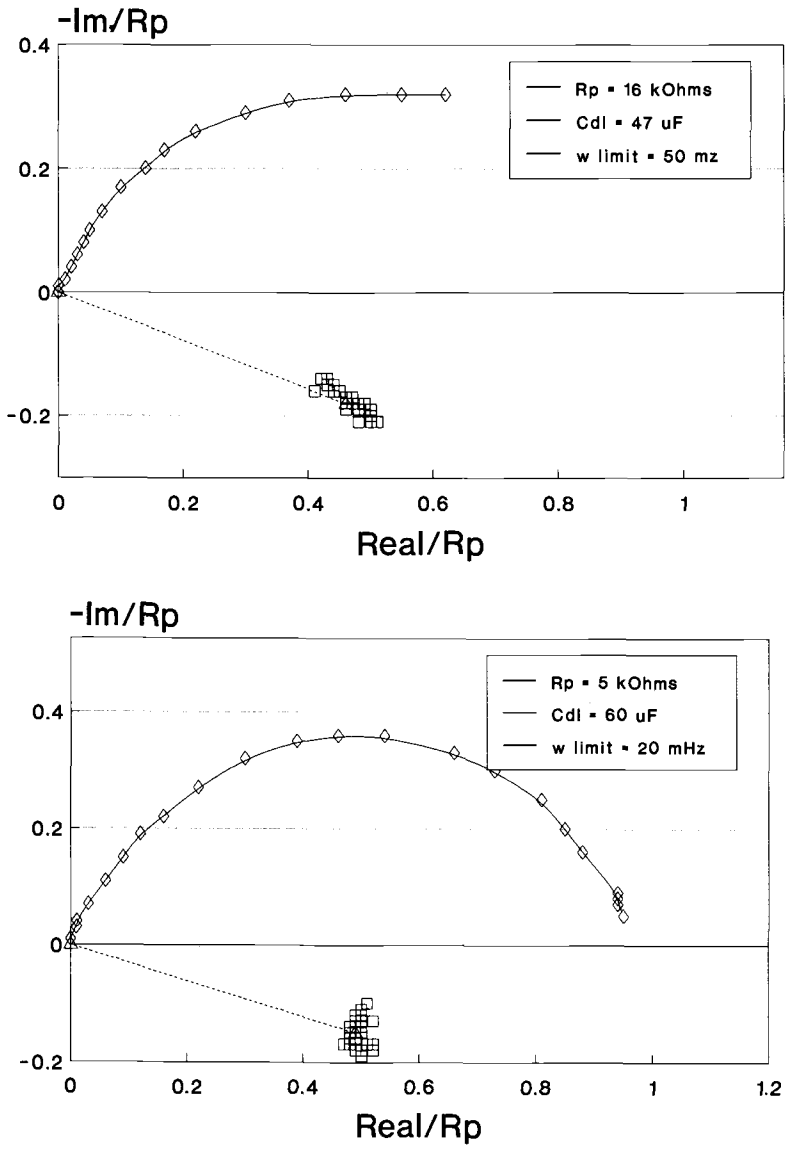

FIG. 6—*Normalized impedance diagrams made with a five-day prepassivated 70-30 Cu-Ni alloy containing 0.4% Nb and exposed to a 3% NaCl aerated solution:* (a) *in a quiescent condition;* (b) *after 8 h of rotation at 5000 rpm;* (c) *in a quiescent condition 16 h after the rotation period.*

Corrosion of Aluminum Alloys

The resistance to corrosion of various bare faces of aluminum alloys exposed to an aerated saline solution was also investigated with EIS and the results analyzed by the systematic permutation of data points. The specimens were mounted in a manner that would expose only one face of each of the orthogonal planes that were related to the

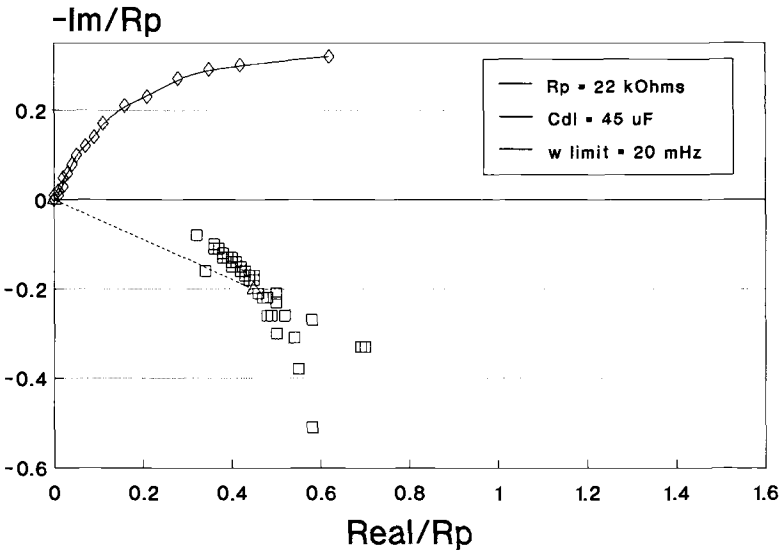

FIG. 6—(continued)

rolling direction of the commercial sheet material used for this study. For each experiment a pair of identical aluminum specimens were immersed in a 2 l beaker containing a solution of aerated 3% NaCl. At the completion of these experiments (14 days) the specimens were removed and examined with both optical and scanning electron microscopy to observe any difference in corrosion morphologies.

The results obtained during this study with EIS were compared with results independently obtained on panels made from 2090 and 8090 Al-Li along with 2024, 6061, and 7075 aluminum alloys subjected to exposure to sea water fog and full or partial immersion in sea water [*28*].

Some typical EIS normalized Nyquist plots obtained with high-strength Al-Li and aluminum alloys are presented in Fig. 11. While the centers projected in the case of Al-Li alloys even after an exposure period of 13 days (Fig. 11*a*) are quite focused, the centers projected from EIS data obtained with the 7075-T6 aluminum specimens produced characteristic depressed tailing patterns (Fig. 11*b*) normally associated with widespread localized corrosion attack.

Long-term exposure tests and microscopic examination of the EIS tested specimens revealed that the 8090-T8 sheet material had a lower overall corrosion rate and was less prone to pitting-exfoliation corrosion than its more conventional 7075-T6 counterpart. The depression angles obtained during the analysis of these EIS data could be correlated to the extent of surface pitting but seemed to be unrelated to the seriousness or depth of attack.

Analyzed Simulated Results

Among the numerous equivalent circuits that have been used to describe electrochemical interfaces, only a few really apply in the context of a freely corroding interface at or close to a kinetic equilibrium. These have recently been reviewed [*11,31,40*] and discussed in detail. Additionally, a circuit that was used to model the impedance of the pitting process of aluminum-based materials [*41,42*] will be considered here.

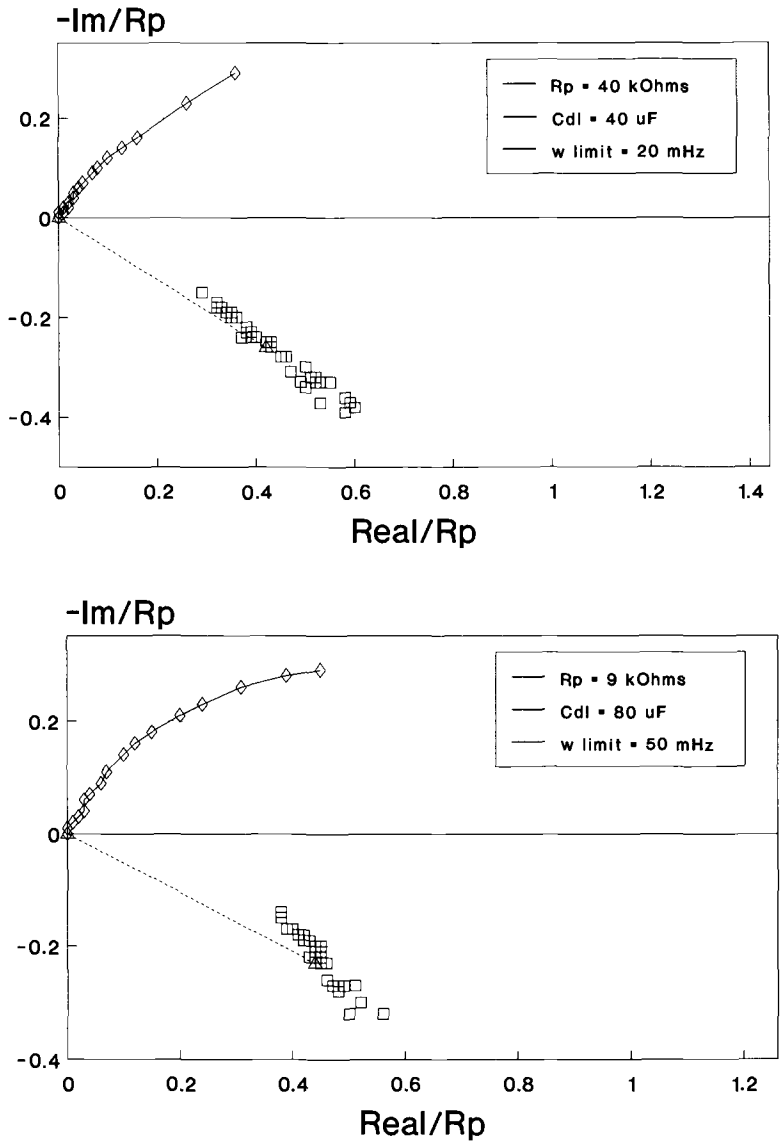

FIG. 7—*Normalized impedance diagrams made with a five-day prepassivated 70-30 Cu-Ni alloy containing 2.1% chromium and exposed to a 3% NaCl aerated solution:* (a) *in a quiescent condition;* (b) *after 8 h of rotation at 5000 rpm.*

Beside the simple circuit assumed by the geometrical extrapolation method, another circuit (Fig. 5*b*), commonly used to model the impedance of coated materials, would generate nearly perfect arcs [*43*] when presented in the Nyquist fashion.

On the other hand, the circuit represented in Fig. 5*c* contains a diffusion limited component [*40,44*] that can greatly affect the appearance of EIS plots (Fig. 12). The impedance ($Z(\omega)$) of the diffusion limited or Warburg component in this circuit can be described in a

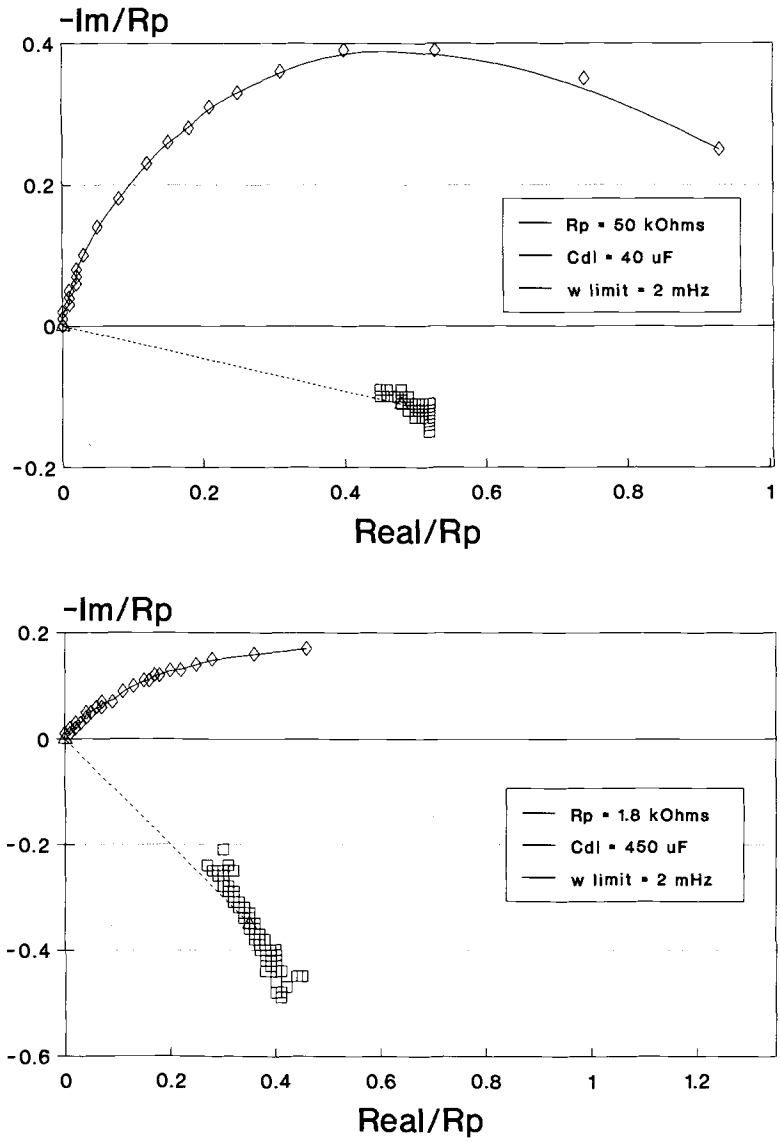

FIG. 8—*Normalized impedance diagrams made with C-steel specimens exposed to a deaerated 1.2% Na molybdate solution for 6 days before adding 3% NaCl (day 7) and air (day 10):* (a) *on day 6;* (b) *on day 14.*

simplistic fashion using Eq 6, where ω is the probing frequency, and R and C the resistance and capacitance associated with the distributed R-C line of infinite length.

$$Z(\omega) = (\text{Factor} \times R/C)^{0.5} \times \omega^{-0.5} \tag{6}$$

The Nyquist plots of Fig. 5*b* were obtained by giving R and C the values associated with

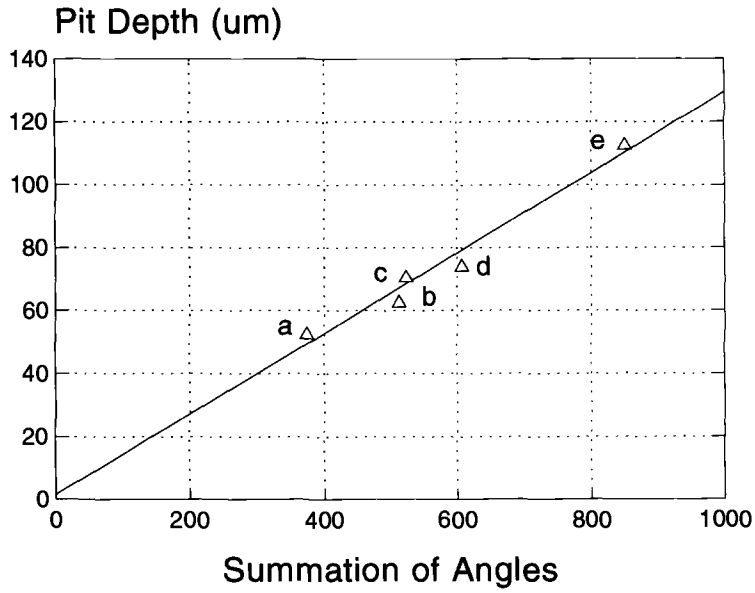

FIG. 9—*Summation of calculated depression angles as a function of measured deepest pit depths for steel specimens exposed during:* (a) *20 days in a 3% NaCl deaerated solution (2 h air intake);* (b) *35 days in a 1.2% Na molybdate solution (continuous air intake day 9, 3% NaCl day 22);* (c) *17 days in a 1.2% Na molybdate solution (3% NaCl day 7, continuous air intake day 9);* (d) *21 days in a 1.2% Na molybdate solution (12% NaCl day 6, continuous air intake day 12);* (e) *26 days in 1.9% K chromate solution (12% NaCl day 4, continuous air intake day 15).*

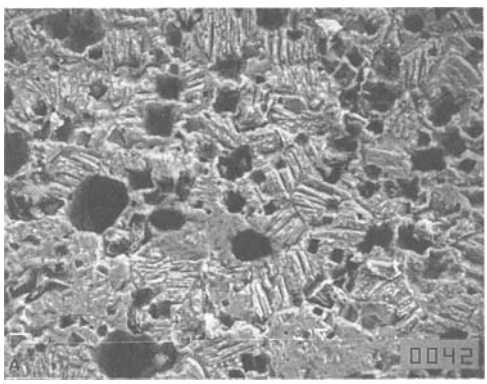

FIG. 10—*SEM micrographs (×750) of steel specimens exposed for 20 days to an aerated solution containing:* (a) *2M (12%) NaCl,* (b) *2M NaCl + 0.1 M K chromate, and* (c) *2M NaCl + 0.1M Na molybdate.*

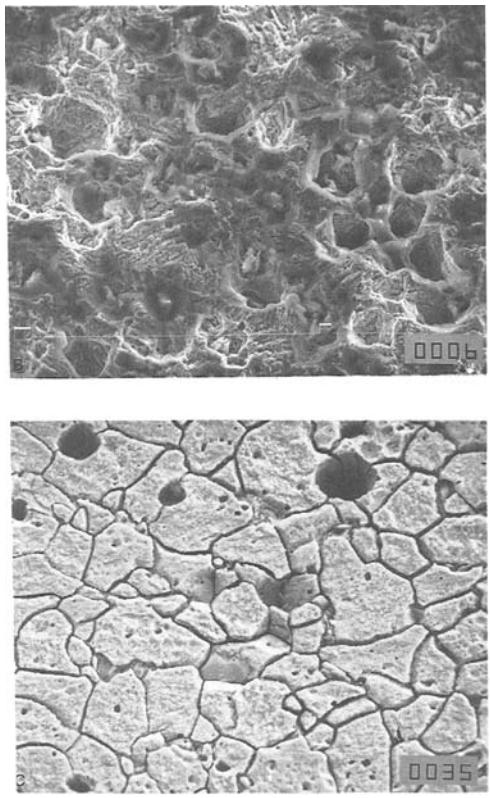

FIG. 10—(continued)

R_p and C_{dl} while changing the coefficient (Factor) multiplying the ratio of these components. The synthetic data were then analyzed with the geometric extrapolation technique which also produced the results presented in the legend (Fig. 12).

The presence of a Warburg component tends to produce the tailing patterns associated with many of the experimental data. But its presence does not by itself create the depression angle commonly associated with real data nor does it hinder excessively the calculation of both R_p and C_{dl}. With a Factor as high as 30% the difference between R_p and C_{dl} calculated with the geometric projection method and the values used for the simulation of this circuit is only 20% in the case of R_p and nil in the case of C_{dl} (legend, Fig. 12*a*).

This good agreement between the values used in the simulation and those calculated with the projection technique disappeared when the model proposed by Mansfeld and coauthors [*41,42*] to represent the pitting process of aluminum-based materials (Fig. 5*d*) was used and the resulting synthetic data analyzed (Fig. 13). The main reason for the discrepancy between the simulated and calculated values of R_p and C_{dl} (or C_p in this case) is surely the very low value given to R_{pit} in this model. Since the pitting surface is, in this model, considered to be a circuit in parallel to the rest of the exposed metallic surface, such a low value would dominate the impedance characteristic of EIS measurements as a function of the ratio (F) of pitted to nonpitted surface area.

The patterns produced during the analysis of these synthetic data (Fig. 13) contained the tailing and depression angle obtained with real data. But in no case were the high angles

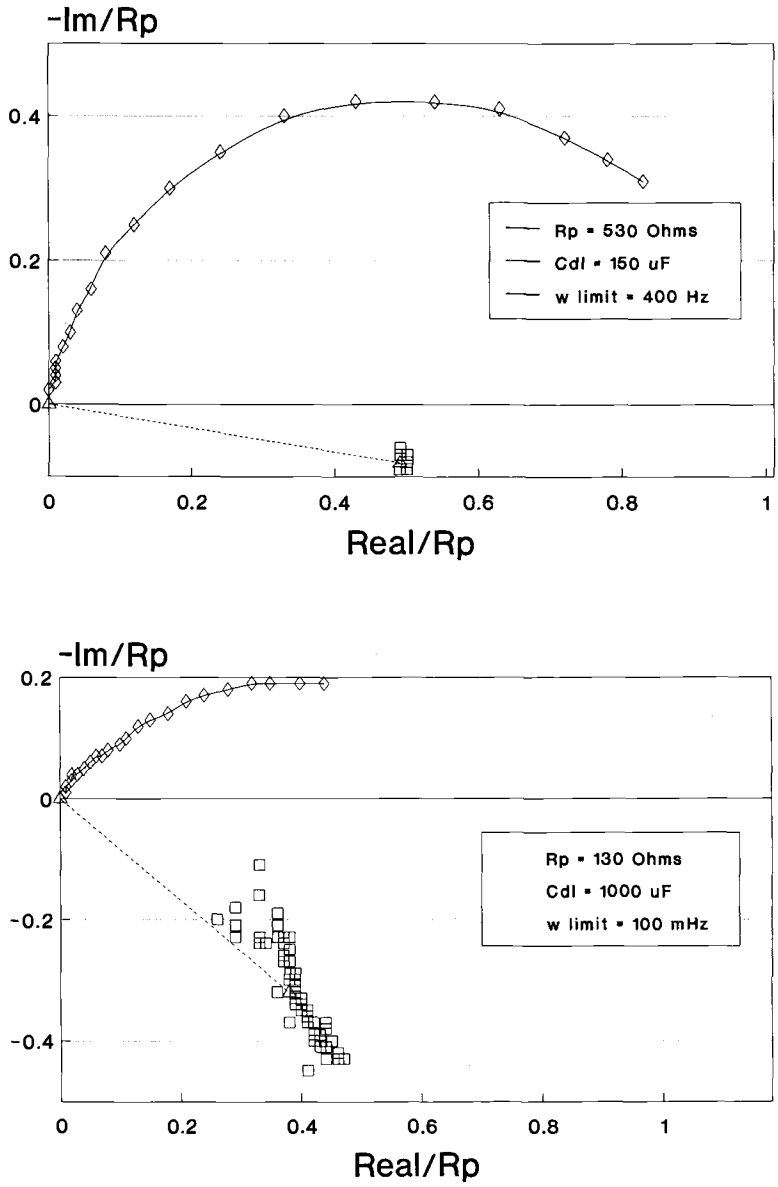

FIG. 11—*Normalized impedance diagrams made with long transverse edge specimens exposed for 13 days in an aerated 3% NaCl solution:* (a) *8090-T8 Al-Li and* (b) *7075-T6 Al.*

observed for obviously pitting systems reproduced with such a model. The highest depression angle was obtained when an F corresponding to 50% of the surface was used in the simulation. The tailing patterns obtained with this model also contained a curvature that is absent of the tailing patterns produced with experimental pitting systems (Fig. 7, Fig. 8*c*, and Fig. 11*b*).

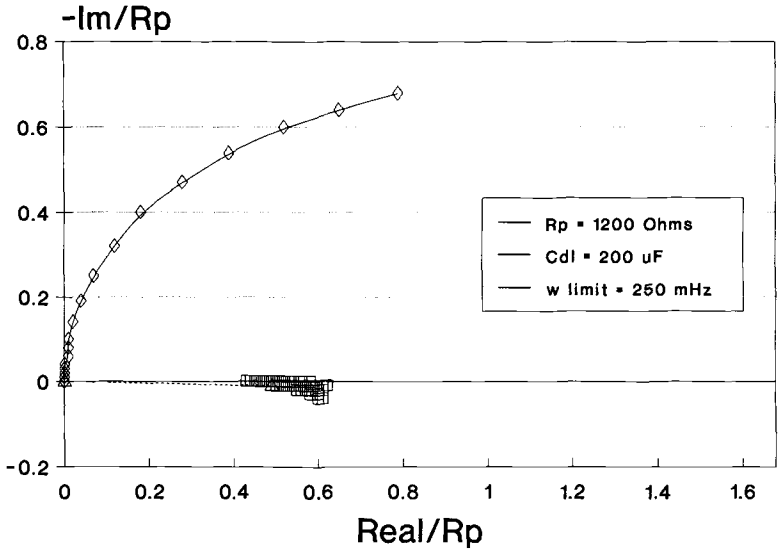

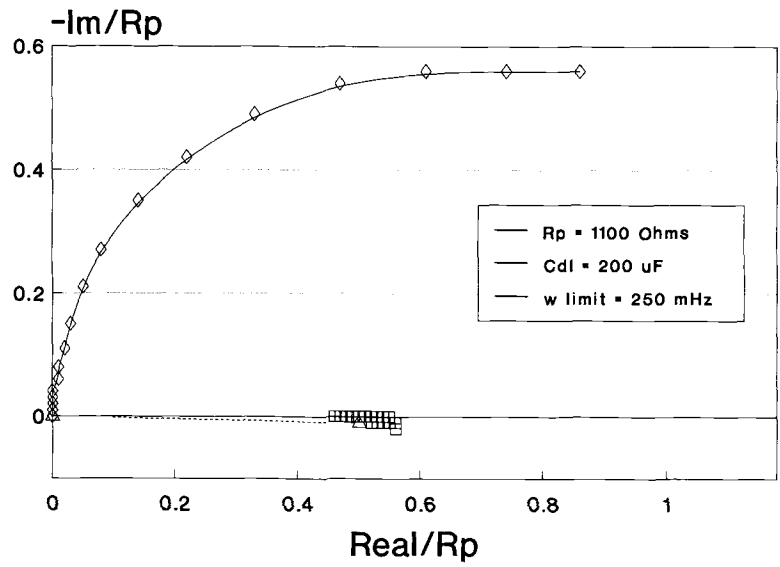

FIG. 12—*Simulated results obtained with the circuit of Fig.* 5c (R_p = *1000* Ω, C_{dl} = *200* μF*; Factor of* (a) *30%* (b) *10%;* (c) *1%.*

Conclusion

The patterns typically produced during the analysis of experimental EIS results by the geometric extrapolation technique could only be partly reproduced when synthetic data were analyzed. Since a prerequisite to use EIS with confidence for corrosion studies and monitoring is the development of appropriate models which could explain the observed EIS spectra this would indicate that a few improvements are still desired. One om-

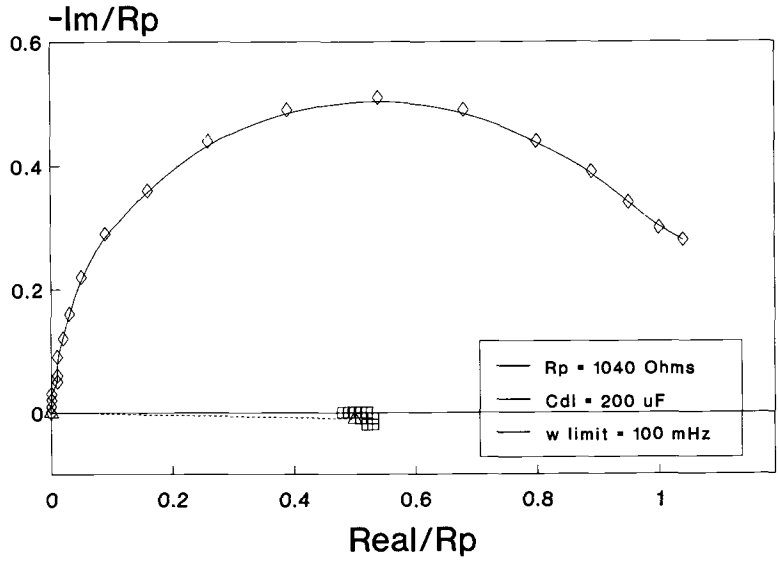

FIG. 12—(continued)

nipresent characteristic of these spectra that really has to be addressed properly in terms of its significance in corrosion is the CPE or angle of tilt of Nyquist plots.

The unavoidable crystallographic heterogeneity of a rough surface severely restricts the range of validity of any model describing its electrochemical behavior. Microscopic roughening of the solid surface provides an additional complication that can only be

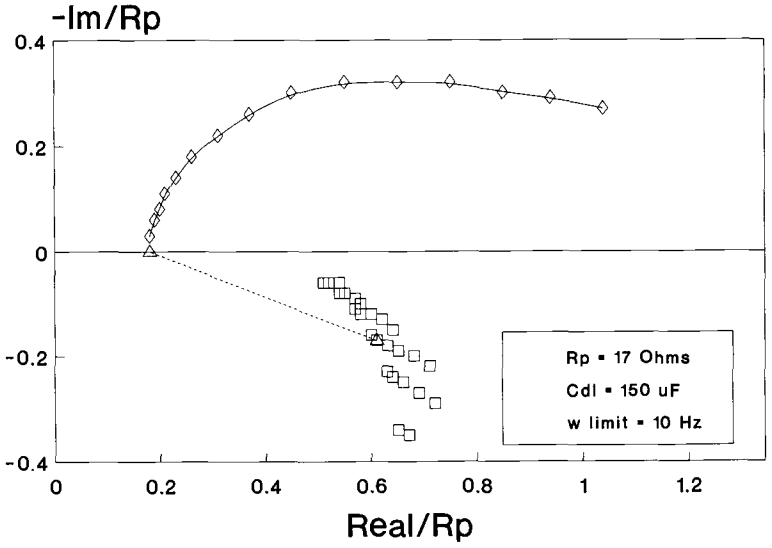

FIG. 13—*Simulated results obtained with the circuit of Fig.* 5d (R_p = *1000* Ω, C_p = *200* μF, R_{pit} = *2.5* Ω, C_{pit} = *80* mF)*; Factor of* (a) *50%;* (b) *5%;* (c) *0.5%.*

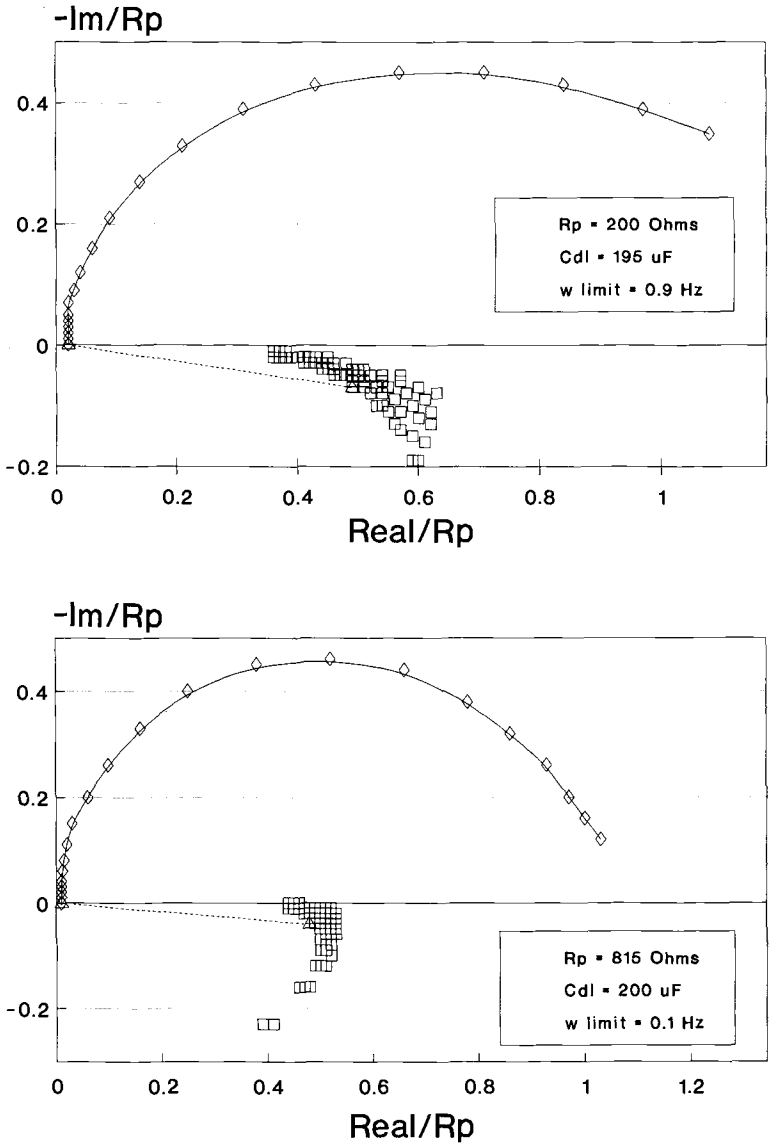

FIG. 13—(continued)

addressed by using complex models with fractal geometries [*45,46*]. But on a practical level the relation between the absolute value of this CPE and the extent of localized corrosion attack could be of great value for monitoring purposes provided proper calibration are performed.

References

[*1*] Zeller III, R. L. and Savinell, R. F., *Corrosion Science,* Vol. 26, No. 8, 1986, pp. 591–599.

[2] Epelboin, I., Keddam, M., and Takenouti, H., *Journal of Applied Electrochemistry*, Vol. 2, 1972, pp. 71–79.
[3] Mansfeld, F., Kendig, M., and Tsai, S., *Corrosion Science*, Vol. 22, No. 5, 1982, pp. 455–471.
[4] Bonnel, A., Dabosi, F., Deslouis, C., Duprat, M., Keddam, M., and Tribollet, B., *Journal of the Electrochemical Society*, Vol. 130, No. 4, April 1983, pp. 753–766.
[5] Duprat, M. and Dabosi, F., *Proceedings of the 9th International Congress on Metallic Corrosion*, Toronto, Canada, Vol. 4, June 3–7, 1984, pp. 104–409.
[6] Mansfeld, F., Kendig, M. W., and Lorenz, W. J., *Journal of the Electrochemical Society*, Vol. 132, No. 2, 1985, pp. 290–296.
[7] Sekine, I., Ohkawa, H., and Handa, T., *Corrosion Science*, Vol. 22, No. 12, 1982, pp. 1113–1123.
[8] Rothwell, A. N., Walsh, T. G., and Cox, W. M., *CORROSION/91*, Paper 170, National Association of Corrosion Engineers, Houston, TX, 1991.
[9] Lorenz, W. J. and Mansfeld, F., *Corrosion Science*, Vol. 21, No. 9–10, 1981, pp. 647–672.
[10] Roberge, P. R. and Beaudoin, R., *Journal of Applied Electrochemistry*, Vol. 18, 1988, pp. 38–42.
[11] Silverman, D. C. and Carrico, J. E., *Corrosion*, Vol. 44, No. 5, May 1988, pp. 280–287.
[12] Epelboin, I. and Keddam, M., *Journal of the Electrochemical Society*, Vol. 117, 1970, pp. 1052–1061.
[13] Roberge, P. R., "Analyzing Electrochemical Impedance Corrosion Measurements by the Systematic Permutation of Data Points," *Computer Modeling in Corrosion, ASTM STP 1154*, R. S. Munn, Ed., American Society for Testing and Materials, Philadelphia, 1992.
[14] Cole, K. S. and Cole, R. H., *Journal of Chemical Physics*, Vol. 9, April 1941, pp. 341–351.
[15] Davidson, D. W. and Cole, R. H., *Journal of Chemical Physics*, Vol. 19, December 1951, pp. 1484–1490.
[16] Jonscher, A. K., "Dielectric Relaxation in Solids," Chelsea Dielectrics Press, London, U.K., 1983.
[17] Kendig, M. W., Meyer, E. M., Lindberg, G., and Mansfeld, F., *Corrosion Science*, Vol. 23, 1983, pp. 1007–1016.
[18] De Levie, R., *Electrochimica Acta*, Vol. 10, 1965, pp. 113–122.
[19] Bottelbergs, P. H. and Broers, G. H. J., *Journal of Electroanalytical Chemistry*, Vol. 72, 1976, pp. 257–266.
[20] Bates, J. B., Wang, J. C., and Chu, Y. T., *Solid State Ionics*, Vols. 18 & 19, 1986, pp. 1045–1054.
[21] Roberge, P. R. and Beaudoin, R., *Journal of Applied Electrochemistry*, Vol. 18, 1988, pp. 601–607.
[22] Roberge, P. R. and Halliop, E., *CORROSION/90*, Paper 15, National Association of Corrosion Engineers, Houston, TX, 1990.
[23] Roberge, P. R., Halliop, E., Asplund, M., and Sastri, V. S., *Journal of Applied Electrochemistry*, Vol. 20, 1990, pp. 1004–1008.
[24] Roberge, P. R., Halliop, E., and Sastri, V. S., "Monitoring Localized Corrosion in Sour Media," Paper 216, *Proceedings of the 11th International Corrosion Congress*, Florence, Italy, April 2–6, 1990.
[25] Roberge, P. R., Sastri, V. S., and Maxwell, V., "Electrochemical Studies of Mild Steel in Sodium Chloride Solutions Containing Inorganic Inhibitors," *CANMET Report MTL 90-65 (TR)*, Energy, Mines & Resources, Ottawa, Canada, 1991.
[26] Roberge, P. R., Halliop, E., and Sastri, V. S., "A Study of Passivation/Depassivation of Carbon Steel: Electrochemical Impedance Spectroscopy vs Potential Noise Fluctuations," *Proceedings of the 4th International Symposium on Electrochemical Methods in Corrosion Research*, Espoo, Finland, July 1–4, 1991.
[27] Roberge, P. R., Sastri, V. S., and Maxwell, V., "Electrochemical Evaluation of Inhibitors in Sour Media," *CANMET Report MTL 90-68 (TR)*, Energy, Mines & Resources, Ottawa, Canada, 1991.
[28] Lenard, D. R., Moores, J. G., Roberge, P. R., and Halliop, E., "Maine Corrosion of Aluminum-Lithium Alloy Steel," *TTCP-P-TP1 Report*, Defence Research Establishment Pacific, Victoria, B.C., Canada, 1991.
[29] Roberge, P. R., Halliop, E., and Yousri, S., "Potentiodynamic Polarization and Electrochemical Impedance Spectroscopy for the Statistical Process Control of Aluminum Anodizing," *Electrochemical Impedance: Analysis and Interpretation, ASTM STP 1188*, J. R. Scully, D. C. Silverman, and M. W. Kendig, Eds., American Society for Testing and Materials, Philadelphia, 1993 (this publication).
[30] Roberge, P. R., Halliop, E., and Sastri, V. S., *Corrosion*, June 1992, in press.

[31] Silverman, D. C., *CORROSION/90*, Paper 135, National Association of Corrosion Engineers, Houston, TX, 1990.
[32] *Impedance Spectroscopy*, J. R. MacDonald, Ed., John Wiley & Sons, New York, 1987.
[33] Hladky, K., Callow, L. M., and Dawson, J. L., *British Corrosion Journal*, Vol. 15, No. 1, 1980, pp. 20–25.
[34] Lane, P. L., "An AC-Impedance Study of Corrosion Inhibitors for Aluminum Alloys," *Technical Report 87046*, Royal Aircraft Establishment, Farnborough, U.K., 1987.
[35] Hitzig, J., Juttner, J., Lorenz, W. T., and Paatsch, *Corrosion Science*, Vol. 24, No. 11/12, 1984, p. 945.
[36] Hitzig, J., Juttner, K., Lorenz, W. J., and Paatsch, W., *Journal of Electrochemical Society*, Vol. 133, No. 5, 1986, p. 887.
[37] Mansfeld, F., *Corrosion*, Vol. 44, No. 12, 1988, pp. 856–868.
[38] Walker, C. K. and Maddux, G. C., *Corrosion*, Vol. 45, No. 10, 1989, pp. 847–852.
[39] Patton, C. C., *Oilfield Water Systems*, Campbell Petroleum Series, Norman, OK, 1981.
[40] Silverman, D. C., *Corrosion*, Vol. 46, No. 7, 1990, pp. 589–598.
[41] Mansfeld, F., Lin, S., Kim, S., and Shih, H., *Journal of the Electrochemical Society*, Vol. 137, No. 1, 1990, pp. 78–82.
[42] Mansfeld, F., Lin, S., Kim, S., and Shih, H., *Werkstoffe und Korrosion*, Vol. 39, 1988, pp. 487–492.
[43] Mansfeld, F., *Corrosion*, Vol. 44, No. 8, 1988, pp. 558–559.
[44] Dawson, J. L. and John, D. C., *Journal of Electroanalytical Chemistry*, Vol. 110, 1980, p. 37.
[45] Keddam, M. and Takenouti, H., *Electrochimica Acta*, Vol. 33, No. 3, 1988, pp. 445–448.
[46] De Levie, R., *Journal of Electroanalytical Chemistry*, Vol. 281, 1990, pp. 1–21.

Kevin C. Stewart,[1] *David G. Kolman,*[1] *and S. Ray Taylor*[2]

The Effect of Parasitic Conduction Pathways on EIS Measurements in Low Conductivity Media

REFERENCE: Stewart, K. C., Kolman, D. G., and Taylor, S. R., **"The Effect of Parasitic Conduction Pathways on EIS Measurements in Low Conductivity Media,"** *Electrochemical Impedance: Analysis and Interpretation, ASTM STP 1188,* J. R. Scully, D. C. Silverman, and M. W. Kendig, Eds., American Society for Testing and Materials, Philadelphia, 1993, pp. 73–93.

ABSTRACT: Artifacts are ubiquitous to electrochemical impedance measurements at sufficiently high frequency. These artifacts, which are exacerbated by low conductivity solutions, can arise from the measurement electronics, the reference electrode, the electrical leads, or the electrochemical cell, or a combination thereof. This study has systematically examined the factors that may contribute to the occurrence of artifacts in low conductivity media. The frequency regime over which artifacts exist was identified for steel in lake water. The value and occurrence of the solution resistance was identified by adjusting the conductivity and comparing the results with calculated values. Possible contributions from the frequency response analyzer, potentiostat, reference electrode, and cell geometry were studied using a series of test resistors. The major contributors to artifacts appear to arise from the potentiostat and associated leads, and the ratio of the resistances between the working and reference and the reference and counter electrodes in the electrochemical cell. The problem of fitting complex spectra was approached by combining nodal analysis with simplex fitting. A model was determined that accurately reproduces the spectra for a set of current measuring resistors used in the voltage-drop configuration for two electrode measurements using a particular make of potentiostat.

KEYWORDS: impedance, artifacts, low conductivity, equivalent circuit, modeling

In the application of impedance spectroscopy to electrochemical systems, it is tacitly assumed that the high-frequency limit is the electrolyte resistance. Application of network analysis or transfer function theory to any interfacial model will invariably bear out this conclusion. In practice, however, electrochemists and corrosion scientists realize that there is typically an upper frequency limit, beyond which the high-frequency impedance data are corrupted by one or more factors. High-frequency artifact is often attributed to additional time constants associated with the reference electrode [*1*], the Luggin capillary [*2*], limitations of the potentiostat [*1,3*], poor cell design [*4*], cell geometry, electrical leads, and connectors [*5–10*]. Other sources proposed for high-frequency artifact are viscoelastic properties of the electrolyte [*11*] and surface porosity [*12–14*]; however, these latter theories are less widely supported and have been argued [*15*]. Although many of these explanations have resulted in methods for minimizing high-frequency measurement error in electrolytes having good conductivity, artifacts remain, making it common practice among experimentalists to ignore impedance data above frequencies of approximately 10^4

[1]Graduate research assistants and [2]research assistant professor, respectively, Center for Electrochemical Science and Engineering, University of Virginia, Charlottesville, VA 22903.

to 10^5 Hz to eliminate risk of interpretational error. If the solution resistance has been identified within the spectrum, deletion of higher frequency data is certainly justifiable. However, it may be unsafe to assume that lower frequency interfacial data are uncorrupted by the factors that caused the high-frequency artifacts.

Recently, these authors and others have observed that application of electrochemical impedance spectroscopy (EIS) to low-conductivity solutions such as lake water [*16*], glacial acetic acid [*17*], and polyamic acid, significantly decreases the frequency at which "high frequency" artifacts begin. In these cases, the solution resistance may not be observed with adequate fidelity until frequencies as low as 10 to 100 Hz are reached. The impedance data from 65 kHz (or higher) to 100 Hz may take the form of a high-frequency capacitive arc followed by a low-frequency inductive arc or several capacitive arcs connected with loops. This can be disconcerting to the adventuring experimentalist, who upon first observation may misinterpret artifacts as interfacial properties (e.g., oxide characteristics, polarization resistance) because they occur in frequency regimes where interfacial properties are expected. Of even more concern is the possibility that the resulting artifact can obscure altogether the behavior of the electrochemical interface under study. Hence, it is of great interest to determine the source of these errors and eliminate them from the measurement.

Previous investigators have attributed artifacts observed in low-conductivity electrolytes to parasitic conduction paths within the electrochemical cell and measurement system [*17,18*]. Receiving most interest have been parasitic pathways produced by the stray capacitances between the reference and working electrode and the reference and counter electrode, as well as the stray capacitance associated with the current measuring resistor. Although the proposed circuit models have adequately simulated the high-frequency artifact observed for stainless steel in glacial acetic acid [*17*], this laboratory has found that they do not adequately explain impedance data observed for steel in fresh lake water. Because of the importance of understanding the corrosion behavior of steel in fresh waters and the ubiquity of high-frequency artifact, it is the long-term objective of this research to determine a more universal model which can account for all low-conductivity environments. The motivation for this work is based on the belief that the source of the artifacts extends beyond the electrochemical cell and reference electrode, but must also include the electronics within the potentiostat.

Although it may seem logical to just ignore data above some critical frequency, it is quite possible that the circuitry responsible for the artifact may contribute to the spectra in the frequency range pertaining to the interface under study, and in some cases totally mask it [*19*]. The objective of this study is to develop an appropriate model for the combined stray current paths within the cell and the measuring electronics, so that their contribution to the impedance can be deconvoluted from the total spectra. This will in theory provide a means to extract a concise description of the interfacial impedance from which an accurate assessment of corrosion rates, etc. can be made.

In the case of low-conductivity electrolytes there are three perceived variables that contribute to high-frequency impedance artifact that must be accounted for: the measurement electronics, the electrochemical cell (including geometry, reference electrode, wiring, and connections), and the solution resistance. This paper has examined all three of these variables individually within two phases of experimentation. Because experimentation with steel in fresh lake water was the impetus for this project, the first phase of research examined the effect of changing solution conductivity for this system, holding all other variables constant. The second phase of experiments that will be presented examines the contribution of the electronics, and to some extent, cell geometry, by examining and modeling the artifacts observed for a range of precision resistors. By using a resistor for the test cell, issues related to stray pathways within the cell (other than the stray capaci-

tance associated with the resistor) can be ignored, thus allowing an examination of the contribution of the electronics, wiring, and connections. In this second phase of investigation, a powerful algorithm which fits impedance data to complex ladder networks is introduced. It should be noted, however, that the circuit presently used only incorporates a two-electrode measurement. This model is an initial step in detailing the response of the electronics, including three-electrode measurements, as most laboratory measurements use a three-electrode configuration.

The goal of this study is to generate a universal model that can be used to extract artifactual data from impedance spectra corrupted by artifacts. The intention of this study is not to analyze one particular brand of instrument because artifacts are inherent to instruments of all makes. This study currently addresses only one particular make of instrumentation; however, it is believed that much of the instrument modeling can be extrapolated to other brands with slight modifications. These modifications will be the origin of future work.

Part I. The Effects of Changing Solution Conductivity

Experimental Methods

Mild carbon (A36) steel cylindrical electrodes (1.9 cm by 0.9 cm diameter) were dry polished to a 600 grit SiC finish, followed by ultrasonic cleaning in hexane. The test cell consisted of the steel cylindrical electrode, a concentric cylindrical platinized niobium mesh counter electrode, and a saturated calomel reference electrode (SCE) in a glass well possessing a Luggin capillary. All experiments were performed under nonflowing conditions, in aerated solution. It should be noted that experiments performed with a silver wire reference electrode inserted into the glass well in place of the SCE yielded identical results. Because of the similarity, the experiments comprising the silver wire are not shown.

EIS measurements were performed with a Schlumberger 1286 potentiostat and a model 1255 frequency response analyzer (FRA). All impedance scans were run in a three-electrode configuration at the open circuit potential using potentiostatic control and a 10 mV rms ac voltage signal. All data were integrated over ten cycles and the current measuring resistor was optimized for each measurement using the autorange feature in ZPLOT software.

Lake water was obtained from Lake Anna in Mineral, Virginia. The lake water had a resistivity of approximately 19 000 Ω-cm with the ionic content shown in Table 1. Solution resistivity was decreased by the addition of KCl and $NaMoO_4$ and increased by the addition of distilled deionized water (resistivity = 18 MΩ-cm). Solution resistivities (conductivities) were measured with a YSI 32 conductance meter.

TABLE 1—*Summary of ion content of water obtained from Lake Anna as determined by ion chromatography.*

Anion	Composition, ppm
Sulfate (SO_4^{2-})	8.1
Chloride (Cl^-)	4.1
Nitrate (NO_2^-)	2.1
Phosphate (PO_4^{2-})	<1
Fluoride (F^-)	0.32

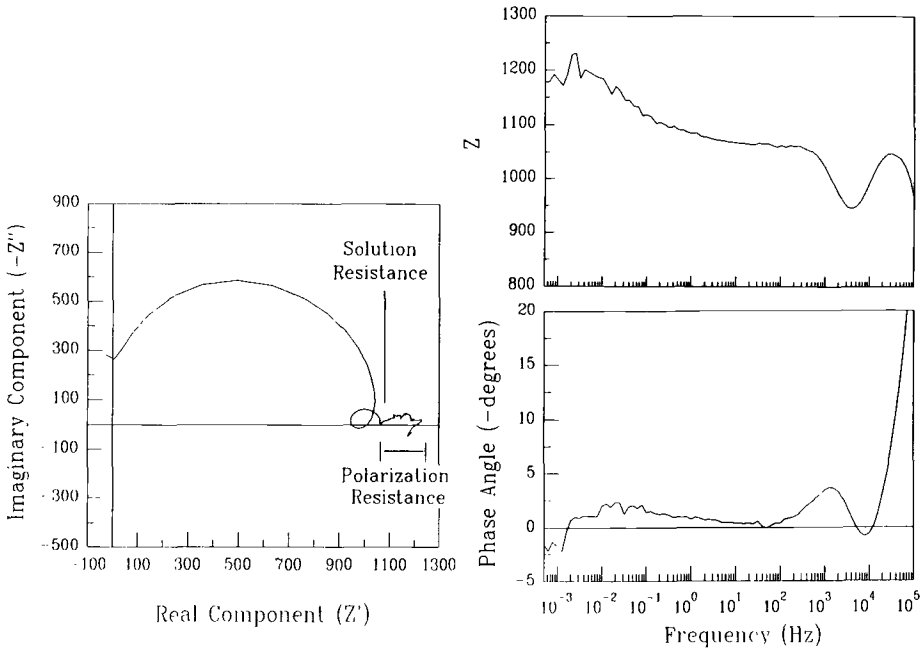

FIG. 1—*Impedance spectrum of A36 steel exposed to lake water, scanned from 1 MHz to 0.5 mHz.*

Results and Discussion

A resulting impedance spectrum for A36 steel in lake water is shown in Fig. 1. The spectrum was measured from 1 MHz to 0.5 mHz and is uncorrected for specimen area (5.32 cm). Three capacitive arcs and one inductive arc can be seen. Upon initial inspection, it is not clear how to analyze the data to determine the solution resistance, much less the interfacial behavior. It is clear, however, that artifacts are present as evidenced by the negative real behavior displayed at approximately 1 MHz. Thus, there is a need to perform additional experiments that can assist in the deconvolution of the spectra so that interfacial behavior is revealed.

Although the conductivity of a solution can be increased by the addition of a supporting electrolyte, the supporting ions may alter the interfacial phenomena that are of interest. However, low conductivity is not the only source of artifacts in an impedance spectrum. Both the electronic instrumentation and the cell geometry also contribute to artifacts in an impedance spectrum. It is of interest, therefore, to vary some or all of these three primary components to delineate the frequency range over which they contribute to the impedance spectrum. Ideally, it is of interest to vary only one of the contributors while holding the other two constant in order to reveal the effect of each singular contribution on the artifacts as a whole.

The ability to vary each of the three primary contributors (the electronics, the cell, and the solution resistivity) to the artifacts can be limited. The electronics generally may be considered fixed, with the only controlled variations arising from the selection of a current measuring resistor. Varying the geometry of the cell may be somewhat easier. Previous research has detailed the effects of changing the position of the reference electrode with respect to the working electrode [*17,19,20*]. This allows control of the magnitudes of the

solution resistance both between the reference and working electrodes (R_s) and between the counter and reference electrodes (R'_s). Unfortunately, as these parameters are changed, artifacts arising from other effects may occur, such as screening of the working electrode by the reference electrode [*20*]. The values of R_s and R'_s that may be examined, therefore, are limited to a narrow range, wherein it can be assumed that changes in the spectrum are arising solely from changing R_s and R'_s. Another drawback of this method is that for a given cell and test solution, (R_s + R'_s) is constant so each may not be varied independently when moving the reference electrode. Therefore, in order to examine a wide range of solution resistances, the resistivity of the solution must be changed.

Sets of experiments using a change in solution resistivity have been performed in order to better understand the impedance spectrum of Fig. 1. The solution resistivity was changed in three different manners in order to discern the scope of the artifacts and extract the interfacial behavior. The first set of experiments involved the addition of KCl to the solution in varying amounts. The results of these experiments may be seen in Fig. 2, a set of spectra scanned from 1 MHz to 1 Hz (the low-frequency capacitive loop seen in Fig. 1 is not shown in these spectra). It is seen that as the solution resistivity decreases, there is a decrease in size of the intermediate-frequency loop, which initially shows inductive behavior, but then becomes capacitive, disappearing altogether at the lowest solution resistivity. The size of the high-frequency capacitive arc is seen to decrease with decreasing resistivity. Additionally, as the solution resistivity is decreased, the high-frequency arc (see also Fig. 3) is seen to intersect the intermediate frequency capacitive arc at continually lower impedances relative to the intermediate-frequency arc. This continues until, at the lowest resistivities, the high-frequency arc no longer intersects the intermediate arc, and the loop disappears.

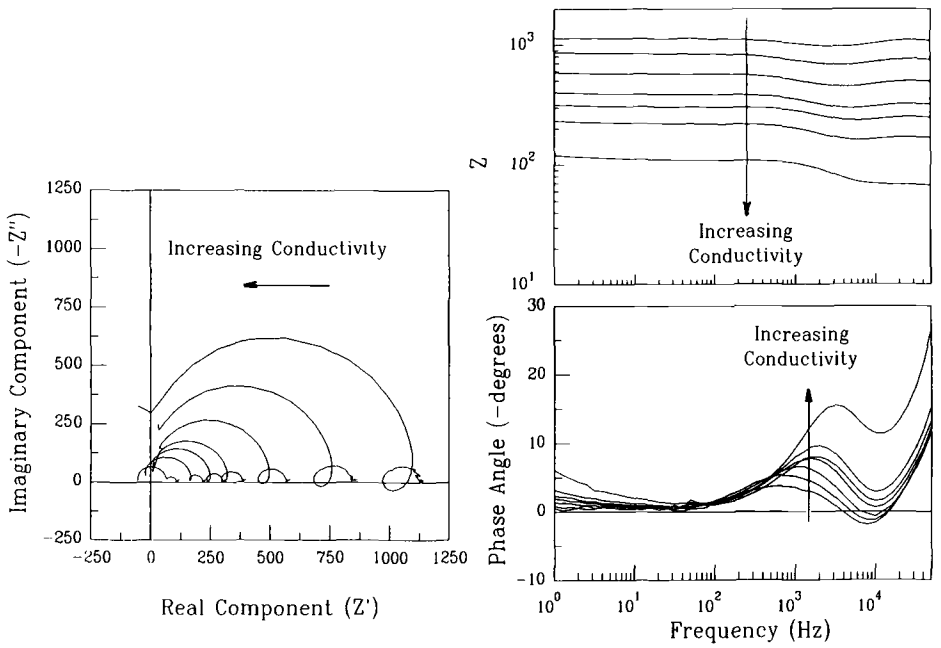

FIG. 2—*Impedance spectra for A36 steel exposed to lake water with different solution resistivities resulting from the addition of KCl. Solution resistivities and resistances of experiments A–G are given in Table 2.*

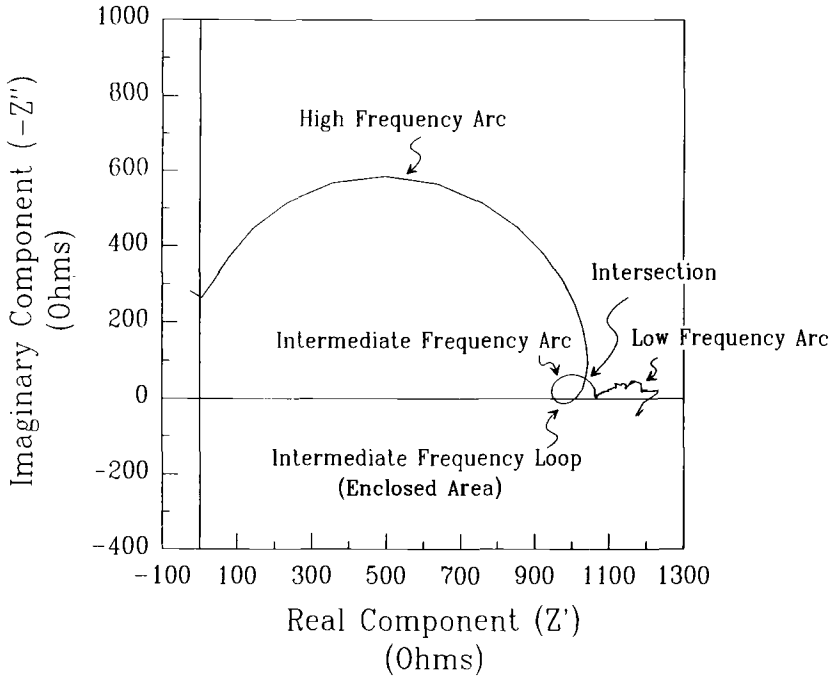

FIG. 3—*Labelled Nyquist plot of impedance spectrum of Fig. 1.*

It was hypothesized that the solution resistance was the real component of impedance in the 1 to 100 Hz region, because at low resistivities this is the only region in which $Z'' \rightarrow 0$. Support of this hypothesis may be found from simple calculations. It is known that

$$\rho(\Omega - cm) = R_s(\Omega)X(cm) \tag{1}$$

where ρ is the solution resistivity and X is the cell constant. X is constant because the geometry of the cell is fixed for a given set of experiments, therefore the ratio of the resistivity of the solution to the measured solution resistance should be constant. That is,

$$X = \frac{\rho}{R_s} = \text{Constant} \tag{2}$$

Table 2 shows the results of the calculations for each experiment, wherein ρ was measured with a conductivity probe and R_s was obtained from the spectra as the real component of

TABLE 2—*Summary of the measured resistivities, measured solution resistances and calculated cell constants of the spectra of Fig. 2. The average cell constant is 15.6 cm and the standard deviation is 0.755 cm.*

	A	B	C	D	E	F	G
ρ (kΩ-cm)	19.5	13.6	8.83	6.20	4.95	3.61	1.76
R_s (Ω)	1140	865	585	400	317	233	121
X (cm)	17.1	15.7	15.1	15.5	15.6	15.5	14.6

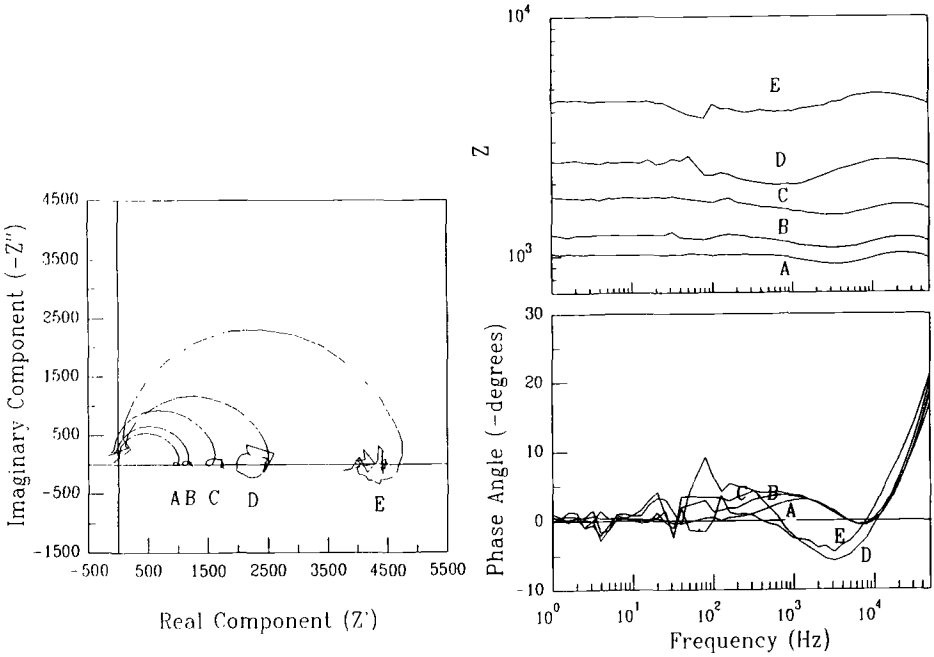

FIG. 4—*Impedance spectra for A36 steel exposed to lake water with different solution resistivities resulting from the dilution of the lake water with distilled deionized water. Solution resistivities and resistances of experiments A–E are given in Table 3.*

the impedance in the 1 to 100 Hz region. It may be seen that the cell constant is indeed approximately equal for each experiment, supporting the hypothesis. Further support for the hypothesis arises from a qualitative observation. It can be seen from the Bode angle plot, that although the phase angle (and hence Z'') approaches zero at three separate places in the spectrum, it is only in the 1 to 100 Hz region where the phase angle is approximately zero over a relatively wide range of frequencies, which is indicative of a resistive element. In the high-frequency region, Z'' (and the phase angle) approaches zero at two (or more) separate frequencies. As the resistivity is reduced, the phase angle becomes further removed from zero at frequencies above 100 Hz. It may be reasoned that because the phase angle behavior of the spectrum in the 1 to 100 Hz region is unchanged with changing solution resistivity, the approach of the phase angle (and Z'') to zero in this region is indeed an expression of the solution resistance. Because the higher frequency data are affected by changes in the solution conductivity, it is reasoned that the behavior above 100 Hz is caused in part by low solution conductivity.

A second set of experiments supported this result. In this set of experiments, the lake water was diluted with distilled, deionized water. Therefore, the ion concentrations were all changed equally in these experiments, without the addition of foreign elements. It is seen from Fig. 4 that as the resistivity is increased by increased dilution, the spectra change in a manner consistent with that seen in the experiments comprising the addition of KCl. It is seen that the size of the high-frequency arc increases with increasing resistivity. As before, the cell constants were computed for these experiments and are shown in Table 3. It is seen that, although the data are noisy at the lower frequencies, the cell constants

TABLE 3—*Summary of the measured resistivities, measured solution resistances, and calculated cell constants of the spectra of Fig. 4. The average cell constant is 19.0 cm and the standard deviation is 0.713 cm.*

	A	B	C	D	E
ρ (kΩ-cm)	78.1	47.6	32.8	24.0	20.0
R_s (Ω)	4370	2470	1750	1220	1030
X (cm)	19.5	19.6	18.7	19.3	17.9

are approximately equal and, again, the hypothesis that the solution resistance lies in the 1 to 100 Hz region may be supported.

A change in the solution resistivity may result in more than a variation of R_s and R'_s. The addition or deletion of aggressive anions such as chloride can also change double layer and Faradaic processes. The concentration change, therefore, causes many parameters to vary. In the case of the addition of chloride, it would be expected that the polarization resistance would decrease with increasing chloride concentration. The data above 100 Hz that have been hypothesized to be artifactual also shrink with increasing chloride concentration. Therefore, it may be argued that because the high-frequency data shrink with increasing chloride concentration, the high-frequency data may not be solely artifactual but may also include the polarization resistance. Thus, a third set of experiments was performed using additions of sodium molybdate to the solution. It is known that the molybdate ion is a corrosion inhibitor for steel in neutral water [*16,21,22*]. Therefore, addition of molybdate should decrease R_s and increase the polarization resistance of the steel. A resulting decrease in the magnitude of the high-frequency data coupled with an increase in the magnitude of the low-frequency data would further support the hypothesis that the data above 100 Hz is artifactual while that below 100 Hz is interfacial.

Figure 5 shows the results of experiments involving the addition of sodium molybdate. Sodium molybdate was added in sufficient concentrations to achieve resistivities comparable to the KCl experiments (see Table 4). It may be seen that for essentially equivalent resistivities, the high-frequency behavior of the steel exposed to sodium molybdate is similar to that observed when exposed to potassium chloride. If the data above the 50 Hz region were indeed due to an interfacial process, the impedances would increase with increasing conductivity (i.e., increasing molybdate concentration). This is not observed. As previously observed, the presumed solution resistance is seen to occur in the 1 to 100 Hz region of the data. Again, the cell constant calculations shown in Table 4 confirm the hypothesis that the solution resistance indeed lies in the 1 to 100 Hz region. The low-frequency capacitive arc (see Fig. 3), which was attributed to the interfacial behavior, has been found to increase in size with increasing molybdate concentration. This further confirms the argument that the data above the 1 to 100 Hz region are due to artifacts and that the data below this region originates from the interfacial behavior.

Part II. Contributions of the Electronics

It was of great interest to model the impedance data obtained from experiments with lake water in order to adequately explain and possibly mitigate the artifacts. Initial efforts resulted in models that could mimic the behavior of the experimental data but required circuit element values and configurations that were physically unrealizable. It became obvious that the effects of the electronics, which had been previously ignored, must be taken into consideration so that a realistic model could be produced. It is known that the

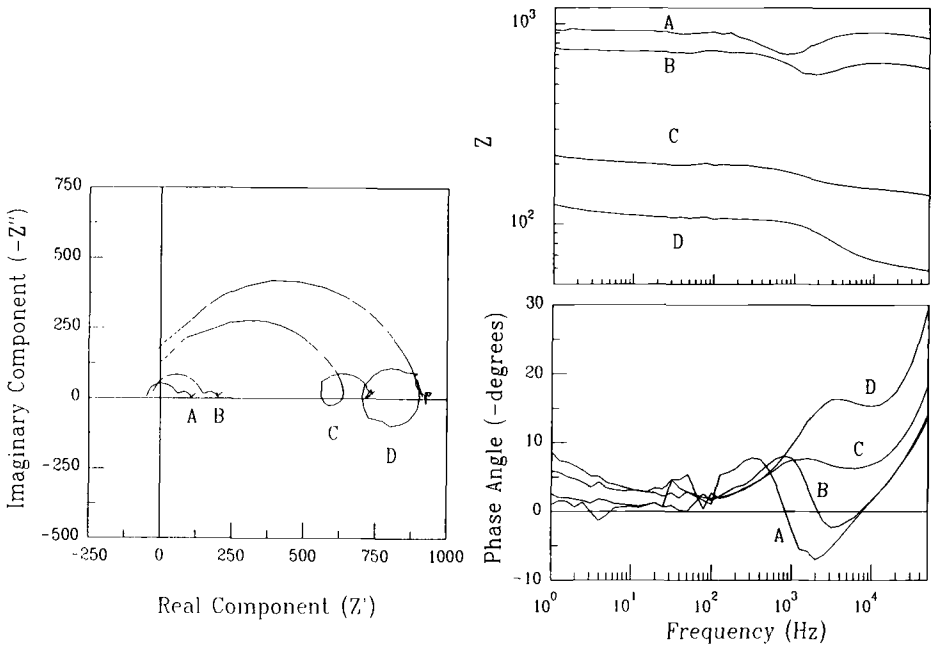

FIG. 5—*Impedance spectra for A36 steel exposed to lake water with different solution resistivities resulting from the addition of sodium molybdate. Solution resistivities and resistances of experiments A–D are given in Table 4.*

electronics can contribute to a measured impedance spectrum [*23*]. Furthermore, it is known that the solution resistance between the reference and working electrodes (R_s) and the solution resistance between the counter and reference electrodes (R_s') have a deleterious synergistic relationship with the electronics such that increased resistances produce increased artifacts [*16*]. Therefore, it was the object of this phase of the study to detect the origin of the artifacts arising from the electronics and to study the effect of R_s and R_s' on a resulting impedance spectrum.

Errors in impedance measurements can arise in five physical locations: the test cell, the leads from the cell to the potentiostat, inside the potentiostat itself, in the leads from the potentiostat to the frequency response analyzer (FRA), or finally, inside of the FRA. The ability to control the extent of these errors varies. Artifacts caused by the test cell are at least partially under the control of the experimenter. Cell geometry may be modified, and it may be possible to alter the solution resistance by reducing the solution resistivity or by altering the cell geometry. The leads to the potentiostat should not be altered by the experimenter because potentiostats are calibrated to the lead length supplied at purchase. Errors from the potentiostat are inevitable and can only be compensated for after the measurement is made. These errors are of the greatest concern. Finally, errors arising from the FRA and its leads have been found to be negligible and of little concern. This is discussed in greater detail in the following paragraphs.

While the parasitic pathways inside the potentiostat and its leads (hereafter collectively referred to as the potentiostat) are not controllable, they are independent of the test cell and should be constant for a given test condition. Thus, a model that may explain errors caused by the potentiostat should be portable and applicable to a variety of different

TABLE 4—*Summary of the measured resistivities, measured solution resistances and calculated cell constants of the spectra of Fig. 5. The average cell constant is 18.1 cm and the standard deviation is 2.00 cm.*

	A	B	C	D
ρ (kΩ-cm)	19.0	13.3	3.60	1.70
R_s (Ω)	920	729	201	108
X (cm)	20.6	18.2	17.9	15.7

experiments conducted on the same physical potentiostats and possibly on other potentiostats of the same model. One way to evaluate the artifacts caused by the potentiostat is to conduct an impedance scan on a simple, stable, and linear test cell with known values. The simplest test cell chosen was a resistor measured in a two-electrode configuration, thus eliminating contributions of a reference electrode.

There are two possible ways to circumvent the errors introduced by the measuring apparatus: (1) determine and operate the test equipment in a region where it is known to produce accurate results, or (2) explain and account for the artifacts created in the frequency regime being examined so that useful data can be extracted. This project sought to use both ways of resolving these artifacts. The response of the potentiostat/FRA combination to a variety of test conditions was mapped out experimentally and a partial model that explains many of the observed artifacts was developed.

Experimental Methods

Contributions of the FRA—The FRA receives two voltage signals from the potentiostat representing voltage and current, which it compares in phase angle and in magnitude, thereby producing a scaled impedance. To test the response of the Schlumberger 1255, the output signal it produces was fed back through the coaxial cables which normally connect the FRA to the potentiostat into the Channel 1 and Channel 2 inputs. This was done for 150 mV, 1 V and 1.5 V signals. These signals cover the range of possible inputs to the FRA.

Contributions of the Potentiostat—Ignoring all electrochemical interfaces, any electrochemical cell will have a parallel resistor/capacitor (RC) combination between both the counter and reference electrodes and the reference and working electrodes due to the resistivity of solution and the geometric capacitance. The simplest way to mimic these RC combinations is to place resistors between the counter and reference, and reference and working electrode leads in a three-electrode configuration. The geometric capacitance will be modeled by the stray capacitance that exists in any real resistor.

In order to evaluate the response of the potentiostat, a test matrix of two-electrode measurements comprising resistors in half-decade increments from 10 Ω to 100 kΩ was performed. Fixed current measuring resistors of the same value or, for the half-decades, both the value above and below, were used. To observe the effect of a reference electrode to counter electrode path, three-electrode measurements were made by inserting a second resistor, R_s', between the counter and reference electrodes. The geometric positioning of the reference electrode within an electrochemical cell was simulated by changing the ratio of R_s' to R_s. These ratios were 1:10, 1:1, 10:1, and 100:1. Thus, a test matrix was formed by varying both the magnitude of R_s (10 Ω to 100 kΩ) and the ratio of R_s' to R_s. All results were confirmed by two or more experiments.

Each test was conducted at 0 V dc using a 10 mV sinusoidal test signal. The 1286

electrochemical interface was set to bandwidth type 'C'. The FRA was set to short integration, 100 cycles maximum on the current measuring channel and scanned from 20 MHz to 100 Hz at 25 points/decade. It should be noted that although the FRA is able to scan frequencies as high as 20 MHz, the potentiostat is unable to function adequately beyond 1 MHz. The frequency range beyond 1 MHz was scanned solely for the sake of completeness.

A series of 5% carbon resistors used for the test matrix were mounted in an Archer Universal Breadboard and the potentiostat leads were attached to the resistor leads. Care was taken to orient the leads in a consistent manner, since it has been observed that repositioning of the leads may alter very high frequency results. The resistors were measured to have a capacitance of less than 10 pF across them when mounted in the breadboard.

Results and Discussion

Contributions of the FRA—Figure 6 shows the response of the FRA to its own output signal. Scans to 20 MHz using both extremes of the possible range of input voltages (150 mV and 1.5 V) indicate that both the magnitude and the phase angle responses are extremely constant and never deviate more than 0.5% from the expected value. Therefore, it is unlikely that the FRA contributes to observed impedance artifacts.

Contributions of the Potentiostat—The completed matrix of test resistors (9 total) and R_s to R_s' ratios (5 total) is too large to display the spectra in their entirety. Figure 7 displays a subset of the matrix, a series of four plots for a 330 Ω test resistor (2 R_s':R_s ratios, 1:10

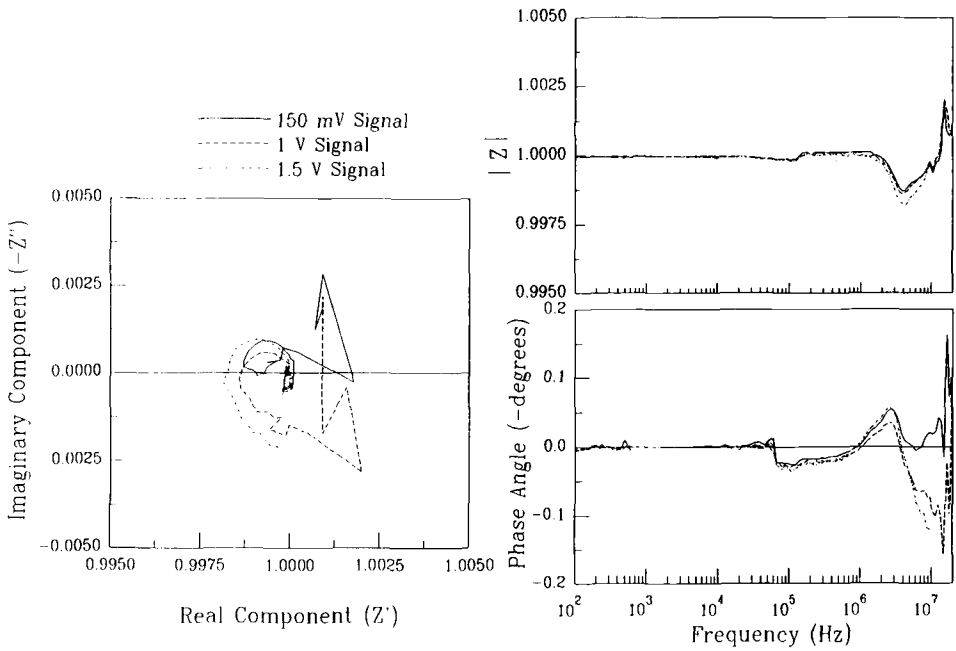

FIG. 6—*Response of the FRA to identical signals on Channel 1 and Channel 2. Spectrum scanned from 20 MHz to 100 Hz.*

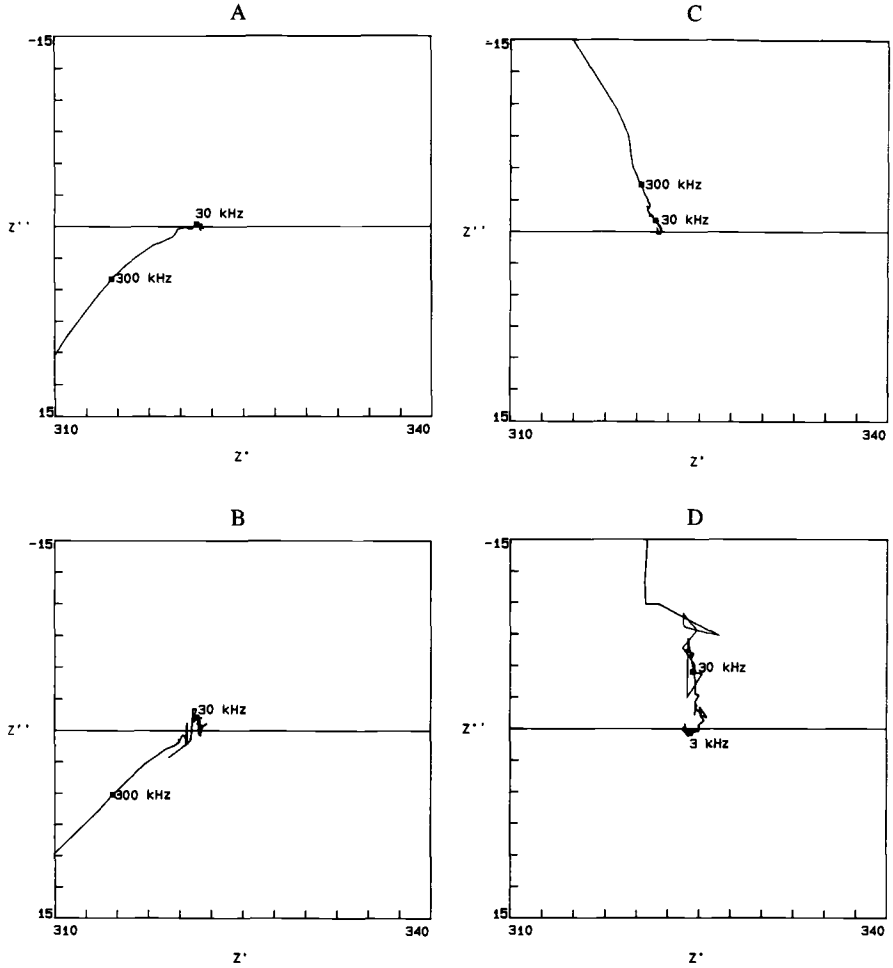

FIG. 7—*Nyquist plots of a 330 Ω test resistor varying R_s':R_s and the current measuring resistor. Plots a and b are measurements with R_s':R_s equal to 1:10 and 100:1, respectively, with a 100 Ω measuring resistor. Plots c and d are measurements with R_s':R_s equal to a 1:10 and 100:1, respectively, with a 1 kΩ measuring resistor.*

and 100:1, for both the 100 Ω and 1 kΩ measuring resistors). These plots display the general features discovered throughout the matrix. The most prominent feature of the plots is that all the tests conducted using the 1 kΩ measuring resistor display capacitive behavior while each test conducted using the 100 Ω measuring resistor display inductive behavior. This may be caused by the switch in measuring techniques from virtual-earth to voltage-drop in this make of potentiostat. Another important observation is that the R_s' to R_s ratio has a definite effect on the shape of the artifact produced and on the frequency range over which the artifacts are observed. The variations due to the changing ratios must be caused by parasitic pathways because, theoretically, the value of R_s' should not affect an impedance spectrum.

One manner of representing the degree to which artifacts affect an impedance spectrum is the use of percentage error boxes. An "*n*% box" was chosen arbitrarily as a figure of merit and is defined as the frequency closest to the point where the Nyquist diverges by $\pm n\%$ of the actual magnitude of the resistance in either the real or imaginary components. A more accurate method would use a divergence of *n*% in the magnitude of the impedance. That is, it would be more accurate to use a circle rather than a square to measure the error. However, because of the limited resolution of frequencies, the additional error caused by the *n*% box method is acceptable.

Each experiment used a measuring resistor which was of the same magnitude as the test resistor for test resistors of whole-decade magnitudes (e.g., 100 Ω, 1 kΩ). The measuring resistor immediately smaller than the test resistor was used for test resistors of half-decade magnitudes (e.g., 330 Ω, 3.3 kΩ). The *n*% box calculations give approximate boundaries for the maximum frequency that can be trusted to a desired level of accuracy at any particular impedance. An example of these calculations may be seen in graphical form in Fig. 8 where $R_s':R_s$ = 10:1 and *n*% = 1%, 5%, 10%, and 20%. Additionally, Table 5 displays the entire matrix for the 1% box calculations. It should be noted that for errors smaller than 1% the data may be considered to be unaffected by artifacts arising from the potentiostat. On the contrary, errors larger than 20% may be considered to be greatly affected by artifacts arising from the potentiostat and should be discarded. It may be seen from Table 5 that, in general, as the ratio of R_s' to R_s is increased for a given R_s, the *n*% box frequencies decrease. This indicates that the artifacts are occurring at lower frequencies as the ratio is increased. It may also be seen from both Table 5 and Fig. 8 that as the magnitude of the test resistor is increased, a peak in the *n*% box frequency is seen at 1 kΩ. This is curious because it is commonly believed that as a solution resistance is increased, the artifacts at a given frequency should increase. This perplexing behavior may be somewhat explained. It is known that the potentiostat uses two different types of current

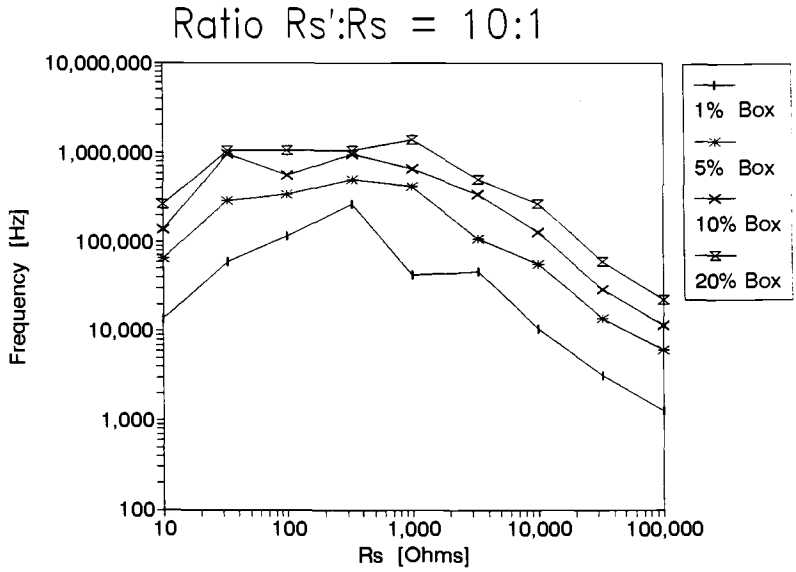

FIG. 8—*Plot of n% box frequencies for a* $R_s':R_s$ *of 10:1.*

TABLE 5—*Summary of the 1% box frequencies obtained for various combinations of test resistors and measuring resistors.*

Test Resistance (Measuring Resistor)	2-Electrode, kHz	1:10 ratio, kHz	1:1 ratio, kHz	10:1 ratio, kHz	100:1 ratio, kHz
10Ω (10Ω)	12.6	34.6	13.8	13.8	24
33Ω (10Ω)	50.2	—	60.4	60.4	16.6
33Ω (100Ω)	38.1	—	50.2	45.8	31.7
100Ω (100Ω)	126	115	126	115	264
330Ω (100Ω)	240	264	200	264	12.6
330Ω (1kΩ)	264	264	264	138	20.0
1kΩ (1kΩ)	105	105	95.7	41.8	9.57
3.3kΩ (1kΩ)	46.8	41.8	38.1	16.6	2.64
3.3kΩ (10kΩ)	105	95.7	79.6	28.9	4.58
10kΩ (10kΩ)	26.4	26.4	2.89	10.5	2.40
33kΩ (10kΩ)	10.5	8.73	7.26	3.17	—
33kΩ (100kΩ)	240	13.8	9.57	3.17	—
100kΩ (100kΩ)	3.48	3.48	2.64	1.26	0.166

measuring systems [*24*]: the voltage-drop technique for the 0.1 Ω to 100 Ω current measuring resistors and the virtual-earth technique for the 1 kΩ to 100 kΩ current measuring resistors. These two systems are discussed in greater detail in the following paragraphs. The calculations from the virtual-earth method follow the expected trend, namely that the *n*% box frequency decreases with increasing current measuring resistance. However, the calculations from the voltage-drop technique indicate opposite behavior. It is currently unclear why the *n*% box frequencies increase with increasing measuring resistor as a result of the voltage-drop technique.

In the experiments comprising steel exposed to lake water, it was found that artifacts occurred down to approximately 100 Hz. The solution resistances for these experiments were on the order of 100 Ω to 1 kΩ. However, Table 5 shows that the potentiostat should not contribute below approximately 9.57 kHz assuming the worst case of $R_s':R_s$. This implies that the cell geometry and reference electrode are contributing significantly below 10 kHz.

Potentiostat Modeling—There are several possible non-idealities in potentiostats that can contribute to the observed artifacts: (1) the current measuring resistors contain stray capacitances, (2) there are capacitances between the signal carrying wire and the driven shield, and (3) the voltage measuring devices do not have infinite input impedance.

The potentiostat in this study uses two different methods of measuring current: the voltage-drop method (for 0.1 Ω to 100 Ω current measuring resistors) and the virtual-earth method (for 1 kΩ to 100 kΩ current measuring resistors). Both of these methods can introduce errors into an impedance measurement because of stray capacitances in the measuring resistors.

Figure 9 shows a schematic of the voltage-drop measuring system. In the voltage-drop technique, the test current flows through the measuring resistor, actually a measuring impedance (Z_{meas}), producing a voltage. This voltage is scaled by $1/R_{meas}$ and output on Channel 1. The measured voltage between the reference and working electrodes is output on Channel 2.

The relationships may be summarized as

$$\text{Channel 2} = V_{test} \tag{3}$$

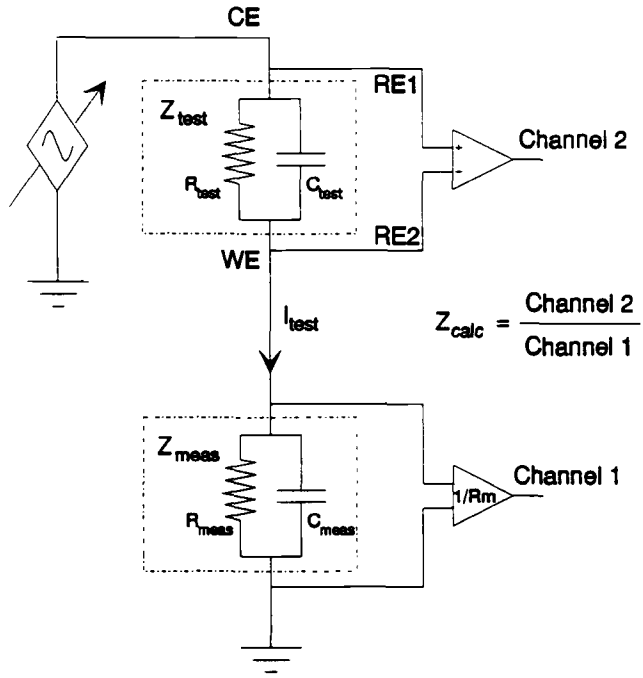

FIG. 9—*Schematic of the voltage-drop measuring system.*

$$\text{Channel 1} = \frac{I_{\text{test}} \times Z_{\text{meas}}}{R_{\text{meas}}} \tag{4}$$

The impedance of the test cell is defined as

$$Z_{\text{test}} = \frac{V_{\text{test}}}{I_{\text{test}}} \tag{5}$$

$$Z_{\text{calc}} = \frac{\text{Channel 2}}{\text{Channel 1}} \tag{6}$$

Thus, substituting (3), (4) and (5) into (6),

$$\begin{aligned} Z_{\text{calc}} &= \frac{V_{\text{test}}}{\text{Channel 1}} \\ &= \frac{V_{\text{test}}}{I_{\text{test}}} \times \frac{R_{\text{meas}}}{Z_{\text{meas}}} \\ &= Z_{\text{test}} \times \frac{R_{\text{meas}}}{Z_{\text{meas}}} \end{aligned} \tag{7}$$

Since Z_{meas} is actually the parallel combination of R_{meas} and C_{meas} then

$$\begin{aligned} Z_{meas} &= R_{meas} \| C_{meas} \\ &= \frac{R_{meas}}{1 + j\omega R_{meas} C_{meas}} \end{aligned} \tag{8}$$

Substituting (7) into (6),

$$Z_{meas} = Z_{test}(1 + j\omega R_{meas} C_{meas}) \tag{9}$$

Therefore,

$$\begin{aligned} Z_{meas} &= Z_{test} + j\omega R_{meas} C_{meas} Z_{test} \\ &= Z_{test} + j\omega L' \end{aligned} \tag{10}$$

Thus, the net result of the stray capacitance across the current measuring resistor is to add a pseudo-inductance, L', in series with the test element. The magnitude of this inductor is $R_{meas} C_{meas} Z_{test}$.

A schematic of the virtual-earth measuring arrangement is seen in Fig. 10. If the op-amp in the virtual-earth arrangement was ideal (infinite gain and infinite bandwidth), then this arrangement would produce exactly the same pseudo-inductance as the voltage-drop technique. In reality, the finite gain-bandwidth product of the op-amp can introduce additional phase-shifts when used in this manner. The virtual-earth measuring apparatus has yet to be modeled and will be the subject of future work.

An additional source of artifacts can originate from the capacitive coupling through the coaxial cable between the signal line and the driven shield (see Fig. 11). In an effort to reduce the capacitance "seen" by the signal, the shield surrounding it is driven to the same voltage as the line it encases. Since there is no resulting voltage differential across the capacitor, no current flows through the capacitor and the signal effectively does not "see" a capacitance. However, the signal that drives the shield passes through a 600 kHz low pass filter (240 ns pole) [25] as well as a finite gain-bandwidth amplifier. Therefore, as the frequency increases, the voltage applied to the shield can no longer follow the main

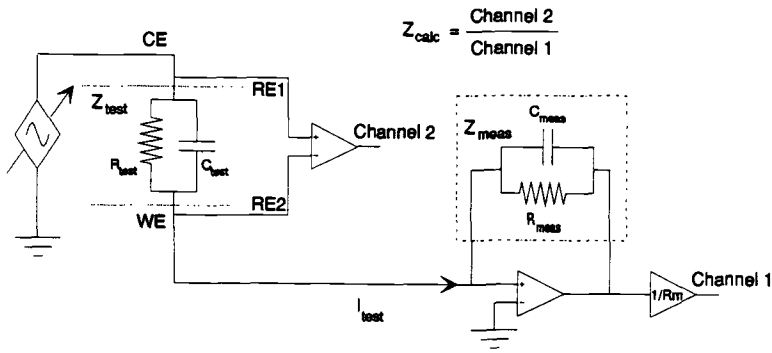

FIG. 10—*Schematic of the virtual-earth measuring system.*

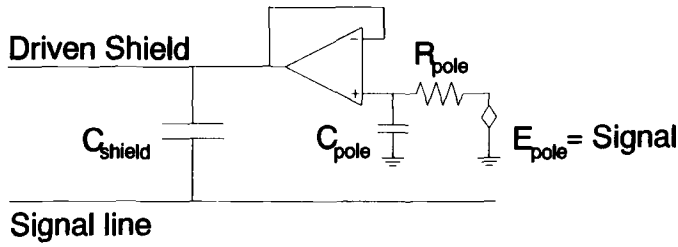

FIG. 11—*Schematic of the signal line/driven shield arrangement.*

signal and the apparent capacitance increases. This effect is difficult to represent in equation form, but can be modeled using circuit analysis programs.

Circuit Modeling of the Potentiostat—There are two major problems with modeling the error introduced by the measurement instrumentation. One problem is that, while it is possible to create a transfer function for non-ideal op-amps, it is a slow error-prone process that has to be repeated each time elements are added or removed from the circuit. The other problem is that the circuits involved are typically ladder networks. The impedances of ladder networks, circuits that do not reduce to a series of nested two-terminal elements, cannot be expressed as polynomials or even as ratios of polynomials. Instead, the values of the circuit elements can only be found by solving a set of simultaneous equations.

These two difficulties make it necessary to use some sort of circuit modeling program to calculate the impedance. PSpice [*26*], a commercially available program for circuit emulation, is usable but cumbersome for repetitively evaluating slight changes in a circuit. For this project, a more useful program was written that allows both emulation and fitting of ladder networks. Both PSpice and the present program solve the circuits by nodal analysis. Circuit modeling by nodal analysis offers increased flexibility and shortened development time for new models. The price for this flexibility is increased time to calculate the impedance for a given set of values. However, given the speed of personal computers and their ability to calculate repetitively while unsupervised, the nodal analysis methods are superior to other methods for analyzing the present circuit networks.

A problem that results from the modeling of complex ladder networks is that it is impossible to use many of the standard data fitting techniques. Present commercially available fitting programs use algorithms that take advantage of the fact that at a local minimum, the partial derivative of χ^2 with respect to each parameter equals 0 (χ^2 is the overall fitting parameter). This shortcut allows the routine to quickly move along the error surface to a minima. The problem with this method for ladder networks is that the "function" that relates experimental parameters to impedance is a set of simultaneous equations. This makes it difficult to find the partial derivative. Fortunately, another methodology called simplex-fitting routines [*27,28*] can be used iteratively to handle problems of this type. This is the method used in the program written by the authors.

An internally consistent model (Fig. 12) has been developed that is able to largely explain the observed two-electrode impedance behavior for the measuring resistors used in conjunction with the voltage-drop technique. The model simulates behavior from 100 Hz to 200 kHz. It is a goal of future work to model experimental data beyond 200 kHz. The model of Fig. 12 is able to mimic the behavior while varying only two of the many possible non-idealities in the potentiostat. The first parameter is a parasitic capacitance present in the measuring resistor. This produces an inductive shift and the value obtained for that element (~10 pF) is reasonable. The varied element is the capacitance

due to the driven shield present on the working electrode lead. The signal driving the shield passes through a 660 kHz low pass filter and is driven by an op-amp in the voltage follower configuration with a gain-bandwidth product of 10^6 Hz. The capacitance between the driven shield and the line has been modeled as 200 pF. This value may be slightly large because the lead itself has only about 50 pF although the rest of the capacitance may appear in the connections beyond the lead.

Figure 12 shows the values obtained for the model of the voltage-drop measuring apparatus. It should be noted this model assumes that the test resistor is actually in series with a 1 μH inductor. This is an inductance in addition to the pseudo-inductance L'. Although the presence of this inductor makes the model behave according to experimental data, there is no physical justification for its presence.

Figure 13 shows the extremely close fit between the experimental and simulated data. These fits are for the model of Fig. 12 wherein only the value of the test resistor and measuring resistor were changed between each simulated spectrum. Thus, the element values shown in Fig. 12 have been adjusted from the individual fits performed on each of the five data sets and have not been optimized for any particular combination of test resistor/measuring resistor. These conditions may be overly stringent. It is reasonable to allow the parasitic capacitance C_{meas} to vary for different measuring resistors because the stray capacitance associated with each physical measuring resistor will be different. Also, the values of C_{test} and L_{test} may be expected to change slightly for different test resistors.

Without the incorporation of a model of the potentiostat, it is impossible to adequately model any other artifacts. Future research will incorporate the model of Fig. 12 into analyses of the effects of the solution resistance, reference electrode and cell geometry on

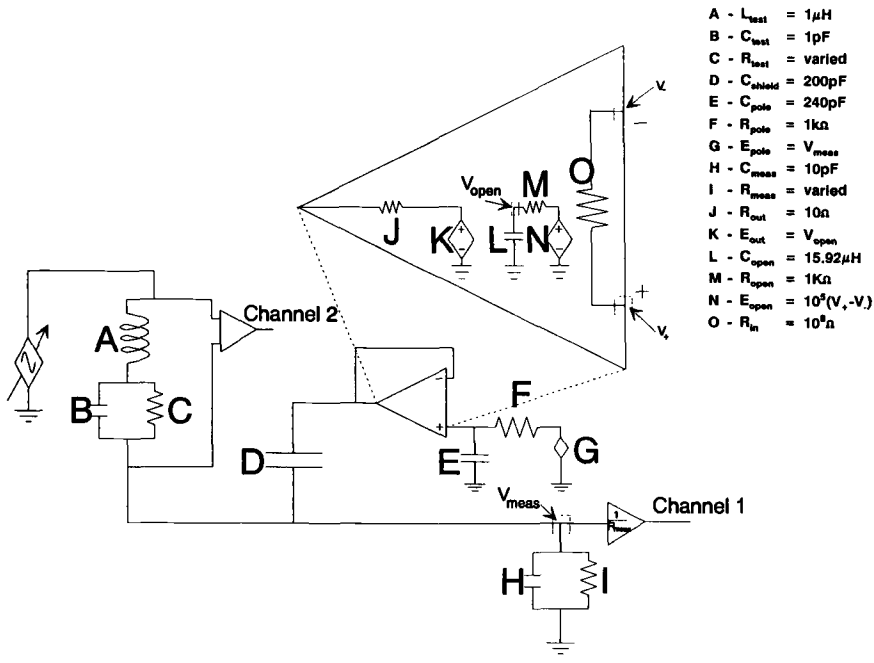

FIG. 12—*Schematic drawing of the model used to simulate the behavior of the voltage-drop measuring apparatus. Optimized values of the elements obtained by computer modeling are shown at right.*

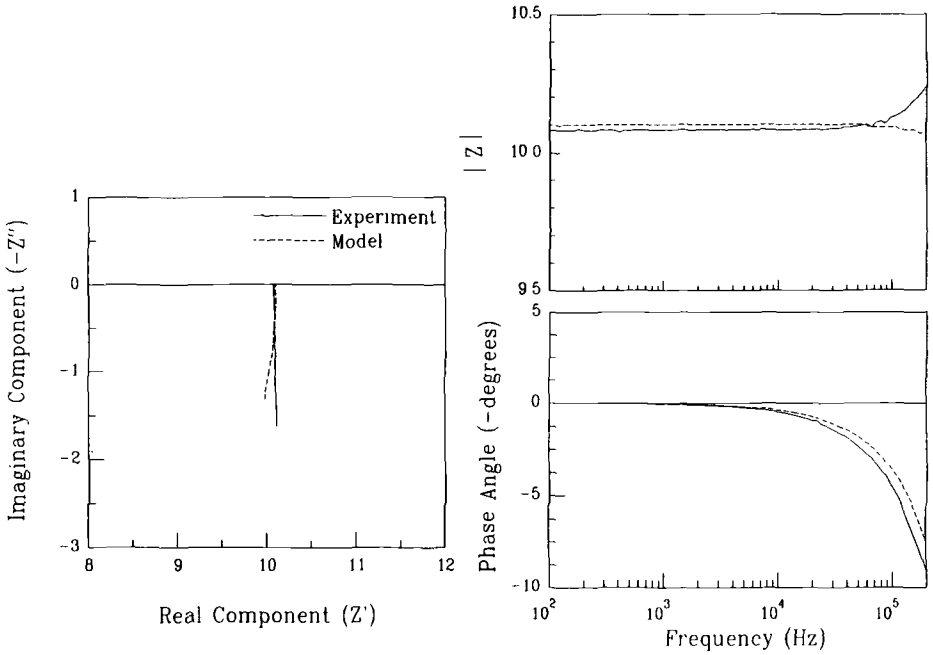

FIG. 13—*Comparison of experimental data and simulated data for a 10 Ω test resistor and 10 Ω measuring resistor.*

artifacts. By including the model of the potentiostat, modeling of these other artifact sources may be performed safely because the deleterious synergistic behavior of artifact sources will be incorporated.

Conclusions

It is well-documented that EIS experiments in low-conductivity environments can produce artifacts. These extraneous phase shifts can obscure experimental data and cloud the true interpretation of a spectrum. It is possible to resolve the causes of these artifacts using both experimental and mathematical techniques.

Experiments comprising steel in natural lake water have shown that the solution resistance within an impedance spectrum may be isolated. The solution resistivity of the lake water was changed by the introduction supporting ions and by dilution with distilled deionized water. A series of changes in conductivity resulted in the differentiation of artifacts from interfacial data, allowing the determination of the solution resistance.

Although it is useful to be able to identify the solution resistance, it is desirable to model and thus remove the test artifacts. This would increase confidence that other parts of the spectrum have been correctly identified. Tests on simple test cells (e.g., resistors) show that the potentiostat and its associated leads introduce artifacts by themselves. Several factors, including the magnitude of the resistance being scanned, the measuring resistor selected, and the ratio of the impedances $R_s':R_s$, have been found to affect the shape of the spectrum.

The problem of interpreting complex spectra was approached by combining circuit modeling by nodal analysis with the simplex method. The simplex method is a powerful numerical fitting technique that fits without calculating partial derivatives. This combination of approaches offers the advantage of quickly being able to model and fit complex circuits of any configuration, including ladder networks.

The model that was developed was able to accurately reproduce the spectra produced for a range of test resistances on two different current measuring resistors that are used in a voltage-drop configuration. It is robust for the range of data tested, since small changes from the ideal fit for each data set can be tolerated in producing average values for all fits. The major problems with the model are the inclusion of an extra 1 μH inductor in the physical test resistor, an inability to account for artifacts appearing above 500 kHz, and the non-inclusion of measuring resistors which are used in a virtual-earth configuration.

Future work for this project includes modeling of the virtual-earth current measuring technique, explaining the higher frequency artifacts, evaluating the accuracy of fitting by Monte Carlo methods, and modeling electrochemical cells by attaching them to the completed potentiostat model.

References

[1] Mansfeld, F., Kendig, M. W., and Tsai, S., *Corrosion*, Vol. 38, 1982, p. 570.
[2] Feng, Y., Zhou, G., and Cai, S., *Electrochimica Acta*, Vol. 36, 1991, p. 1093.
[3] Mansfeld, F., Kendig, M. W., and Tsai, S., *Corrosion*, Vol. 38, 1982, p. 570.
[4] Macdonald, D. D. and Urquidi-MacDonald, M., *Journal of the Electrochemical Society*, Vol. 132, 1985, p. 2316.
[5] Savova-Stoynov, B. and Stoynov, Z. B., *Journal of Applied Electrochemistry*, Vol. 17, 1987, p. 1150.
[6] Willihngunz, E., *Journal of the Electrochemical Society*, Vol. 102, 1955, p. 99.
[7] Euler, J. and Dehmelt, K., *Zeitschrift fuer Electrochemie*, Vol. 61, 1957, p. 1200.
[8] Lander, J. and Nelson, E. E., *Journal of the Electrochemical Society*, Vol. 107, 1960, p. 722.
[9] Keddam, M., Stoynov, Z., and Takenouti, H., *Journal of Applied Electrochemistry*, Vol. 7, 1977, p. 539.
[10] Laman, F. C., Matsen, M. W., and Stiles, J. A. R., *Journal of the Electrochemical Society*, Vol. 133, 1986, p. 2441.
[11] Gutman, F., *Journal of the Electrochemical Society*, Vol. 112, 1965, p. 90.
[12] Gopikanth, M. L. and Sathyanarayana, S., *Journal of Applied Electrochemistry*, Vol. 9, 1979, p. 369.
[13] Darby, F., *Journal of the Electrochemical Society*, Vol. 113, 1966, p. 396.
[14] Hampson, N. A., Karunathylaka, S. A. G. R., and Leek, R., *Journal of Applied Electrochemistry*, Vol. 10, 1980, p. 3.
[15] Keddam, M., Rakatomavo, C., and Takenouti, H., *Journal of Applied Electrochemistry*, Vol. 14, 1984, p. 437.
[16] Kolman, D. G., "An Investigation of the Effects of Molybdate on a Mild Steel Cooling Water System," M.S. Thesis, University of Virginia, 1991.
[17] Chechirlian, S., Eichner, P., Keddam, M., Takenouti, H., and Mazille, H., *Electrochimica Acta*, Vol. 35, 1990, p. 1125.
[18] Gohr, H., Mirnik, M., and Schiller, C. A., *Journal of Electroanalytical Chemistry*, Vol. 180, 1984, p. 273.
[19] Faidi, S. E. and Scantlebury, J. D., *Journal of the Electrochemical Society*, Vol. 136, No. 4, 1989, p. 990.
[20] Fiaud, C., Keddam, M., Kadri, A., and Takenouti, H., *Electrochemica Acta*, Vol. 32, No. 3, 1987, p. 445.
[21] Robertson, W. D., *Journal of the Electrochemical Society*, Vol. 98, 1951, p. 94.
[22] Cartledge, G. H., *Corrosion*, Vol. 24, 1968, p. 223.
[23] Rodgers, Robert S., EG&G Princeton Applied Research, personal communication 1991.
[24] *1286 Electrochemical Interface Operating Manual*, Issue 3, June 1985.
[25] Luckhurst, Geoff, Schlumberger Instruments, personal communication 1991.

[26] Tuinega, P. W., *SPICE: A Guide to Circuit Emulation Using PSpice,* Prentice-Hall, Inc., Englewood Cliffs, NJ, 1988.
[27] Demas, J. N. and Demas, S. E., *Interfacing and Scientific Computing on Personal Computers,* Allyn and Bacon, Boston, 1990.
[28] Press, W. H., Flannery, B. P., Teukolsky, S. A., and Vetterling, W. T., *Numerical Recipes in Pascal,* Cambridge University Press, 1989.

Robert G. Kelly,[1] *Alison J. Young,*[2] *and Roger C. Newman*[2]

The Characterization of the Coarsening of Dealloyed Layers by EIS and Its Correlation with Stress-Corrosion Cracking

REFERENCE: Kelly, R. G., Young, A. J., and Newman, R. C., **"The Characterization of the Coarsening of Dealloyed Layers by EIS and Its Correlation with Stress-Corrosion Cracking,"** *Electrochemical Impedance: Analysis and Interpretation, ASTM STP 1188,* J. R. Scully, D. C. Silverman, and M. W. Kendig, Eds., American Society for Testing and Materials, Philadelphia, 1993, pp. 94–112.

ABSTRACT: The origin of the reversibility of the environmental embrittlement of an Ag-20 at. % gold alloy in 1 M $HClO_4$ has been investigated. The structure of the porous gold layer formed on this alloy under potentiostatic polarization has been studied by electrochemical impedance spectroscopy (EIS). In the as-dealloyed state, a 50-μm layer has impedance behavior electrically equivalent to a layer containing 10^{11} cylindrical pores/cm^2 (geometric area) each with a radius of 9 nm. Upon aging, the pores closest to the substrate coarsen first, destroying the ability of the layer to inject a brittle crack into the uncorroded substrate. This change in structure is observable as a change in the low-frequency portion of the impedance spectrum. The observed potential dependence of this coarsening indicates that it occurs due to surface diffusion of gold atoms.

KEYWORDS: dealloying, stress-corrosion cracking (SCC), porous electrodes, surface diffusion, coarsening, film-induced cleavage

The film-induced cleavage model of stress-corrosion cracking (SCC) predicts an intimate connection between environmental cracking and the size of the porosity of a surface film [*1,2*]. According to this model, anodic dissolution can form a nanoporous surface layer that has a low fracture toughness. Since many of these layers are dealloyed layers, there is a high degree of coherency between the film and the substrate from which it forms. Thus, when the dealloyed layer is strained, a crack which forms in the layer can attain sufficient velocity to penetrate the underlying substrate for some distance. Since the size scale of the porosity controls the mechanical properties of the layer [*1,2*], it has been proposed that allowing these layers to age would destroy their ability to inject a crack into the underlying substrate due to an increase in pore size by coarsening. Such aging has been shown to reverse the embrittlement in both α-brass [*3*] and Ag/Au [*4*], two systems for which hydrogen embrittlement can be ruled out on the basis of thermodynamics [*5,6*].

While experimental support for the film-induced cleavage model has been increasing in recent years [*3,4,7–9*], there is a lack of direct evidence of the pore coarsening which is proposed to reverse the embrittlement. In most SCC systems, a direct, *in-situ* measurement of the porosity is not possible due to the occurrence of faradaic reactions in the

[1]Research assistant professor, Center for Electrochemical Science and Engineering, Department of Materials Science, University of Virginia, Charlottesville, VA 22903.

[2]Research student and reader, respectively, Corrosion and Protection Centre, University of Manchester Institute of Science and Technology, Manchester, England M60 1QD.

potential range of interest. Such a measurement would be extremely useful in determining the nature of the process that controls the coarsening, as well as generating direct experimental evidence of its existence under conditions relevant to SCC. High temperature coarsening (200 to 800°C for 10 min) of nanoporous gold sponges (analogous to dealloyed layers) has been shown to result in a brittle-to-ductile transition [*10,11*]. Li and Sieradzki completely dealloyed small, three-point bend bars of an Ag-Au alloy, producing a Au-rich sponge with extremely fine porosity (approximately 5 nm pore radius). The as-dealloyed specimens were then exposed to a range of heat treatments before being mechanically tested. These heat treatments allowed the effects of pore coarsening of over an order of magnitude to be investigated. The results showed a brittle-to-ductile transition at a pore diameter of approximately 50 nm. At pore sizes greater than this, the toughness was dramatically higher, while at smaller pore sizes, very little energy was absorbed during fracture, i.e., the specimens failed in a brittle manner. While that work supplied strong support for the relation between pore size and the mechanical behavior of a dealloyed material, it was necessarily done *ex-situ*. The objective of the present work was to follow the coarsening of the dealloyed layers *in-situ* and to relate changes in the physical structure of the layers to the ability of these layers to inject a brittle crack into the underlying, uncorroded substrate.

In Ag/Au alloys, the dealloyed layer is non-faradaic over a wide range of potential. This allows electrochemical measurements to be used to probe the surface area distribution as well as changes in it. Since the SCC behavior of this system has been previously shown to be consistent with the film-induced cleavage model [*4*], this system provides an opportunity to investigate the relation between the reversible embrittlement observed and changes in the structure of the porosity of the dealloyed layer.

Theory of Porous Electrode Impedance Measurements

While there are many electrochemical techniques that are capable of measuring electrochemically active surface area, and thus, indirectly, the degree of porosity of a non-faradaic interface, most give only *total* surface area. No information concerning the pore shape or the distribution of pore size can be extracted. Electrochemical impedance spectroscopy (EIS) can probe the dealloyed film and provide information concerning the shape, size, and distribution of the porosity.

deLevie provided the classic description of the impedance of porous electrodes in a series of papers [*12–14*]. More recently, Candy et al. [*15*] developed an analysis for the impedance of a set of N right cylindrical pores whose walls and bases are non-faradaic. They were able to derive a relation which allows the estimation of a set of equivalent cylindrical pore parameters for porous electrodes from impedance measurements. The basis for these calculations is the recognition that a number of the parameters of the pore system affect the measurement; pore depth and length, pore solution conductivity, and pore interfacial impedance all affect the impedance with which the measurement signal interacts. For example, an excitation signal of a given frequency penetrates to a greater and greater depth of the pore for wider pores or in solutions of higher conductivity. deLevie showed that this geometry results in the measured impedance being equal to $\sqrt{\tilde{Z}}$, where $\tilde{Z}$ is the impedance of the flat interface [*12–15*]. For non-faradaic, right cylindrical surfaces, this results in a line in the complex plane plot at 45° with respect to the real axis. At a critical frequency (ω_{crit}), the excitation signal just reaches the bottom of the pore and the entire surface area of the porous electrode is sensed. Further lowering of the frequency results in an increase in impedance characteristic of a purely capacitive interface, but no increase in the amount of sensed surface area. This results in a vertical line in the complex

plane. Thus, at ω_{crit}, a singularity occurs. At this frequency, the pore solution resistance (R_{pore}) equals the capacitive impedance of the total surface area ($|\vec{Z}_{C_{tot}}|$). Therefore, at ω_{crit}

$$R_{pore} = \frac{\rho l}{3N\pi r_{pore}^2} \tag{1}$$

$$|\vec{Z}_{C_{tot}}| = \frac{1}{2N\omega_{crit} r_{pore} \pi l C_{dl}} \tag{2}$$

where

R_{pore} = total resistance of the electrolyte in the pores, Ω,
ρ = solution resistivity, Ω-cm,
l = length of pore, cm,
N = number of pores,
r_{pore} = radius of pore, cm,
$|\vec{Z}_{C_{tot}}|$ = capacitive impedance of the porous layer, Ω,
ω_{crit} = critical frequency, rad s^{-1}, and
C_{dl} = specific interfacial capacitance, F/cm^{-2}.

Therefore, upon rearrangement

$$r_{pore} = \frac{2l^2 C_{dl} \omega_{crit} \rho}{3} \tag{3}$$

and

$$N = \frac{1}{4\pi l C_{dl} |Z(\omega)| \omega r_{pore}} \tag{4}$$

Thus, measurements of ω_{crit} and $|Z_{C_{tot}}|$ allow an estimation of the equivalent cylindrical pore parameters for a dealloyed layer whose potential is in the non-faradaic region. In addition, the shape of the high-frequency portion of the complex plane has been shown to be characteristic of the structure of the pores, with more re-entrant pores exhibiting more of a pseudo-charge transfer resistance [*16*]. It is also possible to ascribe portions of the impedance spectrum to portions of the porous layer based upon the frequency, with lower frequencies corresponding to regions closer to the porous film/substrate interface. This can be of great importance for pore structures that change with distance from the bulk solution/layer interface.

Experimental

Materials and Specimen Preparation

The material used for this investigation was an Ag-20 at.% Au alloy supplied by Johnson-Matthey, plc (Hertfordshire, United Kingdom). The ingot was homogenized and rolled to a thickness of 0.5 mm. For the electrochemical tests, specimens of 2 mm by 2 mm were cut and small holes were added for electrical connection to a Pt wire. For the mechanical testing, small three-point bend bars were cut with a width of 3 mm. Both types of specimen were polished lightly with 4000 grit abrasive paper, and rinsed in deionized

water, acetone, and finally methanol before annealing for 1 h at 900°C in air, followed by air cooling. The resultant grains were essentially equiaxed and approximately 30 μm in diameter. After annealing, each specimen was rinsed again in methanol, and all but 0.04 cm^2 (one side) was insulated with lacquer. All tests were performed in perchloric acid solutions of either 1 M, 50 mM or 10 mM concentration at room temperature or 70°C. The electrochemical tests were conducted in $HClO_4$ solutions that had been deaerated for at least 2 h with nitrogen. A standard three-electrode arrangement was used. In most cases, a saturated calomel electrode (SCE) was in a separate compartment and was connected to the test cell via a Luggin capillary. In cases where this arrangement might have interfered with the measurement due to frequency response limitations, the SCE was moved into the test cell for the measurement.

Testing Methods

Dealloying was accomplished by potentiostatically holding the specimen at +1.05 V(SCE). This results in perfectly selective oxidation of silver as the reversible potential for gold oxidation is well above this potential in this solution. The thickness of the dealloyed layers so formed was estimated based upon the charge passed. Thickness for the thicker films was correlated to the charge passed by examination of fractured specimens in a scanning electron microscope.

The mechanical tests involved growing a dealloyed layer on the three-point bend bar while it was under zero stress and then rapidly (> 100%/s) straining it in a single shot to a permanent deformation of over 45°. Recent work [*3,4*] has shown the benefits of rapidly straining thin foils in order to test the applicability of different SCC models. The key aspect of these experiments is the decoupling of the stress from the corrosion. Once hydrogen embrittlement is excluded [*5,6*], the only model that is consistent with the formation of a crack in the absence of dissolution is the film-induced cleavage model. By introducing the stress in a "single-shot" manner, other SCC mechanisms are not rapid enough to account for any observed cracking. Other experimental details of work showing the applicability of the film-induced cleavage model to the SCC of Ag/Au have appeared elsewhere [*4*]. In some experiments, the dealloyed layer was allowed to age at room temperature or 70°C *in-situ* for up to 6 h before the single-shot straining was imposed. For the specimens to be aged for long periods at 70°C, the potential was stepped to +0.7 V(SCE) after completion of the dealloying and held there for 1 min to prevent plating of silver. The effects of aging were studied when allowed to occur under both open circuit conditions and when holding the specimen potentiostatically at various potentials in the non-faradaic region. Under these conditions, no dissolution can occur.

One of the goals of this work was to study the changes in the nature of the porosity of dealloyed layers during aging. An advantage of working with noble metal alloys is the existence of a wide non-faradaic region of potential. This allows for the probing of the surface area with electrochemical methods; the interface behaves as a pure capacitor over a wide range of frequencies. Three types of electrochemical methods were used to evaluate the surface area of the dealloyed layers and how it changed with time: potential steps, potential triangle waves, and EIS. Potential steps from 0 V(SCE) to +0.05 V(SCE) were applied and the current recorded. Some measurements were made at other potentials, but all were in the non-faradaic region and were 50 mV in amplitude. The integration of the current waveform yielded a measure of the capacitive charge at the interface. By comparing these measurements to those made on smooth electrodes, changes in surface area could be easily calculated. For purely capacitive interfaces, a potential triangle requires the imposition of a current square wave whose magnitude is directly proportional to the surface area. Triangular waveforms of 50 mV peak to peak and a period of 4 s were used

to follow the initial coarsening (10 to 1000 s) at different potentials. EIS was performed in order to probe the structure of the dealloyed layer, and was also used as an additional method to measure the total active surface area by measurement of the low-frequency capacitance. Impedance measurements were made from 20 kHz to 10 mHz using an amplitude of 10 mV rms and a dc potential of 0 V(SCE). A Solartron 1250 Frequency Response Analyzer was coupled to a Sycopel Ministat potentiostat for these measurements.

Results

Mechanical Tests

Typical results of the mechanical tests are shown in Figs. 1 and 2. Figure 1 shows a metallographic cross-section of a specimen that was rapidly strained immediately after growth of the dealloyed layer. The brittle dealloyed layer cracked in many places, and in two, the cracks extended into the bulk, undealloyed material for distances of over 60 μm. Figure 2 shows a cross-section of a similar specimen for which the layer was allowed to age for 4 min under open circuit conditions. While the layer still fractures in a macroscopically brittle manner, no cracks are able to propagate past the dealloyed layer. Many other experiments were performed in order to demonstrate that when cracking did occur it took place during the application of the single-shot strain and these have been presented in detail elsewhere [*4*]. Figure 3 shows that this brittle-to-ductile transition takes time to occur. If specimens were strained within 1 min after the layer was grown and the dealloying potential was removed, cracks propagated past the dealloyed layer (labeled as filled circles). However, longer term open circuit decays resulted in no cracking past the dealloyed layer (labeled as an open circle). Table 1 shows the results of tests performed with the specimen held at constant potential during aging after growth of a dealloyed layer approximately 5 μm thick. In these tests, the potential was stepped from the dealloying potential of +1.05 V(SCE) to the coarsening potential.

In order to evaluate this brittle-to-ductile transition in more depth, a series of experiments were conducted to determine the time to the transition at constant potential. Table 2 shows these results. At 0 V(SCE), the brittle-to-ductile transition begins to occur within

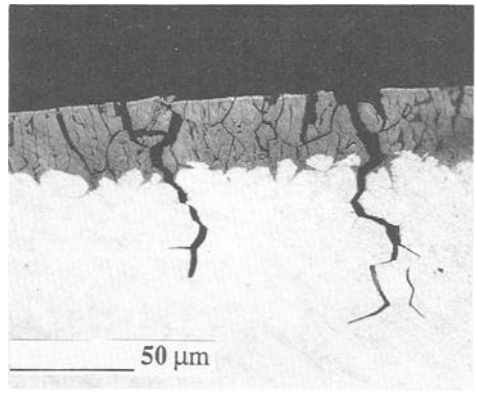

FIG. 1—*Metallographic section of 0.5 mm sheet specimen of an 80Ag-20Au alloy strained rapidly after growing a 20-μm-dealloyed layer. The dealloyed layer is at the top, and cracks which propagate well past the dealloyed layer can be seen. Also, note the preferential attack of the dealloying at the grain boundaries. Dealloying performed at +1.05 V(SCE) in 1 M* $HClO_4$.

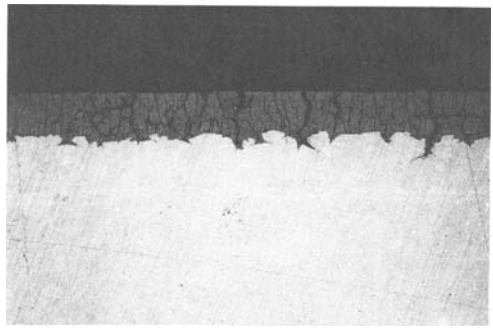

FIG. 2—*Metallographic section of 0.5 mm sheet specimen of an 80Ag-20Au alloy strained after allowing the sample to age at room temperature in air for 5 min. Note the many cracks in the dealloyed layer, but none propagate into the bulk material. Dealloying performed at +1.05 V(SCE) in 1 M $HClO_4$.*

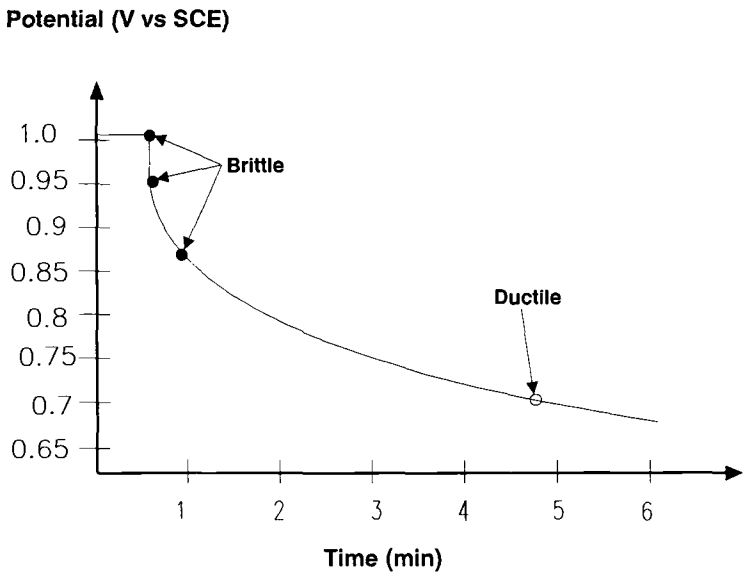

FIG. 3—*Potential decay transient obtained after removing applied potential (+1.05 V(SCE)) from an 80Ag-20Au alloy. Specimens were stressed rapidly to failure at the indicated points and the type of fracture was determined by examination in the SEM.*

15 min, but is not complete for 3 h. At +0.6 V(SCE), some brittle fracture also remains for at least 1 h. More testing is presently underway to more accurately define the beginning of the transition under potentiostatic conditions and will be reported later [*17*].

Electrochemical Tests

The complex plane plot of a flat Ag-Au electrode in deaerated 10 mM $HClO_4$ at 0 V(SCE) is shown in Fig. 4. Over the frequency range of interest (10 mHz to 1 kHz), no

TABLE 1—*Fracture mode results of potentiostatic coarsening mechanical tests on 25-μm-thick 80Ag-20Au alloy specimens with five μm dealloyed layers at room temperature. Dealloying performed at +1.05 V(SCE) in 1 M $HClO_4$.*

Test No.	Coarsening Potential (V versus SCE)	Coarsening Time, min	Fracture Mode[a]
1	+0.75	1	I
2	+0.1	1	I
3	+0.75	5	I
4	+0.1	5	I
5	+0.1	100	I/D

[a]I = intergranular fracture; I/D = mixture of intergranular and ductile fracture.

TABLE 2—*Fracture mode[a] results of potentiostatic coarsening mechanical tests for 25-μm-thick 80Ag-20Au alloy specimens with five μm dealloyed layers at room temperature. Dealloying performed at +1.05 V(SCE) in 1 M $HClO_4$. Specimens were coarsened at 70°C.*

	Coarsening Time, h						
Potential, V(SCE)	0	0.25	1	2	3	4	6
0	I	I/D	I/D	I/D	D		D
+0.6	I		I/D		D		D

[a]I = intergranular fracture; I/D = mixture of intergranular and ductile fracture; D = ductile.

faradaic processes are seen; the interface behaves as a pure capacitor. A specific capacitance of 8 μF/cm² can be calculated that is slightly (±10%) frequency dependent. Figure 5 shows the spectrum generated for a specimen with a 50-μm-thick dealloyed layer. While the low-frequency portion (<0.08 Hz) is similar in form to that of the flat electrode, it represents a much larger surface area, as shown in a comparison of the impedance magnitude plots of the two specimens of the same apparent surface area (Fig. 6). The specimen with the dealloyed layer has the purely capacitive portion of the spectrum shifted to much lower frequencies, characteristic of a large capacitance. The most dramatic differences in the spectra appear between 0.08 Hz and 20 kHz. The electrode with a dealloyed layer shows a dispersion in the impedance due to the physical structure of the layer. As discussed earlier, the combination of the resistivity of the solution, the structure of the pore (length and radius) and the specific double layer capacitance of the interface determine the degree of dispersion of the impedance according to Eqs 3 and 4. The character of the dispersion contains information about the details of the porous structure.

If the dealloyed layer is allowed to coarsen at elevated temperature (in air at 400°C for 1 h), a marked change in the structure of the porous layer occurs as revealed by the complex plane plot shown in Fig. 7. While there appears to be little change in the high-frequency portion of the plot, a striking change in the 0.08 to 5 Hz region occurs. This portion of the complex plane plot is much more vertical in the aged specimen, as can be easily seen in Fig. 7*b*. The shift in the high-frequency intercept for the two spectra is due to a slightly different solution resistance due to a slight change in specimen to reference electrode distance upon reintroduction of the specimen into the electrochemical cell after aging.

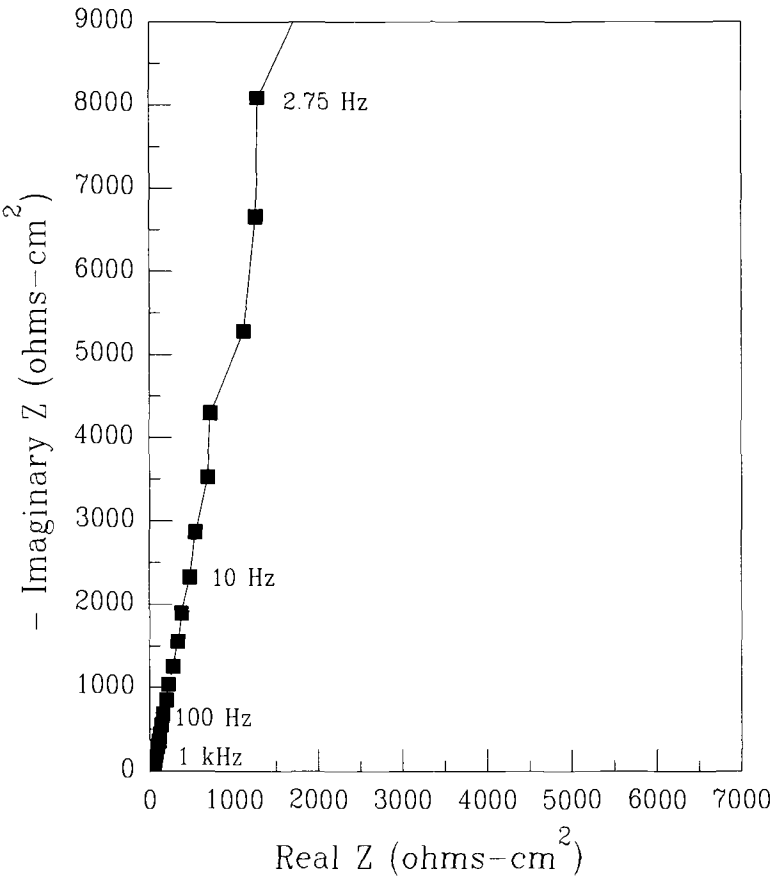

FIG. 4—*Complex impedance plot of a smooth gold wire in 10 mM $HClO_4$ at 0 V(SCE).*

A similar change in the complex plane plot occurs during aging in solution at 70°C and 0 V(SCE). Figure 8 shows the progression in the low-frequency portion of the plot with time to a higher and higher degree of verticality (see Fig. 8*b*). The loss of total surface area that occurs during this coarsening can be most easily seen in Fig. 9 in which the effects of the potential at which the coarsening was allowed to occur are illustrated. These results are from the potential step experiments. The logarithm of the ratio of the charge under the current transient measured at time $t = 0$ to that measured at time t is plotted as a function of the logarithm of the coarsening time. At the three lower potentials (0, +0.45 and +0.6 V(SCE)), the degree of coarsening is similar, with about 70% of the original area of the dealloyed layer being lost over 55 h. At the higher potential of +0.75 V(SCE), the coarsening is much faster. The slopes of the lines indicate that the coarsening has a $t^{1/4}$ time dependence.

Figure 10 compares the results of coarsening measurements made early on in the coarsening process for a variety of potentials between −0.1 V and +0.5 V(SCE). These measurements were made by the application of a potential triangle wave, which, for a purely capacitive interface, results in a square current wave. The large increase in the rate of coarsening at +0.5 V(SCE) is apparent.

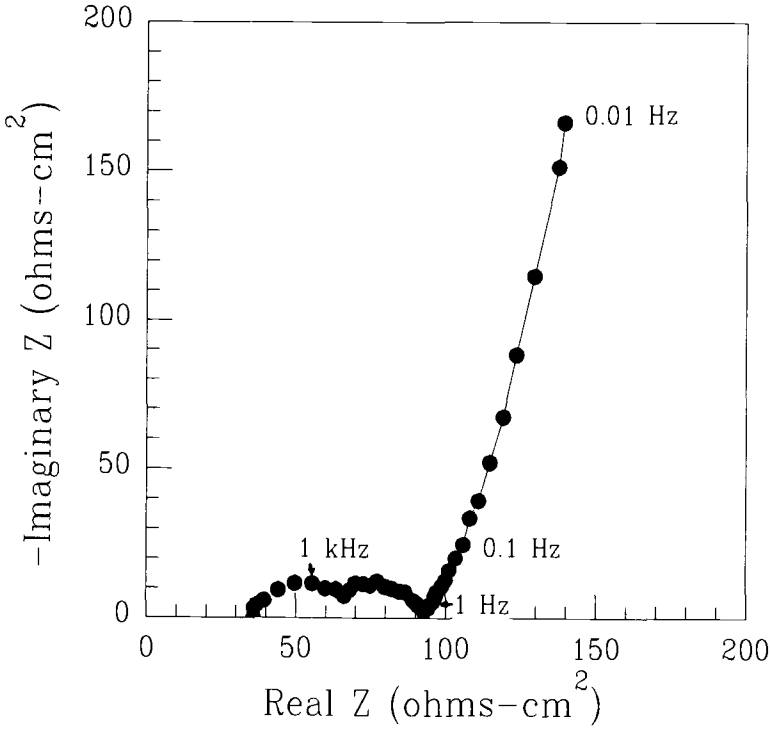

FIG. 5—*Complex impedance plot of an 80Ag-20Au alloy with a freshly-formed 50 μm dealloyed layer. Note the structure at both high and intermediate frequencies. Spectrum measured at 0 V(SCE) in 10 mM $HClO_4$.*

Estimations of the effective cylindrical pore parameters (radius and number) for the different aging treatments can be made based upon the work of Candy et al. [*15*] and are shown in Table 3. While the coarsening at 70°C has no discernible effect on either parameter, the specimen coarsened at 400°C for 1 h shows both a large increase in r_{pore} and a large decrease in N.

Discussion

Mechanical Test Results

A series of recent publications [*1–4*] has shown that normally ductile materials such as α-brass [*3*] and Ag-Au [*4*] can be made to undergo brittle cracking when a nanoporous, dealloyed layer is present. In order for this cracking to occur, the layer must not be allowed to age excessively, even at room temperature; otherwise, the embrittlement is reversed. Hydrogen embrittlement can be ruled out for both systems on the basis of thermodynamic calculations [*5,6*]. By showing that this cracking can occur under conditions of rapid straining in addition to slow strain rate conditions, models based upon anodic dissolution, including surface diffusion models, have been shown to be inappropriate for explaining the cracking phenomenology in these systems. Calculations have shown that no dissolution-based model can explain either the observed crack velocities or the reversibility of the embrittlement [*4*]. This is particularly true for the cracking observed at

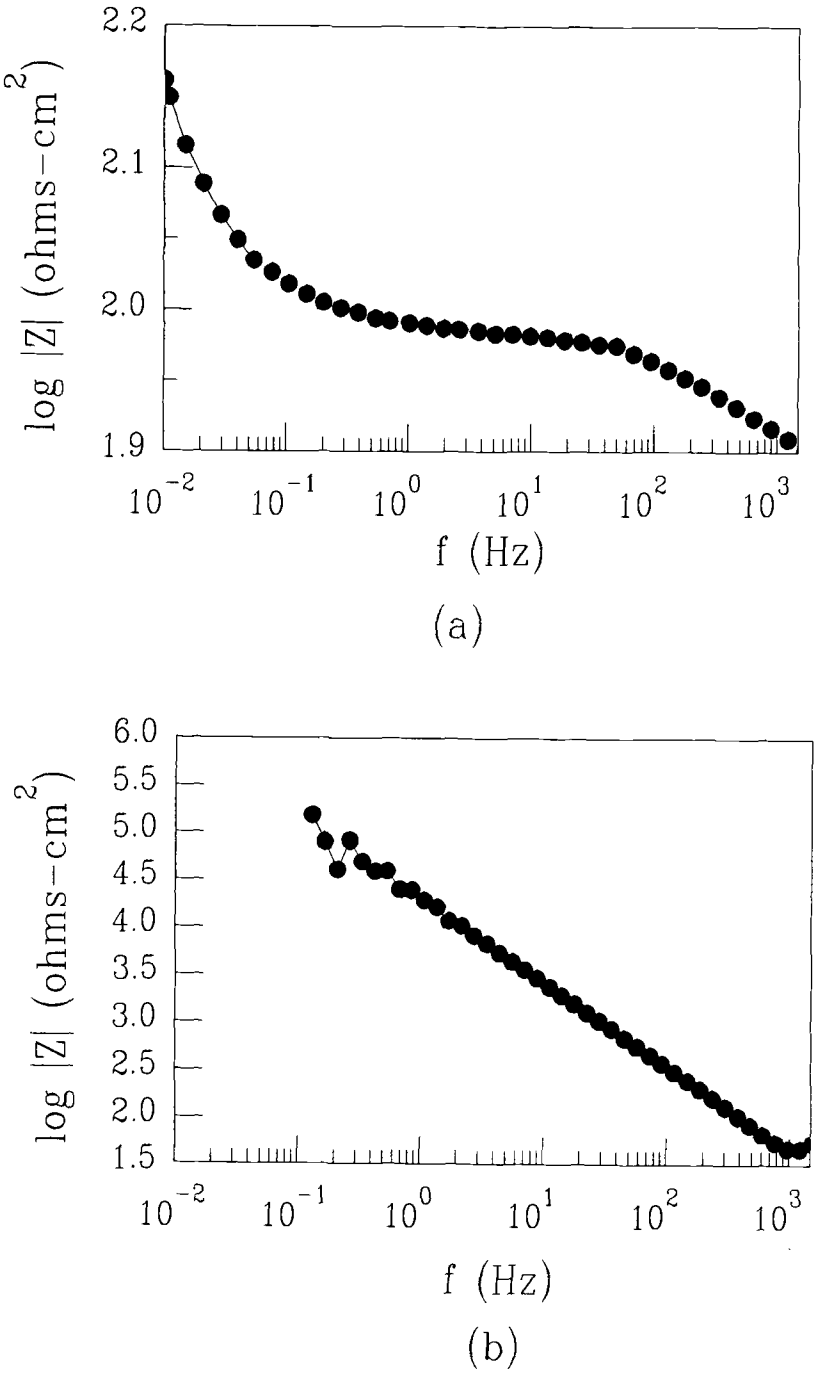

FIG. 6—*Impedance magnitude spectra of* (a) *an as-dealloyed 80Ag-20Au specimen and* (b) *a smooth gold wire in 10 mM* $HClO_4$. *The much lower impedance of the as-dealloyed specimen is due to the much higher surface area (note the difference in scales). The dispersion of the impedance due to the structure of the layer is also apparent above 100 mHz. Spectra measured at 0 V(SCE).*

potentials where there is no faradaic reaction. A film-induced cleavage model is, however, consistent with all of the experimental results.

One of the cornerstones of the film-induced cleavage model is the prediction that only nanoporous surface layers would have the combination of a low strain-to-failure and intimate connection to the substrate that is required for a brittle crack to propagate into a ductile substrate [*1,2*]. Dealloyed layers can meet these criteria when they are formed. However, such as-dealloyed layers experience an extremely large driving force for surface rearrangement due to their very large surface areas. Thus, if experimental conditions were to allow for the dealloyed layer porosity to coarsen before the imposition of the stress, no crack extension past the boundary of the dealloyed layer would be predicted to occur. One of the advantages of the rapid foil testing used in the present investigation is the opportunity to implement different aging treatments and observe the effects on the cracking behavior for a single cracking event. In slow strain rate testing, the constantly increasing stress usually prevents sufficient time for this coarsening to occur at the crack tip; the cracking rate is controlled by the time it takes the dealloyed layer to form to the critical thickness at the crack tip. Once again, it should be emphasized that, once hydrogen

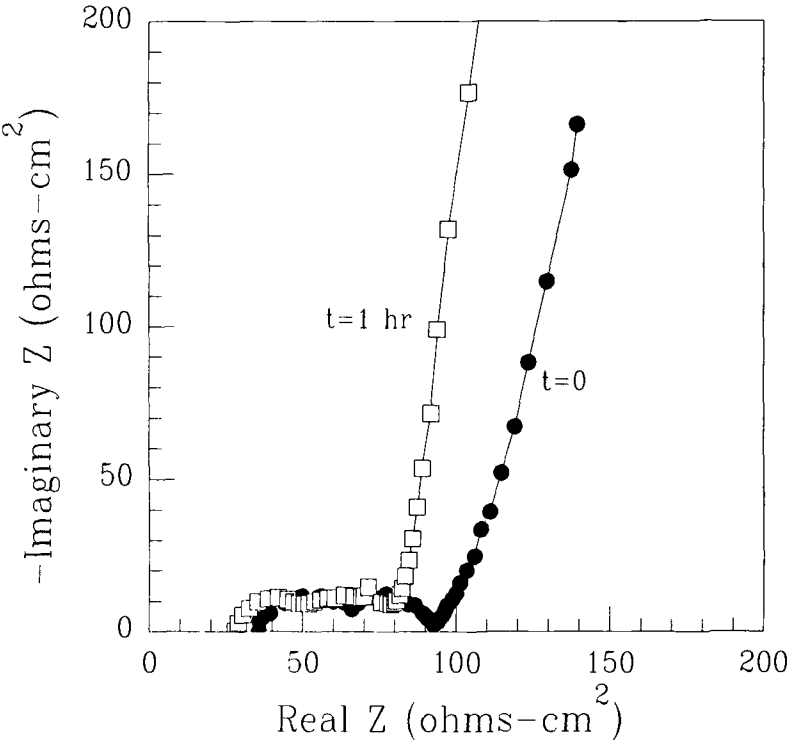

FIG. 7—(a) *Comparison of the complex impedance plot of an 80Ag-20Au alloy with a freshly-formed 50-μm dealloyed layer (filled circles) and after 1 h at 400°C in air (open squares). Note the change in the low-frequency portion of the plot.* (b) *Complex impedance plot of the layer after 1 h at 400°C showing the high degree of verticality of plot even at very low frequencies. Spectrum measured at 0 V(SCE) in 10 mM $HClO_4$.*

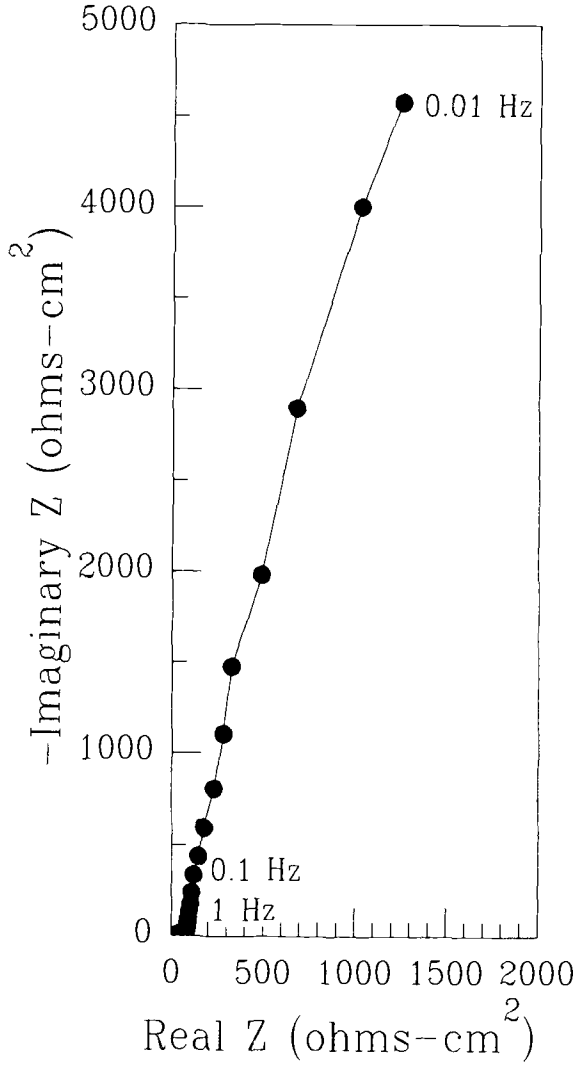

FIG. 7—(continued)

embrittlement is excluded, no other theory of SCC would predict a reversibility in the embrittlement.

Thus, one key to understanding the physical origin of film-induced cleavage is understanding the cause of the reversibility of the embrittlement. For hydrogen embrittlement, reversibility has been ascribed to diffusion of hydrogen either out of the specimen (for high-temperature treatments [*10,11*]) or diffusion to less deleterious sites at more moderate temperatures (i.e., a more even distribution throughout the test specimen). These suggestions have been supported by high-temperature baking combined with detection of the escaping hydrogen by mass spectrometry [*18*]. For aging dealloyed layers, the evidence to this point has been less direct. For example, it has been shown [*3,4*] that by immediately

plunging specimens with freshly-dealloyed surfaces into liquid nitrogen, brittle cracking of these FCC alloys can occur. This has been ascribed to the prevention of layer coarsening by surface diffusion at 77 K. As previously discussed, a brittle-to-ductile transition can be observed in bulk samples after *ex-situ* treatments [*10,11*] as well as *in-situ* at constant potential (Table 2). However, more direct measurements of the changes in the pore size under *in-situ* conditions would provide stronger evidence for a link between the pore coarsening and the brittle crack advance.

Such coarsening would have to be able to occur rapidly at room temperature in order to explain the results shown in Figs. 1 and 2; bulk diffusion of silver (or gold) would not be nearly rapid enough to cause sufficient coarsening at such a low value of the homologous temperature. Thus, surface diffusion would appear to provide the most plausible explanation. Surface diffusion of metals in solution is known to be potential dependent though not smoothly so [*18,19*], with the reasons for this being a topic of some debate. Kolb [*18*] has shown that gold surface diffusion occurs faster at higher potentials in $HClO_4$, with very slow coarsening occurring at potentials below which specific adsorption of different anions occurs. This appears to be the case in the present study as well. The results shown in Figs.

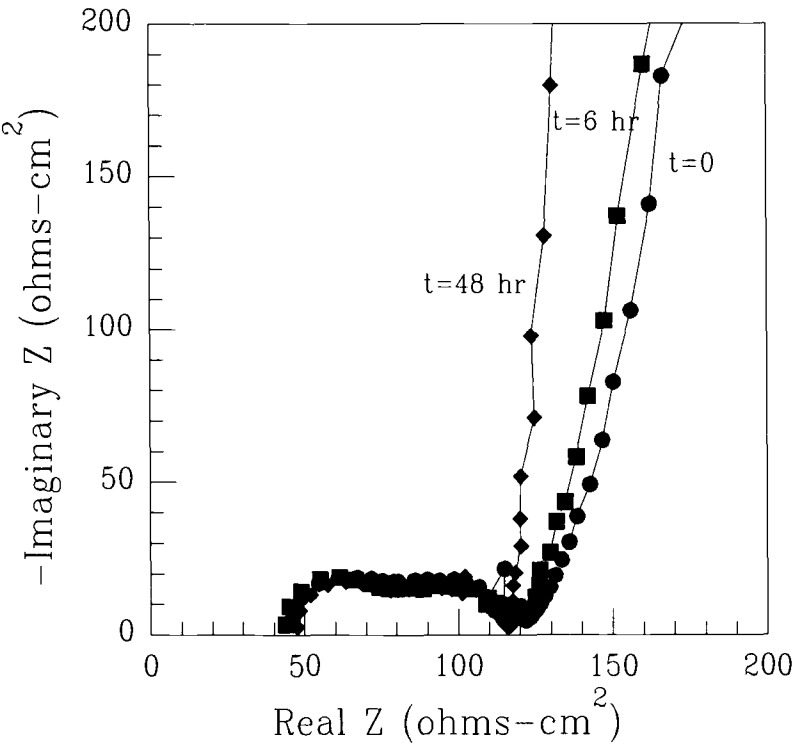

FIG. 8—(a) *Comparison of the complex impedance plot of an 80Ag-20Au alloy with a freshly-formed 50-μm-dealloyed layer (filled circles) and after 6 h (filled squares) and 48 h (filled diamonds) at 70°C and 0 V(SCE) in 1 M $HClO_4$. Note the change in the low-frequency portion of the plot.* (b) *Complex impedance plot of the layer after 48 h at 70°C and 0 V(SCE) in 1 M $HClO_4$ showing the high degree of verticality of plot even at very low frequencies. All spectra measured at 0 V(SCE) in 10 mM $HClO_4$.*

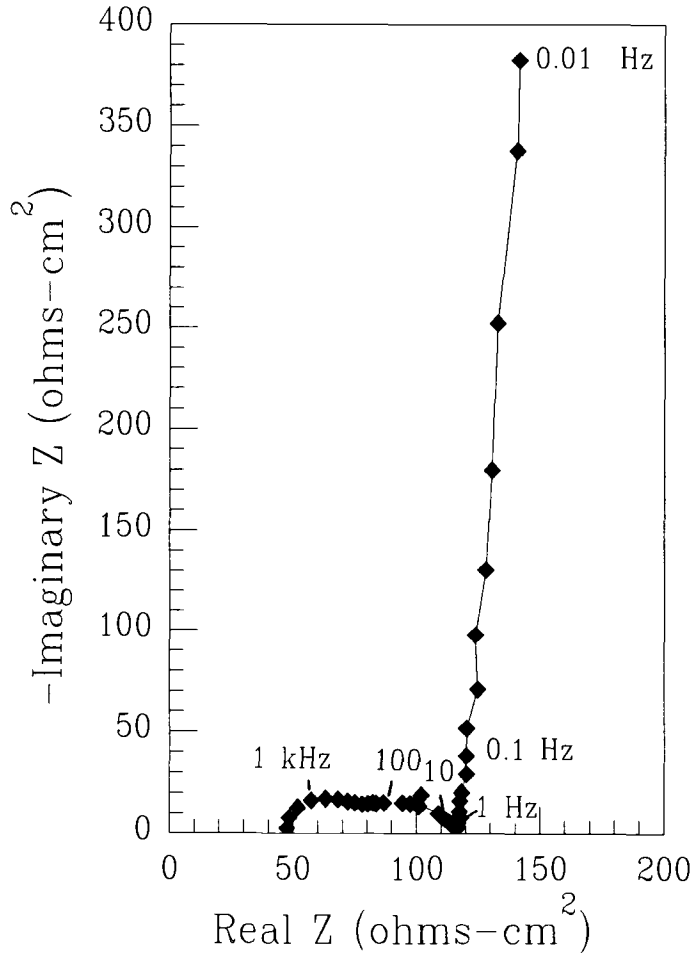

FIG. 8—(continued)

3 and 9 support this when combined with those displayed in Table 1. Figure 3 shows that as the potential falls below +0.7 V(SCE) after approximately 4 min at open circuit, the layer loses its ability to inject a crack into the substrate. If this were simply a time effect, then Tests 2 and 4 in Table 1 would have shown no crack extension past the dealloyed layer. However, the potential steps that were used in the tests in Table 1 freeze the porosity in its as-dealloyed state. At these lower potentials, the coarsening occurs slowly, and the layer retains its ability to inject a brittle crack into the uncorroded substrate for extended periods of time. For the experiments whose results are shown in Fig. 3, the specimens were allowed to spend a significant amount of time at a higher potential.

Figure 1 and Table 2 both demonstrate that when the specimen remains in solution, the brittle-to-ductile transition takes time to occur. That is, while the embrittlement is reversible, the kinetics of the recovery are slow and affected by the presence of solution, temperature, and potential, as one would expect for a process controlled by surface diffusion.

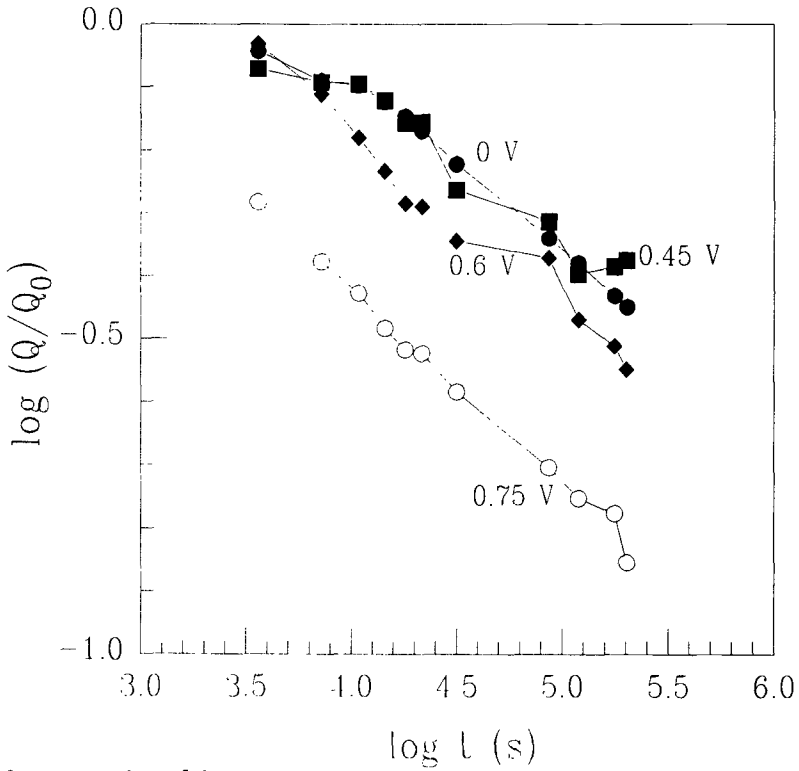

FIG. 9—*Logarithm of the ratio of the charge passed during a 50 mV step at time t*(Q) *to that at t = 0*(Q_o) *versus the logarithm of time for specimens held potentiostatically at the potentials indicated. The charge is directly proportional to the total active surface area of the electrode. Measurements made in 1 M* $HClO_4$ *at 0 V(SCE).*

Electrochemical Results

The impedance results lend insights into details of the dealloying process and the nature of the porosity that the dealloying produces. Using Eqs 3 and 4, along with the impedance data from dealloyed samples, an estimate can be made of the equivalent cylindrical pore parameters. As previously discussed, this analysis results in a description of a set of N parallel pores, each with a radius of r_{pore}, and a length l (taken as the thickness of the dealloyed layer, 50 μm). For as-dealloyed specimens, this results in approximately 10^{11} pores/cm^2 of 9-nm-radius. The dealloying process is able to produce such a fine porosity due to its high selectivity; all of the silver atoms are removable, while the gold atoms are inert. Since the alloy is 80 at.% Ag, the result of the selective removal of the silver is a fine network of gold ligaments which experience a large driving force for surface rearrangement.

As discussed earlier and elsewhere [*12–15*], uniform, cylindrical pores whose surfaces are under non-faradaic conditions will exhibit a single line in the complex plane at frequencies above f^* which will be at 45° to both axes. The more re-entrant the pores, the more the locus of the complex plane impedance plot will deviate from the 45° phase angle, and will begin to resemble a relaxation due to a faradaic process. The frequency at which the relaxation due to a set of pores appears depends upon their distance from the outer surface

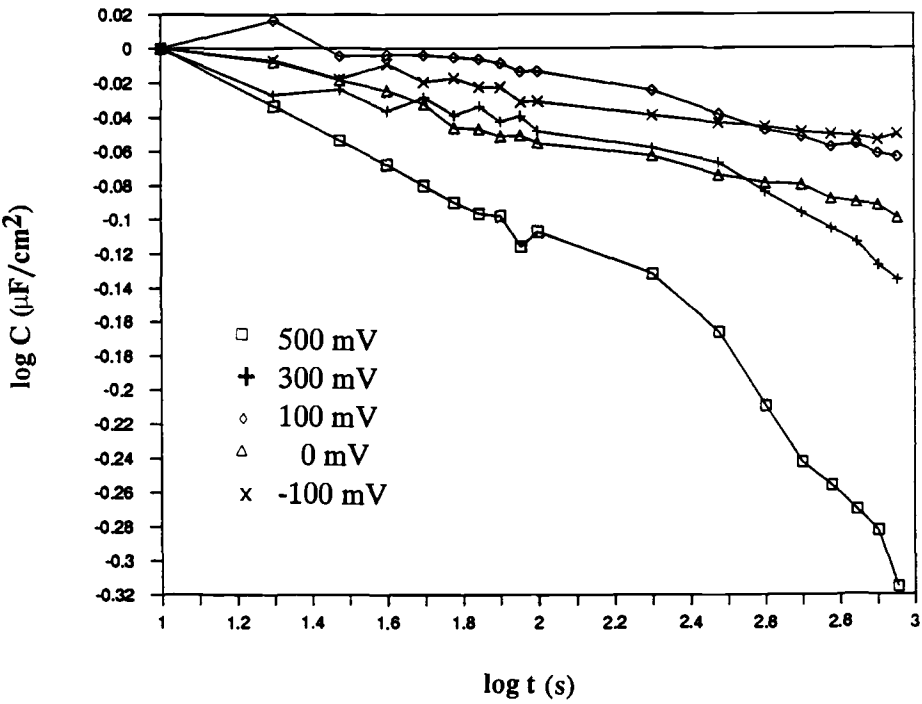

FIG. 10—*Logarithm of the ratio of the low-frequency capacitance at time t to that at t = 0 versus the logarithm of time for specimens held potentiostatically at the potentials indicated. The capacitance is directly proportional to the total active surface area of the electrode. These measurements were made by applying a potential triangle waveform and monitoring the resulting current square wave. Measurements made in 1 M $HClO_4$ at the indicated potential.*

and the tortuosity of the path to the bulk solution. The nonuniform porosity of the dealloyed layer manifests itself in a three-stage dispersion of the impedance. Figure 5 shows two relaxations at high frequency, possibly due to two populations of pore sizes, with the one closer to the outer surface having a relaxation at higher frequencies. The near semicircular shape of these features indicate that the outer pores are (or behave as if they are) somewhat re-entrant. Impedance data generated at other potentials in the non-

TABLE 3—*Effects of coarsening on the equivalent cylindrical pore parameters of dealloyed layers on 80Ag-20Au alloy specimens. All specimens were 500 μm thick and had dealloyed layers of 50-μm-thickness, which was the value used in the calculations of the pore parameters as the length. Dealloying performed at +1.05 V(SCE) in 1 M $HClO_4$.*

Treatment	f^* (Hz)	r_{pore} (nm)	N, ($\times 10^{11}$ pores/cm^2)
70°C/t = 0	3.72	9	2.7
70°C/t = 6 h	3.72	9	2.3
70°C/t = 48 h	2.6	6	2.5
400°C/t = 0	5.1	12	2.4
400°C/t = 1 h	25.8	61	0.022

faradaic region showed no voltage dependence for these features, pointing once again to a geometric origin. The residual dc current under these conditions (<1 $\mu A/cm^2$ based on geometric area) also indicates that any faradaic process that is occurring is doing so at a slow rate and would, therefore, exhibit a much larger impedance than the 75 Ω-cm^2 measured for these features. The use of the dealloyed layer thickness (50 μm) as the pore length may be questioned for such tortuous pores. However, the aim of the modeling is to represent the dealloyed layer in terms of an electrode containing cylindrical pores. This approach allows the effects of experimental conditions imposed after the layer is formed to be studied. Since none of these experimental conditions changed the thickness of the dealloyed layer, the use of the thickness of the dealloyed layer as the length of the equivalent cylindrical pore appears to be reasonable.

The second stage of the frequency dispersion occurs in the range of 100 to 50 mHz and corresponds to the beginning of the near vertical section of the plot. For ideally flat capacitive interfaces, this section is truly vertical. Well-coarsened dealloyed layers show such behavior at low frequencies as shown in Fig. 7*b*. For as-dealloyed layers (Fig. 5) and slightly coarsened layers (Fig. 8), this region is not quite vertical. If this were due to a slow faradaic process, it would continue to lower frequencies and would be unaffected by aging. However, at lower frequencies, the plot does indeed become more vertical (Fig. 5), and the feature is strongly affected, even by low-temperature aging (Fig. 8). The finest pores would be found at the dealloying front; the region closest to the interface of the dealloyed layer with the underlying substrate contains the most recently formed pores. These pores would therefore manifest themselves in the impedance measurement at lower frequencies than pores in the bulk of the dealloyed layer that are closer to the interface of the layer with the bulk electrolyte. While the small radius of these pores would lead to a high pore impedance, they would have the highest driving force for coarsening due to their high surface area-to-volume ratio. Thus, they would be the pores most likely to coarsen under mild aging conditions where no new dealloying was occurring.

At the lowest frequencies (<50 mHz), the interface behaves identically to a flat, non-faradaic electrode with an extremely large surface area. For example, the low-frequency data from the as-dealloyed specimen shown in Fig. 7 represents a capacitance of 0.16 F/cm^2 of geometric area. This represents an active surface area of approximately 20 000 cm^2 per cm^2 of geometric area based on the specific capacitance of 8 $\mu F/cm^2$ measured on a gold wire in the same solution. These extremely high surface areas are the result of the efficiency of the dealloying process in removing the silver from this 80 at.% Ag alloy. The resultant network of extremely fine gold ligaments, while space-filling, consists of over 10^{11} pores per cm^2. A separation of this effect from pseudo-capacitances due to residual oxygen reduction is possible from analysis of the phase angle of the impedance with frequency. In these solutions, the phase angle, adjusted for the shift due to the pore impedance, remained constant at 83 $\pm$ 3° from 1 Hz down to 10 mHz for well-coarsened layers (70°C for 48 h, Fig. 8*b*). Below this, indications of the presence of a very slow faradaic process start to become apparent. Estimates of the reaction resistance for this process (thought to be reduction of trace oxygen) gives a value of 20 k Ω-cm^2. This further supports the assertion above that the higher frequency structure in the complex plane plot is due to the geometry of the pores, and not the relaxation of a faradaic reaction.

During coarsening, it would be expected that the majority of the change occurs in the finest pores. These pores would have the highest driving force for the coarsening, which would allow them to reduce their surface energy through a reduction in their surface area. Both aging treatments cause a major change in the middle frequency portion (50 to 100 mHz) of the complex plane plot, as shown by Figs. 7 and 8 and Table 3. This change is gradual for lower temperature aging treatments, as shown in Fig. 8. The results shown in

Table 3 illustrates that 70°C aging in solution has little effect on the average pore parameters because the finest pores make up a small fraction of the total surface area of the 50-μm-thick layer. However, their effect on the middle-frequency range data is apparent in both Figs. 7 and 8. The higher temperature aging affects both the finest pores (Fig. 7) and the larger pores (Table 3). While the effects on the larger pores (note these "large" pores are still <100 nm radius) is apparent in Table 3, these changes are still subtle in Fig. 7. Longer coarsening times or higher coarsening temperatures, or both, do make observable changes in the complex plane plots, though the qualitative appearance of the plots remains. This is not surprising in light of the self-similar coarsening noted by Li and Sieradzki [*10,11*] during high-temperature aging of completely dealloyed bars. The finest pores close to the interface are expected to be the most important in terms of the film-induced cleavage model [*1,2,4*]. It is the condition of these pores that determines whether or not a crack formed in the dealloyed layer continues into the substrate. If they are extremely small and have an intimate connection with the substrate, then brittle cracks formed in the layer during straining would be able to continue into the bulk. Such a condition can occur most easily during slow dealloying at a crack tip. When the layer reaches a critical thickness for the applied stress, the layer cracks and the crack penetrates some distance into the substrate. However, if these extremely fine pores are allowed to coarsen, they lose this ability to transmit the crack.

The potential dependence of the coarsening as shown in Figs. 9 and 10 indicates that it is clearly not associated with bulk phenomena. Surface diffusion rates are, however, potential dependent [*19–21*] and have been measured to be as high as 2.5×10^{-3} cm^2 s^{-1} [*21*] for bulk gold samples. In cases where the surface diffusion is assisted by anion adsorption, such as gold in sulfate solution, higher potentials lead to higher rates [*20*]. The surface diffusion rate is not linear with potential; below the adsorption potential for the anion, the rate is low and relatively insensitive to potential, while above the potential of adsorption, the rate increases dramatically. In the present case, the perchlorate anion may assist in the surface diffusion, as may residual chloride, above +0.7 V(SCE). Thus, open circuit potential decays, which spend approximately 3 min above +0.7 V(SCE), have sufficient time *at a high enough potential* to coarsen the layer sufficiently to remove its ability to inject a crack. Potential steps from the dealloying potential to a potential in the nonfaradaic region are capable of retarding the surface diffusion process, and thereby preserve the fine porosity necessary for brittle cracking. Other methods of preventing surface diffusion, such as quickly cooling the specimen in liquid nitrogen before fracturing, are also effective in maintaining the layer's ability to inject a brittle crack into the underlying FCC material [*3,4*].

Summary and Conclusions

(1) The coarsening of dealloyed layers controls the ability of these layers to inject brittle cracks into the underlying substrate.

(2) This coarsening can be followed *in situ* in detail through the use of electrochemical measurements.

(3) The impedance measurements indicate that the pores in the outer portion of the layer are re-entrant. In addition, the finest pores, which are closest to the substrate, are the most sensitive to coarsening.

(4) The potential and time dependence of the coarsening implies that the controlling process is surface diffusion of gold atoms.

Acknowledgments

One of the authors (R.G.K.) acknowledges the financial support of the Fulbright Commission and the National Science Foundation through a Fulbright Scholarship and an NSF/NATO Post-doctoral Fellowship, respectively. The Research Corporation Trust is acknowledged for additional financial support, as is Johnson Matthey, plc for the loan of the materials. Discussions with Prof. D. E. Williams are also gratefully acknowledged, as are contributions by G. Smith and M. Suleiman with the mechanical testing.

References

[1] Sieradzki, K. and Newman, R. C., *Philosophy Magazine A*, Vol. 51, 1985, p. 95.
[2] Sieradzki, K. and Newman, R. C., *Journal of Physics and Chemistry of Solids*, Vol. 48, 1987, p. 1101.
[3] Newman, R. C., Shahrabi, T., and Sieradzki, K., *Scripta Metallurgica*, Vol. 23, 1989, p. 71.
[4] Kelly, R. G., Frost, A. J., Shahrabi, T., and Newman, R. C., *Metallurgical Transactions A*, Vol. 22A, 1991, p. 531.
[5] Bertocci, U., *J. Electrochem. Soc.*, Vol. 136, 1989, p. 1887.
[6] Pickering, H. W., *International Congress on Metallic Corrosion*, Vol. 2, National Research Council of Canada, Ottawa, Ontario, 1984, p. 246.
[7] Newman, R. C., Zheng, W., Tilley, C. R., and Procter, R. P. M., Paper 568, *Corrosion '89*, National Association of Corrosion Engineers, Houston, TX, 1989.
[8] Cassagne, T. B., Flanagan, W. F., and Lichter, B. D., *Metallurgical Transactions A*, Vol. 19A, 1988, p. 281.
[9] Hannah, I. M., Procter, R. P. M., and Newman, R. C., *Proceedings, 4th International Conference on Hydrogen Effects on Material Behavior*, N. R. Moody and A. W. Thompson, Eds., TMS-AIME, Warrendale, PA, 1990, pp. 965–973.
[10] Li, R., "Studies of the Mechanical Properties of Solids with Random Porosity," Ph.D. Dissertation, Queens College, City Univ. of New York, Queens, NY, 1989.
[11] Li, R. and Sieradzki, K., submitted to *Physical Review Letters*.
[12] deLevie, R., in *Advances in Electrochemistry and Electrochemical Engineering*, P. Delahay, Ed., Vol. 6, Interscience, New York, 1967, p. 329.
[13] deLevie, R., *Electrochimica Acta*, Vol. 8, 1963, p. 751.
[14] deLevie, R., *Electrochimica Acta*, Vol. 9, 1964, p. 1231.
[15] Candy, J. P., Fouilloux, P., Keddam, M., and Takenouti, H., *Electrochimica Acta*, Vol. 26, 1981, p. 1029.
[16] Keiser, H., Beccu, K. D., and Gutjahr, M. A., *Electrochimica Acta*, Vol. 21, 1976, p. 539.
[17] Kelly, R. G., Smith, G., Suleiman, M., and Newman, R. C., in preparation.
[18] Lee, S. M. and Pyun, S. I., *Scripta Metallurgica et Materialia*, Vol. 24, 1990, p. 1629.
[19] Kolb, D., Lehmpfuh, G., and Zei, M., *Journal of Electroanalytical Chemistry*, Vol. 179, 1984, p. 298.
[20] Kolb, D. M. and Schneider, J., *Surface Science*, Vol. 162, 1985, p. 764.
[21] Alonso, C., Salvarezza, R. C., Vara, J. M., and Arvia, A. J., *Electrochimica Acta*, Vol. 35, 1990, p. 1331.

Applications of Kramers-Kronig Transformations

Pankaj Agarwal,[1] *Mark E. Orazem,*[1] *and Luis H. Garcia-Rubio*[2]

Application of the Kramers-Kronig Relations in Electrochemical Impedance Spectroscopy

REFERENCE: Agarwal, P., Orazem, M. E., and Garcia-Rubio, L. H., **"Application of the Kramers-Kronig Relations in Electrochemical Impedance Spectroscopy,"** *Electrochemical Impedance: Analysis and Interpretation, ASTM STP 1188,* J. R. Scully, D. C. Silverman, and M. W. Kendig, Eds., American Society for Testing and Materials, Philadelphia, 1993, pp. 115–139.

ABSTRACT: The Kramers-Kronig equations and the current methods used to apply them to electrochemical impedance spectra are reviewed. Measurement models are introduced as a tool for identification of the frequency-dependent error structure of impedance data and for evaluating the consistency of the data with the Kramers-Kronig relations. Through the use of a measurement model, experimental data can be checked for consistency with the Kramers-Kronig relations without explicit integration of the Kramers-Kronig relations; therefore, inaccuracies associated with extrapolation of an incomplete frequency spectrum are resolved. The measurement model can be used to determine whether the residual errors in the regression are due to an inadequate model, failure of data to conform to the Kramers-Kronig assumptions, or noise.

KEYWORDS: Kramers-Kronig relations, impedance spectroscopy, error structure, measurement models, deconvolution

In principle, the Kramers-Kronig relations can be used to determine whether the impedance spectrum of a given system has been influenced by time-dependent phenomena. Although this information is critical to the analysis of impedance data, the Kramers-Kronig relations have not found widespread use in the analysis and interpretation of electrochemical impedance spectroscopy data due to difficulties with their application. The integral relations require data for frequencies ranging from zero to infinity, but the experimental frequency range is often constrained by instrumental limitations or by noise attributable to the instability of the electrode.

The Kramers-Kronig relations have been applied to electrochemical systems by direct integration of the equations, experimental observation of stability and linearity, or regression of electrical circuit models to the data. Each of these approaches has its advantages and disadvantages. This paper will review the Kramers-Kronig equations and the methods used to apply them to electrochemical impedance spectra. This paper will then suggest that the disadvantages associated with current methods used to check experimental data for consistency with the Kramers-Kronig relations can be circumvented by application of measurement models to impedance spectra.

[1]Graduate student and professor, respectively, Department of Chemical Engineering, University of Florida, Gainesville, FL 32611.

[2]Professor, Department of Chemical Engineering, University of South Florida, Tampa, FL 33620.

The Kramers-Kronig Relations

The Kramers-Kronig relations, developed for the field of optics, are integral equations which constrain the real and imaginary components of complex quantities for systems that satisfy conditions of causality, linearity, and stability [*1–4*]. Bode [*5*] extended the concept to electrical impedance and tabulated various forms of the Kramers-Kronig relations. Several transformations used in the electrochemical literature are shown. The imaginary part of the impedance can be obtained from the real part of the impedance spectrum through

$$Z_i(\omega) = -\left(\frac{2\omega}{\pi}\right) \int_0^\infty \frac{Z_r(x) - Z_r(\omega)}{x^2 - w^2}\, dx, \tag{1}$$

where $Z_r(\omega)$ and $Z_i(\omega)$ are the real and imaginary components of the impedance as functions of frequency ω. The real part of the impedance spectrum can be obtained from the imaginary part through

$$Z_r(\omega) = Z_r(\infty) + \frac{2}{\pi} \int_0^\infty \frac{x\, Z_i(x) - \omega Z_i(\omega)}{x^2 - w^2}\, dx, \tag{2}$$

if the high-frequency asymptote for the real part of the impedance is known, and through

$$Z_r(\omega) = Z_r(0) + \frac{2\omega}{\pi} \int_0^\infty \frac{x/\omega Z_i(x) - Z_i(\omega)}{x^2 - w^2}\, dx \tag{3}$$

if the zero-frequency asymptote for the real part of the impedance is known. A relationship between the phase angle $\phi(\omega)$ and modulus $|Z(\omega)|$ is also available, e.g.,

$$\phi(\omega) = \frac{2\omega}{\pi} \int_0^\infty \frac{\ln\, (|Z(x)|}{x^2 - w^2}\, dx \tag{4}$$

In response to the integration limits, a fourth constraint, which the impedance approaches finite values at frequency limits of zero and infinity, is commonly added. This constraint, sometimes claimed to prevent application of the Kramers-Kronig relations to capacitive systems, is in fact not needed because a simple variable substitution [*5*] can be used if the imaginary part of the impedance tends to infinity according to $1/\omega$ as $\omega \rightarrow \omega_0$ (see also Ref *6*).

Review of Methods for Determining Consistency with the Kramers-Kronig Relations

The usual approach in interpreting impedance spectra is to regress a model to the data. The models employed are typically linear and assume conditions of a sinusoidal steady state. It is important, therefore, that the impedance response be characteristic of a system that is causal, linear, and stable. The condition of linearity can be achieved by using sufficiently small amplitude perturbations. The condition of stability requires that the sys-

tem return to its original condition when the perturbing signal is terminated. An additional implied constraint of stationary behavior may be difficult to achieve in electrochemical systems (such as corrosion) where the electrode may change significantly during the time required to collect impedance data. It is therefore of practical importance to the experimentalist to know whether the data taken do in fact satisfy the Kramers-Kronig relations. The approaches taken to ascertain the degree of consistency include direct integration of the Kramers-Kronig relations, experimental replication of data, and regression of electrical circuit analogues to the data.

Direct Integration of Kramers-Kronig Relations

The Kramers-Kronig relations provide a unique transformation that can be used to predict one component of the impedance if the other is known over the frequency limits of zero to infinity. The usual way of using the Kramers-Kronig equations, therefore, is to calculate the imaginary component of impedance from the measured real component using, for example, Eq 1, and to compare the values obtained to the experimental imaginary component. Alternatively, the real component of impedance can be calculated from the measured imaginary values using Eqs 2 or 3. The major difficulty in applying this approach is that the measured frequency range may not be sufficient to allow integration over the frequency limits of zero to infinity. Therefore, discrepancies between experimental data and the impedance component predicted through application of the Kramers-Kronig relations could be attributed to use of a frequency domain that is too narrow as well as to failure to satisfy the constraints of the Kramers-Kronig equations. The Kramers-Kronig relations can, in principle, be applied with a suitable extrapolation of the data into the unmeasured frequency domain. Several methods for extrapolation have appeared in the electrochemical literature.

Kendig and Mansfeld [7] proposed extrapolating an impedance spectrum into the low-frequency domain under the assumption that the imaginary impedance is symmetric, thus, the polarization resistance R_p, otherwise obtained from

$$R_p = Z_r(\infty) - Z_r(0) = \frac{2}{\pi}\int_0^\infty \left[\frac{Z_i(x)}{x}\right] dx \tag{5}$$

would be obtained from

$$R_p = Z_r(\infty) - Z_r(0) = \frac{4}{\pi}\int_{\omega_{max}}^\infty \left[\frac{Z_i(x)}{x}\right] dx \tag{6}$$

where ω_{max} is the frequency at which the maximum in the imaginary impedance is observed. This approach is limited to systems which can be modeled by a single relaxation time constant [8,9]. The limitation to a single time constant is severe because multiple elementary processes with different characteristic time constants are usually observed in electrochemical impedance spectra.

Macdonald and Urquidi-Macdonald [8] have presented an approach based on extrapolating polynomials fit to the data. The experimental frequency domain was divided into several segments, and the individual impedance components $Z_r(\omega)$ and $Z_i(\omega)$ were fitted to a polynomial expression given by

$$Z_r = \sum_{k=0}^{n} a_k \omega^k \tag{7}$$

and

$$Z_i = \sum_{k=0}^{n} a_k \omega^k \tag{8}$$

which was extrapolated into the unmeasured frequency domain. The Kramers-Kronig equation (e.g., Eq 1 or 3) was integrated numerically using the extrapolated piece-wise polynomial fit for either the real or the imaginary component of the impedance, respectively [*10,11,12*]. While the extrapolation algorithm was applied successfully to a variety of systems (including synthetic impedance data derived from equivalent electrical circuits and experimental systems such as TiO_2-coated carbon steel in aqueous HCl/KCl solutions), such extrapolation of polynomials is unreliable over a broad frequency range.

Haili [*13*] provided an alternative approach based on the expected asymptotic behavior of a typical electrochemical system. For extrapolation to $\omega = 0$, the imaginary component $Z_i(\omega)$ was assumed to be proportional to ω as $\omega \rightarrow 0$ consistent with the behavior of a Randles-type equivalent circuit. This approach would apply as well to a Warburg impedance, which is also nearly proportional to ω as $\omega \rightarrow 0$. The real impedance approaches a constant limit which is the sum of the Ohmic solution resistance and the polarization resistance. The extrapolation in this region involves only one adjustable parameter whose value will approach $Z_r(\omega_{min})$ if ω_{min} is sufficiently small. At high frequencies, the imaginary component was assumed to be inversely proportional to frequency as $\omega \rightarrow \infty$ and the real component was assumed to approach a constant equivalent to the Ohmic solution resistance R_∞. The method of Haili guarantees well-behaved extrapolation of the impedance spectrum at upper and lower frequency limits with only five adjustable parameters. Haili's work confirmed the importance of extrapolating impedance data to both zero and infinite frequency when evaluating the Kramers-Kronig relations.

Esteban and Orazem, et al. [*14,15*] presented an approach which circumvented the problems associated with extrapolations of polynomials and yet avoided making *a priori* assumption of a model for asymptotic behavior. Esteban and Orazem suggested that, instead of predicting the imaginary impedance from the measured real impedance using Eq 1 or, alternatively, predicting the real impedance from the measured imaginary values using Eq 2 or 3, both equations could be used simultaneously to calculate the impedance below the lowest measured frequency ω_{min}. The low-frequency limit ω_0 is an adjustable parameter that is typically three or four orders of magnitude smaller than ω_{min}. The calculated impedance, in the domain $\omega_0 \leq \omega < \omega_{min}$, "forces" the experimental data set to satisfy the Kramers-Kronig relations in the frequency domain $\omega_0 \leq \omega \leq \omega_{max}$. The parameter ω_0 is chosen to satisfy the requirements that the real component of the impedance spectrum attains an asymptotic value and that the imaginary component approaches zero as $\omega \rightarrow \omega_0$. Internal consistency between the impedance components also requires that the calculated functions be continuous with the experimental data at ω_{min}. These requirements cannot simultaneously be satisfied by data from systems that do not satisfy the constraints of the Kramers-Kronig relations; therefore, discontinuities between experimental and extrapolated values were attributed to inconsistency with the Kramers-Kronig relations. The approach described by Esteban and Orazem [*14,15*] is different from other algorithms presented here because the Kramers-Kronig relations themselves were used to extrapolate

data to frequencies below the lowest measured frequency. Extrapolation of polynomials or *a priori* assumption of a model was thereby avoided.

While each of the algorithms described here have been applied to some experimental data with success, any approach toward extrapolation can be applied over only a small frequency range and cannot be applied at all if the experimental frequency range is so small that the data do not show a maximum in the imaginary impedance. The extrapolation approach for evaluating consistency with the Kramers-Kronig relations cannot be applied, therefore, to a broad class of experimental systems for which the unmeasured portion of the impedance spectrum at low frequencies is not merely part of a "tail" but instead represents a significant portion of the impedance spectrum.

Experimental Checks for Consistency

Experimental methods can be applied to check whether impedance data conform to the Kramers-Kronig assumptions. A check for linear response can be made by observing whether spectra obtained with different magnitudes of the forcing function are replicate. Stationary behavior can be identified experimentally by replication of the impedance spectrum. Spectra are replicate if the spectra agree within the expected frequency-dependent measurement error. If the experimental frequency range is sufficient, the extrapolation of the impedance spectrum to zero frequency can be compared to the corresponding values obtained from separate steady state experiments.

The experimental approach to evaluating consistency with the Kramers-Kronig relations shares constraints with direct integration of the Kramers-Kronig equations. Because extrapolation is required, the comparison of the dc limit of impedance spectra to steady state measurement is possible only for systems for which a reasonably complete spectrum can be obtained. Experimental approaches for verifying consistency with the Kramers-Kronig relations by replication are further limited in that, without an *a priori* estimate for the confidence limits of the experimental data, the comparison is more qualitative than quantitative. A method is therefore needed to evaluate the error structure, or frequency-dependent confidence interval, for the data that would be obtained in the absence of nonstationary behavior.

Regression of Electrical Circuit Analogues

Electrical circuits consisting of passive and distributed elements satisfy the Kramers-Kronig relations (see, for example, the discussion in Refs *16*, *17*, and *18*). Therefore, successful regression of an electrical circuit analogue to experimental data implies that the data satisfy the Kramers-Kronig relations [*19,20*]. This approach has the obvious advantage that integration over an infinite frequency domain is not required; therefore, a portion of an incomplete spectrum can be identified as being consistent without use of extrapolation algorithms.

It should be noted that the regression is, however, sensitive to the weighting applied to the data, an important consideration for impedance data which vary over many orders of magnitude [*21*]. With no weighting (or unity weighting), the real part of the spectrum at low frequencies and the imaginary part of the spectrum at intermediate frequencies are emphasized. Information about physical processes that influence the spectrum at high frequencies may therefore be lost. A better approach is to provide proportional weighting to each data point, achieved by dividing the objective function at each frequency by the experimental observation at that frequency. The processes that appear at high-frequency are given the same weight in the regression as the processes that are important at low-

frequency. The proportional weighting approach has the disadvantage that the regression can be overly influenced by the portions of the spectrum that have the largest uncertainty. The most desirable approach, therefore, is to divide the objective function at each frequency by the variance of the experimental observation at that frequency [*21*]. Normalization by the variance will yield proportional weighting if the percent error is not a function of frequency. The problem here is that consistency is determined by regression of a model, and the most reliable regression is obtained only if the frequency dependence of the error structure of the data is known. Also, *a priori* knowledge of the error structure may be needed to decide whether a given regression provides a "good fit." As an alternative to *a priori* knowledge of the error structure, Macdonald has recently suggested that model parameters for error structure be included in the regression of a model to data [*22,23*].

Perhaps the major problem with the use of electrical circuit models to determine consistency is that interpretation of a "poor fit" is ambiguous. A poor fit is not necessarily the result of an inconsistency of the data with the Kramers-Kronig relations. A poor fit could also be attributed to use of an inadequate model or to regression to a local rather than global minimum (caused perhaps by a poor initial guess).

Application of Measurement Models

In this work, models are classified as being one of two types: process models or measurement models. Process models are used to predict the response of a system from physical phenomena that are hypothesized to be important. Regression of process models to data allows identification of physical parameters based upon the original hypothesis. In contrast, measurement models are built by sequential regression of line shapes to the data. This type model can be used to identify characteristics of the data set that could facilitate selection of an appropriate process model.

The regression of measurement models as a means of determining consistency with the Kramers-Kronig relations is an extension to the use of electrical circuit analogues. Because the model itself is consistent with the Kramers-Kronig relations, successful regression of the model to a given spectrum implies that the data are consistent. Integration over zero to infinity in frequency is not required. The measurement model is composed of a summation of lineshapes that will, with a sufficient number of terms, provide a statistically adequate fit to any consistent data set. Use of the measurement model eliminates the ambiguity in the interpretation of a "poor fit" to the data. Since the model will provide an adequate representation of a consistent spectrum, failure to fit the data can be attributed to inconsistency with the Kramers-Kronig relations. Another result of the adequacy of the model is that the model can be used to identify the frequency-dependent error structure of impedance spectra. The error structure can then be used to weight the data during regression and to provide a means of deciding whether a given regression provided a "good fit." In this section, the measurement model is presented along with a demonstration of applicability to impedance data, its use in determining the frequency-dependent error structure, and its use to determine consistency with the Kramers-Kronig relations.

Structure of Measurement Model

A simple measurement model was obtained for electrochemical impedance spectroscopy [*24*] by analogy to the classical theories of optical dispersion in which the complex dielectric constant is calculated as a function of the frequency of light [*25,26,27*]. Since the line shape of the Debye model for the complex dielectric constant was similar to that seen for the complex impedance, an analogue of the multiple Debye model was used, i.e.,

$$Z(\omega) = Z_0 + \sum_k \frac{\Delta_k}{(1 + j\tau_k\omega)} \tag{9}$$

which corresponds to the Voight model (Fig. 1) in series with a solution resistance. The time constant τ_k for element k is equivalent to R_kC_k in the Voight model, and Δ_k is equivalent to R_k. The impedance response of a single Voight element is usually attributed to the electrical response of a linearized electrochemical reaction [*28,29*]. Equation 9 satisfies one requirement of a measurement model in that it is consistent with the Kramers-Kronig relations.

The tenets underlying the use of measurement models for impedance spectroscopy are:

(1) By including a sufficient number of terms, a general measurement model based on Eq 9 can fit impedance data for typical stationary electrochemical systems.
(2) Because the measurement model does fit stationary impedance data, an inability to fit an impedance spectrum can be attributed to failure of the data to conform to the assumptions of the Kramers-Kronig relations rather than to failure of the model. Thus, the measurement model can be used to assess the consistency of impedance data with the Kramers-Kronig relations without integration.

Demonstration of Applicability to Impedance Spectra

The measurement model presented here is most effective in modeling systems that can be modeled otherwise with passive elements such as resistors, capacitors, and inductors. It is perhaps no surprise that, with only two elements, the measurement model can provide a good representation of a circuit developed for painted metals that does not include diffusion or constant phase elements [*30*]. The electrical circuit is presented as Circuit 1 in Fig. 2. The fit to synthetic data obtained from a model for painted steel is presented in Fig. 3. The normalized sum of squares for this fit was found to be 2.055×10^{-14} [*24*]. The measurement model indicates that two time constants can be resolved from the synthetic data, and this result is consistent with the circuit used to generate the synthetic data.

The appearance of a positive imaginary component of the impedance has been attributed at high frequencies to the stray capacity of the current measuring resistor [*31*] and at low frequencies to adsorption phenomena at the electrode surface [*28*]. Transport based models for this behavior are rare, and most electrical circuit models account for this behavior by incorporating either an inductor or a capacitor with a negative value for the capacitance. The measurement model was applied to pseudo-capacitive data reported by Lorenz and Mansfeld [*32*] for corrosion of iron in 0.5 M H_2SO_4. Their model, shown as Circuit 2 in Fig. 2, incorporated an inductor to fit the pseudo-capacitive response at low frequencies. The Voight model can account for inductive behavior if the magnitude (Δ_k) is allowed to have a negative sign. The regression to Circuit 2 is given in Fig. 4. The measurement model indicates that three time constants can be resolved from the synthetic

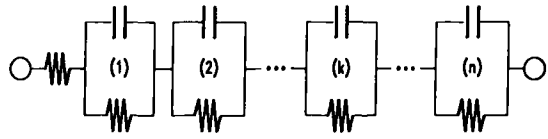

FIG. 1—*The Voight electrical circuit analogue corresponding to the measurement model used in this work (Eq 9).*

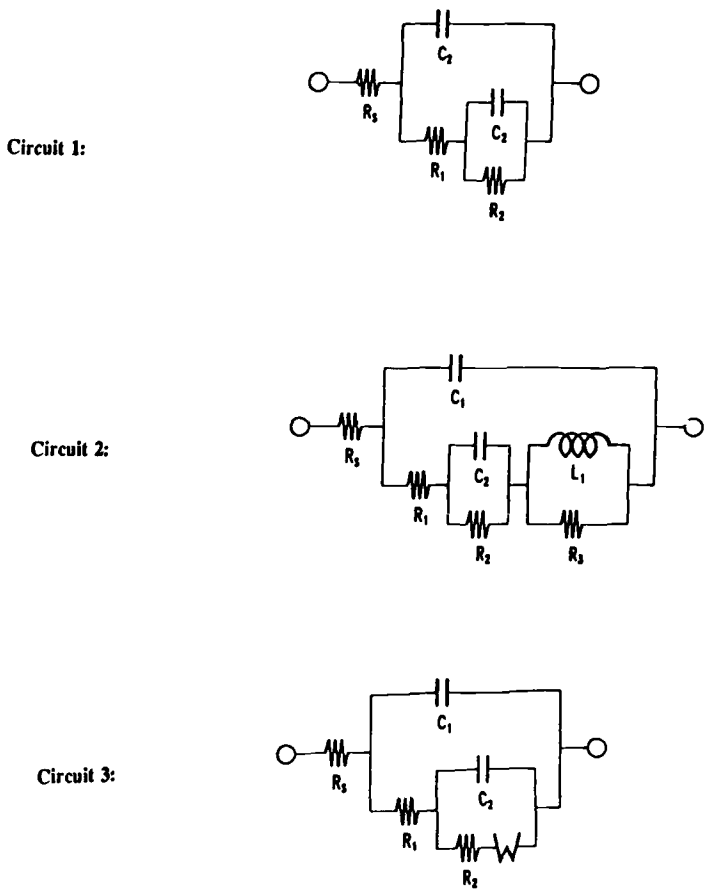

FIG. 2—*Electrical circuit analogues for: (1) corrosion of a painted metal* [30]*; (2) corrosion of iron in 0.5 M* H_2SO_4 *at the corrosion potential* [32]*; and (3) hydrogen evolution on* $LaNi_5$ [15].

data, and this result is fully consistent with the circuit. Complete agreement is obtained because the circuit is composed of only passive elements (one inductor, three resistors, and two capacitors). The residual sum of squares for this fit was found to be 3.221×10^{-14}. The measurement model provides a good fit to data exhibiting an inductive response.

Additional measurement model elements were needed to provide a good fit to systems which contain distributed elements such as are associated with mass transfer limitations and frequency dispersion. In accordance with Eq 9, a measurement model is constructed by sequentially adding k Voight elements with parameters Δ_k and τ_k until the fit is no longer improved by addition of yet another element. This procedure is illustrated for synthetic data obtained from the electrical circuit model proposed for evolution of hydrogen on a $LaNi_5$ ingot electrode [*15*]. A diffusional resistance was observed in this system as a result of the incorporation of hydrogen into the metal. The electrical circuit model presented as Circuit 3 in Fig. 2 accounted for mass transfer of hydrogen with a Warburg element, and three time constants are evident in the circuit analogue. The complex Warburg impedance, given by

$$Z_W = R_W \frac{\tanh\ (\sqrt{j\tau_W\omega})}{(\sqrt{j\tau_W\omega})} \tag{10}$$

can be derived from the solution of $\nabla^2 c_i = 0$ for a film of thickness δ [28,29]. The time constant can be expressed in terms of diffusivity and film thickness as $\tau_W = \delta^2/D_i$. The Warburg element is sometimes called a distributed element because it can be modeled by a distribution of relaxation times [28]. The optimal regression of the measurement model to synthetic data from Circuit 3 in Fig. 2 required five Voight elements. The fit is presented in Fig. 5, and the resultant residual sum of squares was 4.915×10^{-10}.

The residual sum of squares obtained by fitting the measurement model to the synthetic data is presented as a function of the number of Voight elements in Fig. 6. Figure 6 can be used to show that a maximum of five Voight elements can be resolved from the synthetic data because the sixth Voight element did not improve the quality of the fit. Figure 6 also shows that, while visual inspection of Fig. 5 suggests that a fit obtained with three elements might be acceptable (resulting in residual errors less than 0.1 percent), addition of the fourth and fifth elements provided significant improvement in the residual error. Several points must be made here. The average residual error with five Voight elements was less than 2×10^{-4} percent. The measurement model based on a summation of Voight elements, therefore, provided an excellent fit, despite the fact that the circuit included a Warburg element which has an impedance response that differs significantly from that obtained for a resistor and capacitor in parallel. The measurement model fit the synthetic data to within seven significant figures; therefore, the measurement model can be considered to be statistically adequate to fit the corresponding experimental impedance data for which only three or four significant figures can be expected. To explore the potential influence of experimental error, random noise with a maximum amplitude of five percent was added to the results of Circuit 3. The optimal regression of the measurement model yielded only three Voight circuit elements as shown in Fig. 6. Only three elements could be resolved because the contribution of the fourth circuit element was insignificant as compared to the noise of the data. The normalized sum of squares obtained by regression of the measurement model was slightly lower than the noise level which is shown as a dashed line in Fig. 6.

The comparison of the measurement model to synthetic data, as presented in this section, is meant to illustrate the applicability of the measurement model lineshapes to models that have been developed for "typical" impedance data. The summation of lineshapes associated with the Voight model can be applied to data that can be otherwise modeled by passive elements such as resistors, capacitors, and inductors. It can also be applied to distributed elements such as Warburg and constant phase elements. The model can therefore be used to identify the error structure of impedance data and to evaluate data for consistency with the Kramers-Kronig relations.

Identification of Error Structure

The regression of a measurement model with four Voight elements is presented in Fig. 7 for three replicate impedance spectra obtained for an $In_{0.05}Ga_{0.95}As/GaAs$ superlattice structure on a semi-insulating GaAs substrate [33]. The three data sets are in good agreement, although a larger degree of scatter is evident at low frequencies. The residual error corresponding to Fig. 7 is presented in Fig. 8 as a function of frequency. The scatter evident in the regression can be associated with the frequency-dependent error structure of the data. In this data set, the scatter in the real part of the impedance is largest at high frequencies where the real part of the impedance has become small as compared to the

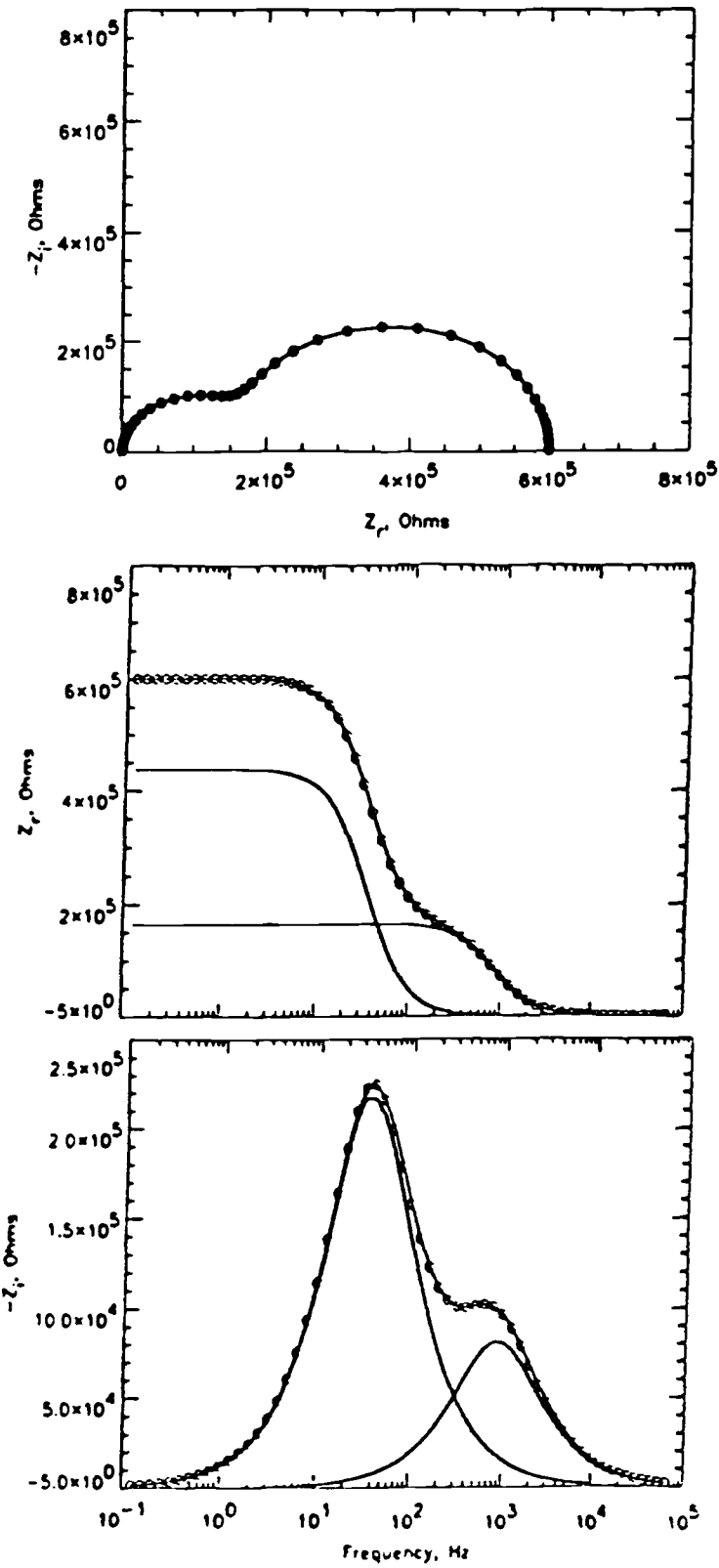

FIG. 3 — *Regression of a measurement model with two Voight elements to synthetic data (○) obtained from Circuit 1 (corrosion of a painted metal* [30]*). The residual sum of squares for the fit was 2.055 × 10⁻¹⁴. Solid lines in all figures are the results of the model fit. The lines presented in the lower two figures are the model fit and its deconvolution into the contribution of each Voight element. Taken from Ref* 24 *with permission of the publisher.*

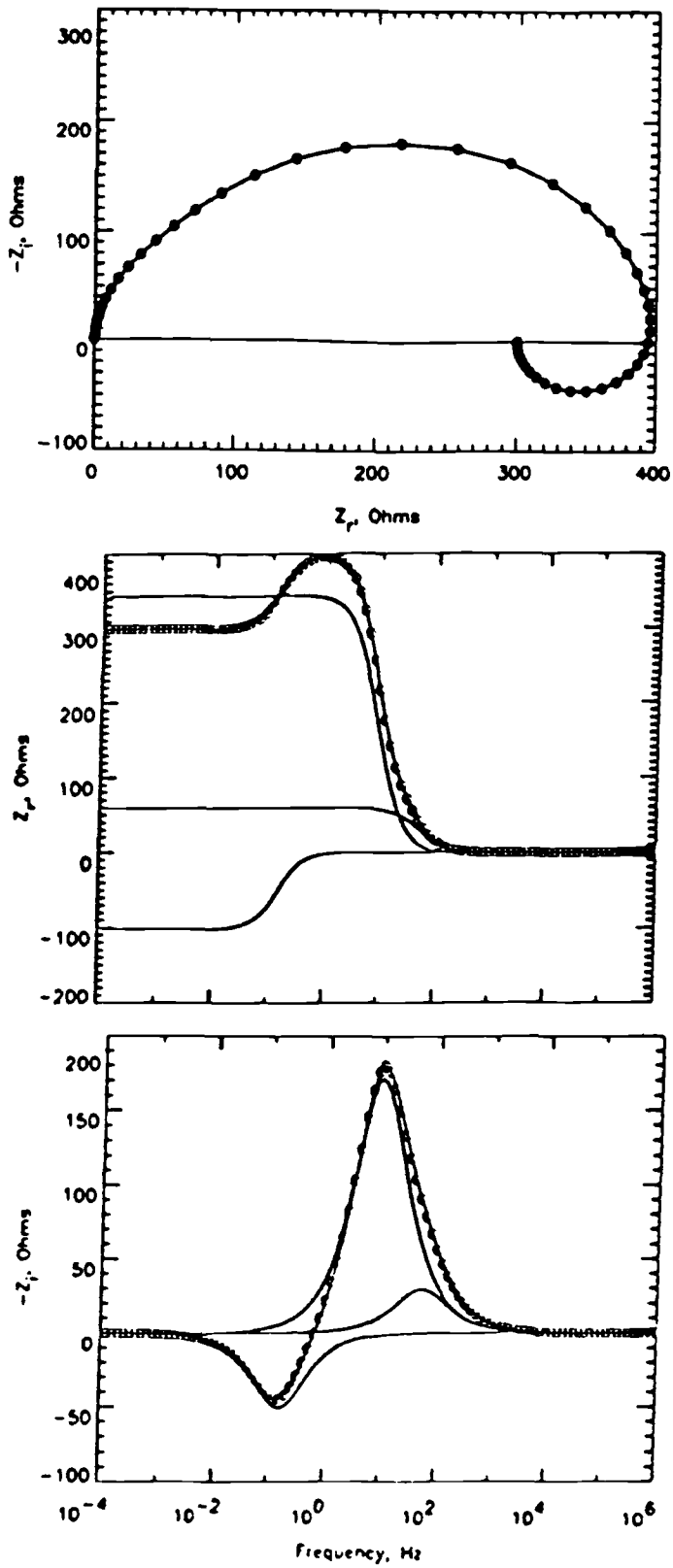

FIG. 4—*Regression of a measurement model with three Voight elements to synthetic data (○) obtained from Circuit 2 (corrosion of iron in 0.5 M H_2SO_4 at the corrosion potential [32]). The residual sum of squares for the fit was 3.221 × 10^{-14}. Solid lines in all figures are the results of the model fit. The lines presented in the lower two figures are the model fit and its deconvolution into the contribution of each Voight element. Taken from Ref* 24 *with permission of the publisher.*

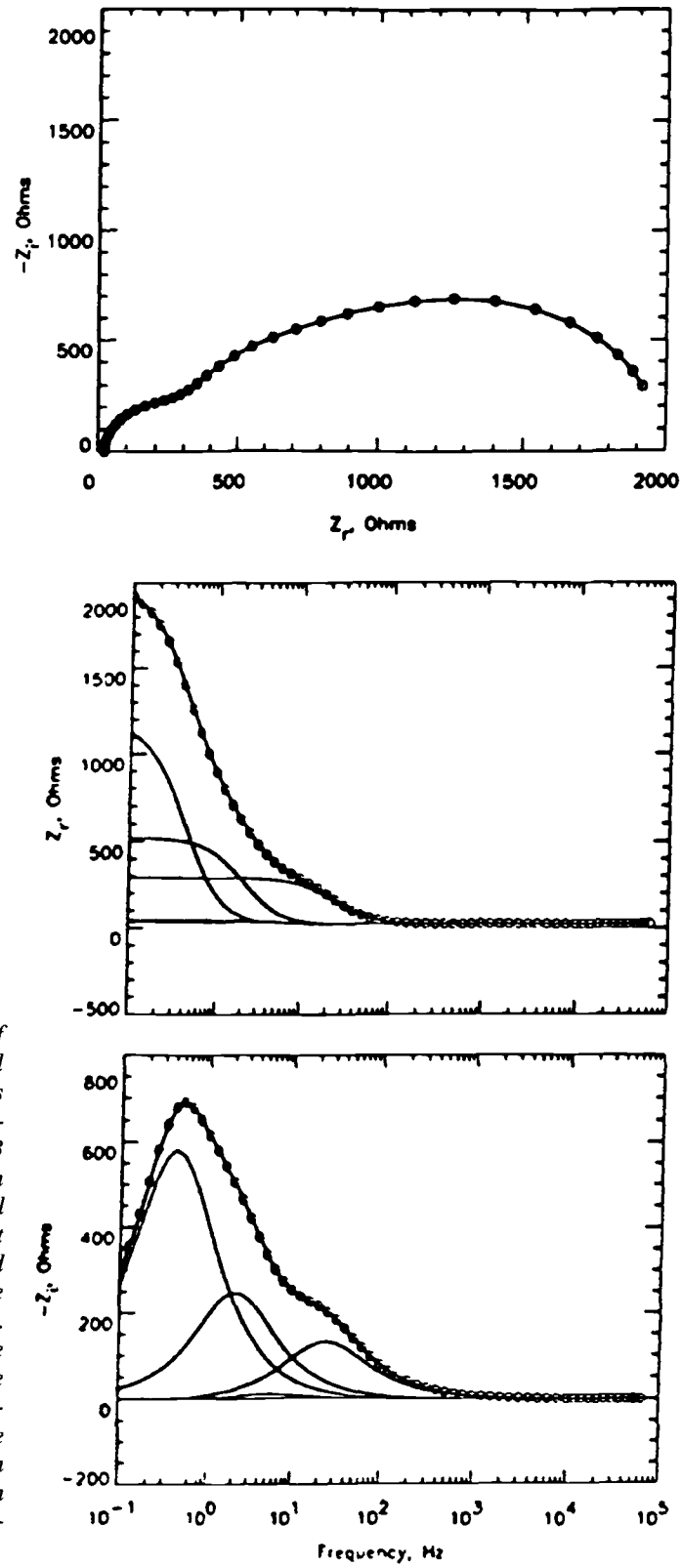

FIG. 5—*Regression of a measurement model with five Voight elements to synthetic data* (○) *obtained from Circuit 3 (hydrogen evolution on* $LaNi_5$ [15]). *The residual sum of squares for the fit was* 4.915×10^{-10}. *Solid lines in all figures are the results of the model fit. The lines presented in the lower two figures are the model fit and its deconvolution into the contribution of each Voight element. Taken from Ref* 24 *with permission of the publisher.*

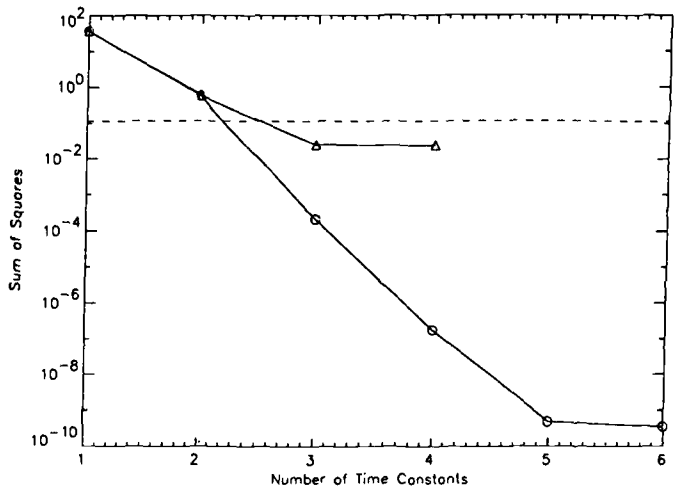

FIG. 6—*Normalized sum of squares for the regression of a measurement model to synthetic data obtained from Circuit 3 (hydrogen evolution on $LaNi_5$ [15]) as a function of the number of Voight time constants employed in the model:* (○) *regression to synthetic data;* (Δ) *regression to synthetic data with random noise added; and (dashed line) normalized noise level. Taken from Ref* 24 *with permission of the publisher.*

value of the imaginary component. Conversely, the scatter in the imaginary component is largest at low frequencies where the real component is dominant.

The dashed line in Fig. 8 is given by

$$\epsilon = \pm 0.01\sqrt{Z_i^2 + Z_r^2}, \tag{11}$$

such that the 95 percent confidence interval for the experimental data is estimated to be

$$Z_r = Z_r^{\text{expt}} \pm \epsilon \tag{12}$$

and

$$Z_i = Z_i^{\text{expt}} \pm \epsilon \tag{13}$$

The error for each component of the impedance was assumed to be one percent of the magnitude of the impedance at that frequency. The value of one percent was suggested by the specification of the Solartron 1250 frequency response analyzer for variance of the results at 90 percent confidence using a "long integration mode" with a signal greater than 0.02 percent of the range [*34*]. The value used would, of course, be dependent upon the instrumentation used as well as upon other aspects of experimental technique. Work is continuing on identification of more complete models for the frequency-dependent error structure [*35*]. Given its simplicity, however, Eq 11 is in remarkable agreement with the apparent error structure of the data. In the absence of replicate data, Eq 11 could provide an estimate for the variance of the data. Normalization of data by the variance is preferred in regression techniques because least reliance is placed on the least reliable data.

The *a priori* estimate of the error structure of the impedance data can provide a powerful

tool when used in combination with the measurement model. For example, knowledge of the frequency dependence of the expected noise level can be used to interpret the results of "replicate" experiments. The regression of a measurement model with seven Voight elements is presented in Fig. 9 for eight consecutive impedance experiments on $LaNi_5$ at the potential of -0.8 V (Hg/HgO), cathodic to open circuit [*36,37*]. The data presented in Fig. 9 appear replicate, but examination of the residual errors in Fig. 10 reveals that, though the residuals are within twice the standard deviation of the data, the standard deviation of the data is much larger than the expected error structure. The solid lines in Fig. 10 represent twice the standard deviation of the data, and the dashed lines show the estimated error in the data using Eq 11. The errors are not random as would be expected for a truly replicate data set; therefore, the impedance response indicates time-dependent behavior. This analysis shows that the seven runs are not replicate and, instead, reflect the condition of the electrode at different points in time. It is appropriate, therefore, to treat these data as seven independent experimental spectra.

Identification of Consistency with Kramers-Kronig Relations

Most electrochemical impedance data do not adequately approximate the infinite frequency domain required for direct integration of the Kramers-Kronig equations. Experimental spectra can be evaluated for consistency using measurement models without performing integration because measurement models satisfy the Kramers-Kronig relations implicitly. To check for the consistency of the data, the measurement model is regressed to the real or the imaginary part of the experimental spectrum. The model can then be used to predict the other part of the spectrum (i.e., the real part if the regression was done to the imaginary and the imaginary part if the regression was done to the real). From the estimated variance of the model parameters, a 95-percent confidence interval can be found for the model predictions using Monte-Carlo simulation. If the data are within the 95-percent confidence interval, the system can be regarded as being stationary during the course of the experiment. If a significant portion of the data falls outside of the 95-percent confidence interval, the system is likely to be nonstationary. The details of the algorithm for Monte-Carlo simulation are given in Ref *38*. The random number generator used for the simulation was taken from Ref *39*. Five thousand simulations were performed at each frequency to ensure that impedance values follow a Gaussian distribution.

Though the system changed over the period of seven experiments at -0.8 V (Hg/HgO), the measurement model approach demonstrates that a pseudo-steady state approximation applies for each individual run. The applications of the measurement model approach to one experimental data set at -0.8 V (Hg/HgO) is presented in Fig. 11. The measurement model was fit to the imaginary part of the impedance and the confidence interval was predicted for the real part. The circles in Figs. 11 and 12 represent the experimental data, the solid lines represent the 95-percent confidence interval for the model, and the dashed lines in Fig. 12 represent the model for the error structure of the data. The imaginary part of the residuals lie within the proposed error structure, indicating a satisfactory fit of the model to the imaginary part of the data. The use of the error structure to indicate satisfactory regression removes the possibility that a poor fit could be attributed to a local rather than global minimum in the nonlinear regression. Since the real part of the residuals lie within the confidence interval, the data can be deemed to be consistent with the Kramers-Kronig relations. The sharp discontinuity in the residuals at 1000 Hz can be explained by an inappropriate choice of frequency for change of current measuring resistor during the course of the experiment. The measurement model approach can therefore be used to suggest improvements to experimental design.

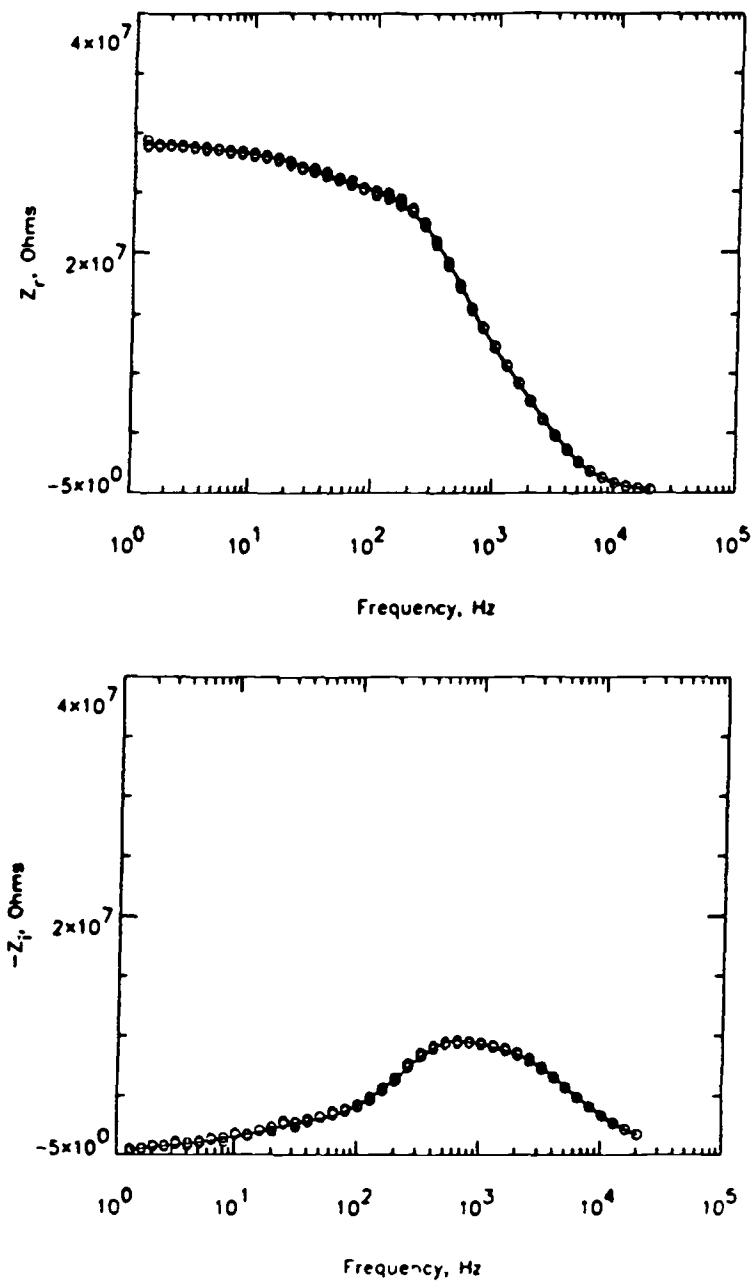

FIG. 7—*Regression of a measurement model with four Voight elements to replicate experimental data* (○) *obtained for an* $In_{0.06}Ga_{0.95}As/GaAs$ *superlattice structure on a semi-insulating GaAs substrate* [33].

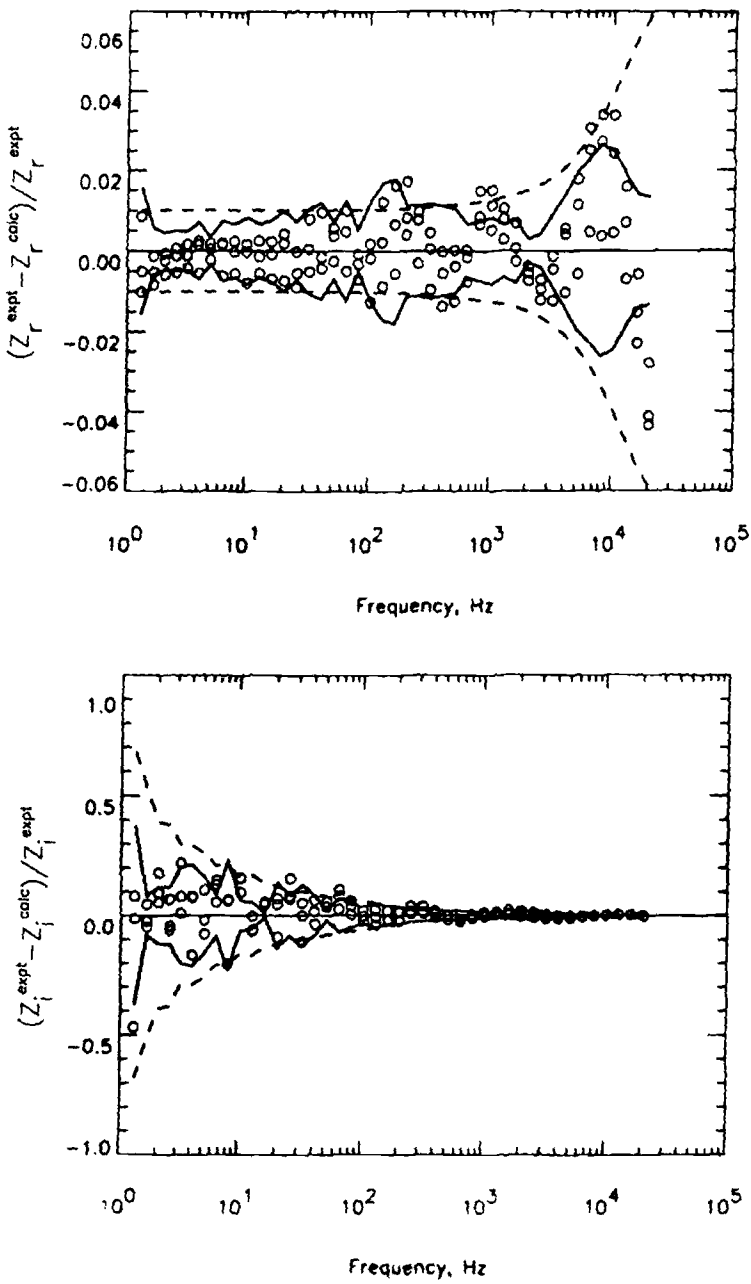

FIG. 8—*Residual error of the regression of a measurement model with four Voight elements to replicate experimental data* (○) *obtained for an* $In_{0.05}Ga_{0.95}As/GaAs$ *superlattice structure on a semi-insulating GaAs substrate. The dashed lines represent a simple model for the error structure of the data given by Eq 11. The solid lines represent the 95-percent confidence interval for the data given at each frequency by twice the standard deviation of the data.*

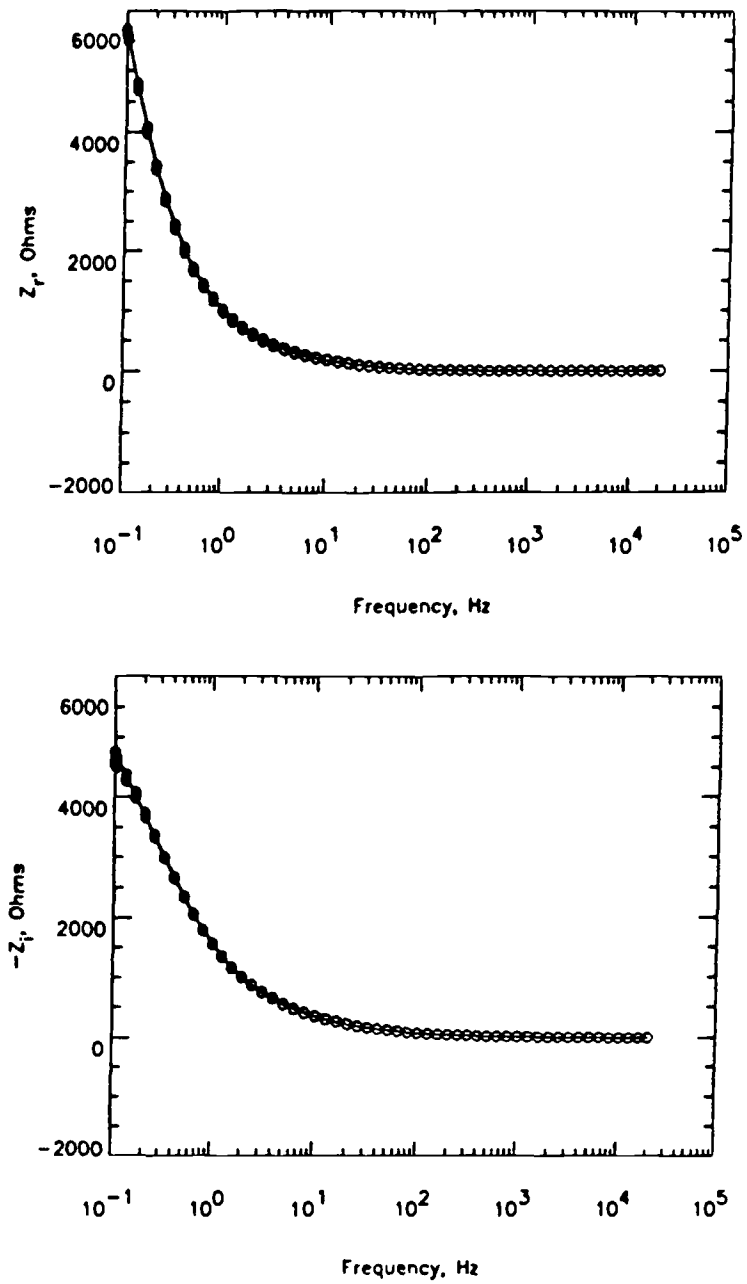

FIG. 9—*Regression of a measurement model with seven Voight elements to eight consecutive impedance scans obtained for a $LaNi_5$ ingot in 31 wt % KOH at a potential of −0.8 V (Hg/HgO)* [35,36]. *The circles represent the experimental data and the lines represent the results of the regression.*

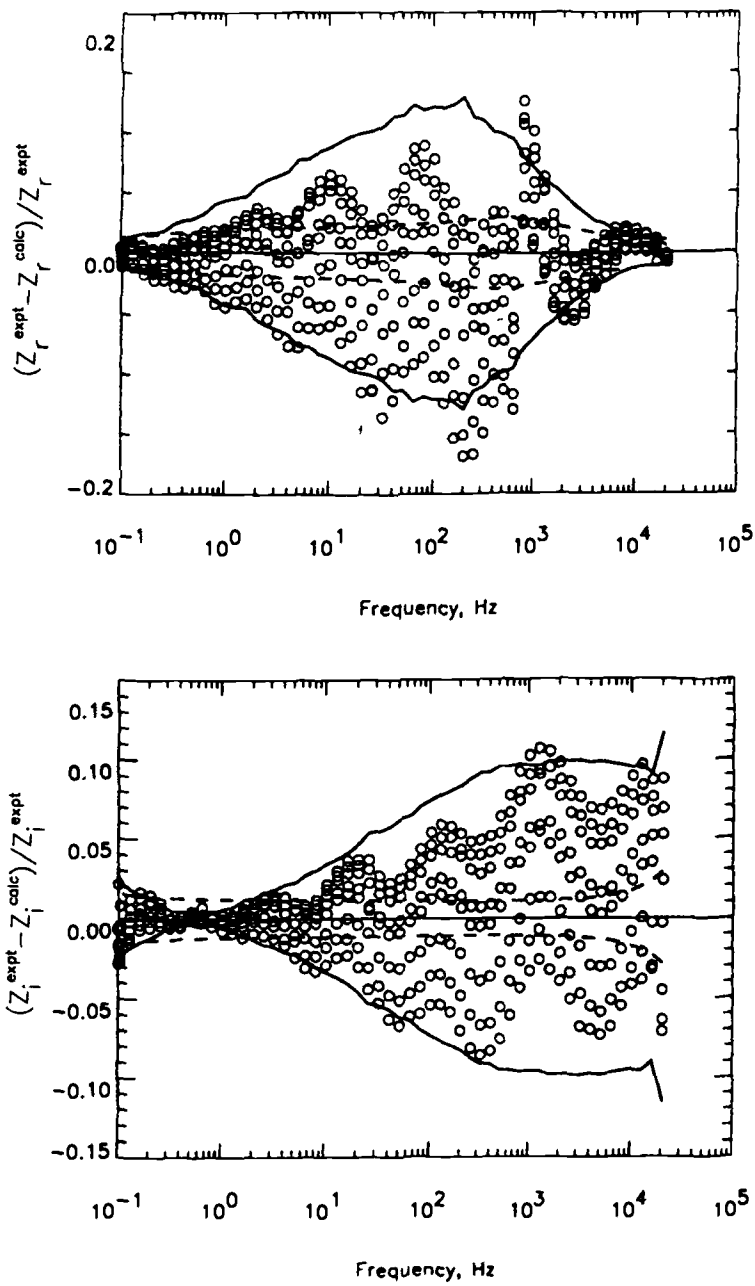

FIG. 10—*Residual errors as a function of frequency for the regression presented in Fig. 9* [35,36]. *The circles represent the residual errors, the solid lines represent twice the standard deviation of the data and the dashed lines represent the model for the error structure given by Eq 11.*

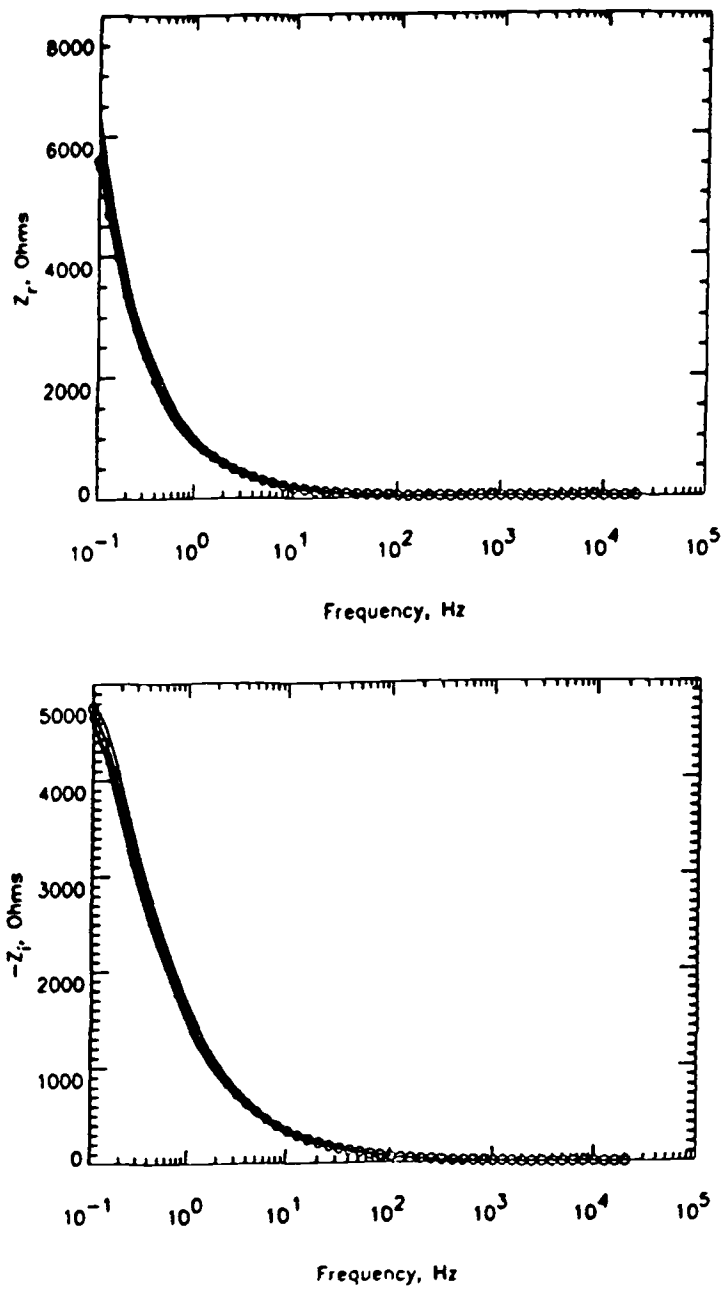

FIG. 11—*Optimal regression of the measurement model to the imaginary part of the impedance spectrum for experimental data obtained for hydrogen evolution at a $LaNi_5$ metal hydride electrode at a potential of −0.8 V (Hg/HgO)* [35,36]. (a) *The real part of the impedance and* (b) *the imaginary part of the impedance. The lines represent the results of the model regression, and the upper and lower lines represent the predicted 95 percent confidence interval for the regression.*

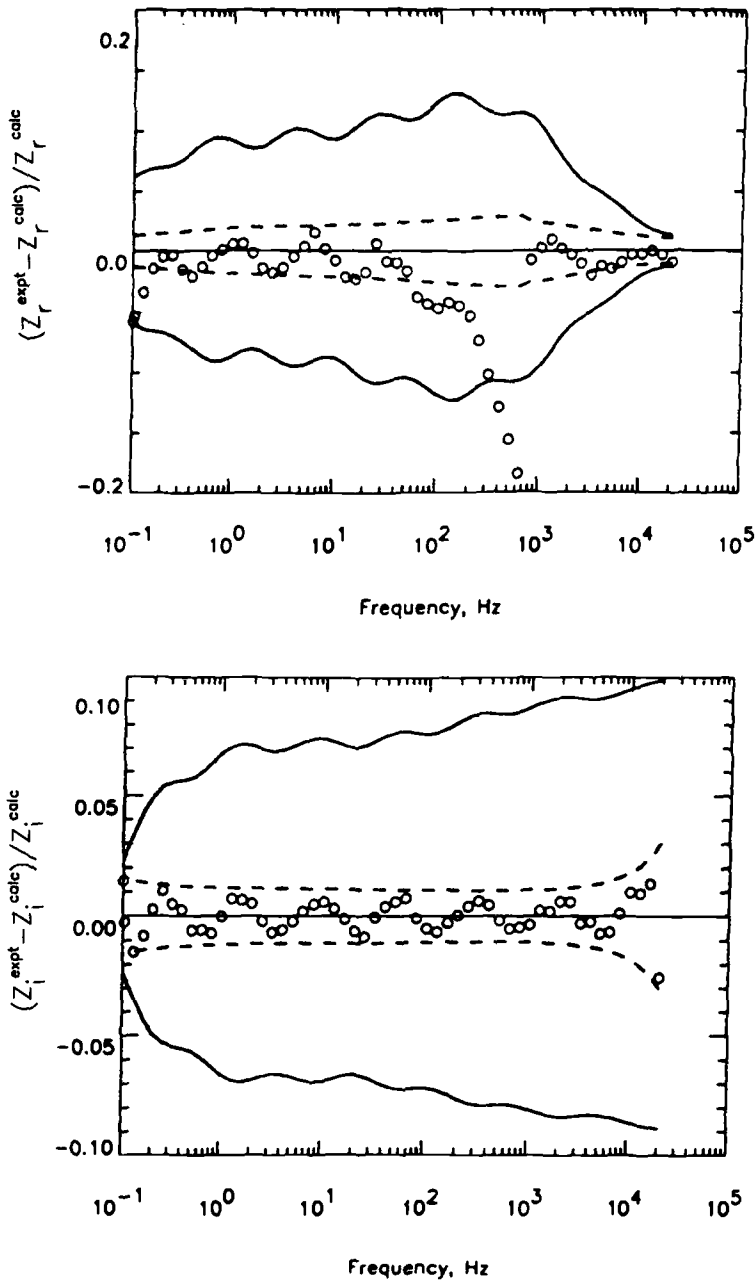

FIG. 12—*Comparison between the residual errors and the predicted 95 percent confidence interval for the model fit to the imaginary part of the impedance spectrum for experimental data obtained for hydrogen evolution at a* $LaNi_5$ *metal hydride electrode at a potential of −0.8 V (Hg/HgO)* [35,36]. (a) *The real part of the impedance and* (b) *the imaginary part of the impedance. Dashed lines represent the estimated error structure for the data.*

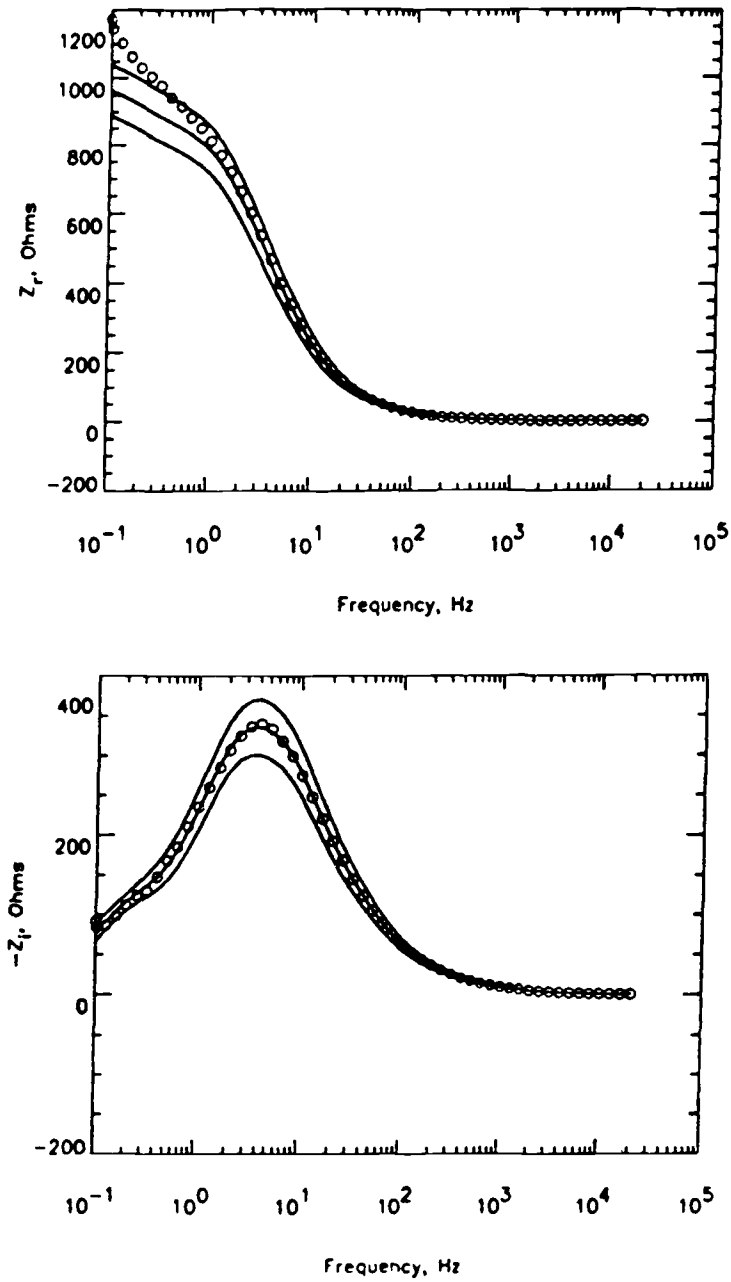

FIG. 13—*Optimal regression of the measurement model to the imaginary part of the impedance spectrum for experimental data obtained for hydrogen evolution at a $LaNi_5$ metal hydride electrode at a potential of −1.1 V (Hg/HgO)* [35,36]. (a) *The real part of the impedance and* (b) *the imaginary part of the impedance. The lines represent the results of the model regression, and the upper and lower lines represent the predicted 95 percent confidence interval for the regression.*

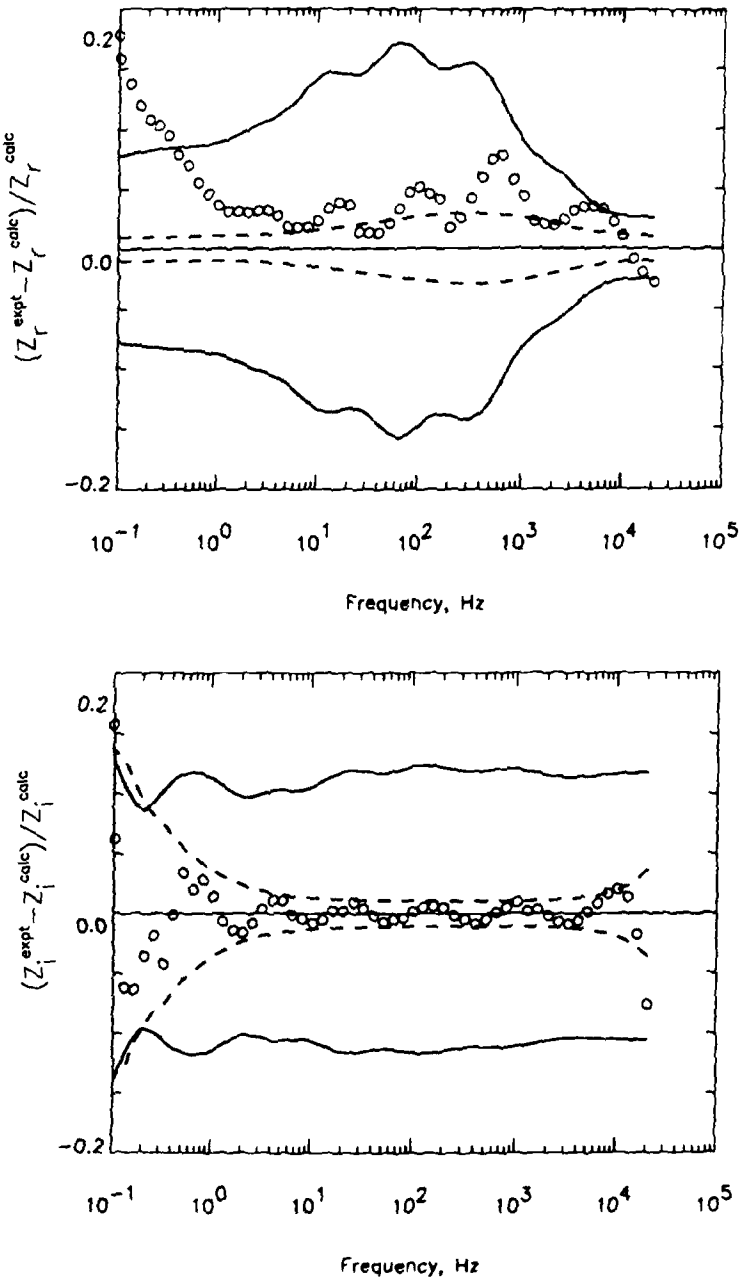

FIG. 14—*Comparison between the residual errors and the predicted 95 percent confidence interval for the model fit to the imaginary part of the impedance spectrum for experimental data obtained for hydrogen evolution at a $LaNi_5$ metal hydride electrode at a potential of −1.1 V (Hg/HgO)* [35,36]. (a) *The real part of the impedance and* (b) *the imaginary part of the impedance. Dashed lines represent the estimated error structure for the data.*

A corresponding analysis is presented in Figs. 13 and 14 for experimental data obtained at −1.1 V (Hg/HgO). The measurement model was regressed to the imaginary part of the impedance and the confidence interval for the real part was predicted. A significant portion of the real part of the spectrum lies outside the 95-percent confidence interval; thus, the data do not satisfy the constraints of the Kramers-Kronig relations. These results are very important for the analysis of the data because most physico-chemical models are developed under the assumption of a pseudo-steady state. These models cannot be used to interpret nonstationary data. The results of the measurement model analysis can be used to suggest changes in the experimental design or to encourage development of models which take the time dependent-behavior of the system into account.

Conclusions

The use of measurement models is superior to the use of polynomial fitting because fewer parameters are needed to model complex behavior and because the measurement model satisfies the Kramers-Kronig relations implicitly. Experimental data can therefore be checked for consistency with the Kramers-Kronig relations without actually integrating the equations over frequency. The use of measurement models does not require extrapolation of the experimental data set; therefore, inaccuracies associated with an incomplete frequency spectrum are resolved. For the application to a preliminary screening of the data, the use of measurement models is superior to the use of more specific electrical circuit analogues because one can determine whether the residual errors are due to an inadequate model, failure of data to conform to the Kramers-Kronig assumptions, or experimental noise.

Acknowledgment

The portion of this work performed at the University of Florida (PAN and MEO) was conducted in support of a series of projects supported by the Office of Naval Research under Grant N00014-89-J-1619 (A. J. Sedriks, Program Monitor), Gates Energy Products, Gainesville, Florida, the National Science Foundation under Grant EET-8617057, and by DARPA under the Optoelectronics program of the Florida Initiative in Advanced Microelectronics and Materials. The work performed at the University of South Florida (LHGR) was supported by the National Science Foundation under Grants RII-8507956 and INT-8602578.

References

[1] Kronig, R. de L., "On the Theory of Dispersion of X-Rays," *Journal of the Optical Society of America and Review of Scientific Instruments,* Vol. 12, 1926, p. 547.

[2] Kronig, R. de L., "Dispersionstheorie im Röntgengebiet," *Physikalische Zeitschrift,* Vol. 30, 1929, p. 521.

[3] Kramers, H. A., "Die Dispersion und Absorption von Röntgenstrahlen," *Physikalische Zeitschrift,* Vol. 30, 1929, p. 522.

[4] Davies, B., "Integral Transforms and Their Applications," in *Applied Mathematical Series 2nd Ed.,* Vol. 25, Springer-Verlag, New York, 1985, p. 101.

[5] Bode, H. W., *Network Analysis and Feedback Amplifier Design,* D. Van Nostrand Company, Inc., NY, 1945.

[6] Gabrielli, C., Keddam, M., and Takenouti, H., "Kramers-Kronig Transformation in Relation to the Interface Regulating Device," *Electrochemical Impedance: Analysis and Interpretation, ASTM STP 1188,* J. R. Scully, D. C. Silverman, and M. W. Kendig, Eds., American Society for Testing and Materials, Philadelphia, 1993 (this publication).

[7] Kendig, M. and Mansfeld, F., "Corrosion Rates From Impedance Measurements: An Improved Approach for Rapid Automatic Analysis," *Corrosion,* Vol. 39, 1983, p. 466.

[8] Macdonald, D. D. and Urquidi-Macdonald, M., "Application of Kramers-Kronig Transforms in the Analysis of Electrochemical Systems: I. Polarization Resistance," *Journal of the Electrochemical Society*, Vol. 132, 1985, p. 2316.

[9] Mansfeld, F., Kendig, M. W., and Lorenz, W. J., "Corrosion Inhibition in Neutral Aerated Media," *Journal of the Electrochemical Society*, Vol. 132, 1985, p. 290.

[10] Urquidi-Macdonald, M., Real, S., and Macdonald, D. D., "Application of Kramers-Kronig Transforms in the Analysis of Electrochemical Systems: II. Transformations in the Complex Plane," *Journal of the Electrochemical Society*, Vol. 133, 1986, p. 2018.

[11] Urquidi-Macdonald, M., Real, S., and Macdonald, D. D., "Applications of Kramers-Kronig Transforms in the Analysis of Electrochemical Impedance Data—III. Stability and Linearity," *Electrochimica Acta*, Vol. 35, 1990, p. 1559.

[12] Dougherty, B. J. and Smedley, S. I., "Validation of Experimental Data from High Impedance Systems Using the Kramers-Kronig Transforms," *Electrochemical Impedance: Analysis and Interpretation, ASTM STP 1188*, J. R. Scully, D. C. Silverman, and M. W. Kendig, Eds., American Society for Testing and Materials, Philadelphia, 1993 (this publication).

[13] Haili, C., "The Corrosion of Iron Rotating Hemispheres in 1M Sulfuric Acid: An Electrochemical Impedance Study," M.S. Thesis, University of California, Berkeley, June 1987.

[14] Esteban, J. M. and Orazem, M. E., "On The Use of the Kramera-Kronig Relations to Evaluate the Consistency of Electrochemical Impedance Data," *Journal of the Electrochemical Society*, Vol. 138, 1991, p. 67.

[15] Orazem, M. E., Esteban, J. M., and Moghissi, O. C., "Practical Applications of the Kramers-Kronig Relations," *Corrosion*, Vol. 47, 1991, p. 248.

[16] Macdonald, D. D. and Urquidi-Macdonald, M., "Kramers-Kronig Transformation of Constant Phase Impedances," *Journal of the Electrochemical Society*, Vol. 137, 1990, p. 515.

[17] Townley, D., "Comments: Evaluation of Kramers-Kronig Transforms for Electrochemical Impedance Data," *Journal of the Electrochemical Society*, Vol. 137, 1990, p. 3305.

[18] Urquidi-Macdonald, M. and Macdonald, D. D., "Comments: Evaluation of Kramers-Kronig Transforms for Electrochemical Impedance Data," *Journal of the Electrochemical Society*, Vol. 137, 1990, p. 3306.

[19] McKubre, M. C. H., Macdonald, D. D., and Macdonald, J. R., "Corrosion of Materials: Kramers-Kronig Transforms," in *Impedance Spectroscopy: Emphasizing Solid Materials and Systems*, J. R. Macdonald, Ed., John Wiley & Sons, New York, 1987, p. 274.

[20] Brachman, M. K. and Macdonald, J. R., "Generalized Immitance Kernels and the Kronig-Kramers Relations," *Physica*, Vol. 20, 1956, pp. 141–148.

[21] Macdonald, J. R. and Potter, Jr., L. D., "A Flexible Procedure for Analyzing Impedance Spectroscopy Results: Description and Illustrations," *Solid State Ionics*, Vol. 23, 1987, pp. 61–79.

[22] Macdonald, J. R., "Impedance Spectroscopy: Old Problems and New Developments," *Electrochimica Acta*, Vol. 35, 1990, pp. 1483–1492.

[23] Macdonald, J. R. and Thompson, W. J., "Strongly Heteroscedastic Nonlinear Regression," *Communication in Statistics—Simulation and Computation*, Vol. 20, 1991, pp. 843–886.

[24] Agarwal, P., Orazem, M. E., and Garcia-Rubio, L. H., "Measurement Models for Electrochemical Impedance Spectroscopy: 1. Demonstration of Applicability," *Journal of the Electrochemical Society*, Vol. 139, 1992, pp. 1917–1927.

[25] Debye, P., *Polar Molecules*, Chemical Catalog Company, New York, 1929.

[26] Christy, R. W., "Classical Theory of Optical Dispersion," *American Journal of Physics*, Vol. 40, 1972, pp. 1403–1419.

[27] Elicabe, G. E., Garcia-Rubio, L. H., and Brandolin, A., "Approximations to the Refractive Index for Light Scattering Measurements," submitted to *Journal of Applied Polymer Science*, 1991.

[28] Raistrick, I. D., Macdonald, J. R., and Franceschetti, D. R., "Theory," Chapter 2 of *Impedance Spectroscopy Emphasizing Solid Materials and Analysis*, J. Ross Macdonald, Ed., John Wiley and Sons, New York, 1987.

[29] Gabrielli, C., *Identification of Electrochemical Processes by Frequency Response Analysis*, Solartron Instrumentation Group Monograph, The Solartron Electronic Group Limited, Farnborough, England, 1980.

[30] Walter, G. W., "A Review of Impedance Plot Methods Used for Corrosion Performance Analysis of Painted Metals," *Corrosion Science*, Vol. 26, 1986, p. 681.

[31] Stewart, K. C., Kolman, D. G., and Taylor, S. R., "The Effect of Parasitic Conduction Pathways on EIS Measurements in Low Conductivity Media," *Electrochemical Impedance:*

Analysis and Interpretation, ASTM STP 1188, J. R. Scully, D. C. Silverman, and M. W. Kendig, Eds., American Society for Testing and Materials, Philadelphia, 1993 (this publication).

[*32*] Lorenz, W. J. and Mansfeld, F., "Determination of Corrosion Rates by Electrochemical DC and AC Methods," *Corrosion Science*, Vol. 21, 1981, p. 647.

[*33*] Wojcik, P. T., "Thermally Stimulated Deep-Level Impedance Spectroscopy," M.S. Thesis, University of Florida, August 1992.

[*34*] *Solartron 1250 Frequency Response Analyzer Operator's Manual*, Schlumberger, Hampshire, England, 1982, p. 17.2.

[*35*] Agarwal, P., Orazem, M. E., and Garcia-Rubio, L. H., "Measurement Models for Electrochemical Impedance Spectroscopy: 2. The Error-Structure of Impedance Data," in preparation.

[*36*] Agarwal, P., Orazem, M. E., and Hiser, A., "Application of Electrochemical Impedance Spectroscopy to Metal Hydrides," presented at the 180th Meeting of the Electrochemical Society, Phoenix, AZ, October 13–18, 1991.

[*37*] Agarwal, P., Orazem, M. E., and Hiser, A., "Application of Electrochemical Impedance Spectroscopy to Metal Hydrides," *Hydrogen Storage Materials, Batteries, and Electrochemistry*, D. A. Corrogan and S. Srinivasan, Eds., The Electrochemical Society, Pennington, NJ, in press.

[*38*] Agarwal, P., Orazem, M. E., and Garcia-Rubio, L. H., "Measurement Models for Electrochemical Impedance Spectroscopy: 3. Evaluation of Data for Consistency with the Kramers-Kronig Relations," in preparation.

[*39*] Press, W. H., Flannery, B. P., Teukolsky, S. A., and Vetterling, W. T., *Numerical Recipes, The Art of Scientific Computing*, Cambridge University Press, New York, 1989.

Claude Gabrielli,[1] *Michel Keddam,*[1] *and Hisasi Takenouti*[1]

Kramers-Kronig Transformation in Relation to the Interface Regulating Device

REFERENCE: Gabrielli, C., Keddam, M. and Takenouti, H., **"Kramers-Kronig Transformation in Relation to the Interface Regulating Device,"** *Electrochemical Impedance: Analysis and Interpretation, ASTM STP 1188,* J. R. Scully, D. C. Silverman, and M. W. Kendig, Eds., American Society for Testing and Materials, Philadelphia, 1993, pp. 140–153.

ABSTRACT: The Kramers-Kronig transforms constitute in principle a powerful tool to validate experimental impedance data. However, some ambiguities remain in this method; thus, its use needs some care. For instance, the negative resistance generated by the passivation process is often considered an impedance feature that cannot be verified by the Kramers-Kronig transforms. Clarifying this fundamental aspect on the basis of experimental results is not easy. To overcome this difficulty, the problem is addressed in this paper by considering impedance functions numerically simulated by a simple dummy cell. Then the applicability of the Kramers-Kronig transform is verified by evaluating:

(a) The real part of the impedance from its imaginary part,
(b) The imaginary part of the impedance from its real part,
(c) The real part of the admittance from its imaginary part, and
(d) The imaginary part of the admittance from its real part.

The calculated impedance spectra are then compared with the original ones.

From these calculations for different types of impedance, it is concluded that the choice of the proper immittance to be submitted to the Kramers-Kronig criterion is of basic importance. If the impedance is measured under potential regulation, the validity test should be performed with admittance. Conversely, if transfer functions are obtained under current regulation, the Kramers-Kronig transform should be applied to the electrode impedance.

KEYWORDS: stability, electrochemical impedance spectroscopy (EIS), passivation, transpassive dissolution, validation criterion

The impedance technique is increasingly applied to various electrochemical systems. Therefore, one may encounter impedance diagrams showing a shape never met before. It is important in these situations to make sure that such diagrams obtained experimentally are really significant before devising an electrochemical model. In this context, the Kramers-Kronig transforms offers a useful tool to validate the measured results before undertaking any further investigation. Some authors claimed that a certain impedance feature cannot be verified through the Kramers-Kronig transforms even though the results are reproducible and verify the linearity [*1–3*]. Then, they even concluded that the Kramers-Kronig transforms cannot be fully applied to the electrochemical impedance data. This problem arises often for diagrams obtained during the passivation or the transpassive dissolution of metals [*1,4,5*].

Thorough examination of this aspect is a rather difficult task, so we tried to verify the applicability of the Kramers-Kronig transforms on numerically generated data simulating

[1]Directeur de Recherche, CNRS, Physique des Liquides et Électrochimie, Laboratoire de l'Université P&M Curie, 75252 Paris Cedex 05, France.

different diagram shapes. The synthetic data include negative resistances or negative capacitances, or both.

The applicability of the Kramers-Kronig transforms requires four conditions: linearity, causality, stability, and a finite value of the immittance. The last aspect was recently discussed thoroughly by Esteban and Orazem [6]. We are particularly interested in the stability effect. We will recall, therefore, some fundamental features of the theory of stability applied to the electrode impedance [7]. We will then briefly describe the algorithm used for the Kramers-Kronig transforms.

Principles

Stability

Stability concerns the interface response to a small perturbing signal. It depends on both intrinsic interface dynamics and characteristics of the regulating device supplying a perturbing signal and maintaining the electrode at the steady state polarization conditions. Stability deals with the behavior of the whole system to the perturbation regime. However, sometimes this concept is confusingly used with the existence of a steady state, i.e., conditions that the system does not evolve during the experiment [1].

In terminology of the theory of stability, two types of stability can be distinguished. If the response vanishes with time after withdrawing the perturbation, the system is called asymptotically stable. Conversely, if the response does not vanish but remains bounded (e.g., an oscillation is maintained), the system is called stable. If the system diverges from its steady state when a perturbing signal is applied, the system is considered unstable [8]. In this paper, we will use the term "stable" for the system exhibiting the asymptotically stable state.

The electrochemical impedance can be defined as $Z(s)$ where s is the Laplace parameter ($s = \sigma + j\omega$). When $s = j\omega$, then the impedance is defined in the usual way. The current flowing through an electrochemical cell with impedance $Z(s)$ controlled by a potential regulating device is equivalent to a voltage source E_s in series with an output resistance R_s

$$I(s) = \frac{E_s}{R_s + Z(s)} \tag{1}$$

In the same way, if the electrochemical system is polarized by a current source I in parallel with a conductance G_s, the potential across the cell is

$$E(s) = \frac{I}{G_s + 1/Z(s)} \tag{2}$$

It is known that the system is stable if the poles of $I(s)$ in the potential, and $E(s)$ in current control, have a negative real part. For instance, if the electrochemical system has only one time constant τ, the time response to a perturbing signal can be written as

$$\text{Response} = K \times \exp(\sigma t) \tag{3}$$

Since time dependence of the response vanishes with time when $\sigma < 0$, the system is stable. The general analysis in time domain is not straightforward. In the frequency domain, stability criteria were elaborated in servo system theory. (Readers who are particularly interested in this aspect will find details in Refs 7 and 8.) Summarizing briefly,

the Laplace transform leads one to analyze in the Nyquist plot in the frequency range $-\infty < \omega < \infty$ [8]. The physical impedance is defined in the positive frequency domain; mathematical theory leads to extend to negative ω values by completing the diagram symmetrically with respect to the real axis (analytic function of complex variable). Then one counts the number of turns T around the origin. This number is positive if the Nyquist diagram turns clockwise with increasing frequency. Inversely, it is negative if the diagram turns counterclockwise. The number of poles with a positive real part P can be determined by the number of clockwise rotations of the diagram. The number of zero with a negative real part N is derived by

$$N = P - T \tag{4}$$

If N is equal to zero, then the system is stable under potential control. On the contrary, if P is zero, the electrochemical interface is stable under current control. Table 1 summarizes the stability of the interface when there is only one relaxation phenomenon related to a faradaic process in addition to the charge transfer resistance R_t and the double layer capacitance C_d. R_{sol} stands for the solution resistance. R_p is the polarization resistance defined as the low-frequency limit of the impedance.

The diagrams displayed in Table 1 such as 2b and 3a, present very common features. The diagram 3d is relative to the passivation process. It is also well known that the passivation characteristic can only be obtained by using a potentiostat and is not observable under galvanostatic control. This agrees with the stability diagnostic indicated in

TABLE 1—*Stability of the system with one faradaic time constant.*

Resistances	$Im(Z_F) > 0$	P	G	$Im(Z_F) < 0$	P	G
Rsol<Rt<Rp	2a 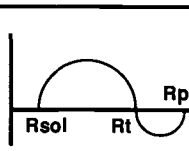	-	-	3a 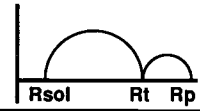	+	+
Rsol<Rp<Rt	2b 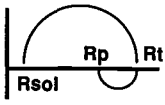	+	+	3b 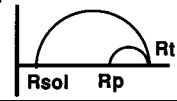	-	-
0<Rp<Rsol<Rt	2c 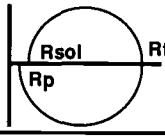	+	+	3c 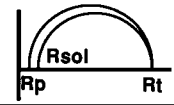	-	-
Rp<0<Rsol<Rt	2d 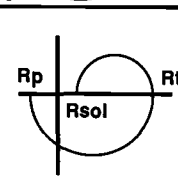	-	+	3d 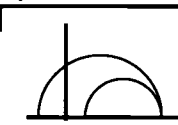	+	-

P : Under voltage , G : Under current regulations, + : Stable, - : Unstable

Table 1. The diagrams exhibiting the shapes similar to diagrams 2c and 2d were found during *Zn* electrodeposition. The polarization curve in this case is S-shaped. These features are interpreted on the basis of an electrochemical reaction mechanism involving an autocatalytic process [9]. The diagrams 3b and 3c were experimentally observed during the passivation of iron in sulfuric acid when the electrode was polarized by a regulation device having a negative output impedance [10]. A diagram such as 2a was never observed to our knowledge.

Kramers-Kronig Transforms

Numerically simulated impedance data fulfill the conditions of linearity. Except for the diverging impedance such as the Warburg or that of the blocking electrode, the finite value of the impedance can easily be calculated. For experimental data the problems are somewhat more complex. The linearity can be verified, in principle, by measuring the impedance with a perturbing signal of a small enough amplitude. If the measured impedance is independent of the amplitude of the perturbing signal, the linearity is considered to be satisfied. The causality is somewhat a more intricate term; if the impedance (or the admittance) is determined experimentally and reproducible, the requirement for the causality might likely be fulfilled.

The Kramers-Kronig transforms are based on the fact that the impedance measurement (more generally, immittance measurement) on both the real and the imaginary parts at each frequency is redundant. If the frequency change of one part is known *for the whole frequency range*, one can mathematically derive the other one. Let us consider the immittance $A(\omega)$ as

$$A(\omega) = Re(\omega) + j \times Im(\omega) \tag{5}$$

Then the Kramers-Kronig transforms lead to

$$Re(\omega) = Re(0) + \left(\frac{2\omega}{\pi}\right) \int_0^\infty \frac{\left(\frac{\omega}{x}\right) Im(x) - Im(\omega)}{x^2 - \omega^2} dx \tag{6}$$

$$Re(\omega) = Re(\infty) - \left(\frac{2}{\pi}\right) \int_0^\infty \frac{x \times Im(x) - \omega \times Im(\omega)}{x^2 - \omega^2} dx \tag{7}$$

$$Im(\omega) = -\left(\frac{2\omega}{\pi}\right) \int_0^\infty \frac{Re(x) - Re(\omega)}{x^2 - \omega^2} dx \tag{8}$$

where

$j = \sqrt{-1}$,
ω = angular frequency ($= 2\pi f$) (s^{-1}),
$Re(\omega)$ = Real part of $A(\omega)$,
$Im(\omega)$ = Imaginary part of $A(\omega)$,
$Re(0)$ = $A(\omega)$ at $f = 0$, i.e., R_p, and
$Re(\infty)$ = $A(\omega)$ at $f = \infty$, i.e., R_{sol}.

Computing Techniques

The Kramers-Kronig transforms were performed from the impedance Z as well as from the admittance Y. For the latter, the impedance was transformed into the admittance ($Y = Z^{-1}$) and then the Kramers-Kronig transforms were performed. At last, the results were displayed under the form of the electrode impedance ($Z = Y^{-1}$). In the following, we will represent the real and the imaginary parts of the impedance respectively by $Re(Z)$ and $Im(Z)$. Similarly, $Re(Y)$ and $Im(Y)$ stand for the real and the imaginary parts of the admittance. It is worth noting that if the impedance goes toward infinity in a low-frequency range, the admittance tends towards zero, thus yielding a finite value. The admittance meets, therefore, the requirement of the finite value for the application of Kramers-Kronig transforms.

The impedance data were numerically simulated on the basis of the equivalent electrical network displayed in Fig. 1. The value of α different from unity is introduced to represent a frequency dispersion (Constant Phase Element at high frequencies). We used positive as well as negative values for C_1 and R_1. Then, all diagrams displayed in Table 1 are simulated. We also examined, as can be seen later, an example having two faradaic time constants corresponding to that observed during the transpassive dissolution of metals.

Algorithm for the Kramers-Kronig Transforms

The numerical integration is generally performed with a constant increment Δx. Since the impedance measurements are spread over several decades, the Kramers-Kronig transforms were often carried out by dividing the frequency range in several segments. To avoid an arbitrary division in segments, we used a geometrical progression of Δx. The Newton method for integration was then slightly modified to meet this change. Since the integration was performed with a frequency step size five times smaller than that used in the simulation data, a cubic spline was used to interpolate the impedance data [*11*]. Further, to avoid the division by zero in Eqs 6 through 8, the initial value of x was selected such that $x = \omega$ never took place. We used Eq 7 to evaluate the real part of the immittance rather than Eq 6. The computer code for the calculations was written in FORTRAN.

Results and Discussion

Figures 2 and 3 display the simulated impedance data on the basis of the equivalent circuit displayed in Fig. 1. The figure numbers correspond to those indicated in Table 1. Table 2 showed the value of electrical elements used. Instead of the capacitance value C,

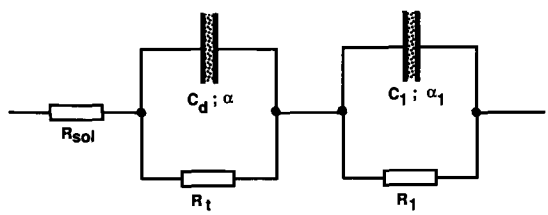

FIG. 1—*Electrical equivalent circuit for simulated impedance.* R_{sol} = *Solution resistance,* C_d = *Double layer capacitance,* R_t = *Charge transfer resistance,* C_l *and* R_l *generate a relaxation phenomenon due to an electrochemical process.* C_d *and* C_l *are frequency distributed elements.*

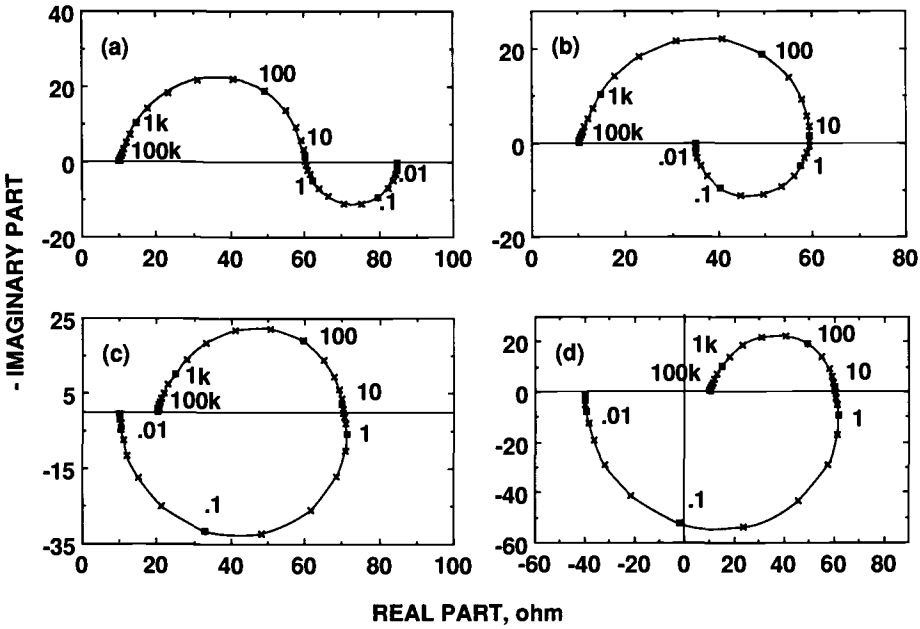

FIG. 2—*Simulated impedance diagrams with one faradaic time constant showing positive imaginary part corresponding to those marked respectively by 2a to 2d in Table 1. The parameter values are displayed in Table 2.*

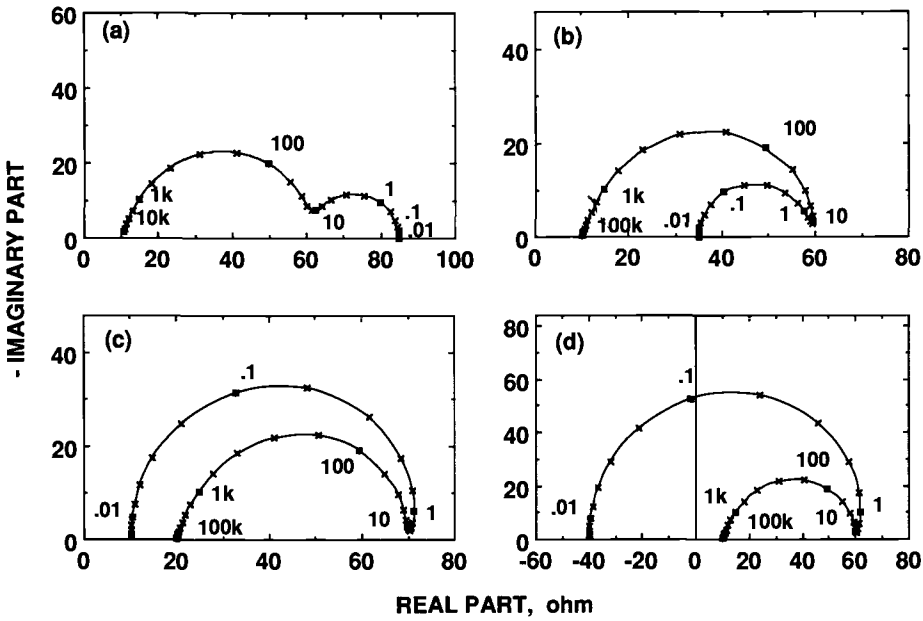

FIG. 3—*Simulated impedance diagrams with one faradaic time constant showing negative imaginary part corresponding to those marked respectively by 3a to 3d in Table 1. The parameter values are displayed in Table 2.*

we introduced the time constant τ defined by the product of resistance by capacitance ($\tau = RC$) as a parameter. The impedance $Z(\omega)$ was then derived by

$$Z(\omega) = R_{sol} + \frac{R_t}{(1 + j\omega\tau)^{\alpha}} + \frac{R_1}{(1 + j\omega\tau_1)^{\alpha 1}} \tag{9}$$

This expression corresponds to the Cole-Davidson type distribution of the time constant τ and τ_1.

The Kramers-Kronig transforms were performed in all cases by the four different manners as previously indicated. Figure 4 shows, for example, the result of four transforms for the impedance data of Fig. 3*a*. When the system is stable under both the potential and the current regulations, i.e., 2b, 2c, and 3a in Table 1, the result of four transforms agree quite well with the initial data as can be seen by the comparison of Fig. 3*a* and Figs. 4*a* through 4*d*.

Figures 2*a*, 3*b*, and 3*c* correspond to the impedances of unstable systems under both regulations, thus the Kramers-Kronig transforms do not agree in all cases with the initial impedance data. For the case in Fig. 2*a*, the result calculated from the real part of the impedance *Re*(*Z*) generated the diagram displayed in Fig. 3*a*. In fact, these two diagrams have the same frequency dependence on *Re*(*Z*). From the imaginary part of the impedance *Im*(*Z*), the Kramers-Kronig transforms showed the diagram displayed in Fig. 2*b* but shifted by 50 Ω on the real axis (Fig. 5*a*). The frequency dependence of *Im*(*Z*) is, in this case, also equal to that of Fig. 2*b*. However, the algorithm used for the calculation set the low-frequency limit of immittance equal to that of the initial immittance data as can be seen in Eq 6. If Eq 7 were used instead for the Kramers-Kronig transforms, one finds indeed the same diagram as in Fig. 2*b*. When the Kramers-Kronig transforms are performed for the impedance of an unstable system, we always produced the impedance of the stable system with the same frequency dependence of the initial set of data. For instance, from the data of the diagram 3b, the result displayed in Fig. 2*b* was calculated from *Re*(*Z*) and that corresponding to the diagram 3a from *Im*(*Z*). Similarly, from the initial data of Fig. 3*c*, one finds the diagram 2c when the Kramers-Kronig transforms are carried out from *Re*(*Z*). These observations can be made because the diagrams are simulated with parameters whose absolute values are often the same.

The observation made from the admittance data was somewhat more complex. The admittance *Y* for each frequency can be calculated from the impedance *Z* by

TABLE 2—*The values used for synthetized impedance data (cf Fig. 1).*

Diagram	R_{sol}/Ω	R_t/Ω	τ/s	α	R_1/Ω	τ_1/s	α_1
2*a*	10	50	10^{-3}	0.8	25	−1	0.8
2*b*	10	50	10^{-3}	0.8	−30	1	0.8
2*c*	20	50	10^{-3}	0.8	−60	1	1.25
2*d*	10	50	10^{-3}	0.8	−100	1	1.25
3*a*	10	50	10^{-3}	0.8	25	0.1	0.8
3*b*	10	50	10^{-3}	0.8	−30	−1	0.8
3*c*	20	50	10^{-3}	0.8	−60	−1	1.25
3*d*	10	50	10^{-3}	0.8	−100	−1	1.25

Capacitance of each network can be calculated by: $\tau = RC$.

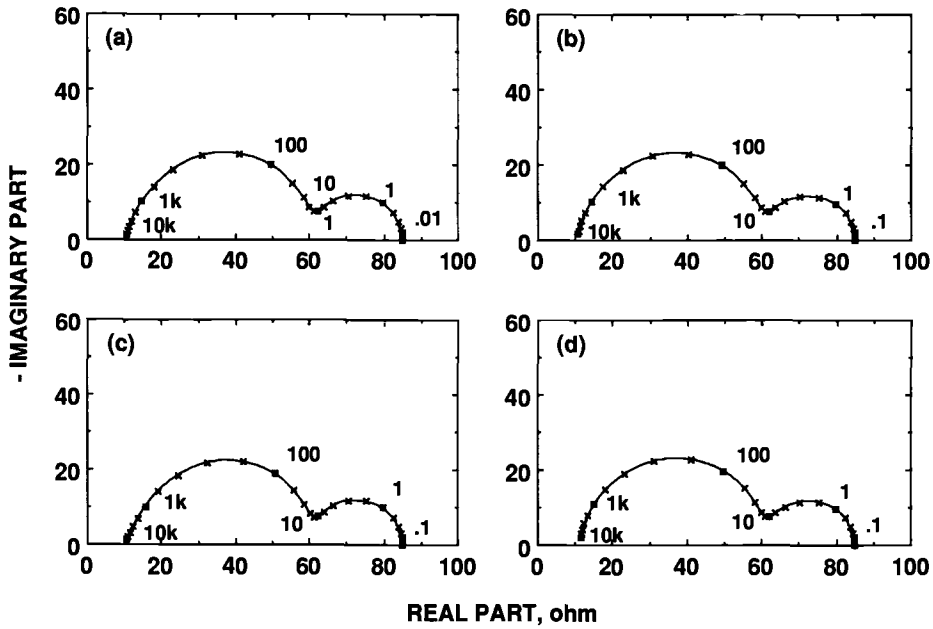

FIG. 4—*Result of the Kramers-Kronig transforms for the diagram 3a (results in agreement with the original data).* (a) *Re(Z) calculated from Im(Z).* (b) *Im(Z) calculated from Re(Z).* (c) *Re(Y) calculated from Im(Y).* (d) *Im(Y) calculated from Re(Y).*

$$Z = Re - j \times Im$$

$$Y = \frac{1}{Z} = \frac{Re}{Re^2 + Im^2} + \frac{j \times Im}{Re^2 + Im^2} \tag{10}$$

Therefore, both the absolute values of $Re(\omega)$ and $Im(\omega)$ should follow the same frequency dependence to find a synthetized data $Z(\omega)$ of stable system. This is indeed verified for the diagram 2a when the Kramers-Kronig transforms are performed from the real part of admittance. The calculated diagram is equal to the diagram 3a. In the same way, from the diagrams 3b and 3c, the Kramers-Kronig transforms from $Re(Y)$ showed respectively the diagrams 2b and 2c.

If the Kramers-Kronig transforms were performed for the diagram 2a from $Im(Y)$, then one finds a diagram similar to 2b, but of a larger size (Fig. 5*b*). Figures 5*c* and 5*d* are, respectively, the Kramers-Kronig transforms of the diagram 3b calculated from $Im(Z)$ and $Im(Y)$, respectively. Figure 5*c* corresponds to the diagram 2b, but the low-frequency limit is shifted to be coincident with $Re(0)$ of the initial data. Figures 6*a* and 6*b* are the diagrams calculated from $Im(Z)$ and $Im(Y)$ of the impedance data of Fig. 3*c*. The remarks formulated with Figs. 5*c* and 5*d* apply as well to Figs. 6*a* and 6*b*.

Let us examine now the system that satisfies the stability conditions (diagrams 2d and 3d) when polarized by only one of the two regulation devices. If the Kramers-Kronig transforms from the admittance were made for the diagram 2d, the results verify the initial impedance data. Conversely, for the impedance diagram 3d, the Kramers-Kronig transforms from the impedance agree with the initial data. On the contrary, if the Kramers-

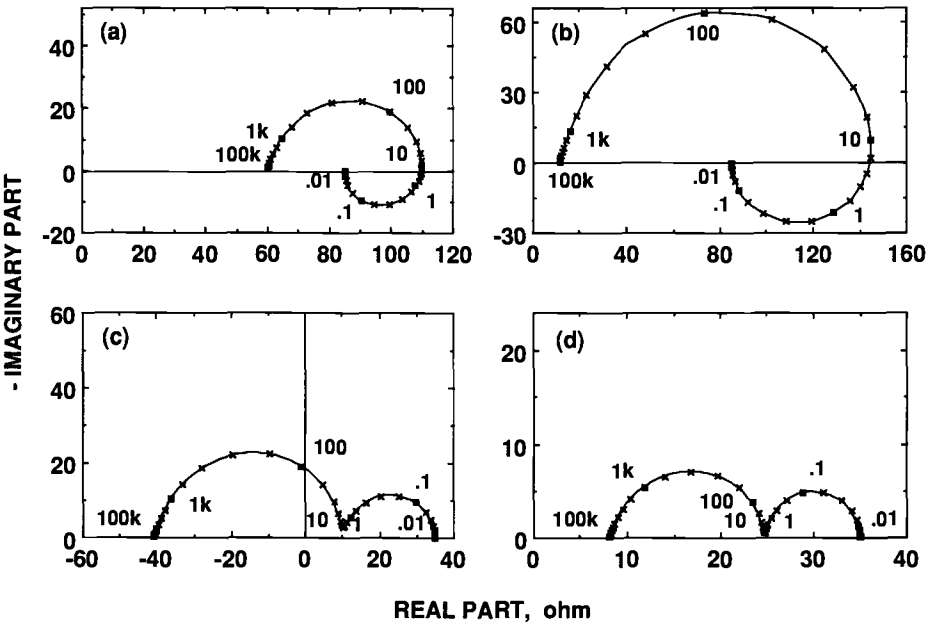

FIG. 5—*Result of the Kramers-Kronig transforms in contradiction with the original data.* (a) *Re(Z) calculated from Im(Z) for 2a.* (b) *Re(Y) calculated from Im(Y) for 2a.* (c) *Re(Z) calculated from Im(Z) for 3b.* (d) *Re(Y) calculated from Im(Y) for 3b.*

Kronig transform was proceeded from *Re(Z)* for the diagram 3d, one found the diagram 2d (see Fig. 6*c*) and from *Im(Z)*, the diagram displayed in Fig. 6*d*. Figures 7*a* and 7*b* illustrate the results of Kramers-Kronig transforms of the diagram 2d from *Re(Y)* and *Im(Y)* respectively. The diagram in Fig. 7*a* is identical to the diagram 3d.

It can be concluded, therefore, that there is a close relationship between the Kramers-Kronig transforms and the stability of the system. The Kramers-Kronig transforms from the impedance lead to the original results only if the system is stable under current control (galvanostat) depending on whether the transforms were made from the real or the imaginary part. Similarly, the Kramers-Kronig transforms from the admittance conform with the initial data provided that the system is stable under the potential control (potentiostat). This is a very important feature for the validation of the impedance data from the Kramers-Kronig criterion.

Figure 8*a* is a simulated impedance for the Randle-type electrode process. Figure 8*c* is relative to the Kramers-Kronig transforms from *Im(Y)*, and agrees relatively well with Fig. 8*a*. Figure 8*b* is the Kramers-Kronig transform from *Im(Z)*. One may find a further good agreement with Fig. 8*a* if Eq 7 were used instead of Eq 6. On the contrary, if the Kramers-Kronig transform was performed from *Re(Z)*, as reported by Shih and Mansfeld [*12*], a marked difference in the calculated impedance was observed: The diagram bends significantly towards the real axis. From the viewpoint of stability, Fig. 8*a* is stable under both regulations provided that the impedance diagram shows a finite value at zero frequency. Since the potential regulation is best appropriate to polarize such a system, the Kramers-Kronig transforms from the admittance will be performed. The impedance tends to a very high value in low frequencies; then the admittance tends to zero, i.e., remains bounded.

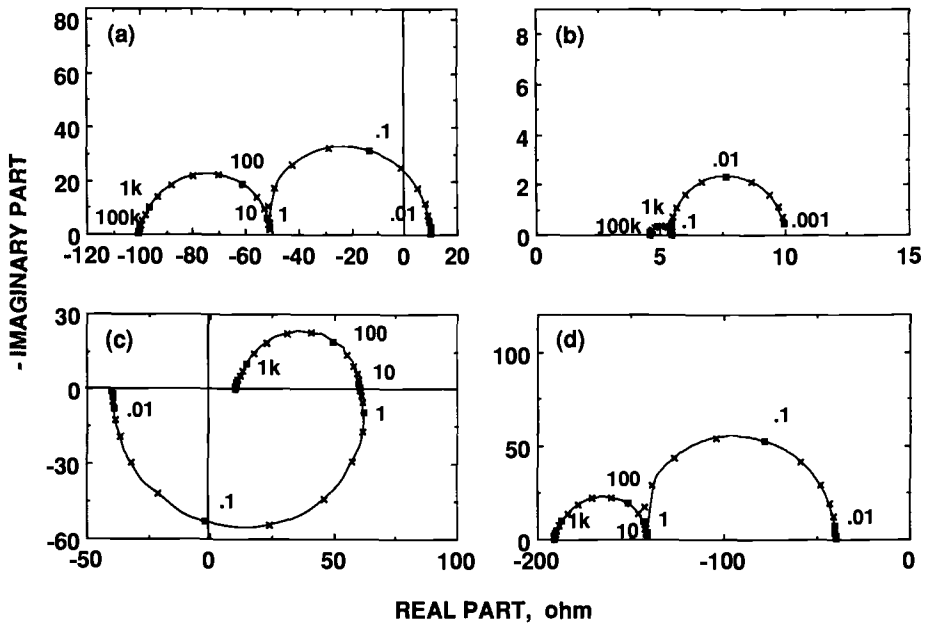

FIG. 6—*Result of the Kramers-Kronig transforms in contradiction with the original data.* (a) *Re(Z) calculated from Im(Z) for 3c.* (b) *Re(Y) calculated from Im(Y) for 3c.* (c) *Im(Z) calculated from Re(Z) for 3d.* (d) *Re(Z) calculated from Im(Z) for 3d.*

Indeed, the Kramers-Kronig transform from *Im(Y)* was found close enough to the initial data to validate the impedance data, though a significant difference can be seen at low frequencies. The frequency range used for the Kramers-Kronig transforms was likely not large enough (particularly on the low-frequency side) to eliminate completely the truncation effect on the integration calculation.

Figure 9 is relative to the simulated impedance for the transpassive dissolution. We added in series another parallel R-C circuit in the equivalent electrical network given earlier (Fig. 1). This diagram is stable only under potential control. The diagrams illus-

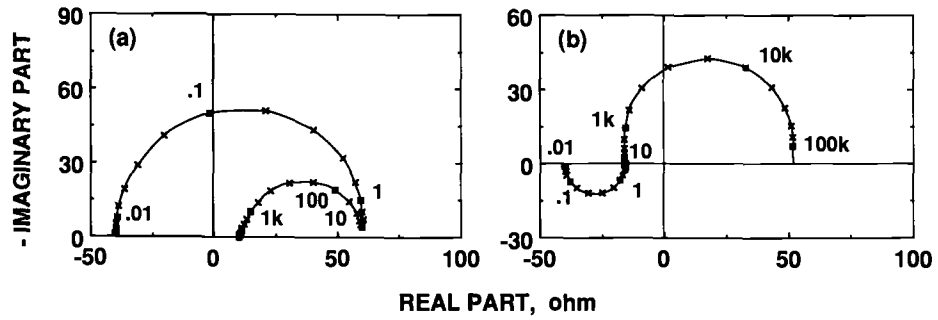

FIG. 7—*Result of the Kramers-Kronig transforms in contradiction with the original data.* (a) *Im(Y) calculated from Re(Y) for 2d.* (b) *Re(Y) calculated from Im(Y) for 2d.*

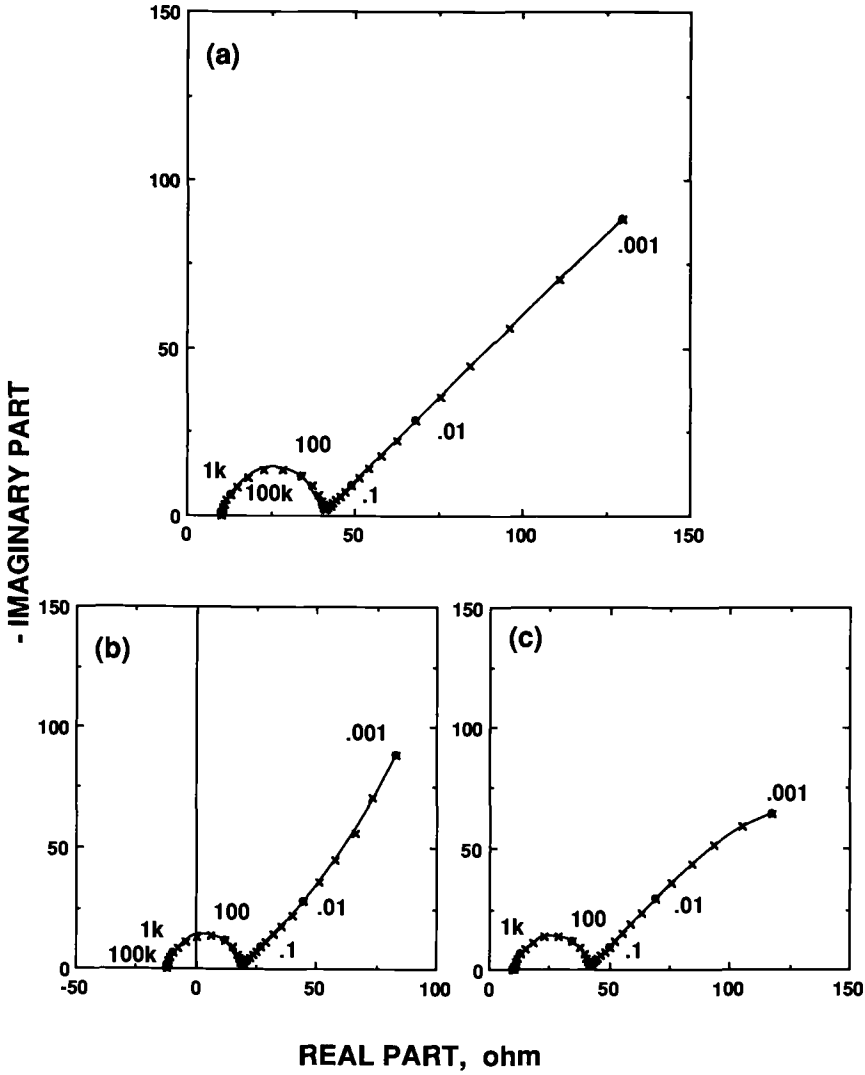

FIG. 8—*Randles type impedance.* (a) *simulated by* $R_{sol} = 10\ \Omega$, $R_t = 30\ \Omega$, $t = 10^{-3}$ *s*, $\alpha = 0.8$, $R_l = 10^3\ \Omega$, $t = 10^4$ *s and* $\alpha_l = 0.5$. (b) *calculated Re(Z) from Im(Z).* (c) *calculated Re(Y) from Im(Y).*

trated in Figs. 10*a* and 10*b* are obtained by the Kramers-Kronig transforms respectively from *Re(Z)* and *Im(Z)*. Figure 10*a* looks similar to Fig. 9, but if the diagram is examined closely, one may remark that the low-frequency loop turns the opposite direction. Figure 10*b* does not exhibit a negative real part. It is worth noting that these two diagrams are stable under current control.

Figures 10*c* and 10*d* are obtained by the Kramers-Kronig transforms for *Re(Y)* and *Im(Y)*, respectively. Though a slight difference was found at intermediate frequencies on the diagram 10*d*, these diagrams agree with that displayed in Fig. 9. The close relationship between the regulating device and the Kramers-Kronig transforms is again verified for a

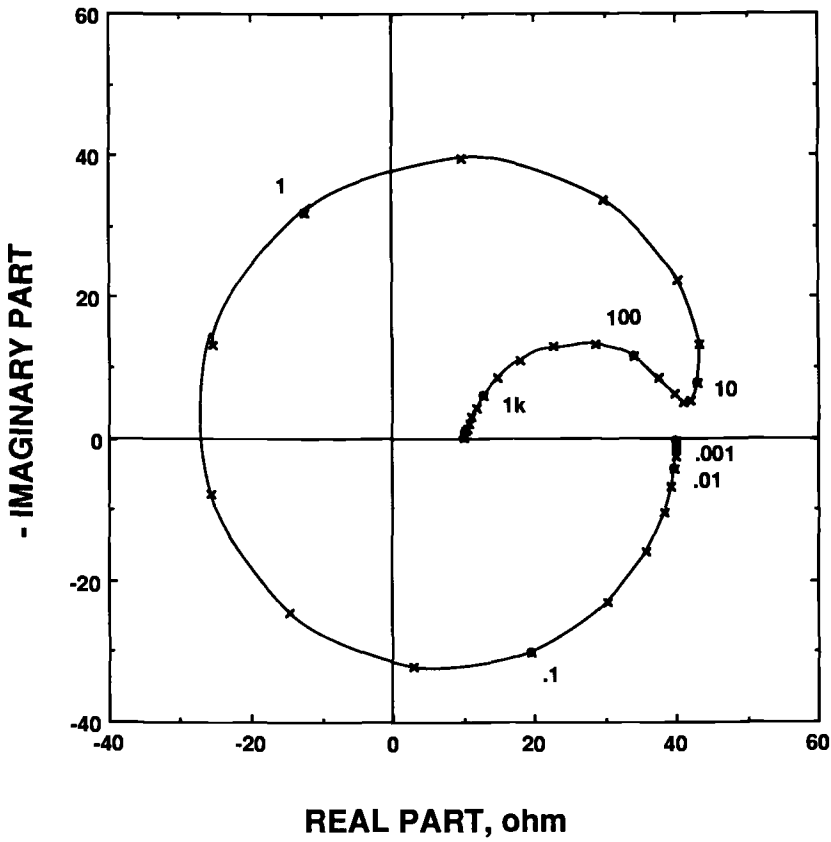

FIG. 9—*Simulated impedance for the transpassive dissolution.* $R_{sol} = 10\ \Omega$, $R_t = 30\ \Omega$, $t = 10^{-3}$ *s*, $\alpha = 0.8$, $R_1 - 100\ \Omega$, $t = -1$ *s*, $\alpha_1 = 1.25$, $R_2 = 100\ \Omega$, $t = -0.1$ *s*, $\alpha_1 = 0.8$.

more complicated electrochemical system. We determined experimentally how the requirement of stability is related to the applicability of the Kramers-Kronig transforms.

Conclusion

The Kramers-Kronig transforms may, in principle, constitute a useful tool to validate the experimental impedance data. We particularly emphasized the stability of the electrochemical interface with respect to the interface regulating device, one of the four requirements to the applicability of this criterion, by using synthetized impedance data. It was found that if the impedance was measured under potential regulation, the Kramers-Kronig transforms have to be applied to the electrode admittance. Conversely, if the electrode impedance was determined under current control, the impedance data should be submitted to the Kramers-Kronig transforms. It is worth noting that if the system is unstable under a given regulation device, the electrode interface cannot be correctly polarized. Thus, no impedance data will be yielded.

If the stability condition is not fulfilled, the transformed data correspond to those obtained under the regulating device at which the interface is stable and having the same frequency dependence. For impedance data similar to those in diagrams 2a, 3b, and 3c, the

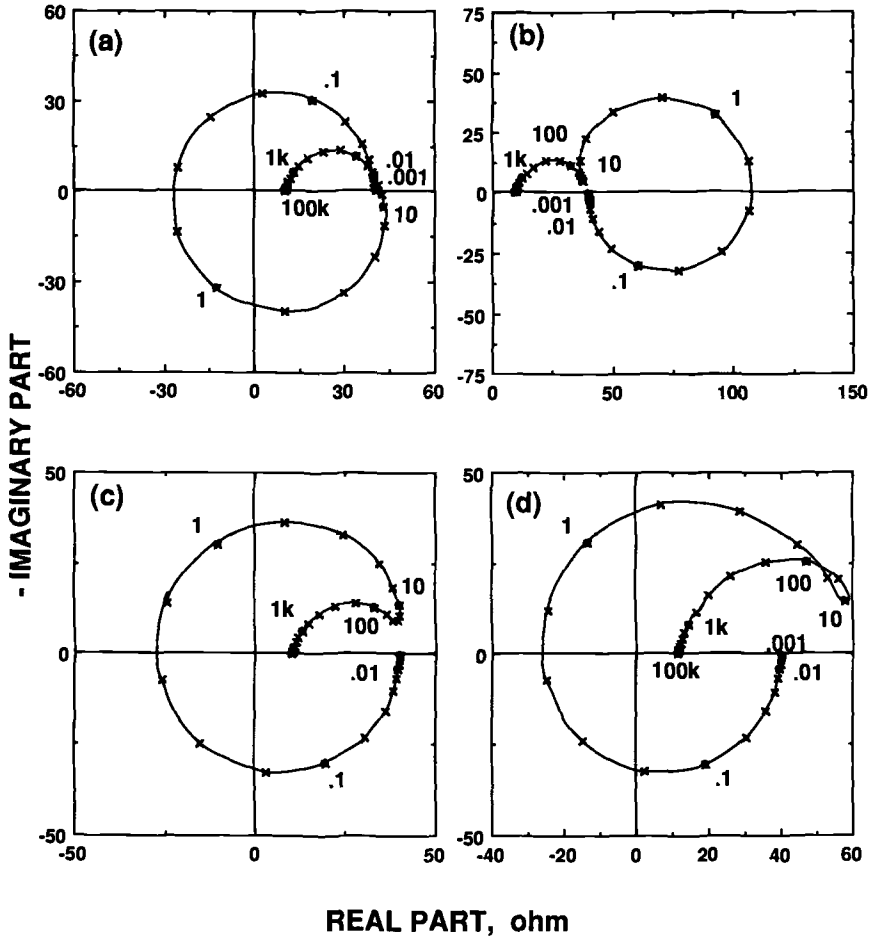

FIG. 10—*Result of the Kramers-Kronig transforms for the impedance shown in Fig. 9.* (a) *Re(Z) calculated from Im(Z).* (b) *Im(Z) calculated from Re(Z).* (c) *Re(Y) calculated from Im(Y).* (d) *Im(Y) calculated from Re(Y).*

interface cannot be polarized adequately by a potentiostat or a galvanostat. In this case the Kramers-Kronig transforms cannot be applied. In other words, the knowledge about the stability of the system allows one to definitely discard certain features of electrode impedance without using the Kramers-Kronig transform criteria.

Further, it was found that if the impedance becomes very high at low frequencies, the Kramers-Kronig transforms from the admittance may likely verify the validity of experimental data.

References

[1] Macdonald, D. D., *Corrosion*, Vol. 46, 1990, p. 229.
[2] Macdonald, D. D. and Urquidi-Macdonald, M., *Journal of the Electrochemical Society*, Vol. 132, 1985, p. 2316.

[3] Urquidi-Macdonald, M., Real, S., and Macdonald, D. D., *Journal of the Electrochemical Society,* Vol. 133, 1986, p. 2018.
[4] Cahan, B. and Chen, C. T., *Journal of the Electrochemical Society,* Vol. 129, 1982, p. 474.
[5] Gabrielli, C. and Keddam, M., *Journal of the Electrochemical Society,* Vol. 129, 1982, p. 2872.
[6] Esteban, J. M. and Orazem, M. E., *Journal of the Electrochemical Society,* Vol. 138, 1991, p. 67.
[7] Epelboin, I., Gabrielli, C., Keddam, M., and Takenouti, H., "The Study of the Passivation Process by the Electrode Impedance Analysis," in *Comprehensive Treatise of Electrochemistry,* J. O'M. Bockris, B. E. Conway, E. Yeager, and R. White, Eds., Vol. 4, Plenum Press, New York, 1981, p. 151.
[8] Parmentier, R. D., "Neutristor Analysis Technique for Non-linear Distributed Electronic System," *Proceedings of the Institute for Electrical and Electronic Engineers,* Vol. 58, 1970, p. 1829.
[9] Epelboin, I., Ksouri, M., and Wiart, R., *Journal of the Electrochemical Society,* Vol. 122, 1975, p. 1206.
[10] Epelboin, I., Gabrielli, C., Keddam, M., and Takenouti, H., *Zeitschrift fur Physikalische Chemie,* Neue Folge, Vol. 98, 1975, p. 215.
[11] Press, W. H., Flannery, B. P., Teukolsky, S. A., and Vetterling, W. T., *Numerical Recipes,* Cambridge University Press, Cambridge, MA, 1986.
[12] Shih, H. and Mansfeld, M., *Corrosion,* Vol. 45, 1989, p. 325.

Brian J. Dougherty[1] *and Stuart I. Smedley*[1]

Validation of Experimental Data from High Impedance Systems Using the Kramers-Kronig Transforms

REFERENCE: Dougherty, B. J. and Smedley, S. I., **"Validation of Experimental Data from High Impedance Systems Using the Kramers-Kronig Transforms,"** *Electrochemical Impedance: Analysis and Interpretation, ASTM STP 1188*, J. R. Scully, D. C. Silverman, and M. W. Kendig, Eds., American Society for Testing and Materials, Philadelphia, 1993, pp. 154–170.

ABSTRACT: Impedance data measured for the high impedance aluminum/methanol and aluminum/methanol/water systems have been validated using the Kramers-Kronig Transforms (KKT). The real-to-imaginary and imaginary-to-real transforms gave accurate results for experimental data which met the linearity, causality, stability, and continuity and finiteness criteria. In cases in which only the continuity and finiteness criterion was violated, the magnitude of the real impedance calculated from the imaginary-to-real transform and the maximum value of the imaginary impedance calculated from the real-to-imaginary transform were smaller than the experimental values. The real-to-imaginary transform was more sensitive to errors of this type than the imaginary-to-real transform. Neither transform produced accurate results when the linearity, stability, and causality requirements were violated.

KEYWORDS: Kramers-Kronig Transforms (KKT), impedance, corrosion, aluminum, methanol, water

Impedance spectroscopy is an increasingly important technique in the study of electrochemical phenomena. In a typical impedance experiment, the electrochemical system is perturbed by an electrical stimulus, and the response monitored as a function of the perturbation frequency. The general relationship between the response and the perturbation can be represented by [*1*]

$$R(s) = H(s,P) \times P(s) \tag{1}$$

where $R(s)$ is the response; $P(s)$ the perturbation; and $H(s,P)$ is the transfer function. The Laplace variable, s, $= j\omega$, where ω is the angular frequency and $j^2 = -1$. $H(s,P)$ constitutes a valid impedance provided that the following criteria are met [*1*]:

- Causality: The response of the system must be determined entirely by the perturbation.
- Linearity: The perturbation/response characteristics of the system must be described by a series of linear differential equations.
- Stability: Once the perturbation has been removed the system must return to its original state.

[1]SRI International, Menlo Park, CA 94025-3493.

- Continuity and finiteness: The impedance must be finite-valued and continuous over the frequency range $0 < \omega < \infty$. In particular, the impedance must tend to a constant, real value as $\omega \rightarrow 0$ and $\omega \rightarrow \infty$.

For impedance data to satisfy these criteria, very careful control of the experimental conditions is required. To some extent, the requirements of these criteria conflict, so that in practice a compromise must be accepted. Relatively few researchers establish the validity of their data in a phenomenological sense, other than to note that the spectra recorded are independent of the signal amplitude, thereby demonstrating that the system behaves linearly, or that the system is stable in the sense that it returns to its original state on completion of the experiment.

In our study of the high impedance system of aluminum in methanol and in methanol-water mixtures [2], the quality of the spectra at frequencies below 10 mHz was degraded by data scatter due to noise. This problem was alleviated somewhat by the use of a large signal amplitude (20 mV); however, such a large amplitude could have resulted in spurious components due to harmonics of the excitation frequency, in possible contradiction to the causality and linearity criteria. In addition, the results were averaged over several cycles at each test frequency. This increased the total measurement time, raising questions as to the stability of the system. A further consequence of signal averaging is that it increases the minimum frequency at which the impedance of the system could be measured. The impedance of the aluminum/methanol/water system often retained a significant reactive component at frequencies below 1 mHz, so that the fourth criterion was not always obeyed. It is apparent that a reliable method of evaluating the validity of experimentally measured impedance spectra was warranted.

Kramers-Kronig Transforms

Kramers-Kronig Transforms (KKT) are mathematical relationships that permit the real component of a complex variable to be calculated solely from the imaginary component of the same variable, and vice versa. They arise directly from the causality principle of physics [3,4] and can be applied to any system described by Eq 1 and satisfying the aforementioned criteria [1]. The most useful forms of the KKT are [1,5]:

$$Z'(\omega) - Z'(\infty) = \left(\frac{2}{\pi}\right) \int_{x=0}^{\infty} \frac{xZ''(x) - \omega Z''(\omega)}{x^2 - \omega^2} dx \tag{2}$$

$$Z''(\omega) = \left(\frac{2\omega}{\pi}\right) \int_{x=0}^{\infty} \frac{Z'(x) - Z'(\omega)}{x^2 - \omega^2} dx \tag{3}$$

$$R_p = \left(\frac{2}{\pi}\right) \int_{x=0}^{\infty} \frac{Z''(x)}{x} dx \tag{4}$$

Z' and Z'' are the real and imaginary components of the impedance, respectively, at the angular frequencies x (integrand) and ω (the "pole" frequency); R_p is the polarization resistance; and $Z'(\infty)$ is the value of the real component of the impedance as $\omega \rightarrow \infty$. Although Eqs 2 to 4 are integrations from 0 to ∞, the integration can be truncated at some finite frequency within these limits provided the impedance tends to a finite, constant real value at both high and low frequency. The apparent singularity at $x = \omega$ in Eqs 2 to 4 is avoided, since [1,4]

$$\lim_{x \to \omega} = \left[\int_{x=0}^{\infty} \frac{dx}{x^2 - \omega^2} \right] = 0 \tag{5}$$

The use of the KKT as diagnostic tools for the verification of experimental impedance data has been evaluated by Macdonald et al. [*1,5*], who showed that the transforms could successfully detect errors of a few percent in either or both the real or imaginary components of the impedance. Since the KKT are purely mathematical relationships, they provide an independent means by which to establish the validity, or otherwise, of experimental impedance data. In the present paper, we describe the application of these transforms to test the validity of experimental impedance data measured for the high impedance aluminum/methanol/water system.

Calculation Procedure

The KKT were calculated using the method of Urquidi-Macdonald et al. [*1*], except as otherwise noted.

(1) A polynomial of general formula

$$Z(x_i) = \sum_{n=0}^{n=n_{max}} a_n x_i^n \tag{6}$$

where a_n is the coefficient of the n^{th} power of the frequency, x_i, and $1 \leq n_{max} \leq 6$, was fitted sequentially over segments of the experimental data. The minimum and maximum frequency of each data segment and the maximum degree of the polynomial were selected so as to optimize the fit of the polynomial.

(2) Equation 6 was used to interpolate each segment of the experimental data set, thereby generating an extended data set for use in the transformation calculations. For a given segment, m, covering the frequency range ${}_m x_0$ to ${}_m x_{max}$, the frequencies in the extended data set, ${}_m x_i$, were calculated using

$$\log_{10}({}_m x_i) = \log_{10}({}_m x_0) + 0.02 \times (i - 1) \tag{7}$$

where i is an integer between 0 and i_{max}

$$i_{max} = 50 \times \log_{10}\left(\frac{x_{max}}{x_0}\right) \tag{8}$$

This generated 50 points per decade in the extended data set, spaced 0.02 log units apart, compared to 10 points per decade in the experimental data set. This interpolation procedure is necessary to ensure the accuracy of the transforms, which must be calculated by numerical methods.

The largest contribution to Eqs 2 to 4 occurs when the denominator is small, i.e., when $x \approx \omega$. Since the magnitude of the real impedance, $|Z'(x)|$, is largest at low frequency, significant error can be introduced into the calculations if the frequency resolution in the extended data set is too large. The use of a logarithmic step rather than a linear one as used by Macdonald et al. [*5*] improves the accuracy of the transform by increasing the density of points at the low-frequency end of each segment.

(3) The real-to-imaginary (Eq 2) and imaginary-to-real (Eq 3) transforms were evaluated numerically using their discrete forms (Eqs 9 and 10, respectively) [*5*]

$$Z'(\omega) - Z'(\infty) = \left(\frac{2}{\pi}\right) \sum_{x=x_{min}}^{x=x_{max}} \frac{xZ''(x) - \omega Z''(\omega)}{x^2 - \omega^2} \Delta x \tag{9}$$

$$Z''(\omega) = \left(\frac{2\omega}{\pi}\right) \sum_{x=x_{min}}^{x=x_{max}} \frac{Z'(x) - Z'(\omega)}{x^2 - \omega^2} \Delta x \tag{10}$$

Δx denotes the frequency interval and x_{min} and x_{max} are the minimum and maximum frequencies in the experimental data set, respectively; the other terms have the same meanings as in Eqs 2 to 4. R_p was calculated directly from Eq 11, substituting the polynomial for $Z''(x)$, integrating between the limits ${}_m x_0$ and ${}_m x_{max}$ for each segment, and then summing up the results of all segments [5].

$$R_p = \left(\frac{2}{\pi}\right) \sum_{x=x_{min}}^{x=x_{max}} \frac{Z''(x)}{x} \Delta x \tag{11}$$

The calculations were performed using a cubic spline integration algorithm, running in BASIC 5.0 on an HP 9816 computer.

(4) The results were analyzed by comparing the transformed data with the original data, using a statistical error function given by [1]

$$AE = \frac{100 \times \sum_{x=1}^{N} |Z_{ex}(x) - Z_{KK}(x)|}{N \times Z_{max}} \tag{12}$$

where $|Z_{ex}(x) - Z_{KK}(x)|$ represents the absolute magnitude of the difference between the value of the experimental impedance ($Z_{ex}(x)$) and that calculated via the KKT, ($Z_{KK}(x)$); Z_{max} is the maximum value of the experimental impedance, and N is the number of points in the experimental data.

Evaluation of Transform Algorithm

Experimental impedance data measured for the high impedance aluminum/methanol/water system typically contained two capacitive-type loops separated by an inductive-type loop [5]. Furthermore, the frequency distribution around the low-frequency capacitive loop was such that at 1 mHz (the lowest frequency at which the impedance could be measured in practice), only the leading arc of this loop could be discerned. This is an apparent violation of the fourth criterion.

To ascertain whether or not the KKT procedure would transform impedance data of this type accurately, the KKT algorithm was tested using synthetic impedance data derived for an electrical circuit containing two parallel RC elements and one parallel RL element, linked together in series (i.e., RC-RL-RC). Two cases were tested:

(a) Using a wide frequency range, 10^{-6} Hz to 10^{4} Hz, in which all relaxations were fully characterized.
(b) Using a limited frequency range, 10^{-3} Hz to 10^{4} Hz, in which the low-frequency relaxation was not fully characterized.

Case A was chosen to provide a test of the accuracy of the algorithm; Case B to test the ability of the transform procedure to detect the sensitivity of the transform to cases where the fourth criterion is not met. Case B more accurately reflects the type of impedance data measured at an aluminum electrode in methanol/water mixtures.

The transformed data are compared to the experimental data in Figs. 1 and 2, for Cases A and B, respectively. In Case A, an excellent fit between the transformed and experimental data was achieved, demonstrating the accuracy of the algorithm itself when presented with impedance data of the type described earlier. In Case B, deviations occur at low frequencies in both transforms: the imaginary-to-real transform (Fig. 2*a*) shows a small deviation to lower values of the impedance at low frequency. The real-to-imaginary transform (Fig. 2*b*) gives a smaller maximum value of the imaginary impedance of the low-frequency capacitive loop. In contrast, the maximum value of the imaginary impedance of the high-frequency capacitive loop is almost unaffected. These differences are quantified in Table 1. (*AE* is defined by Eq 12). In Case A, *AE* was less than 0.4 for both transforms, and the value of R_p calculated from the KKT deviated from its theoretical value by less than 0.2%. In Case B, *AE* was an order of magnitude larger than in Case A, particularly for the real-to-imaginary transform. In addition, the calculated value of R_p was 32% smaller than that used to generate the data.

These cases demonstrate that the KKT procedure adopted here is capable of accurately transforming impedance data of the type described, and that the procedure is capable of detecting instances when there is insufficient data at low frequencies to characterize the impedance spectrum fully. The real-to-imaginary transform and the calculation of R_p are particularly sensitive indicators in this context.

Application of the KKT to Aluminum Electrodes Corroding in Methanol/Water Solutions

In our impedance study of the corrosion of aluminum in methanol/water solutions, an extensive body of impedance spectra was recorded at various electrode potentials and at various solvent compositions [2]. Each series of data consisted of an initial spectrum, measured at the corrosion potential, E_{corr}, followed by steady-state polarization to cathodic and anodic potentials. Next, a second impedance scan was measured at E_{corr}. Then, the electrode was polarized cathodically and the impedance spectra were measured as the potential was stepped anodically. At the completion of this set of experiments, a final spectrum was measured at E_{corr}. Details of the electrode preparation and other aspects of the experimental conditions pertaining to this study are described elsewhere [2].

The large body of data gathered together with the long time required to perform the KKT analysis (approximately 2 h per spectrum using the HP 9816; more modern computers could undoubtedly perform the calculations more quickly, but were not available to this study) meant that it was not possible to test each spectrum individually. Therefore, evaluation of the experimental impedance data was limited to spectra selected from the bulk of the data as follows:

(1) The first and last spectrum recorded in each series of experiments.
(2) Three spectra were tested from those measured at elevated polarization potentials: one from each of the cathodic and anodic regimes and the third at E_{corr}.
(3) Spectra in which data scatter at low frequencies indicated a poor signal-to-noise ratio.

The first and last spectra provide information regarding the initial behavior of the electrode and show that once it had been polarized to elevated anodic and cathodic

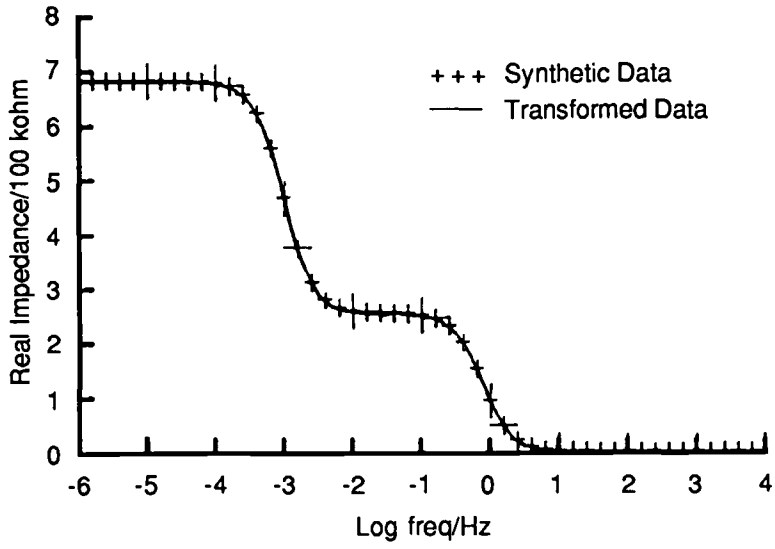

(a) Imaginary-to-real transform

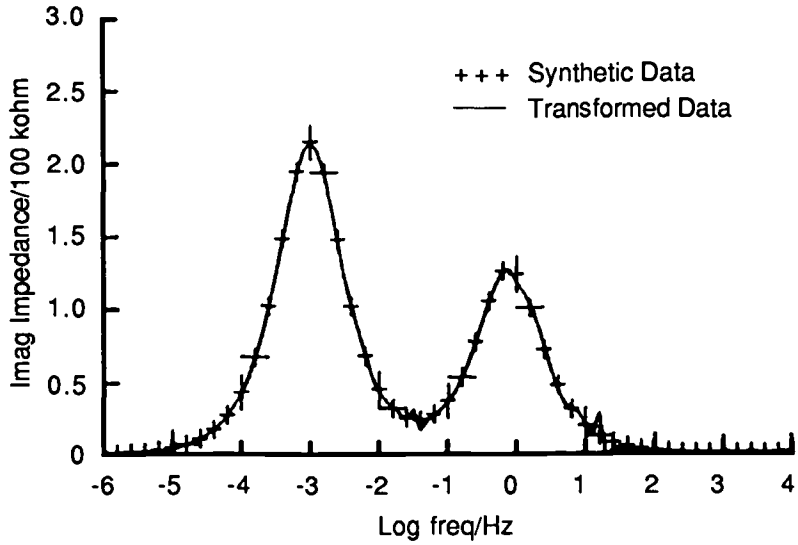

(b) Real-to-imaginary transform

FIG. 1—*Kramers-Kronig Transforms of synthetic impedance data, calculated over an extensive frequency range (Case A). Synthetic data calculated for an electrical circuit comprising three elements connected in series: two parallel RC circuits (R_1 = 254 kΩ, C_1 = 5.12 μF; R_2 = 428 kΩ, C_2 = 2.35 μF); and one parallel RL circuit (R = 1000 Ω; L = 100 kH).*

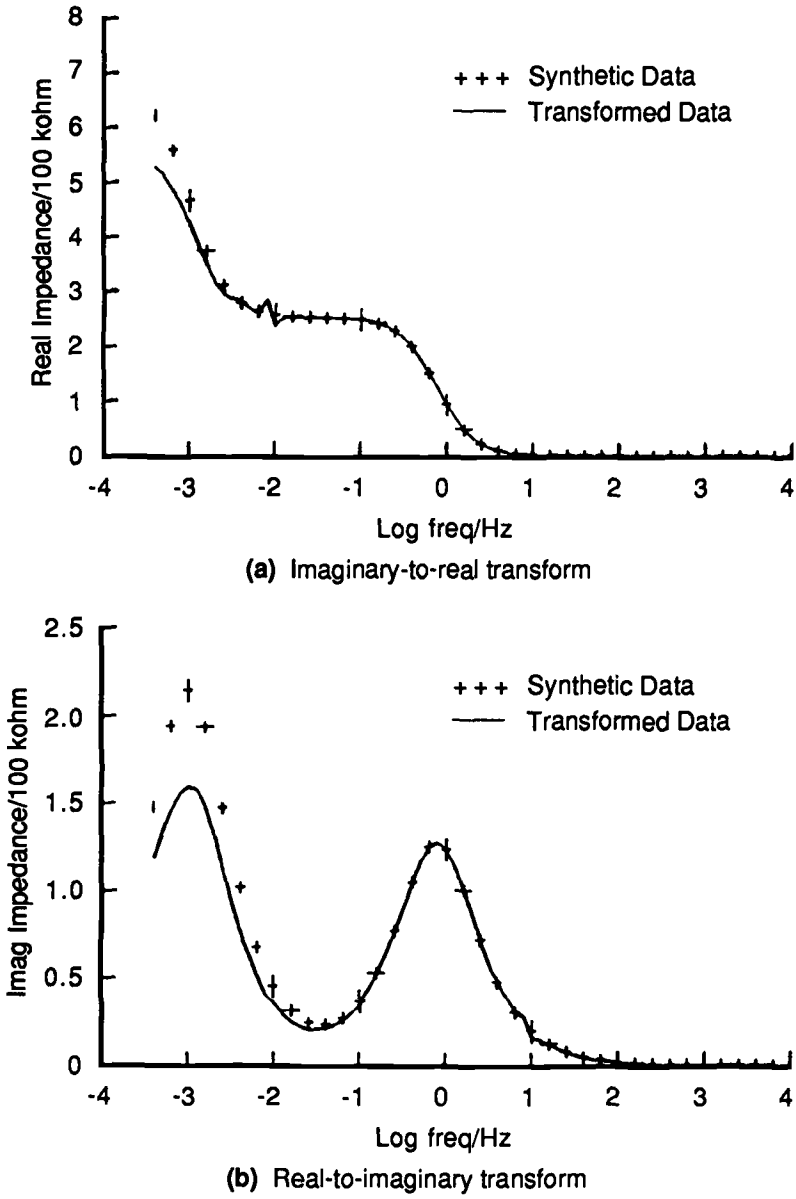

FIG. 2—*Kramers-Kronig Transforms of synthetic impedance data, calculated over a truncated frequency range (Case B). Synthetic data calculated for circuit described in caption to Fig. 1.*

TABLE 1—*Average errors of transformation for synthetic impedance data.*

	Average Error		Polarization Resistance	
	Imag→Real	Real→Imag	$k\Omega$ cm^2	% Deviation
Case A	0.103	0.375	681	−0.2
Case B	1.2	5.2	466	−31.8
Theoretical	...	...	682	...

potentials. The behavior of these two spectra in the KKT process gives an indication as to whether or not the four criteria were maintained throughout the course of the experiment. The spectra chosen from the series at elevated polarization potentials were usually in the mid-to-high polarization potential range, since the system was further from equilibrium and tended to be noisier in these cases, so that the system was less likely to obey all the criteria. Finally, obviously noisy spectra were tested, since the data scatter itself indicates that spurious electrical signals or that system instabilities may be a problem. Therefore, an overall picture of the validity of a series of spectra could be obtained without individually testing each one.

Results and Discussion

Figure 3 depicts typical Nyquist plots of the impedance of aluminum in methanol/water solutions under a variety of experimental conditions. These spectra have been chosen to demonstrate the results of the KKT process for each of three types of spectra selected for validation as described earlier. Figures 3*a* to *c* depict spectra recorded at an aluminum electrode immersed in anhydrous methanol, pure water, and a 50 wt% mixture of the two, respectively. The spectra shown were measured for an aluminum electrode maintained at its corrosion potential, recorded within 24 h of its immersion in the test solution. Figures 3*d* and *e* depict the impedance spectra of aluminum in a 50 wt% methanol/water solution, at an overpotential within each of the anodic and cathodic regimes. These spectra form part of the same series as the one in Fig. 3*c*. Time constraints here meant that the measurement could not be extended to frequencies below 1.3 mHz. Inspection of these figures reveals that a second RC-type relaxation is almost certainly present at very low frequency, and is not adequately characterized within the experimental frequency range. These two spectra are analogous to Case B for the synthetic impedance data described earlier. Finally, Fig. 3*f* depicts a spectra in which there is much data scatter at low frequencies. This spectrum was recorded at an aluminum electrode which had been immersed in anhydrous methanol for a week and marked the final spectrum recorded in one of the experimental series.

The results of the transformation of the impedance spectra in Figs. 3*a*, *b*, and *c* are displayed in Figs. 4 to 6, respectively. In these figures, Plot A compares the result of the imaginary-to-real transform to the real component of the experimental impedance; Plot B compares the result of the real-to-imaginary transform to the imaginary component of the experimental impedance. In all cases, a good fit between the experimental and calculated data was achieved. For each case, the value of AE (Eq 12) is listed in Table 2. In the case of the imaginary-to-real transform, AE values less than 1.5 were obtained. AE for the real-to-imaginary transform was less than 2.5. In all cases, AE was larger for the real-to-imaginary transform than for the imaginary-to-real one. Table 2 also lists the value of R_p calculated from various sources: that measured directly from the appropriate spectrum in Fig. 3; the zero-frequency extrapolation of imaginary-to-real transform (Eq 11); and that

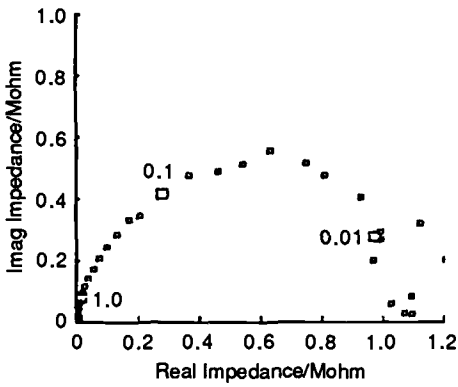

(a) Anhydrous methanol. E_{corr} = -0.21 V; immersion time = 6 hours; spectrum measured at E_{corr}.

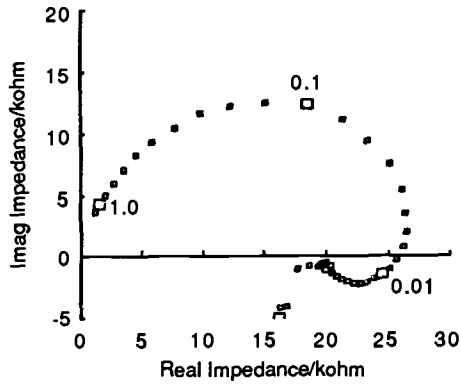

(b) Pure water. E_{corr} = -0.51 V; immersion time = 24 hours; spectrum measured at E_{corr}.

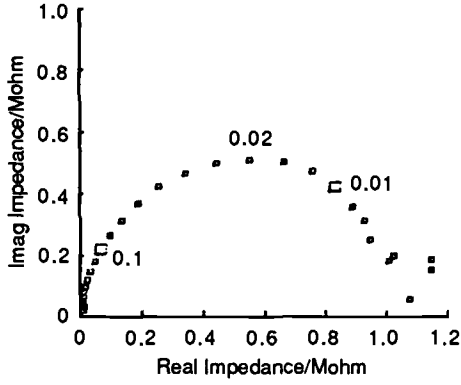

(c) 50 wt% methanol/water. E_{corr} = -0.64 V; immersion time = 3 hours; spectrum measured at E_{corr}.

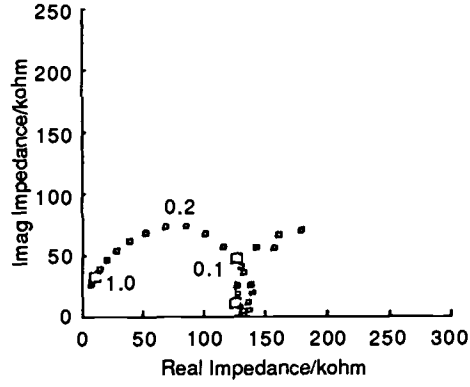

(d) 50 wt% methanol/water. E_{corr} = -0.91 V; immersion time = 53 hours; spectrum measured at E = -0.71 V.

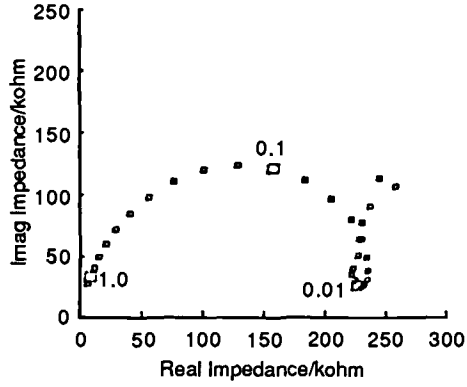

(e) 50 wt% methanol/water. E_{corr} = -0.91 V; immersion time = 91 hours; spectrum measured at E = -1.11 V.

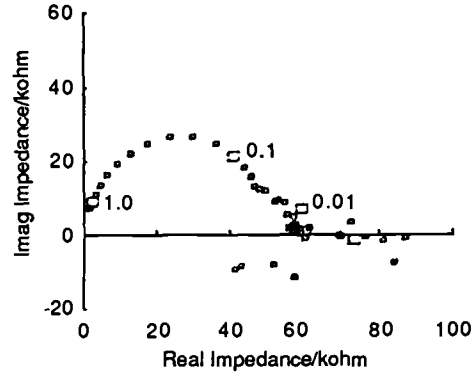

(f) Anhydrous methanol. E_{corr} = -0.25 V; immersion time = 173 hours; spectrum measured at E_{corr}.

FIG. 3—*Nyquist plots of the impedance of aluminum in methanol/water solutions. Electrode rotation speed = 500 rpm;* ΔE_{ac} *= 20 mV rms; T = 298 K; 0.1 mol* dm^{-3} NH_4ClO_4 *used as supporting electrolyte in all cases. All potentials are relative to SCE. Frequency in Hz is denoted on the spectra.*

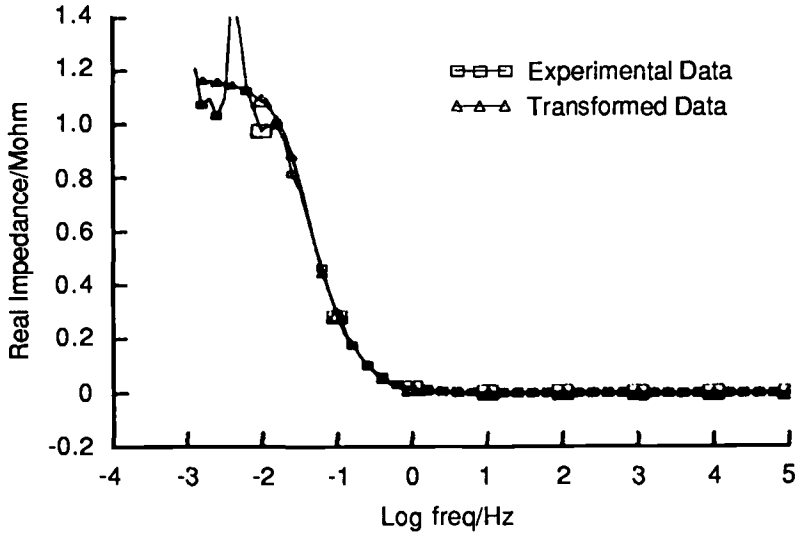

(a) Imaginary-to-real transform

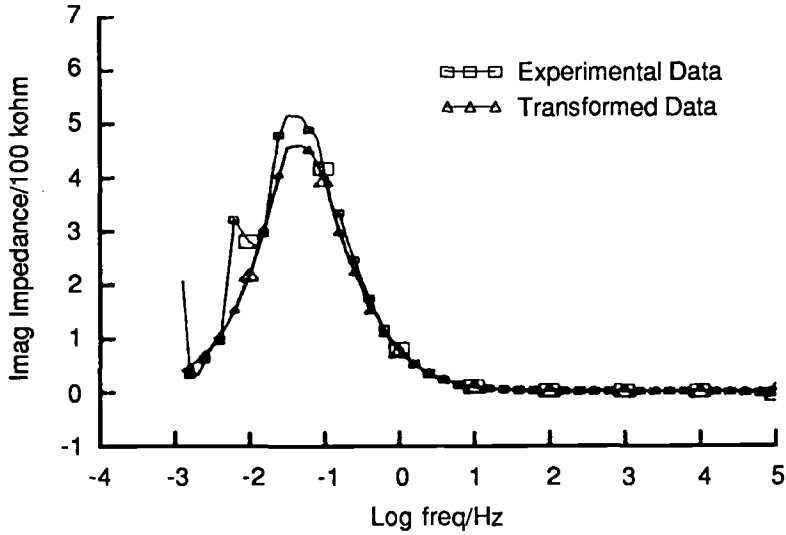

(b) Real-to-imaginary transform

FIG. 4—*Kramers-Kronig Transforms of impedance data in Fig. 3*a.

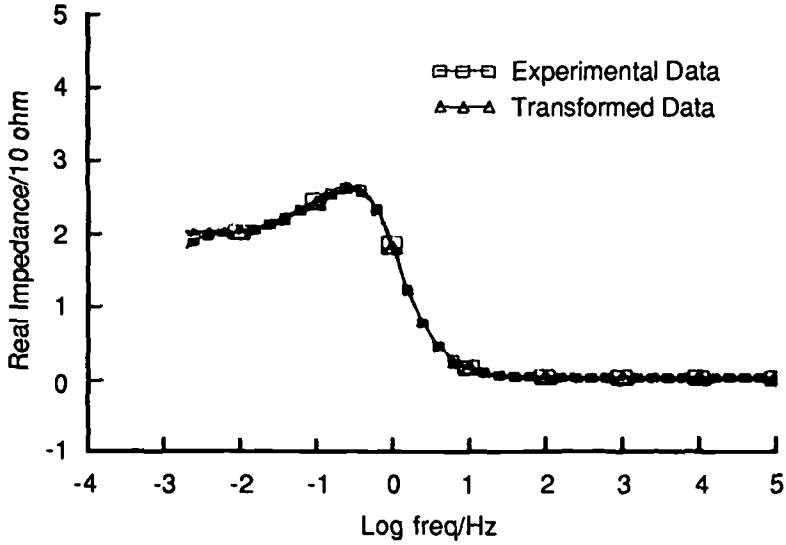

(a) Imaginary-to-real transform

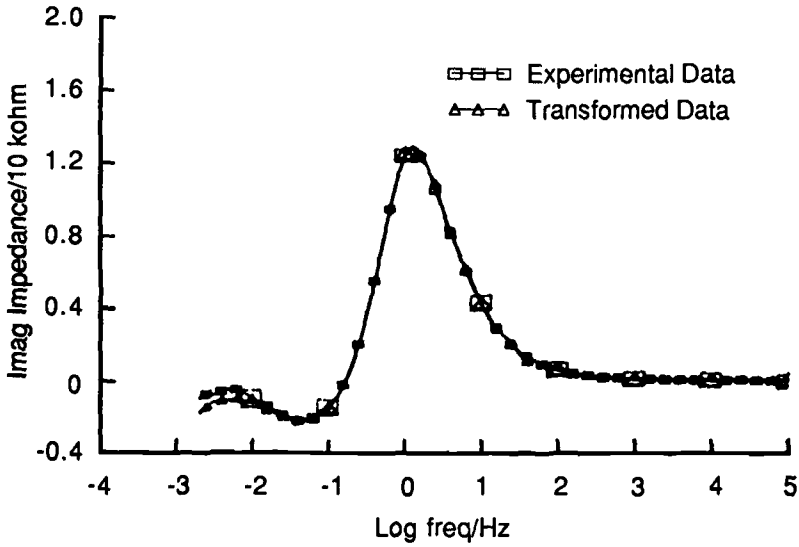

(b) Real-to-imaginary transform

FIG. 5—*Kramers-Kronig Transforms of impedance data in Fig. 3*b.

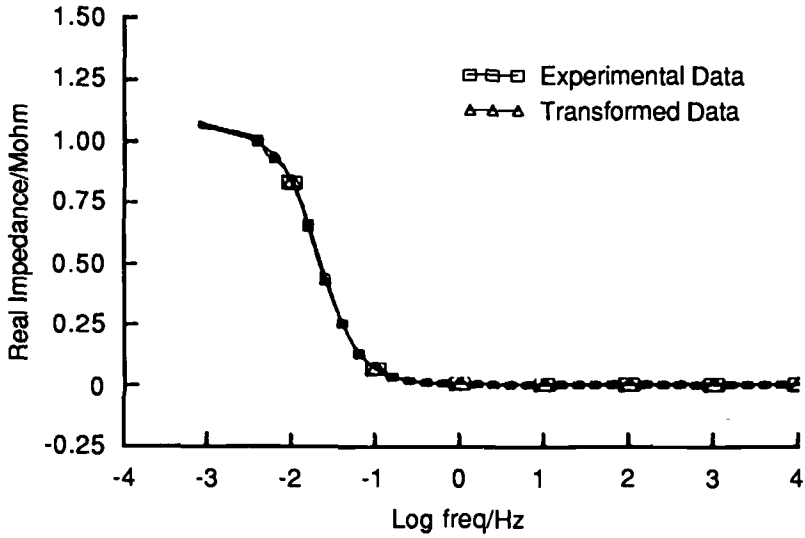

(a) Imaginary-to-real transform

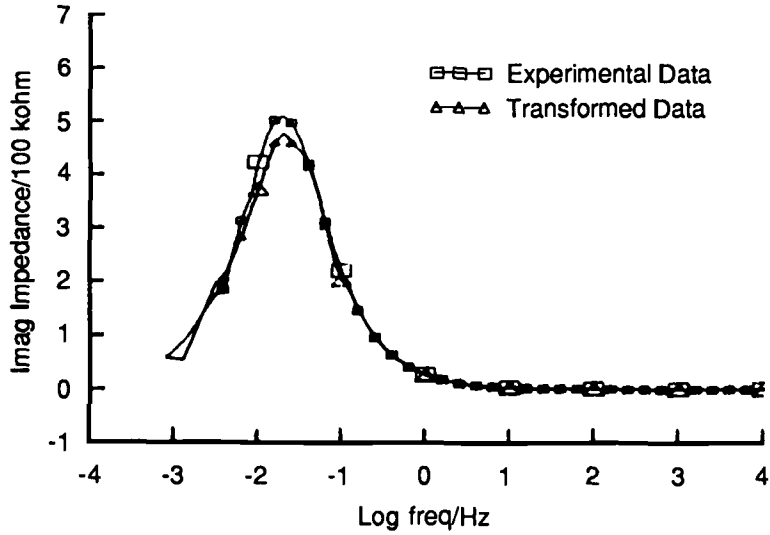

(b) Real-to-imaginary transform

FIG. 6—*Kramers-Kronig Transforms of impedance data in Fig. 3c.*

TABLE 2—*Average errors of transformation and calculated values of* R_p *for experimental impedance data.*

	Average Error		Polarization Resistance/$k\Omega$ cm^{2}[a]			
Figure	I→R	R→I	Fig. 3	Eq 9	Eq 10	dev(%)
3*a*	1.42	2.51	1120	1170	1160	+3.6
3*b*	0.80	1.00	20.0	20.2	19.7	−1.5
3*c*	0.54	1.24	1050	1060	1080	−2.8
3*d*	1.55	4.66	(264)	...	179	−32
3*e*	0.29	7.00	(600)	...	320	−50
3*f*	2.95	9.48	(51.9)	58.2	56.5	+8.9

[a]Entries in brackets are extrapolations of the low frequency loop.

calculated using Eq 12. The deviation in the value of R_p calculated using Eq 11 from that measured from Fig. 3, as a percentage of the latter value, is listed in the seventh column of Table 2. This deviation is relatively small, of the order 2 to 4% for each of Figs. 3*a*, *b*, and *c*.

The transformed data for Figs. 3*d* and *e* are shown in Figs. 7 and 8. The imaginary-to-real transform (Figs. 7*a* and 8*a*) displays a small deviation to lower values of the impedance in the transformed data at low frequencies. *AE* in these cases (Table 2) is small, and comparable to that obtained earlier for well-behaved data. However, the real-to-imaginary transforms show a significant deviation to low values of the imaginary impedance for the low-frequency maximum; this is manifest by a large value of *AE* for this transform. This deviation and the value of the error function are consistent with that for synthetic impedance data which has not been taken over a wide enough frequency range. R_p calculated via the transforms are significantly lower than those measured experimentally; however, the experimental values themselves had to be measured by extrapolating the lowest frequency semicircle over a large distance, so that these are approximations only.

The transforms for the spectrum in Fig. 3*f* are displayed in Fig. 9. Here, the imaginary-to-real transform behaves quite well, except at low frequency where it fails to follow the rapid increase in the magnitude of the experimental impedance. *AE* (Table 2) in this case is twice that of the other systems. The real-to-imaginary transform, Fig. 9*b*, shows significant deviations from the experimental data, in fact predicting a second RC-type relaxation not present in the experimental data and characterized by a large value of the error function. The predicted value for R_p in this case is similar to that measured experimentally; however, the noisy nature of the spectrum in Fig. 3*f* means that the value of R_p is difficult to ascertain experimentally.

Spectra which transformed as for the examples in Figs. 3*a* to *c*, exhibiting average errors less than 3 for both the real-to-imaginary and imaginary-to-real transforms, were considered to pass the KKT test. If the behavior was as for Figs. 3*d* and *e*, the result was also considered passing, since despite the large error in the real-to-imaginary transform, the average error of the imaginary-to-real transform was less than 2, and the results appeared to indicate that failure of the transformation process was due solely to the lack of data at low frequency rather than an inherent instability in the data itself. These results do not extend to a sufficiently low frequency to be used to evaluate R_p, and hence cannot be used to calculate meaningful corrosion rate data, but nevertheless do provide valuable mechanistic information. Spectra for which the average error of transformation was larger than 3 for both transforms, such as that shown by the case in Fig. 3*f*, were considered to fail the KKT test.

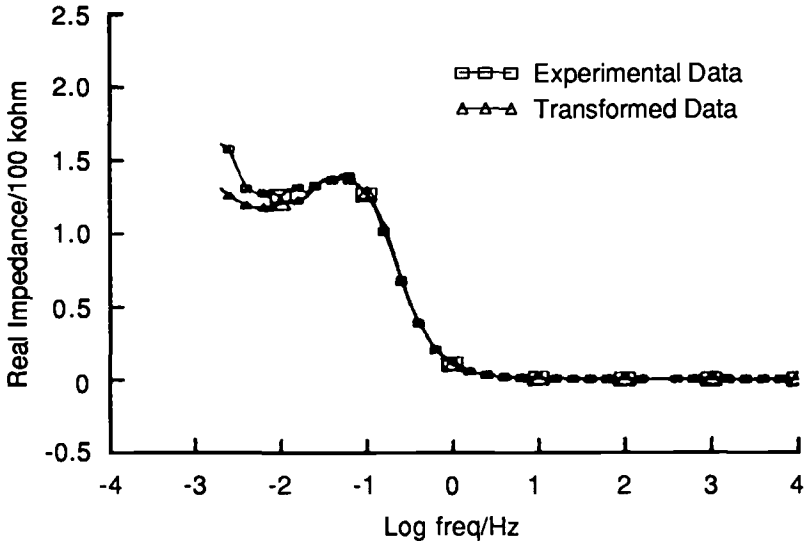

(a) Imaginary-to-real transform

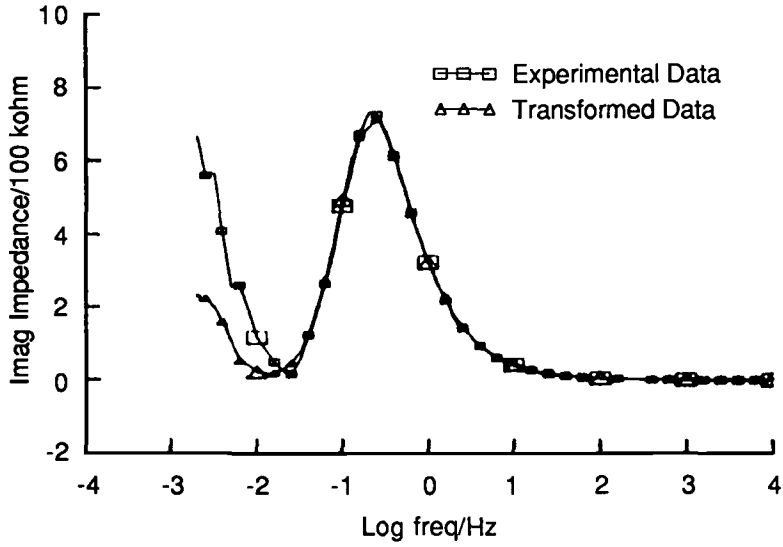

(b) Real-to-imaginary transform

FIG. 7—*Kramers-Kronig Transforms of impedance data in Fig. 3*d.

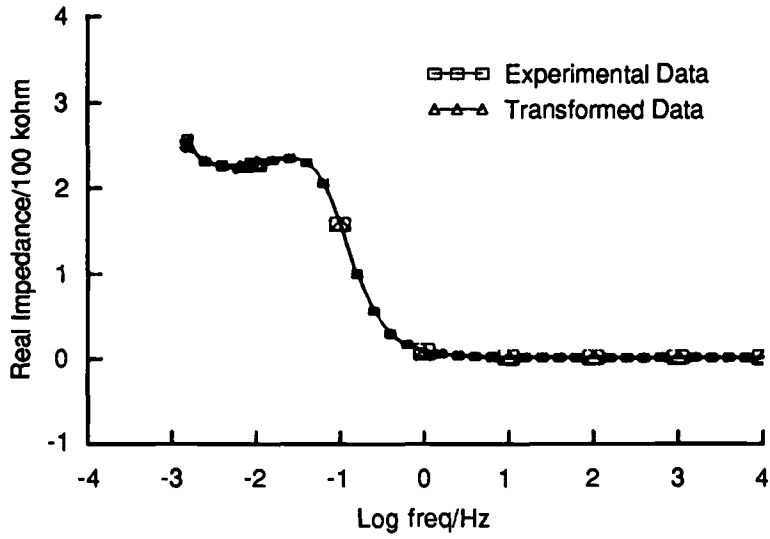

(a) Imaginary-to-real transform

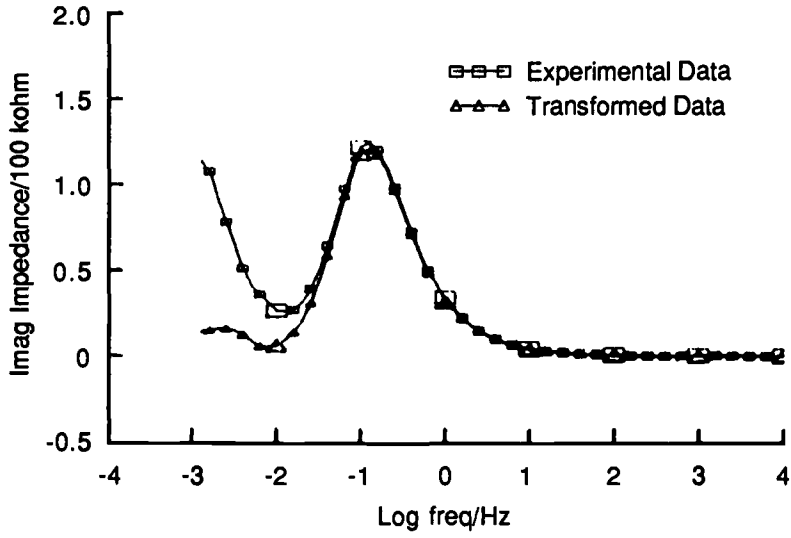

(b) Real-to-imaginary transform

FIG. 8—*Kramers-Kronig Transforms of impedance data in Fig. 3e.*

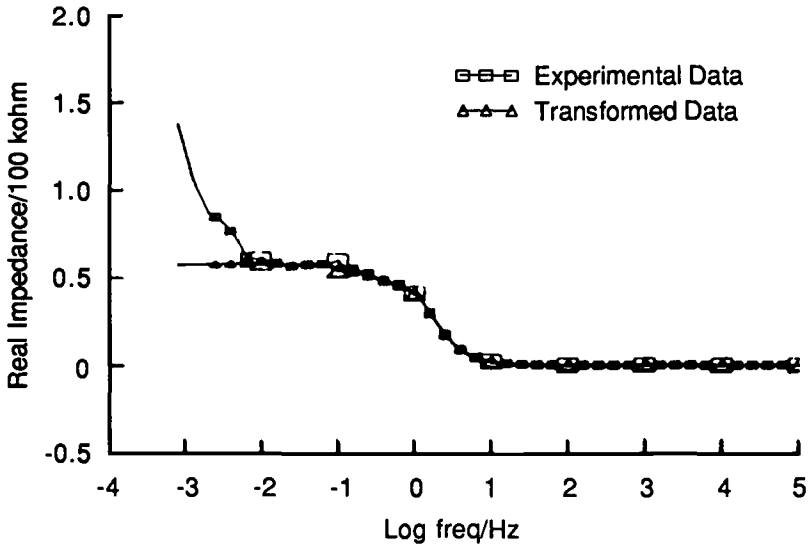

(a) Imaginary-to-real transform

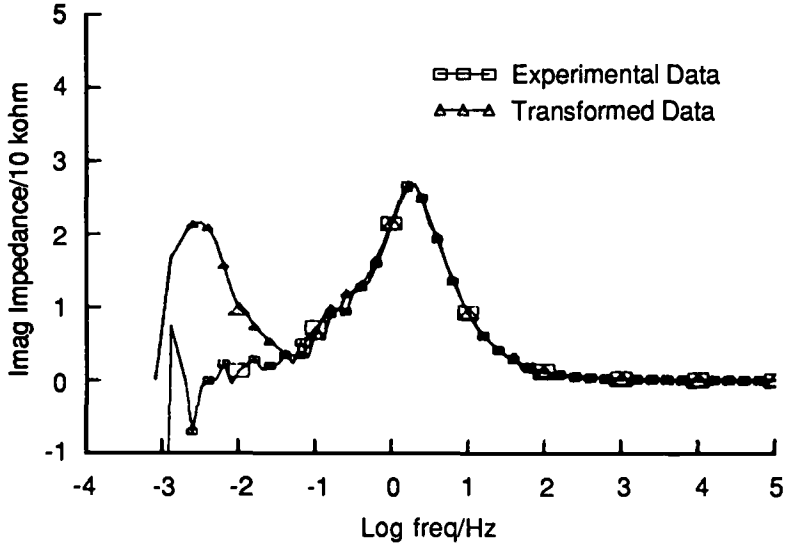

(b) Real-to-imaginary transform

FIG. 9—*Kramers-Kronig Transforms of impedance data in Fig. 3f.*

The results of the application of the KKT procedure highlight various aspects of the experimental data which can serve as indicators of possible violations of the four criteria which must be met for an impedance experiment to be valid.

The spectra in Figs. 3*a* to *c* were well-behaved at low frequency, lacked spurious noise effects, and exhibited good stability with respect to time, thereby permitting the measurement to be extended to quite low frequencies. Transformation of these three cases gave transformed data which accurately reproduced the experimental data, and gave low values of *AE* for both the real-to-imaginary and imaginary-to-real transforms. The spectra in Figs. 3*d* and *e* show little sign of spurious noise effects and the system itself was fairly stable; however, only the leading arc of the low frequency capacitive loop could be characterized at the minimum frequency used in this study. In this case, the imaginary-to-real transform was well-behaved, but significant error was generated during the real-to-imaginary transform. Finally, neither transform gave good results in the case of an obviously noisy spectrum.

Conclusions

Experimental impedance data measured in the high impedance aluminum/methanol/water system has been subjected to a validation procedure using KKT. It is apparent that:

- The KKT are sensitive to cases where the impedance data contain more than one relaxation, including inductive-type loops;
- Instances where the experimental data set contains insufficient data at low frequency to fully characterize the spectrum can be detected;
- The real-to-imaginary transform is particularly sensitive to errors in the experimental data;
- In general, spectra which were well-behaved at low frequency, lacked spurious noise effects, and exhibited good stability with respect to time transform accurately, and gave a small error in both the imaginary-to-real and real-to-imaginary transform;
- Lack of data at low frequency resulted in a large error in the real-to-imaginary transform, but the imaginary-to-real transform was accurate;
- Obviously noisy spectra transform to give large errors in both transforms;
- Deviations such as data scatter and lack of low-frequency data often indicate that at least one of the four criteria is not obeyed.

Acknowledgments

The authors are grateful to the New Zealand Ministry of Energy and New Zealand University Grants Committee for their financial support of this study. This work was performed at Victoria University, Wellington, New Zealand.

References

[*1*] Urquidi-Macdonald, M., Real, S., and Macdonald, D. D., *Journal of the Electrochemical Society*, Vol. 133, 1986, p. 2018.
[*2*] Dougherty, B. J., "The Dissolution Mechanism of Aluminum in Methanol and in Methanol/Water Solutions," Ph.D. thesis, Victoria University of Wellington, Wellington, New Zealand, 1990.
[*3*] Landau, L. D. and Lifschitz, E. M., *Electrodynamics of Continuous Media*, Pergamon Press, New York, 1986, pp. 256, 279.
[*4*] Jaksic, M. M. and Newman, J., *Journal of the Electrochemical Society*, Vol. 133, 1986, p. 1097.
[*5*] Macdonald, D. D. and Urquidi-Macdonald, M., *Journal of the Electrochemical Society*, Vol. 132, 1985, p. 2316.

Corrosion and Inhibition

S. Turgoose[1] *and R. A. Cottis*[1]

The Impedance Response of Film-Covered Metals

REFERENCE: Turgoose, S. and Cottis, R. A., "**The Impedance Response of Film-Covered Metals,**" *Electrochemical Impedance: Analysis and Interpretation, ASTM STP 1188*, J. R. Scully, D. C. Silverman, and M. W. Kendig, Eds., American Society for Testing and Materials, Philadelphia, 1993, pp. 173–191.

ABSTRACT: This paper derives the expected electrochemical impedance response of a corroding film-covered metal. The film is assumed to be nonelectroactive and uniform corrosion and transport by diffusion are considered. A generalized equivalent circuit for such a corroding system is presented. All terms in this equivalent circuit are defined by physical, chemical, or electrochemical constants of the system, which applies constraints to the possible values of equivalent circuit elements. It is shown that use of expressions derived for redox systems at their equilibrium potential can introduce significant errors in the analysis of data from corroding metals. The correlation between corrosion rate and polarization or charge transfer resistance is also discussed.

KEYWORDS: electrochemical impedance response, corrosion, surface films

The corrosion of metals in near-neutral solutions often occurs in the presence of surface films but the effect of these films on both the dc and ac electrochemical responses has not been widely discussed. The reduction in corrosion rate due to the reduced diffusion rate of oxygen through surface films is well known [*1*] and is the basis of the action of cathodic inhibitors but the effect of restricted diffusion of metal ions away from the surface has not been given much, if any, attention.

Electrochemical impedance spectroscopy (EIS) has been widely used for the study of corroding metals, and data analysis is often accomplished by means of equivalent circuit models. The commonest referred to is the Randles circuit [*2*], Fig. 1, which models the Faradaic part of the impedance by a charge transfer resistance in series with a diffusional impedance, with this branch in parallel with the double layer capacitance. This is a well documented rigorous approach to the impedance response of a redox system with two solution species, as given by Eq 1

$$O + ne^- = R \tag{1}$$

For this reaction, assuming semi-infinite linear diffusion, the diffusional component of the impedance (a Warburg impedance) is given by Eq 2, with the Warburg coefficient defined by Eq 3

$$Z_{\text{real}} = \sigma\omega^{-1/2}; Z_{\text{imag}} = \sigma\omega^{-1/2} \tag{2}$$

[1]Corrosion and Protection Centre, UMIST, Manchester M60 1QD, United Kingdom.

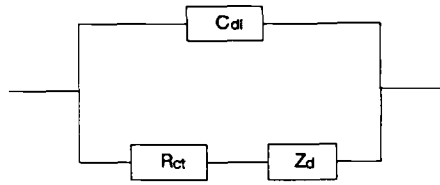

FIG. 1—*Randles equivalent circuit for an electrochemical process.*

$$\sigma = \frac{RT}{n^2F^2\sqrt{2}}\left(\frac{1}{D_O^{1/2}C_O} + \frac{1}{D_R^{1/2}C_R}\right) \tag{3}$$

The derivation of the expression for the Warburg coefficient, Eq 3, involves the assumption that the kinetics of the redox process are sufficiently fast that the steady state surface concentrations of *O* and *R* are related by the Nernst equation. For corroding metals, where both anodic and cathodic reactions are often far from equilibrium, this is not generally true. Also, it is not immediately apparent that the circuit in Fig. 1 is applicable to a corroding metal interface. For such an interface, there are at least two essentially independent reactions occurring at the corroding metal surface, only linked by the fact that under free corrosion conditions, i.e., in the absence of any external current source, there must be no net current through the interface. Some workers have proposed modified equivalent circuits, generally to explain the impedance response of film covered surfaces, which do consider the two-electrode processes occurring, these processes appearing in parallel as regards an applied signal. Bonnel et al. [*3*] used the circuit in Fig. 2*a*, which considers the anodic branch to be represented by a charge transfer resistance with a series charge transfer resistance-diffusional impedance for the cathodic branch. Juttner et al. [*4*] used the circuit of Fig. 2*b*, which again represents the anodic branch as a charge transfer resistance but now considers the cathodic branch as a series combination of several diffusional impedances, associated with linear diffusion in bulk solution, hemispherical diffusion at the approach to the mouths of pores in the surface film, and in the pores. In this latter case no series charge transfer resistance was included in the cathodic branch. Both of these equivalent circuit models make the assumption that the anodic branch can be represented simply by a resistor.

While both of these equivalent circuits can be used to explain the impedance responses observed, they both allow arbitrary attribution of numerical values to equivalent circuit elements, whereas in reality the anodic and cathodic charge transfer resistances must be related at the corrosion potential. This imposes constraints on the possible relative values of various circuit components which are not always apparent with an equivalent circuit approach. Also, the assumption that the anodic branch of the corrosion process, at the corrosion potential, can be modeled simply by a resistance with no diffusional elements has not been justified and does not appear self-evident in the case of film-covered electrodes. The assumption that there is no diffusional impedance in this branch is essentially the same as assuming that the reverse (metal ion to metal reduction) reaction is insignificant, i.e., that the anodic process is far from equilibrium. If we consider iron corroding in neutral solution, with mass transfer controlled oxygen reduction as the only cathodic reaction, then with a bulk oxygen concentration of 0.00025 M (8 ppm) the surface ferrous ion concentration will be 0.0005 M, assuming no subsequent reactions of ferrous ions and equal diffusion coefficients for oxygen and ferrous ion. The equilibrium potential for the iron–ferrous ion system at this concentration is about −750 mV (sce). This is not very

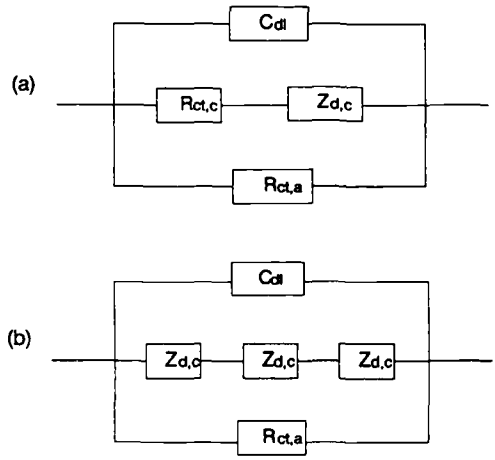

FIG. 2—*Equivalent circuits for film covered electrodes from* (a) *Ref* 2 *and* (b) *Ref* 3.

much lower than commonly observed corrosion potentials, especially in the presence of cathodic inhibitor films. Further, if diffusion of ferrous ion is more restricted than that of oxygen, or if there is a second, activation-controlled, cathodic reaction, such as hydrogen evolution from water, then the surface ferrous ion concentration will be higher than above, as will the equilibrium potential. Thus, it can not necessarily be assumed that the anodic reaction is irreversible in such systems.

This paper considers the expected impedance response of a corroding metal surface without making the assumption of irreversibility of the anodic reaction. It should be stressed that it is not assumed here that the reverse reaction is significant, but simply that it should not necessarily be ignored. Equivalent circuits are developed which reflect the electrochemical responses and in which the numerical values of the elements can be related to physical (diffusion coefficients and diffusion layer thickness), chemical (bulk concentrations), or electrochemical (exchange current densities and Tafel slopes) parameters of the system. At the same time the dc response is also considered, and therefore the correlation between polarization resistance and corrosion rate.

The systems considered here are a metal with uniform corrosion and diffusion processes with transport of species to and from the electrode surface solely by diffusion. The effects of migration or the effects of modifications to steady state concentration profiles due to homogeneous chemical reactions, are not discussed. The transport is assumed to be dominated by one diffusion barrier (i.e., solution or film), and the parameters used in most of the calculations assume film-controlled transport. The film is assumed not to be electroactive. Also, simple reaction mechanisms for the electrode processes are assumed. Even with these simplifications the impedance spectra calculated can be complex and these simplifying assumptions are not considered to fundamentally affect the relevance of the approach to the interpretation of experimental data.

Components of the Corroding System

The system considered is a corroding metal, with allowance for the possibility of the metal ion to metal reduction reaction. The cathodic reactions considered are both oxygen reduction and reduction of water. These three processes occur in parallel on the metal

surface, and so the overall impedance can be obtained from a parallel combination of their individual impedances, with the addition of a double layer capacitance. Initially these three processes will be treated individually and both their dc and ac responses will be considered.

Anodic Branch

dc Behavior—Considering a metal dissolution reaction

$$M \rightleftharpoons M^{n+} + ne \tag{4}$$

If, for a simple process, the dissolution current at an electrode potential, E, is given by

$$i_f = i_{0,a}\exp\left(\frac{E - E_a^0}{\beta_f}\right) \tag{5}$$

and the reverse, deposition, current is given by

$$i_b = i_{0,a}C_s\exp\left(\frac{-(E - E_a^0)}{\beta_b}\right) \tag{6}$$

where C_s is the surface concentration of metal ions, β_f and β_b are the Tafel coefficients for the forward and reverse reactions, given by Eq 7

$$\beta_f = \frac{RT}{(1 - \alpha)\text{nF}}\,;\ \beta_b = \frac{RT}{\alpha\text{nF}} \tag{7}$$

and $i_{0,a}$ and E_a^0 are the exchange current density and equilibrium electrode potential for C_s = 1 mol/cm^3 (this choice of concentration unit is taken to give consistency with that later used in the diffusion expressions).

The net dissolution current, defined by

$$i_{\text{net}} = i_f - i_b \tag{8}$$

also defines the net flux (i_{net}/nF) of metal ions across the metal-solution interface. Considering the transport of metal ions away from the metal surface to be by diffusion, then, under steady state conditions, this flux across the interface must equal the diffusional flux across the diffusion boundary layer. Hence

$$i_{\text{net}} = \frac{\text{nF}D(C_s - C_b)}{\delta} \tag{9}$$

where D is the diffusion coefficient for metal ions, cm^2/s, δ is the diffusion layer thickness, cm, and C_b is the bulk concentration, mol/cm^3, of metal ions.

Letting $\eta = E - E_a^0$ then Eqs 5, 6, 8, and 9 give Eq 10. Thus, substituting C_s from Eq 10 into Eq 9 enables the net anodic current to be calculated as a function of potential, given i_0,

the Tafel coefficients, the ratio D/δ and

$$C_s = \frac{C_b + \frac{i_{0,a}\delta}{nFD} \exp\left(\frac{\eta}{\beta_f}\right)}{1 + \frac{i_{0,a}\delta}{nFD} \exp\left(\frac{-\eta}{\beta_b}\right)} \tag{10}$$

the bulk concentration of metal ions.

ac Behavior—To consider the response of the system to a small amplitude applied current or voltage the time dependence of the current needs to be considered.

The response of a redox system with two solution species can be found in many standard texts and the derivation below for the corroding metal follows the approach given for a redox system in Ref *5*. The potential is a function of the current and surface concentration of metal ions

$$E = f(i,C_s) \tag{11}$$

from which the response of the electrode to a time dependent perturbation is given by

$$\frac{dE}{dt} = \left(\frac{\partial E}{\partial i}\right)_{c_a} \frac{di}{dt} + \left(\frac{\partial E}{\partial C_s}\right)_i \frac{dC_s}{dt} \tag{12}$$

For a sinusoidal current of angular frequency ω (rad/s), applied in addition to the dc current, the dependence of current on time is given by Eq 13

$$i(t) = i_{dc} + i^0 \sin \omega t \tag{13}$$

where i^0 (A/cm^2) is the peak current density and i_{dc} is the value of i_{net} under the dc conditions defined by Eq 8. Writing the current at a given potential as

$$i = i_{0,a} \exp\left(\frac{\eta}{\beta_f}\right) - i_{0,a}C_s \exp\left(-\frac{\eta}{\beta_b}\right) \tag{14}$$

and differentiating with respect to η at constant C_s we get Eqs 15 and 16, which define the charge transfer resistance, R_{ct} (Ω-cm^2).

$$\left(\frac{\partial i}{\partial \eta}\right)_{C_s} = \frac{i_{0,a}}{\beta_f} \exp\left(\frac{\eta}{\beta_f}\right) + \frac{i_{0,a}C_s}{\beta_b} \exp\left(-\frac{\eta}{\beta_b}\right) \tag{15}$$

Hence,

$$\left(\frac{\partial E}{\partial i}\right)_{C_s} = \left(\frac{\partial \eta}{\partial i}\right)_{C_s} = R_{ct} = \frac{\beta_f \beta_b}{\beta_f i_b + \beta_b i_f} \tag{16}$$

Similarly, differentiating Eq 14 with respect to η at constant i gives

$$0 = \frac{i_{0,a}}{\beta_f}\exp\left(\frac{\eta}{\beta_f}\right) + \frac{i_{0,a}}{\beta_b}C_s\exp\left(-\frac{\eta}{\beta_b}\right) - i_{0,a}\exp\left(-\frac{\eta}{\beta_b}\right)\left(\frac{\partial C_s}{\partial \eta}\right)$$
$$= \frac{i_f}{\beta_f} + \frac{i_b}{\beta_b} - \frac{i_b}{C_s}\left(\frac{\partial C_s}{\partial \eta}\right) \tag{17}$$

and therefore

$$\left(\frac{\partial E}{\partial C_s}\right)_i = \left(\frac{\partial \eta}{\partial C_s}\right)_i = \left(\frac{\beta_f\beta_b}{\beta_f i_b + \beta_b i_f}\right)\frac{i_b}{C_s} \tag{18}$$

The other two terms in Eq 12 are the same as for a solution redox system and are derived in Refs *5* and *6*, as shown in the following equations. Differentiating Eq 13 with respect to time gives

$$\frac{di}{dt} = i^0\omega\cos\omega t \tag{19}$$

The final term in Eq 12 is obtained by solving

$$\frac{\partial C(x,t)}{\partial t} = D\left(\frac{\partial^2 C(x,t)}{\partial x^2}\right) \tag{20}$$

where $C(x,t)$ is the concentration of metal ions at distance x from the surface at time t. This can be solved by Laplace transformation [*5,6*] with initial and boundary conditions

$$C(0,0) = C_{s,dc}$$
$$\lim_{x\to\infty} C(x,t) = C_b \text{ (for all } t) \tag{21}$$
$$\left(\frac{\partial C(x,t)}{\partial x}\right)_{x=0} = \frac{i(t)}{nFD}$$

where $C_{s,dc}$ is the steady state value of the surface concentration of metal ions, defined by Eq 10.

Assuming semi-infinite linear diffusion, the solution is [*5,6*] Eq 22, which on differentiation gives Eq 23.

$$C_s = C(0,t) = C_{s,dc} + \frac{i^0}{nF(2D\omega)^{1/2}}(\sin\omega t - \cos\omega t) \tag{22}$$

$$\frac{dC_s}{dt} = \frac{i^0}{nF}\left(\frac{\omega}{2D}\right)^{1/2}(\sin\omega t + \cos\omega t) \tag{23}$$

Substituting 16, 18, 19 and 23 into Eq 12 gives

$$\frac{dE}{dt} = (R_{ct} + \sigma\omega^{-1/2})i^0\omega \cos \omega t + \sigma\omega^{1/2}i^0 \sin \omega t \tag{24}$$

where the Warburg coefficient, σ, is given by Eq 25

$$\sigma = \left(\frac{\beta_f\beta_b}{\beta_f i_b + \beta_b i_f}\right)\frac{i_b}{nF\sqrt{2D}C_s} \tag{25}$$

Equating this to the response of a series resistor(R)-capacitor(C) circuit to a sinusoidal current

$$\frac{dE}{dt} = Ri^0\omega \cos \omega t + \frac{i^0}{C} \sin \omega t \tag{26}$$

where

$$Z_{real} = R; Z_{imag} = \frac{1}{\omega C} \tag{27}$$

enables the impedance of the system to be expressed as a series combination of a charge transfer resistance, given by Eq 16, and a Warburg impedance such that

$$\begin{aligned} Z_{real} &= R_{ct} + Z_{d,real} = R_{ct} + \sigma\omega^{-1/2} \\ Z_{imag} &= Z_{d,imag} = \sigma\omega^{-1/2} \end{aligned} \tag{28}$$

The expression for σ is different from the expression given in Eq 3 for a redox system with two solution species perturbed about its equilibrium potential, although the expression in Eq 3 has been used for corroding systems [7].

However, for a system where the reduced species is a metal, the second term in brackets in Eq 3 is zero, and if we introduce the equilibrium condition, $i_f = i_b$, Eq 25 reduces to Eq 3, since

$$\frac{\beta_f\beta_b}{\beta_f + \beta_b} = \frac{RT}{nF} \tag{29}$$

For a corroding metal, not at the equilibrium metal-metal ion potential, the use of forms of Eq 3 can introduce significant errors in the determination of physical constants from impedance spectra.

If the diffusion layer is of finite thickness, δ, such that at distance δ from the surface the concentration of diffusing species is fixed, then, at low frequencies, the diffusional impedance deviates from the straight line in the Nyquist plot predicted by Eq 28 [8]. The real and

imaginary parts of the diffusional impedance are then given by Eq 30 [8].

$$Z_{D,real} = \sigma\omega^{-1/2}\left(\frac{\sinh(u) + \sin(u)}{\cosh(u) + \cos(u)}\right)$$
$$Z_{D,imag} = \sigma\omega^{-1/2}\left(\frac{\sinh(u) - \sin(u)}{\cosh(u) + \cos(u)}\right) \tag{30}$$

where

$$u = \delta\left(\frac{2\omega}{D}\right)^{1/2} \tag{31}$$

The low-frequency limit of the diffusional impedance (Eq 30 as u tend to 0) is such that $Z_{imag} = 0$ and the real impedance is given by Eq 32 or 33

$$Z_{D\omega\to 0} = \sigma\delta\left(\frac{2}{D}\right)^{1/2} \tag{32}$$

$$Z_{D\omega\to 0} = \left(\frac{\beta_f\beta_b i_b}{\beta_f i_b + \beta_b i_f}\right)\left(\frac{\delta}{nFDC_s}\right) \tag{33}$$

If we now consider the case where the bulk concentration of metal ions is very small, as commonly true for corroding metals, then Eqs 9 and 33 give Eq 34

$$Z_{D\omega\to 0} = \left(\frac{\beta_f\beta_b}{\beta_f i_b + \beta_b i_f}\right)\frac{i_b}{i_{net}} = R_{ct}\frac{i_b}{i_{net}} \tag{34}$$

Equating the low frequency limit of the impedance with the polarization resistance gives Eq 35. The values of R_p, calculated from Eq 35, are identical to

$$R_p = R_{ct} + Z_{D\omega\to 0} = R_{ct}\frac{i_f}{i_{net}} \tag{35}$$

those obtained by numerical methods from the slope of the dc curves calculated according to the Eqs 5 through 10.

Figure 3 shows the products $i_{net}\cdot R_{ct}$ and $i_{net}\cdot R_p$ against potential for $D/\delta = 0.00001$ cm/s, with other parameters as given in Table 1. It can be seen that it is R_p and not R_{ct} that should be used for determination of corrosion rate, but even $i_{net}\cdot R_p$ shows some variation with potential. This variation in $i_{net}\cdot R_p$ is due to the two limits of Eq 35. Rewriting Eq 35 as

$$i_{net}R_p = \frac{\beta_f\beta_b}{\beta_f i_b + \beta_b i_f} i_f \tag{36}$$

then

$$\text{as } i_b \to 0 \quad i_{net}R_p \to \beta_f \tag{37}$$

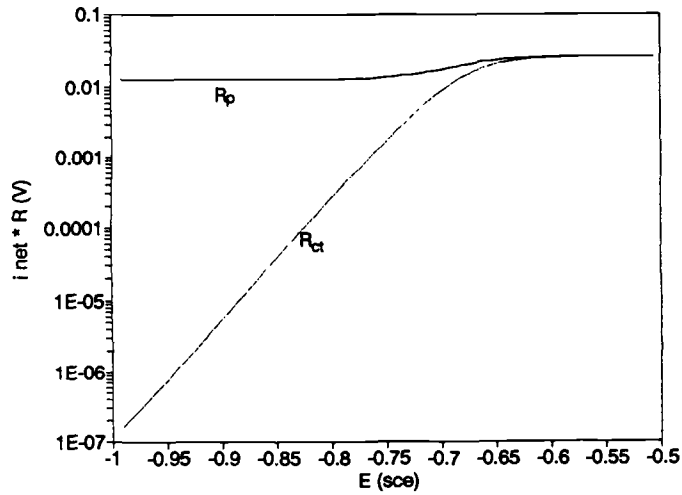

FIG. 3—*Variation of* $i_{net} \cdot R_p$ *and* $i_{net} \cdot R_{ct}$ *with potential for the anodic process with* D/δ = *0.00001 cm/s. Other parameters as Table 1.*

and

$$\text{as } i_b \rightarrow i_f \quad i_{net}R_p \rightarrow \frac{\beta_f\beta_b}{\beta_f + \beta_b} \tag{38}$$

Overall, the ac response of this anodic reaction is given by a series combination of a charge transfer resistance and a diffusional impedance. Both the charge transfer resistance and the polarization resistance are defined by E, i_0, the Tafel coefficients, and the ratio D/δ, and these also define the net dissolution current. However, to define the frequency response of the system we also need to define $\delta/\sqrt{D}$, and as a result of this the impedance spectra can vary significantly even if the low frequency resistance and hence net dissolution rate remain constant. As will be seen later, the effect of decreasing the ratio $\delta/\sqrt{D}$ is to shift the contribution of the diffusional impedance to higher frequency, to the extent that the charge transfer resistance may become hard to distinguish in the spectra.

TABLE 1—*Parameters used for calculations.*

E_a^0	−0.32
$i_{0,a}$	0.01 A/cm^2
β_f	RT/F
β_b	RT/F
E_{ox}^0	1.23
$i_{0,ox}$	4×10^{-10} A/cm^2
β_{ox}	2RT/F
E_h^0	0.00
$i_{0,h}$	5×10^{-11} A/cm^2
β_h	2RT/F
$C_{ox,bulk}$	2.5×10^{-7} mol/cm^3

The Cathodic Reduction of Oxygen—For the reaction

$$O_2 + 2H_2O + 4e \rightarrow 4OH^- \tag{39}$$

neglecting the reverse reaction, oxygen evolution, the current may again be given by the standard electrochemical kinetic equation [5]

$$i_{ox} = i_{0,ox} C_{s,ox} \exp\left(\frac{-(E - E^0_{ox})}{\beta_{ox}}\right) \tag{40}$$

and in the same manner as before Eqs 41 and 42 result

$$R_{ct,ox} = \frac{\beta_{ox}}{i_{ox}} \tag{41}$$

$$\sigma_{ox} = \frac{\beta_{ox}}{4F\sqrt{2D_{ox}}C_{s,ox}} \tag{42}$$

Equation 42 could also be obtained from Eq 25 with $i_f = 0$. The low frequency limit of the diffusional impedance is again given by Eq 32, which here gives Eq 43

$$Z_{D,\omega\rightarrow 0} = \beta_{ox} \frac{\delta}{4FDC_{s,ox}} \tag{43}$$

The limiting diffusion current, i_{lim} is given by Eq 44

$$i_{lim} = \frac{4FDC_{bulk}}{\delta} \tag{44}$$

and the dependence of surface concentration on current by Eq 45

$$C_{bulk} - C_{s,ox} = \frac{i_{ox}\delta}{4FD} \tag{45}$$

Combination of 40, 44, and 45 give an alternative expression for the dc current

$$i_{ox} = i_{0,ox}\left(1 - \frac{i}{i_{lim}}\right) C_{bulk} \exp\left(\frac{-(E - E^0_{ox})}{\beta_{ox}}\right) \tag{46}$$

From 43 to 45 it follows that

$$Z_{D,\omega\rightarrow 0} = \frac{\beta_{ox}}{i_{lim} - i_{ox}} \tag{47}$$

and that

$$R_{p,ox} = \frac{B_{ox}}{i_{ox}} \frac{i_{lim}}{(i_{lim} - i_{ox})} \tag{48}$$

The value of R_p for this reaction tends to infinity as the current approaches the limiting current. In this case it is the charge transfer resistance that gives information about the dc current and not the polarization resistance.

Hydrogen Evolution from Water

Again, assuming a simple reaction mechanism, the rate of this reaction is given by Eq 49

$$i_H = i_{0,H} a_{H_2O} \exp\left(-\frac{(E - E_H^0)}{\beta_H}\right) \tag{49}$$

and if it is assumed that the presence of surface films does not affect the activity of water at the surface and a $H_2O \simeq 1$, i.e., dilute solutions, this reaction has a charge transfer resistance given by Eq 50 and no diffusional impedance

$$R_{ct,H} = \frac{\beta_H}{i_H} \tag{50}$$

Calculated Responses of Corroding Metal Surfaces

The equivalent circuit for a corroding interface, considering the three aforementioned reactions is given by Fig. 4, although the contributions of the various components will vary depending on the detailed corrosion mechanism.

Consideration of a metal at its corrosion potential introduces an additional constraint not yet considered, that there must be no net current through the interface. In the case here this can be expressed as

$$i_f - i_b = i_{ox} + i_H = i_{corr} \tag{51}$$

It is interesting to note that for the equivalent circuits of Fig. 2, where both i_b and i_H are assumed to be zero, Eq 51 reduces to $i_f = i_{ox} = i_{corr}$. In this case it follows that

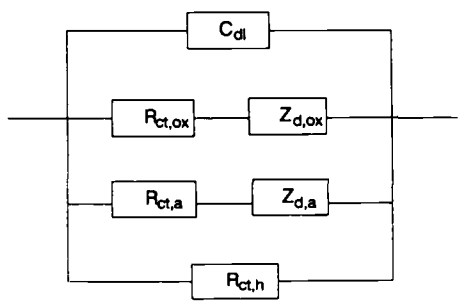

FIG. 4—*Equivalent circuit for the corroding interface considered here.*

$$\frac{R_{ct,a}}{R_{ct,ox}} = \frac{\beta_f}{i_f}\frac{i_{ox}}{\beta_{ox}} = \frac{\beta_f}{\beta_{ox}} \tag{52}$$

and so the two resistances are related and since typically β_{ox} will be of the same order as β_f the cathodic charge transfer resistance cannot be greatly different from the anodic. It is necessary in the use of this simplified equivalent circuit to introduce this constraint. The circuits of Fig. 2 shows a diffusional impedance only if the oxygen reduction reaction is under mixed control and the resistance associated with the low frequency time constant cannot be significantly greater than the high frequency resistance.

In the equivalent circuit here, if either i_b or i_H are significant, this simple condition is removed.

To illustrate the types of dc and ac response obtained from the system considered here numerical values are needed for exchange current densities and Tafel slopes. The values taken here are given in Table 1. With these values the oxygen reduction current is under mass transport control in the vicinity of the calculated corrosion potentials.

Initially it will be assumed for the purposes of these calculations that the diffusion coefficients for oxygen and metal ions are equal, which is generally approximately true in dilute solution but may not be for diffusion through surface films. Also the following calculations assume a uniform corrosion process.

The dc behavior is shown by the calculated (from Eqs 5, 6, 10, 46, and 49) polarization curves in Fig. 5 for different values of D/δ. These curves are similar to those obtained for corroding iron under static conditions, and correspond to no surface film (D/δ = 0.001 cm/s) and approximately 90% (0.0001 cm/s) and 99% (0.00001 cm/s) inhibition of the oxygen reduction reaction. The partial currents for D/δ = 0.00001 cm/s are shown in Fig. 6. The polarization resistances for different values of δ/D, with corrosion potentials, corrosion rates and Stern-Geary constants ($= i_{corr} \cdot R_p$) are given in Table 2.

It should be noted that there are two reasons for the variation of these Stern-Geary constants. The first, already mentioned, is the varying influence of the reverse reaction under the different conditions, and the second, which occurs even without this reversible

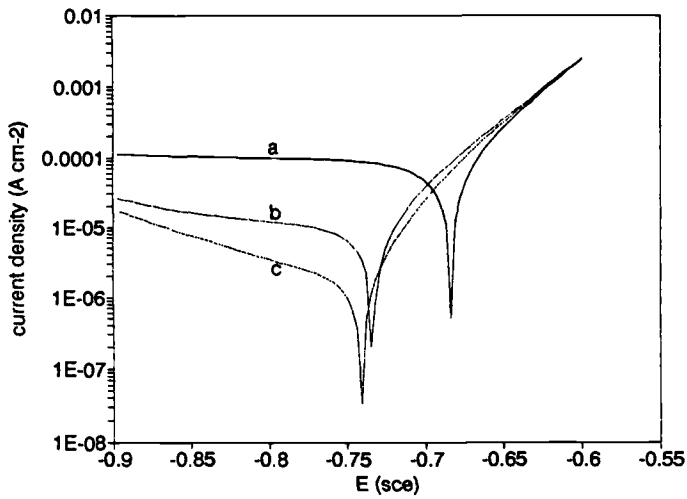

FIG. 5—*dc current density-potential curves for:* (a) D/δ = *0.001 cm/s;* (b) D/δ = *0.0001 cm/s;* (c) D/δ = *0.00001 cm/s. Other parameters as Table 1.*

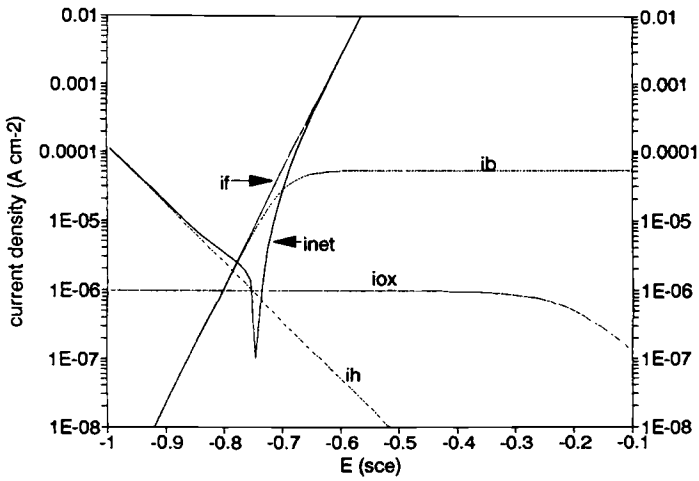

FIG. 6—*Partial current densities corresponding to Curve* (c) *in Fig. 5.*

anodic reaction, is that hydrogen evolution becomes relatively more important as the film becomes less permeable.

With the aforementioned values for the individual Tafel slopes and using Eq 53 to give the overall polarization resistance, then

$$\frac{1}{R_{p,\text{tot}}} = \frac{1}{R_{p,an}} + \frac{1}{R_{p,ox}} + \frac{1}{R_{p,H}} \tag{53}$$

for an irreversible anodic reaction with mass transport limited oxygen reduction as the cathodic reaction a value of RT/F (25.6 mV) is expected, Eq 26. In the limit (i_f and $i_b \gg i_{\text{net}}$) the reversible anodic reaction with the same cathodic reaction gives a value of RT/2F (12.8 mV), Eq 27. However if the reduction of oxygen is sufficiently hindered that hydrogen evolution becomes the dominant cathodic reaction then the corresponding values are 2RT/3F (17.1 mV) and 2RT/5F (10.2 mV). The third case is not seen but the others correspond to values of δ/D of 10^3, 10^5 and 10^7 in Table 2. The fact that even within a given system the growth of a surface film with time may cause the Stern-Geary constant to change, because the detailed reaction mechanism changes, obviously has implications in the use of linear polarization to obtain accurate corrosion rates, and the same qualifications must also apply to the use of polarization resistances obtained from impedance measurements.

TABLE 2—*Effect of varying film permeability on dc behavior.*

log, δ/D	E_{corr}	i_{corr}, A/cm^2	R_p, Ω-cm^2	$i_{\text{corr}}*R_p$
3	−0.684	9.61e-05	265	25.4
4	−0.734	1.03e-05	1911	19.7
5	−0.741	1.75e-06	7124	12.5
6	−0.726	6.79e-07	15 808	10.7
7	−0.704	3.89e-07	26 654	10.4

ac Behavior

The spectra here are calculated for the corrosion potential. This is determined by solving Eqs 9, 10, 46, and 49 with the free corrosion condition defined by Eq 51. The impedance at each frequency is then calculated by summing the admittance of the four parallel branches, essentially by calculating the values of equivalent parallel resistors and capacitors for each branch, then summing the capacitances and the inverse of the resistances to obtain one equivalent resistor-capacitor parallel combination. From this the impedance at the given frequency was calculated. This was carried out with a Turbo PASCAL (Borland) program on an AT-compatible personal computer.

The impedance spectra depend not only on the ratio D/δ but also on $\sqrt{D}/\delta$, and on the value chosen for the double layer capacitance. Figure 7 shows the impedance spectra for systems corresponding to the polarization curves in Fig. 5, with a double layer capacitance of 20μF/cm² and with the value of $\delta/\sqrt{D}$ fixed at 3.16. This corresponds to values of D of 10^{-5}, 10^{-7} and 10^{-9} cm²/s with values of δ of 0.01, 0.001, and 0.0001 cm, respectively. It can be seen that the impedance response for the former case, which approximates to film-free conditions, shows little diffusional effect. However, even slightly restricted diffusion introduces a second time constant into the spectrum, and the lower the permeability (D/δ) of the film the more significant the low frequency (diffusional) impedance becomes.

Figure 8 shows the impedances of the anodic branches alone, with a double layer capacitance of 20 μF/cm², for the same conditions as Fig. 7. Comparison of Figs. 7 and 8 shows that the impedance of the anodic branch dominates the overall spectrum. In the presence of surface films the overall polarization resistance, Fig. 7, is slightly lower than that for the anodic process, Fig. 8, due to the parallel hydrogen evolution charge transfer resistance. With the mass transport limited cathodic reduction of oxygen this reaction path has a sufficiently high impedance to have almost no influence on the total impedance.

These spectra are all for a fixed value of $\delta/\sqrt{D}$ but variation of this also affects the

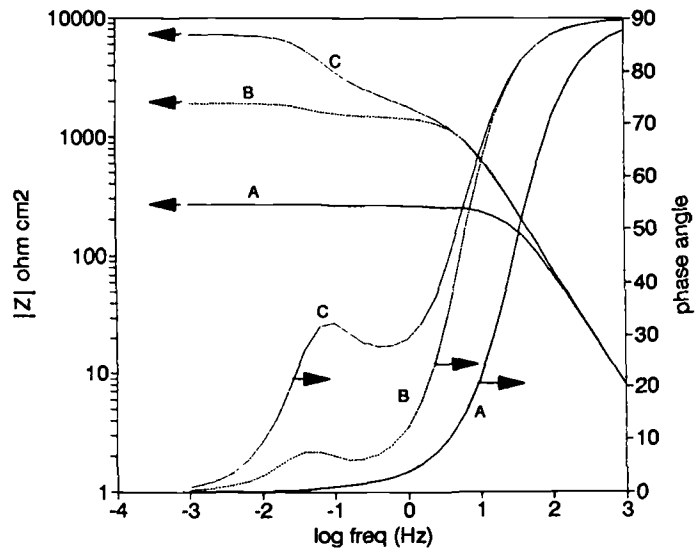

FIG. 7—*Bode plots of impedance response of corroding interface with varying D/δ, fixed $\delta/\sqrt{D}$.* (A) $D = 10^{-5}$ *cm²/s,* $\delta = 10^{-2}$ *cm;* (B) $D = 10^{-7}$ *cm²/s,* $\delta = 10^{-3}$ *cm;* (C) $D = 10^{-9}$ *cm²/s,* $\delta = 10^{-4}$ *cm.*

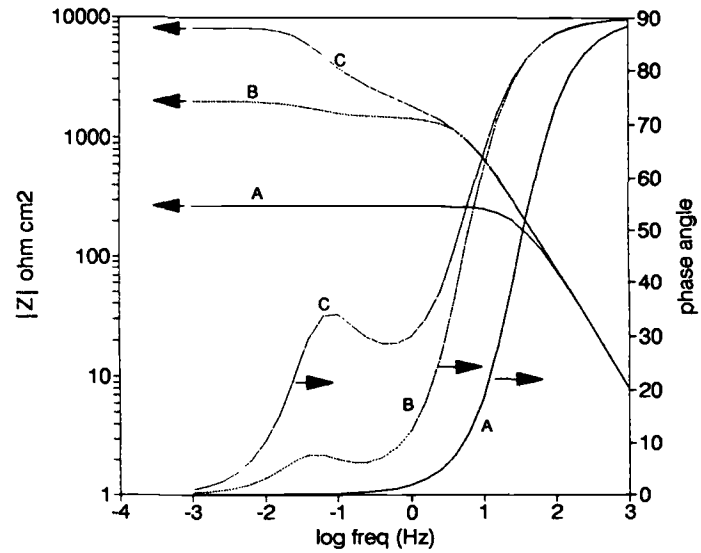

FIG. 8—*Bode plots for impedance of anodic process with all conditions as in Fig. 7.*

impedance. Figure 9 shows the impedance spectra at the corrosion potential for D/δ = 10^{-5} cm/s^{-1} for various values of D (10^{-7} to 10^{-11} cm^2/s^{-1}), corresponding to film thicknesses of 0.01 cm to 10 nm, and with a double layer capacitance of 20 μF/cm^2.

It should be stressed that for all the plots in Fig. 9 the charge transfer resistances ($R_{ct,a}$ = 1342 Ω-cm^2, $R_{ct,ox}$ = 53 210 Ω-cm^2, $R_{ct,h}$ = 65 240 Ω-cm^2), the overall polarization resistance (7124 Ω-cm^2), the corrosion potential (−741 mV sce) and the net dissolution rate (1.75 μA/cm^2) are the same. The differences arise from changes in the Warburg

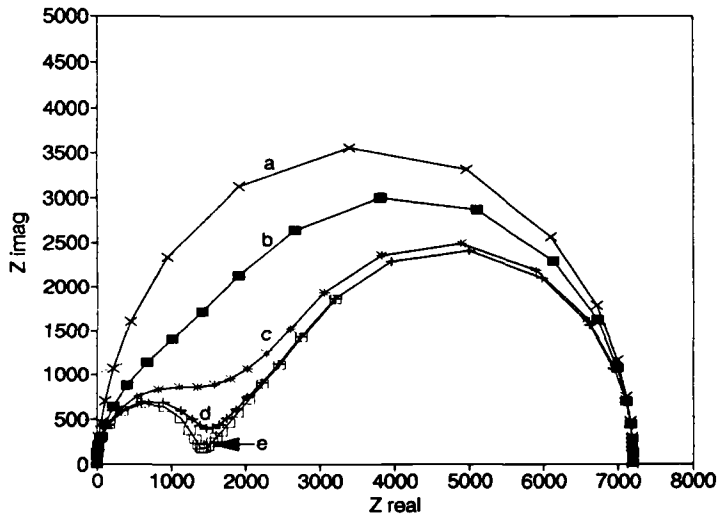

FIG. 9—*Nyquist plots for corroding interface with D/δ = 0.00001 cm/s.* (a) $\delta = 10^{-6}$ *cm;* (b) $\delta = 10^{-5}$ *cm;* (c) $\delta = 10^{-4}$ *cm;* (d) $\delta = 10^{-3}$ *cm;* (e) $\delta = 10^{-2}$ *cm.*

TABLE 3—*Parameter values for plots in Fig. 9.*

D, cm^2/s	δ, cm	$\delta/\sqrt{D}$, $s^{1/2}$	σ (anodic), Ω-cm^2
10^{-11}	10^{-6}	.316	14 900
10^{-10}	10^{-5}	1	4710
10^{-9}	10^{-4}	3.16	1490
10^{-8}	10^{-3}	10	471
10^{-7}	10^{-2}	31.6	149

coefficients, especially that due to the anodic process, and $\delta/\sqrt{D}$, as shown in Table 3. The effect of $\delta/\sqrt{D}$ on the impedance spectrum is shown by the plot of Z_{imag} against frequency in Fig. 10, for the same conditions as Fig. 9.

Figure 11 shows the Nyquist plots for $D/\delta = 10^{-4}$ cm/s, with the same range of film thicknesses.

Thus, in the presence of surface films which restrict diffusion the reversibility of the anodic process generates two time constants in an impedance spectrum. The high frequency response is due to the charge transfer resistance-double layer capacitance combination, and the lower frequency one is due to diffusional effects. The charge transfer resistance in this case relates to the exchange current density of the M/M^{n+} system and not to the net dissolution rate. Even with the same film permeability and corrosion rate the impedance response is markedly dependent on the film thickness. This arises since the angular frequency where the imaginary diffusional impedance is maximum is proportional to D/δ^2 (approximately 2.5 D/δ^2 s^{-1}) [7]. With the thinnest films, e.g., Fig. 9*a*, the diffusional impedance occurs at sufficiently high frequency that the Nyquist plot appears to be a single semicircle. The plot in Fig. 10*a* shows only a slight deviation from that expected

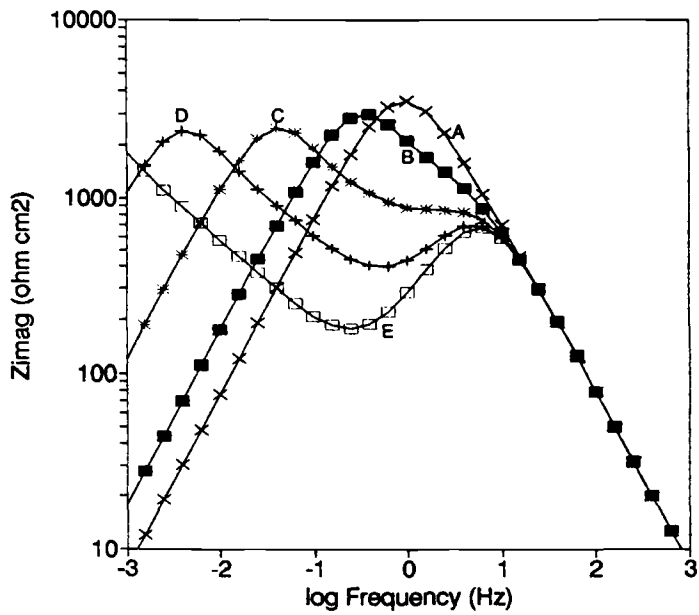

FIG. 10—*Imaginary impedance against frequency for plots in Fig. 9.*

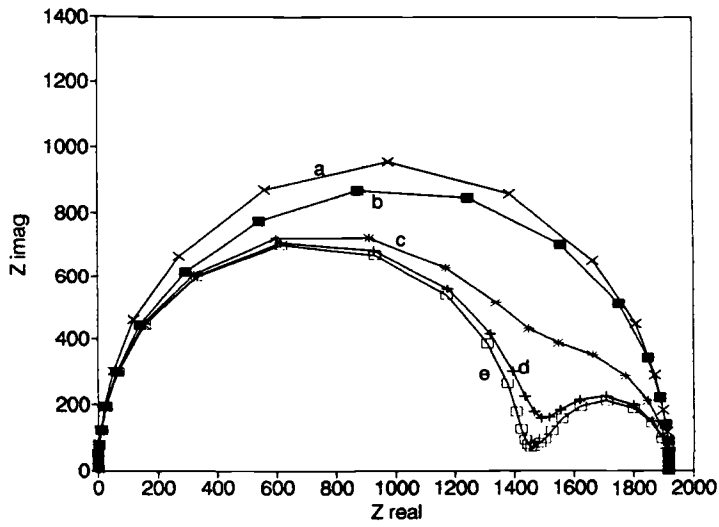

FIG. 11—*Nyquist plots for corroding interface with D/δ = 0.0001 cm/s.* (a) $\delta = 10^{-6}$ *cm;* (b) $\delta = 10^{-5}$ *cm;* (c) $\delta = 10^{-4}$ *cm;* (d) $\delta = 10^{-3}$ *cm;* (e) $\delta = 10^{-2}$ *cm.*

for one semicircle and it is doubtful if this could be detected with experimental measurements. With thicker films two features are resolvable and eventually the diffusional impedance occurs at sufficiently low frequency that the limited diffusion length effect is not seen in the frequency range usually studied, Fig. 9*e*. In this latter case the corrosion rate would not be available from the impedance data.

The conditions for Fig. 9*b* are not untypical of those for cathodic inhibitors (R_p around 10 000 Ω-cm^2 with a 100-nm-thick film), although some effective cathodic inhibitors will give higher R_p with thinner films than this, and similar impedance spectra are often obtained. Typically spectra obtained in the presence of surface films show features predicted by the calculations here. First, the Nyquist plot is depressed in the high frequency region and second the capacitance calculated if one depressed semicircle were assumed is higher than typical double layer capacitances, the first may have other explanations (surface roughness, porous conducting films, etc.) but arises here from the overlap of the two time constants. The second arises here because the calculated capacitance has a significant contribution from the "capacitance" of the diffusional impedance.

The effect of allowing the metal ion diffusion coefficient to vary with a fixed oxygen diffusion coefficient is shown in Fig. 12. The shape of the Nyquist plot changes considerably as does the low frequency intercept, even though the corrosion rate only varies by less than 5% in these calculations, as shown by the data in Table 4.

Conclusions

It has been shown that in neutral solutions, under conditions where diffusion is restricted by surface films, allowance for the reversibility of the anodic reaction may significantly affect the calculated impedance spectra.

A general equivalent circuit has been developed for the corroding interface in which the numerical values of the components are related to physical, chemical, and electrochemical parameters of the system.

With only slightly restricted diffusion, as compared to bulk solutions, the reversible

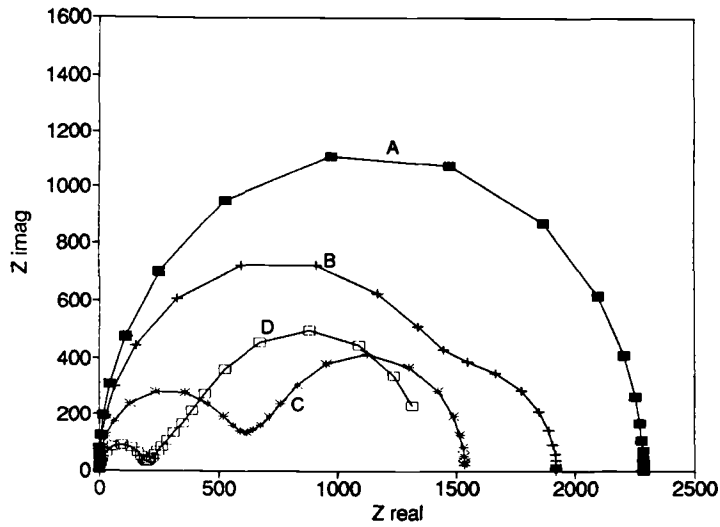

FIG. 12—*Nyquist plots for corroding interface for different diffusion coefficients (D_m) for metal ions with $D_{ox} = 10^{-8}$ cm²/s and $\delta = 0.0001$ cm.* (A) $D_m = 10^{-7}$ cm²/s; (B) $D_m = 10^{-8}$ cm²/s; (C) $D_m = 10^{-9}$ cm²/s; (D) $D_m = 10^{-10}$ cm²/s.

anodic reaction gives rise to two time constants in an impedance spectrum. The first of these relates to the kinetics of the reversible metal-metal ion reaction in parallel with a double layer capacitance and the second arises from a finite length diffusional impedance.

It has been shown that the low frequency limit of the impedance relates to the corrosion rate, although the "constant" depends on the detailed reaction mechanism and will change as surface films develop. This clearly has implications for the use of both dc and ac techniques for corrosion rate measurement. In principle it is possible to get more accurate corrosion rates from impedance than from dc methods in these systems. Equations 16, 34, and 35, for the charge transfer, polarization and diffusional resistances associated with the anodic reaction lead to the expression for the net dissolution rate in Eq 54.

$$\frac{1}{i_{\text{net}}} = \frac{(\beta_f + \beta_b)R_p}{\beta_f \beta_b} + \frac{R_{ct}}{\beta_b} \tag{54}$$

Consideration of the reversibility of the anodic reaction enables prediction of the depression of the high frequency region of the "semicircles" in the Nyquist plots and the occurrence of large "capacitances," both of which are commonly seen in practice.

TABLE 4—*Parameter values for plots in Fig. 12.*

log, Dm	E_{corr}, mV/sce	i_{corr}, μA/cm²	R_p, Ω-cm²	$i_{corr}*R_p$, mV
−7	−0.740	10.4	2277	23.7
−8	−0.734	10.3	1911	19.7
−9	−0.715	10.1	1520	15.4
−10	−0.690	9.93	1371	13.6

These conclusions arise from a relatively simple system. Full explanation of impedance spectra in neutral solutions requires that we allow for more complex systems, including some or all of factors such as nonuniform films (and thus localized corrosion processes), variation of the relative values of diffusion coefficients through films as compared to in solution, homogeneous chemical kinetics (e.g., ferrous ion-oxygen reactions), effects of surface pH changes on electrochemical kinetics, and transport by migration. Some of these will be considered in subsequent papers but it is felt that consideration of the simple system here contributes to understanding of the impedance responses commonly observed in neutral solutions.

References

[1] Lorentz, W. J. and Mansfeld, F., *Electrochimica Acta*, Vol. 31, 1986, p. 467.
[2] Randles, J. E. B., *Discussion Faraday Society*, Vol. 1, 1947, p. 11.
[3] Bonnel, A., Dabosi, F., Delouis, C., Duprat, M., Keddam, M., and Tribollet, B., *Journal of the Electrochemical Society*, Vol. 130, 1983, p. 753.
[4] Juttner, K., Lorentz, W. J., Kendig, M. W., and Mansfeld, F., *Journal of the Electrochemical Society*, Vol. 135, 1988, p. 332.
[5] Bard, A. J. and Faulkner, L. R., *Electrochemical Methods*, John Wiley and Sons, New York, 1980.
[6] Southampton Electrochemistry Group, *Instrumental Methods in Electrochemistry*, Ellis Horwood, Chichester, U.K., 1985.
[7] Dawson, J. L. and John, D. G., *Journal of Interfacial and Analytical Chemistry*, Vol. 110, 1980, p. 37.
[8] Sluyters-Rehbach, M. and Sluyters, J. H., *Electroanalytical Chemistry*, Vol. 4, 1970, p. 1.

David C. Silverman[1]

Corrosion Prediction from Circuit Models Application to Evaluation of Corrosion Inhibitors

REFERENCE: Silverman, D. C., **"Corrosion Prediction from Circuit Models Application to Evaluation of Corrosion Inhibitors,"** *Electrochemical Impedance: Analysis and Interpretation, ASTM STP 1188,* J. R. Scully, D. C. Silverman, and M. W. Kendig, Eds., American Society for Testing and Materials, Philadelphia, 1993, pp. 192–204.

ABSTRACT: Detailed kinetic models are not often available to predict the efficacy of inhibitors of iron corrosion in water at near neutral pH from electrochemical impedance spectra. Circuit models offer a way of using the spectra to estimate corrosion and of making practical conclusions about the mechanism in the absence of kinetic models. Circuit elements estimated from regression of the models against the impedance spectra are shown to provide information for the estimation of corrosion rates and for insights into corrosion behavior. However, simultaneous agreement between calculated and measured impedance spectra, and between predicted and measured corrosion rates, does not necessarily mean that the circuit model is a unique representation of the spectra. Results are presented that show that similar values of the circuit elements can be obtained from regression of two different models against the measured spectra.

KEYWORDS: electrochemical impedance spectroscopy (EIS), polarization resistance, corrosion, modeling, inhibitor, iron, steel, amino-trimethyl phosphonic acid (ATMP), circuit models, corrosion rate, velocity, rotating cylinder electrode

Evaluation of corrosion inhibitors for steel is of practical importance because of the ubiquitous use of steel in contact with a number of corrosive environments. One important application area is the protection of steel during containment and transport of aqueous solutions at near neutral pH ($5 < pH < 9$). The ability to rapidly evaluate and screen inhibitors for this type of application is important in order to choose an appropriate inhibitor quickly.

Numerous workers have shown that electrochemical impedance spectroscopy (EIS) can be applied successfully to the evaluation of corrosion inhibitors in acid solutions [*1–3*]. Far fewer studies have been reported on the use of EIS for rapid evaluation of corrosion inhibitors for steel in water in the near neutral pH region. As inferred from a number of recent papers [*4–10*], the major problem is lack of a clear understanding of the mechanism by which the inhibitor interacts with the three-dimensional oxide layer that forms on iron or steel at near neutral pH. Lorenz and Mansfeld have discussed that one reason for this paucity in knowledge is the difficulty in measuring the inhibition kinetics by electrochemical or nonelectrochemical means [*5*]. These kinetics depend in a complex manner on exposure time, properties of the surface layers, and hydrodynamic conditions. From a practical standpoint, this complexity means that any technique used to screen corrosion inhibitors for this application must be able to provide reliable estimates of corrosion rates

[1]Fellow, Monsanto Company, St. Louis, MO 63167.

and indications of the relationship among those corrosion rates and the environmental variables, all in the absence of *a priori* knowledge about the degree of importance of many of the variables themselves.

In a recent evaluation of corrosion of steel in an inhibited waste stream, the electrochemical impedance technique was shown to be very powerful for predicting corrosion in the absence of a definitive understanding of the corrosion mechanism [*11*]. Analysis by curve-fitting to analogous circuit models was shown to be extremely powerful for extracting the polarization resistances (and corrosion rates) from the rather complex impedance spectra in the absence of a kinetic model. The estimated corrosion rates were shown to be valid indicators of observed electrode mass loss and in-plant corrosion. The in-plant results showed that corrosion decreased after the process changes recommended from the electrochemical impedance results were implemented [*12*]. This agreement means that the electrochemical impedance technique can be used to perform practical evaluations of steel corrosion in inhibited, aqueous environments having a pH near 7 even if the corrosion mechanism is not known and the environment is not well-characterized.

One of the factors that complicates evaluation of corrosion inhibitors for steel is hydrodynamic conditions. As shown by Mahato et al. [*13*], not only does the mass transfer rate of oxygen which often controls corrosion in this system increase with flow rate (agitation), but at a constant flow rate the rate of mass transfer to the corroding interface can actually decrease. The oxide/hydroxide corrosion product layer can decrease the rate of transfer of oxygen from the fluid/surface boundary to the steel below the surface [*6,7*]. In the presence of an inhibitor, this deleterious effect of fluid velocity on corrosion rate can be greatly diminished or can even disappear [*5,10*]. There are also indications that adding the inhibitor while the fluid is in motion can decrease the amount of inhibitor required to passivate the surface relative to that which would be required if the addition is made in a stagnant fluid [*14*]. Fluid motion must be included as a variable when evaluating corrosion inhibitors for steel. As discussed elsewhere, the rotating cylinder electrode can provide information that can be used to make predictions in other flow geometries [*15*]. Combining the electrochemical impedance technique with the rotating cylinder electrode should enable practical corrosion predictions to be made under dynamic conditions.

The work in this paper was undertaken to examine the effectiveness of combining EIS with the rotating cylinder electrode for rapid (order of days) screening of corrosion inhibitors in aqueous systems at near neutral pH. The inhibitor chosen is DEQUEST® (Registered Trademark of Monsanto Company) 2000 (amino trimethyl phosphonic acid or ATMP). The mechanism by which this material can inhibit corrosion of steel is unclear but the compound has been shown to decrease corrosion of steel [*8,10,16,17*]. The goal of the paper is to illustrate how EIS could be used for such evaluation, the type of information that might be acquired, and ambiguities that might arise when the only way to analyze the data is through the use of circuit analogues.

Experimental

The experimental arrangement and algorithm for deriving the spectra have previously been discussed in detail [*16*] and are only summarized here. The experiment is guided by a Hewlett-Packard 9816S microcomputer with the impedance spectra being measured by a Solartron 1250A Frequency Response Analyzer and a PAR 173D potentiostat with 276 programmable interface. The algorithm first optimizes the gain of the potentiostat every half-decade by finding the maximum gain of the potentiostat that does not cause a current overload. This gain is implemented at each half-decade of frequency during the measurement. The minimum gain (1 Ω) is used between 10 kHz and 100 Hz. The potentiostat filter

is activated below 0.5 Hz so that only one sine wave is needed at each frequency below that point. The excitation amplitude for these experiments was 5 mV. Polarization resistances were estimated for some of the conditions by dc type of measurements to compare to those estimated by modeling of the impedance spectra. The method of generating and analyzing these dc curves has been discussed in detail elsewhere [*16*]. Some of the curves, especially those generated in the presence of the inhibitor, were analyzed by assuming that the voltage versus current curve is a straight line over this ±20 mV range. A straight line was fit through the points and the polarization resistance was assumed to be the slope.

The electrochemical cells used in the static and dynamic (rotating cylinder electrode) studies are described in detail elsewhere [*16,18*]. The rotating cylinder electrode was maintained at 200 r/min except for short durations (about 1 h each) at 1000 r/min and 2000 r/min. The electrode was allowed to rotate at the higher speeds for about 0.5 h before generating spectra to 0.01 Hz at those rates. These additional rotation rates were used to examine the sensitivity of corrosion to fluid motion. Spectra were generated to 0.001 Hz at 200 r/min. Rotation was begun immediately upon immersion of the electrode. Temperatures of 35°C and 80°C were used in the dynamic tests and temperatures of 35°C and 70°C were used in the static tests.

The aqueous environment was an aggressive water composed of 0.088 g/l Ca^{+2} added as $CaSO_4 \cdot 2H_2O$, 0.024 g/l of Mg^{+2} added as $MgCl_2 \cdot 6H_2O$, 0.040 g/l of HCO_3^- added as $NaHCO_3$, and 0.328 g/l SO_4^{-2} added as Na_2SO_4. Deionized water and ACS reagent grade salts were used. The pH was adjusted with reagent grade HCl to a pH of 7. The steel used for both types of experiments was UNS G10180. The electrodes were sanded with 600 grit silicon carbide paper. The chloride concentration was increased to 1000 ppm by weight in the static studies. The DEQUEST 2000 was product grade added at 30 ppm active material by weight in the dynamic studies and 50 ppm by weight in the static studies.

Analysis of Impedance Spectra

The impedance spectra were uploaded to an IBM mainframe. The spectra were analyzed using the first two circuits shown in Fig. 1. Analysis using the last circuit is discussed later. The subroutine used to estimate the circuit elements performs a nonlinear regression of the data against the equations which describe the circuit. The sum of the squares of the residuals is minimized automatically between the calculated and actual impedance spectra in real and imaginary coordinates. How well the model fits is judged by overlaying the impedance spectrum calculated from the model and that measured. Merely showing that the sum of the squares of the residuals is minimized for the function chosen does not necessarily mean that the function represents the data adequately. In addition, some of the spectra were analyzed using EQUIVCRT by Boukamp [*19*]. Only minor differences were found among the results from the two algorithms.

Circuit 1 in Fig. 1 models one relaxation time constant. This circuit is usually used to represent a single charge transfer reaction. Circuit 2 models two relaxation time constants and is often used to represent an imperfectly covered electrode as might be found with an inhibitor or imperfect coating. This circuit could also model a mechanism with an adsorbed electroactive intermediate [*3*]. Circuit 3 also represents two relaxation time constants. Use of this circuit is discussed later. The first two circuits were used to model most of the spectra. All of the models allow for dispersion of the time constants by means of the term $(j\omega\tau)^{\beta}$ where ω is the frequency in rad/s, τ (equivalent to RC, resistance times capacitance) is a time a constant of the process being affected by the excitation, and β is a phenomenological exponent expressing degree of dispersion of the time constant. It usually lies between 0.5 and 1 (1 being no dispersion). The maximum number of adjustable parameters

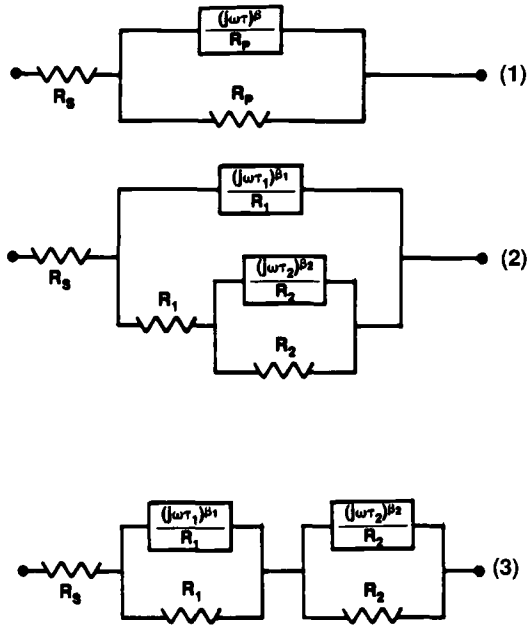

FIG. 1—*Circuit elements used to model the impedance spectra.*

is three for Circuit 1 and six for Circuits 2 and 3. The solution resistance was estimated as the intersection of each spectrum with the real axis at high frequency. The value was kept constant during the regression analysis. The solution resistance was about 50 ± 10 Ω-cm^2 in all cases.

Results

Slow drift of the corrosion potential can be a problem when making electrochemical measurements of steel in aqueous solutions at near neutral pH [*5,10*]. In the case of these studies, the corrosion potential was found to reach steady state after about 24 to 36 h of immersion. Therefore, the impedance spectra obtained at or after 48 h of immersion can be reasonably assumed not to contain possible instability artifacts (nonlinearities) caused by a drifting corrosion potential; that is, all of the data in any one spectrum should correspond to the same corrosion process at least when the lowest frequency is 0.001 Hz. Spectra obtained before steady state was reached had to be examined carefully to eliminate such artifacts. Those portions of the spectra that seemed to be affected by drift of the corrosion potential were ignored in the analysis.

Figures 2 and 3 show examples of the electrochemical impedance spectra for steel in water at 80°C, at a pH of 7, and at 200 r/min. Figure 2 shows the spectrum without DEQUEST 2000. Figure 3 shows the spectrum with 30 ppm of DEQUEST 2000 added. Only the Bode format is shown. The figures demonstrate the amount of agreement between the models and the actual spectra. The corrosion rates estimated from models of the impedance spectra and those estimated from mass loss of the *same* electrode used for the electrochemical measurements are shown in Table 1. The time-averaged corrosion rates of the electrodes derived from the impedance spectra were estimated by assuming that the resistance associated with the corrosion rate measured at a given time remained constant

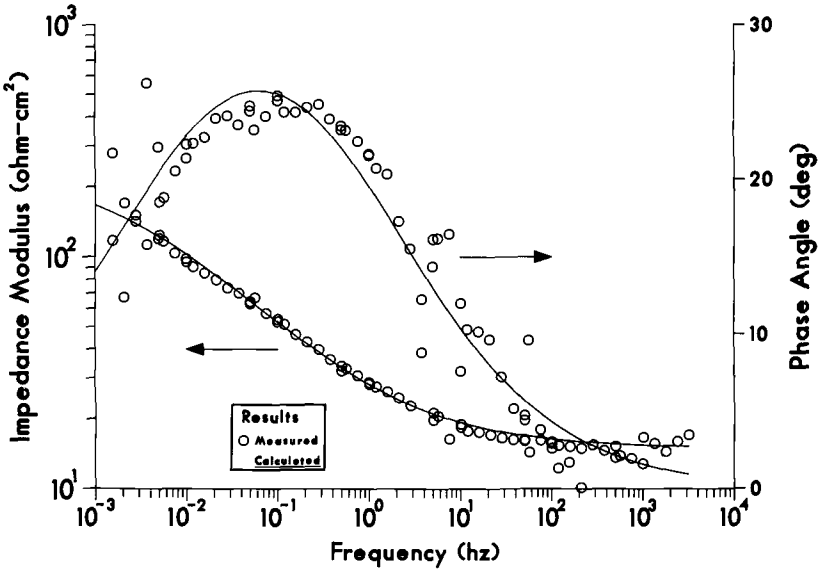

FIG. 2—*Impedance spectrum of steel at 200 r/min in water solution at 80°C with no inhibitor at 66 h of exposure. Modeled using Circuit 1 in Fig. 1.*

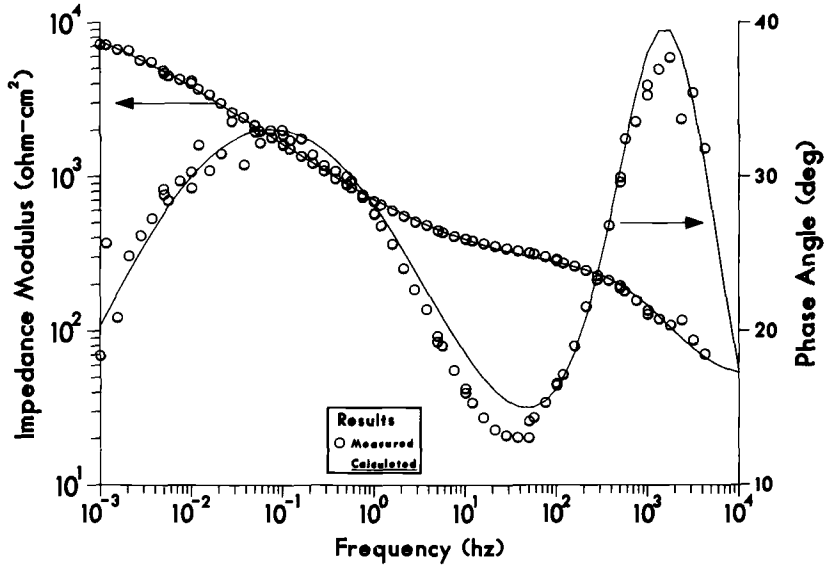

FIG. 3—*Impedance spectrum of steel at 200 r/min in water solution with 30 ppm DEQUEST 2000 at 80°C after 65 h of exposure. Modeled using Circuit 2 in Fig. 1.*

TABLE 1—*Corrosion rate of steel in aggressive water solutions.*

Conditions	Temperature, °C	Time-Averaged Corrosion Rate, mm/year	
		Impedance	Mass Loss
Dynamic—	35	0.86	1.3
uninhibited	80	1.8	2.5
Dynamic—	35	0.04	0.089
30ppm DEQ 2000	80	0.10	0.14
Static—	35	0.50**	0.22**
uninhibited*	70	0.51	0.41
Static—	35	0.043**	0.020**
50ppm DEQ 2000*	70	0.043	0.051

*The water solution for these cases was the same as that shown in the experimental section except that the chloride ion concentration was 1000 ppm by weight.
**From Ref *11*.

until the next change in rotation rate. For the inhibited systems, the polarization resistance changed quickly over the first 24 h and then much more slowly for the next 24 h. The reciprocals of the appropriate resistances measured at 200 r/min were fit to a polynomial function of time and that fitted function was time-averaged by integration. The resistances measured at various rotation rates were included in the estimate of corrosion for the uninhibited solutions because of the large effect that fluid velocity had on corrosion in that system.

Spectra for steel in uninhibited water at 35°C had two relaxation time constants after about 24 h of exposure. The resistance associated with the capacitive element that relaxes at high frequency was used for the estimate of the mass loss shown in Table 1 for this system. The reasons for using this circuit element are discussed in detail later. The value of B was assumed to be 0.025 V for the uninhibited system and 0.05 V for the inhibited system, independent of temperature. Neither value is unreasonable for steel corrosion in aqueous media [*20*]. The value of 0.025 V might be expected to underestimate the corrosion rate because the value may increase above that value with time [*16*]. In addition, Duprat et al. [*10*] have estimated values of 0.033 V in the absence of inhibitor and 0.064 V in the presence of an inhibitor comprised of 1 g/L of ATMP and oleylamino acid. Their water contained 200 mg/L NaCl with no other ions. These values are similar to those assumed in this study. The measured current in the presence of the inhibitor was near the noise threshold of the system for dc type of measurements. Note that in view of these assumptions, the agreement in Table 1 is reasonable.

The effect of fluid velocity was examined by plotting the reciprocal of the resistance as a function of time and rotation rate. The results when the inhibitor was included are shown in Fig. 4. Two time constants were observed for the inhibited system at both temperatures in agreement with previous results [*8,10,16*]. However, as discussed later the high-frequency time constant is not believed to be related to the charge transfer resistance when the inhibitor is present but to some other process. The resistance associated with that time constant was almost independent of rotation rate but was slightly dependent on exposure time and temperature. Therefore, only the resistance associated with the low-frequency time constant is included in Fig. 4.

Table 2 shows the comparison of the resistances estimated from the dc measurements and the electrochemical impedance technique for the experiments run under dynamic

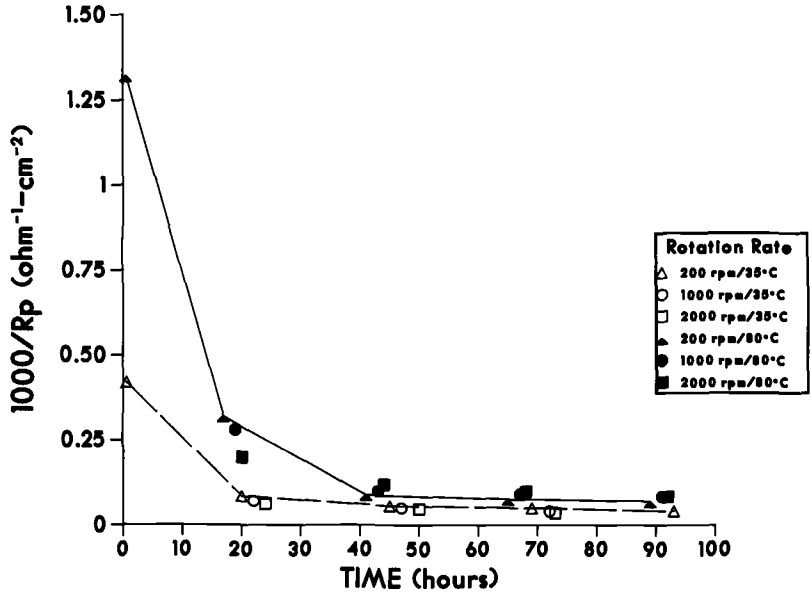

FIG. 4—*Reciprocals of resistances estimated from impedance spectra for steel in water containing inhibitor as a function of time and rotation rate.*

TABLE 2—*Comparison of polarization resistance measurements* (dynamic conditions only).*

Temperature	Rotation Rate, RPM	Estimated Polarization Resistance, Ω-cm²	
		Impedance	DC Technique
Uninhibited, 35°C	200	429 & 449	930
	200	434 & 329	795
	200	205 & 550	1021
	200	143 & 1040	1020
Uninhibited, 80°C	200	205	187
	200	232	208
	1000	138	128
	200	199	215
30 ppm	200	1.16×10^4	1.13×10^4
DEQUEST 2000,	200	1.78×10^4	1.44×10^4
35°C	200	2.02×10^4	1.68×10^4
	1000	2.52×10^4	1.72×10^4
	200	2.43×10^4	1.89×10^4
30 ppm	200	3.11×10^3	3.75×10^3
DEQUEST 2000,	200	1.12×10^4	6.14×10^3
80°C	200	1.33×10^4	6.59×10^3
	200	1.43×10^4	7.18×10^3
	1000	1.17×10^4	6.36×10^3

*Results correspond to exposure at increasing times. The first 200 rpm result is after 3 to 5 h of exposure. Afterwards, spectra were generated at 200 rpm every 24 h. The spectrum at 1000 rpm was generated within one h after the preceding spectrum at 200 rpm.

conditions. Note that at 35°C without inhibitor the polarization resistance estimated from the dc measurements is approximately equal to the sum of the two resistances obtained from the electrochemical impedance technique. As previously mentioned, when inhibitor was present a straight line was fit through the data so as to estimate the polarization resistance from the slope. The resistances for these latter systems as obtained from dc results tend to differ by a factor of 1.5 to 2 from those obtained by the impedance technique. This difference could easily have been caused by assuming linear behavior to obtain the dc polarization resistances. However, in all cases, the agreement is acceptable for practical corrosion screening.

The resistances shown in Table 2 as measured by the impedance technique are the resistances used for the mass loss estimate in Table 1. The resistances are the resistances associated with the high-frequency time constant (first value) in uninhibited water at 35°C, the resistance associated with the single time constant in uninhibited water at 80°C, and the resistances associated with the low-frequency time constants for the exposures to water with inhibitor at both temperatures. The resistance associated with the high-frequency time constant in the presence of inhibitor was about 200 to 400 Ω-cm^2, about two orders of magnitude less than the resistances associated with the low-frequency time constants in those environments (1×10^4 to 3×10^4 Ω-cm^2). This large difference means that using only the resistance associated with the low-frequency time constant would give a reasonable estimate because adding the resistance associated with the high-frequency time constant to the values shown would only affect the second decimal place. The hypothesis is that only the resistance associated with the low-frequency time constant in the inhibited system is related to the corrosion rate.

Discussion

Figures 2 and 3 show examples of the agreement between the measured impedance spectra and those calculated by the best regression fit using the first two circuit models in Fig. 1. The agreement strongly suggests that the circuits can model the spectra. As discussed later, they are not necessarily unique. The agreement shown in Table 1 strongly suggests that the single resistance in water at 80°C and the low-frequency resistances in water containing DEQUEST 2000 at each temperature are associated with (inversely proportional to) the corrosion rate. The resistance associated with the high-frequency time constant was used to estimate the corrosion rate shown at 35°C. The reason for choosing this resistance is discussed in the following paragraphs. The practical conclusion, though, is that inhibitors for steel in near neutral pH water can be screened rapidly by this approach even when the corrosion mechanism is unclear. Steady state must be reached (approximately 48 h) to make reliable predictions.

Note that use of only the low-frequency resistance at 35°C in uninhibited water would have also resulted in a corrosion rate that is in fair agreement with that estimated from mass loss. Thus, agreement between the corrosion rate estimated from a resistance in a model element to that calculated from mass loss is not always a valid criterion for deciding which part of the model to use to estimate the corrosion rate. Such agreement is a necessary but not a sufficient condition for a model to be valid.

The polarization resistance in the uninhibited solution at 35°C measured under the dc technique is approximately equal to the sum of the resistances measured by the electrochemical impedance technique. Use of the dc derived values would lead to an estimated corrosion rate of about 0.3 to 0.4 mm/y using a B value of 0.025 V. This rate is less (by a factor of two to four) than that estimated by mass loss (about 1 mm/year). According to the model of Bonnel, et al. [7], the resistance associated with the high-frequency portion of the

spectrum is hypothesized to contain anodic and cathodic contributions to the charge transfer reaction. The resistance associated with the low-frequency portion is hypothesized to contain the explicit contribution from mass transport both through the fluid and through the porous corrosion products on the surface. If so, the resistance as measured by the dc method would contain contributions from both relaxation time constants.

Previously [*16*], corrosion in a comparably aggressive water at 35°C but under static conditions was found to be modeled by the approach of John and Dawson [*21*]. At that time, the corrosion rate was shown to be related to the resistance associated with the high-frequency time constant under static conditions. The resistance associated with the high-frequency time constant in such an environment is written by Bonnel [*7*] as the addition of resistances caused by the anodic and cathodic contributions to charge transfer acting in parallel ($R_1R_2/(R_1 + R_2)$). The *hypothesis* is that the parallel combination of the resistances created by the anodic and cathodic charge transfer processes allows the resulting composite resistance associated with the high-frequency time constant to be used for *screening* steel corrosion rates in uninhibited, near neutral pH water at low temperature under dynamic conditions. The complex interaction among charge transfer, hydrodynamics, and time does suggest that this hypothesis might not always be valid.

The discussion of Mansfeld and the reply by Bonnel et al. [*9*] also strongly suggest that screening cannot be done in under 24 h. Mansfeld has presented results which indicate that at low temperature, steel shows one relaxation time constant in near neutral pH water containing 0.5N NaCl after 2 h of exposure. In the present study, one relaxation time constant was observed after only several hours of exposure. However, two time constants emerged after 24 h. This observation agrees with the reply by Bonnel et al. who state that a second capacitive time constant is observed after longer exposure times. Note that only one relaxation time constant appeared in the spectra generated at 80°C at all times. The resistance associated with it was assumed to be inversely proportional to the corrosion rate.

Figure 4 shows the plot of the reciprocals of the low-frequency resistances for steel in water at the two temperatures and in the presence of 30 ppm by weight DEQUEST 2000. These resistances are hypothesized to be related to the corrosion rate. They were used for the estimates in Table 1. As previously stated, the resistance associated with the high-frequency time constant tended to remain in the range of 200 to 400 Ω-cm^2. Corrosion rates estimated from this resistance would have been of the order of 1 mm/year, far higher than those observed from mass loss of the electrode.

Addition of DEQUEST 2000 to the aqueous environment changes the corrosion behavior. As shown in Fig. 4, the sensitivity of corrosion to fluid velocity virtually disappears. The corrosion rate is decreased by one to two orders of magnitude relative to that in the absence of DEQUEST 2000. This decrease demonstrates the corrosion inhibition properties of DEQUEST 2000. At 80°C under dynamic conditions and at 70°C under static conditions, the exponent on the low-frequency element does approach 0.5 at long times. This behavior may suggest that there is a diffusional contribution to the corrosion process, at least at elevated temperature. Since the corrosion rate remains independent of fluid velocity up to this time, any diffusional resistance should lie within the oxide film of the electrode, not within the fluid boundary layer. However, this behavior was not observed at lower temperature where the exponent on the low-frequency element remained in the range of 0.65 to 0.7.

This change in behavior of the exponent on the relaxation time constant associated with the polarization resistance is not caused by a decrease in oxygen solubility with increased temperature. The Henry's Law type constant only decreases by about 40% over this

temperature range [*22*]. The solubility in salt water at 25°C is about 2.6×10^{-7} mol/cc. Using the Sherwood versus Reynolds–Schmidt number relationship for the smooth rotating cylinder electrode [*23*] and assuming that this oxygen concentration is rate limiting, results in a predicted corrosion rate of about 2.5 to 3 mm/year at 200 r/min. This predicted rate is orders of magnitude greater than that found in the inhibited system at all temperatures indicating that the small decrease in oxygen solubility cannot cause the different behavior of the exponents on the time constant that emerges at low frequency.

The presence of inhibitor has a marked effect on the values of the capacitances. Figure 5 shows plots of the capacitance versus time for each of the time constants (constant phase elements) for steel in the uninhibited and inhibited environments under dynamic conditions. The capacitance associated with the high-frequency time constant in the presence of inhibitor is about 10^{-6} F/cm^2 (1 μF/cm^2) or less, showing a slight decrease with exposure time and a slight dependence on temperature. Such low-capacitance values associated with the high-frequency time constant have been observed before for steel in solutions containing this inhibitor [*4,8,10*]. This low value has been attributed to the formation of a more compact and protective film.

One possible way to estimate the film thickness is to use the relationship $C/A = \epsilon\epsilon_0/d$ (where C/A is the capacitance per unit area, ϵ is the dielectric constant, ϵ_0 is the permittivity in free space (8.854×10^{-12} F/m), and d is the thickness) [*24*]. Using a value of C/A of 10^{-6} F/cm^2 and ϵ of 5 to 20 (the range of values for a number of oxidized metal solids [*25*]) results in a film thickness d of the order of 50 to 200 Å. The resistance in parallel with this capacitance might be considered to represent the resistance to movement of ions (possibly oxygen) through the surface region. These resistances are independent of fluid velocity. An hypothesis would be that the inhibitor incorporates into or strongly interacts with the upper layers of the iron oxide/hydroxide surface region to make it more compact and more impervious to oxygen (or oxide) mass transfer from the fluid to the metal-oxide interface where the iron is oxidized. Indeed, evidence exists that phosphonic

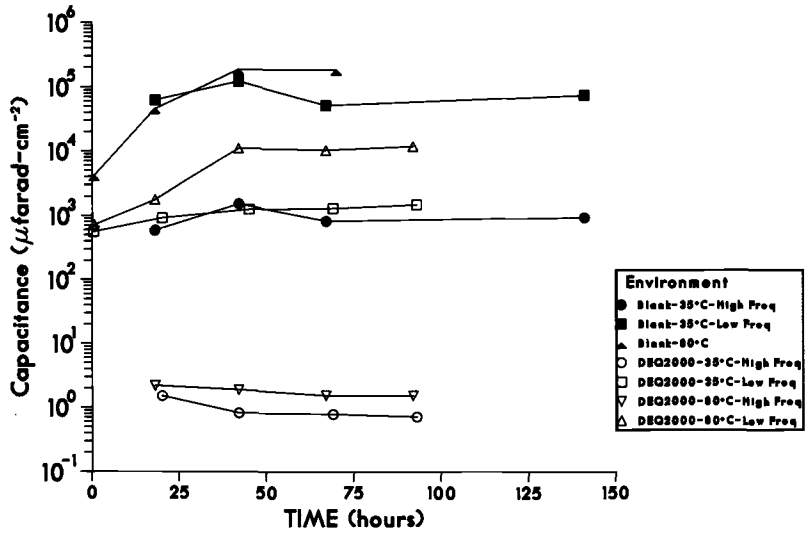

FIG. 5—*Magnitude of capacitances estimated from relaxation time constants as a function of environment and time.*

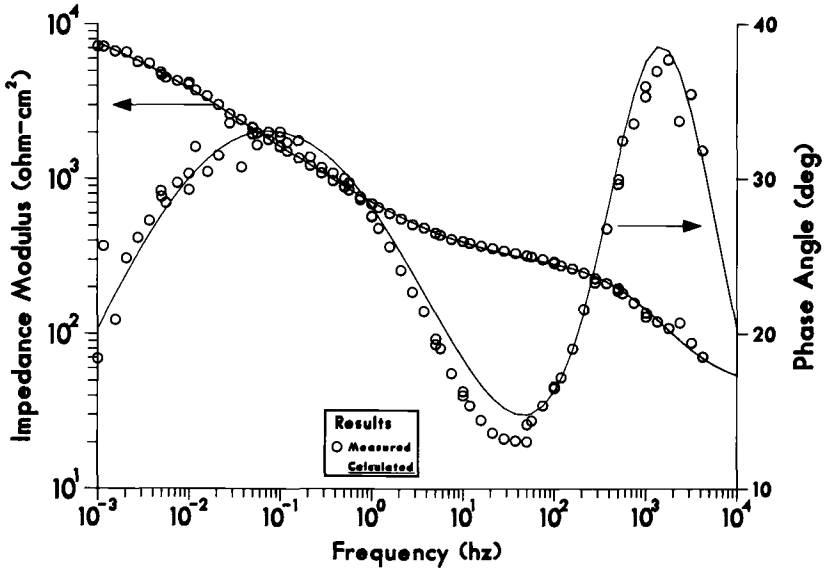

FIG. 6—*Impedance spectrum of steel at 200 r/min in water solution with 30 ppm DEQUEST 2000 at 80°C after 65 h of exposure. Modeled using Circuit 3 in Fig. 1.*

acids in concert with calcium either can become predominant constituents in the upper portions of the surface region [*26*] or incorporate through the surface region [*27*]. Auger electron spectroscopy has been used by Neagle [*28*] to examine the surface composition of steel exposed to cooling water containing calcium ions and inhibited by hydroxy phosphono-acetic acid. He estimated that the thickness of the surface film containing phosphorous and calcium is about 200 to 800 Å. Agreement with the value estimated above is fair considering that the two inhibitors are not the same (though they have similar phosphonate functional groups) and both techniques lead to very gross estimates of the surface layer thickness. The capacitance associated with the high-frequency time constant is probably not a double layer capacitance which would be expected to be in the range of 2×10^{-5} F/cm^2.

One question that often arises is if the structure of the circuit model itself can be used to relate the circuit elements to actual physical processes. As previously shown [*29*], Circuits 2 and 3 can model the same spectrum having two relaxation time constants when the ratio of the constant phase elements (capacitances) associated those time constants differs by several orders of magnitude. As shown in Fig. 5, the capacitances associated with the two time constants in the inhibited system differ by four orders of magnitude (10^{-6} F/cm^2 versus 10^{-2} F/cm^2). Figure 6 shows the results in Bode format of a regression using Circuit 3 against the same spectral data as in Fig. 3. Figures 3 and 6 are identical. Table 3 shows the circuit elements as estimated by regression analysis for the two models. All comparable circuit elements are similar. More important, the resistances used for the corrosion rate estimate (1.3×10^4 Ω-cm^2) are the same. *Thus, either model could have been used to extract that information necessary for both corrosion rate estimation and the previous mechanistic discussion.* This observation implies that agreement between corrosion rates as estimated from mass loss and as estimated from impedance results is at most a necessary but definitely not a sufficient condition for the chosen model to be the only valid representation of the corrosion process. Care must be exercised when trying to use only

TABLE 3—*Comparison of circuit elements estimated from Circuits 2 and 3 in Fig. 1*.*

Element	Circuit 2	Circuit 3
R_s-Solution Resistance, Ω-cm^2	4.86×10^1	4.23×10^1
R_1-High Freq. Resistance, Ω-cm^2	2.02×10^2	2.00×10^2
R_2-Low Freq. Resistance, Ω-cm^2	1.34×10^4	1.35×10^4
β_1-High Freq. Exponent	9.35×10^{-1}	8.88×10^{-1}
C_1-High Freq. Capacitance, F/cm^2	1.95×10^{-6}	3.66×10^{-6}
β_2-Low Freq. Exponent	4.73×10^{-1}	4.72×10^{-1}
C_2-Low Freq. Capacitance, F/cm^2	8.00×10^{-4}	7.96×10^{-4}

*The calculated circuit elements are for Fig. 3 (Circuit 2) and Fig. 6 (Circuit 3).

circuit models to explain corrosion mechanisms because more than one analogous circuit can model a given spectrum. However, corrosion rates can still often be estimated reliably and conclusions can be made about the corrosion mechanism, even though there is ambiguity in the models used to obtain the polarization resistance.

Acknowledgment

I want to thank J. E. Carrico who ran all of the experiments.

References

[1] Growcock, F. B. and Jasiniki, R. J., *Journal of the Electrochemical Society,* Vol. 136, No. 8, 1989, p. 2310.
[2] Lorenz, W. J. and Kendig, F., *Corrosion Science,* Vol. 21, 1981, p. 647.
[3] Gabrielli, C., Keddam, M., and Takenouti, H., "The Use of AC Impedance Techniques in the Study of Corrosion and Passivity," in *Treatise Material Science,* J. C. Scully, Ed., Academic Press, San Diego, Vol. 23, 1983, p. 395.
[4] Mansfeld, F., Kendig, M. W., and Lorenz, W. J., *Journal of the Electrochemical Society,* Vol. 132, No. 2, 1985, p. 290.
[5] Lorenz, W. J. and Mansfeld, F., *Journal of the Electrochemical Society,* Vol. 139, No. 2, 1988, p. 332.
[6] Juttner, K., Lorenz, W. J., Kendig, M. W., and Mansfeld, F., *Journal of the Electrochemical Society,* Vol. 139, No. 2, 1988, p. 332.
[7] Bonnel, A., Dabosi, F., Deslouis, C., Duprat, M., Keddam, M., and Tribollet, B., *Journal of the Electrochemical Society,* Vol. 130, No. 4, 1983, p. 753.
[8] Duprat, M., Moran, F., and Dabosi, F., *Corrosion Science,* Vol. 23, No. 9, 1985, p. 1047.
[9] Mansfeld, F., *Journal of the Electrochemical Society,* Vol. 132, No. 1, 1985, p. 255 and reply by Bonnel, A., Dabosi, F., Deslouis, C., Duprat, M., Keddam, M., and Tribollet, B., *Journal of the Electrochemical Society,* Vol. 132, No. 1, 1985, p. 256.
[10] Duprat, M., Lafont, M. C., and Dabosi, F., *Electrochimica Acta,* Vol. 30, No. 3, 1985, p. 353.
[11] Silverman, D. C., *Corrosion,* Vol. 46, No. 7, 1990, p. 589.
[12] McGuire, R. E. and Silverman, D. C., "Complementary Use of Laboratory and Plant Tests to Solve Complex Chemical Plant Corrosion Problems," *Corrosion,* Vol. 47, No. 11, 1991, p. 894.
[13] Mahato, B. K., Cha, C. Y., and Shemilt, L. W., *Corrosion Science,* Vol. 20, 1980, p. 421.
[14] El Din, A. M., Shams, El Din, A. M. K. Tag, and El Sum, E. A., *Metaux: Corrosion-Industrie,* Vol. 63, No. 752, 1988, p. 123.
[15] Silverman, D. C., *Corrosion,* Vol. 44, No. 1, 1988, p. 42.
[16] Silverman, D. C. and Carrico, J. E., *Corrosion,* Vol. 44, No. 5, 1988, p. 280.
[17] Kuznetsov, Y. I. and Popkov, Y. A., *Zhurnal Prikladnoi Khimii,* Vol. 63, No. 5, 1990, p. 1042.
[18] Silverman, D. C., *Corrosion,* Vol. 40, No. 5, 1984, p. 220.
[19] Boukamp, B., "Equivalent Circuit (EQUIV.PAS)," Version 3.97 with (80)2(87) Support, 1989.
[20] Mansfeld, F., "The Polarization Resistance Technique for Measuring Corrosion Currents," in

Advances in Corrosion Science and Technology, M. G. Fontana and R. W. Staehle, Eds., Vol. 6, Ch. 3, Plenum Press, New York, 1976, p. 163.

[*21*] John, D. G. and Dawson, J. L., *Journal of Electroanalytical Chemistry*, Vol. 110, 1980, p. 37.

[*22*] *International Critical Tables*, Vol. 3, McGraw-Hill Book Co., New York, 1928, p. 257.

[*23*] Eisenberg, M., Tobias, C. W., and Wilke, C. R., *Journal of the Electrochemical Society*, Vol. 101, No. 6, 1954, p. 306.

[*24*] Kendig, M. and Scully, J. R., *Corrosion*, Vol. 46, No. 1, 1990, p. 22.

[*25*] *Handbook of Physics and Chemistry, 59th ed.*, R. C. Weast, Ed., 1978, p. E58–E61.

[*26*] Koehler, S., Bilz, H. J., and Gast, R., *Chemische Technik (Leipzig)*, Vol. 42, No. 6, 1990, p. 245.

[*27*] Sullivan, P. and Yeoman, A., "Performance and Mechanism of Cooling Water Programs Based on Hydroxyphosphonic Acid (HPA)," Paper 45, International Water Conference, Pittsburgh, PA, 1988.

[*28*] Neagle, W., "Hydroxy Phosphono Acetic Acid (HPA)—A Mechanistic Investigation of Corrosion Inhibition Under Cooling Water Conditions," Paper 568, *CORROSION/91*, Cincinnati, OH, March 11–15, 1991.

[*29*] Silverman, D. C., *Corrosion*, Vol. 47, No. 2, 1991, p. 87.

Stanley T. Hirozawa[1] *and David E. Turcotte*[1]

Use of Electrochemical Noise in the Study of Inhibitor Systems: Part I—The Effect of Silicate Polymerization on the Inhibition of Aluminum

REFERENCE: Hirozawa, S. T. and Turcotte, D. E., "**Use of Electrochemical Noise in the Study of Inhibitor Systems: Part 1—The Effect of Silicate Polymerization on the Inhibition of Aluminum,**" *Electrochemical Impedance: Analysis and Interpretation, ASTM STP 1188,* J. R. Scully, D. C. Silverman, and M. W. Kendig, Eds., American Society for Testing and Materials, Philadelphia, 1993, pp. 205–219.

ABSTRACT: Electrochemical noise appearing in corrosion potential (E_{corr})–time plots and electrochemical impedance (EI) spectra were used to study the synergism between nitrate and different silicates in the inhibition of aluminum. Individually, nitrate and some of the silicates did not protect aluminum; however, by combining them, the protection was greatly enhanced as deduced from the reduction of noise and the elevation of both E_{corr} and polarization resistance (R_p). The SiO_2 to Na_2O ratio (R) had a significant influence on the reaction of a silicate with aluminum. This was attributed to the amphoterism of aluminum as well as the polymerization of the silicate.

Unstable protective films are probably the cause of electrochemical noise. It then follows that the elimination or reduction of noise would indicate improvement in the protectiveness of a film. Thus, noise reduction in E_{corr}–time plots and EI spectra complements the elevation of E_{corr} and R_p as tools in the improvement of inhibitor interaction with metal surfaces.

KEYWORDS: electrochemical impedance spectroscopy (EIS), corrosion potential, electrochemical noise, silicate, nitrate, inhibitors, aluminum, polymerization

Numerous inhibitors raise the breakdown potential (E_b) of aluminum, but only nitrate was found to raise its protection potential (E_{prot}) [*1*]. E_{prot} was found to be the true pitting potential (E_{pit}) of aluminum in a given medium. Nitrate is very effective in preventing the localized corrosion of aluminum. However, it cannot protect aluminum under physically depassivating processes, e.g., cavitation, sand abrasion, and nucleate boiling. These processes occur in automotive cooling systems. Silicate was found to be very synergistic with nitrate under these depassivating conditions. However, in the absence of nitrate, silicate is incapable of protecting against the depassivating processes occurring in the cooling system.

In the past decade, we have witnessed the rapid development of applied electrochemical impedance spectroscopy (EIS), thanks to the work of Epelboin, Mansfeld, Lorenz and others [2–5]. We decided to use EIS to explore the observations described in the previous paragraph.

[1]Senior research associate and research chemist, respectively, BASF Corporation, Wyandotte, MI 48192.

Chemical Properties of Aluminum

The potential-pH diagram of aluminum is given in Fig. 1 [*6*]. The large separation of the immunity boundary from Line a implies that bare aluminum can displace hydrogen from water at all pH's. However, at around neutral pH, it is passivated due to the formation of Al_2O_3.

$$2Al^\circ + 3H_2O \rightarrow Al_2O_3 + 3H_2 \tag{1}$$

Aluminum may also be oxidized directly by oxygen.

$$4Al^\circ + 3O_2 \rightarrow 2Al_2O_3 \tag{2}$$

The rate of corrosion of aluminum is controlled by the rate of hydrolysis of the oxide [*7*].

$$Al_2O_3 + 3H_2O \rightarrow 2Al(OH)_3 \tag{3}$$

The corrosion regions in the acidic and basic media in Fig. 1 imply that the corrosion products are amphoteric.

$$Al(OH)_3 + 3OH^- \rightleftarrows Al(OH)_6^{-3} \tag{4}$$

$$Al(OH)_3 + 3H^+ \rightleftarrows Al^{+3} + 3H_2O \tag{5}$$

The number of hydroxyl groups per aluminum atom can vary from 0 to 6 depending on the pH. Potential-pH diagrams are based on thermodynamic data and give no kinetic information. From the consideration of practicality, we have found that passivation current-pH ($i_{pass'n}$-pH) curves are extremely useful, particularly for aluminum [*8*]. An example of such a curve is given in Fig. 2 for 3003 Al in an aqueous solution containing 1% borax and 0.5% $NaNO_3$ at room temperature. The passive region is extended to lower pH by nitric acid but the aluminum is vulnerable above pH 8. The breakpoint of the curve, pH 8 in this case, will be referred to as the critical pH. When the temperature is raised to 82.2°C, the critical pH is lowered to 7. The data in this graph was obtained from galvanostaircase polarization [*9*] (see also ASTM G100, Method for Conducting Cyclic Galvanostaircase Polarization).

Chemistry of Silicates

Silicates are manufactured by fusing silica with sodium carbonate using a silica to sodium oxide weight ratio (R) of 3.2.

$$3.2\ SiO_2 + Na_2CO_3 \rightarrow Na_2O(SiO_2)_{3.2} + CO_2 \tag{6}$$

This product will be referred to as 3.2R silicate. The 3.2R glass is treated with appropriate amounts of caustic and dissolved in water to make the other silicates: 1.0R, 1.8R, 2.0R, 2.5R, and 3.2R. Generally, the manufacture of lower-ratio glasses is avoided because the high caustic content wears down the fusing vessels although 2.0R glass may be prepared to be converted to 1.0R.

Silicic acid is a weak acid where $pK_{a1} = 9.4$. When the pH drops below ~10, polymerization commences.

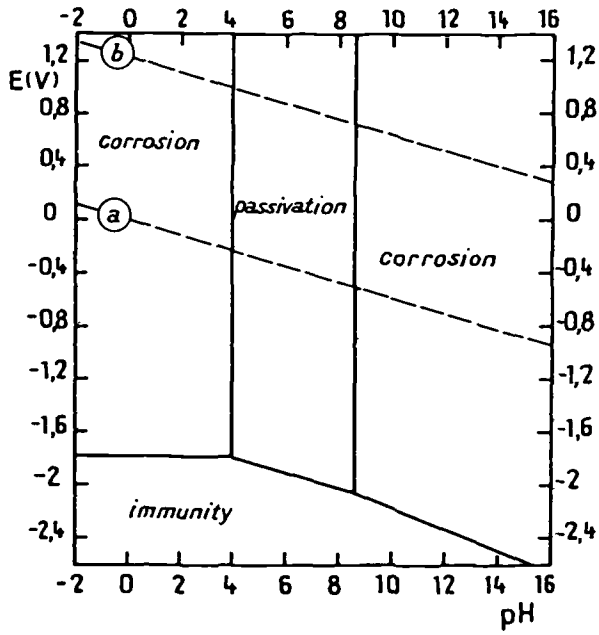

(*a*) Passivation by a film of hydrargillite $Al_2O_3.3H_2O$.

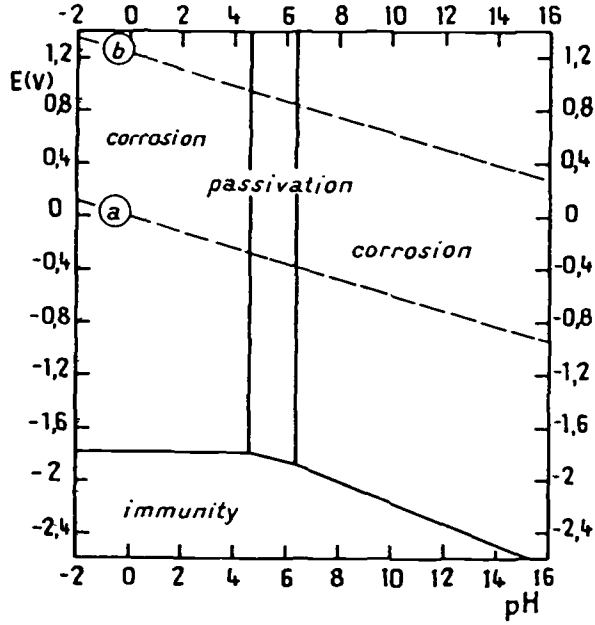

(*b*) Passivation by a film of böhmite $Al_2O_3.H_2O$.

FIG. 1—*Theoretical conditions of corrosion, immunity, and passivation of aluminum at 25°C.*

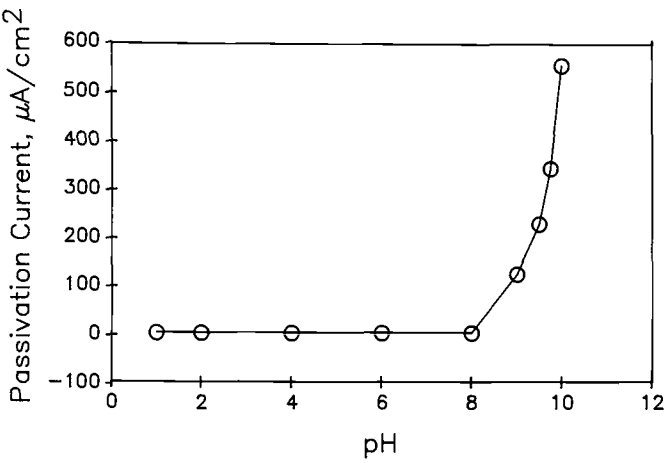

FIG. 2—$i_{pass'n}$-*pH curve for aluminum in 0.5% $NaNO_3$ and 1% borax.*

$$n\ HOSiOOH \rightarrow H(OSiO)_nOH + nH_2O \quad (7)$$

The n value can be very large in the planar polymers, but in solutions, geodesic spheres form with a definite n, e.g., 15 is commonly reported [*10*].

Objective

With the knowledge that the amphoterism of $Al(OH)_3$ and the polymerization of silicate are directly related to pH, the objective of this study was to explore the interaction of aluminum with silicate as a function of R and pH using electrochemical noise and E_{corr} and EIS data.

Experimental Procedure

Materials

Reagent grade sodium chloride, sodium nitrate, and sodium metasilicate were used. Silicates with R of 1.8, 2.0, 2.5, and 3.2 were obtained commercially as specially filtered solutions containing 37 to 44% solid; henceforth, these materials will be referred to as 1.8R, 2.0R, 2.5R, and 3.2R silicates. Distilled water was used to prepare all solutions.

Equipment

Keithley Model 616 and 614 digital electrometers were used to measure the corrosion potentials which were recorded on a two channel Houston Instrument recorder. For EIS, the Solartron 1255 frequency analyzer/EG&G PARC Model 273 Potentiostat/Galvanostat combination was used. The experiments were run by the EG&G PARC Model 388 software and the modeling and graphics were carried out using the Boukamp [*11,12*] software.

The test cell consisted of a 500-mL flat-bottomed beaker as described in Refs *1* and *8* except that the silver/silver polysulfide reference electrode [*13*] was substituted for the saturated calomel electrode (SCE). The working electrode was 3003-H14 (UNS A93003) Al in sheet form. 1.5-cm-diameter circles were cut and prepared according to ASTM G1, Recommended Practice for Preparing, Cleaning, and Evaluating Corrosion Test Speci-

mens, using 600 grit diamond slurry on a flat lapping machine by Metal Samples Co. and used without further preparation. The specimens were mounted in flat specimen holders [*13*] where 1 cm^2 was exposed to the solution. The counter electrode was a pair of ultrafine grade graphite rods.

Procedure

Prepare the solution in the cell and attach it to the cell cover which has provisions for the electrodes and thermocouple. Connect the positive lead of the electrometer to the working electrode, the negative lead to the reference electrode, and start recording. Turn on the magnetic stirrer and the heater. After the temperature stabilizes at 82.2°C (180°F) for 15 min, remove any gas bubbles that might be adhering at the TEFLON-WE-solution interface and turn off the stirrer. Start EIS at E_{corr} 5.5 h after the heater is turned on. The 5.5-h immersion time allowed E_{corr} to stabilize (for the inhibited system but not necessarily for the uninhibited systems).

Results and Discussion

Corrosion Potential-Time Plots

Curve A in Fig. 3 is the E_{corr}-time plot for **aluminum in 165 ppm NaCl** at room temperature. The curve is noise-free except for the first 15 min. When the temperature is raised to 82.2°C (180°F) (see Curve B), noise appears with 10 mV peak-to-peak short period noise superimposed on a long period 120 mV peak-to-peak noise with a period of 12 to 14 min and with round tops and pointed bottoms. The selected inhibitor must form a protective film that will overcome this noise at the elevated temperature. This noise is suggestive of the instability of the oxide/hydroxide film. All of the remaining experiments were carried out at 82.2°C.

Curve A in Fig. 4 is the reference for 165 ppm NaCl (same as curve 3B). Curve 4B was obtained in 0.25% **$NaNO_3$ in the absence of NaCl.** There is long term instability and the short period noise increases after about 3 h. **$NaNO_3$ in the presence of NaCl** (Curve C)

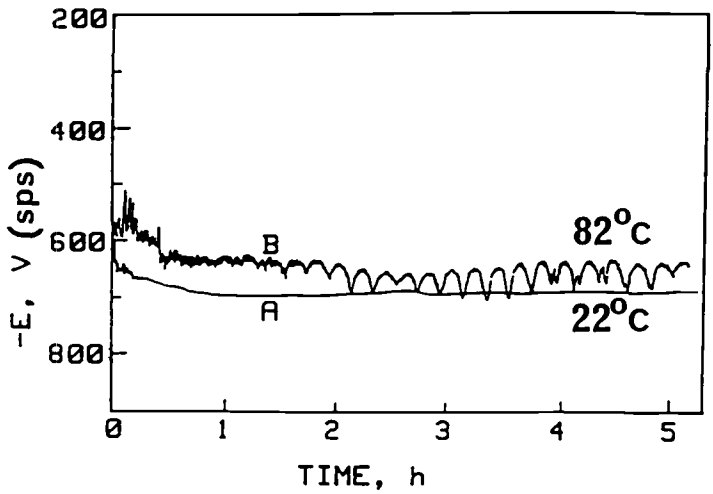

FIG. 3—*E_{corr}-time plots of aluminum in 165 ppm NaCl.* (a) *22°C.* (b) *82°C.*

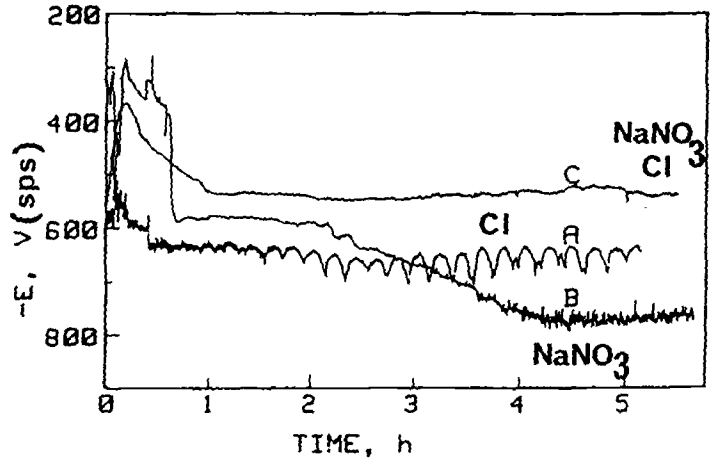

FIG. 4—*E_{corr}-time plots of aluminum at 82°C.* (a) *165 ppm NaCl.* (b) *0.25% $NaNO_3$.* (c) *165 ppm NaCl/0.25% $NaNO_3$.*

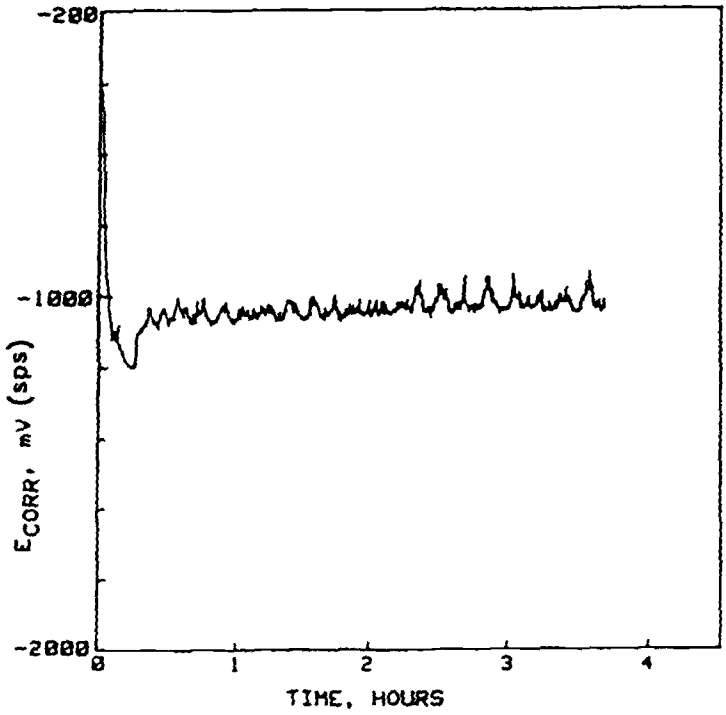

FIG. 5—*E_{corr}-time plot of aluminum in 1.0R (0.0566% SiO_2).*

shows an unexpected synergism that is indicated by the lessening of the noise and elevation of E_{corr}.

Figure 5 was obtained from aluminum in 0.2% **$Na_2SiO_3 \cdot 5H_2O$ in the absence of NaCl.** The metasilicate will be referred to as 1.0*R*. All of the silicate solutions in this study contained 0.0566% SiO_2 to enable comparisons. The large noise and low E_{corr} indicate that 1.0*R* cannot protect aluminum even in the absence of chloride. When **NaCl is added to 1.0*R*,** instead of synergism, the instability of the "protective" film worsens as shown by Fig. 6. When **$NaNO_3$ is added to Na_2SiO_3/NaCl,** E_{corr} is raised by about 500 mV but there is large, long period noise which diminishes somewhat when the immersion time goes beyond 2 h (Curve 7B). But note that the short-term noise has been eliminated.

In Figure 7, Curve A was obtained in 1.8*R* silicate/$NaNO_3$/NaCl medium. Note the great improvement over Curve B. The 1.8*R* silicate eliminated the noise and raised E_{corr} about 230 mV. The 2.0*R* silicate gave completely noise-free curves even in the absence of nitrate while the 2.5*R* and 3.2*R* silicates were noisy at first, and then quieted down slightly (not shown here).

EIS

Figure 8 gives the EIS Nyquist plot for aluminum in 165 ppm NaCl. The large noise agrees with Fig. 3*b*. It appears that Cl^- at elevated temperatures destroys the oxide film. This data set is plotted in Fig. 9 in the Bode format. Both the log $|Z|$ and phase angle plots show the noise, but the linear Nyquist plot gives a much greater emphasis to the noise. Henceforth, the Nyquist plot will be used. Nitrate in the absence of chloride gave a noisy Nyquist plot (see Fig. 10). When **$NaNO_3$ is added to the NaCl,** the resulting Nyquist plot is

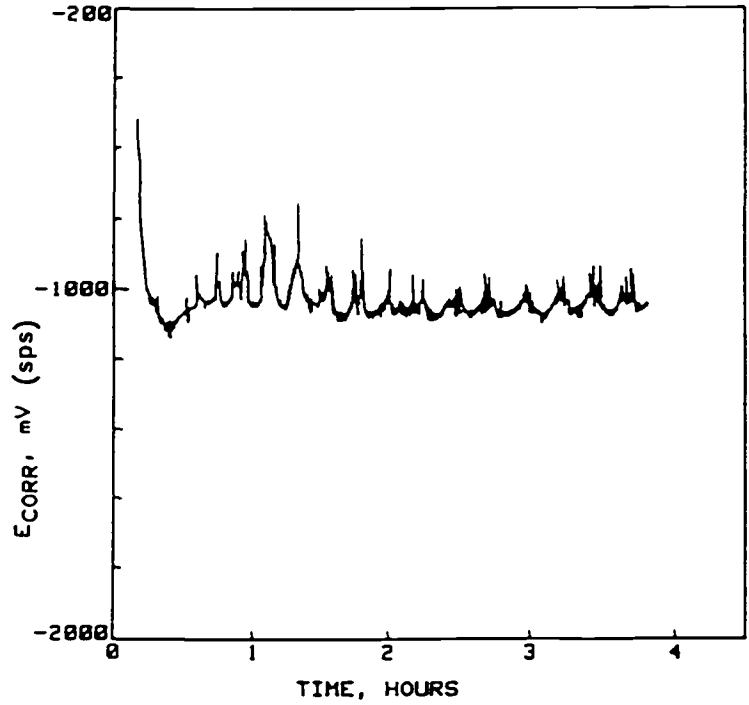

FIG. 6—*E_{corr}-time plot of aluminum at 82°C in 165 ppm NaCl/1.0R (0.0566% SiO_2).*

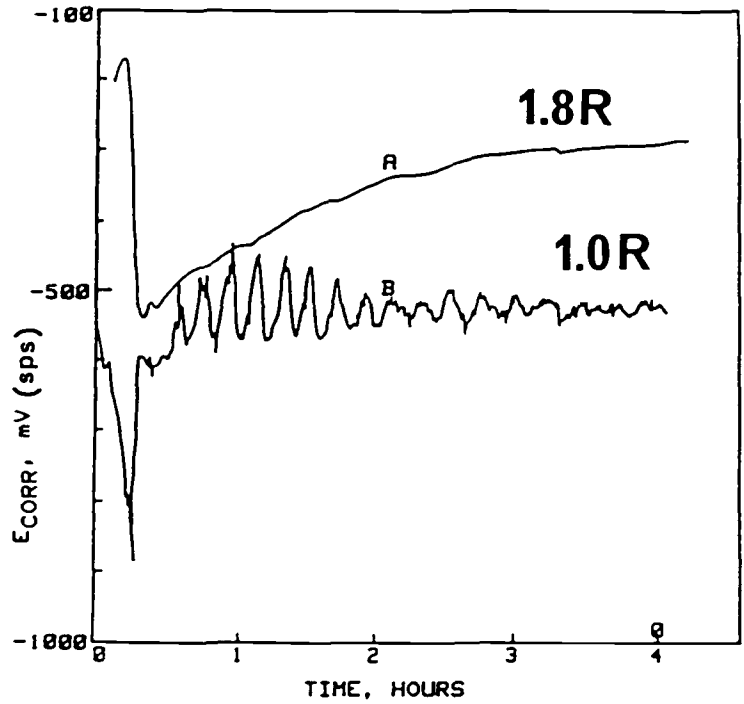

FIG. 7—*E_{corr}-time plots for aluminum at 82°C.* (a) *1.8R (0.0566% SiO_2)/0.25% $NaNO_3$/ 165 ppm NaCl.* (b) *1.0R (.0566% SiO_2)/0.25% $NaNO_3$/165 ppm NaCl.*

given in Figure 11*a*. Note that much of the noise in the critical semicircle region is eliminated. This corroborates the synergism shown by the E_{corr} recordings of Fig. 4.

Figure 12 gives the Nyquist plot for 1.0*R* system. There appear to be two time constants. The first time constant with R_p of about 100 Ω-cm^2 probably indicates that the barrier layer is very thin. The inability of the second semicircle to develop probably

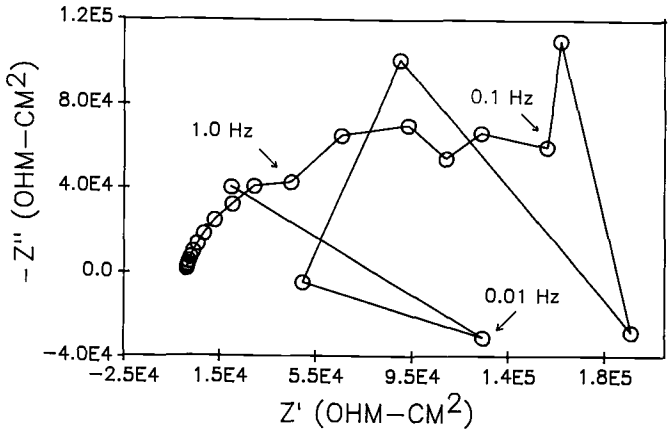

FIG. 8—*EIS Nyquist plot for aluminum in 165 ppm NaCl at 82°C.*

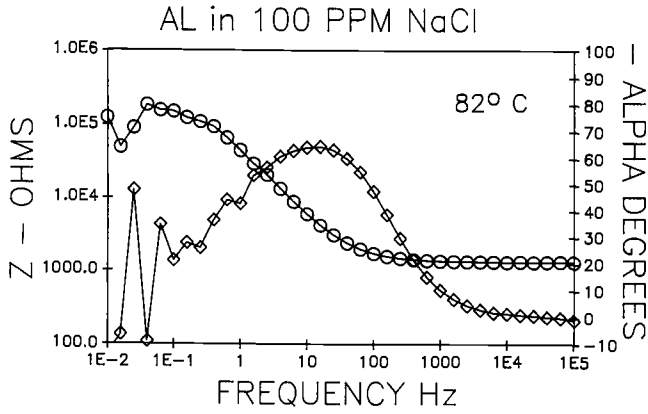

FIG. 9—*EIS Bode plots for aluminum in 165 ppm NaCl at 82°C.*

indicates that a stable Al silicate layer cannot form under the present conditions. When **$NaNO_3$ is added to the NaCl/1.0*R*** system (see Fig. 11*b*), most of the noise is eliminated and the R_p is increased about a one hundred-fold. However, a R_p of 4×10^4 Ω-cm^2 implies inadequate corrosion protection since the R_p's of commercial coolants range from 1×10^5 Ω-cm^2 to 1×10^6 Ω-cm^2. In most silicate studies with nitrate, the result of the synergistic pair is greater than both of the individual results. In the present case, the R_p for $NaNO_3$ is greater than the R_p for $NaNO_3/Na_2SiO_3$ as shown in Fig. 11. Therefore, nitrate and metasilicate are antisynergistic in the presence of chloride at elevated temperature.

Figure 13 shows the effect of R on the Nyquist plots of the silicates in the absence of nitrate. 1.0R is so poor that it does not show up at this sensitivity. 2.5R and 3.2R are rather noisy and the R_p's are too low. 1.8R and 2.0R both are noise-free, which means that they are laying down a protective film, but 2.0R seems definitely superior. It appears that a significant change has occurred between 2.0R and 2.5R. This is corroborated by the E_{corr}-time plots shown in Fig. 14. The 2.0R plot is very smooth while the 2.5R plot is very noisy. The R_p values estimated from Fig. 13 are plotted in the lower curve in Fig. 15. The upper

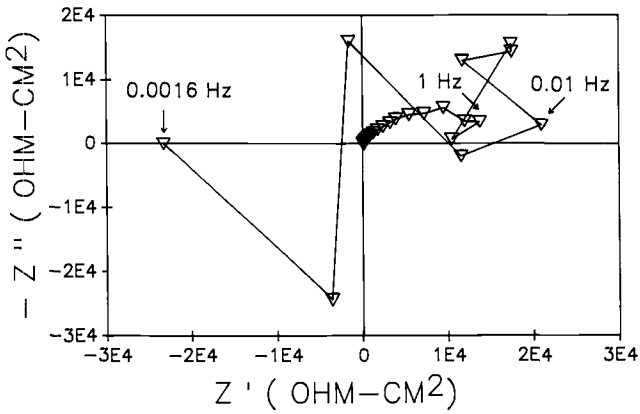

FIG. 10—*EIS Nyquist plot of aluminum in 0.25% $NaNO_3$ at 82°C in absence of chloride.*

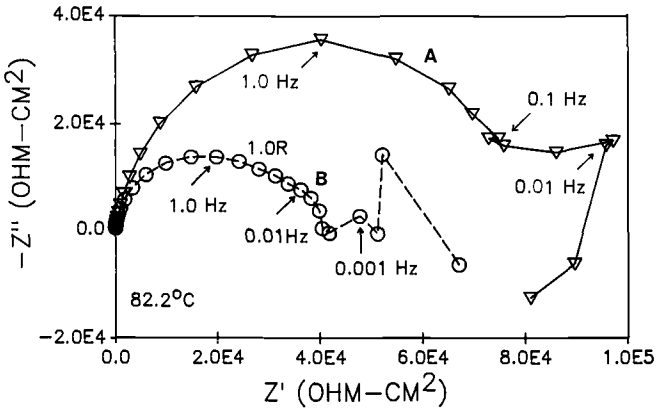

FIG. 11—*EIS Nyquist plots of aluminum at 82°C.* (a) *165 ppm NaCl/0.25% $NaNO_3$.* (b) *0.01% NaCl/0.25% $NaNO_3$/1.0R (0.0566% SiO_2).*

curve shows that nitrate is synergistic with all of the silicates but the synergism is greatest for 2.0*R*.

Modeling and electron microscopic studies have been omitted from this paper because they were discussed in Ref *16*.

Effect of Silicate Polymerization on Corrosion Inhibition

Figure 16 gives the pH as a function of *R*. Open triangles represent solutions without nitrate; these are the natural pH for the respective silicates (at 0.0566% SiO_2) and they are expected to maintain the extent of polymerization. At 1.0*R* the silicate species are metasilicate monomers, at 2.0*R* dimers, and at >2.4*R* geodesic spheres containing 15 SiO_2 groups [*11*]. The poor performance of 1.0*R* is due to the fact that it has exceeded its critical pH (see Fig. 2).

There are two reasons for the good performance of 2.0*R*. First, the pH is in the passive region of the $i_{pass'n}$-pH curve, and second, the dimers can attach to the outer $Al(OH)_3$ layer

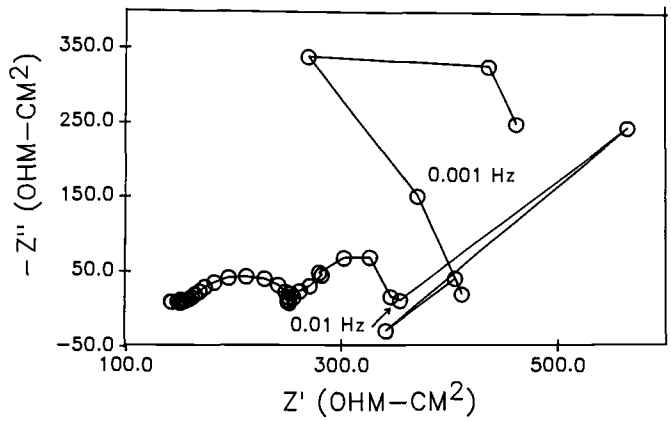

FIG. 12—*EIS Nyquist plot of aluminum in 1.0R (0.0566% SiO_2)/165 ppm NaCl at 82°C.*

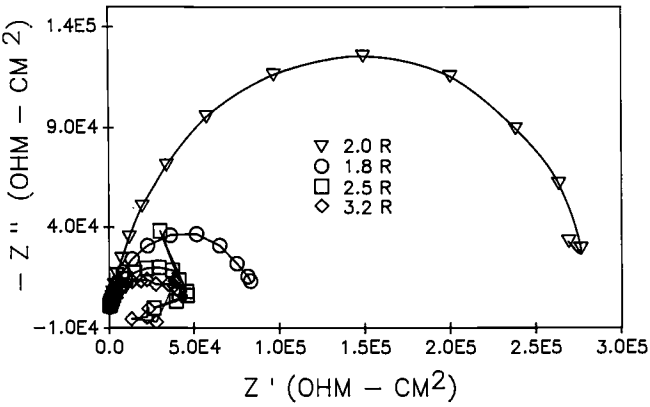

FIG. 13—*EIS Nyquist plots of aluminum at 82°C in 165 ppm NaCl containing 0.0566% SiO_2 as: 2.0R, 1.8R, 2.5R, and 3.2R.*

by chelating the aluminum. Since $Al(OH)_4^-$ is geometrically similar to $Si(OH)_4$, the ion can be inserted or exchanged into the silicate structure thus creating an aluminosilicate site having fixed negative charge. It is quite likely that aluminum and silicon are forming a planar structure as illustrated in Fig. 17*a* [*10*]. The high negative charge facing the solution is preventing the chloride from entering the domain of the inner oxide layer as deduced from the noise-free E_{corr}-time and EI curves.

The noise in both the E_{corr}-time and EI curves as well as the low R_p's for 2.5*R* and 3.2*R* can be explained in the following manner. The packing of the geodesic spheres (see Fig. 17*b*) on to the aluminum surface is expected to be much less efficient than forming the planar structure. About twice the amount of silicate compared to 2.0*R* would be required to cover the entire surface and the chloride can pass through the spaces between the spheres. Phosphate which is often used in conjunction with silicate probably serves as "mortar" to fill up these cracks.

The closed triangles in Fig. 16 show the effect of nitrate on the pH of the silicates. The pH is elevated at the higher *R*'s. It was interesting to note that at 1.8*R* and above, nitrate

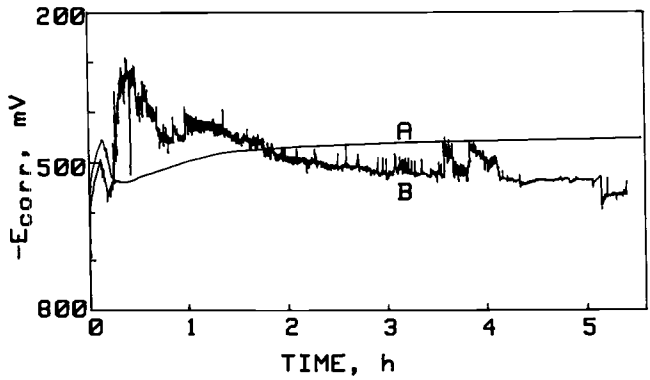

FIG. 14—*E_{corr}-time plots of aluminum at 82°C in 165 ppm NaCl containing 0.0566% SiO_2 as:* (a) *2.0R and* (b) *2.5R.*

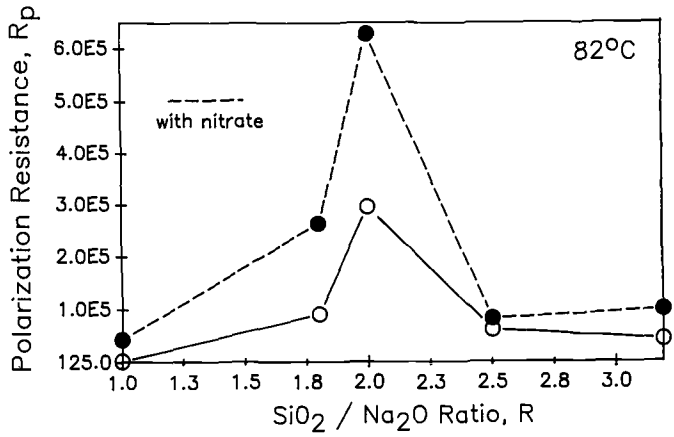

FIG. 15—*Dependence of R_p on R and nitrate.*

increased the noise in the E_{corr}-time curves and EI spectra and synergism was insignificant. It could be that the expected synergism was counteracted by the rise in pH beyond the critical point (see Fig. 2). The significant synergism for 1.8*R* and 2.0*R* observed in Fig. 15 was obtained by dropping the pH to the original pH.

The rate of polymerization of silicates upon lowering the pH is rapid. For example, when the pH of 1.0*R* is brought down to the level of 2.0*R*, the electrochemical behavior is identical to the latter. When the pH is brought down further below 10, the behavior is the same as for 2.5*R* and 3.2*R*. The reverse process, i.e., depolymerization of the polysilicates by raising the pH is very slow. The Si–O–Si bond is hard to break in solution and this difficulty is multiplied by the geodesic structure of the polysilicate. An analogy from the polymolybdate chemistry can be cited. The Mo–O–Mo bond is said to decompose in basic solution [*14*]. When these bonds found in the geodesic spheres of heteropoly 12- and 18-molybdates were refluxed at pH 10 to 10.5 for two months, their effectiveness as inhibitors was not diminished to the level of the inferior molybdates [*15*]. This proved that the geodesic structure enhanced the stability of the Mo-O-Mo bond and the same should hold true for the Si–O–Si bond in a geodesic sphere.

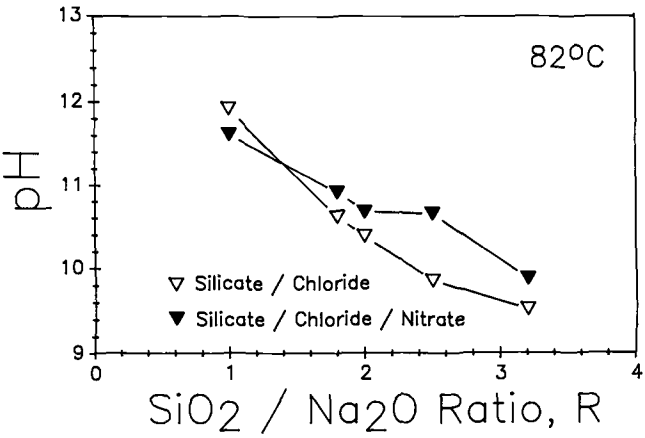

FIG. 16—*Dependence of pH on R and nitrate.*

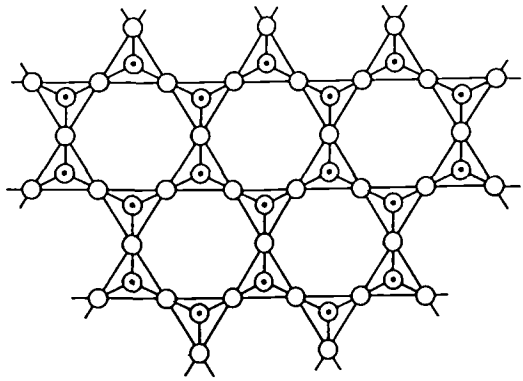

A. Sheet silicate anion structure idealized. [For a real example see A. K. Pant *Acta Cryst., B*, 1968, 24, 1077.]

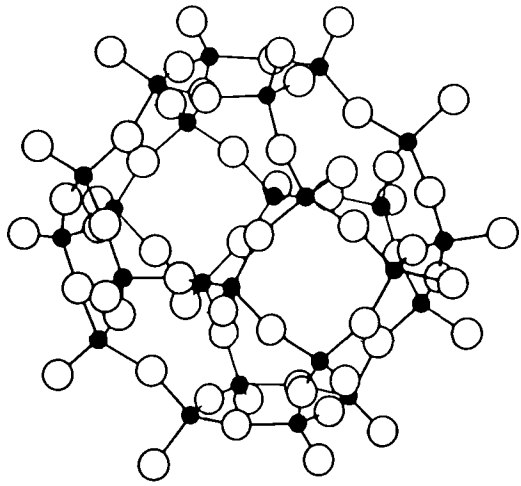

B. The arrangement of AlO_4 and SiO_4 tetrahedra which gives the cubo-octahedral cavity in some zeolites and felspathoids. • represents Si or Al.

FIG. 17—*Structure of polysilicates.* (a) *planar.* (b) *geodesic sphere.*

Requirements of a Good Inhibitor System

A good inhibitor system for aluminum must be able to maintain the Al_2O_3 inner barrier layer and also form a tough outer layer that can withstand the depassivating processes described earlier. Nitrate was found to be the only inhibitor that satisfied all of the requirements of a model of an inhibitor of localized corrosion of aluminum [*1*]. Silicate can form a tough outer layer but the toughness depends on the R value as well as on the presence of a sturdy foundation of Al_2O_3 provided by nitrate [*16*].

Reference Electrode

An attempt was made to use SCE as the reference. At the elevated temperature, gas bubbles formed in the Luggin capillary which caused large noise followed by break in the circuit. The silver/silver chloride electrode was not used because of its instability at high temperature as well as chemical instability where chloride can be replaced by anions that form silver salts more insoluble than AgCl, e.g. mercaptans and H_2S. The silver polysulfide electrode was immersed in the test solution and provided a stable anchor for many of the overnight experiments. Seven reference electrodes averaged −40 mV versus saturated calomel in 0.1M KCl at room temperature. The preparation and properties of this reference electrode are described elsewhere [*13*].

Conclusion

Noise occurring in E_{corr}-time plots and EI spectra was successfully applied in studying synergistic/antisynergistic behavior among potential inhibitors for aluminum. Chloride causes localized corrosion while nitrate can prevent localized corrosion in the presence of chloride. Synergism between nitrate and silicate depends on the SiO_2/Na_2O ratio (R). Low R (1.0) causes the medium to surpass the critical pH resulting in excessive corrosion in the absence of nitrate, while in the presence of nitrate, only a minor degree of synergism is observed. High R (>2.3) causes the formation of large geodesic spherical polysilicates that are cumbersome and have difficulty forming a good protective film, and synergism with nitrate is minimal. Maximum synergism with nitrate is observed at $2.0R$ and $1.8R$; moreover, even in the absence of nitrate they seem able to lay down protective films that appear to prevent the penetration of the oxide layer by chloride.

Acknowledgment

The authors are grateful to Dr. John Conville, BASF Corporation, for many useful discussions.

References

[*1*] Hirozawa, S. T., "Study of the Mechanism for the Inhibition of Localized Corrosion of Aluminum by Galvanostaircase Polarization," in *Corrosion Inhibition*, R. H. Hausler, Ed., NACE, Houston, TX, 1988, pp. 105–112.
[*2*] Epelboin, I., Keddam, M., and Takenouti, H., *Journal of Applied Electrochemistry*, Vol. 2, 1972, p. 71.
[*3*] Mansfeld, F., *Corrosion*, Vol. 36, 1981, p. 301.
[*4*] Mansfeld, F., Kendig, M. W., and Tsai, S., *Corrosion*, Vol. 38, 1982, p. 570.
[*5*] Lorenz, W. J. and Mansfeld, F., *Corrosion Science*, Vol. 21, 1981, p. 647.
[*6*] Pourbaix, M., *Atlas of Electrochemical Equilibria in Aqueous Solutions*, 2nd Ed., NACE, Houston, TX, 1974.
[*7*] Videm, K., "The Electrochemistry of Uniform Corrosion and Pitting of Aluminum," Kjeller Report, Institute of Atomenergi, 1974.
[*8*] Hirozawa, S. T., "Corrosion Monitoring by Galvanostaircase Polarization" in *Electrochemical Techniques in Corrosion Engineering*, R. Baboian, Ed., National Association of Corrosion Engineers, Houston, TX, 1986.
[*9*] Hirozawa, S. T., *Journal of the Electrochemical Society*, Vol. 130, 1983, p. 1718.
[*10*] Iler, R. K., *The Chemistry of Silica*, Chap. 2, John Wiley and Sons, New York, 1979.
[*11*] Boukamp, B. A., *Equivalent Circuit-Users Manual*, Second Revised Ed., University of Twente, May 1989.
[*12*] Boukamp, B. A., "Non-Linear Least Squares Fit of AC-Impedance Measurements" in *Computer Aided Acquisition and Analysis of Corrosion Data*, M. W. Kendig, U. Bertocci, and J. E. Strutt, Eds., Electrochemical Society, 1985, p. 146.

[*13*] Hirozawa, S. T., "Silver/Silver Polysulfide Reference Electrode," *Journal of the Electrochemical Society*, in publication.

[*14*] Cotton, F. A. and Wilkinson, G., *Advanced Inorganic Chemistry*, Interscience Publishers, New York, 1972, p. 952.

[*15*] Hirozawa, S. T., "Antifreeze Concentrates and Coolants Containing Heteropolymolybdate Compounds," U.S. Patent 4,743,393, May 1988.

[*16*] Hirozawa, S. T. and Turcotte, D. E., "Use of Electrochemical Noise in the Study of Inhibitor Systems for Aluminum" in *Materials Performance Maintenance*, R. W. Revie, V. S. Sastri, M. Elboujdaini, D. L. Piron, P. R. Roberge and P. Mayer, Eds., The Metallurgical Society of the Canadian Institute of Mining, Metallurgy and Petroleum, Vol. 25, 1991, p. 207.

Harvey Hack[1] *and Howard Pickering*[2]

The Influence of Corrosion Product Film Formation on the Corrosion of Copper-Nickel Alloys in Aqueous NaCl

REFERENCE: Hack, H. and Pickering, H., **"The Influence of Corrosion Product Film Formation on the Corrosion of Copper-Nickel Alloys in Aqueous NaCl,"** *Electrochemical Impedance: Analysis and Interpretation, ASTM STP 1188,* J. R. Scully, D. C. Silverman, and M. W. Kendig, Eds., American Society for Testing and Materials, Philadelphia, 1993, pp. 220–236.

ABSTRACT: The corrosion resistance of copper-nickel alloys in seawater is known to be due to the development of a protective corrosion-product film. This study is an attempt to elucidate the reason for the protective nature of these films. A rotating disk electrode was used to study the corrosion product formation on three copper-nickel alloys in aqueous 3.4% NaCl. The three alloys studied were 70-30 copper-nickel (C71500), 90-10 copper-nickel (C72200), and pure copper. Electrochemical impedance spectroscopy (EIS), palladium sputter-coating of the corrosion product, and removal of the outer corrosion product layers with adhesive tape were used to follow the growth of the inner and outer film layers. It is concluded that in copper-nickel corrosion, oxygen reduction occurs at the bottom of pores in the outer corrosion product layers, and the corrosion rate is determined by the diffusion of oxygen through the pore electrolyte to these sites.

KEYWORDS: corrosion resistance, electrochemical impedance spectroscopy (EIS), pore electrolyte, copper-nickel alloys

Until fairly recently, the corrosion mechanism of copper-nickel alloys was not well understood. The formation of a corrosion product film has been found to greatly reduce the corrosion rate of copper alloys. The role of this film in reducing corrosion is unclear, however. The corrosion product of 90-10 copper-nickel is known to consist of a loosely adherent porous layered structure consisting primarily of cupric hydroxychloride over a thin tightly adherent layer of cuprous oxide [*1–4*]. The iron and nickel from the alloy are concentrated in the inner part of the porous layer [*2*]. Until recently, copper-nickel was believed to get its corrosion resistance from nickel doping of the inner cuprous oxide semiconductor layer [*3,4*].

More recently, Kato and Pickering [*1,5*], have developed a more highly supported mechanism for copper-nickel's corrosion resistance, as follows: These authors looked at the effect of stripping of the outer corrosion product layers on anodic and cathodic polarization behavior. Only cathodic polarization was affected by the presence of the corrosion products, indicating a cathodically controlled corrosion process on alloy covered with corrosion products. The low rate of the cathodic reaction, assumed to be oxygen reduction, increased some when the outer porous corrosion product layer was stripped off

[1]David Taylor Research Center, Annapolis, MD 21402.
[2]The Pennsylvania State University, Department of Materials Science and Engineering, University Park, PA 16802.

[5]. Thus the inner cuprous oxide could provide a diffusion barrier to the cathodic reaction [3] as well as being, along with the outer layer, a poor catalyst for the oxygen reduction reaction [1,5].

Palladium coating of the inner layer greatly increased the (oxygen reduction) reaction kinetics to the diffusion limited value, an effect attributed by the experimenters to either electrical shorting through the resistive inner cuprous oxide layer or to an increased catalytic activity of the corrosion product surface for oxygen reduction. These results eliminated the possibility that the effect was due to low ionic conductivity in the corrosion product [1,2]. Kato et al. [6] later proved that the catalytic effect was the correct one by developing a corrosion product film in sulfide-containing solutions. This film showed high oxygen reduction rates, presumably because the sulfide is a good catalyst, but the reaction rate slowed when the loosely adherent layers were removed. This is a good argument in favor of the poor catalytic nature of the porous corrosion product as the basic cause of the good corrosion resistance of the Cu-Ni alloys [5,6]. During the initial formation of the corrosion product layer, this factor is thought to mainly control the corrosion rate. Thereafter, during the growth of the outer porous layer when the corrosion rate further decreases in accord with the parabolic law ($\geq$10 h [1]), slow oxygen diffusion through the pore electrolyte to reduction sites deep in the corrosion-product structure near the inner/outer layer interface is most consistent with the data [1,2,5–7].

The effect of nickel and iron is not understood sufficiently to explain differences in behavior between pure copper, 90-10 copper-nickel, and 70-30 copper-nickel. The present research was designed as a first step in filling gaps in the knowledge about the action of the corrosion product layers on these alloys.

Approach

The metals studied were pure copper, commercial 90-10 copper-nickel, and commercial 70-30 copper-nickel. A rotating disk electrode apparatus was used because of the mathematically well-established and reproducible nature of the flow which this apparatus provides across the specimen surface [8,9]. A base rotation speed of 1000 r/min was used.

The specimen preparation and testing procedures used have been described elsewhere [7]. Briefly, the specimens were polished through 600 grit, then exposed for 28 days (672 h) while rotating in aerated 3.4% sodium chloride solution. Degreasing of specimens was initially performed, but was found to have no significant effect on the results and was therefore discontinued. The specimen was mounted in a plexiglass mount and spun face down. Specimen area was 1.277 cm^2 (0.5 in. diameter). Connection between the specimen and the rotator shaft was accomplished with a spring-loaded contact assembly. Potentials were measured using a saturated calomel half-cell electrode with a Luggin capillary equipped with a Vycor fritted tip. The tip was located just above the plane of specimen rotation and 1 to 3 mm from the edge of the specimen holder. Counter electrodes were densified graphite and were located inside containers separated from the cell electrolyte by porous glass frits. Two counter electrodes were used for current symmetry.

The corrosion rate of the specimen and the corrosion product film properties were studied using electrochemical impedance spectroscopy (EIS) [10]. The applied signal was 10 mV, small enough to have little effect on the corrosion of the specimen as it was being studied. This allowed the time-dependent formation of the corrosion product film to be studied as it occurred. Frequencies used ranged from 10^5 to 10^{-3} Hz. Both swept-sine and Fast Fourier Transform (FFT) techniques were employed, and gave similar results where the frequencies overlapped. The total time required to get data for all frequencies was about 2 h. All data from 100 000 to .01 Hz were obtained in the first 15 min of this interval,

however. Thus, for short (1 to 7 h) exposures the low-frequency data could have been significantly influenced by exposure time effects. These short exposures tended to have all of the significant data occur above .01 Hz, so this effect in practice was minimal. Exposure time effects would be expected to be insignificant over the two-hour measurement period for exposures of 24 h or greater, since the rate of change in the corrosion system decreased with exposure time.

Potentiodynamic polarization curve generation was also used to characterize the corrosion behavior. Cathodic polarization curves were generated in the aerated solution while anodic polarization curves were generated after first deaerating the test cell for one hour with nitrogen or argon. Scans were always conducted from the most electronegative potential to the most electropositive potential at a scan rate of 0.01 $mV\text{-}s^{-1}$ and at a rotation rate of 1000 r/min. Cathodic curves were generated after holding at the starting potential for 10 min to allow for stabilization of the current. Anodic curves were generated after a ten-minute stabilization period at the corrosion potential.

Impedance data were gathered after only a one-hour exposure, when the corrosion resistance imparted by the corrosion product layers presumably was still undeveloped, and after varying periods of time up to 28 days exposure at 1000 r/min, when the corrosion product was presumably well established. After growth of the corrosion product layers for 28 days, impedance measurements were taken at rotation speeds of 500 and 2000 r/min.

A unique method for determining whether the film was limiting the corrosion reaction by (1) having an electrically insulating effect, or (2) affecting the catalysis of the cathodic reaction, is sputter-coating of palladium on the corrosion product surface. Since palladium is a good catalyst for the cathodic reaction (oxygen reduction), but its use on top of the film would not effect film resistance, this technique provides a good method for separating out the relative effects of these two possible rate-limiting steps. After the 28-day testing of each specimen, it was dried, then re-wet and retested to first determine the effect of drying. Although drying the specimens did, in some cases, slightly affect the shape of the impedance curves, this change was small enough to have no bearing on the results reported in the following section. Since the drying effect was usually minimal, the specimens were next dried again, placed in a device to mask off the specimen holder, then sputter-coated with palladium until the surface appeared silvery in color. This usually took three to five minutes at 20 mA current. The specimen was sputter coated at a 45° angle, then reversed and sputter coated at a 45° angle from the opposite direction. This procedure minimized the possibility of plating through cracks in the film, which could result in electrical shorting through the film to the metal surface. After re-wetting the coated specimen and retesting, the loosely adherent layers were stripped off using adhesive tape. This procedure has been shown to remove the outer porous layers of the corrosion products and the palladium layer while leaving intact the inner, tightly adherent layer [*1,2*]. By comparing the data with no film, a full film, and a stripped film (inner layer only), the effect of the various film layers could be studied independently. After stripping off the outer corrosion product layer and the palladium layer, the remaining specimen surface was analyzed for palladium. If palladium had plated through a crack in the corrosion products until it contacted the surface to create an electrical short-circuit through the film, then some palladium should remain on the surface when the outer corrosion product is removed. Analysis was conducted on the 90-10 copper-nickel specimen using energy dispersive X-ray analysis in a dot-mapping mode to detect local areas of palladium concentration. Analyses were also conducted on specimens of the other two materials using a comparatively new technique called energy dispersive X-ray diffraction. Residual palladium on the surface was below the level of detectability for all analyses conducted.

This supports the supposition that the sputter-coated palladium film did not develop an electrical short-circuit through the corrosion product layers to the metal surface.

Results and Discussion

Copper

Figure 1 is a Nyquist plot showing the effect of exposure time on the impedance behavior of copper at 1000 r/min. Each curve for copper exhibits an approximate semicircle indicative of one time constant. The polarization resistance, which is the right-hand intercept of the semicircle with the real axis, increased systematically with exposure time from less than 1 kΩ-cm^2 after one hour up to about 15 kΩ-cm^2 after 670 hours. Figure 2 is a Bode Phase plot showing the phase shift as a function of frequency for a number of exposure durations. The single phase shift peak for most exposure durations indicates that any time constants associated with the corrosion process must be close in frequency. The maximum phase shift is centered at about 500 Hz after one hour, and systematically shifts to lower frequencies as exposure time increases, reaching a value of about 5 Hz after 670 hours of exposure. This shift to lower frequencies is an indication of the increased polarization resistance, and can occur without a shift in interfacial capacitance.

Figures 3 and 4 indicate that a palladium coating over the outer corrosion product layer slightly increases the low frequency intercept on the real impedance axis. This is probably because of the barrier effect of the coating to oxygen diffusion through the layer, although this could also be due to decreased surface roughness of the plated surface. It follows that the corrosion reaction on copper could at least in part be controlled by diffusion through, or catalysis on the surface of, the inner corrosion product layer. Removal of the outer layer has little effect on the polarization resistance. A palladium coating has little effect,

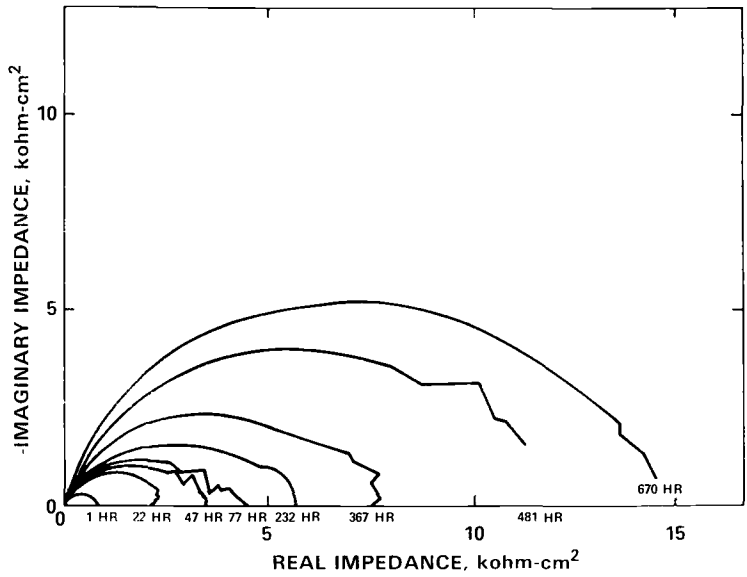

FIG. 1—*Copper Nyquist plot showing effect of exposure duration in aerated 3.4% NaCl solution at 1000 r/min.*

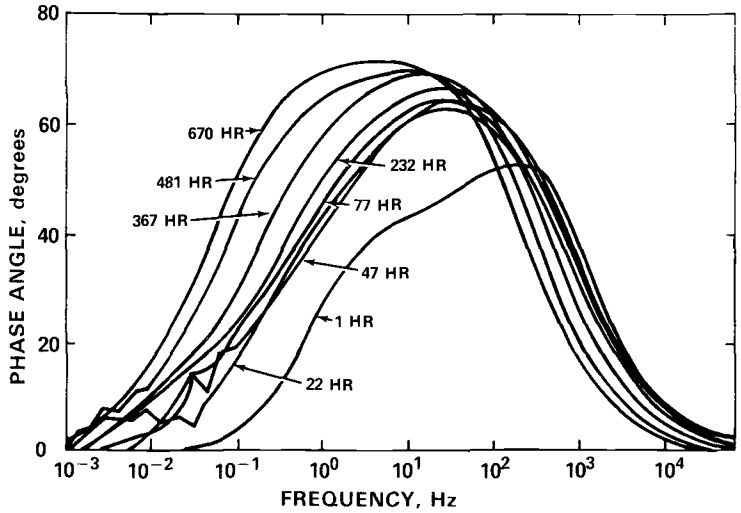

FIG. 2—*Bode phase plot for the data in Fig. 1.*

and stripping of the outer corrosion product also has little effect on the value of the time constant after 670 hours.

Figures 5 and 6 present the results of varying rotation speed on the impedance behavior of copper with a well developed corrosion product film. Changing rotation speed from 1000 r/min to 500 or 2000 r/min had no effect on the behavior of copper in either plot. This indicates that the corrosion reactions are not controlled by diffusion through a fluid boundary layer, but must be controlled by a process on the surface such as diffusion through the corrosion product film, surface adsorption or desorption, or electron exchange on the surface.

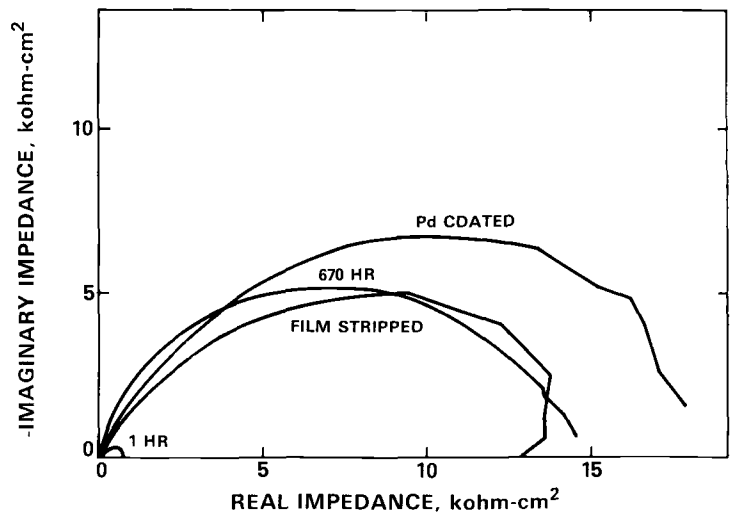

FIG. 3—*Copper Nyquist plot showing effect of palladium coating and stripping of outer layers for the conditions in Fig. 1.*

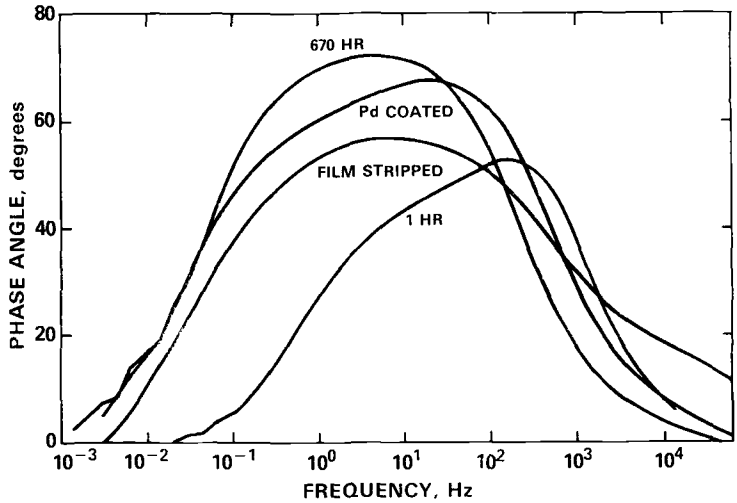

FIG. 4—*Bode phase plot for the data in Fig. 3.*

Figure 7 is a composite of a number of polarization curves generated during the exposure at 1000 r/min in a manner similar to that described in the **Approach** section. The anodic curves can be considered a true representation of the anodic reactions, since deaeration removes interference from the oxygen reduction reaction. The cathodic curves still retain distortion near the corrosion potential due to the presence of significant anodic reactions at this location. If this distortion is not too great, the intersection of the anodic curve with the cathodic curve for the material under the same conditions should still roughly define a current density that can be related through Faraday's Law to the corrosion rate of the material under those conditions. The current density for copper exposed

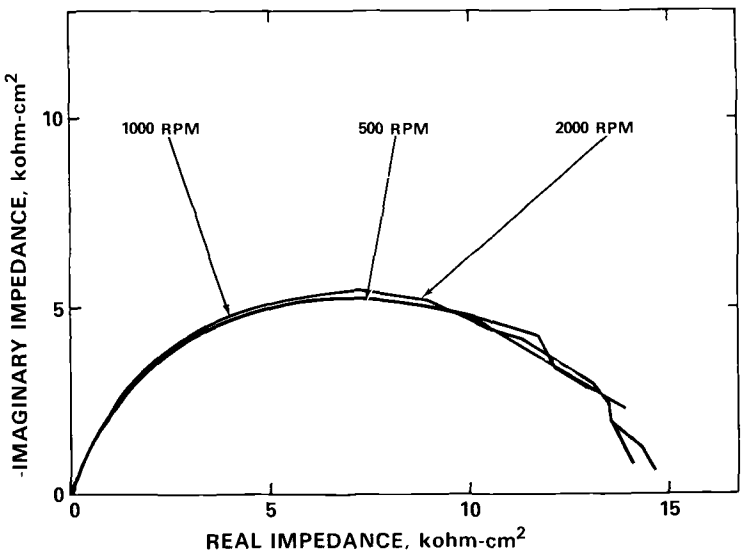

FIG. 5—*Copper Nyquist plot in aerated 3.4% NaCl as a function of rotation speed.*

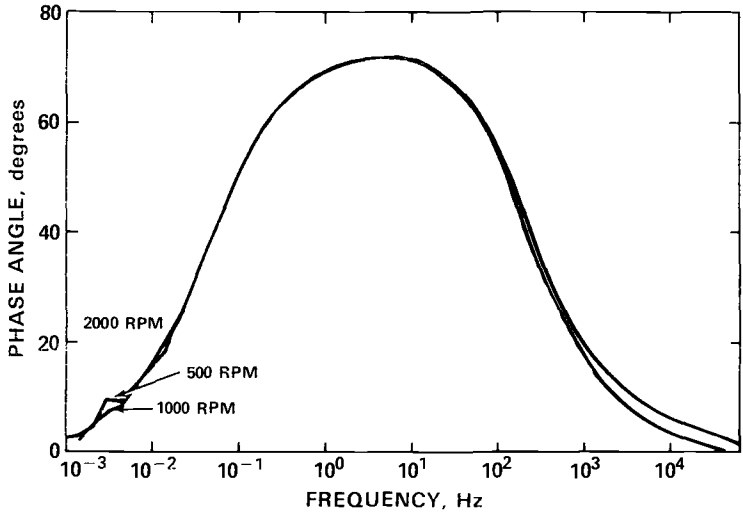

FIG. 6—*Bode phase plot for the data in Fig. 5.*

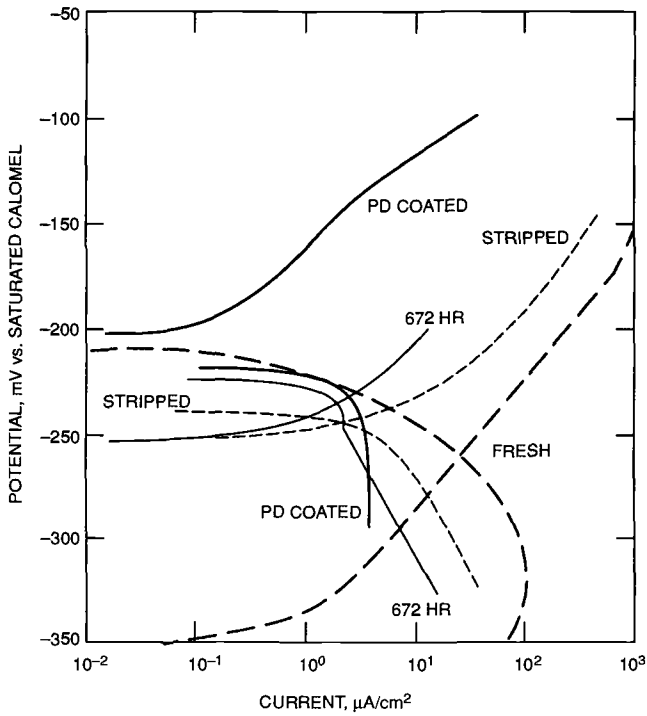

FIG. 7—*Anodic and cathodic polarization behavior in the vicinity of the corrosion potential for copper in 3.4% NaCl at 1000 r/min.*

for 1 h (curve labeled FRESH in Fig. 7) was about 30 $\mu A\text{-}cm^{-2}$, and has a limiting value of cathodic current density of about 100 $\mu A\text{-}cm^{-2}$. The limiting value for cathodic current density based on oxygen diffusion calculated from the Levich Equation [*8*] is about 310 $\mu A\text{-}cm^{-2}$ at 1000 r/min on a disk electrode. All other curves intersect at a value of 2 to 5 $\mu A\text{-}cm^{-2}$. As with the impedance data, this shows that palladium coating or stripping of the outer corrosion product film had little effect on the corrosion rate of copper exposed for 672 h. Notice that 2 to 5 $\mu A\text{-}cm^{-2}$ is equivalent to a corrosion rate of 2 to 5 mils per year. This is very close to the reported corrosion rate range for copper of 1 to 4 mils per year [*11*].

90-10 Copper-Nickel

The data from 90-10 copper-nickel, shown in Figs. 8 and 9, are more complex. Although after one hour a reasonable semicircle is obtained with a polarization resistance of approximately 0.7 $k\Omega\text{-}cm^2$, 240-hour exposures result in corrosion product films that create dramatic increases in impedance, where a low enough frequency cannot be reached for the higher real axis intersection to be seen. This intersection point can thus only be exactly obtained by appropriate mathematical modeling of the data, although a rough estimate indicates a value exceeding 200 $k\Omega\text{-}cm^2$. The shape of the curves at high frequencies indicates a deviation from a semicircular shape. This effect becomes more pronounced with increasing exposure duration. The phase data indicate that a second, low-frequency, phase peak develops at longer exposure times. This indicates that the spectrum is resolvable into two close time constants, suggesting two mechanisms. The second phase peak is centered at a very low frequency, about 0.002 Hz, which is the reason why the lowest frequency used in the test was unable to record a real value of polarization resistance. The phase data verify the appearance of the second time constant after 240 hours of exposure, and a shift in the peak frequency from about 10 Hz after one hour to 30 Hz after 240 hours.

Figures 10 and 11 illustrate the effect of stripping and palladium coating. Stripping of the corrosion product film reduces the polarization resistance to 2 $k\Omega\text{-}cm^2$, a value closer to one-hour exposure values, and removes the second time constant. Thus, the very high resistance and the second time constant appear to be related to the formation of the loosely adherent outer layers. Consequently, these outer layers must be the reason for the good corrosion performance of the 90-10 alloy as compared to copper. Palladium coating prior to stripping also dramatically reduces the polarization resistance and removes the second time constant. Thus, the outer porous layer must be a poor catalytic surface for the oxygen reduction reaction, which is subsequently improved by the palladium coating. The palladium coating greatly increases the exchange current density, and possibly the active area, for the oxygen reduction reaction and removes the need for the (slow) oxygen diffusion process through the porous layer to the more catalytic sites deep in the porous layer structure. This is in agreement with potentiodynamic work performed by other investigators [*1,2,5,6*].

The data as a function of rotation speed for 90-10 copper-nickel are presented in Figs. 12 and 13. The low-frequency peak in this test run occurred at a much higher frequency than that of curves presented in Figs. 9 and 11 for this material; however, the behavior was qualitatively similar. Rotation speed had little effect, indicating that diffusion processes in the bulk electrolyte are not a factor in determining the corrosion rate.

Composite potentiodynamic curves for 90-10 copper-nickel are shown in Fig. 14. These data are consistent with the behavior indicated by the impedance data. The one-hour exposure resulted in a current density of 30 $\mu A\text{-}cm^{-2}$, whereas this corrosion current dropped to around 0.2 $\mu A\text{-}cm^{-2}$ after 672 hours of exposure. This is equivalent to a

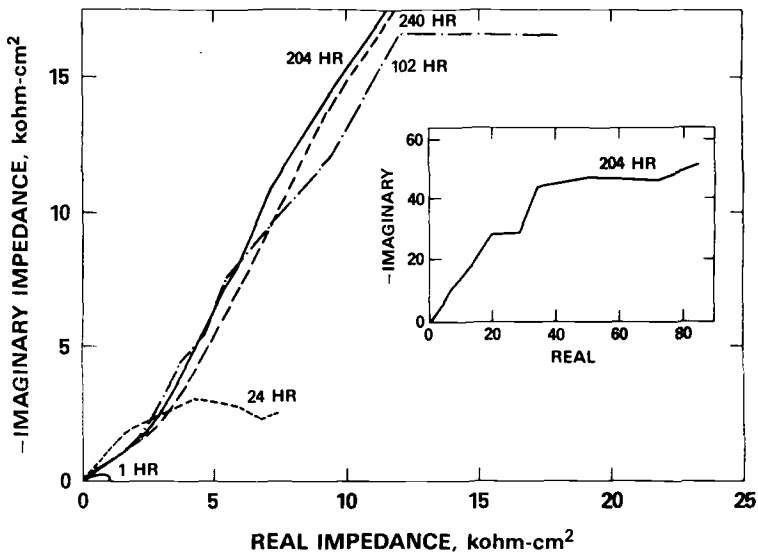

FIG. 8—*90-10 copper-nickel Nyquist plot showing effect of exposure duration in aerated 3.4% NaCl at 1000 r/min.*

corrosion rate of about 0.2 mils per year, which is consistent with the corrosion rates published for 90-10 copper-nickel in seawater [*11*]. Palladium coating increased the current to 3 μA-cm^{-2}, a value approaching that of freshly exposed material, and stripping of the outer layer increased the current slightly more, to 6 μA-cm^{-2}.

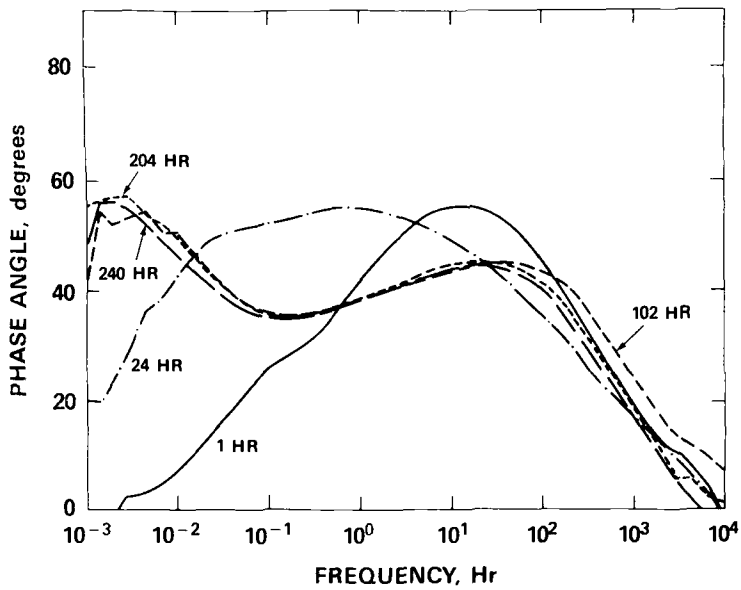

FIG. 9—*Bode phase plot for the data in Fig. 8.*

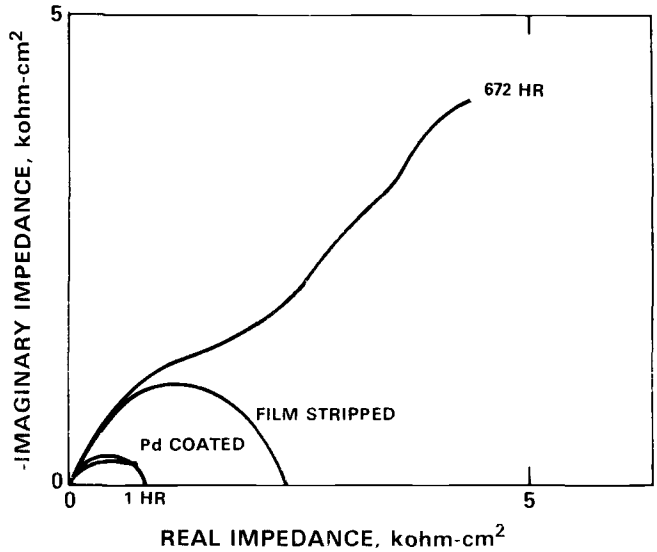

FIG. 10—*90-10 copper-nickel Nyquist plot showing effect of palladium coating and stripping of outer layers for the conditions in Fig. 8.*

70-30 Copper-Nickel

Figures 15 and 16 show the time-dependent behavior of impedance for 70-30 copper-nickel. The Nyquist plot for this material appears to be one semicircle that almost closes on the real axis at short and long exposure durations. The intermediate exposure durations show indications of two time constants (two semicircles). The value of the polarization resistance increases from about 1 kΩ-cm² after one hour to about 20 kΩ-cm² after 485 hours. Although the phase data at short and long exposure durations show only one peak, the width of this peak is too great for a simple one-time-constant model. These data are

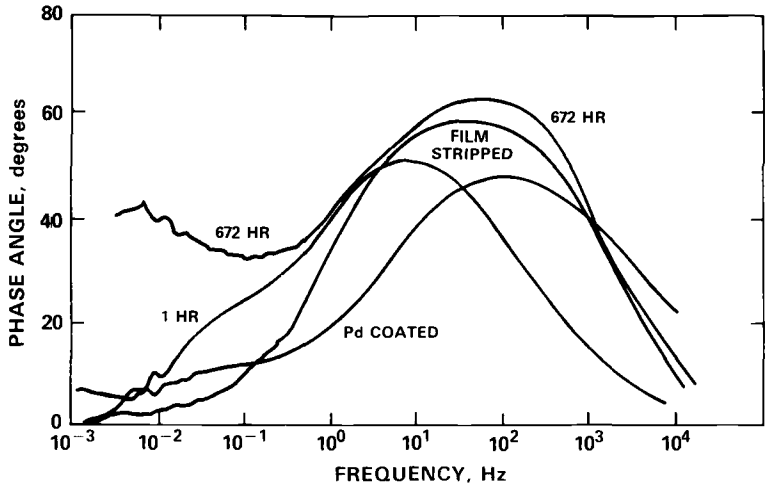

FIG. 11—*Bode phase plot for the data in Fig. 10.*

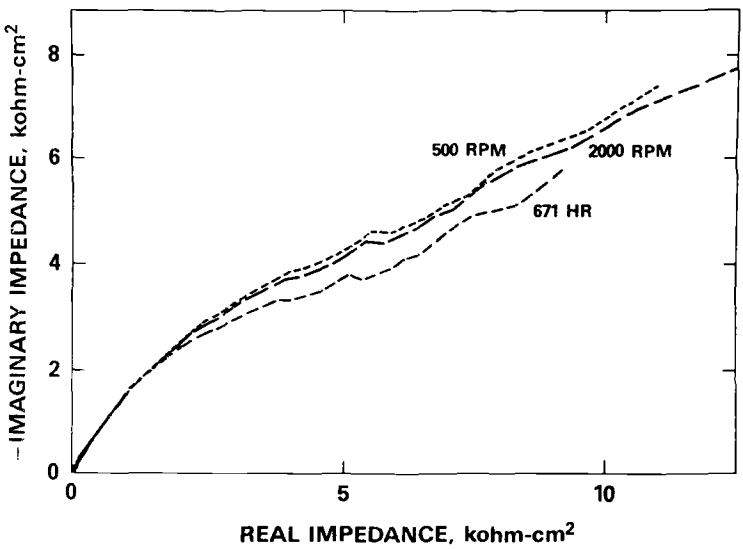

FIG. 12—*90-10 copper-nickel Nyquist plot in aerated 3.4% NaCl as a function of rotation speed.*

likely due to the presence of two, overlapping time constants, one centered at about 50 Hz and the other becoming visible only after longer exposure durations and centered at about 2 Hz. Thus the apparent single semicircles on the Nyquist plot are, in fact, probably resolvable into two closely overlapping time constants. Although the impedance of the filmed material is high, about 38 kΩ-cm², it is not as high as the 90-10 alloy, an observation

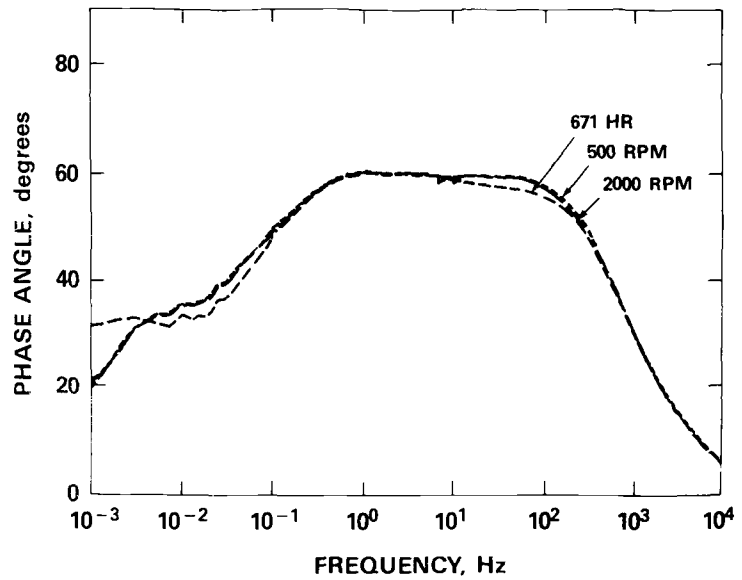

FIG. 13—*Bode phase plot for the data in Fig. 12.*

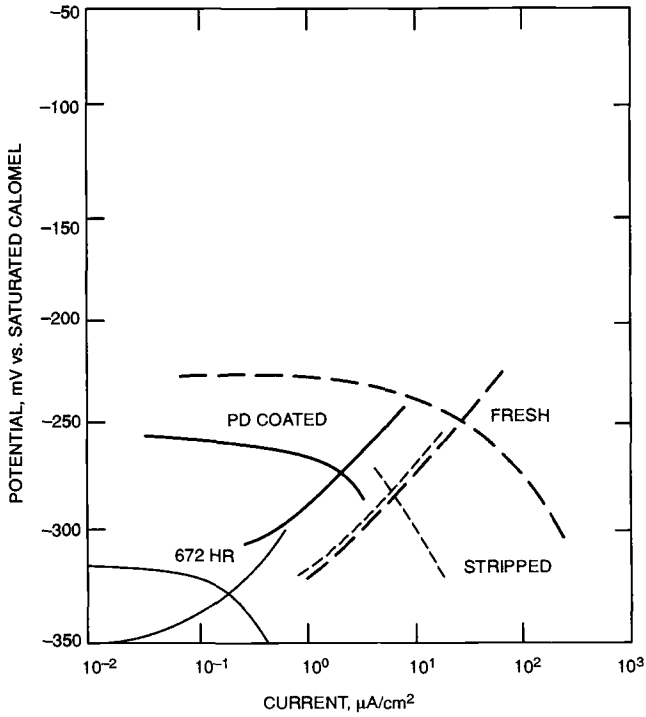

FIG. 14—*90-10 copper-nickel polarization behavior in 3.4% NaCl at 1000 r/min.*

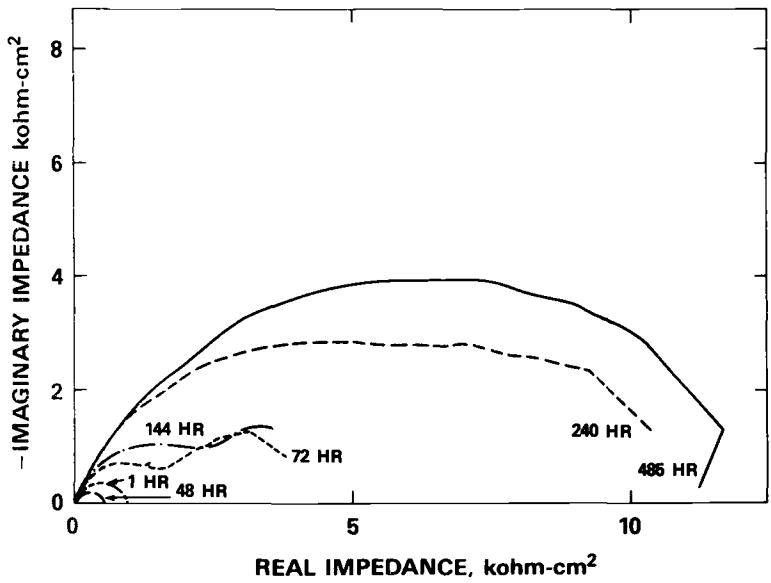

FIG. 15—*70-30 copper-nickel Nyquist plot showing effect of exposure duration in aerated 3.4% NaCl at 1000 r/min.*

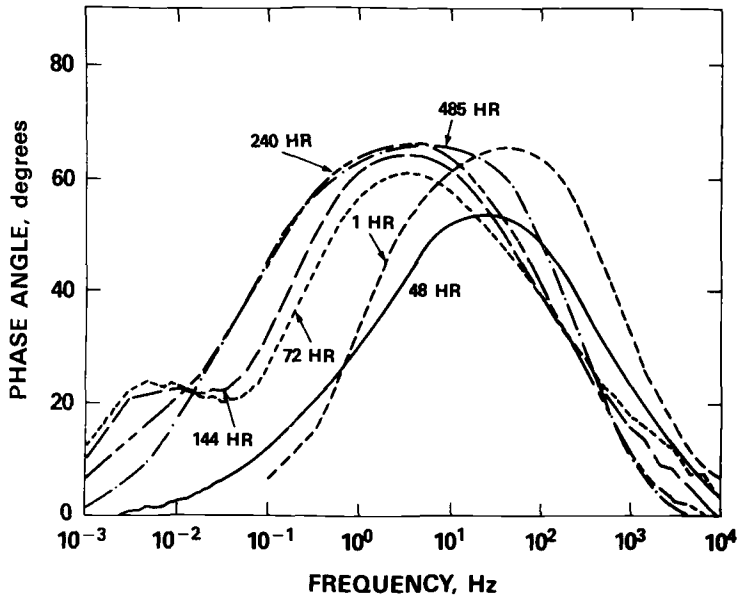

FIG. 16—*Bode phase plot for the data in Fig. 15.*

that is at odds with this material's better corrosion resistance and with other measurements on these alloys at 360 hours by the small amplitude cyclic voltametry (SACV [*12*]) technique [*13*].

Like the 90-10 alloy, Figs. 17 and 18 show that either palladium coating or stripping of the outer corrosion product layers greatly reduces the impedance to a level roughly

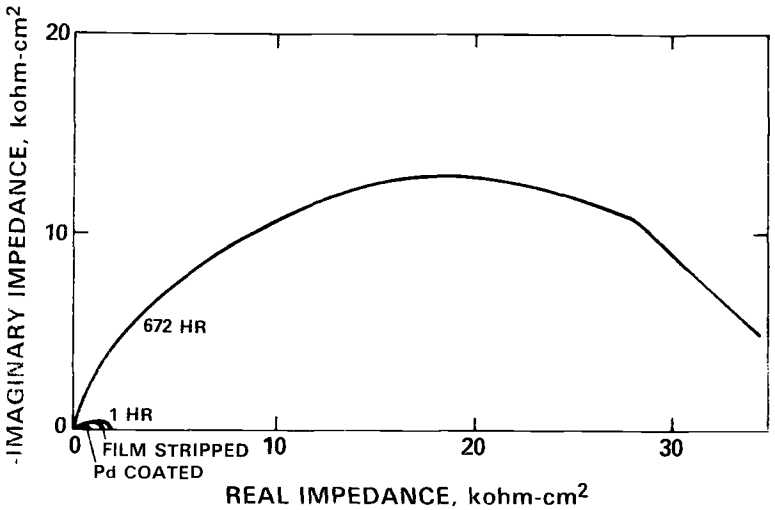

FIG. 17—*70-30 copper-nickel Nyquist plot showing effect of palladium coating and stripping of outer layers for the conditions in Fig. 15.*

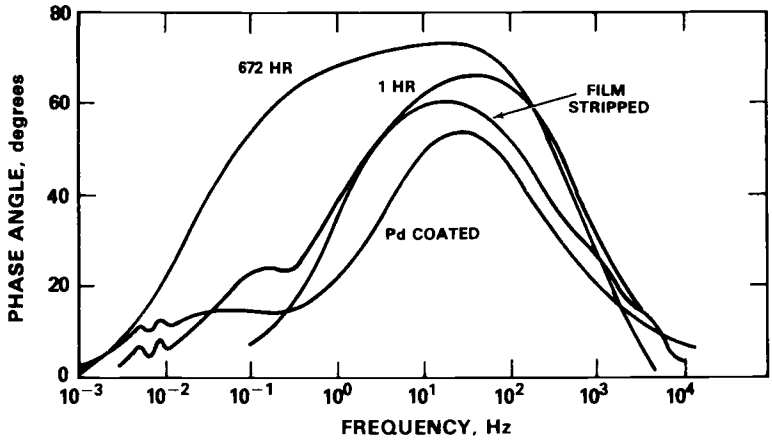

FIG. 18—*Bode phase plot for the data in Fig. 17.*

equivalent to freshly exposed material, about 1 kΩ-cm^2. In addition, the lower overlapping frequency peak in Fig. 18 is also removed by palladium coating or stripping of the outer layers.

The rotation-speed data for 70-30 copper-nickel are presented in Figs. 19 and 20. Rotation speed had little effect, just as on 90-10 copper-nickel, indicating that diffusion in the bulk electrolyte solution was not controlling the corrosion rate.

Composite potentiodynamic curves for 70-30 copper-nickel are shown in Fig. 21. Material exposed for 672 hours had a corrosion current of 0.7 μA-cm^{-2}, as compared to 3 μA-cm^{-2} for freshly exposed material. The 672-hour data are equivalent to 0.7 mils per year, which compares favorably to 0.3 mils per year for one year seawater exposure [*11*]. The current was increased somewhat by stripping, indicating that the outer layers are part of the barrier, and by palladium coating, indicating that the outer layer is a poor catalytic surface for oxygen reduction. This is in agreement with the impedance data, and is similar to the behavior of the 90-10 copper-nickel alloy.

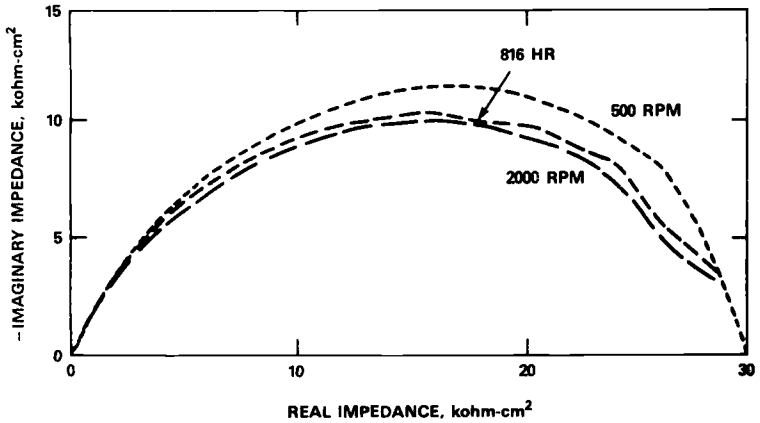

FIG. 19—*70-30 copper-nickel Nyquist plot in aerated 3.4% NaCl as a function of rotation speed.*

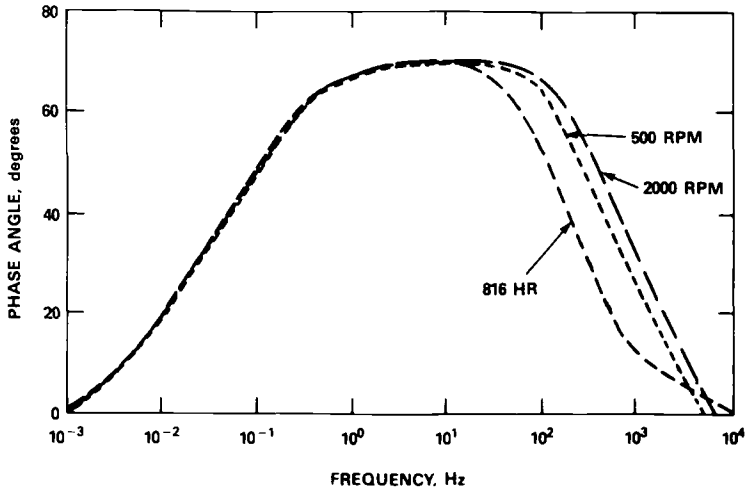

FIG. 20—*Bode phase plot for the data in Fig. 19.*

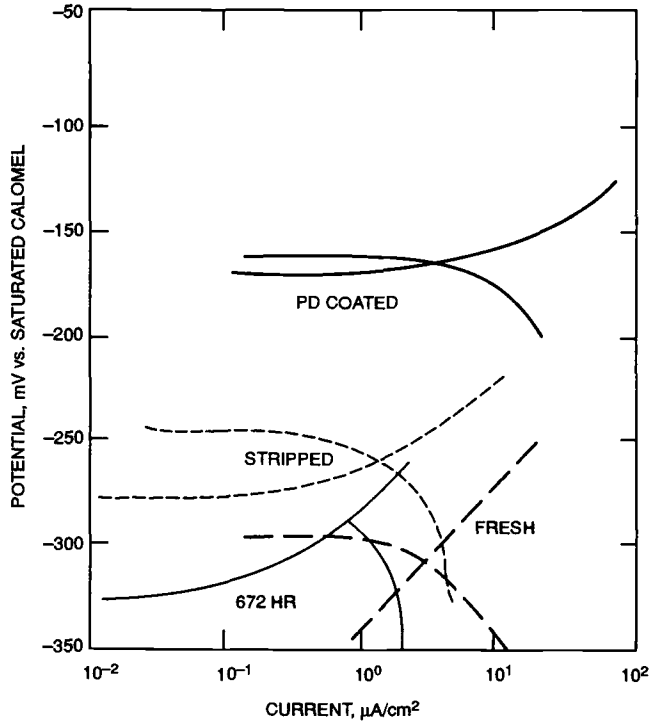

FIG. 21—*70-30 copper-nickel polarization behavior in 3.4% NaCl at 1000 r/min.*

Conclusions

The effect of exposure duration on these alloys can be explained by assuming an initially similar behavior on all alloys, resulting from double-layer capacitance and faradaic resistance, that results in a semicircular Nyquist behavior with a polarization resistance of 0.5 to 1 $k\Omega\text{-}cm^2$. As a corrosion product forms, an alloy-dependent second time constant is evidenced. This second time constant results in a systematic increase in the polarization resistance of the material, with the effect being least for pure copper.

On all of the alloys tested, the enhanced corrosion resistance was due to a process associated with the specimen surface, such as diffusion through the corrosion product layer or limited catalysis of the cathodic reaction, rather than by diffusion through a Nernst-like fluid boundary layer. The latter was evidenced by a lack of rotation speed dependence of the polarization resistance. The inner layer provides protection for pure copper. The greater corrosion resistance of the copper-nickel alloys, 90-10 copper-nickel and 70-30 copper-nickel, appears to be due to the outer, loosely adherent corrosion product layers, since the rate increases when these layers are removed. Since palladium coating prior to removal of these outer layers significantly increases the reaction rate, the corrosion product surface must have a poor catalytic nature for the oxygen reduction reaction. This would force oxygen to diffuse within the pore electrolyte to sites deep in the porous layer where the surface is more catalytic for the oxygen reduction reaction and where electrons are readily available for oxygen reduction. The oxygen diffusion step in the pore electrolyte is partially or completely rate limiting for the overall corrosion reaction, in accord with the parabolic kinetics reported after the first period ($\geq$10 h) of corrosion-product layer formation [*1*].

Acknowledgments

This work was sponsored by the National Science Foundation, Division of Materials Research, Metallurgy Program, Grant 83144168, the International Copper Association, and by the David Taylor Research Center, Bethesda, Maryland.

References

[*1*] Kato, C., Ateya, B. G., Castle, J. E., and Pickering, H. W., "On the Mechanism of Corrosion of Cu-9.4Ni-1.7Fe Alloy in Air Saturated Aqueous NaCl Solution, I. Kinetic Investigations," *Journal of the Electrochemical Society*, Vol. 127, 1980, p. 1890.

[*2*] Kato, C., Castle, J. E., Ateya, B. G., and Pickering, H. W., "On the Mechanism of Corrosion of Cu-9.4Ni-1.7Fe Alloy in Air Saturated Aqueous NaCl Solution, II. Composition of the Protective Surface Layer," *Journal of the Electrochemical Society*, Vol. 127, 1980, p. 1897.

[*3*] North, R. F. and Pryor, M. J., "The Influence of Corrosion Product Structure on the Corrosion Rate of Cu-Ni Alloys," *Corrosion Science*, Vol. 10, 1970, p. 297.

[*4*] Popplewell, J., Hart, R., and Ford, J., *Corrosion Science*, Vol. 13, 1973, p. 295.

[*5*] Kato, C. and Pickering, H. W., "A Rotating Disk Study of the Corrosion Behavior of Cu-9.4Ni-1.7Fe Alloy in Air Saturated Aqueous NaCl Solution," *Journal of the Electrochemical Society*, Vol. 131, 1984, p. 1219.

[*6*] Kato, C., Pickering, H. W., and Castle, J. E., "Effect of Sulfide on the Corrosion of Cu-9.4Ni-1.7Fe Alloy in Aqueous NaCl Solution," *Journal of the Electrochemical Society*, Vol. 131, 1984, p. 1225.

[*7*] Hack, H. and Pickering, H. W., "AC Impedance Study of Copper and Copper-Nickel Alloys in Aerated Salt Water—I. Pd Coating and Corrosion Product Stripping," *Journal of the Electrochemical Society*, Vol. 138, 1991, p. 690.

[*8*] Levich, V. G., *Physicochemical Hydrodynamics*, Prentice-Hall, Inc., Englewood Cliffs, NJ, 1962, pp. 345–357.

[*9*] Riddiford, A. C., "The Rotating Disk System," in *Advances in Electrochemistry and*

Electrochemical Engineering, Vol. 4-Electrochemistry, P. Delahay, Ed., John Wiley and Sons, NY, 1965, pp. 46–116.

[*10*] Gabrielli, C., *Identification of Electrochemical Processes by Frequency Response Analysis,* The Solartron Electronic Group Limited, Irvine, CA, 1981.

[*11*] Uhlig, H. H., *The Corrosion Handbook,* John Wiley and Sons, New York, 1948, pp. 394ff.

[*12*] Shih, H. and Pickering, H. W., "Analysis of the Small Amplitude Cyclic Voltametry Technique for Measuring Polarization Resistance and Interfacial Capacitance," *Journal of the Electrochemical Society,* Vol. 134, 1987, p. 1943.

[*13*] Shih, H. and Pickering, H. W., "SACV Measurement of the Polarization Resistance and Capacitance of Copper Alloys in 3.4 wt.% NaCl Solution," *Journal of the Electrochemical Society,* Vol. 134, 1987, p. 1949.

DISCUSSION

F. Mansfeld[1] *(written discussion)*—It is surprising that you did not find an effect of mass transport on the corrosion rates of copper and Cu-Ni. It is well known that in chlorine-containing media the anodic reaction is mass transport controlled. The reaction has been discussed by Pickering et al., among others. In our studies of copper-based materials in natural and artificial seawater we found that E_{corr} was independent of rotation speed of a rotating cylinder electrode, while i_{corr} increased. This is the result of *both* the cathodic and the anodic reactions being mass transport controlled.

Your conclusion that oxygen reduction occurs at the bottom of pores in the outer corrosion product layer is interesting. We reached the same conclusion and are applying the inhomogeneous surface model (Jüttner et al.) for the analysis of EIS data. This model considers mass transport of oxygen through porous layers.

H. Hack and H. Pickering (authors' closure)—In this corrosion system, the cathodic reaction is much slower than the anodic reaction. Therefore, regardless of the rate-controlling step of the anodic reaction, the overall rate of both reactions will be controlled by the rate-controlling step of the slower cathodic reaction. Oxygen mass transport through the fluid boundary layer controls the rate of the cathodic reaction, and thus the anodic rate, in the early stages of the corrosion process before the corrosion product film is fully developed. After the development of the film the rate of the cathodic reaction drops well below this mass-transport-limited rate. The authors conclude that this is due to the film's ability to slow down the cathodic reaction by providing pores through which the oxygen must diffuse in order to react. The formation of the corrosion product film is sensitive to small changes in the environment. It is possible that a less protective film was formed in Dr. Mansfeld's experiments than in ours due to some environmental difference. His film may not have reduced the cathodic reaction rate below the fluid mass-transport-limited rate for his experimental setup. It would be instructive to compare the experimental setup and environmental parameters of Dr. Mansfeld's experiments and ours. We are pleased that he has independently come to the same conclusion as this research regarding oxygen reduction occurring at the bottom of pores, and look forward to his analysis using the inhomogeneous surface model.

[1]University of Southern California, Los Angeles, CA, 90089-0241.

A. Neil Rothwell,[1] *John L. Dawson,*[1] *David A. Eden,*[1] *and James W. Palmer*[2]

Interpreting Electrochemical Impedance Spectra from Segmented Electrode Arrangements

REFERENCE: Rothwell, A. N., Dawson, J. L., Eden, D. A., and Palmer, J. W., **"Interpreting Electrochemical Impedance Spectra from Segmented Electrode Arrangements,"** *Electrochemical Impedance: Analysis and Interpretation, ASTM STP 1188,* J. R. Scully, D. C. Silverman, and M. W. Kendig, Eds., American Society for Testing and Materials, Philadelphia, 1993, pp. 237–251.

ABSTRACT: Differential corrosion of carbon steels and in particular welded joints has long been recognized as a problem in aqueous environments. Minor differences in composition and microstructure can cause severe differential galvanic corrosion effects that lead to rapid rates of corrosion on particular types of steel or weld consumables.

To study this mode of corrosion a monitoring technique was developed that allows corrosion rates and galvanic currents to be assessed. The design of this instrumentation facilitates the use of impedance measurements on single electrodes while they are effectively coupled as part of a mixed metal system. The individual impedance responses may be analyzed to give information on the rates of corrosion for each element together with information on the separate anodic and cathodic reaction mechanisms.

The effects of differential galvanic corrosion have been studied in a range of environments both in the laboratory and in the field. Data are presented for aerated and deaerated seawater and also CO_2 brine system with inhibitor additions.

KEYWORDS: electrochemical impedance spectroscopy (EIS), weld corrosion, CO_2 corrosion, inhibitors

Galvanic effects or differential corrosion resulting from mixed metal combinations is a well-recognized phenomenon. Materials selection, insulating gaskets, cathodic protection, and coatings are standard methods of minimizing such problems in practical engineering situations. However, there are many cases where differential effects resulting from relatively minor differences in alloy composition cannot be prevented, as in welded structures. Hence, the use of appropriate weld consumables and weld procedures is crucial in primary control of the corrosion problem.

One practical means of preventing weld metal corrosion with carbon steels is to add traces of more noble elements to the weld consumables with the aim of producing a more resistant weld metal; the parent plate then acts as a large anode. However, such an approach may also result in increased attack of the heat-affected zone (HAZ).

The oil and gas production industry has found that corrosion of weld metal or heat affected zones, or both, is increased significantly by high fluid turbulence in lines containing produced fluids or where treated seawater injection is used to maintain reservoir

[1]CAPCIS MARCH Limited, Manchester, M1 2PW, England.
[2]CAPCIS Limited, Manchester, M1 2PW, England.

pressure. Corrosion penetration rates of up to 15 mm/yr have been found. The detailed mechanisms involved in these macrocorrosion cells are the subject of continuing research, but the galvanic corrosion effects appear to be enhanced by the morphology of the semiprotective films formed under the high turbulence of the fluids.

Measurements of electrochemical processes associated with relative anodic and cathodic areas of differential corrosion cells is therefore of practical and scientific interest. The ability to make simultaneous measurements of such areas, while individual electrodes comprising the differential cell remain coupled at the common corrosion potential, offers an obvious advantage. For example, on-site studies of inhibition weld corrosion in an operating flow line in offshore oil and gas production require that the electrode test assembly responds rapidly to process conditions, such as change of fluid velocity and composition. Alternative measurement methods where each electrode is held at a common potential by means of potentiostats is not feasible particularly as it requires insertion of a reference electrode into the line. This paper describes how segmented but coupled electrodes can be used to evaluate differential corrosion behavior of weldments by measuring the response of each element across separate zero resistance ammeters.

In the case of flowlines and manifolds in production systems, the corrodant is carbon dioxide dissolved in the aqueous brine and oil phases; with seawater injection, as used for secondary recovery, it is typically traces of oxygen or reducible species remaining after deaeration and scavenging treatments that cause the corrosion problem. Practical means of controlling such corrosion first require the selection of appropriate weld procedures and then the use of inhibitor treatments or adequate control of oxygen and chemical additions.

Laboratory tests, involving a range of electrochemical measurements, are invaluable for the selection of materials and inhibitors for specific duties. Electrochemical techniques can be employed in the laboratory and on site under field conditions to optimize weld corrosion control programs using process control dosage procedures.

Electrochemical Techniques

The increasing use of electrochemical impedance spectroscopy (EIS) can be traced back to the development of digital frequency response analyzers and spectrum analyzers during the early 1970s. EIS is an ideal and widely used technique for the investigation and monitoring of general or uniform corrosion. It is also effective in studies of inhibition and evaluation of change in dielectric constant of both organic coatings and anodized aluminum.

As a method of general applicability for investigation of localized corrosion, EIS has limitations. This is particularly true for stress corrosion cracking and pitting studies where electrochemical noise, that is the analysis of the random current and potential transients, is a more appropriate technique. For example, although EIS may be used to identify pitting corrosion from the scatter of the low-frequency range of the impedance plot such data do not conform to the Kramers-Kronig Transform because the corrosion system is unstable. Additionally the scatter noted in the spectra may not be purely due to localized corrosion and may be as a result of changes in the environment. EIS has, however, been used to model specific cases of localized corrosion such as that produced by diffusion within crevices [*1,2*], and the effect of local anodes positioned within a passive layer [*3*].

One area of investigation where we have successfully exploited electrochemical impedance is in the investigation and control of corrosion produced by differential or galvanic effects in carbon manganese steels. These galvanic cells can be associated with differences in metal and alloy composition, geometric effects, and differences in local hydrodynamics that give rise to flow assisted corrosion and erosion corrosion.

Impedance data from differential systems can be relatively complex to interpret and it is essential that they are analyzed in conjunction with galvanic current measurements and differential polarization. It is the combination of these techniques that provides the most powerful means of assessing differential corrosion behavior.

Galvanic Measurements

The standard method used in evaluation of mixed metal corrosion is to couple two different electrodes through a zero resistance ammeter (ZRA). The current between the couple is then monitored by the ZRA and is used to assess galvanic effects when, for example, the electrode area ratio is changed. A major disadvantage with this basic technique is an inability to obtain individual polarization or kinetic data from each electrode without disconnection of the couple. A standard polarization measurement can provide curves for the overall couple, with the coupled electrodes as the working electrode in the polarization circuit. The individual polarizations have to be inferred or extrapolated from the curves by using the change in coupling current.

One means of obtaining individual polarization information is to couple each electrode through its individual ZRA to a common earth. The galvanic current into, or out of, each electrode is then monitored separately by each ZRA. Also, any externally applied polarization current, as supplied by a potentiostat, and the resultant current flowing through each electrode, can be measured by the ZRAs. This approach, proposed by D. A. Eden, was first assessed in 1983 [*4*], and reported in 1986 [*5*]. Experimental polarization data obtained from such an arrangement for a two-electrode couple would comprise three polarization curves, one for each electrode in the couple, plus an overall or composite curve from the external polarizing potentiostat.

Electrochemical impedance spectra can also be obtained from such an interface arrangement. An illustrative example of impedance data from an extreme macrogalvanic cell which was obtained from connecting mild steel to zinc can be seen in Fig. 1. The zinc electrode has a distinct charge transfer relaxation and a Warburg diffusion, presumed to be zinc dissolution coupled to oxygen reduction, while the steel cathode appears largely diffusion-controlled with limited charge transfer indicating that the oxygen reduction response is essentially from the limiting current density portion of the polarization curve.

The overall impedance response from the two electrodes is a combined response from the steel plus zinc; the difference in solution resistance arising from the relative positions of the working electrodes and the reference electrode. Coupling-current measurements showed that the electron flow was from the zinc to the steel, as expected. The experimental impedance curve from the couple can also be derived or simulated mathematically in complex number notation from the individual anodic and cathodic electrode responses.

All the EIS and LPR data presented in this paper have been generated from a "coupled" system where all electrodes are electrically formed together to a common earth through individual ZRAs. In this configuration the external polarization is applied by the potentiostat to the coupled system which is held at the combined rest potential; the individual LPR and EIS is then measured across each ZRA. In the case of weldment corrosion studies the five-electrode array was produced by sectioning two samples of pipe material (P1 + P2), two heat-affected zones (H1 and H2) and the weld metal (W), as shown in Fig. 2.

Methodology

The corrosion of weld metal can be attributed to the differences in composition of the weld metal, the microstructure of an as-cast metal, and the high distribution of micro

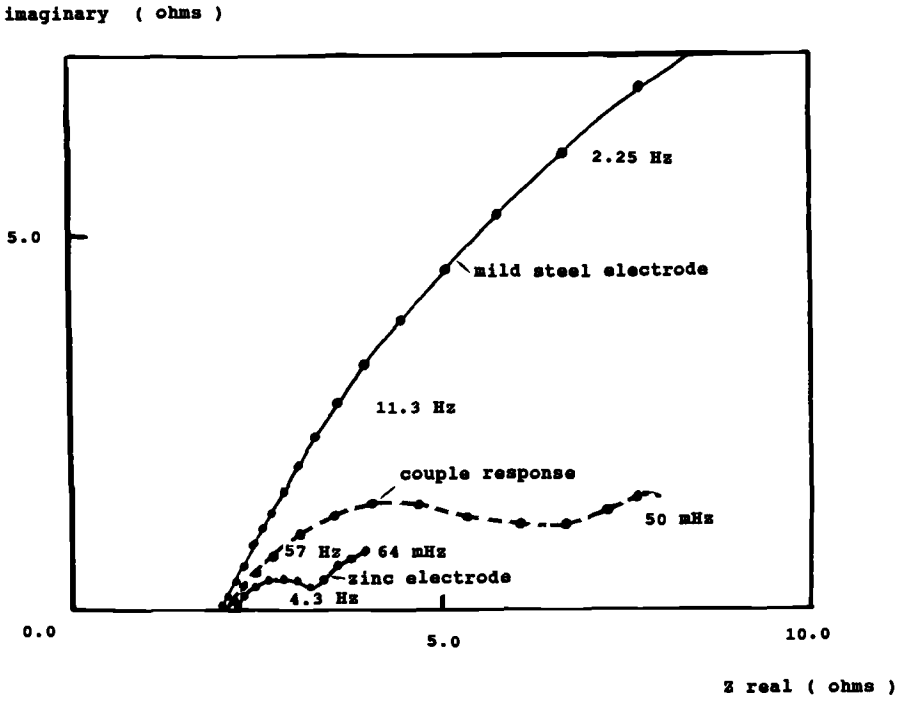

FIG. 1—*EIS for coupled steel and zinc electrodes.*

inclusions resulting from deoxidation practices [*6,7*]. The corrosion of a heat-affected zone (HAZ) occurs where a noble weld metal is laid in combination with a parent of high hardenability. Low-temperature transformation products such as martensite and upper and lower bainite may, in the absence of sufficient alloy content, produce an active HAZ. It is not generally the low-temperature transformation products that corrode preferentially; however, their presence in an HAZ results in a matrix of ferrite that is "driven" by the cathodic martensitic and bainitic structures [*8*].

Micro-Structural Effects

In order to assess basic metallurgical effects, a range of microstructures was produced in an EN3B carbon steel by quenching, austempering, and solution annealing. In this manner, five structures were produced: as-wrought, martensitic, lower bainite, upper bainite, and solution annealed. Electrodes of each of these materials were machined, to 10 mm diameters after heat-treating. An electrical connection was made to the rear face and the specimens were encapsulated as a composite electrode in epoxy resin in an equispaced circular array on a 25-mm diameter. The electrodes were polished to a 1200 grit finish prior to testing in an aerated seawater solution at 20°C.

The impedance responses for these materials coupled together are shown in Fig. 3. As would be expected for seawater systems, the corrosion is under control by the diffusion of oxygen, and thus it is difficult to estimate corrosion rates from the spectra. It can be seen, however, that the traces can be used for ranking of corrosion performance. The overall

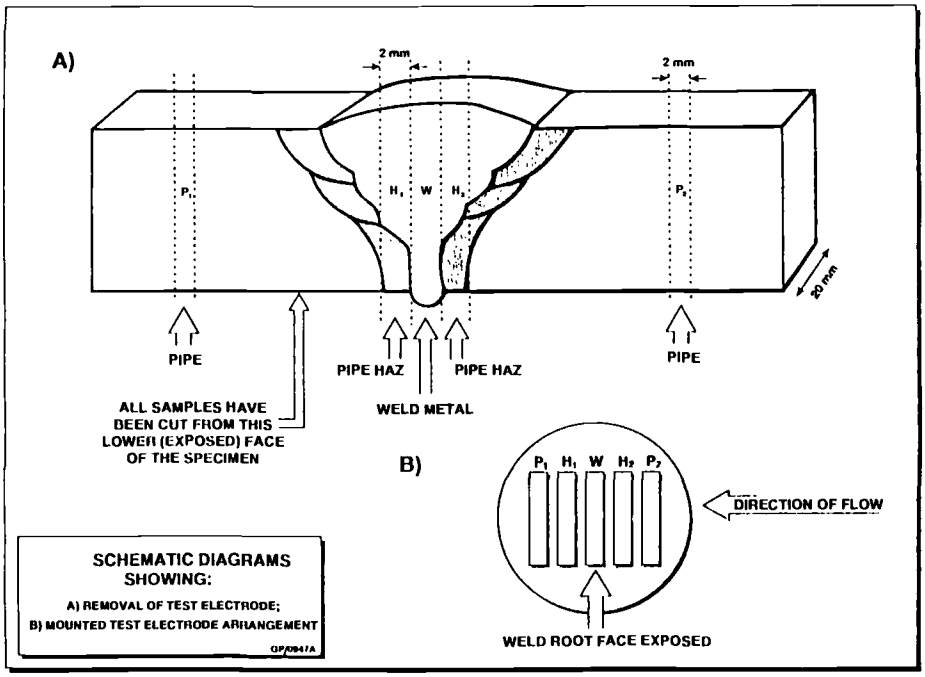

FIG. 2—*Schematic representation of weld sectioning.*

trace shows the composite response, the data indicating the solution annealed structure to be the most anodic with the other elements showing more noble behavior in the increasing order; martensitic, pearlitic (wrought), upper bainite, and lower bainite. This ranking correlated with the galvanic currents measured and the linear polarization responses measured across the individual ZRAs (Table 1). The ZRA current rankings, the linear polarization resistance (LPRM), and the corrosion rates from EIS show good correlation for this system.

These results show that minor changes in microstructures can result in differences in corrosion rate in the coupled condition of up to one order of magnitude. It is therefore not surprising that alloy additions of up to 1% can greatly affect the corrosion behavior of welded joints.

Welded Joints

The traditional Manual Metal Arc (MMA) weld consumable for high-integrity welded joints in C-Mn pipeline steel has been E7016. This consumable has led to rapid corrosion attack in a range of systems [*9*].

This has led to a range of alloyed consumables being adopted, typically containing either nickel or a combination of copper and nickel (E7018G, E8018G) [*10*].

Welds were prepared from an E7016 and an E7018G consumable in X52 pipeline steel. These were cut into 10-mm transverse sections, polished to 1 μm on all faces and etched in 2% Nital. Sections of the weld metal, HAZ (including fusion line), and parent metal on both sides of the joint were carefully taken. An electrical connection was made to the rear

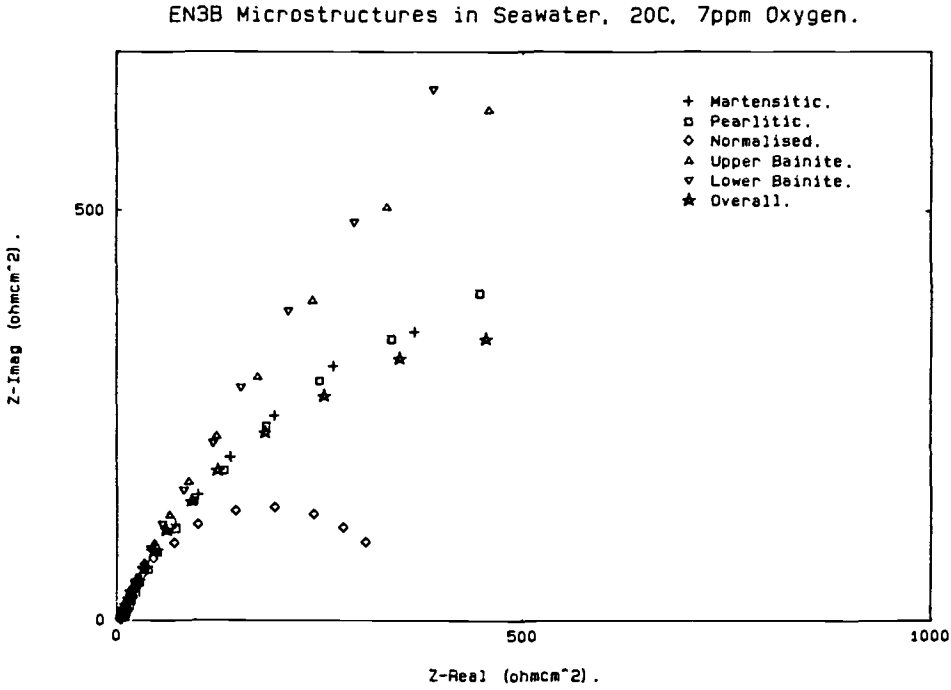

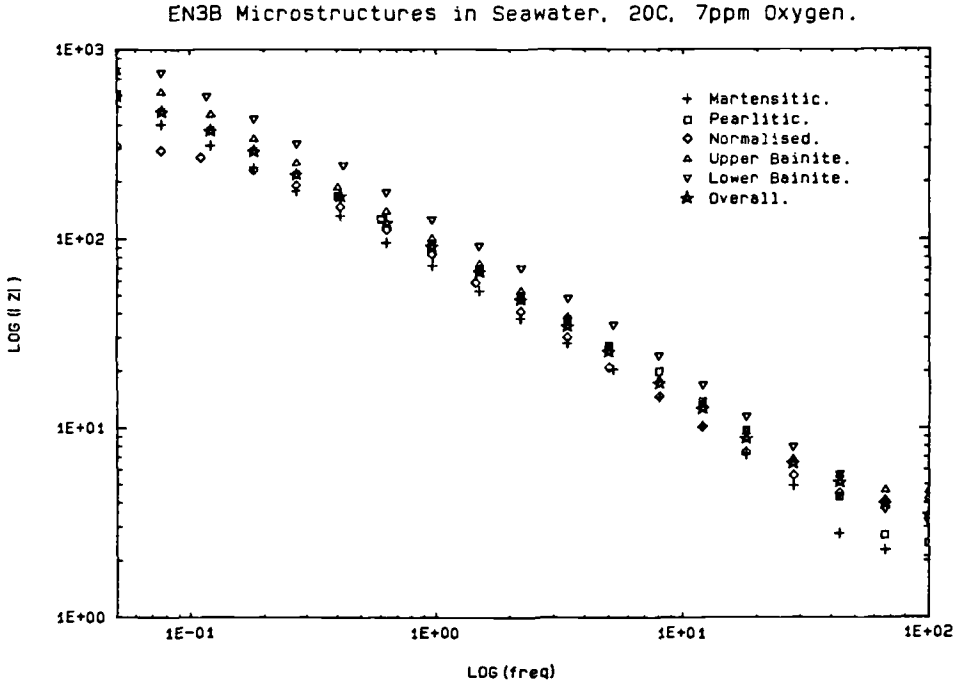

FIG. 3—*EIS for EN3B microstructures.*

TABLE 1—*Corrosion rates of EN3 microstructures in seawater.*

	ZRA (mA/cm²)	LPR (mm/y)	EIS (mm/y)
Martensitic	−14.6	0.18	—
Pearlitic	−8.9	0.2	—
Solution Annealed	+56.5	1.2	0.96
Upper Bainite	−16.5	0.17	—
Lower Bainite	−16.5	0.17	—
Overall	−	0.38	=0.3

TABLE 2—*EIS results for weld type 1 (E7018-G).*

	R_{ct} (Wcm²)	Cdl (F/cm²)	Corrosion Rate (mm/y)	ZRA (mA/cm²)
Parent1	46	0.0026	6.3	+28
HAZ1	44	0.0036	6.6	+32
Weld	53	0.0022	5.4	−37
HAZ2	76	0.0022	3.8	−54
Parent2	44	0.0026	6.6	+31

TABLE 3—*EIS results for weld type 2 (E7016).*

	R_{ct} (Wcm²)	Cdl (F/cm²)	Corrosion Rate (mm/y)	ZRA (mA/cm²)
Parent1	85	0.001	3.4	−53
HAZ1	38	0.0016	7.6	−30
Weld	20	0.0038	14.4	+200
HAZ2	52	0.0031	5.5	−37
Parent2	84	0.001	3.4	−80

face and mounted in epoxy (Fig. 2). The electrodes were then polished to a 1200 grit finish prior to testing in 3.5% sodium chloride at 60°C saturated with carbon dioxide.

The results of these tests are shown in Figs. 4 and 5. As would be expected the most anodic (positive current) elements on the ZRA traces also show the most anodic or active corrosion on the impedance spectra. It can be seen from this data that the differences between alloy levels in the weld metal can be easily determined by the individual impedance spectra. Type 1, E7018G, weld alloyed with nickel shows lower corrosion rates than one HAZ region and both parent steels but a slightly higher rate than the other HAZ region. Type 2, E7016G weld metal, unalloyed C-Mn weld, shows up to four times the corrosion rate of the parent steel (Tables 2 and 3).

The accepted route for enhanced weld performance has been to alloy the weld metal. However, in "sweet" carbon dioxide (no hydrogen sulfide present) systems the base corrosion rate is unacceptably high, so inhibition is often the preferred option. This approach to weld corrosion monitoring presented earlier can also be applied to inhibition studies.

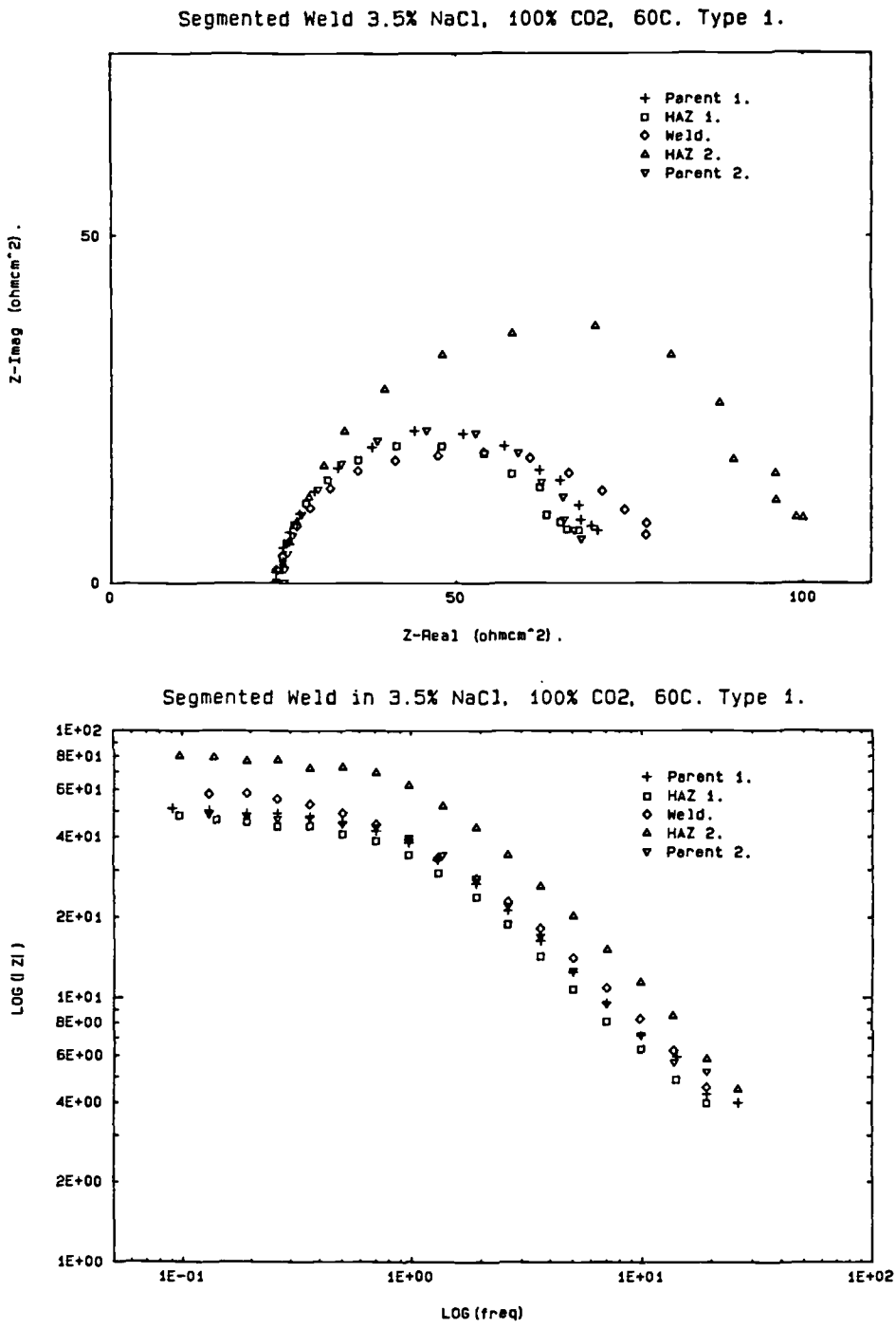

FIG. 4—*EIS for E7018-G segmented weld.*

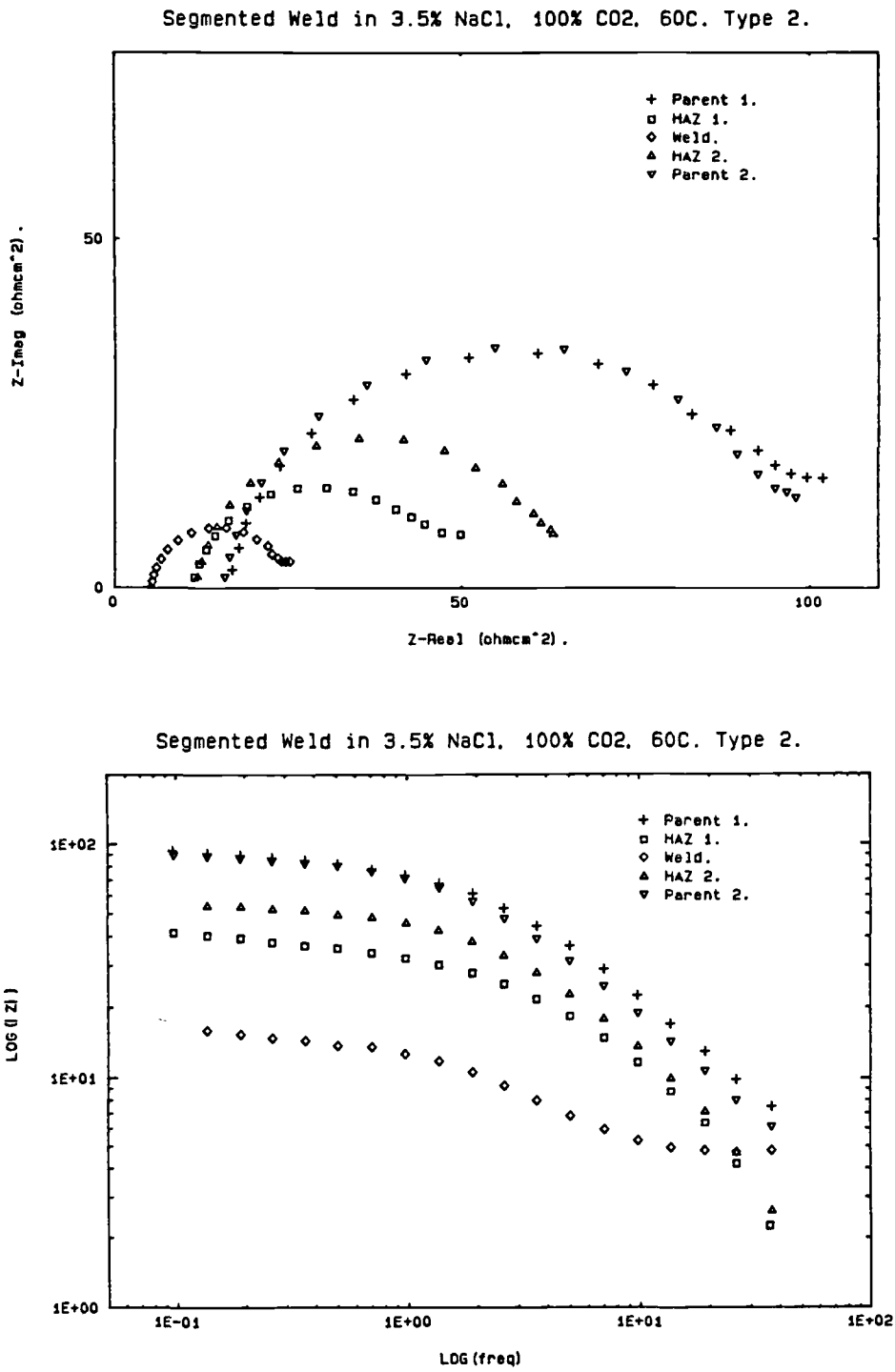

FIG. 5—*EIS for E7016-1 segmented weld.*

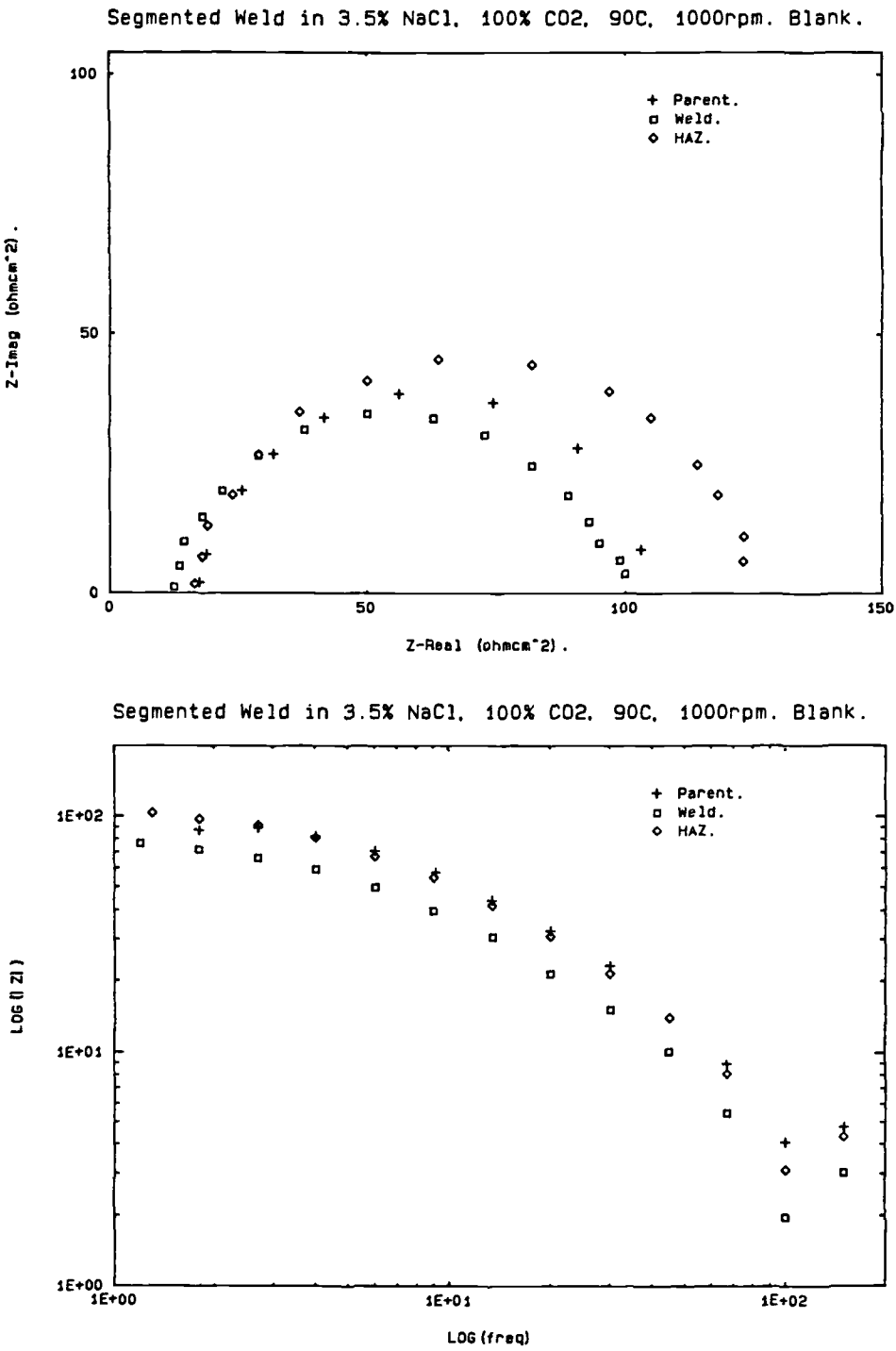

FIG. 6—*EIS for rotating segmented weld electrodes 0 ppm inhibitor.*

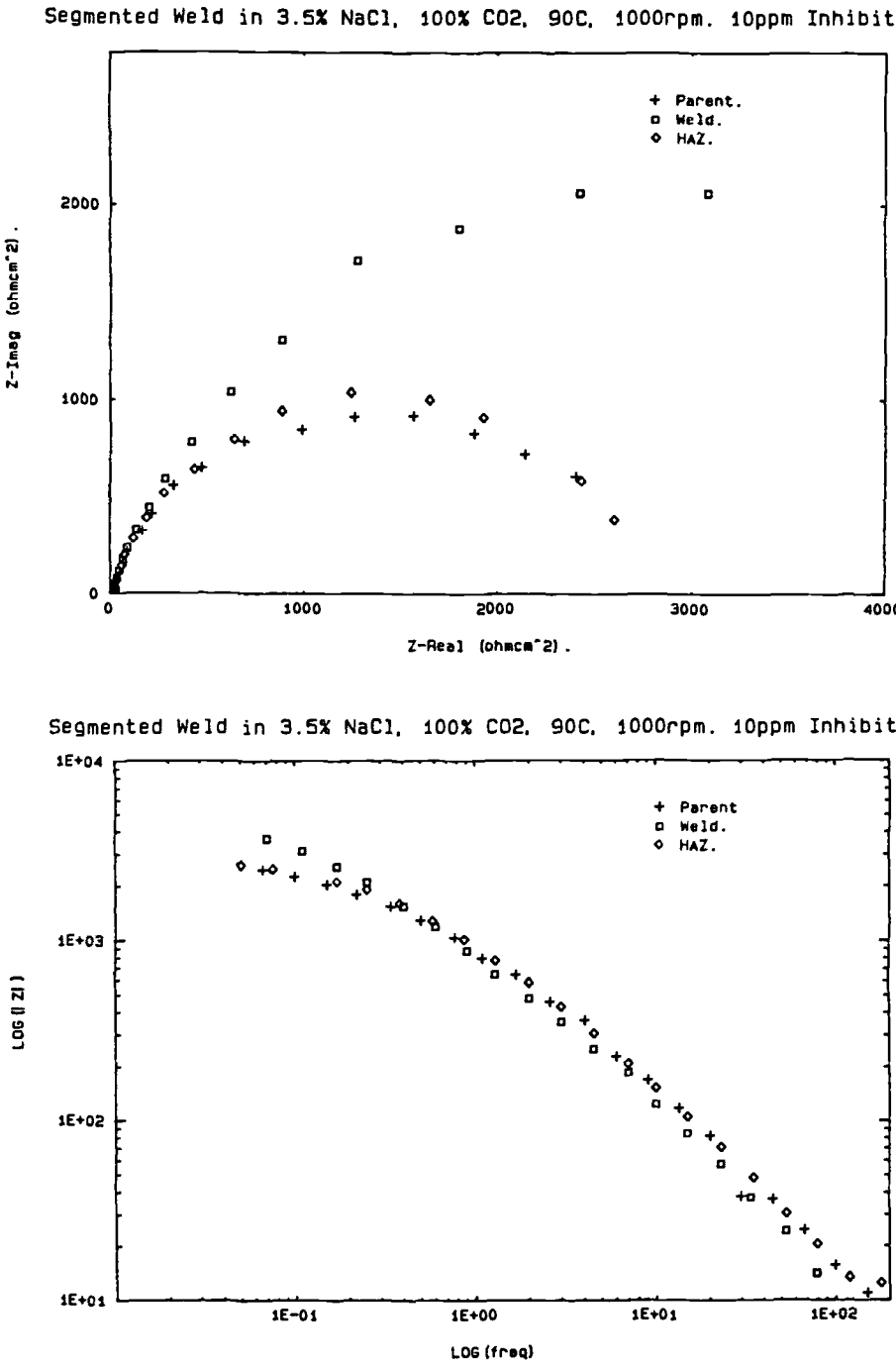

FIG. 7—*EIS for rotating segmented weld electrodes 10 ppm inhibitor.*

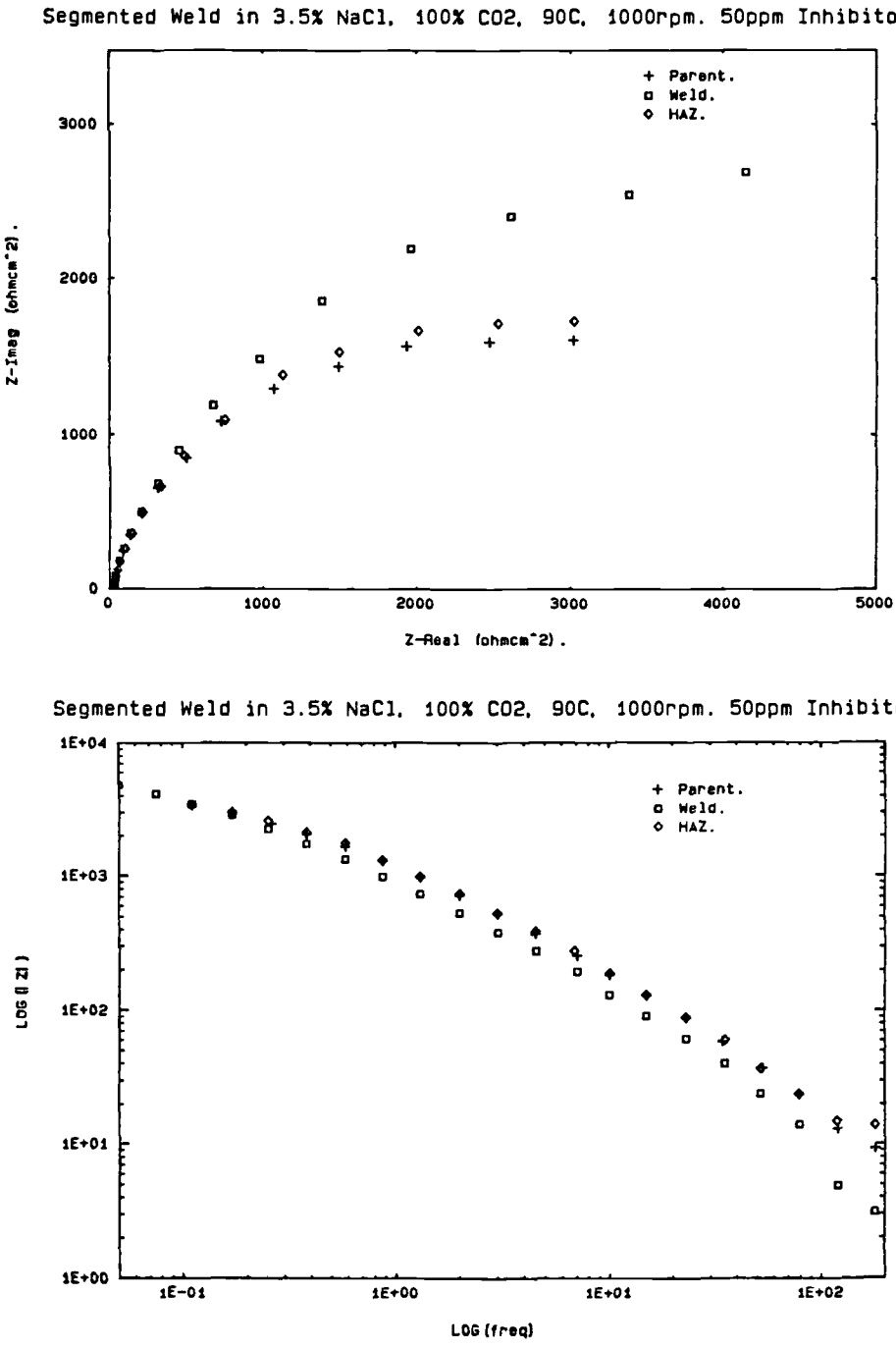

FIG. 8—*EIS for rotating segmented weld electrodes 50 ppm inhibitor.*

TABLE 4—*Results from rotating segmented electrodes inhibitor trials.*

Element	R_{ct} (Wcm²)	Cdl (F/cm²)	Corrosion Rate (mm/y)	Efficiency (%)
Blank				
Parent	85	0.0002	3.4	
Weld	86	0.0003	3.4	
HAZ	106	0.00025	2.7	
10 ppm Inhibitor				
Parent	2500	0.0002	0.12	96%
Weld	4100	0.0006	0.07	98%
HAZ	2050	0.0002	0.14	94%
50 ppm Inhibitor				
Parent	3170	0.0002	0.09	97%
Weld	8300	0.0004	0.03	99%
HAZ	5000	0.0002	0.06	98%

Inhibition Effect

A T1G E8018G consumable was laid in X52 pipeline steel and sectioned as per the previous work. Electrodes of weld metal, HAZ, and parent steel were mounted equispaced in a 34-mm diameter cylindrical mold in epoxy resin. The cylinder was polished to a 1200 grit finish prior to testing. The results presented in Figs. 6 through 8 and Table 4 were obtained at 90°C, 100% carbon dioxide using a Rotating Cylinder at a rotational speed of 1000 r/min with a 90:10 formation water:brine solution.

These results show that the individual response of each element to inhibition can be determined. These data demonstrate that inhibitor packages can be formulated to effec-

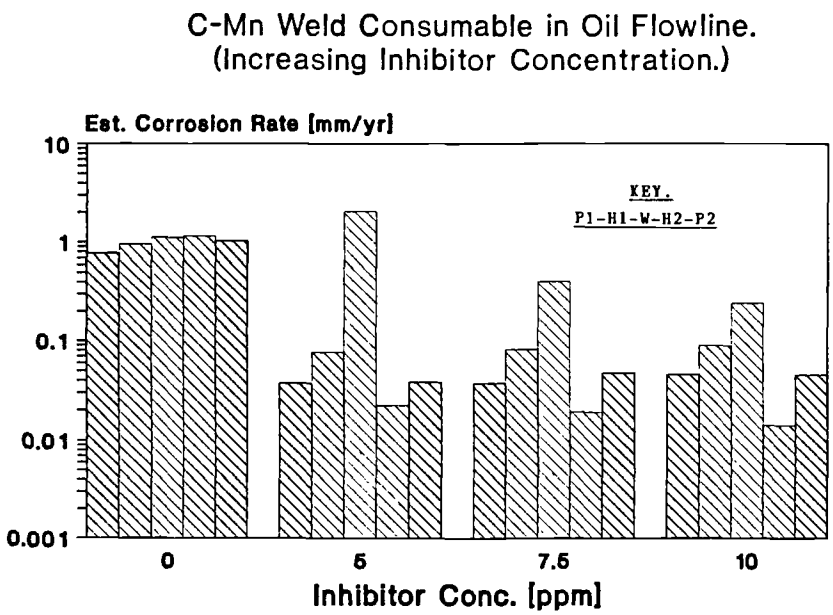

FIG. 9—*Field data for E7016 consumable during inhibitor trials in an oil flowline.*

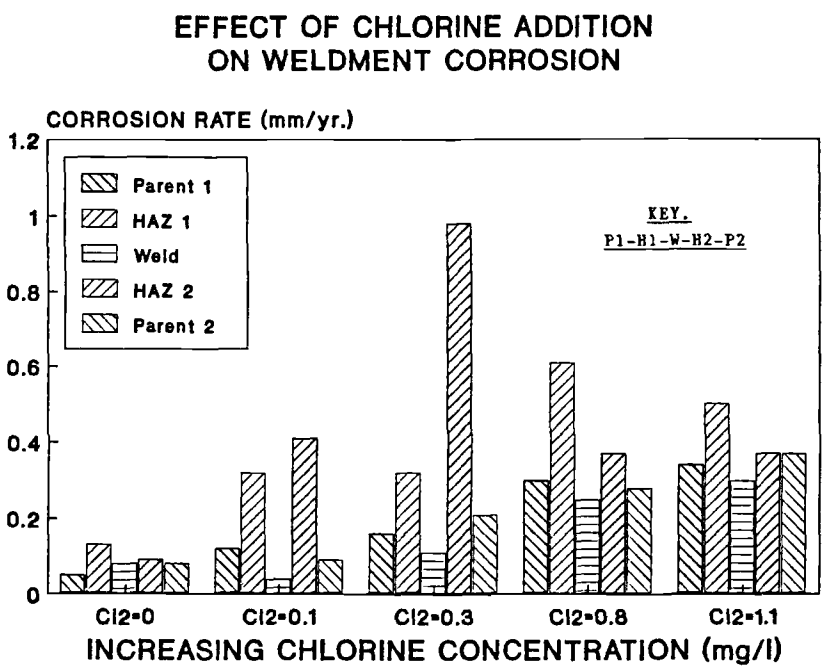

FIG. 10—*Field data for E7018-G consumable during chlorination trials in a seawater injection system* [9].

tively protect the entire weld area. It is not appropriate to take a standard inhibitor package, test it on parent steel, and expect uniform performance across a welded joint.

Similarly, data on parent plate during chlorination of a seawater injection system or inhibition in oil flow lines cannot be applied to a weld. Examples of what may happen are shown in Figs. 9 and 10. These data were obtained during offshore trials in the North Sea using weld sectioned probes and the techniques described in this paper. In both these cases the weld/HAZ corrosion was exacerbated when data from parent electrode probes indicated the effect to be insignificant.

Conclusions

Electrochemical impedance spectra from segmented electrodes can be used to determine the corrosion mechanisms and corrosion rates occurring on separate electrodes while these are effectively coupled together so as to form one component.

EIS analysis can be used to determine the performance of welded joints in a range of environments both in the laboratory and in the field. This allows parent/consumable combinations to be assessed for compatibility and the effectiveness of inhibitor treatments to be determined.

As with all electrochemical techniques the data interpretation is more effective when analyzed in conjunction with zero resistance ammetry and linear polarization measurements.

References

[1] MacDonald, D. D. and McKubre, M. C. H., "Corrosion of Materials," *Electrochemical Impedance Methods*, J. R. MacDonald, Ed., Wiley-Interscience, New York, 1986.
[2] Sagues, A., *Paper No. 25, Corrosion/89*, National Association of Corrosion Engineers, Houston, TX, 1990.
[3] Oltra, R. and Keddam, M., *Electrochemica Acta*, Vol. 35, 1990, pp. 1619–1629.
[4] Woollam, R. C., "Electrochemical Corrosion Studies on Coupled Electrodes," MSc dissertation, UMIST, 1983.
[5] Dawson, J. L., Gill, J. S., Al-Zanki, A. A., and Woollam, R. C., *Dechema-Monograph 101*, Vol. 235, VCH, Frankfurt, 1986.
[6] Rothwell, A. N. and Turner, M. E. D., *Metals and Materials*, June 1989, pp. 350–354.
[7] Rothwell, A. N., "The Preferential Corrosion of Weldments in Seawater Service," MSc dissertation, UMIST, 1986.
[8] Rothwell, A. N., "Corrosion of Carbon Manganese Steel Welds," Ph.D. thesis UMIST, submitted October 1992.
[9] Nice, P. I., Georgie, W. J., and Rothwell, A. N., Symposia Q, UK Corrosion, 22–24 October, 1991.
[10] CAPCIS/The Welding Institute, *Report 5563/28/89*, February 1989.

DISCUSSION

F. Mansfeld[1] *(written discussion)*—You mentioned that you have determined experimentally the B-values for the conversion of R_p into corrosion rates. Please give experimental value of B for the parent metal, the weld metal, and the HAZ, and indicate how these values were determined experimentally.

[1]University of Southern California, Los Angeles, CA, 90089-0241.

Corrosion of Aluminum

J. L. Dawson,[1] *G. E. Thompson,*[2] *and M. B. H. Ahmadun*[3]

Evolution of Electrochemical Impedance During Sealing of Porous Anodic Films on Aluminum

REFERENCE: Dawson, J. L., Thompson, G. E., and Ahmadun, M. B. H., **"Evolution of Electrochemical Impedance During Sealing of Porous Anodic Films on Aluminum,"** *Electrochemical Impedance: Analysis and Interpretation, ASTM STP 1188,* J. R. Scully, D. C. Silverman, and M. W. Kendig, Eds., American Society for Testing and Materials, Philadelphia, 1993, pp. 255–275.

ABSTRACT: Electrochemical impedance spectrocopy (EIS) has been used to study the hydrothermal sealing of porous anodic films on aluminum. The 5-μm and 15-μm-thick films, originally formed by anodizing 99.99% wt% aluminum in sulphuric acid, were immersed in boiling distilled water and *in-situ* impedance measurements were made continuously *during* the sealing process. Comparisons of the spectra were also made *after removal* of the films from the boiling water bath after various times and immersion in distilled water at ambient temperature.

Analysis of the EIS data, presented as Bode plots of impedance and phase angle against frequency, showed development of hydrated films and decrease of the original barrier layer thickness. Electrical equivalent circuit models were used to interpret the detailed changes in solution resistance, hydration of the films (R_h and C_h) and the barrier layer (R_b and C_b). The major difference between the *in-situ* boiling water and the cold water spectra was considered to be the result of alumina gel formation at higher temperatures, with distinct precipitation at lower temperatures. Evidence of precipitation, at the outer film surface, pore mouth blocking, and eventual hydration within the pores is also presented.

KEYWORDS: electrochemical impedance spectroscopy (EIS), anodized aluminum, hydrothermal sealing, film hydration, modeling

Sealing of porous anodic alumina films as a result of immersion in boiling water is a standard method of improving the protection of aluminum to atmospheric corrosion. Thus, aluminum is first anodized in appropriate electrolytes with the resulting films having a typical porous honeycomb morphology, with a barrier layer separating the electrolyte next to the base of the pores from the aluminum substrate. The color of the anodized article depends on the alloy, bath composition, and time of anodizing, whereas the major anodic film parameters (pore and cell diameters and barrier layer thickness) are directly dependent on the anodizing voltage.

The purpose of hydrothermal treatment, or sealing, is to develop pore plugging of the porous film. This process is generally accepted as being associated with the formation of crystalline material on the outer film surface [*1–4*], and more subtle changes in the film

[1]Senior consultant, CAPCIS Ltd/CAPCIS-MARCH Ltd, Manchester, M1 2PW, United Kingdom.
[2]Professor of Corrosion Science and Engineering, Corrosion and Protection Centre, UMIST, Manchester M60 1QD, United Kingdom.
[3]Scientist, Metal Protection and Finishing Department, Metal Industry Development Centre, Selangor, Malaysia.

depths, including dissolution of the cell-walls, precipitation of hydrated alumina within the pores, and development of intermediate layers [*4*].

Electrical impedance measurements were first proposed in 1962 as a practical means of characterizing the sealing process [*1*]. Further, measurement of pore electrolyte resistance after sealing is a standard guide to the extent of pore filling [*5*] and provides an *ex-situ* assessment of the sealing quality and likely performance. However, the subtle changes associated with the sealing of films are only partly revealed by conventional single frequency admittance measurements, typically performed at 1k Hz [*6–8*].

The development of digital frequency response analyzers has enabled researchers to obtain a wide frequency range of electrochemical impedance spectra. Consequently improved process or quality control [*9,10*] can be achieved by evaluation of the various contributions to the impedance and understanding of their influence on the overall sealing mechanisms [*10,11*]. Additionally, assessment of corrosion processes can be obtained by analysis of low frequency (<1 Hz) impedance changes [*12,13*].

Hydrothermal sealing processes appear to involve three distinct overlapping stages [*3,4*]; first, precipitation of material in the pores occurs, especially near the outer film surface. The second stage is formation of crystalline material at the film surface, which is considered to be of relatively minor significance. The final stage is associated with continuing changes within the film depths, possibly involving aggregation of alumina material and a redistribution of porosity. There is also evidence of an intermediate layer, probably of decreased porosity, located below the surface crystals and extending into the film; the development of the intermediate layer occurs at a progressively decreasing rate with sealing time.

The present paper reports on *in-situ* impedance data obtained on anodized aluminum during immersion in boiling distilled water. The objective was to assess the value of the impedance technique as an *in-situ* monitoring approach. The *in-situ* data are compared with more conventional measurements, reported by other workers [*1,2,9–16,18–21*]; these are performed *ex-situ* by immersion in cold distilled water. Impedance measurements were also made during intermittent sealing, that is during both reimmersion in boiling water after immersion in cold water and on further removal. The observed differences between spectra obtained in boiling water and cold water, together with the evolution of impedance with time, are interpreted in terms of electrical circuit analogues or equivalent circuits. Such circuit models also include the contributions from morphological features observed during *ex-situ* electrochemical examination of hydrothermally treated anodic films [*2–4,24*].

Experimental

Electrodes, 1 by 1 cm surface area, were prepared from a sheet of aluminum (99.99 wt% Al; 0.002% Cu; 0.004% Fe; 0.003% Si) by cutting a spade-shaped sample and masking all but one face with epoxy resin. The exposed surface was electropolished in a perchloric acid/methanol mixture at 20 V for 5 min at 5°C, then washed in distilled water and finally dried in a cool air stream.

Individual specimens were anodized at a constant voltage of 17 V in 1.5 M sulphuric acid at 20 ± 1°C for various fixed times to provide film thicknesses of 2.5, 5.0, and 15 μm. Such conditions reflect those used commercially. After anodizing, the specimens were washed in distilled water for 5 min followed by two further rinses in fresh distilled water; this standard procedure was followed throughout the work. Immediately after final rinsing, the anodized specimens were sealed in boiling distilled water under reflux. Water conduc-

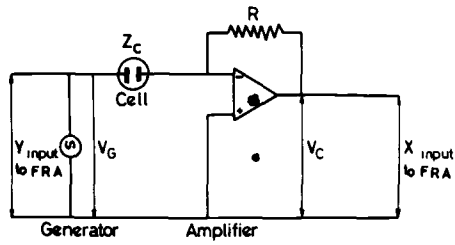

FIG. 1—*Schematic arrangement for "two-electrode" frequency response analysis.*

tivity was 1.8 μS cm^{-1}; the pH was 5.5 at 20°C, which was not adjusted further. After sealing, specimens were dried immediately in a cool air stream.

EIS data were obtained using two identically prepared specimens held 1 cm apart in the test cell; for *in-situ* measurements, the frequency range or number of data points, or both, were reduced to decrease the measurement duration to between 4 and 10 min. A Solartron-Schlumberger 1250 FRA, with a Thompson Ministat as interface, controlled by a Hewlett Packard HP85 personal computer by means of IMPED Software [25] were employed. The two-electrode arrangement used for impedance measurements is shown in Fig. 1.

Results and Interpretation

Typical Ex-Situ Data and Previous Equivalent Circuit Models

Complex plane impedance plots illustrate the major changes observed after the sealing process (Fig. 2). Thus, although the overall film impedance decreases with hydrothermal treatment, there is development of a high-frequency response; this detail is partially resolved by expansion of the axis as indicated in the inset. The more appropriate method

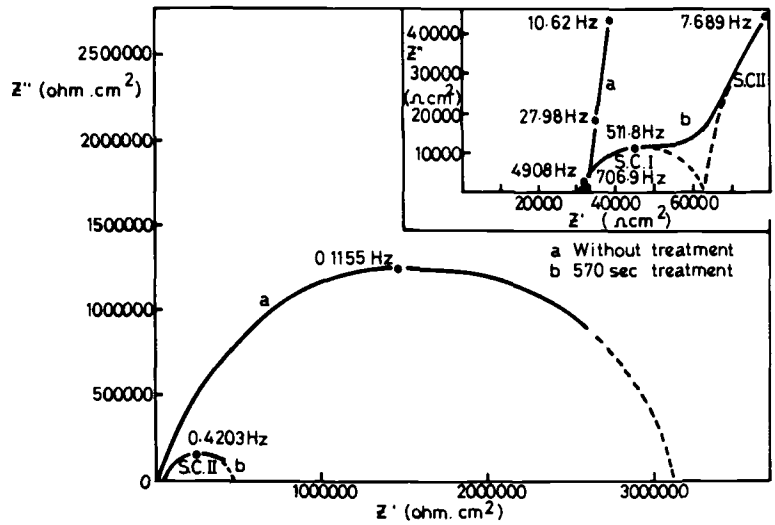

FIG. 2—*Complex phase plots of* (a) *the unsealed 2.5-μm thick porous film and* (b) *the film after sealing for 570 s. The inset in the diagram reveals the data on an expanded Z axis.*

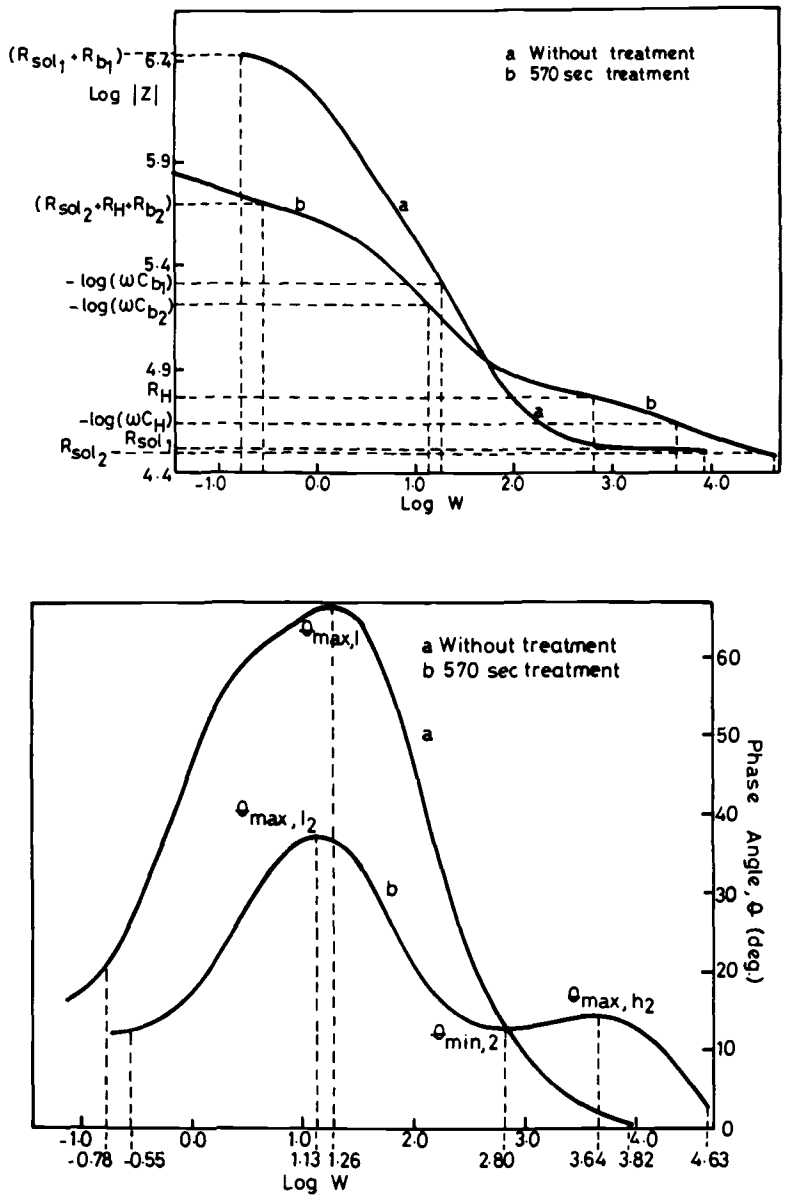

FIG. 3—*Bode plots for the* (a) *unsealed and* (b) *sealed 2.5-μm thick films of Fig. 2.*

of presenting the data is in the form of Bode plots of impedance and phase angle against measurement frequency, log $|Z|$ versus log ω and log θ versus log ω (Fig. 3).

Change in response of aluminum, anodized to produce a 2.5-μm-thick film, before and after sealing for 570 s, but obtained *ex-situ* in cold water, are indicative of capacitive (high phase angle) and resistive (low phase angle) components. The approximate magnitudes of

the RC components can be extracted using the conventional methods of impedance analysis, as indicated in Fig. 3. Values of the RC components may then be fed back into an appropriate model equivalent circuit; adjustment of the model or of the component values, or both, so that the simulated model curves fit the experimental data provides an assessment and analysis method.

For the unsealed anodic film, a simple circuit model of a solution resistance, R_s, in series with a parallel RC combination of barrier layer resistance, R_b, and barrier layer capacitance, C_b, describes most of the data. However, there is some evidence in the low-frequency phase angle data of a secondary film component, possibly due to a hydration process. In the present work a limitation is recognized in the analysis since when the solution resistance is high, as in relatively low-conductivity distilled water, and where R_s approaches R_b, it may not be a simple procedure to extract values of C_b. However, the capacitance data of Fig. 3 suggest a barrier layer thickness of 17 nm, assuming a dielectric constant of 10 and using the relationship between capacitance and thickness of a parallel plate condensor $C = \epsilon_0 \epsilon A/d$, where ϵ_0 is the permittivity in free space, ϵ is the dielectric constant, A is the area, and d is the thickness. This is the expected value for films formed in sulphuric acid and was independent of the overall film thickness (2.5, 5, and 15 μm).

A schematic diagram of the simplified cross-section of a porous anodic film on aluminum is given in Fig. 4*a*; the equivalent circuit and nomenclature adopted by Jason and Wood [*14*] is given in Fig. 4*b*. The circuit was developed from the observed change in the capacitance of electrical condensers with adsorbed water content. Considering Fig. 4*b*, the capacitance between two conducting layers, separated by a mixed alumina, air, and water dielectric of total thickness d is C_o and the leakage resistance is R_o. The pore base capacitance and resistance are represented by C_2 and R_2 respectively and R_1 is the resistance of the pore. Under 100% relative humidity conditions, R_1 represents the resistance of the pore electrolyte (R_s). This circuit is similar to that first used to describe an unsealed porous anodic film [*1*].

For partly sealed films, a modified circuit (Fig. 5) has been proposed by Hoar and Wood [*1*]. This circuit simulates pore filling and a degree of pore end plugging, $R_{1\text{-}2}$, $C_{1\text{-}2}$ and $R_{1\text{-}1}$, $C_{1\text{-}1}$, respectively, in agreement with the results of Hunter, Towner, and Robinson [*15*].

Impedance spectroscopy measurements on anodic films formed in oxalic acid and sealed in hot water at 99.5°C led Koda et al. [*11*] to suggest that an equivalent circuit comprising the barrier layer, R_b and C_b, porous layer, R_p and C_p, and solution resistance, R_{sol}, should, in principle, described the system (Fig. 6). This is similar to the circuit proposed by Hitzig et al. [*16*], which was used to describe the sealing of sulphuric acid formed films; the

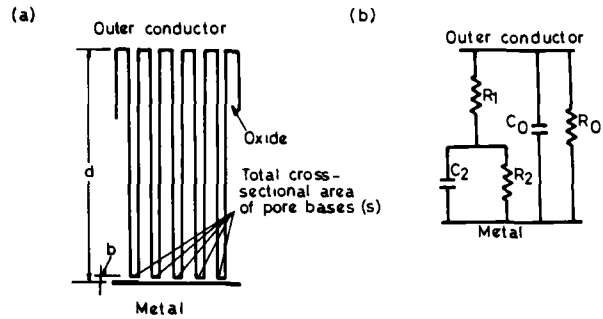

FIG. 4—*Schematic diagrams of* (a) *simplified section of the porous anodic film and* (b) *equivalent circuit of single pore* [4].

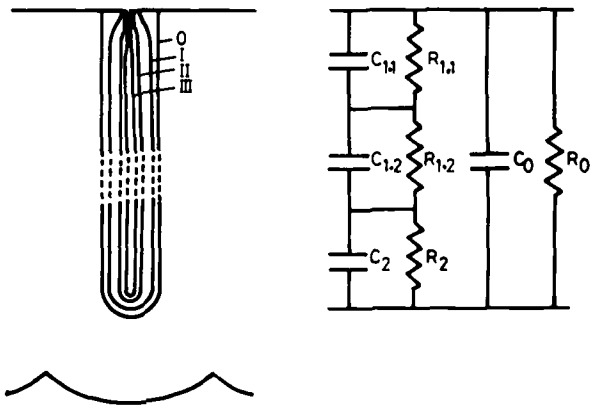

FIG. 5—*Schematic diagram of the change in pore morphology during sealing and the modified circuit analogue* [1].

increase in R_p and decrease in C_p with sealing time were considered to be due to partial pore filling (Fig. 7). Koda et al. concluded that hydration of the porous layer gave rise to pore filling, while development of the higher frequency response, R_h and C_h, was the result of hydrated film formation (Fig. 8).

A more appropriate circuit for the present study, based on electronoptical evidence [*2–4,24*] and incorporating elements of previous models, would appear to include the solution resistance, R_s, hydrated film components, R_h and C_h, and the barrier layer, R_b and C_b (Fig. 9). As shown later, although this may be a simplified model, it is useful in many cases; however, more detailed consideration has to be given to specific hydration processes and conductivity changes to describe fully the response from amorphous alumina films produced by anodic oxidation.

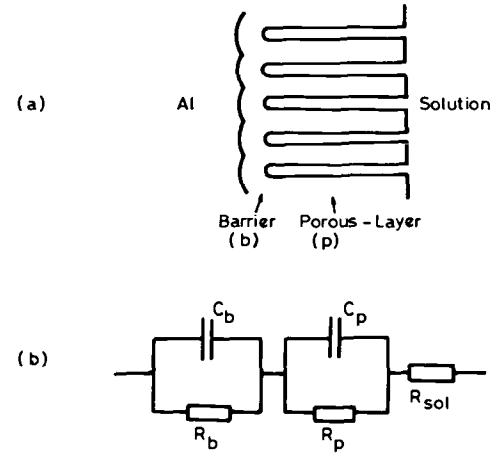

FIG. 6—*Schematic diagram of the porous anodic film and equivalent circuit* [11].

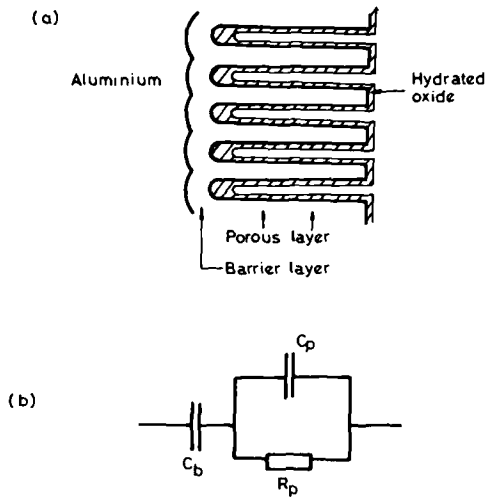

FIG. 7—*Schematic diagram of the partially sealed anodic film and modified circuit analogue* [16].

In-Situ Impedance Measurements and Models for Continuous Sealing in Boiling Water

Bode plots obtained from aluminum, supporting 5-μm-thick porous alumina films, immersed in boiling water, are shown in Fig. 10. Thus, although a general decrease in the overall impedance, $|Z|$, was observed during extended immersion, there was also an initial increase in the high-frequency range during the first 4 min of immersion. The dashed line shows the expected high-frequency response based on the low-frequency data. Figure 11 shows that this increase in high-frequency impedance was more pronounced with a 15-μm porous film [*17*]. The phase angles also showed a general decrease over the first 60 min, associated with the higher frequency ranges, but this was then followed by an increase in the lower frequency phase angle response on prolonged immersion. A similar trend was observed with the film formed to 15 μm.

The use of a suitable equivalent circuit can generate simulations of the impedance data. A general model for the *in-situ* responses observed during immersion in boiling water incorporates an apparent solution resistance, R'_{sol}, and apparent hydrated film, R'_H and C'_H, and apparent barrier layer, R'_b and C'_b components (Fig. 12*a*). However, this model can be initially simplified depending on the values of C'_H and R'_H, (Fig. 12*b*) or even simplified further to incorporate R'_{sol} and $R'_H C'_H$ into R''_H, Fig. 12*c*. R''_H then represents the apparent hydrated pore resistance.

Understanding of the physical meaning of the previous components is assisted by following their evolution with time of immersion in boiling water. The early changes, proceeding over the initial 4 min with the 5-μm film and over the initial 20 min for the 15-μm film, appear to involve leaching of residual acid from the porous morphology (the specimens were previously anodized in a sulphuric acid bath). Changes in pH during sealing in nickel sulphate have been reported [*18*], although Spooner and Forsyth [*19*] suggest that physically adsorbed water and retained anodizing electrolyte are lost before the film reaches 100°C. The presence of soluble species from the dissolution of alumina and the release of adsorbed/absorbed electrolyte anions should increase the pore solution and boiling water conductivity; hence R'_{sol} and R'_H should decrease initially. This low

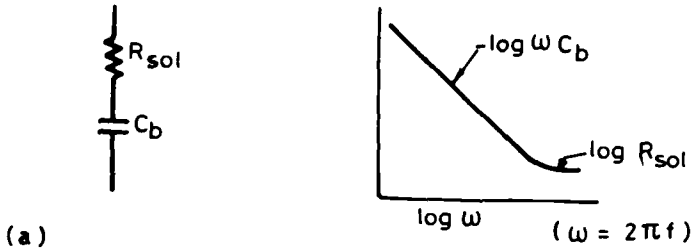

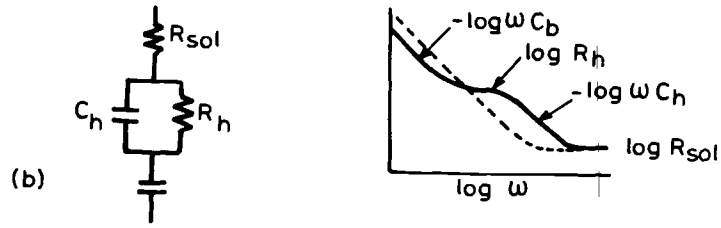

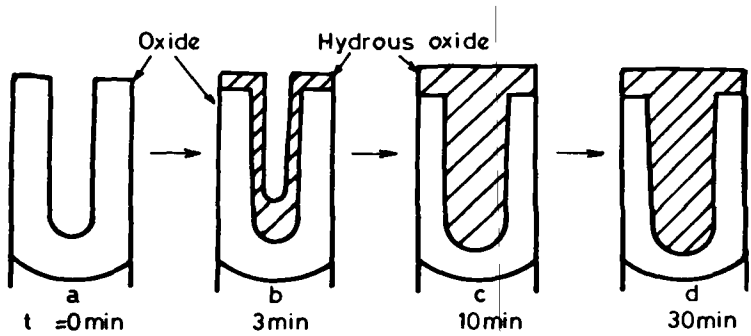

FIG. 8—*Schematic diagrams depicting circuit responses for the partially sealed anodic films* [20,21].

conductivity and lack of hydration accounts for the early, relatively low magnitude of the impedance in the higher frequency data above 100 Hz (Figs. 10*a* and 11*a*).

The experimental values of R''_H, C''_b and R''_b, observed by curve fitting of the EIS data, were then replotted against immersion time (Fig. 13). This indicates the trends of decreases in apparent resistances and increase in apparent capacitance associated with barrier layer thinning. The increase in C''_b appears to involve two stages (Fig. 13*b*); a relatively

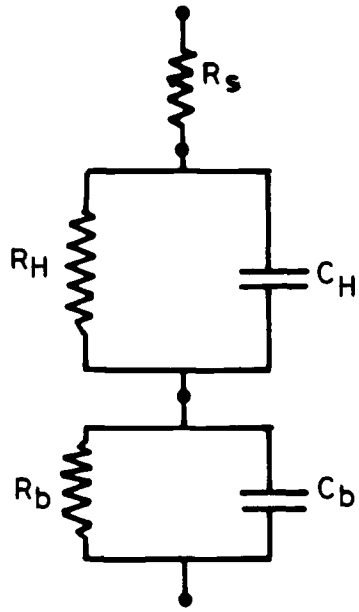

FIG. 9—*Simplified equivalent circuit for a porous anodic film.*

slow process, of duration up to 50 min, is followed by an increasing rate of change. This is reflected in the changes in apparent barrier layer resistance, R''_b (Fig. 13*c*), which also occur over the first 45 min, and the more gradual decrease of hydrated pore resistance, R''_H, (Fig. 13*a*).

The data for the 15-μm film, obtained during continuous sealing, and replotted against time of immersion in boiling water show similar trends of decrease in R''_H, (Fig. 14*a*) and increase in C''_b, although the capacitance reached a maximum that was followed by a slight decrease, (Fig. 14*b*). However, the apparent barrier layer resistance increased with time (Fig. 14*c*). Thus, even though similar trends are observed as a result of the hydration processes, there are also some differences resulting from changes in the original porous film thickness.

The progress of sealing results in the dissolution of the porous film skeleton, releasing Al^{3+} ions and eventual formation of hydrated alumina; these contribute to the decrease of R''_H. The increase in C''_b is indicative of barrier layer thinning, although the slight decrease with the 15-μm film after 150 min immersion also suggests hydration of the barrier layer. It is evident that decreasing the barrier layer thickness decreases R''_b for the 5-μm film but, with a thicker film, the thinning is compensated not only by hydration but also by possible precipitation and agglomeration processes, which occur close to the barrier layer as suggested by O'Sullivan and Wood [*2*].

Ex-Situ Impedance Measurements, Distilled Water at 20°C

Comparisons were made between specimens monitored in boiling water and the more "conventional" measurements obtained *ex-situ* by immersion in cold water. Here the two identical specimens were removed after a specific time from the boiling water hydrothermal bath, immersed in distilled water at 20°C, and EIS measurements were made.

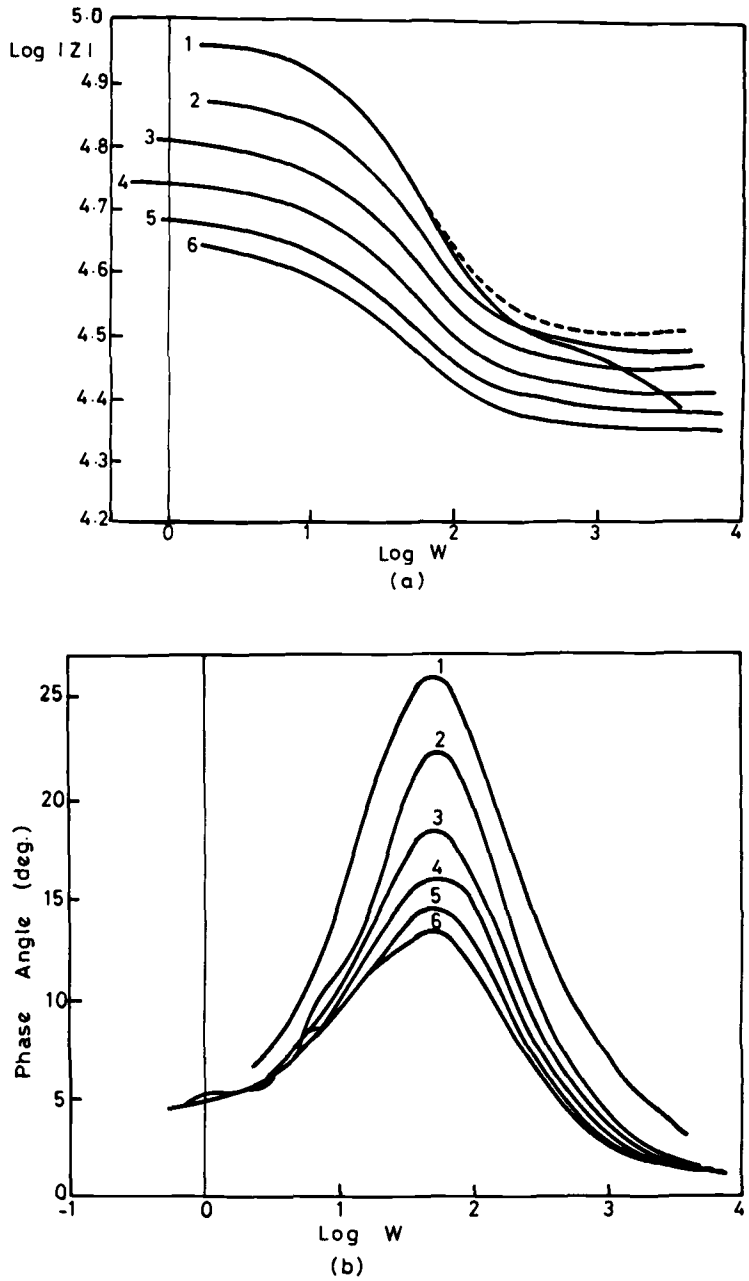

FIG. 10—*Impedance results from 5-μm film during continuous sealing in boiling water; (1) 4 min; (2) 6 to 9 min; (3) 11 to 15 min; (4) 17 to 27 min; (5) 24 to 28 min; (6) 30 to 32 min.*

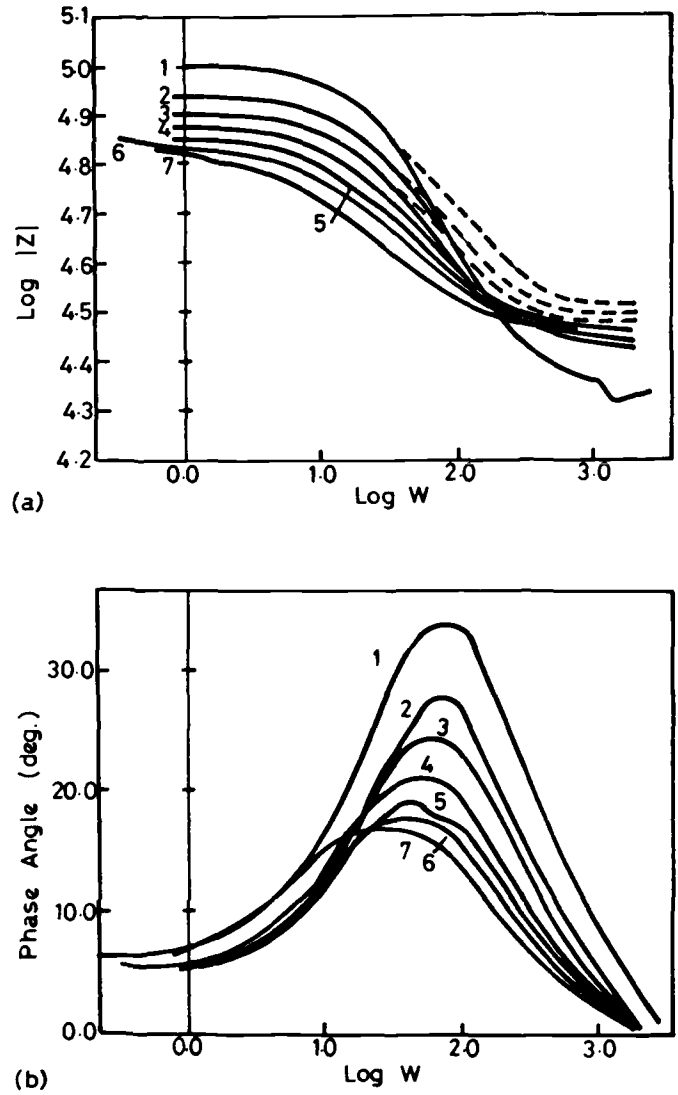

FIG. 11—*Impedance results from 15-μm film during continuous sealing in boiling water; (1) 0 to 5 min; (2) 7 to 11 min; (3) 12 to 16 min; (4) 17 to 21 min; (5) 22 to 28 min; (6) 27 to 33 min; (7) 35 to 44 min.*

The specimens were then returned to the boiling water for further sealing and the cycle repeated. The evolution of the conventional impedance with time was therefore determined and the data again interpreted in terms of electrical circuit analogues.

The equivalent circuit models employed (Fig. 15) were derived from consideration of possible components that could be present; these were based on examination of electron micrograph cross-sections of the films [*2–4,24*]. The models were then simplified to correspond more closely to the measured resistance and capacitance values extracted from the

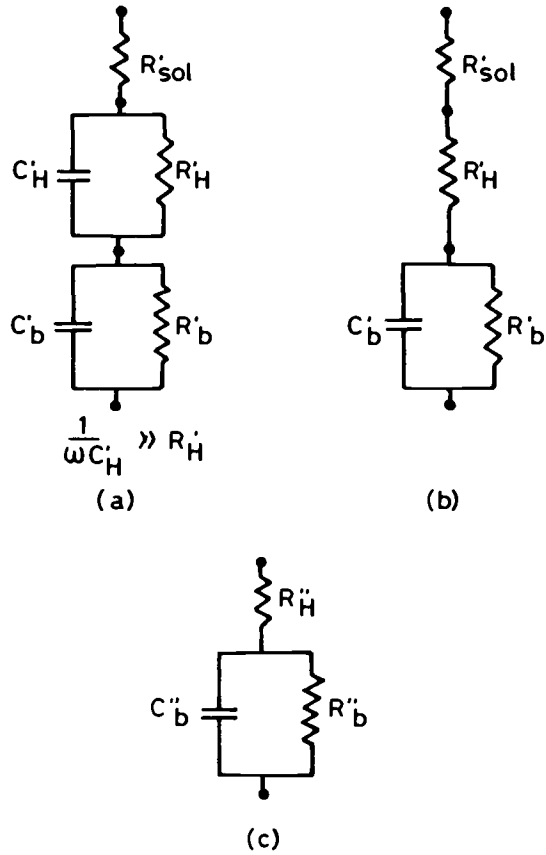

FIG. 12—*Equivalent circuits used to describe the in-situ hydrothermal process, showing possible circuit simplications revealed from* (a) *to* (b) *to* (c).

experimental data. The resistance and capacitance values were inserted into a simulation program and the simulated impedance curves compared to the experimental curves.

The schematic diagram and equivalent circuit of the anodized, but unsealed anodic film (Figs. 15*a,b,c*) identify the cell and electrolyte resistances, pore wall, and barrier layer resistances together with the pore wall and barrier layer capacitances. Since the contribution from the pore electrolyte and porous film appears to be negligible, then a simplified circuit (Fig. 15*c*), comprising the barrier layer, R_B and C_B, and solution resistance, R_s, provides an adequate description of the film and its impedance.

Impedance measurements in distilled water at 20°C after various periods of sealing of the 5-μm film are shown in Fig. 16. The components produced by the hydration process can be represented by an overall hydration resistance, R_H, and hydration capacitance, C_H, as indicated in the schematic diagram of Fig. 15*d* and the equivalent circuit of Fig. 15*e*; Fig. 15*e* can be further simplified to that of Fig. 15*f*, which is similar in some respects to previously proposed models (Fig. 9).

The evolution of the various components with time is given in Fig. 17, which shows the change in R_s, increases in R_H and C_b and decreases of C_H and R_b. The detection of R_H (between G and N in Fig. 15*d*) indicates that changes in R_s, due to the pore blocking, R_{OH},

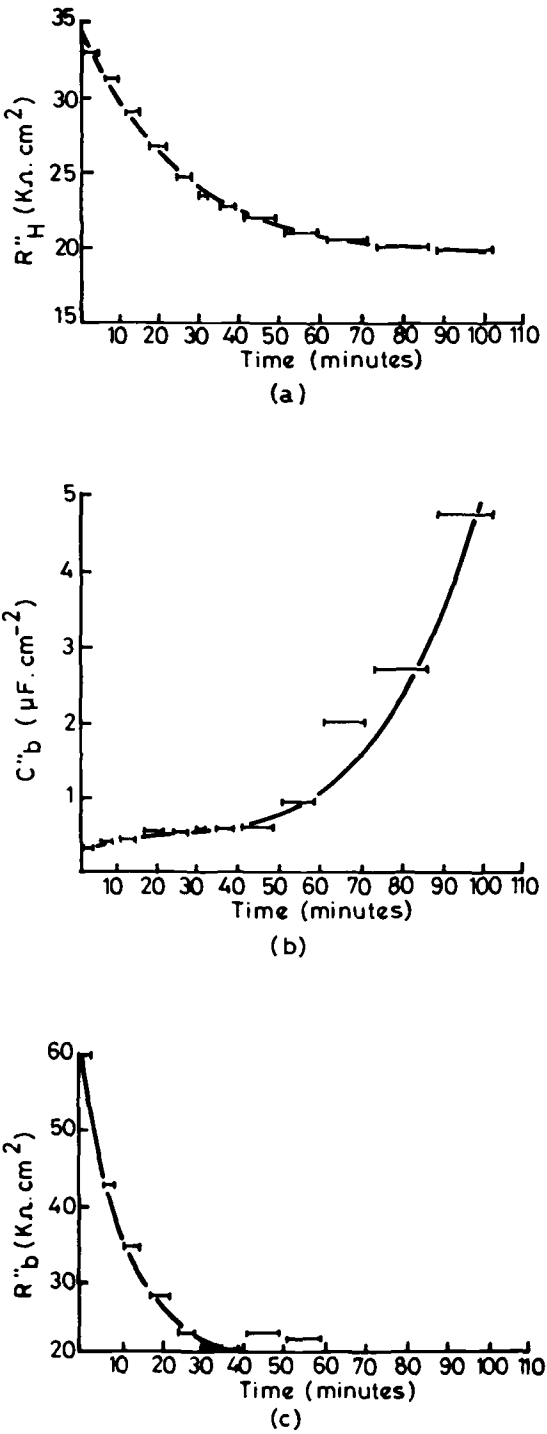

FIG. 13—*Change of* (a) *apparent hydrated pore resistance,* R''_H, (b) *apparent barrier layer capacitance,* C''_b, *and* (c) *apparent barrier layer resistance,* R''_b, *during continuous sealing of the 5-μm porous film.*

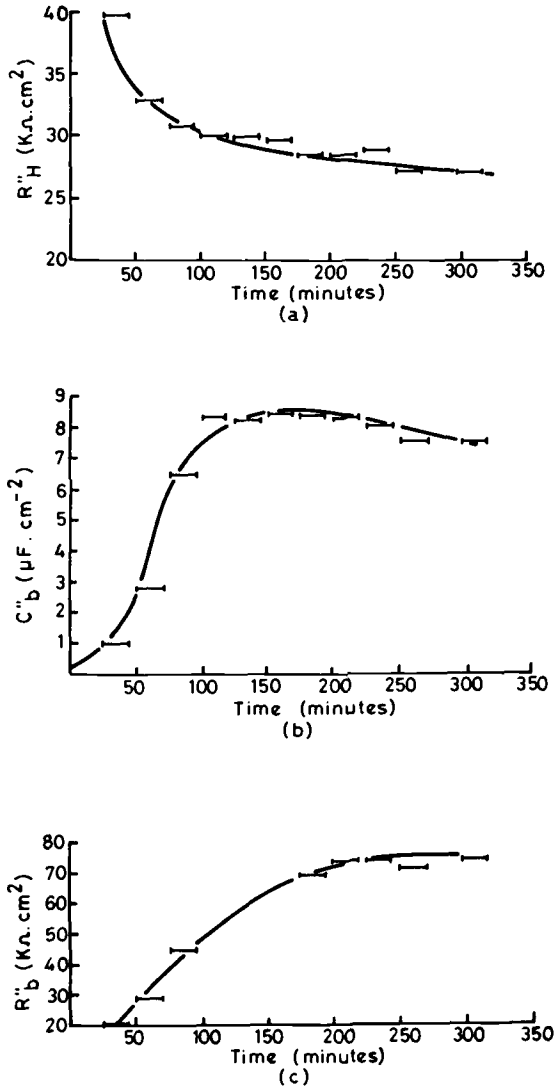

FIG. 14—*Change of* (a) *apparent pore resistance,* R''_H, (b) *apparent barrier layer capacitance,* C''_b, *and* (c) *apparent barrier layer resistance,* R''_b, *during continuous sealing of the 15-μm porous film.*

(between G and E) have occurred. Electron micrographs show that the surface hydration product, pseudoboehmite [*2–4,24*], consists of an acicular or lamellar shaped product, which may eventually obliterate the outer pore surface.

In general, R_H is detected more readily and a more rapid decrease of C_H is evident with thicker films; the rate of increase of C_b is also greater with thicker films. Pore mouth plugging or sealing is achieved after about 5 min of hydrothermal treatment, largely involving development of pseudoboehmite by precipitation. Importantly, the difference between the *in-situ* measurements in hot water and the conventional cold water responses

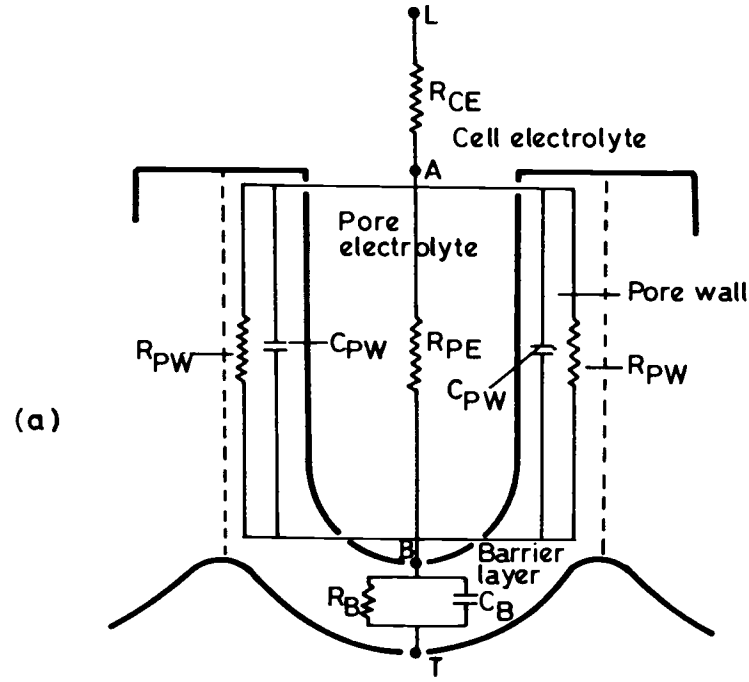

R_{CE} : Cell electrolyte resistance
R_{PE} : Pore electrolyte resistance
R_{PW} : Pore wall resistance
R_B : Barrier layer resistance
C_{PW} : Pore wall capacitance
C_B : Barrier layer capacitance

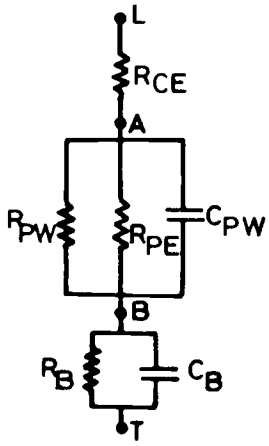

(b)

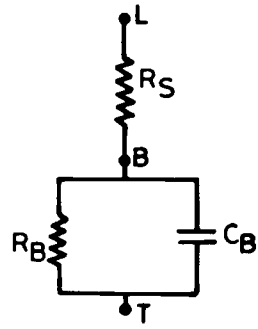

(c)

FIG. 15—*Schematic diagrams and proposed equivalent circuit for unsealed* (a,b,c) *and sealed* (d,e,f) *porous anodic films.*

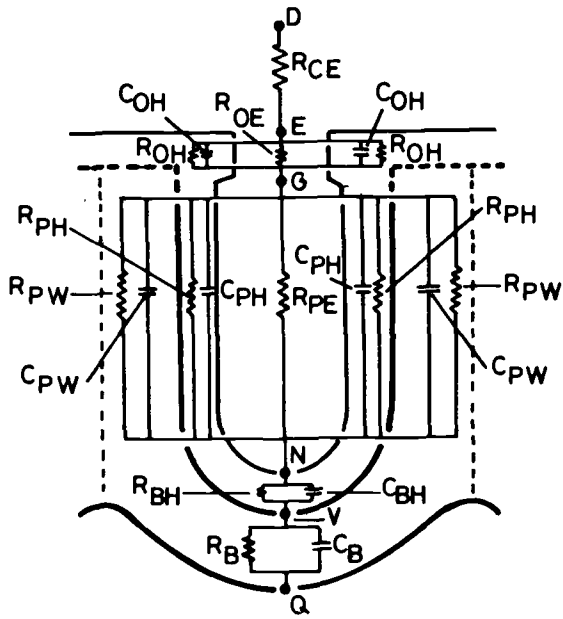

(d)

R_{OH} : Surface crystals and intermediate layer resistance
R_{OE} : Surface crystals and intermediate layer electrolyte resistance
R_{BH} : Barrier layer hydration resistance
R_{PH} : Pore filling material resistance
C_{OH} : Surface crystals and intermediate layer capacitance
C_{PH} : Pore material capacitance
C_{BH} : Barrier layer hydration capacitance

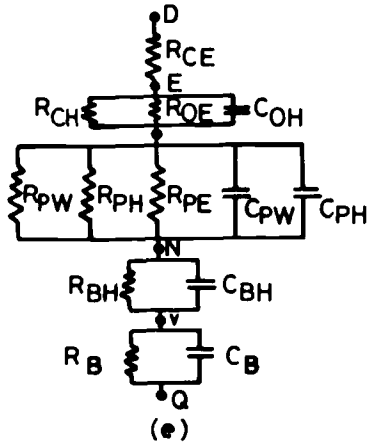

(e)

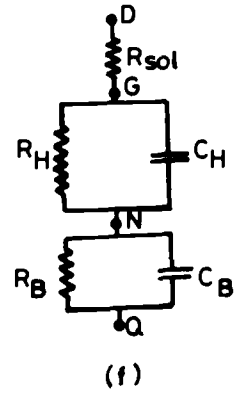

(f)

FIG. 15—(continued)

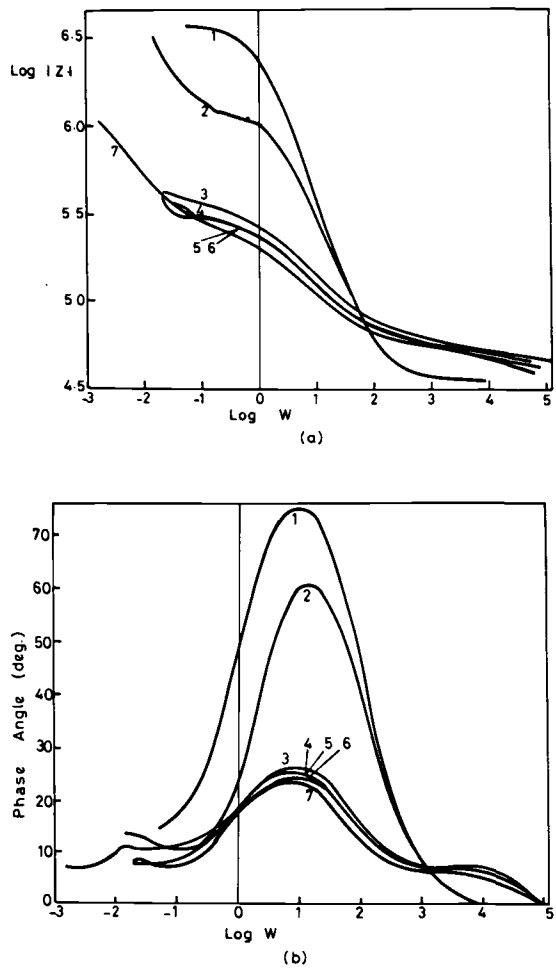

FIG. 16—*Impedance measurements on a 5-μm thick film; the measurements were made in cold water after various times of immersion: (1) 0 s; (2) 30 s; (3) 60 s; (4) 90 s; (5) 120 s; (6) 180 s; (7) 300 s.*

appears to be primarily due to the presence of an alumina gel phase at higher temperatures that transforms into a "solid," precipitated material when the alumina film is removed from the sealing bath and the temperature falls to ambient levels.

In order to test the gel material hypothesis, specimens were continuously monitored using EIS for a period of time in hot water, removed and the impedance in cold water determined, replaced in the hot water and again continuously monitored, and the procedure repeated. The interrupted sealing data gave the same trends as for continuously sealed specimens; thus if the periods of time when the specimen was out of the hot water bath are subtracted from the time scale, then the *in-situ* data were comparable to a continuously immersed specimen. This strongly suggests that the transformation from gel to precipitate, and vice-versa within the pores, is largely reversible. Other experimental data [*24*] for long term sealing (not shown here) clearly reveal the existence of three time

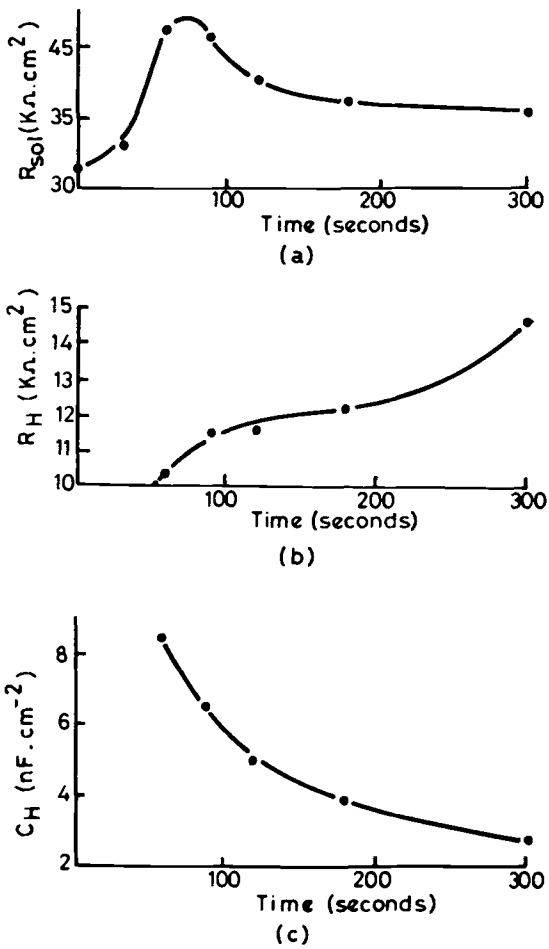

FIG. 17—*Change of* (a) *solution resistance,* R_s, (b) *hydrated pore resistance,* R_H, (c) *hydrated pore capacitance,* C_H, (d) *barrier layer resistance* R_b *and* (e) *barrier layer capacitance,* C_b, *after increasing periods of sealing; the measurements were made in cold water.*

constants or peaks, representing the hydrated pore (R_H and C_H), the section of the pore between the intermediate layer and the barrier layer (R_{H1} and C_{H2}) and the barrier layer (R_b and C_b).

Discussion

The EIS data obtained *in-situ* during hydrothermal treatment of porous anodic films on aluminum provide new, detailed information on the sealing processes. Bode plots of impedance and phase angle against frequency are suitable methods of data presentation for this system in which the impedance response covers a wide frequency range. Electrical circuit analogues are appropriate means of analysis and interpretation of the evolution of the impedance with time of sealing. There are no electrochemical reactions involved in the sealing process and therefore there is no requirement to invoke the over-simplified equivalent circuit representation of kinetic parameters.

The circuit models used in the present work are not entirely new [*13,16,19–23*]. How-

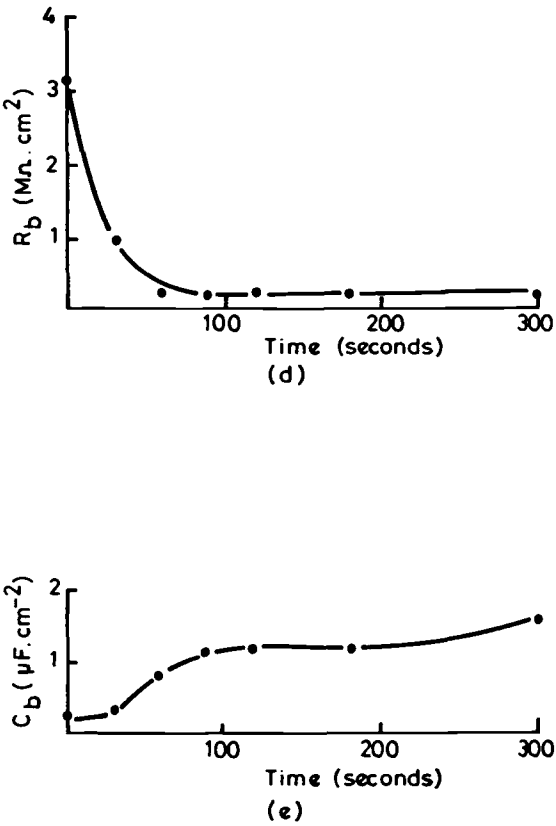

FIG. 17—(continued)

ever, the components used in the present study identify important parameters of the sealed film (Figs. *9, 12* and *15*). In other models, R_s represents solely the resistance of the electrolyte or medium in which the impedance measurements were conducted; this appears to over-simplify the interpretation. R_s incorporates effects from the surface crystals of pseudoboehmite, any intermediate layer as well as the cell electrolyte resistance. Separation of the hydrothermal treatment effects on the film surface (R_s), in the pores (R_H and C_H) and in the barrier layer (R_b and C_b) enables the developments during hydrothermal treatment, or the sealing processes, to be monitored with immersion time.

Sealing is not a simple process of a gradual buildup of hydrous oxide on the barrier layer, pore wall, and film surfaces as suggested by some other workers. Morphological observations from electron microscopy show the progressive development of an outer precipitated film [*2–4,24*], pore plugging and precipitation of solid material within the pores down to the original barrier layer [*2*]. These morphological changes are also reflected in the *in-situ* (boiling water) and *ex-situ* (cold water) impedance spectra and are particularly obvious when these are analyzed by plotting the evolution of extracted values of the appropriate circuit components with time.

Interpretation of the impedance data in terms of development of an outer film, pore mouth plugging followed by barrier layer thinning and further precipitation on pore walls mirrors in general terms the morphological changes.

The mechanisms by which sealing develops can be summarized from comparisons

between the conventional or cold water data and the *in-situ* hot water monitoring. The surprising difference lies in the responses from the hydrated pores during *in-situ* monitoring at the sealing temperature. The important, and possibly controlling, parameter appears to be the development of the hydrated gel produced by dissolution of the alumina cell material enveloping the pore. Precipitation on the outer film surface plays a major role in the development of the plugging of the pore mouth. Hydration within the pore, resulting from dissolution from the surface of the pore wall and the barrier layer proceeds more slowly since it relies on diffusion processes. The presence of a gel at higher temperature facilitates this process, while decreasing the temperature, i.e., by removing the specimen from the sealing bath, transforms the gel to a precipitate which effectively hinders further diffusion processes.

The analysis and interpretation of EIS on sealed and partially sealed porous films produced by anodizing of aluminum in sulphuric acid has provided a more detailed insight into the mechanisms of sealing. The influence of film thickness and differences between different films produced by other anodizing processes requires further investigation. However, the equivalent circuits proposed are able to assist in the understanding of the sealing processes and offer advantages over previous models.

References

[1] Hoar, T. P. and Wood, G. C., *Electrochimica Acta*, Vol. 7, 1962, p. 333.
[2] Wood, G. C. and O'Sullivan, J. P., *Journal of the Electrochemical Society*, Vol. 116, 1969, p. 1351.
[3] Wefers, K., *Aluminum*, Vol. 49, 1973, p. 553.
[4] Thompson, G. E., Furneaux, R. C., and Wood, G. C., *Transactions of the Institute of Metal Finishing*, Vol. 53, 1975, p. 97.
[5] Bradshaw, D. H., Sheasby, P. G., Bancroft, G., and Hack, D. F., *Transactions of the Institute of Metal Finishing*, Vol. 50, 1972, p. 87.
[6] B.S. 1615:1972, Specification for Anodic Oxidation Coatings on Aluminum, British Standards Institution, 2 Park Street, London.
[7] B. S. 3987:1974, Sealing Assessment by Admittance Measurement, British Standards Institution, 2 Park Street, London.
[8] ISO 2931. Anodizing of Aluminium and its Alloys—Assessment of Quality of Sealed Anodic Oxide Coatings by Measurement of Admittance or Impedance, International Standards Organization.
[9] Bodu, J. J., Brunin, M., Epelboin, I., Keddam, M., Sertour, G., and Takenouti, H., *Aluminio*, 1977, p. 277.
[10] Mansfeld, F. and Kendig, M. W., *Corrosion*, Vol. 41, 1985, p. 490.
[11] Koda, M., Takahashi, H., and Nagayama, M., *Kinzoku Hyomen Gijutsu*, Vol. 33, 1982, p. 1.
[12] Mansfeld, F., *Corrosion*, Vol. 44, 1988, p. 538.
[13] Mansfeld, F., *Electrochimica Acta.*, Vol. 35, 1990, p. 1533.
[14] Jason, A. C. and Wood, G. C., *Proceedings of the Physics Society*, London, Vol. B, No. 68, 1955, p. 1105.
[15] Hunter, M. S., Towner, P. F., and Robinson, D. L., 4th Award Tech. *Proceedings of the American Electroplaters Society*, 1959, p. 220.
[16] Hitzig, J., Jutter, K., Lorenz, W. T., and Paatch, W., *Corrosion Science*, Vol. 24, 1984, p. 945.
[17] Ahmadun, M. B. H., Dawson, J. L., and Thompson, G. E., *Transactions of the Institute of Metal Finishing*, Vol. 68 (4), 1990, p. 109.
[18] Wood, G. C. and Marron, V. J. J., *Transactions of the Institute of Metal Finishing*, Vol. 45 (17), 1967, p. 107.
[19] Spooner, R. C. and Forsyth, W. J., *Plating*, Vol. 55, 1968, pp. 336, 341, and 463.
[20] Koda, M., Takahashi, M., and Nagayama, M., *Journal of the Metal Finishing Society*, Japan, Vol. 33, 1982, p. 614.
[21] Koda, M., Takahashi, H., and Nagayama, M., *Journal of the Metal Finishing Society*, Japan, Vol. 33, 1983, p. 44.
[22] Young, L., *Transactions of the Faraday Society*, Vol. 51, 1955, p. 1250.

[23] Young, L., *Transactions of the Faraday Society*, Vol. 55, 1959, p. 842.
[24] Ashmadum, M. B. H., Ph.D. thesis, University of Manchester, 1988.
[25] IMPED Corrsoft™, software package from CAPCIS-MARCH Ltd, Bainbridge House, Manchester, U.K.

DISCUSSION

F. Mansfeld[1] *(written discussion)*—The impedance data shown indicate that the anodic film is dissolving and the pore resistance is decreasing during the sealing process which is just the *opposite* of what one wants to achieve by sealing. In our experience, the changes of the anodic layers observed in your tests occur if the acid used in the anodizing process is not carefully removed before sealing—preferrably in an alkaline bath. Failure to remove acid can lead to corrosion during sealing—exactly what you have observed.

J. L. Dawson, G. E. Thompson, and M. B. H. Ahmadun (authors' closure)—The *in-situ* impedance data show a decrease in resistance as opposed to an increase in resistance which is observed in conventional (cold water) sealing studies. While it is appreciated that a sealed film shows an increased resistance compared with the unsealed film in cold water, this study reveals the trends in behavior in both hot and cold water. Thus, *in-situ* processes proceeding prior to pore filling with solid material are defined. Eventually, in cold water solid products will fill the pores leading to an increased resistance. The general result that sealing results in an increase of resistance, measured at ambient temperature, is not in question.

[1]University of Southern California, Los Angeles, CA, 90089-0241.

John R. Scully[1]

Characterization of the Corrosion of Aluminum Thin Films Using Electrochemical Impedance Methods

REFERENCE: Scully, John R., "**Characterization of the Corrosion of Aluminum Thin Films Using Electrochemical Impedance Methods,**" *Electrochemical Impedance: Analysis and Interpretation, ASTM STP 1188,* J. R. Scully, D. C. Silverman, and M. W. Kendig, Eds., American Society for Testing and Materials, Philadelphia, 1993, pp. 276–296.

ABSTRACT: Characterization of a variety of electrochemical parameters associated with the corrosion of aluminum, Al-Cu, and Al-Si alloy thin films (~1-μm-thickness) in dilute hydrofluoric acid (HF) has been accomplished using electrochemical impedance spectroscopy (EIS). Phenomena characterized include the transition from passive to active dissolution with increasing HF concentration, determination of diffusional impedances associated with ionic transport through the passive oxide, detection of the initiation and repassivation of a population of metastable pits, changes in aluminum oxide resistivity and state of hydration at open circuit potential (OCP), and establishment of trends in oxide film growth with anodic potential. Impedance studies on model intermetallic phases and artificial pits were also conducted in order to aid in the interpretation of these phenomena. A survey of the analyses and interpretation methods utilized to obtain such information from impedance spectra is presented.

KEYWORDS: aluminum oxide film, electrochemical impedance, diffusional impedance, hydrofluoric acid, metastable pitting, oxide capacitance, oxide resistance, passivity, pit capacitance, repassivation, theta phase precipitates

Nomenclature

dc	direct current
CE	Counter electrode
CPE	constant phase element
EIS	electrochemical impedance spectroscopy
ETR	electron transfer reactions
FRA	frequency response analyzer
HF	hydrofluoric acid
hf	high frequency
F	formal
lf	low frequency
IC	integrated circuit
IR	ohmic voltage error
IA	image analysis
NLLS	nonlinear least squares analysis
OCP	open circuit potential

[1]Assistant professor, Department of Materials Science and Engineering, University of Virginia, Center for Electrochemical Sciences and Engineering, Charlottesville, VA 22903.

RE reference electrode
SCE saturated calomel electrode
UHV ultra high vacuum
WE working electrode

α = area fraction of pits (-)
E_{Bd} = Breakdown potential
E_{Rp} = Repassivation potential
C_{cu} = interfacial capacitance of copper electrode ($\mu F/cm^2$)
C_H = Helmholtz or double layer capacitance ($\mu F/cm^2$)
C_{pit} = double layer capacitance of pit ($\mu F/cm^2$)
C_{ox} = oxide space charge capacitance ($\mu F/cm^2$)
C_{tot} = total capacitance for defective oxide surface ($\mu F/cm^2$)
d_{ox} = oxide thickness (nm)
D_{ox} = ion diffusion coefficient in oxide (cm^2/s)
ϵ = dielectric constant (-)
ϵ_o = permittivity of free space ($8.85 \times 10^{-14} F/cm$)
f = frequency of ac signal (Hz, where $\omega = 2\pi f$)
j = $(-1)^{1/2}$
l_ω = distance associated with ionic diffusion at frequency ω (cm)
λ = oxide transfer coefficient, about 0.5 (-)
n = dimensionless constant usually between 0 and 1 associated with CPE, i.e., $Y_{cpe} = Y_o(j\omega)^n$, $n = 1$ for an ideal capacitor and 0.5 for an infinite diffusional impedance
O = finite diffusional impedance parameter (see Ref *8*)
Θ = area fraction of theta-Al_2Cu precipitates
R_θ = interfacial or oxide resistance of theta phase site (Ω-cm^2)
R_{pit} = interfacial resistance of pit site (Ω-cm^2)
R_{sol} = solution resistance between RE and WE (Ω-cm^2)
R_{ox} = oxide resistance for passive Al (Ω-cm^2)
R_{tot} = total resistance of oxide and all defect sites (Ω-cm^2)
ρ = apparent intrinsic resistivity of oxide including defect sites (Ω-cm)
ρ_{ox} = apparent intrinsic resistivity of Al oxide excluding defect sites (Ω-cm)
ρ_{site} = apparent intrinsic resistivity of theta phase defect sites (Ω-cm)
σ = average Warburg impedance coefficient, where $W = \sigma/\omega^{1/2}(1-j)$ (Ω-$cm^2/s^{1/2}$)
σ_{an} = Warburg impedance coefficient for anions diffusing in an oxide film
σ_{ca} = Warburg impedance coefficient for cations diffusing in an oxide film
τ = RC time constant (s)
τ_{ox} = oxide RC time constant obtained from multiplying R_{ox} by C_{ox} (s)
W = symbol representing infinite diffusional impedance parameter (see Ref *8*)
ω = frequency of applied ac signal (rad/s)
Y = magnitude of admittance (mho/cm^2 or mho)
Y_o = admittance constant used in the expression for the constant phase element, (Y_{cpe}) = $Y_o(j\omega)^n$. In the case of the Warburg diffusional impedance, $1/Y_o = \sigma$
Y' = real component of admittance (mho/cm^2 or mho)
Y'' = imaginary component of admittance (mho/cm^2 or mho)
Ψ = voltage field strength (5×10^6 V/cm for Al oxide)
Z = magnitude of impedance such that $Z = (Z'^2 + Z''^2)^{1/2}$, (Ω-cm^2)
Z' = real component of impedance, (Ω-cm^2)
Z'' = imaginary component of impedance, (Ω-cm^2)
Z_d = diffusional impedance associated with diffusion through a passive film, (Ω-cm^2)

Characterization of the corrosion of thin film metallic materials (on the order of 1 μm in thickness) in aqueous solutions is often a difficult task to accomplish using dc electrochemical techniques. For instance, anodic polarization of thin films in solutions that destabilize their passivating oxide can sufficiently accelerate dissolution so as to result in complete penetration of the thin film during the experiment. Alternatively, metastable pit growth in passive aluminum alloys, occurring as a result of galvanic coupling between intermetallic phases resulting from alloying and the solute depleted matrix, cannot be readily probed by dc polarization methods since the localized galvanic cell develops at the prevailing open circuit potential (OCP) without the application of an external current. Gravimetric determination of corrosion rate is also a difficult task for thin metallic films of nanoscale dimensions except with quartz crystal microbalances. Electrochemical impedance spectroscopy (EIS) is a suitable technique for such applications. EIS is also an *in-situ* method capable of monitoring pit initiation and changes in passive film characteristics prior to initiation [*1,2*]. Finally, solution IR voltage errors make dc methods difficult to perform accurately, especially in dilute electrolytes simulating rinse solutions used in integrated circuit (IC) processing or in dilute solutions simulating subsequent exposure to moisture in combination with low levels of contaminants.

In the present study, EIS was used in conjunction with other techniques (dc electrochemical, electron optical, and UHV spectroscopies) to characterize active dissolution, passivity, and metastable pitting of pure aluminum and aluminum alloy thin films in dilute hydrofluoric acid (HF) solutions. The purpose of the present paper is to present a survey illustrating the application of EIS to aid in the characterization of such phenomena. The pertinent application for the metal/electrolyte system described is corrosion of aluminum alloy thin film IC interconnections. Localized corrosion occurs during processing of such components especially when they are exposed to rinse solutions used following HF etching [*3,4*].

Experimental Procedures

High purity aluminum (99.995%), Al–0.5 wt. % Cu, Al-2 wt. % Cu, and Al-2 wt. % Si were sputter deposited (800 to 1200 nm) on either quartz, sapphire, or boron doped silicon wafers with a SiO_2 surface oxide. Al-Cu alloys were processed to produce a microstructure consisting of 1-μm-diameter columnar grains containing Θ-Al_2Cu precipitates at grain boundaries. A more detailed description is provided elsewhere [*3–5*]. Environments consisted of catalytically pyro-distilled water [*6*] with small additions of reagent grade hydrofluoric acid (10^{-5} to 10^{-3} Formal). HF dissociates almost completely to F^- in very dilute concentrations [*4*]. Calculated partitioning of solute between HF, F^-, and HF_2^- in mol/L and measured pH as a function of HF concentration was (a) 4.5×10^{-8} HF, 9.37×10^{-7} HF_2^-, 5.5×10^{-4} F^-, and pH = 3.3 in 10^{-3} F HF; (b) 1.2×10^{-5} HF, 8.8×10^{-5} F^-, and pH = 4.1 in 10^{-4}F HF; and (c) 1.4×10^{-7} HF, 9.9×10^{-6} F^-, and pH = 5.1 in 10^{-4} F HF.

Impedance spectra were collected using systems consisting of either a Solartron Model 1255 FRA, PAR Model 273 potentiostat and PAR M388 software, or Solartron Model 1250 FRA, Solartron Model 1286 potentiostat, and ZPLOT™ software [*7*]. EIS spectra were analyzed using either a MacIntosh IIcx computer and procedures devised by the author or with a 386/16 PC with math co-processor. The equivalent circuit software written by B. Boukamp (EQUIVCRT.PAS) was used with the latter [*8*]. A capacitively coupled (0.1 μF) platinum wire augmented the conventional Hg/Hg_2SO_4 reference electrode at high frequencies. Results are reported versus Hg/Hg_2SO_4 which is +.615 V versus SCE. A flat specimen cell arrangement was employed which placed the working electrode (0.04 cm^2 area)

and counter electrodes (platinum) at opposite ends of a small cylinder. Potentiostat phase shifts were minimized by selection of appropriate measuring resistors but were nevertheless present at frequencies greater than 1000 Hz owing to the low solution conductivities.

EIS data analysis was performed by first selecting an equivalent circuit model based upon a rational physical description of the phenomenon being probed as well as precedence for similar phenomena in the literature. The subsequent analysis procedure was based on the consistent observation of experimental EIS spectra that contained a high frequency (*hf*) process which was quite semicircular in the complex plane and a low frequency (*lf*) process best represented by a constant phase element (CPE) in series with the *hf* parallel resistor. The *lf* process did not return to the real axis in the complex plane over experimentally reasonable (e.g., mHz) excitation frequencies. EIS analyses included the following steps: (a) circle fit and partial nonlinear least squares (NLLS) fit of the clearly distinguished *hf* impedance process; (b) subtraction of solution resistance from the real component of impedance, Z'; (c) determination of the capacitance associated with the *hf* impedance process from linear regression analysis of the calculated imaginary component of admittance, Y'', versus applied frequency, ω, as described elsewhere [*3*]; (d) determination of the parallel resistance and capacitance associated with the *hf* impedance relaxation using (1) a circle fit routine, (2) Kramer-Kronig transformation methods [*3*], or (3) partial NLLS; and finally (e) determination of low-frequency complex impedance from (1) total NLLS fit of entire spectra using either a CPE, infinite diffusional impedance element (*W*), or a finite diffusional impedance element (*O*) in series with the *hf* parallel resistance, or (2) linear regression analysis of Z'' and Z' data plotted versus $\omega^{-1/2}$ data at *lf*. See Ref *8* for a complete description of these procedures. For the *hf* relaxation all analyses methods produced parameters with magnitudes which were identical within $\pm 5\%$.

Results and Discussion

Characterization of the Passive to Active Transition for Pure Aluminum in Dilute HF

Aluminum complexes readily with F^- in aqueous solutions containing HF or NaF. Hence one might hypothesize that the native barrier oxide is gradually converted to a hydrated salt film at the oxide solution interface. Figure 1 illustrates dc polarization results on pure Al as a function of HF concentration. All data are IR corrected. A transition from passive to active behavior is observed with increasing HF. The polarization behavior is consistent with the notion that the native Al_2O_3 film is converted to a nonprotective AlF_3-$3H_2O$ film at all concentrations but the most dilute. A white gel-like film was observed at 10^{-3} F HF but not at the more dilute concentrations. This suggests that the solubility of AlF_3-$3H_2O$ is exceeded at the aluminum surface at high dissolution rates possible in 10^{-3} F HF, but not at the lower dissolution rates observed in the more dilute solutions. This concept is supported by the solubility of AlF_3 which has been reported to be approximately 6×10^{-2} mol/L at 25°C [*9*]. At a mass transport controlled anodic dissolution rate of 10^{-3} A/cm^2 such a surface concentration may be achieved in quiescent solution as long as the diffusion coefficient for Al^{+3} cations in solution is 5×10^{-6} cm^2/s or lower and mass transport is unidirectional. A passive polarization response is observed at 10^{-5} Formal HF and presence of an aluminum oxide was verified by post-exposure XPS and AES analyses [*3,4*]. No white gel was observed. With EIS it is possible to monitor the conversion of the native oxide-covered metal to AlF_3 covered or bare metal with both exposure time and increasing HF concentration. EIS also provides a means to verify the presence of oxide at the most dilute concentration. Figures 2*a–c* illustrate the experimental impedance re-

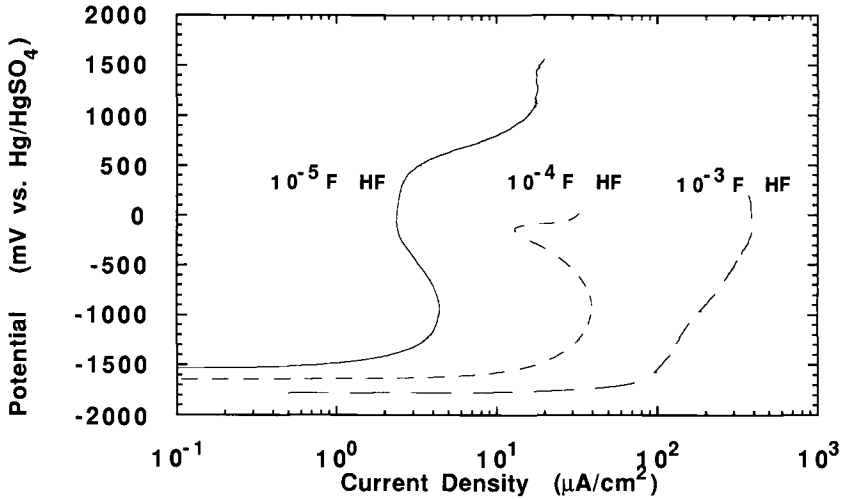

FIG. 1—*Anodic polarization behavior for pure Al thin films in hydrofluoric acid at 10^{-5}, 10^{-4}, and 10^{-3} Formal concentration. All data are IR corrected. Complete dissolution of Al electrodes is observed in more concentrated solutions.*

sponse at an applied potential of −1.0 V and the accompanying NLLS fit. EIS data over the same range of HF concentrations as shown in Fig. 1 are depicted. Table 1 summarizes the parameters associated with the EIS fit assuming the equivalent circuit model illustrated in Fig. 3*a*. According to this model, oxides are characterized by a *hf* parallel RC network consisting of the oxide capacitance in parallel with the oxide resistance and a *lf* diffusional impedance associated with anion and cation transport across the oxide. The oxide imped-

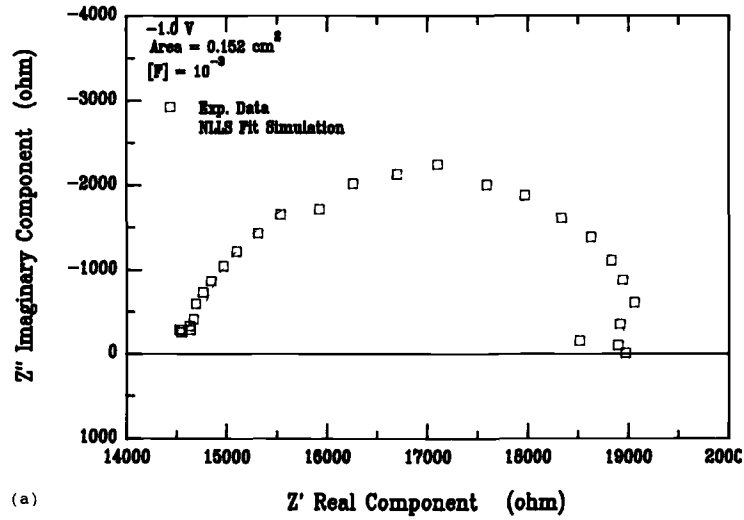

(a)

FIG. 2—*Experimental EIS response (symbols) and Total NLLS Data Fit (solid line) for pure Al at −1.0 V assuming the impedance model shown in Fig. 3.* (a) *10^{-3}*, (b) *10^{-4}*, *and* (c) *10^{-5} Formal HF concentration. In all cases the electrode area is ~0.1 cm^2.*

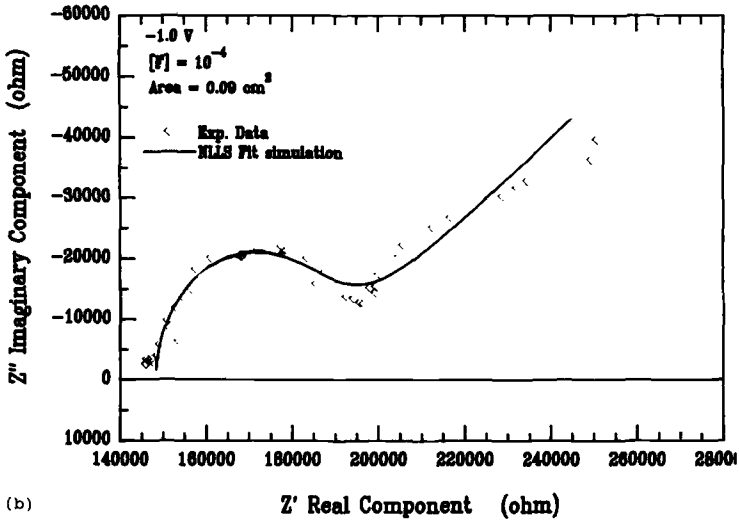

(b)

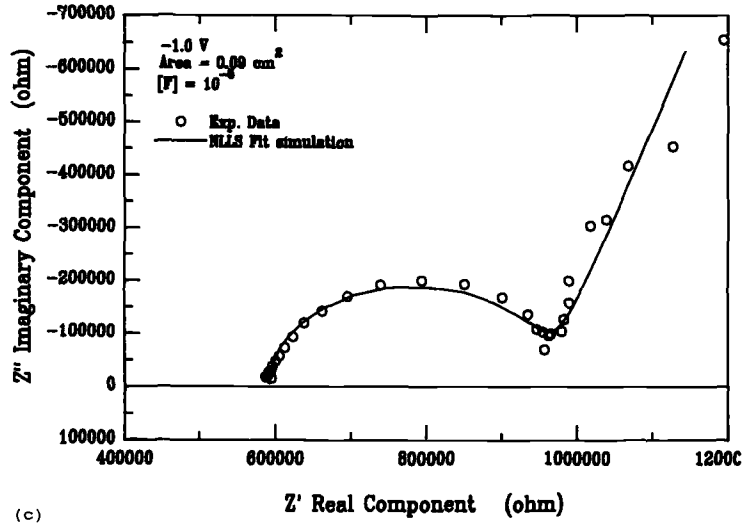

(c)

FIG. 2—(continued)

ance is proportional to oxide thickness and inversely proportional to the ability of the oxide to support both electronic and ionic charge transfer across the oxide. The *lf* EIS response associated with the diffusional impedance of the oxide depends on the Warburg coefficient for both anions and cations, σ. The rationale for choosing this particular model is based upon previous work on oxide-covered metals in the literature [*10*]. The quality of the fit degrades at *lf* (Fig. 2) in a similar manner as observed elsewhere [*11*]. In particular the *lf* CPE slope, n {where $Y_{cpe} = Y_o(j\omega)^n$}, sometimes differed from 0.5, the expected value for an infinite diffusional impedance (see Table 1). The reason for this is not clear. Further discussion of this point will be undertaken elsewhere [*12*]. However, the assump-

TABLE 1—*EIS parameters for the electrical equivalent circuit model shown in Fig. 3a for an oxidized aluminum surface in the passive region at −1.0 V. The parameters shown were obtained from the NLLS fit (solid line) of the experimental data (symbols) shown in Figs. 2a–c.*

HF Conc. (M)	R_{sol} (Ω-cm^2)	R_{ox} (Ω-cm^2)	C_{tot} (μF/cm^2)	$1/Y_o$ *lf* CPE* (Ω-cm^2/s$^{1/2}$)	n (−)
10^{-3}	2.3×10^3	6.5×10^2	6.6	none	n/a
10^{-4}	1.4×10^4	3.1×10^3	9.1	2.3×10^3	0.4
10^{-5}	5.3×10^4	3.5×10^4	5.3	1.0×10^4	0.7

*NOTE: Z_d has been replaced by a CPE for a non-ideal semi-infinite diffusional impedance where $Z_d = 1/(Y_o\omega^n(1-j)$.

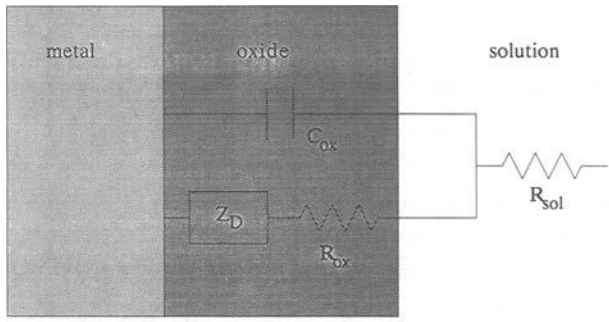

(a) Charge Transfer Across Passive Film

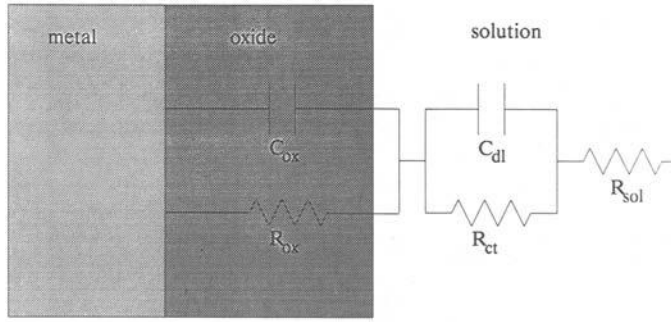

(b) Redox process of film/solution interface

FIG. 3—*Electrical equivalent circuit models for Al electrodes with a compact native oxide film.* (a) *Passive region,* (b) *redox couple at the oxide/solution interface. Z_d has been modeled as a CPE in this paper.*

tion of a semi-infinite (as opposed to finite) diffusional impedance model is not the source of this error. The semi-infinite assumption is valid when

$$l_\omega \ll d_{ox} \text{ where } l_\omega = (D_{ox}/\omega)^{0.5} \quad (1)$$

where d_{ox} is the oxide thickness, D_{ox} is the cation or anion diffusion coefficient and l_ω is the characteristic diffusion length over which the ion can move in the time one cycle is

completed at the frequency of the applied ac signal, ω. This criterion is satisfied if $d_{ox} > 1$ nm, $D < 10^{-16}$ cm^2/s, and $\omega = 0.01$ Hz. It will be shown in the following paragraphs that these requirements are satisfied.

Concerning the *hf* EIS response, the capacitance obtained by EIS is, in principle, given by the space charge capacitance, C_{ox}, in series with the capacitance across the Helmholtz layer at the oxide solution interface, C_H [*13*]

$$1/C_{tot} = 1/C_{ox} + 1/C_H \tag{2}$$

where C_{ox} is given by

$$C_{ox} = \epsilon\epsilon_o/d_{ox} \tag{3}$$

d_{ox} is the oxide thickness and other terms have their usual meaning. C_{ox} is 1.5 to 3 μF/cm^2 just after exposure which yields a 3-nm-thick Al_2O_3 film from Eq 3 assuming $\epsilon = 5$ to 10. This barrier oxide thickness is in good agreement with Auger data from the native oxide prior to exposure [*3,4*]. Since C_H is normally 40 to 60 μF/cm^2, C_{tot} is dominated by C_{ox} in Eq 2 for a homogeneous oxide-covered surface. The assignment of the *hf* CPE to a capacitor is well justified based upon the linear slope associated with plots of Y'' versus ω and the CPE exponent obtained in the NLLS fit, n, $\{Y_{cpe} = Y_o(j\omega)^n\}$ which was always between 0.9 and 1.0 and usually very close to 1.0.

R_{ox} and C_{tot} are shown in Figs. 4*a* and 4*b* as a function of exposure time at OCP for the HF concentrations indicated. Capacitance data indicate thinning of the native barrier oxide with increasing exposure time since (a) C_{tot} at short exposure times is in good agreement with initial oxide thicknesses calculated using Eq 3 and verified by AES-sputter depth profiling, and (b) C_{tot} increases with exposure time indicative of oxide thinning and exposure of bare metal. Note that C_{tot} increases with increasing HF concentration while R_{ox} decreases (Fig. 4) and that the *lf* diffusional impedance is no longer observed at 10^{-3} F HF (Fig. 2). These results further substantiate the claim that the *lf* EIS response observed in dilute HF is indeed attributed to a diffusional impedance associated with the oxide since the conversion of the oxide to gel-like salt resulted in suppression of the *lf* diffusional impedance response. The data in Fig. 4 indicate that the native oxide is dissolved and converted to a salt film within about 10 min in the 10^{-3} F HF solution.

EIS data taken in the passive region (i.e., -1.0 V in Fig. 1) will be dominated by the oxidation process itself. Charge transfer across the passive oxide occurs by anionic and cationic transport. Transport of these species or their vacancies occurring during oxidation is described by the Nernst-Planck equation which includes terms describing D_{ox}, the diffusion coefficient of the anion or cation, concentration, charge, Faraday's constant, and the electric field strength [*10,14–16*]. Assuming that the field strength is independent of oxide thickness or applied potential, this equation has been solved under the ifluence of a sinusoidally modulated potential to yield an impedance describing movement of cations that includes a diffusional impedance term [*10,14*]

$$Z_d = (\sigma_{an}\sigma_{ca}/\sigma_{an} + \sigma_{ca})\,\omega^{-0.5}(1\text{-}j) \tag{4}$$

Operating under the assumption that the *lf* CPE is associated with an oxide diffusional impedance we may now calculate the effective value of σ. Figure 5 illustrates a plot of Z'' versus $\omega^{-0.5}$ in the *lf* range. The parameter $\sigma = (\sigma_{an}\sigma_{ca}/\sigma_{an} + \sigma_{ca})$ is equal to $1/Y_o$, {so that

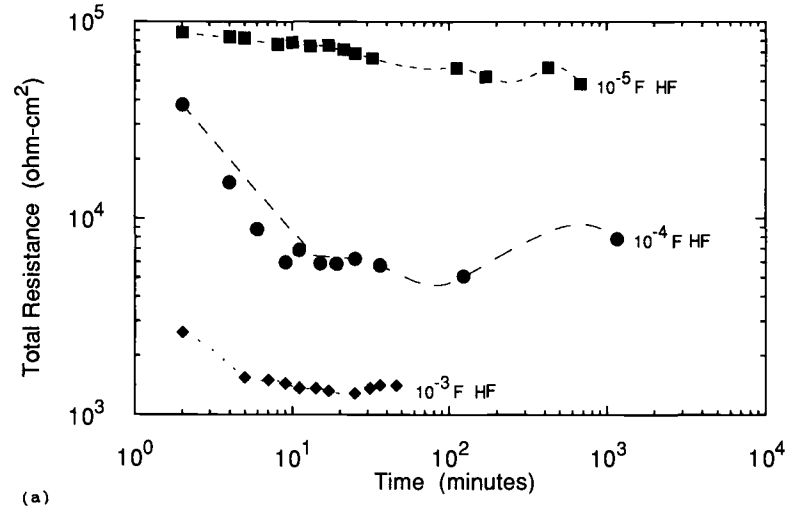

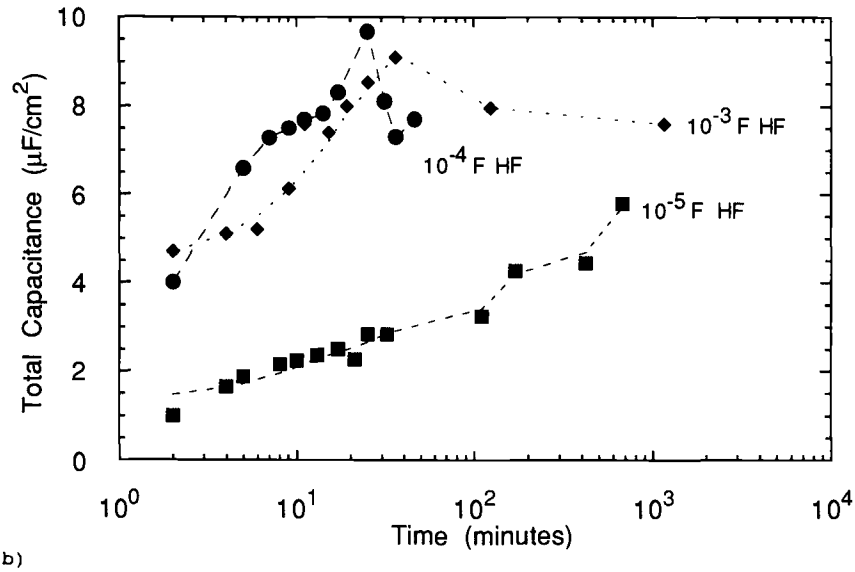

FIG. 4—*Hf resistance and capacitance associated with pure Al exposed at OCP in dilute HF solutions.* (a) *resistance,* (b) *capacitance.*

$Z_d = (1/Y_o)\,\omega^{-n}(1 - j)\}$, where $n = 0.5$ for an ideal infinite diffusional impedance. Table 2 presents the product of the passive current density, i_{pass}, and $1/Y_o$ at -1.0 V in 10^{-3}, 10^{-4}, and 10^{-5} Formal HF. This product should be approximately equal to a constant, that is to say independent of potential or HF concentration if the assumed model is valid [*10,14*]. The product of R_{ox} and i_{pass} is also equal to a constant. These results confirm the presence of an oxide film in dilute HF. The diffusion coefficient associated with anion and cation

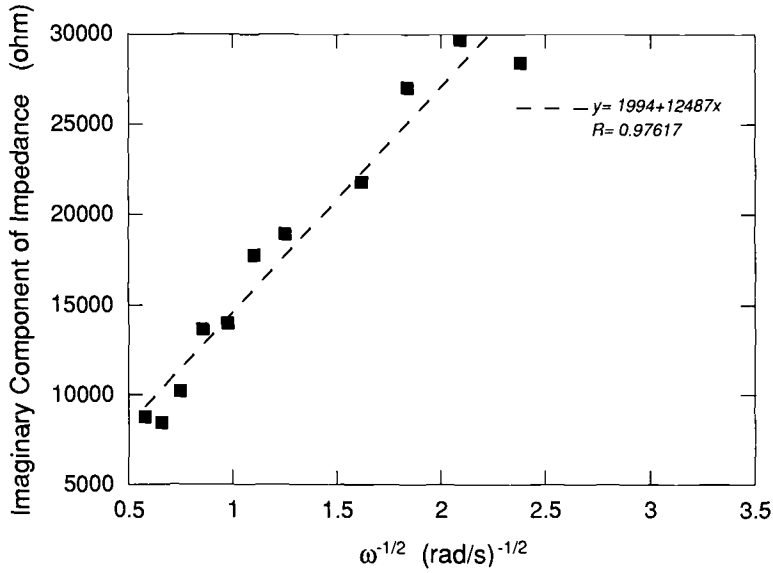

FIG. 5—*Experimental EIS data (symbols) and linear regression fit (dotted line) associated with If imaginary component of impedance (Z") plotted versus* $\omega^{-0.5}$ *for pure Al at* -1.0 *V in* 10^{-4} *Formal HF. A similar trend was noted for Z' versus* $\omega^{-0.5}$. *Electrode area is ~0.1* cm^2.

movement in the oxide is estimated from the product of i_{pass} and σ [*10*]

$$i_{pass}\,\sigma = (D_{ox}/2)^{0.5}\,(\psi/1 - \lambda) \tag{5}$$

where ψ is the voltage field strength reported to be 5×10^6 V/cm for aluminum oxide [*14*] and λ is a transfer coefficient, close to 0.5 for most oxides [*14*]. This expression is only valid if the product $i_{pass}\,\sigma$ as well as the other parameters are independent of potential and pH. The product $i_{pass}\,\sigma$ was found to be independent of potential as well as pH. Equation 5 produces an estimated cation/anion oxide diffusion coefficient on the order of 10^{-17} cm^2/s. This is in reasonable agreement with the literature and much too low to be indicative of a diffusional process occurring in the aqueous solution [*10*]. The criterion described by Eq 1 concerning the assumption of an infinite diffusional impedance is also satisfied.

TABLE 2—*Product of impedance parameter and passive current density for pure Al in dilute HF solutions of various concentrations, and resulting anion-cation diffusion coefficient.*

HF Conc. (M)	$R_{ox} \times i_{pass}$* (Ω-μA)	$1/Y_o \times i_{pass}$* (Ω-$\mu A/s^{0.5}$)	D_{ox} (cm^2/s)
10^{-3}	12×10^4	—	—
10^{-4}	9×10^4	7×10^4	9×10^{-17}
10^{-5}	14×10^4	4×10^4	3×10^{-17}

*The passive current density was obtained at -1.0 V in Fig. 1.
D_{ox} is calculated using Eq 5.

Characterization of Pitting Initiation and Repassivation Using Impedance Methods

Resistance Measurements

Having established in the preceding section that a passive oxide film is maintained on aluminum and aluminum alloys in dilute HF of a concentration below 10^{-4} Formal HF, we now focus on an investigation of passivity and its breakdown due to localized corrosion. Aluminum alloy thin films undergo metastable pitting at OCP in 10^{-5} Formal HF [*3,4*]. In other words, small 1-μm pits are nucleated at potentials well below conservatively determined pitting potentials. EIS is useful for characterizing the initiation of such points *in-situ*. The electrical equivalent circuit model describing a heterogeneous Al-Cu alloy surface in dilute HF is shown in Fig. 6. For Al-Si, the circuit element representing theta (Θ) phase sites is replaced with one describing elemental silicon precipitate sites, while for

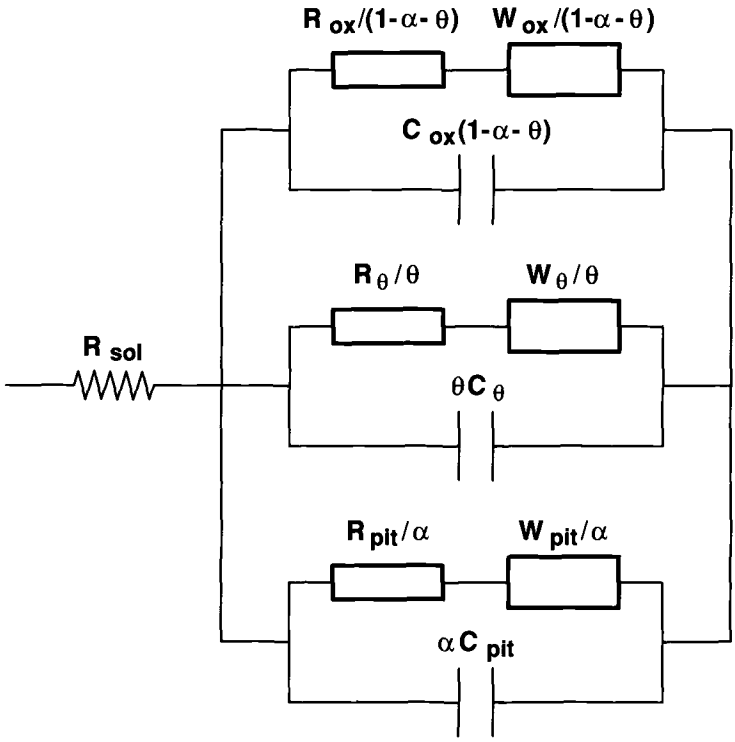

$$\frac{1}{R_{TOT}} = \frac{(1-\alpha-\theta)}{R_{ox}} + \frac{\theta}{R_{\theta}} + \frac{\alpha}{R_{pit}}$$

$$C_{TOT} = (1-\alpha-\theta)\,C_{ox} + \theta C_{\theta} + \alpha C_{pit}$$

FIG. 6—*Proposed electrical equivalent circuit model for Al-Cu alloys undergoing pitting. Circuit model shown is relevant over an intermediate frequency range.* α *is the area fraction of pit sites,* θ *is the area fraction of* Θ*-phase sites, and the subscripts* pit *and* ox *denote the pit sites and oxide covered sites, respectively.*

pure aluminum this circuit element is removed. The model is based on numerous studies presented in the literature [*1–4,17,18*]. It consists of parallel pathways for electron transfer reactions (ETR) at pits, across the aluminum oxide, and either cathodic ETR occurring on or anodic reactions across the Θ-phase oxide. For ETR across an oxide, oxide resistance is a function of the oxide's ionic and electronic characteristics, and its thickness. The total resistance and capacitance of the system can be determined independently of any Warburg diffusional impedance, W, at hf since the real and imaginary components of W are inversely proportional to $\omega^{1/2}$, and are, consequently, minor contributors to the impedance measured at intermediate or high frequencies. The model includes a single solution resistance and is not subject to varying solution resistances as a function of applied frequency or pit activation as discussed elsewhere [*19*]. The reason for this is probably related to the geometry of the thin film system. Here, the reference electrode (RE) was placed a distance of 5×10^3 μm (0.5 cm) from a 0.1 cm^2 WE surface. In comparison, 1-μm-sized pits are formed with an average distance of separation between nearest neighbor pits of 5 μm. This arrangement arguably leads to a relatively uniform current distribution experienced at the RE. It also differs significantly from the situation where the RE is placed within fractions of a cm near a ~0.1-cm-sized pit [*19*]. Under the former conditions the circuit shown in Fig. 6 reduces to a total resistance in parallel with a total capacitance. R_{sol}, R_{tot}, and C_{tot} are determined from the experimental EIS data using the procedures previously discussed. Al-Cu alloys consist of oxide-covered areas, pit sites, and Θ-phase oxide sites. Here, the total resistance, R_{tot}, is given by

$$1/R_{tot} = (1 - \alpha - \theta)/R_{ox} + \theta/R_{\theta} + \alpha/R_{pit} \tag{6}$$

In the present investigation the area fraction of pits, α, is zero until approximately one h after exposure as verified by sequential removals and examination. Θ, the area fraction of oxide covered Θ-phase precipitates, is about 0.01 to 0.001 but depends on Cu concentration. R_{tot}, R_{ox}, and R_{Θ} were readily determined from studies on separate electrodes consisting of the alloy, pure aluminum, and Θ-phase, respectively, R_{ox} is 10^5 Ω-cm^2 just after exposure of pure aluminum, consistent with an oxide resistivity, ρ_{ox}, of the order of 10^{11} Ω-cm for a 3-nm-thick film, in good agreement with the literature [*20*]. R_{Θ} is also 10^5 Ω-cm^2 at OCP which is consistent with independent evidence that an aluminum oxide exists on the Θ-phase [*4*]. However, it is unclear whether the oxide impedance or cathodic ETR at the oxide/electrolyte interface will dominate the impedance spectra of the Θ-phase. R_{pit} represents the polarization resistance for anodically polarized bare aluminum in the pit. R_{pit} was estimated to be about 10 to 100 Ω-cm^2 for bare aluminum based on results for the 10^{-3} Formal HF solution but depends on applied potential. An artificial pit solution represented by a sauturated AlF_3 solution resulted in similar values which decreased with increasing anodic potential. However R_{tot} was difficult to determine for the alloys after pit initiation due to violation of the impedance causality requirement at lower frequencies (i.e., electrochemical noise) (Fig. 7). R_{tot} could be determined from the hf Kramer-Kronig Transformation method but its exact meaning remains unclear. Independent of the noise problem, R_{tot} was not the best indicator of pitting. If $\alpha = 0.001$ and $R_{pit} = 10$ to 100 Ω-cm^2, R_{tot} will only decrease by a factor of 2 to 10, according to Eq 6. Such a modest decrease could also be partially offset by increases in R_{ox} if oxide thickening occurs due to galvanic coupling of the matrix to Θ-phase sites. Consequently, greater emphasis was placed on capacitance measurements for characterizing metastable pitting.

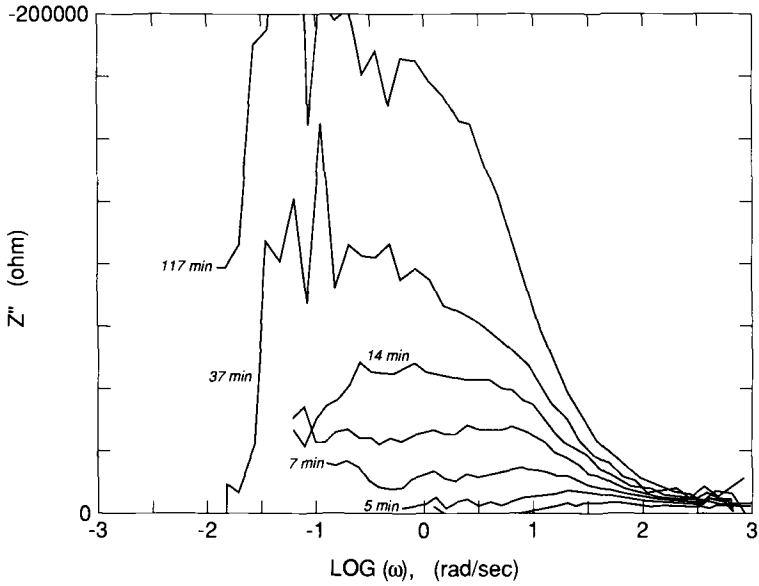

FIG. 7—*Imaginary component of impedance (Z") plotted versus ω for Al-2% Cu in 10^{-5} Formal HF at various exposure times indicating noise at* lf *after pitting initiation.*

Capacitance Measurements

C_{tot} is dominated by C_{ox} in Eq 2 for a homogeneous aluminum oxide covered surface with $d_{ox} > 1$ nm. C_{tot} for a heterogeneous surface consisting of an insulating oxide in parallel with pit or cathodic Θ-phase sites is given by the sum of C_{ox} for Al_2O_3 and C_H developed across the Helmholtz layer for the charge transfer sites, whether they are represented by pit sites, C_{pit}, Θ-phase cathodic sites, C_θ, or pure copper, C_{cu}.

$$C_{tot} = (1 - \alpha - \Theta)C_{ox} + \Theta C_\theta + \alpha C_{pit} \quad (7)$$

C_{cu} and C_θ were obtained from separate studies on Cu and Θ-phase electrodes. C_{cu} was about 100 μF/cm². C_θ was 1 to 2 μF/cm² but increased to 10 μF/cm² after 3 h at OCP. C_{pit} was 100 to 400 μF/cm² for pure aluminum in saturated AlF_3. Since C_{ox} is orders of magnitude smaller than C_H, C_{tot} will increase markedly upon pitting initiation and perhaps cathodic activation of the Θ-phase as shown by Eq 7. C_{tot} can be determined at *hf* using several methods. Since C_{tot} is represented by a passive linear circuit element, its measurement at *hf* was free of spurious noise and constitutes a valid impedance measurement.

Metastable pitting occurs on aluminum alloy thin films as well as pure aluminum in 10^{-5}F HF at their respective OCPs. The OCPs of these alloys are below the average critical pitting potential obtained in potentiodynamic scans [*4*]. Hence EIS is useful for investigating this phenomena. Increases in C_{tot} after about an hour at OCP provide *in-situ* indication of metastable pitting initiation. Initiation was also verified from serial removals and inspection by SEM and optical microscopy. C_{tot} data are shown for Al, Al-Si, and Al-Cu (Fig. 8). The quality of the *hf* data (i.e, frequency dispersion) from which C_{tot} is determined does not change with pit initiation. This was not expected given the flat Al

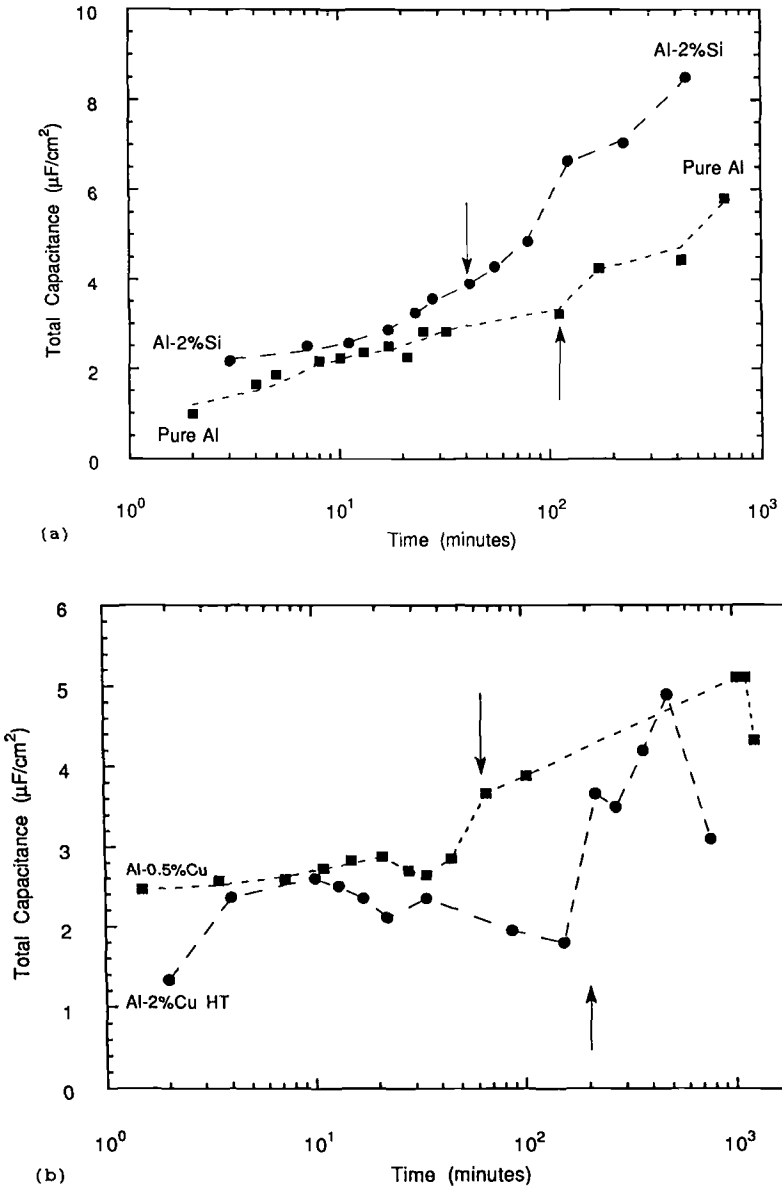

FIG. 8—*Total capacitance as a function of exposure time at OCP in 10^{-5} Formal HF for* (a) *Al relative to Al-Si, and* (b) *Al-0.5% Cu relative to Al-2% Cu alloys. The drop in capacitance corresponds to repassivation of metastable pits.*

surface, cylindrical cell geometry, and resulting uniform current distribution near the reference electrode [3]. Gradual increases in C_{tot} are observed prior to pitting for pure aluminum and Al-Si, corresponding to either film thinning or oxide hydration. The sharp increases in C_{tot} during pit initiation for the Al-2% Cu alloys is attenuated compared to Al-Si and Al-0.5% Cu because a positive shift in OCP from −1.0 V to −0.5 V promotes oxide

growth. These trends in OCP are shown in Fig. 9. One result of oxide growth is a lowering of C_{ox}. Simultaneous decreases in C_{ox} coupled with increases in α have an offsetting effect on Eq 6. Image analysis (IA) was used to determine α, the cumulative area fraction of pit sites as a function of time. C_{tot} should increase linearly with α as indicated by Eq 6 as long as all pits are active during the entire exposure period. IA results are shown for Al-2% Cu in Fig. 10. The pit densities shown were obtained after exposure at OCP for the time indicated. IA results are in excellent agreement with the trends in C_{tot}. IA indicates pit areas fractions of 0.02, 0.10, and 0.14 at 2, 6, and 20 h, respectively. However, after 20 h additional new pits are not observed. One also observes that pits cease to grow in thin films once penetration to the insulating substrate has occurred. Pits readily penetrate the 1-μm-thin films and any larger pits apparently grow radially. Most repassivate before growing to such sizes. This is indicated by the sharp drop in C_{tot} at the end of the exposure period (Fig. 8*b*). C_{pit} cannot be precisely determined from area fractions as attempted elsewhere [*18*] since the exact area fraction of pits that are active at any one period in time is not known. The literature reports that the approximate lifetimes for metastable pits is on the order of 5 to 10 s [*21*]. Hence all pits counted by image analysis at various exposure times cannot be assumed to be active during the entire exposure period. On the other hand, the 0.1 cm^2 test surface exposed contains as many as 10^6 pit sites over the entire exposure period. This results in a cumulative pit lifetime of 10^7 s over a 5×10^4 s exposure period. Hence it is plausible that thousands of active pits existed during the time required to complete the *hf* EIS measurement from which the capacitance data are extracted.

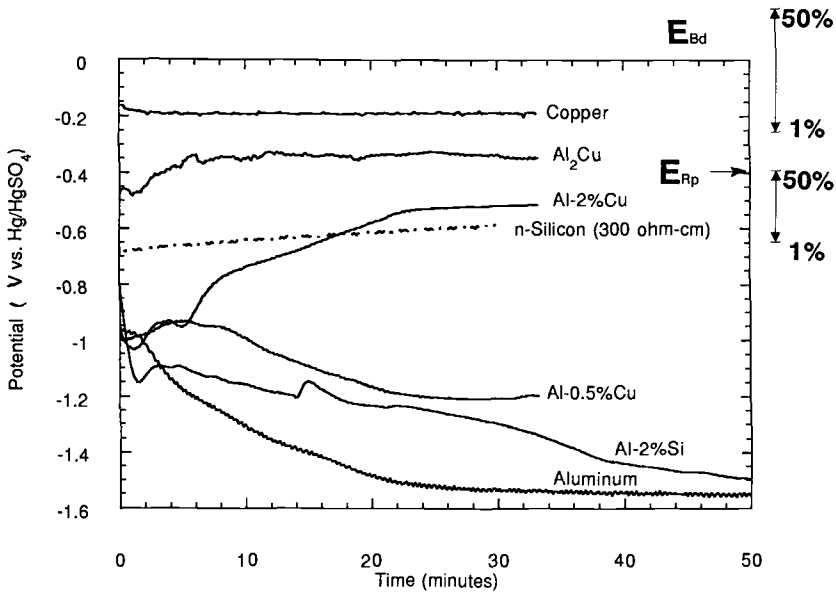

FIG. 9—*Trends in OCP for Al alloys and synthesized electrodes in dilute HF solutions. The vertical bars indicate the normal distribution of the breakdown, E_{Bd}, and repassivation, E_{Rp}, potentials for pure Al. The average values of E_{Bd} and E_{Rp} according to a normal probability distribution are indicated at 50%.*

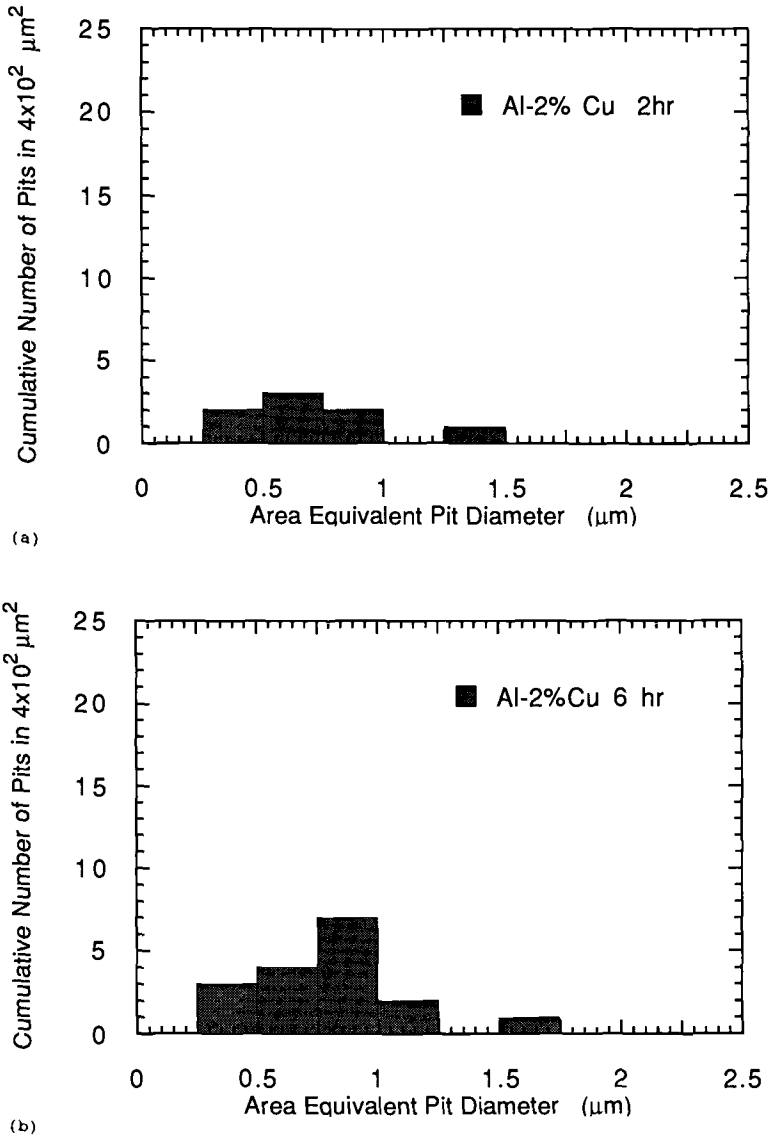

FIG. 10—*Distribution of metastable pit sizes as a function of exposure time for Al-2% Cu in 10^{-5} Formal HF at OCP.* (a) *2 h,* (b) *6 h,* (c) *20 h. The exact specimen area varied for each exposure time.*

Investigation of Oxide Resistivity and State of Hydration

Since pit initiation time could be determined *in situ*, R_{tot} could be examined *prior* to pitting at OCP to determine whether or not the oxide becomes more electronically or ionically conductive by either defect formation or thinning as a precursor to pitting. R_{tot} decreases to a greater extent for Al-Si and Al-Cu alloys than pure aluminum. However, for

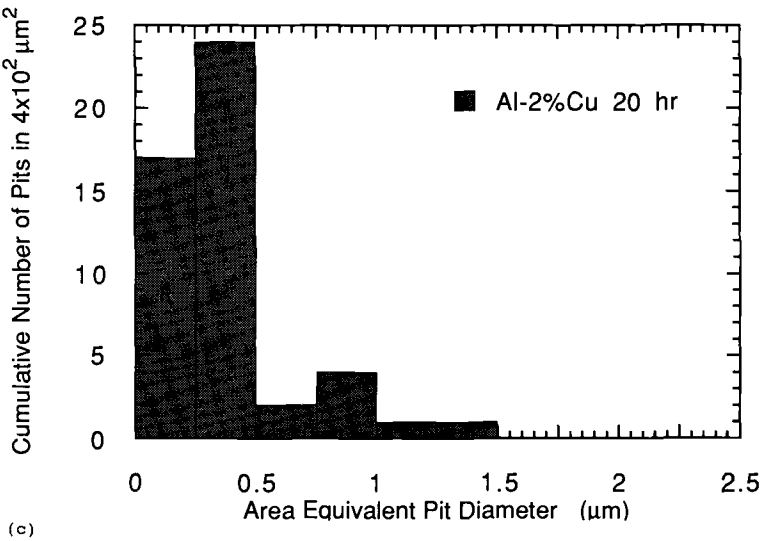

FIG. 10—(continued)

Al-Cu alloys a positive shift in OCP results in oxide growth. In order to separate the geometric effect of increasing thickness on R_{ox} from intrinsic changes in oxide resistivity, we multiply $R_{tot}{}^{*}C_{tot}$. Such multiplication results in a time constant, τ_{ox}. τ_{ox} provides an expression which is independent of oxide thickness

$$\tau_{ox} = R_{ox}C_{ox} = \epsilon\epsilon_o\rho \tag{8}$$

where ϵ is the dielectric constant of the oxide, ϵ_o is the permittivity of free space, and ρ is the apparent oxide resistivity. This expression requires that R_{ox} scales linearly with oxide thickness and that C_{ox} is inversely proportional to oxide thickness. This requirement is fairly well met for oxide thicknesses ranging from 1 to 6 nm in the present study and has been observed elsewhere [*22,23*]. ρ is weighted by the relative area fraction of aluminum matrix and Θ-phase sites

$$\rho = \rho_{ox}\rho_{site}/(\rho_{site} + \Theta\rho_{ox}) \tag{9}$$

This equation is valid only when $\alpha = 0$ (prior to pitting), $\Theta \leq 0.01$, $d_\Theta = d_{ox}$. These conditions are all satisfied during the first hour at OCP. Since $\Theta \leq 0.01$, ρ_{site} must be much less than ρ_{ox} in Eq 9 in order to obtain perceptible decreases in ρ. We can normalize Eq 8 with respect to the same parameter obtained just after exposure in order to monitor the relative changes in oxide characteristics

$$(R_t/R_{t=0})(C_t/C_{t=0}) = (\epsilon/\epsilon_{t=0})\,(\rho/\rho_{t=0}) \tag{10}$$

The normalized parameter given by Eq 10 first increases during exposure at OCP then sharply decreases prior to pit initiation for both Al-Si and Al-Cu alloys (Fig. 11). Slight increases in C_{tot} prior to pit initiation are now clarified (Figs. 8*a,b*). These increases most

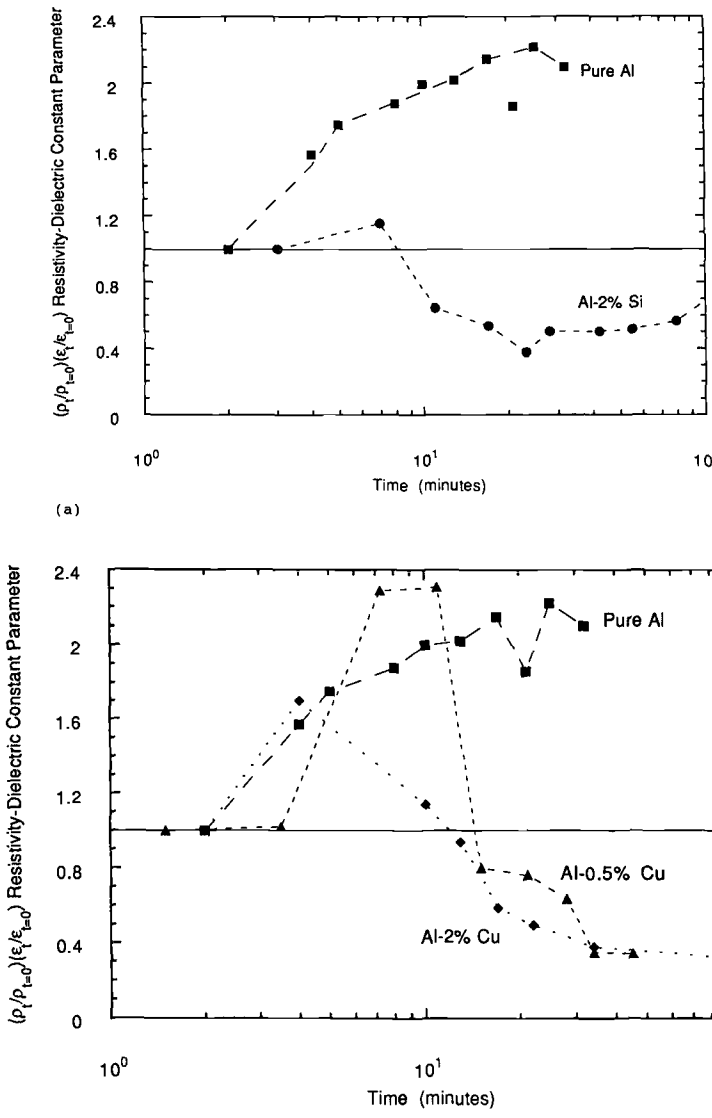

FIG. 11—*Normalized resistivity-dielectric constant parameter as a function of exposure time at OCP in 10^{-5} Formal HF solution prior to pitting initiation. The data illustrated are for* (a) *pure Al compared to Al-Si, and* (b) *pure Al compared to both Al-Cu alloys.*

likely correspond to oxide film hydration given by increasing the ratio $(\epsilon/\epsilon_{t=0})$. Two explanations are possible for the sharp decreases. These are: (a) formation of anodic defective sites in the aluminum matrix that later form pits, or (b) activation of cathodic Θ-phase sites and silicon nodules. Note that formation of pits is ruled out by SEM examination during the time period covered by the data.

In-situ Studies of the Relationship Between Electrode Potential and Oxide Film Thickness

Two methods are available for investigation trends in oxide growth with potential. One is to conduct EIS measurements during the positive drift in the OCP of Al-Cu alloys. The second is to conduct EIS measurements during potential staircase polarization. EIS results from the former method are shown in Fig. 12 for Al-2% Cu. Equation 10 and C_{tot} both decrease linearly with potential. Linear decreases in C_{tot} with increasing potential indicate oxide growth. Independent studies indicate growth rates of 1.3 nm/V [*22,23*] which translates to about 2.5 μF/V-cm^2 in agreement with the plot shown. At the same time the oxide becomes more defective as indicated by the decrease in Eq 10 with increasing potential. Two explanations are possible for the sharp decreases. These are: (a) formation of anodic defective sites in the aluminum matrix that later form pits, or (b) activation of cathodic Θ-phase sites and silicon nodules. To ascertain whether the defects that developed were anodic or cathodic sites, pure aluminum was anodically polarized over the same potential range as experienced by the alloy. Similar decreases in the resistivity were not observed, implying that the development of anodic sites is not the cause for the change. These experiments indicate that the large decrease in relative resistivity noted prior to pitting in Fig. 11 occur at the cathodic Θ-phase and silicon sites. Since the fraction of Θ-phase sites is very small, either the oxide conductivity or the charge transfer resistance of these sites must be significantly less than those on pure aluminum.

Summary

EIS methods are useful in characterizing several electrochemical parameters associated with the corrosion of aluminum thin films. The present paper indicates that impedance can be used to investigate the passivity of aluminum thin films as well as its pitting behavior.

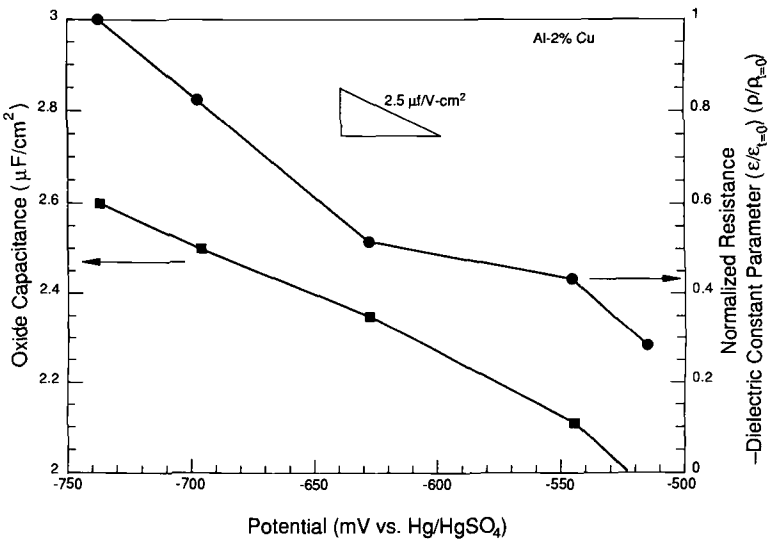

FIG. 12—*Normalized resisitivity-dielectric constant parameter and capacitance for Al-2% Cu as a function of OCP in 10^{-5} Formal HF solution. The EIS data were obtained over the period of time where the OCP drifts positive. The data shown were obtained prior to pitting initiation.*

In-situ information was obtained concerning the diffusion of anions and cations in the passive film, oxide resistance, oxide capacitance, and hence trends in oxide growth and hydration. In 10^{-5} Formal HF, aluminum is passive and behaves in a similar manner to its behavior in dilute sodium chloride solution. An oxide diffusion coefficient of approximately 10^{-17} cm^2/s was estimated for anion and cation movement across the oxide film. In 10^{-3} Formal HF solution, the native Al oxide is replaced with a nonprotective AlF_3-n H_2O salt film over a time period of minutes. The behavior of cathodic Θ-phase sites was also characterized and its oxide thickness was determined to be similar to that of pure aluminum at the most dilute HF concentration. Metastable pitting initiation and repassivation associated with a large population of micrometer sized pits was detected *in situ* at the open circuit potential from increases in C_{tot}. However, complications may arise which place into question the ability to use changes in capacitance in order to quantify the exact density of active pit sites. The oxide time constant, τ_{ox}, was found to be an effective parameter for monitoring oxide hydration and development of electronic defects associated with Θ-Al_2Cu precipitates.

Acknowledgments

Support of various organizations and people at various times is gratefully appreciated. Organizations gratefully acknowledged include AT&T Bell Laboratories, Sandia National Laboratories, and the Center for Electrochemical Sciences and Engineering of the State of Virginia. Francine Bovard and Mike Bode are thanked for performing some of the laboratory measurements.

References

[1] Richardson, J. A. and Wood, G. C., *Journal of the Electrochemical Society*, Vol. 120, No. 193, 1973.
[2] Shih, H. and Mansfeld, F., *Corrosion*, Vol. 45, No. 8, 1989, pp. 610–614.
[3] Scully, J. R., Frankenthal, R. P., Hanson, K. J., Siconolfi, D. J., and Sinclair, J. D., *Journal of the Electrochemical Society*, 137(4), 1365, 1990.
[4] Scully, J. R. and Peebles, D. E., Romig, A. D. Jr., Frears, D. R., and Hills, C. R., "Metallurgical Factors Influencing the Corrosion of Al, Al-Cu and Al-Si Alloy Thin Films in Dilute HF Solution," in *Metallurgical Transactions A*, 23A, 1992, pp. 2641–2655.
[5] Frear, D. R., Sanchez, J. E., Romig, Jr., A. D., and Morris, Jr., J. W., *Metallurgical Transactions A*, Vol. 21A, 1990, p. 2449.
[6] Conway, B. E., Kozlowska, H. A., Sharp, W. R. A., and Criddle, E., *Analytical Chemistry*, Vol. 45, 1973, p. 1331.
[7] ZPlot™ Software, Scribner Assoc. Inc, West Leigh Dr., Charlottesville, VA, 22903.
[8] EQUIVCRT™ Software, B. A. Boukamp, University of Twente, Department of Chemical Technology, PO Box 217, 7500 AE Enschede, The Netherlands.
[9] Seidell, A., *Solubilities of Inorganic and Metal Organic Compounds*, 3rd Ed., Vol. 1, D. Van Nostrand Co., New York, 1940, p. 32.
[10] MacDonald, D. D., Liang, R. Y., and Pound, B. G., *Journal of the Electrochemical Society*, Vol 134, No. 12, 1987, pp. 2981–2986.
[11] MacDonald, D. D., *Electrochimica Acta*, Vol. 35, No. 10, 1990, pp. 1509–1526.
[12] Scully, J. R. and Peebles, D. E., "Active to Passive Transition for Al in Dilute HF Solutions," In preparation for *Journal of the Electrochemical Society*, November 1991.
[13] Diggle, J. W., *Oxides and Oxide Films*, Vol. I, Marcel Dekker, NY, 1972, pp. 319–517.
[14] Macdonald, D. D. and Macdonald, M. U., *Journal of the Electrochemical Society*, Vol. 137, No. 8, 1990, pp. 2395–2402.
[15] Chao, C. Y., Lin, L. F., and Macdonald, D. D., *Journal of the Electrochemical Society*, Vol. 128, Nos. 1187 and 1194, 1981.

[16] Chao, C. Y., Lin, L. F., and Macdonald, D. D., *Journal of the Electrochemical Society*, Vol. 129, No. 1874, 1982.
[17] Mansfeld, F. and Shih, H., *Journal of the Electrochemical Society*, Vol. 135, No. 1171, 1988.
[18] Mansfeld, F., *Electrochimica Acta*, Vol. 35, No. 10, 1990, pp. 1533–1544.
[19] Oltra, R. and Keddam, M., *Electrochimica Acta*, Vol. 35, No. 10, 1990, pp. 1619–1630.
[20] Kingery, W. D., Bowen, H. K., and Uhlmann, D. R., *Introduction to Ceramics*, John Wiley and Sons, New York, 1976, p. 903.
[21] Frankel, G. S., Stockert, L., Hunkeler, F., and Boehni, H., *Corrosion*, Vol. 43, 1987, pp. 429–436.
[22] Frers, S. E., Stefenel, M. M., Mayer, C., and Chierchie, T., *Journal of Applied Electrochemistry*, Vol. 20, 1990, pp. 996–999.
[23] Van Der Linden, B., Terryn, H., and Vereecken, J., *Journal of Applied Electrochemistry*, Vol. 20, 1990, pp. 798–803.

F. Mansfeld,[1] *Y. Wang,*[1] *S. H. Lin,*[1] *H. Xiao,*[1] *and H. Shih*[1]

Detection and Monitoring of Localized Corrosion by EIS

REFERENCE: Mansfeld, F., Wang, Y., Lin, S. H., Xiao, H., and Shih, H., **"Detection and Monitoring of Localized Corrosion by EIS,"** *Electrochemical Impedance: Analysis and Interpretation, ASTM STP 1188* J. R. Scully, D. C. Silverman, and M. W. Kendig, Eds., American Society for Testing and Materials, Philadelphia, 1993, pp. 297–312.

ABSTRACT: Experimental evidence collected by the authors shows that the growth of pits on aluminum alloys and Al-based metal matrix composites can be monitored by EIS. Characteristic changes occur in the impedance spectra when pits have exceeded a certain minimum depth. The phase angle is especially sensitive to the initiation of pits. A model for the impedance of pitted aluminum surfaces has been developed. The procedure for fitting experimental EIS data to this model has been illustrated. The growth of pits and its time dependence can be followed based on the values of the polarization resistance R°_{pit} of a growing pit. Pit growth laws for Al 7075-T6, Al 7075-T73, and Al 6061 exposed to 0.5 N NaCl have been derived. Pit growth rates are inversely proportional to the exposure time.

KEYWORDS: electrochemical impedance spectroscopy (EIS), aluminum alloys, metal matrix composites, pitting, localized corrosion

Localized corrosion in the form of pitting is one of the most common forms of failure of Al-based materials when exposed to corrosive media containing halides. Often the pitting potential E_{pit} is used to estimate the susceptibility of a given material to pitting in a certain environment or to compare the relative resistance of different materials to pitting. This approach is also used to evaluate the effects of surface modification procedures on the resistance to pitting. For aluminum alloys, the use of pitting potentials is unsatisfactory for the characterization of the susceptibility to pitting. In aerated solutions containing halides the corrosion potential E_{corr} and the pitting potential E_{pit} of most aluminum alloys are identical and these materials will pit. However, the total extent of pitting is much higher for Cu-bearing materials such as Al 2024, which has a more noble pitting potential, than for alloys such as Al 6061 or Al 7075, which have a more negative pitting potential. Therefore, the argument that an observed ennoblement of the pitting potential reflects an improvement in the resistance to pitting as the result of surface modification has to be taken with caution. It also has to be considered that once a modified surface layer has been penetrated by pitting, pit growth rates could be the same as for the untreated material. The approach taken by Boehni and Hunkeler [*1*], who have developed a technique for the measurement of pit growth rates, seems therefore to be more promising. Based on the results obtained with this technique, Boehni and Hunkeler were able to determine growth laws for pits in aluminum alloys, which allows one to make extrapolations to longer exposure times. A limitation of this technique is the requirement to polarize the specimen

[1]Corrosion and Environmental Effects Laboratory, Department of Materials Science and Engineering, University of Southern California, Los Angeles, CA 90089-0241.

to $E \geq E_{pit}$ in order to produce active pits. More recently, the authors of this paper have observed that characteristic changes occur in the impedance spectra of aluminum alloys and Al-based metal matrix composites (MMC) when pitting occurred during exposure at the corrosion potential E_{corr} to 0.5 N NaCl (open to air) [*2–11*]. A model has been developed that describes the observed impedance behavior [*2–11*]. Based on this model and certain assumptions, it has been possible to estimate pit growth rates at E_{corr} using electrochemical impedance spectroscopy (EIS) [*5,11*]. A summary of typical results obtained for different materials and a description of the pitting model and methods for the analysis of impedance data will be given in the following.

Experimental Approach and Results

EIS data have been obtained for aluminum alloys and for Al-based metal matrix composites (MMC) in the as-received condition or after surface modification by a chemical process or by a combination of a chemical process with an electrochemical process. The test specimens were immersed in 0.5 N NaCl (open to air) and EIS data were collected as a function of exposure time. The impedance data were analyzed with the software package PITFIT which was developed by the authors [*11,12*]. An estimate of pit growth rates based on the polarization resistance R°_{pit} of the pit was made and the time dependence of pit growth rates was determined.

Materials and Surface Modification Procedures

In earlier tests [*2–10*] surface modification was carried out for Al 6061-T6, Al 7075-T6, and Al 7075-T73 and the MMCs Al/SiC and Al/graphite by immersion in 1000 ppm $CeCl_3$ and other rare earth metal chlorides for 7 days. More recently, surface modification of the aluminum alloys 6061-T6, Al 7075-T6, and Al 7075-T73 has been carried out by immersion in 10 mM $Ce(NO_3)_3$ for 2 h at 100°C followed by immersion in 5 mM $CeCl_3$ for 2 h at 100°C and polarization in 0.1 M Na_2MoO_4 at +500 mV versus SCE for 2 h [*13–15*]. Exceptional corrosion resistance was obtained for Al 6061 with this treatment which will be referred to as the Ce-Mo process. Localized corrosion was not observed visually or by changes in the impedance spectra during exposure to 0.5 N NaCl for 60 days [*13–15*].

Corrosion Tests

The resistance of as-received and modified surfaces to localized corrosion was determined by recording of EIS data as a function of exposure time. As will be discussed, characteristic changes of the impedance spectra are observed when pitting or crevice corrosion are initiated. Analysis of the impedance spectra for such cases allows determination of the polarization resistance R_{pit} of the pit. An estimate of pit growth rates can be made based on the experimental values of R_{pit}. This approach allows determination of the pit growth kinetics for aluminum alloys and Al-based MMCs.

After each test the specimens were observed under an optical microscope. Some specimens were also examined in the scanning electron microscope (SEM) in order to determine pit morphology. The chemistry of the pit environment or the passive surface, or both, were determined by EDAX and Auger electron spectroscopy [*10,14,15*].

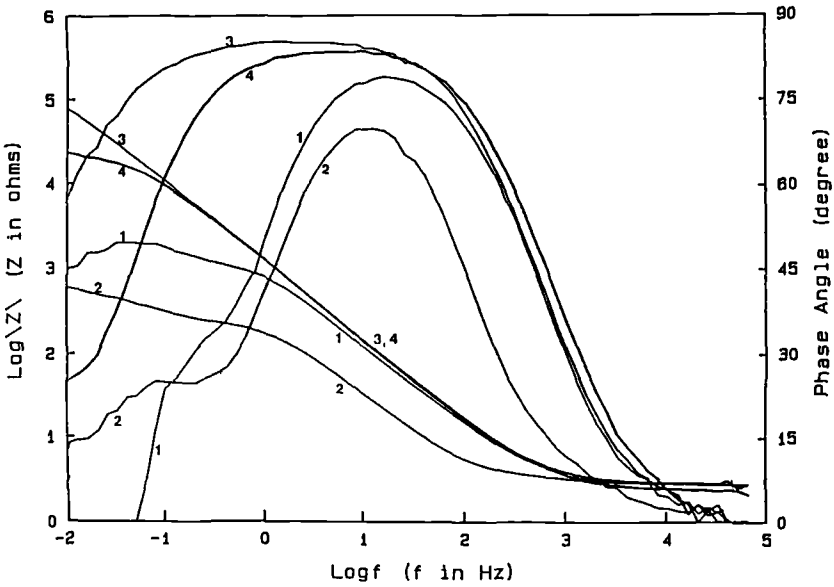

FIG. 1—*Bode-plots for untreated (Curves 1 and 2) and $CeCl_3$-treated (Curves 3 and 4) Al 7075-T6 during immersion in 0.5 N NaCl; immersion times: 2 h for Curves 1 and 3; 4 days for Curve 2; and 23 days for Curve 4.*

EIS Data

EIS data were obtained at E_{corr} as a function of exposure time to 0.5 N NaCl. Figure 1 shows experimental data for Al 7075-T6 in the as-received condition and after passivation by immersion in 1000 ppm $CeCl_3$ for 7 days. For the as-received surface, characteristic changes of the impedance spectra were observed in a very short time, while for the modified surfaces the spectra did not change significantly over a much longer time period. In the first case, a pronounced decrease of the impedance occurred in the capacitive region of the spectra (Fig. 1) at about the time when pitting was first observed visually. In addition, the frequency dependence of the impedance at the lowest frequencies changed to that typical for a transmission line impedance. Sometimes erratic behavior of the impedance data was observed at the lowest frequencies as shown in Curve 1 of Fig. 1, where the phase angle changed sign at about 50 mHz. This problem, which occurred only during the first day of exposure, is probably due to a drift of E_{corr} and polarization of the electrode during the impedance measurement. Such data were eliminated before the analysis of the impedance data with PITFIT.

Figure 2 shows EIS data for Al 6061-T6 in the as-received condition (Fig. 2*a*) and after polishing (Fig. 2*b*). For both cases, the large increase of the capacitance with exposure time, which was determined for as-received Al 7075-T6 (Fig. 1), was not observed; however, the transmission line impedance at the lowest frequencies, which is characteristic of the pitting process, could be clearly recognized after 1 or 2 days of exposure. For both specimens, only a few small pits were observed after 15 days.

Figure 3 shows EIS data for Al 6061-T6 after exposure to 0.5 N NaCl for 30 days. Curve 1 is for the as-received surface, while Curve 2 is for the surface that had been treated in the Ce-Mo process. The spectrum for the as-received surface is typical for localized corrosion,

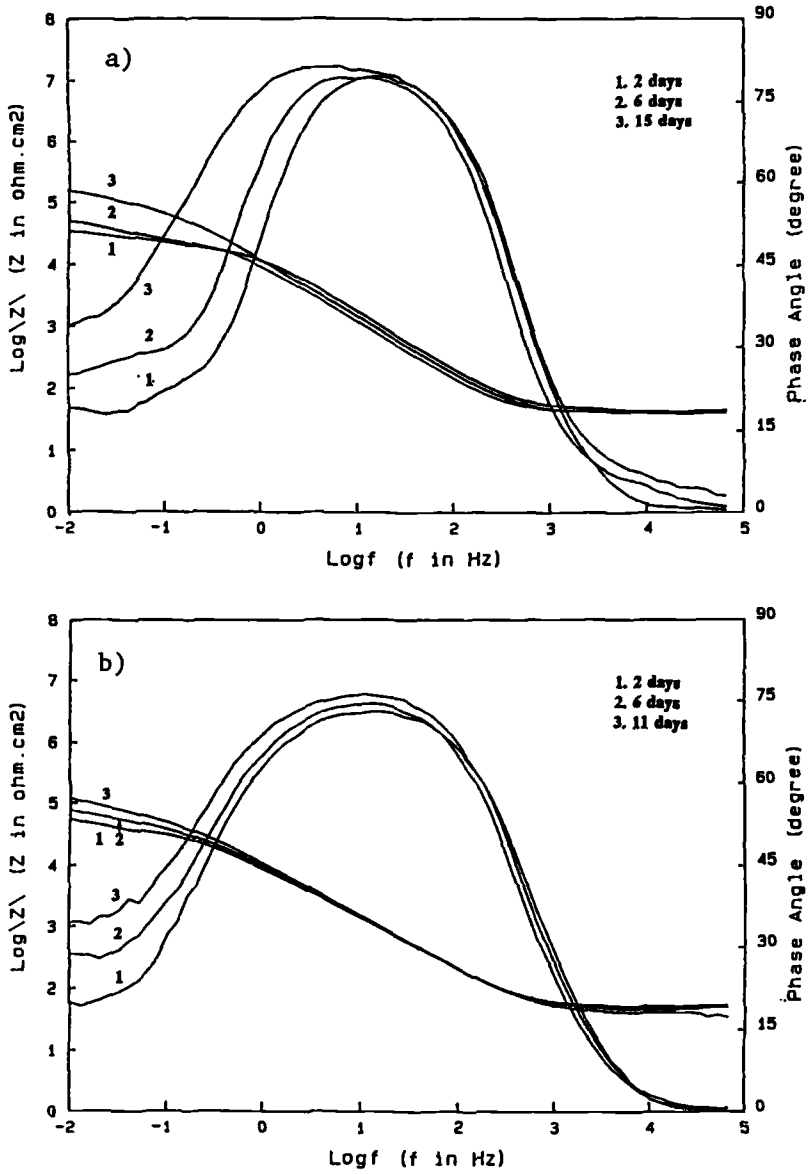

FIG. 2—*Bode-plots as a function of immersion time in 0.5 N NaCl for Al 6061-T6 in the* (a) *as-received and* (b) *polished conditions.*

while Curve 2 is typical for a passive surface for which the polarization resistance R_p exceeds 10^7 Ω-cm^2.

The Pitting Model

The impedance data obtained for untreated specimens during exposure to NaCl for short time periods and for passivated specimens after longer time periods can be described by

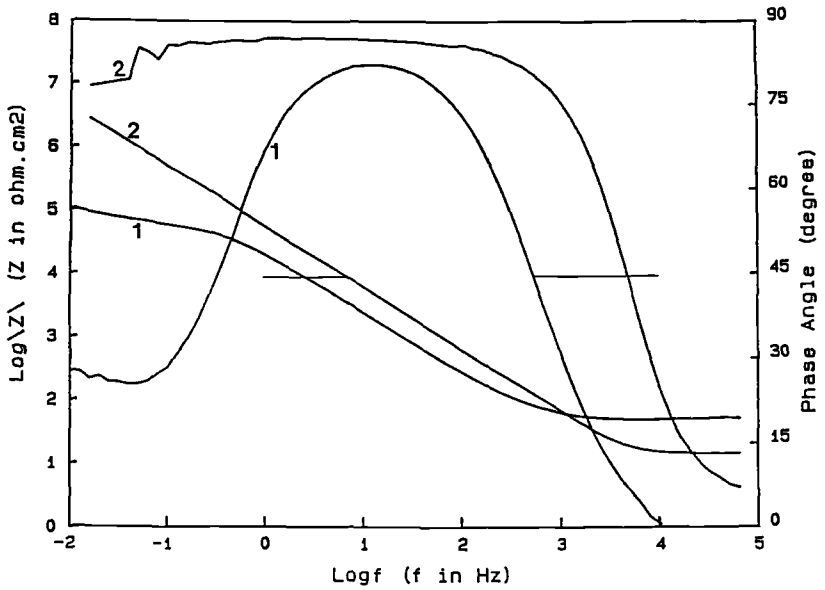

FIG. 3—*Bode-plots for Al 6061-T6 after exposure to 0.5 N NaCl for 30 days; Curve 1: as-received; Curve 2: treated in the Ce-Mo process.*

the pitting model shown in Figure 4 [*2–11*]. This model and the software PITFIT for the analysis of impedance spectra which agree with the pitting model in Fig. 4 have been discussed elsewhere in detail [*11,12*]. In Fig. 4, R_p and C_p are the polarization resistance and the capacitance of the passive surface, respectively, while R_{pit} and C_{pit} are the corresponding parameters for the processes occurring in the growing pit. The frequency dependence of the impedance in the low-frequency range is described by the term $W = K(j\omega)^n/F$, where K and n are experimental parameters and F is the fraction of the surface

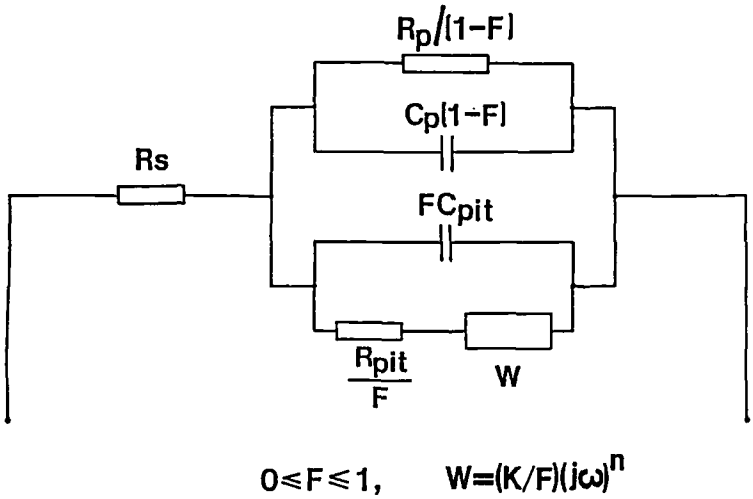

FIG. 4—*Model for the impedance of the pitting process for Al-based materials.*

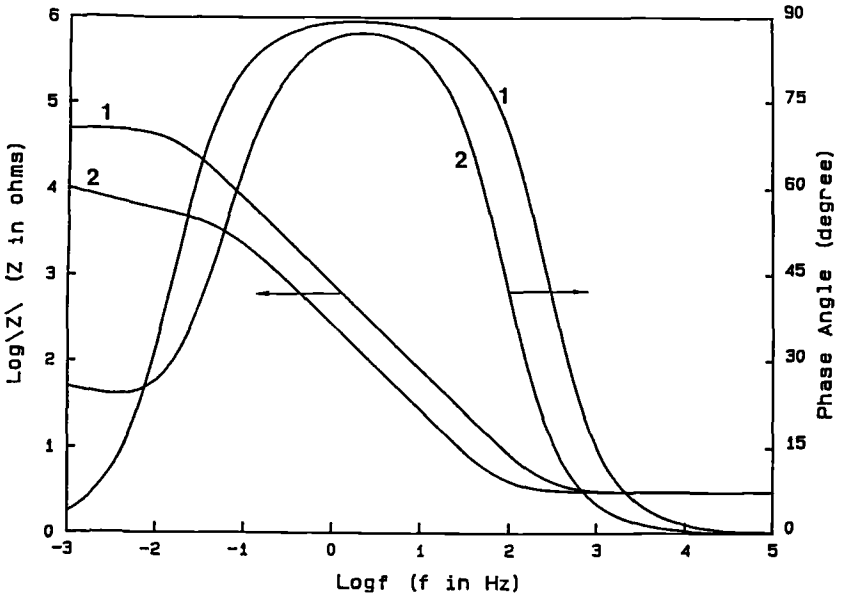

FIG. 5—*Simulated spectra for the model in Fig. 4 for F = 0 (Curve 1) and F = 0.005 (Curve 2);* $R_s = 3\ \Omega$, $R_p = 5 \times 10^4\ \Omega$, $C_p = 2 \times 10^{-4}$ F, $R_{pit} = 25\ \Omega$, $C_{pit} = 0.08$ F, $K = 2.5\ \Omega(rad/s)^{-n}$, $n = 0.50$.

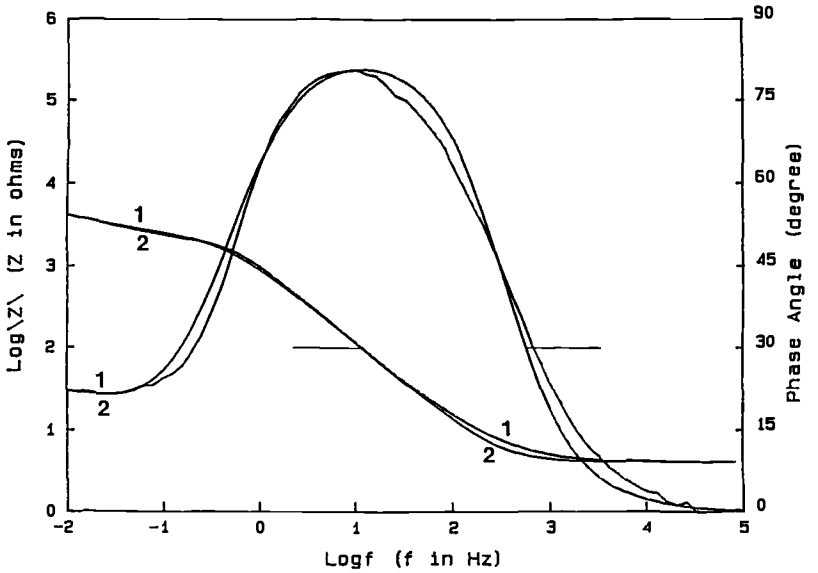

FIG. 6—*Bode-plots for Al 6061-T6; Curve 1–after exposure to 0.5 N NaCl for 24 h; Curve 2–fitted spectra with* $R_s = 4\ \Omega$, $R_p = 14\ 205\ \Omega$, $C_t = 175\ \mu F$, $R_{pit}/F = 2425\ \Omega$, $K/F = 850\ \Omega(rad/s)^{-n}$, $n = -0.53$, $A = 20\ cm^2$.

area on which pitting occurs ($0 \leq F \leq 1$). R_s is the solution resistance between the tip of the Luggin capillary and the surface of the test electrode.

Theoretical spectra for $F = 0$ and $F = 0.005$ are shown in Fig. 5 for parameters that have been found representative of the pitting process in recent studies of aluminum alloys exposed to NaCl [2–11]. Spectra such as those shown in Fig. 5, Curve 1 have been observed for aluminum alloys exposed to NaCl before pits were initiated. Spectra such as those shown in Curve 2 have been obtained for Al 6061 containing an artificial pit [3]. The decrease of the impedance in the capacitive region, the change of the frequency dependence at very low frequencies, and the occurrence of a second maximum of the phase angle at these frequencies are characteristic for the pitting process for aluminum alloys.

Figure 6 shows a comparison of experimental data (Curve 1) and data obtained by a fit (Curve 2) to the model in Fig. 4 for Al 6061 after exposure to 0.5 N NaCl for 24 h. The quality of the fit can be considered to be very good, taking into account the complexity of the impedance spectra.

Analysis of EIS Data

Analysis of experimental EIS data with PITFIT results in the fit parameters R_s, $R_p/(1 - F)$, $C_t = C_p(1 - F) + FC_{pit}$, R_{pit}/F, K/F, and n. Since F is usually very small, $R_p/(1 - F) = R_p$ and $C_t = C_p + FC_{pit}$. Figure 7 shows the time dependence of C_t for Al 7075-T6 in the as-received condition and after passivation, while Fig. 8 gives similar data for Al 6061. A very large increase of C_t is observed for the as-received Al 7075-T6 in the first two days of exposure, while for the passivated specimen C_t remained constant ($C_t = C_p$, $F = 0$) until pits were initiated after about 21 days resulting in an increase of $C_t = C_p + FC_{pit}$ (Fig. 7). For the polished Al 6061, the increase of C_t with time was very small and for the as-received Al 6061 C_t increased significantly only in the first seven days of exposure (Fig. 8).

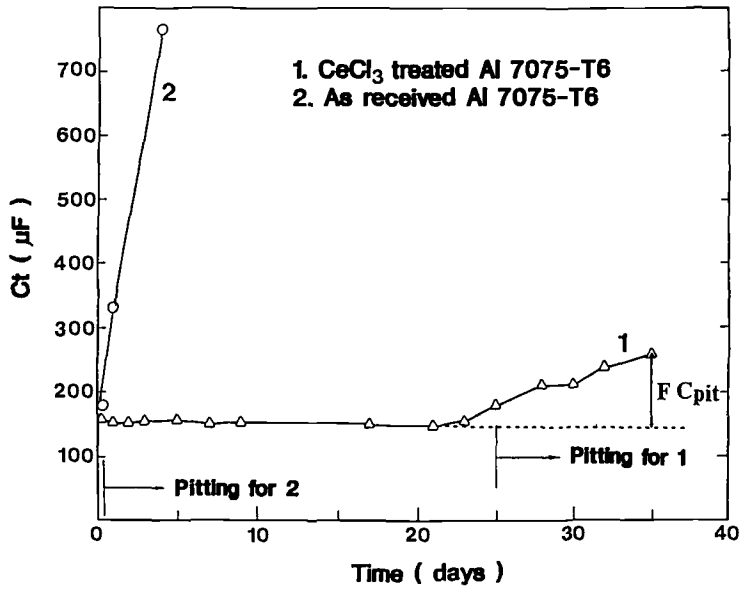

FIG. 7—*Time dependence of C_t for Al 7075-T6 (as-received versus $CeCl_3$ treatment) during exposure to 0.5 N NaCl.*

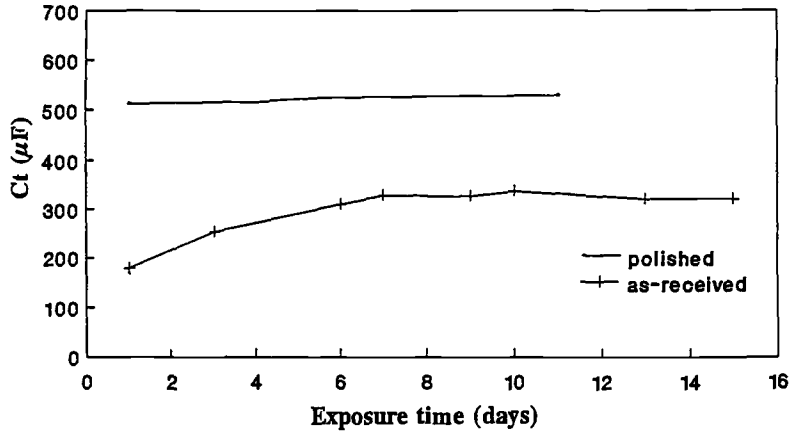

FIG. 8—*Time dependence of C, for Al 6061-T6 (as-received versus polished) during exposure to 0.5 N NaCl.*

Figures 9 and 10 show the time dependence of the fit parameters R_{pit}/F and K/F for Al 7075-T6 (Fig. 9) and Al 6061-T6 (Fig. 10). For Al 7076-T6, R_{pit}/F remained almost constant and only decreased at the last measurement after 37 days. K/F decreased continuously during the same time (Fig. 9). For the as-received Al 6061-T6, R_{pit}/F increased slightly with time and K/F went through a minimum at about 7 days (Fig. 10). For the polished specimen, R_{pit}/F and K/F increase slightly with time (Fig. 10). For the as-received as well as for the polished surface, n had values of about -0.8 (Fig. 11).

Further data analysis and calculation of the specific impedance parameters R°_{p} and R°_{pit} (in Ω-cm^2) and C°_{p} and C°_{pit} (in μF/cm^2) is only possible if the value of F and the pitted area are known as a function of exposure time.

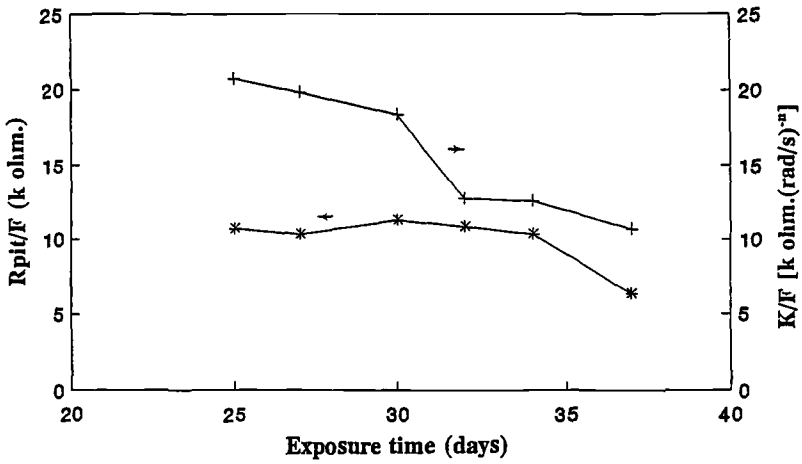

FIG. 9—*Time dependence of R_{pit}/F and K/F for Al 7075-T6 during exposure to 0.5 N NaCl.*

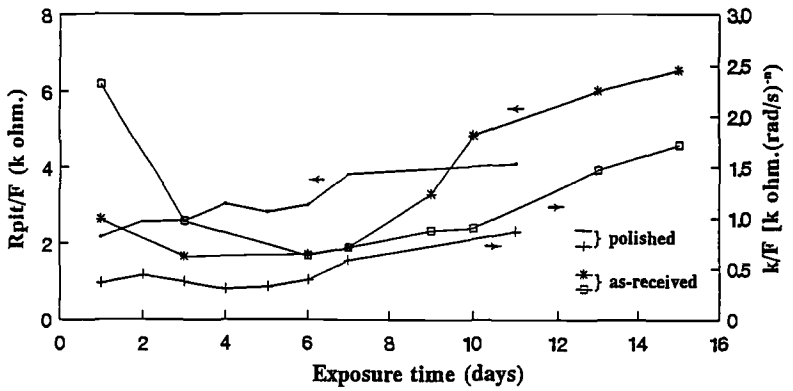

FIG. 10—*Time dependence of R_{pit}/F and K/F for Al 6061-T6 (as-received versus polished) during exposure to 0.5 N NaCl.*

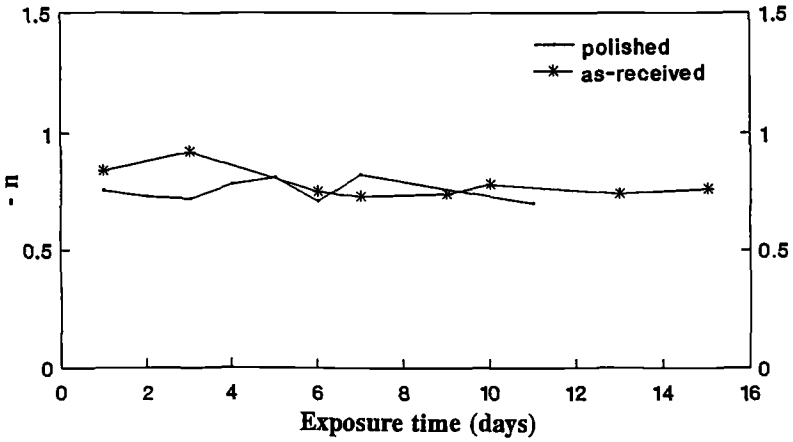

FIG. 11—*Time dependence of n for Al 6061-T6 (as-received versus polished) during exposure to 0.5 N NaCl.*

Determination of Pit Growth Rates

In order to obtain further information concerning pit growth kinetics from the experimental values of R_{pit}/F, the value of F was determined visually at the end of the test by microscopic observation. In addition, the value of FC_{pit} at the end of the test was determined from the C_t data in Figs. 7 and 8 as $FC_{pit} = C_t - C_p$ assuming that C_p, which did not change with time before pits initiated (Fig. 7), remained constant during the entire test. Based on a constant value of $C°_{pit}$ (in $\mu F/cm^2$) it is then possible to calculate F as a function of time. For Al 7075-T6 $C°_{pit}$ was 133 $\mu F/cm^2$, for the as-received Al 6061 $C°_{pit}$ was 500 $\mu F/cm^2$ and for the polished Al 6061 a value of 27.4 $\mu F/cm^2$ was used. $C°_p$ was 25.5 $\mu F/cm^2$ for the polished specimen and 8.5 $\mu F/cm^2$ for the as-received specimen. The latter value has been determined for Al-based materials in many other experiments conducted by the authors. $R°_{pit}$ (in Ω-cm^2) was calculated by multiplying the fit parameter R_{pit}/F with $2FA$, which is the area of a hemispherical pit in a surface with a total area A. This procedure also allows the determination of the transmission line parameter $K°$ and its time dependence.

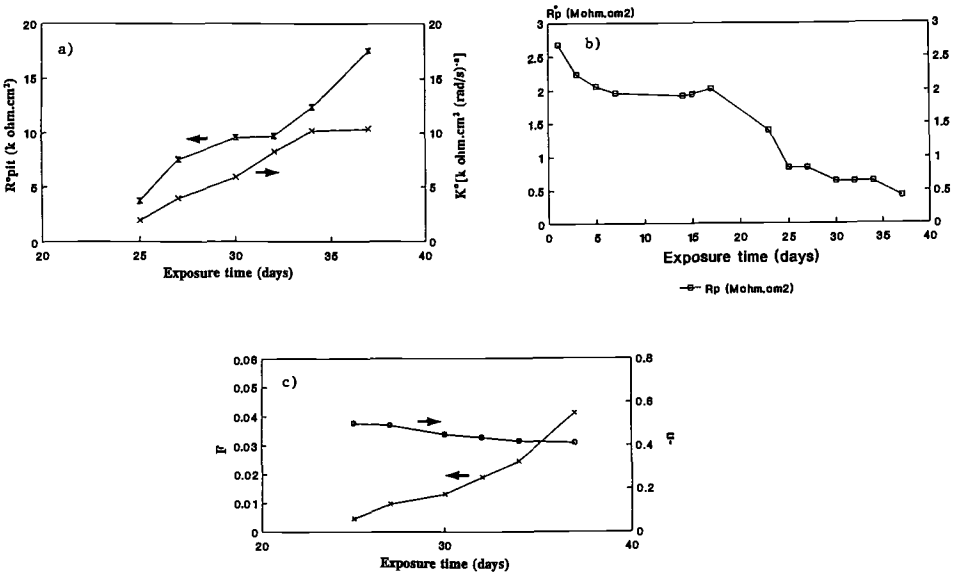

FIG. 12—*Time dependence of $R°_{pit}$ and $K°$, $R°_{p}$, and F and n, for Al 7075-T6 ($CeCl_3$ treatment).*

Figure 12 shows the time dependence of $R°_{pit}$ and $K°$ (Fig. 12*a*), $R°_{p}$ (Fig. 12*b*) and n and F (Fig. 12*c*) for the $CeCl_3$-treated Al 7075-T6. $R°_{pit}$ increased continuously with exposure time (Fig. 12*a*) indicating qualitatively a decrease of pit growth rates with time as the area fraction F at which pits grow increased to a final value of about 0.04 (Fig. 12*c*). $R°_{p}$ showed a slight decrease with time indicating an increase of the corrosion rate of the passive surface with time (Fig. 12*b*). An earlier analysis [*5,10,11*] had indicated a sharp rise of $R°_{p}$ at the time when pits were first detected. However, when the same data were re-analyzed with the final version of PITFIT, the data shown in Fig. 12*b* were obtained. The transmission line parameter $K°$ (units of Ω-cm^2(rad/s)$^{-n}$) also increased with time (Fig. 12*a*). Previously [*5*], the time dependence of K had been reported without normalization to the

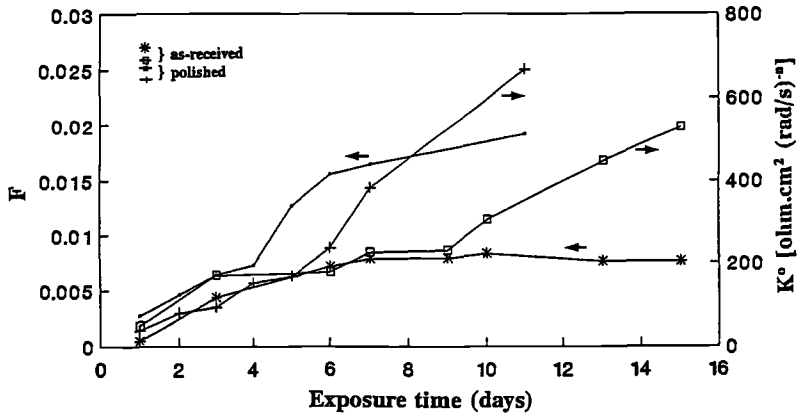

FIG. 13—*Time dependence of F and K° for Al 6061-T6 (as-received versus polished) during exposure to 0.5 N NaCl.*

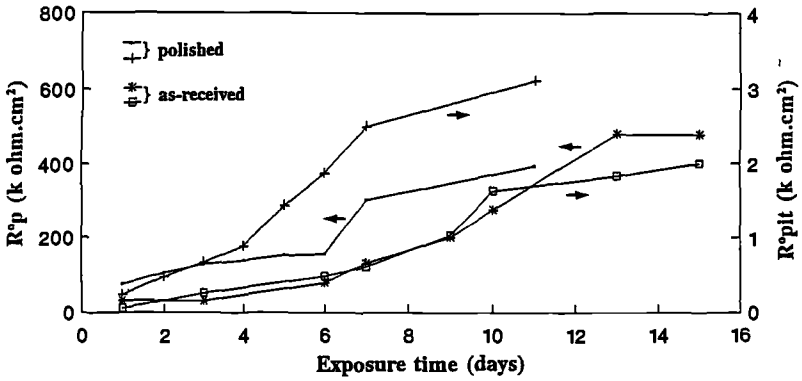

FIG. 14—*Time dependence of* $R°_{pit}$ *and* $R°_{p}$ *for Al 6061-T6 (as-received versus polished) during exposure to 0.5 N NaCl.*

area of the growing pit (units of $\Omega(\text{rad/s})^{-n}$) which produced different numerical values and a different time dependence of K.

The fit parameters for Al 6061 are shown in Figs. 13 and 14. F increased to a final value of about 0.02 after 11 days for the polished specimen, but remained at a much lower value for the as-received specimen (Fig. 13). $K°$ showed a steady increase for both types of surface (Fig. 13). $R°_{p}$ and $R°_{pit}$ also increased continuously with exposure time (Fig. 14).

The time dependence of $R°_{pit}$ for $CeCl_3$-treated Al 7075-T6 is shown again in Fig. 15 as a plot of log $(1/R°_{pit})$ versus log $(t - t_o)$, where t_o is the time at which pit growth was first detected with EIS. Since $1/R°_{pit}$ is proportional to the pit growth rate, the plot in Fig. 15 represents the time dependence of pit growth rate. By curve fitting, the following relationship was obtained

$$\log(1/R°_{pit}) = a + b \log t = -3.00 - 0.99 \log(t - t_o) \quad (1)$$

with t_o = 21d.

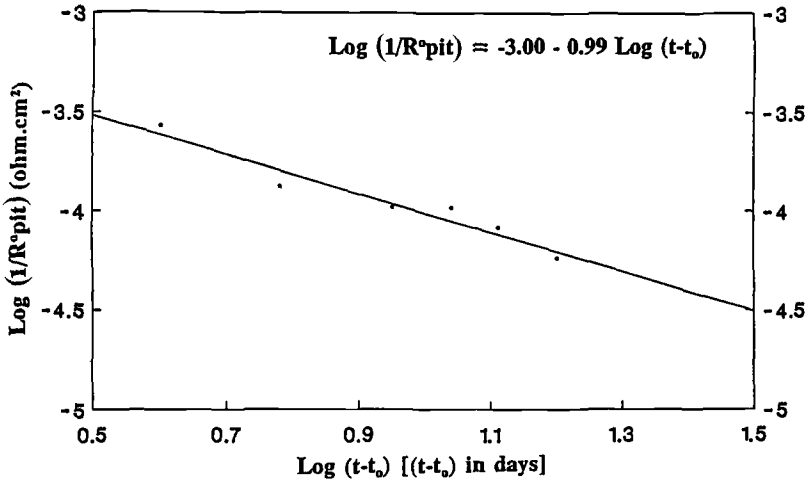

FIG. 15—*Plot of* log $(1/R°_{pit})$ *versus* log $(t - t_o)$ *for Al 7075-T6 passivated by immersion in* $CeCl_3$.

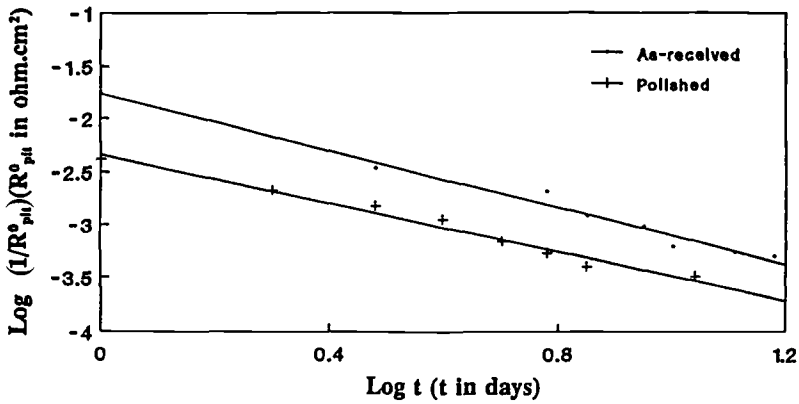

FIG. 16—*Plot of* log $(1/R°_{pit})$ *versus* log t *for Al 6061-T6, as-received and polished.*

For Al 6061-T6, the following time laws were established (Fig. 16)
as-received Al 6061:

$$\log(1/R°_{pit}) = -1.77 - 1.34 \log t \tag{2}$$

polished Al 6061:

$$\log(1/R°_{pit}) = -2.36 - 1.12 \log t \tag{3}$$

Since for Al 6061 pits initiated and grew in the first day of exposure, t_o was close to zero.

For Al 7075 the following results were obtained (Fig. 17*a–c*) using the analysis procedure previously discussed.
polished Al 7075-T6:

$$\log(1/R°_{pit}) = -1.50 - 1.35 \log t \tag{4}$$

with $C°_{pit} = 516\ \mu F/cm^2$.
as-received Al 7075-T73:

$$\log(1/R°_{pit}) = -1.93 - 1.07 \log t \tag{5}$$

with $C°_{pit} = 1200\ \mu F/cm^2$.
deoxidized Al 7075-T73:

$$\log(1/R°_{pit}) = -1.84 - 1.11 \log t \tag{6}$$

with $C°_{pit} = 769\ \mu F/cm^2$.

Minimum Pit Size that can be Detected by EIS

In evaluations of variations of the procedure followed in the Ce-Mo process it was noted occasionally by visual and microscopic observation that a few small pits developed without the occurrence of the characteristic changes in the impedance spectra. In order to determine the minimum pit size that can be detected by EIS, a theoretical calculation was

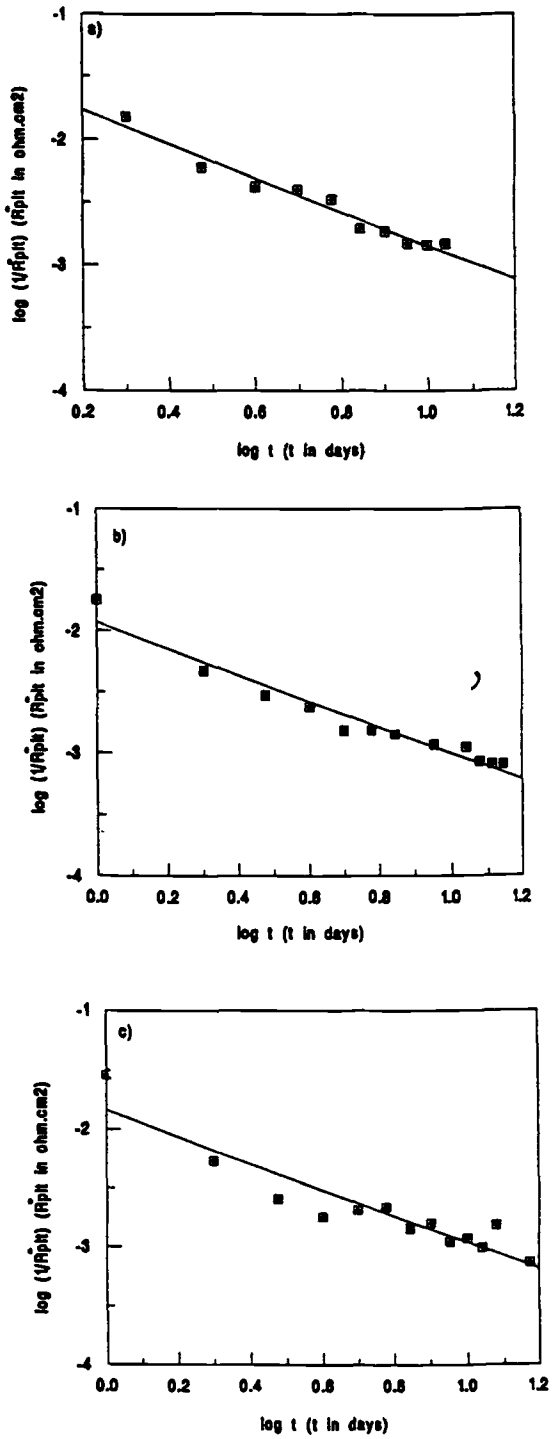

FIG. 17—*Plot of* log $(1/R^{\circ}_{pit})$ *versus* log t *for* (a) *polished Al 7075-T6,* (b) *as-received Al 7075-T73, and* (c) *deoxidized Al 7075-T73.*

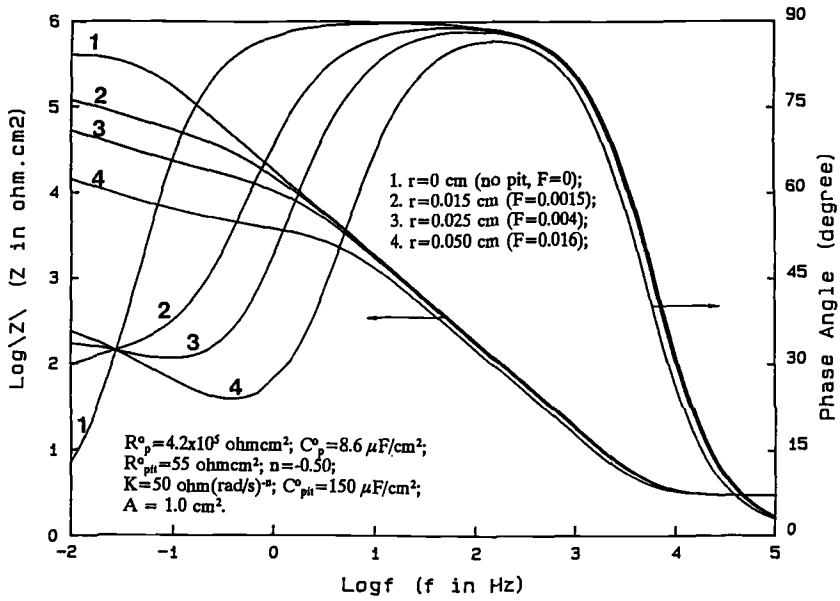

FIG. 18—*Theoretical Bode-plots as a function of pit depth.*

carried out in which the elements in the EC of Fig. 4 were calculated as a function of pit size. It was assumed that one hemispherical pit with a radius r was growing on a passive surface. Figure 18 shows theoretical impedance spectra as a function of r between 0 and 0.05 cm which corresponds to values of F between 0 and 0.016 for $A = 1$ cm^2. The spectra in Fig. 18 are similar to those for Al 6061 in Fig. 2. The characteristic changes of the spectra from those for a passive surface ($F = 0$) to those for a passive surface containing a growing pit occur for a pit radius larger than about 0.015 cm ($F = 0.0015$). For a pit radius of 0.05 cm ($F = 0.016$) a significant increase of C_f and a minimum of the phase angle at about 0.2 Hz can be seen in Fig. 18.

Discussion

The results obtained for aluminum alloys such as Al 6061, Al 7075, and Al 2024 and for Al MMCs such as Al/SiC and Al/graphite have demonstrated that localized corrosion can be detected by characteristic changes of the impedance spectra. A model for the impedance has been presented that describes the events occurring on a surface that contains active and passive areas. An increase of the experimental value of the capacitance C_f is observed which is due to the contribution from the pit capacitance C_{pit}. At low frequencies, a transmission line impedance is observed which is considered to be due to the interaction between the active and passive areas of the surface. The phase angle is a very sensitive indicator for the initiation of localized corrosion once a minimum pit depth has been exceeded. Simulations have shown that the minimum pit radius which can be detected by EIS is about 0.15 mm for one hemispherical pit growing in a surface of 1 cm^2. The pronounced changes of the phase angle that result in a minimum of the phase angle which moves to higher frequencies with increasing pit depth make it relatively easy to detect the presence of active pits. Attempts have been made to estimate pit growth rates and their dependence on exposure time from plots of R°_{pit} versus time. Relationships in the form

$$1/R^{\circ}_{pit} = a(t - t_o)^b \tag{7}$$

which are similar to those of Hunkeler and Boehni [*1*] for pits growth rates as a function of exposure time have been determined. These authors calculated an experimental value of $b = -0.5$ which was used as support for a mechanism of ohmic resistance controlled pit growth [*1,16,17*]. The value of b was found to depend on experimental parameters such as the applied potential $E > E_{pit}$, temperature and solution composition, while a was a system-independent parameter [*17*].

In the present investigation, Eqs 1 through 6 were determined at E_{corr}. For untreated Al 6061-T6 the experimental values of b ranged from -1.12 for the polished specimen to -1.34 for the as-received specimen. For Al 7075-T6, which had been passivated by immersion in 1000 ppm $CeCl_3$ for 7 days, b was found to be -0.99, while for polished (untreated) Al 7075-T6, b was -1.35. For Al 7075-T73, b was -1.07 for the as-received (degreased) specimen and -1.11 for the deoxidized specimen. Since for all cases b is close to -1, it can be assumed that the pit law follows the general equation

$$dr/dt = a_1 (t - t_o)^{-1} \tag{8}$$

which suggests that the radius r of the pits increases logarithmically

$$r = c \log(t - t_o) \tag{9}$$

The parameter a_1 can be defined as the pit growth rate for $t - t_o = 1$ day.

Table 1 presents a summary of the parameters a and b in the pit growth law (Eq 1) and the values of $R^{\circ}_{pit,t=1}$ which is a characteristic parameter for the metal/electrolyte system and represents the specific pit polarization resistance for $t - t_o = 1$ d. The values of C°_{pit} are also listed in Table 1. It is characteristic for C°_{pit} that its values are much larger than C°_{p} for the passive surface. Based on the $R^{\circ}_{pit,t=1}$ values in Table 1, it can be concluded that pits grew at about the same rate for as-received Al 6061, polished Al 7075-T6, as-received Al 7075-T73, and deoxidized Al 7075-T73. Pit growth rates were the lowest for passivated Al 7075-T6 and had intermediate values for polished Al 6061.

Further investigations of the pit growth process under the experimental conditions employed in this study, which is different from all previously reported investigations of localized corrosion, are necessary for a quantitative interpretation of the experimental results. A more detailed evaluation of the assumptions made in the present analysis such as growth of one hemispherical pit is necessary. The assumption that the time dependence of F can be calculated as previously explained has been confirmed in a recent experiment with passivated (Ce-Mo process) Al 6013-T6, in which F was determined after each impedance measurement by microscopic observation of the entire exposed surface. Very

TABLE 1—*Summary of pit growth parameters (Eq 1).*

Alloys	a	$R^{\circ}_{pit,t=1}$(K Ω.cm²)	b	C°_{pit}(μF/cm²)
Al 7075-T6 ($CeCl_3$)	−3.00	1000	−0.99	133
As-received Al 6061-T6	−1.77	59	−1.34	500
Polished Al 6061-T6	−2.36	229	−1.12	27
Polished Al 7075-T6	−1.50	32	−1.35	516
As-received Al 7075-T73	−1.93	85	−1.07	1200
Deoxidized Al 7075-T73	−1.84	69	−1.11	769

good agreement between the F values determined by this method and those calculated for EIS data has been observed [*18*]. It could be argued that F determined at the end of the experiment may not accurately represent the area fraction of pits that are active at this time. This question is more difficult to answer. By assuming that all pits are active, the corroding area may be overestimated and pit growth rates may be underestimated.

Despite some uncertainties in the quantitative determination of pit growth rates, the authors are convinced that EIS is a very powerful tool for detection and monitoring of localized corrosion of aluminum alloys and Al-based materials. It needs to be pointed out here that based on the authors' experience EIS can also be used to detect and monitor localized corrosion of other materials such as stainless steels [*19*] and magnesium [*10,20*]. However, the changes of the impedance spectra in the presence of pits are different for these materials [*18,20*] from those described here for Al-based materials and quantified in the model shown in Fig. 4.

Acknowledgment

This project has been supported by the Office of Naval Research (Dr. A. J. Sedriks) under Contracts N00014-88-K-0034 and N00014-91-J-1041.

References

[*1*] Hunkeler, F. and Boehni, H., *Corrosion*, Vol. 27, 1981, p. 645.
[*2*] Mansfeld, F., Lin, S., Kim, S., and Shih, H., *Corrosion*, Vol. 45, 1989, p. 615.
[*3*] Mansfeld, F., Lin, S., Kim, S., and Shih, H., *Corrosion Science*, Vol. 27, 1987, p. 997.
[*4*] Mansfeld, F. and Shih, H., *Journal of the Electrochemical Society*, Vol. 135, 1988, p. 1171.
[*5*] Mansfeld, F., Lin, S., Kim, S., and Shih, H., *Journal of the Electrochemical Society*, Vol. 137, 1990, p. 78.
[*6*] Mansfeld, F., Lin, S., Kim, S., and Shih, H., *Electrochimica Acta*, Vol. 34, 1989, p. 1123.
[*7*] Mansfeld, F., *Electrochimica Acta*, Vol. 35, 1990, p. 1533.
[*8*] Shih, H. and Mansfeld, F., in *New Methods for Corrosion Testing of Aluminum Alloys, ASTM STP 1134*, V. S. Agarwala and G. M. Ugiansky, Eds., American Society for Testing and Materials, Philadelphia, 1992, p. 180.
[*9*] Mansfeld, F. and Shih, H., *Proceedings of the 11th International Corrosion Congress*, Florence, Italy, 1990, pp. 4–555.
[*10*] Lin, S., "Corrosion Protection of Metal Matrix Composites," Ph.D. thesis, University of Southern California, August 1990.
[*11*] Mansfeld, F. and Shih, H., in *New Methods for Corrosion Testing of Aluminum Alloys, ASTM STP 1134*, V. S. Agarwala and G. M. Ugiansky, Eds., American Society for Testing and Materials, Philadelphia, 1992, p. 141.
[*12*] Shih, H. and Mansfeld, F., *Corrosion*, Vol. 45, 1989, p. 610.
[*13*] Mansfeld, F., Wang, Y., and Shih, H., *Journal of the Electrochemical Society*, Vol. 138, 1991, p. L74.
[*14*] Mansfeld, F., Wang, Y., and Shih, H., "Approaches Towards the Development of a Stainless Aluminum," *Proceedings, EMCR'91*, Espoo, Finland, July 1991, Metals Forum (in press).
[*15*] Mansfeld, F., Wang, Y., and Shih, H., "The Ce-Mo Process for Surface Modification of Al-Based Materials," *Proceedings of the 5th International Fischer Symposium*, Karlsruhe, Germany, June 1991, *Electrochimica Acta* Vol. 37, 1992, p. 2277.
[*16*] Hunkeler, F. and Boehni, H., *Werkstoffe und Korrosion*, Vol. 32, 1981, p. 129.
[*17*] Boehni, H., "Localized Corrosion," in *Corrosion Mechanisms*, F. Mansfeld, Ed., M. Dekker, 1987.
[*18*] Wang, Y. and Mansfeld, F., unpublished results.
[*19*] Mansfeld, F. and Little, B., *Corrosion Science*, Vol. 32, 1991, p. 247.
[*20*] Mansfeld, F., Kim, S., and Lin, S., *Journal of Coatings Technology*, Vol. 61 (744), 1989, p. 33.

Pierre R. Roberge,[1] *E. Halliop,*[1] *and Sid Yousri*[2]

Potentiodynamic Polarization and Electrochemical Impedance Spectroscopy for the Statistical Process Control of Aluminum Anodizing

REFERENCE: Roberge, P. R., Halliop, E., and Yousri, S., **"Potentiodynamic Polarization and Electrochemical Impedance Spectroscopy for the Statistical Process Control of Aluminum Anodizing,"** *Electrochemical Impedance: Analysis and Interpretation, ASTM STP 1188,* J. R. Scully, D. C. Silverman, and M. W. Kendig, Eds., American Society for Testing and Materials, Philadelphia, 1993, pp. 313–327.

ABSTRACT: Industrial and military specifications often require the use of a 300+ h salt spray exposure method to test anodized aluminum coupons and evaluate the quality of anodizing processes. In addition to the salt spray (fog) exposure test being time consuming, its results are highly interpretive and therefore relatively imprecise. The long duration of the test itself makes it a poor tool for monitoring daily plant operation of anodizing baths. An electrochemical procedure has recently been developed to evaluate the quality of anodized aluminum coupons. This procedure is based on the electrochemical activation of the material under test followed by corrosion resistance measurements with either potentiodynamic polarization or electrochemical impedance spectroscopy (EIS) in a cell designed to accept coupons prepared for salt spray testing. Results obtained formed the statistical basis to establish accelerated electrochemical tests as a routine plant monitoring of aluminum anodizing.

KEYWORDS: potentiodynamic, electrochemical impedance spectroscopy (EIS), anodized aluminum, salt spray test

The quality control of aluminum anodizing presents a difficult analytical problem. The use of conventional coating thickness measurements is not satisfactory since the anodizing agents will have dissolved some of the substrate material as the oxide layer was formed. Techniques that determine the coating weight per unit area could be useful to evaluate the extent of anodized film coverage, but these techniques are not sensitive to flaws such as porosity or the presence of contaminants in the coating. Such factors can strongly influence the corrosion protection afforded by the anodized layer.

Specifications such as the Military Specification on Anodic Coatings for Aluminum and Aluminum Alloys (MIL-A-8625 [1]) require the use of ASTM B117, Test Method of Salt Spray (Fog) Testing, which entails a salt spray (fog) exposure of 336 h. In addition to this procedure being rather time consuming, the results are highly interpretive, and therefore relatively imprecise.

ASTM Method for Measurement of Impedance of Anodic Coatings on Aluminum,

[1]Associate professor and research assistant, respectively, Department of Chemistry and Chemical Engineering, Royal Military College, Kingston, Ontario, Canada K7K 5L0.

[2]Chief, Chemical Technology and Purchasing Liaison, Pratt and Whitney Canada Inc., Longueuil, Quebec, Canada J4G 1A1.

(B457) describes a procedure to determine the impedance at 1000 Hz as a measure of the quality of sealing anodized aluminum. While this method is applicable to the rapid, nondestructive testing of anodic coatings, its results were never related to the actual corrosion resistance provided by these coatings.

Because of the problems with the above techniques, an alternative test was still needed to rapidly and accurately evaluate the corrosion protection qualities of various anodized films. Since corrosion resistance was the key evaluation parameter, it was decided to consider electrochemical corrosion measurement techniques as the basis for the development of an accelerated test.

Potentiodynamic Polarization Technique

The technique adopted at Pratt & Whitney Canada [*2*] for daily monitoring aluminum anodizing is one of the most used techniques for studying corrosion [*3*]. Potentiodynamic polarization techniques have been used for both theoretical studies and practical predictions of corrosion behavior. A standard methodology for applying the technique is available in ASTM Standard Reference Test Method for Making Potentiostatic and Potentiodynamic Anodic Polarization Measurements (G 5 87). Typically the potential would be scanned linearly around E_{corr} as a function of time and the current monitored as the potential changes. When the potential is plotted as a function of the log of the current, portions of both the anodic and cathodic regions may be linear and follow a Tafel behavior. In such cases it is possible to extrapolate these linear regions to where they should intersect, at the corrosion potential (E_{corr}), and obtain a value for the corrosion current (i_{corr}).

Several examples of computer programs have been described in the literature [*4–6*] where the application of statistics permit an automatic analysis of experimental data to obtain Tafel constants and calculate i_{corr} according to the Tafel extrapolation technique for measurement of corrosion kinetic parameters introduced by Stern [*7*] and Stern and Geary [*8*]. Commercial corrosion testing software is also available [*9*] if not built into the instrumentation itself.

Electrochemical Impedance Spectroscopy (EIS)

EIS has been successfully applied to the study of corrosion systems for over 20 years [*10*]. Since Epelboin and coworkers published their early work on the system iron-H_2SO_4-propargylic acid [*11*], impedance techniques have found increasing applications in corrosion research because of the possibility of obtaining information on the chemical mechanisms involved. An important advantage of EIS over other laboratory techniques is the possibility of using very small amplitude signals without disturbing the properties being measured.

While the calculation of polarization resistance from EIS spectra is relatively straightforward for many applications, difficulties in data interpretation are still an important obstacle to making practical and friendly routine use of the testing technique [*12*]. In order to overcome some of these difficulties, a method was developed that consisted of geometrically finding the center of an arc formed by three successive data points on a complex impedance diagram [*13*]. The analysis of EIS measurements was further simplified by systematically permuting the data points involved in the projection of centers [*14*]. Such a methodology, which is valid for any frequency domain where the system is dominated by a single time constant (RC), made it possible to automatically estimate, with a calculated degree of confidence, the main impedance parameters used for corrosion monitoring.

Experimental

The Potentiodynamic Technique

The electrochemical instrumentation consisted of an EG&G Princeton Applied Research Model 350-1 Corrosion Measurement System. This system was used to automate the acquisition of Tafel plots, identify linear trends in the plots, and calculate the corrosion rate estimates.

The electrochemical cell used in these studies was designed to accommodate directly standard AMS 4037 test coupons used in salt spray testing. This cell consisted of a hollow plastic cylinder with a 5-cm outside diameter (Fig. 1). The cell was assembled with the test coupon inserted between the hollow cylinder and the solid base. A rubber O-ring was used along with a clamp to create a water-tight seal. In this way, the test coupon surface actually served as the bottom of the cell. To facilitate electrical contact, one corner of the anodized panel was ground to expose bare metal.

The test cell could accommodate a noble metal counter electrode, a reference electrode (SCE), and an air purge which also served as an agitation device. A solution volume of 200 mL was used with a moderate air-stirring rate. This volume of solution was found to be sufficient to negate the effects of metal dissolution that occurred during the course of a typical test. The test solution itself consisted of a buffer made by dissolving 0.2 g of boric acid and 16.0 g of sodium chloride in 1 L of 1.0 N sodium hydroxide solution, and adjusting the resulting solution to pH 10.5. Such a pH control was found to be an important element of the testing procedure and greatly improved the reproducibility of the results. The cell was refilled with fresh solution between each test.

Prior to testing, each specimen panel was solvent degreased, rinsed with deionized water, and activated at a potential of +600 mV versus SCE for 5 min. Following this preconditioning potential, the open circuit potential was monitored and the scan was

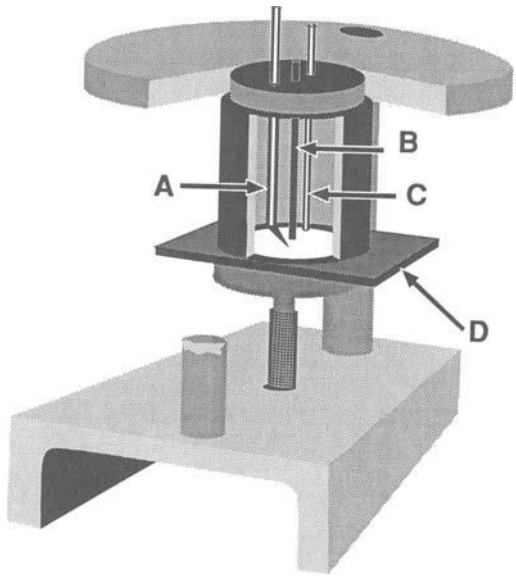

FIG. 1—*Schematic representation of the electrochemical cell;* (a) *Luggin for reference electrode (SCE),* (b) *counterelectrode,* (c) *air purge and* (d) *panel under test.*

initiated once the system had equilibrated (as evidenced by stable open circuit potential). This generally required between 20 s and 5 min.

The instrumentation automatically recorded E_{corr} and executed the applied potential scan from E_{corr} −400 mV to E_{corr} +400 mV. A scan rate of 0.5 mV/s was used, which resulted in a scan time of 27 min.

The EIS Technique

The EIS measurements were carried out with a commercial Frequency Response Analyzer (FRA) system (Solartron model 1255) controlled by a Hewlett Packard model HP86 microcomputer. The probing ac current was kept at a value that would not cause more than 10 mV difference (peak to peak) across the cell. At least five consecutive measurements were made at each frequency to ensure that the system investigated had stabilized.

The cell designed originally for the potentiodynamic studies was modified for the EIS measurements. The main difference was that the cell was operated horizontally in a two-electrode configuration with two half panels, parallel to each other, serving as both working and counterelectrode.

Two types of EIS measurement were made during this project. A first series was made in a fashion described in the literature [*15*] by recording, at a few hour intervals and for a period of over 300 h, the EIS measurements without any initial activation of the panels. The second series of experiments was carried out on panels immediately after their activation at +600 mV versus SCE for a few minutes.

The impedance data analysis technique presented earlier was used to calculate $1/R$ values for each impedance plot gathered. These values were then converted into corrosion rates by multiplying them (Eq 1) with a proportionality constant B [*16*] typical for aluminum exposed to a saline environment.

$$i_{corr} = B/R \tag{1}$$

where

i_{corr} is the corrosion current ($\mu A/cm^2$),
B is a proportionality constant for aluminum in chlorides (24 mV [*16*]), and
R is the resistance calculated from EIS low-frequency measurements ($k\Omega \cdot cm^2$).

Results

Potentiodynamic Versus Salt Spray Testing

Figures 2 and 3 illustrate some typical instrument outputs obtained with two analyzed specimens. Figure 2 shows a Tafel plot measured on a specimen with a relatively good coating while Fig. 3 shows one obtained for a specimen with a poor anodic coating.

Faraday's law (Eq 2) was used to convert the corrosion current estimated from such plots into penetration corrosion rates.

$$\text{Corrosion rate} = \frac{3.3 \times i_{corr} \times EW}{d} \tag{2}$$

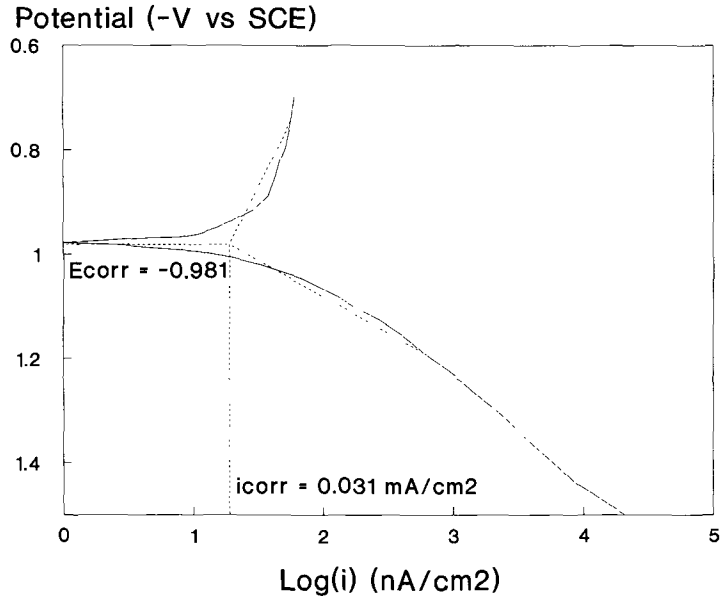

FIG. 2—*A typical potentiodynamic scan made with an anodized* and *sealed aluminum panel (good coating).*

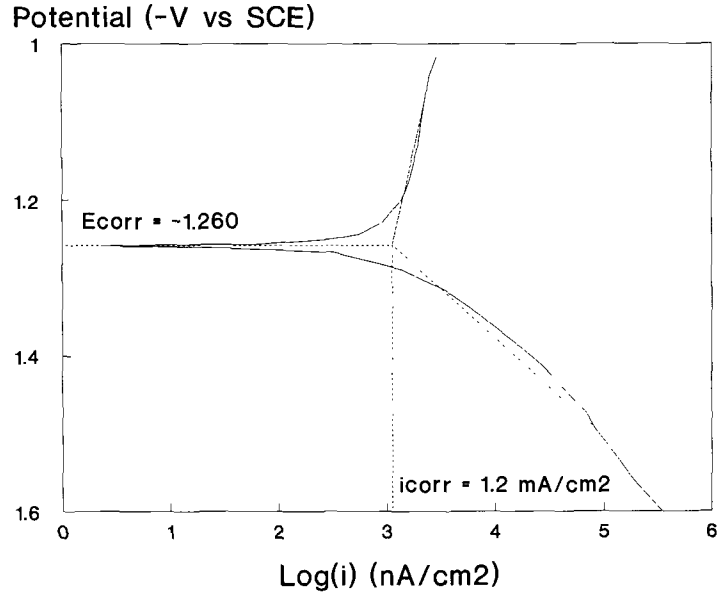

FIG. 3—*A typical potentiodynamic scan made with an anodized but* not *sealed aluminum panel (poor coating).*

where

Corrosion rate is in μm/y,
i_{corr} in μA/cm^2,
EW is the equivalent weight of the element being oxidized (g/equiv.), and
d is the density of the element being oxidized (g/cm^3).

Table 1 contains some corrosion rates that were determined using the potentiodynamic technique for specimens that were anodized by a number of different procedures. A wide range of corrosion rates was observed. The worst case was obviously for bare aluminum coupons while lower corrosion rates were observed for specimens anodized but not sealed. The lowest corrosion rate was found for coupons anodized and sealed in freshly deionized water at pH 5.5.

Four years of tests with panels processed under different conditions helped to establish the following correlation between results obtained with the potentiodynamic technique, conventional salt spray testing, and process control parameters [*2*]:

- Coupons with measured corrosion rates lower than 2.5 μm/y will not fail salt spray testing.
- If the corrosion rates fall between 2.5 and 15 μm/y, a warning is raised that the anodizing process is deteriorating and corrective measures are taken. Panels processed in such conditions would pass the salt spray test 90% of the time.
- When the corrosion rates exceed 15 μm/y, immediate corrective action is required and parts are reprocessed if corrosion rates exceed 25 μm/y. Between 15 and 25 μm/y, a judgment call is made depending on the applications.
- The seal time was optimized. For freshly deionized water an optimum seal time would be 8 min while it could be up to 15 min for a one-month-old seal solution.
- The seal solution temperature was also optimized. Modifications to previous specifications were made when it was discovered that cooler seal solutions produced coupons with higher corrosion rates. The minimum seal solution temperature was raised to 90°C (95 ± 5°C in present specifications).

Additionally, a statistical analysis was performed on 149 pairs of results obtained with potentiodynamic and salt spray testing. Figure 4 illustrates the plot of time-to-failure (salt spray testing) against logarithm of corrosion rate (potentiodynamic) obtained with these results. While it is difficult to establish a direct correlation between these two variables by

TABLE 1—*Comparison of anodizing (chromic acid) operating conditions with corrosion rates obtained with the potentiodynamic technique.*

Anodizing Conditions	Corrosion Rate, μm/y
Bare Aluminum	1200
Anodized + no sealant	130
Anodized + sealed in tap water* (pH = 3)	110
Anodized + sealed in tap water (pH = 4)	50
Anodized + sealed in tap water (pH = 4.5)	0.8
Anodized + sealed in tap water (pH = 7.0)	5.0
Anodized + sealed in tap water (pH = 7.5)	8.9
Anodized + sealed in deionized water (pH = 5.5)	0.025

*All sealing solutions were maintained at 91°C.

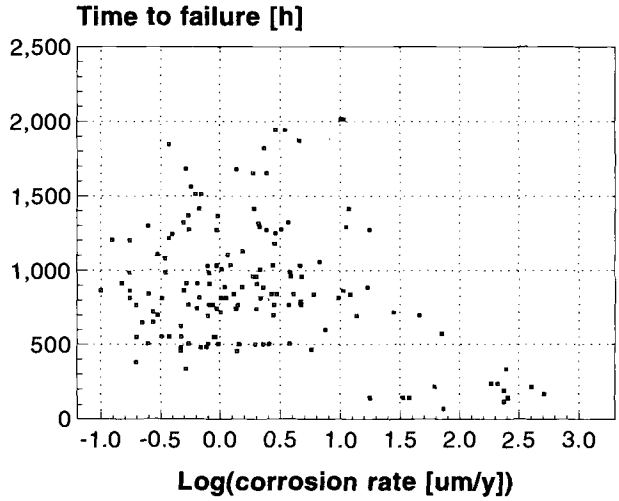

FIG. 4—*Time-to-failure (salt spray) plotted against log [corrosion rate] (potentiodynamic) for tests made on 149 pairs of aluminum panels.*

examining Fig. 4, a more detailed analysis of the results obtained with the potentiodynamic method [*17*] has revealed that two modes were governing the degradation processes measured by potentiodynamic polarization (Fig. 5). By regrouping the pairs of salt spray versus potentiodynamic results into a low corrosion mode (Fig. 6) and a high corrosion mode (Fig. 7) it became possible to establish a statistically valid correlation between the two methods for panels the most susceptible to degrade by corrosion (high corrosion mode (Fig. 8)).

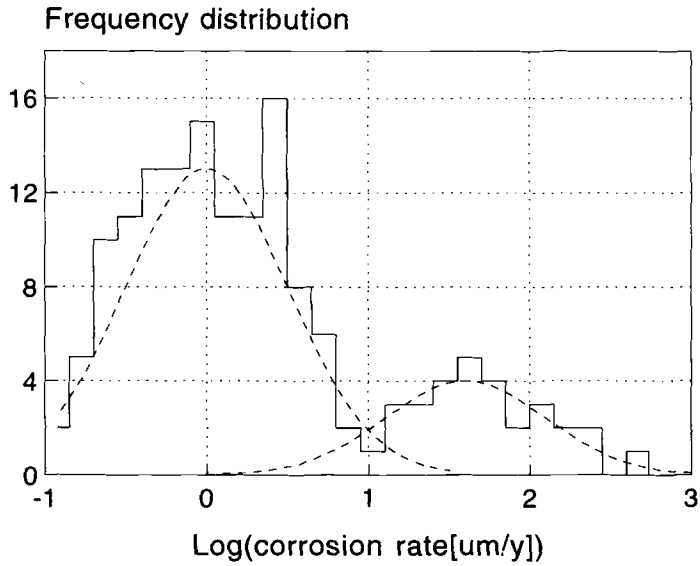

FIG. 5—*Frequency distribution of the potentiodynamic results (Fig. 4) fitted by two normal distribution models at low and high corrosion rates.*

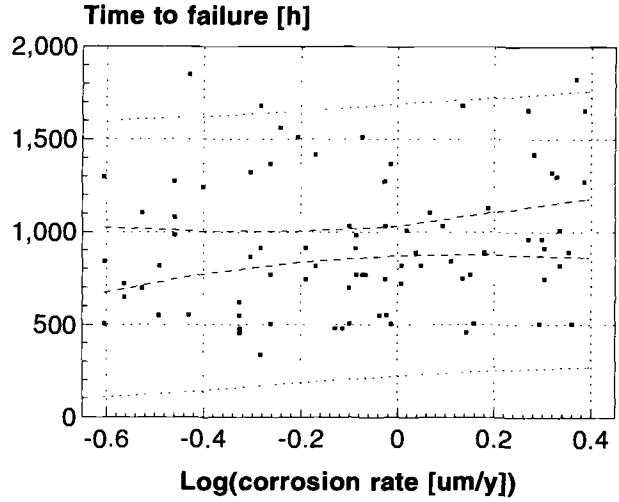

FIG. 6—*Linear regression of time-to-failure (salt spray) and log(corrosion rate) (potentiodynamic) of* low corrosion rate *results of Fig. 4 with parallel lines indicating 95% (---) and 90 (···) % confidence levels.*

A linear regression of the high corrosion rate data obtained with the two techniques showed that the time to failure data decline proportionally with corrosion rates (potentiodynamic technique) according to Eq 3. The correlation coefficient between data obtained with salt spray and potentiodynamic testing was calculated to be 71%.

$$\text{Time-to-failure } [h] = 2850 - 1470 \times \log(\text{corrosion rate } [\mu\text{m/y}]) \quad (3)$$

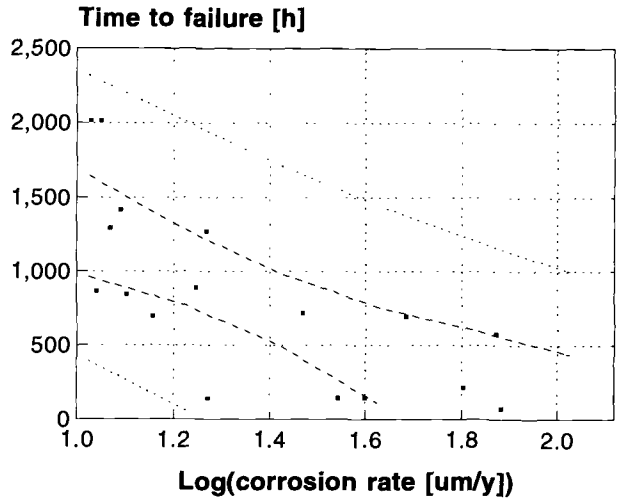

FIG. 7—*Linear regression of time-to-failure (salt spray) and log(corrosion rate) (potentiodynamic) of* high corrosion rate *results of Fig. 4 with parallel lines indicating 95% (---) and 90 (···) confidence levels.*

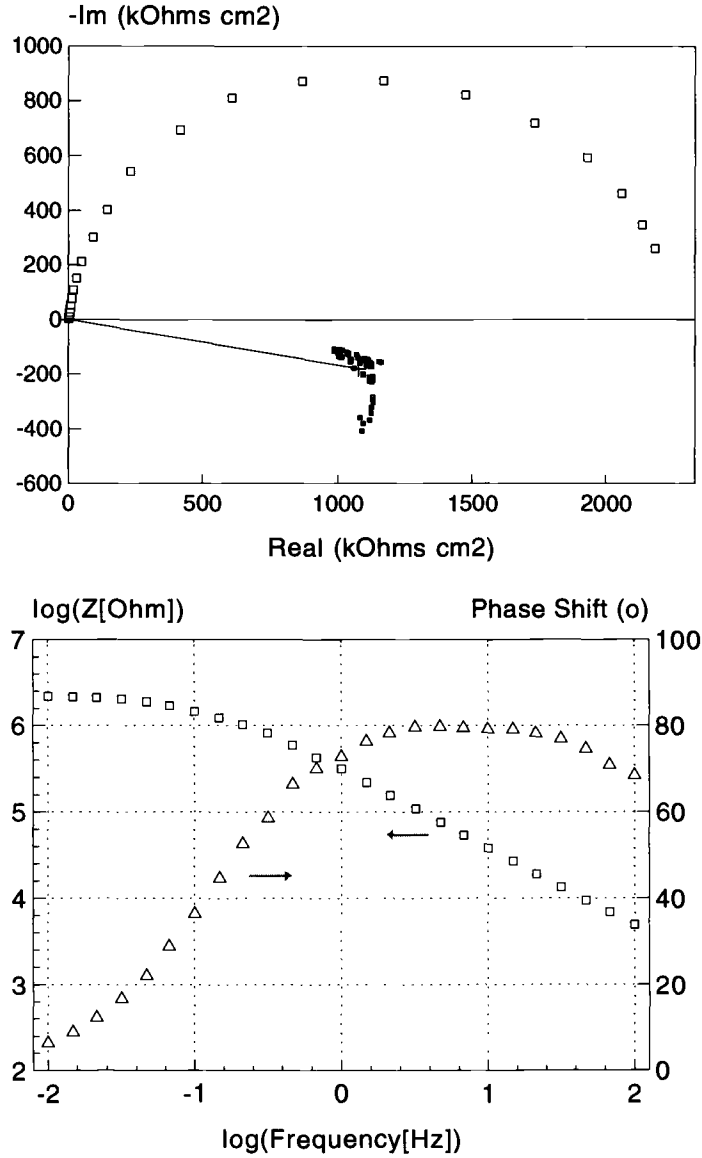

FIG. 8—*Typical EIS results obtained with an anodized and sealed (tap water, pH 4.5) panel during the first day of test in the electrochemical cell:* (a) *Nyquist plot and projected centers obtained with the permutation analysis technique* [13, 14], (b) *Bode representation of the same results.*

EIS

Previous studies [*15,18–21*] have demonstrated that the high-frequency part of EIS spectra can be used to monitor changes in the sealing process of anodized aluminum production. However, some of these studies [*15,21*] have indicated that the corrosion behavior of anodized panels itself cannot be predicted from the high-frequency data. While large differences in the high-frequency portion of EIS spectra can indicate differences in sealing mechanisms, they do not necessarily correlate to differences in the long-term corrosion behavior of anodized aluminum. The experimental data presented in the literature show that the corrosion resistance can best be determined from the low-frequency impedance data. The EIS data presented in [*15*], for example, would indicate that the corrosion behavior of corrosion-resistant anodized aluminum alloys is revealed by following changes observed in the low-frequency portions (<1 Hz) of EIS spectra gathered as a function of exposure time. Based on these studies, a damage function had been established to describe the corrosion resistance from the impedance measured at 0.1 Hz and an exposure time of 7 days.

In the present project, a first series of panels with known anodizing histories and corrosion rates measured by the potentiodynamic method was continuously monitored with EIS during at least 10 days of exposure in the sodium chloride buffered solution. Typical EIS results obtained with sealed anodized panels are presented in Fig. 8 (Day 1) and Fig. 9 (Day 6).

Figures 10 and 11 represent the results of analyzed EIS measurements for two 12-day experiments made with an anodized but *not* sealed panel (Fig. 10) and an anodized *and* sealed panel (Fig. 11). While the results obtained during the first four days of these tests are comparable, the degradation of the corrosion resistance of the panel that was not sealed became quite visible after this initial period when the corrosion rate reached values 50 times higher over the following eight days. The depression angles calculated from the EIS measurements made during these experiments seemed to increase regularly with exposure time.

In a second series of experiments, the EIS measurements were made immediately after the panels had been activated at +600 mV (versus SCE) for a few minutes. The analyzed results are presented in Fig. 12. One can see that the activation step now permits differentiation between panels that had been processed differently.

An indication that the degradation mechanisms differed between the two techniques is presented in Fig. 13. The panels tested with the potentiodynamic technique and measuring a high corrosion rate would typically present a pattern of leached patches after the test (Fig. 13*a*) while the same panels tested with EIS would become increasingly pitted after a few days of the test (Fig. 13*b*).

Conclusions

A preliminary investigation on the application of EIS to the characterization of anodized panels has demonstrated that unless a special electrochemical treatment is applied to the panels before testing them, obtaining results with the large surface cell and the buffered chloride solution would be as tedious and unreliable as it is with salt spray testing.

The quality control of aluminum anodizing with routine potentiodynamic polarization measurements has become an acceptable and reliable replacement of salt spray testing. A detailed statistical analysis of results obtained with these two accelerated testing techniques has demonstrated [*17*] that both methods can reveal relatively easily defective panels. But potentiodynamic polarization or EIS measurements can be performed a thou-

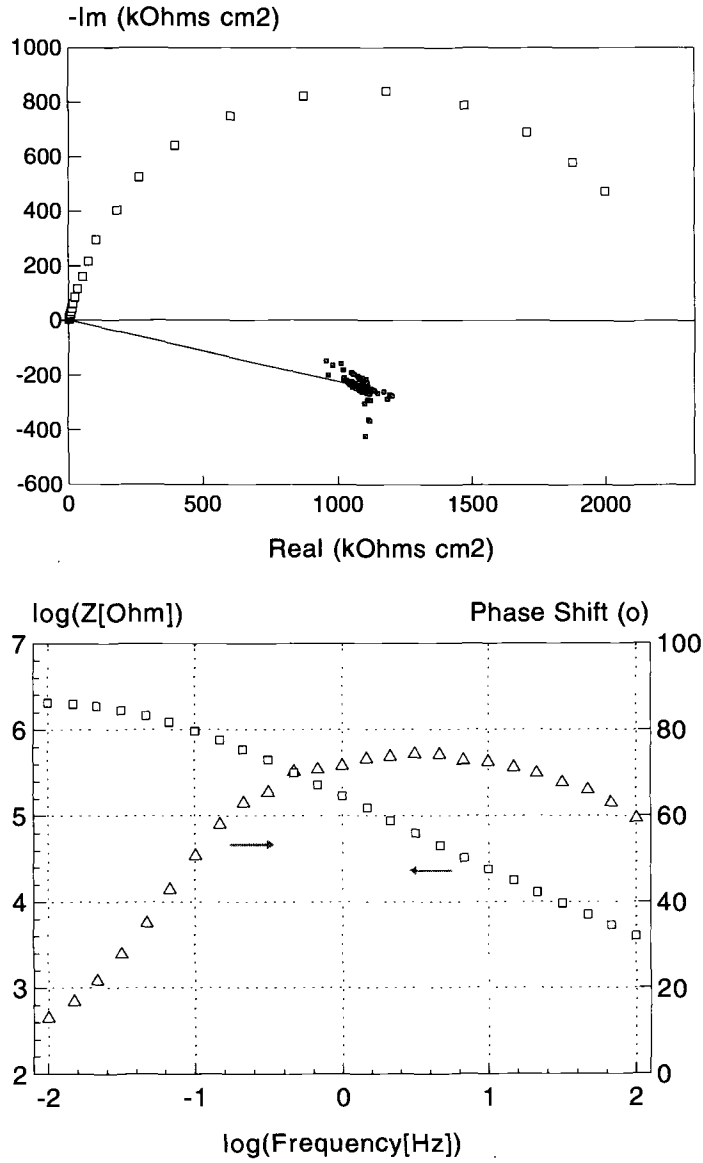

FIG. 9—*Typical EIS results obtained with an anodized and sealed (tap water, pH 4.5) panel during the sixth day of test in the electrochemical cell:* (a) *Nyquist plot and projected centers obtained with the permutation analysis technique* [13, 14], (b) *Bode representation of the same results.*

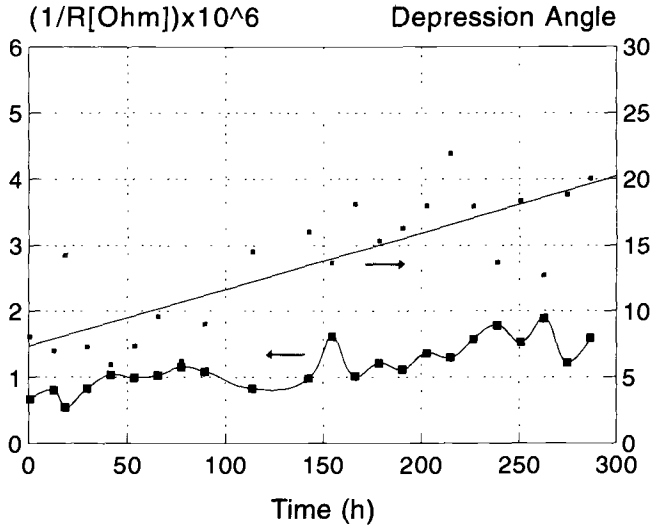

FIG. 10—*Continuous plot of depression angle and corrosion rate (1/*R*) obtained by analyzing EIS measurements with an anodized but* not *sealed aluminum panel.*

sand times faster than classical salt spray exposure and be included in the routine daily operation of a plant. Additionally, the sensitivity of the electrochemical testing techniques to intermediate surface conditions means these techniques could be used to reveal trends in the anodizing chemistry and to fine-tune the process.

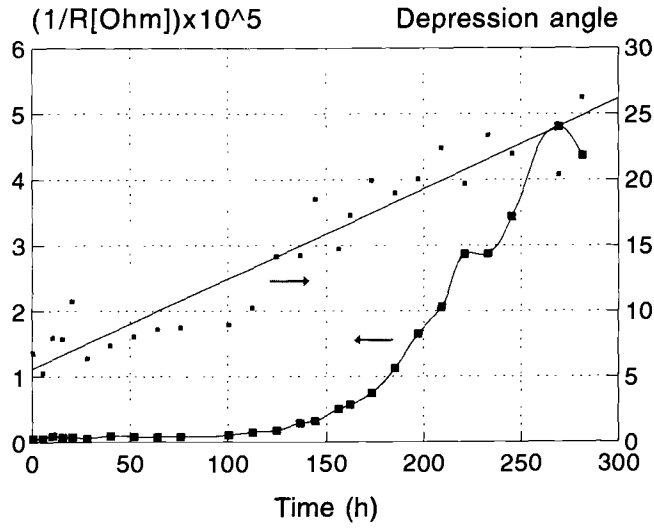

FIG. 11—*Continuous plot of depression angle and corrosion rate (1/*R*) obtained by analyzing EIS measurements made with an anodized* and *sealed aluminum panel.*

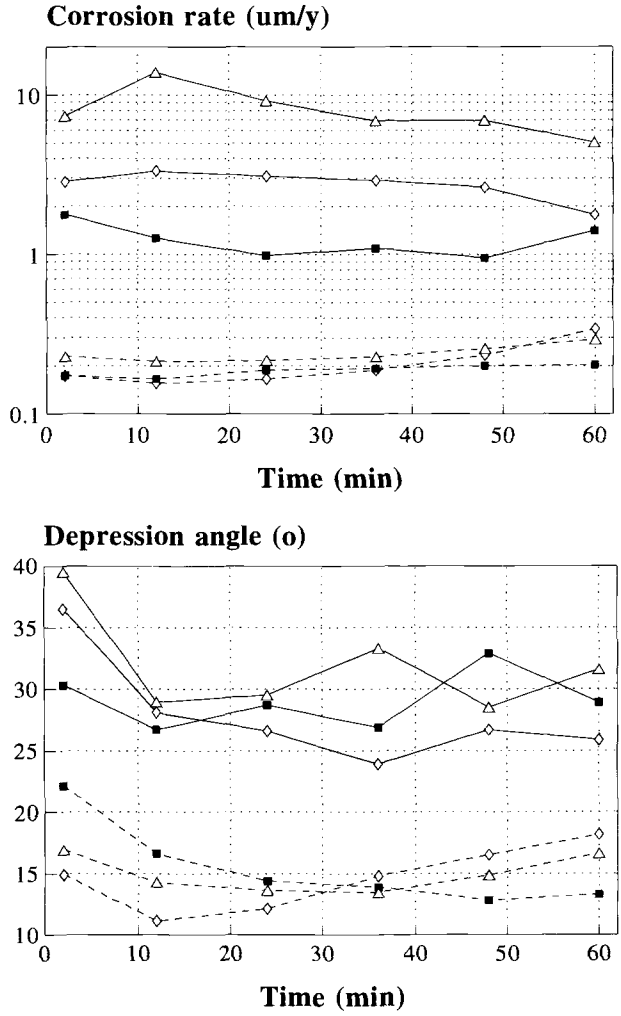

FIG. 12—*Analyzed results of EIS measurements made on two sets of panels (---- sealed in deionized water [corrosion rate = 0.1 μm/y by potentiodynamic measurement] and —— sealed in tap water [corrosion rate = 20 μm/y by potentiodynamic measurement]) after an activation of +600 mV (versus SCE) for 6 (■), 7 (◇) and 8 (△) min:* (a) *calculated EIS corrosion rates,* (b) *calculated depression angles.*

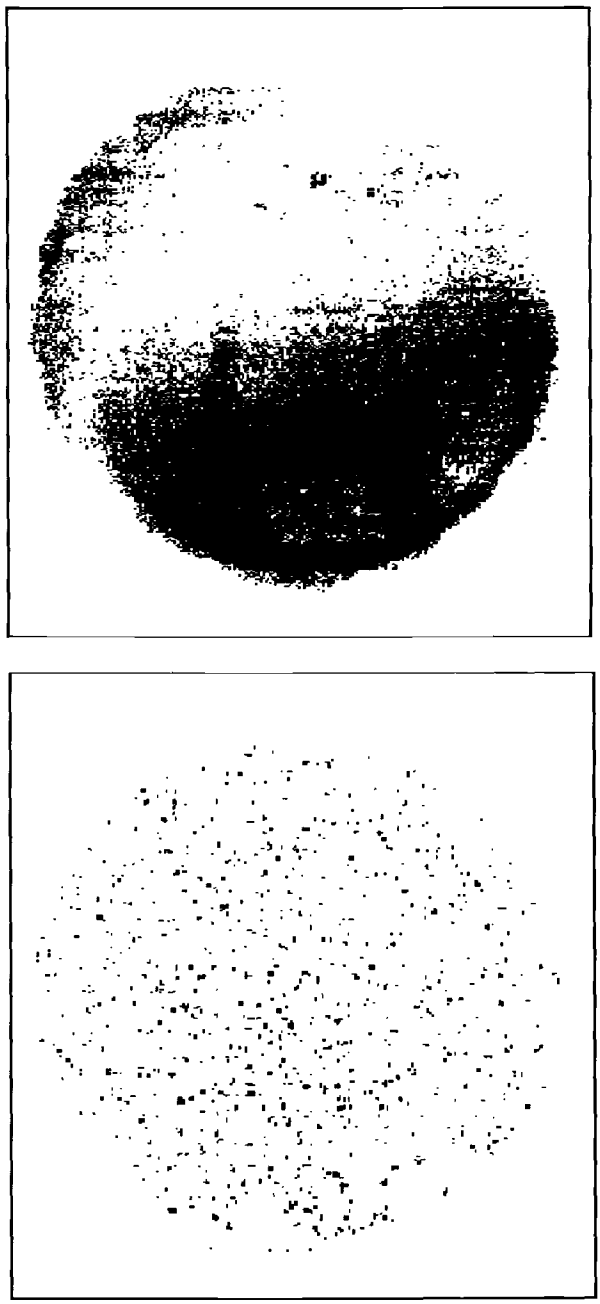

FIG. 13—*Scanned images of anodized but* not *sealed test panels after* (a) *30 min of the potentiodynamic procedure and* (b) *12 days of EIS measurements.*

References

[1] MIL-A-8625C, Military Specification, Anodic Coatings, For Aluminum and Aluminum Alloys, 1969.

[2] Yousri, S. and Tempel, P., *Plating and Surface Finishing*, Vol. 74, No. 11, 1987, pp. 36–43.

[3] Van Orden, A. C., *CORROSION/91*, Paper 140, National Association of Corrosion Engineers, Houston, TX, 1991.

[4] Greene, N. D. and Gandhi, R. H., *Materials Performance*, Vol. 21, No. 7, 1982, p. 34.

[5] Pye, E., "POL-PLOT Software for Electrochemical Testing," *Computers in Corrosion Control, Vol 2*, A. C. Van Orden and R. Erban, Eds., National Association of Corrosion Engineers, Houston, TX, in press.

[6] Mansfeld, F., "The Polarization Resistance Technique for Measuring Corrosion Currents," *Advances in Corrosion Science and Technology Vol. 6*, M. G. Fontana and R. W. Staehle, Eds., Plenum Press, New York, 1976, p. 163.

[7] Stern, M., *Corrosion*, Vol. 14, No. 9, 1958, pp. 440–444.

[8] Stern, M. and Geary, A. L., *Journal of the Electrochemical Society*, Vol. 104, 1957, pp. 56–63.

[9] "Softcorr Corrosion Measurement Software," EG&G, Princeton, NJ, 1986.

[10] Zeller III, R. L. and Savinell, R. F., *Corrosion Science*, Vol. 26, No. 8, 1986, pp. 591–599.

[11] Epelboin, I., Keddam, M., and Takenouti, H., *Journal of Applied Electrochemistry*, Vol. 2, 1972, pp. 71–79.

[12] Silverman, D. C., "Simple Models/Practical Answers Using the Electrochemical Impedance Technique," *Corrosion Testing and Evaluation: Silver Anniversary Volume, ASTM STP 1000*, R. Baboian and S. W. Dean, Eds., American Society for Testing and Materials, Philadelphia, 1990, pp. 379–395.

[13] Roberge, P. R. and Beaudoin, R., *Journal of Applied Electrochemistry*, Vol. 18, 1988, pp. 38–42.

[14] Roberge, P. R., "Analyzing Electrochemical Impedance Corrosion Measurements by the Systematic Permutation of Data Points," *Computer Modeling in Corrosion, ASTM STP 1154*, R. S. Munn, Ed., American Society for Testing and Materials, Philadelphia, 1992, pp. 197–211.

[15] Mansfeld, F. and Kendig, M. W., *Journal of the Electrochemical Society*, Vol. 135, No. 4, 1988, pp. 828–833.

[16] Grauer, R., Moreland, P. J., and Pini, G., "A Literature Review of Polarisation Resistance Constant (B) Values for the Measurement of Corrosion Rate," National Association of Corrosion Engineers, Houston, TX, 1982.

[17] Roberge, P. R. and Sosin, K. A., "Corrosion Cost and Risk Analysis: Coping with Uncertainty," *Proceedings, International Symposium on Materials Performance Maintenance*, 30th Annual Conference of Metallurgists, August 18–21, 1991, Ottawa, Canada.

[18] Hoar, J. P. and Wood, G. C., *Electrochimica Acta*, Vol. 7, 1962, p. 333.

[19] Hitzig, J., Juttner, K., Lorenz, W. J., and Paatsh, W., *Corrosion Science*, Vol. 24, 1984, p. 945.

[20] Hitzig, H., Juttner, K., Lorenz, W. J., and Paatsch, W., *Journal of the Electrochemical Society*, Vol. 133, 1986, p. 887.

[21] Mansfeld, F. and Kendig, M. W., *Corrosion*, Vol. 41, No. 8, 1985, pp. 490–492.

Gayle R. T. Schueller[1] *and S. Ray Taylor*[2]

Equivalent Circuit Modeling of Aluminum/ Polymer Laminates Using Electrochemical Impedance Spectroscopy

REFERENCE: Schueller, G. R. T. and Taylor, S. R., **"Equivalent Circuit Modeling of Aluminum/Polymer Laminates Using Electrochemical Impedance Spectroscopy,"** *Electrochemical Impedance: Analysis and Interpretation, ASTM STP 1188,* J. R. Scully, D. C. Silverman, and M. W. Kendig, Eds., American Society for Testing and Materials, Philadelphia, 1993, pp. 328–343.

ABSTRACT: The electrochemical impedance response of crevice geometries in aluminum polymer structures is investigated using transmission line circuitry in an approach similar to porous electrode impedance analysis. An equivalent circuit is proposed for edge-exposed rectangular defects in aluminum components such as laminates, and its impedance response is calculated as a function of defect dimensions, solution resistivity, and exposed planar surface area. Model laminates were constructed with known rectangular defect dimensions and their measured impedance spectra provided experimental verification of the predicted trends.

KEYWORDS: adhesive bond, aluminum, impedance, laminates, modeling, transmission line theory

Many applications of aluminum, from adhesively bonded structures to metal/polymer laminates used in food and drug packaging, depend on the integrity of an aluminum/polymer bond. Since failure of such components often initiates from pre-existing debonded regions [*1–10*], it is desirable to develop a method that can detect such flaws. The objective of this research is to employ equivalent circuit modeling based on porous electrode theory to quantify the geometry of debonded regions of aluminum polymer laminates from impedance spectra obtained by edge-on examination.

The most easily conceived and commonly used methods for adhesive bond evaluation are mechanical tests that determine the weakest link in a bonded specimen under specific environmental, geometric, and loading conditions [*11–14*]. These tests do not always provide accurate representation of practical failure conditions, and since they assess adhesive bond quality by destructive means, they cannot offer failure prediction for in-service components.

Liquid penetrant [*15–18*] and magnetic particle [*17,18*] testing methods are portable, relatively inexpensive, and often employed for detecting crevices associated with delamination. These methods allow evaluation of defect width and thickness, but provide no information about the debonded depth unless destructive methods are employed to expose dye ingress in the defect plane. Since these techniques rely on electrolyte ingress,

[1]Senior research engineer, 3M Company, Information, Imaging and Electronic Sector Laboratory, 3M Austin Center, Austin, TX 78726-9000.

[2]Research assistant professor, Center for Electrochemical Science and Engineering, Department of Materials Science and Engineering, University of Virginia, Charlottesville, VA 22903.

they are restricted to detection of edge-exposed defects and risk defect masking if the specimen surface has been treated. An additional limitation of magnetic particle testing is its restriction to ferromagnetic materials, thus excluding aluminum.

Ultrasonic [*17–20*], holographic [*17,18*], and radiographic [*17,18,21*] testing methods are independent of specimen magnetic properties, capable of detecting internal defects, and can be extremely sensitive; however, their sensitivity depends strongly on specimen orientation, trained inspectors, and relatively expensive, nonportable equipment. Of these methods, ultrasonic inspection is the least affected by the limitations described and the most commonly employed for evaluation of adhesive bonds. Ultrasonic testing can accurately assess debondment in single adhesive bonds, providing the sensor is perpendicular to the defect plane; however, this detection is significantly compromised in multilayered specimens and when the sensor cannot be aligned appropriately.

Each defect detection technique has strengths and weaknesses, and a complete, accurate analysis of the integrity of adhesive bonds or laminate structures can only be assured by using multiple methods. Electrochemical impedance spectroscopy (EIS) is proposed as a nondestructive evaluation method for use in conjunction with present techniques. The theory is sufficiently general to apply to any system with constricted defect geometries, providing the defect is edge-exposed and an electrically conductive surface is exposed within the flaw. As a technique still under investigation, exact detection limits are not yet determined. It is clear, however, that the external surface area exposed boldly to electrolyte, the surface condition of the electrode, and the test solution resistivity are extremely important to these investigations. Like liquid penetrant inspection, this method requires solution ingress into the defect, but unlike liquid penetrant inspection, it will be demonstrated that impedance provides information about defect dimensions beyond the exposed surface.

Theoretical Development

Evaluation of adhesive bonds by EIS assumes that moisture ingress into an edge-exposed defect at the metal/polymer interface results in an electrolyte-filled crevice whose apparent impedance response is described by transmission line circuitry and can be evaluated within the overall impedance response. For a perfectly bonded specimen, the laminate edge appears electrochemically as a planar surface whose area is equal to the area of metal exposed. Figure 1 illustrates a system where moisture has ingressed into the defective region of a bond. The constricted defect geometry results in potential and current distributions different from planar specimens, and it is proposed that these altered distributions give rise to significant differences between the impedance response of defective laminate specimens and perfectly bonded ones. Previous investigations of the imped-

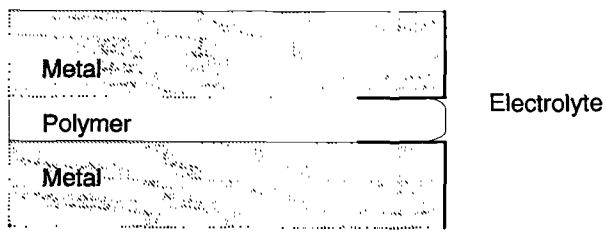

FIG. 1—*Schematic illustration of moisture ingress into an edge-exposed defect.*

ance response of constricted electrochemical systems have ranged from corrosion studies to battery and fuel cell research [*22–28*].

Porous Electrode Theory

Background—DeLevie's derivation of the porous electrode impedance response assumes an electrode dominated by essentially circular, cylindrical pores of uniform diameter and infinite depth with sufficiently high pore density to neglect the external surface [*29–32*]. Assuming negligible electrode impedance and homogeneous electrolyte in the pores, the impedance per unit length, dx, inside a pore was modeled by the circuit in Fig. 2 [*29*] where the incremental solution resistance, $R\ dx$, and surface impedance, $Z/(dx)$, are defined as

$$R\ dx = dR_s = \frac{\rho_s\ dx}{\pi r^2} \quad \text{and} \quad \frac{Z}{dx} = dZ = \frac{Z_p}{2\pi r\ dx} \tag{1}$$

Here, r is the pore radius, ρ_s is the solution resistivity, dR_s is the incremental solution resistance in the pore, and Z_p is the impedance per unit area of the electrode material in a planar configuration at the frequency in question. Employing this model, the incremental change in potential, de, and current, di, were derived, then subjected to the boundary conditions for a porous electrode under an applied ac potential to determine the apparent pore impedance at the specimen surface ($x = 0$) [*30*]

$$Z_a = \frac{e(0)}{i(0)} = \sqrt{Z_p R} = R^{1/2}|Z_p|^{1/2}e^{1/2(i\varphi_p)} = |Z_a|e^{i\varphi_a} \tag{2}$$

Thus,

$$|Z_a| = R^{1/2}|Z_p|^{1/2} \quad \text{and} \quad \varphi_a = 1/2_{\varphi_p} \tag{3}$$

where Z_a is the apparent pore impedance at a given frequency, R is the solution resistance per unit pore length, Z_p is the impedance per unit area of planar surface, φ_a is the phase angle of the pore impedance, and φ_p is the phase angle of the planar specimen impedance. The shift in the electrode impedance in porous electrodes will be referred to as the

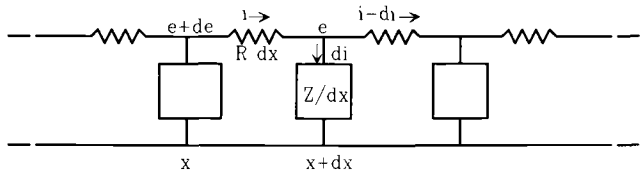

FIG. 2—*Equivalent circuit for an incremental length of an electrolyte-filled pore.*

"squaring" effect whereby: (1) the magnitude of the impedance of a porous electrode is equal to the square root of the impedance of the planar electrode multiplied by proportionality constant $R^{1/2}$; and (2) the phase angle of the impedance of a porous electrode is one half that of the planar electrode. A schematic of this behavior is shown in Fig. 3 [*30*].

One way to assess pore depth is to consider the "penetration depth," λ, for a given frequency of applied signal. DeLevie defines the penetration depth as [*30*]

$$\lambda \equiv \frac{\sqrt{|Z_p(\omega)|R}}{R\cos[1/2\varphi(\omega)]} \tag{4}$$

For semi-infinite pores, defined as pores with depths, d, greater than three times the penetration depth ($d \geq 3\lambda$), the impedance of the pore bottom can be neglected, and the apparent pore impedance is given by Eq 2. For more shallow pores, effects of signal penetration to the base of the pore must be considered. If the boundary conditions are adjusted, the apparent impedance of shallow pores ($d < 3\lambda$) can be defined by [*30*]

$$Z_a = \sqrt{Z_p R}\,\text{cotanh}\,\frac{Rd}{\sqrt{Z_p R}} \tag{5}$$

The cotanh term approaches unity as d increases, thus reducing this general form to that of a semi-infinite pore and providing continuity between shallow and semi-infinite behavior. For pore depths less than 3λ, the apparent pore impedance increases with decreasing pore depth. Since impedances in parallel are dominated by the smallest value, the total low-frequency impedance of a specimen containing both deep ($d \geq 3\lambda$) and shallow ($d < 3\lambda$) pores is dominated by the former. Electrodes with a number of intermediate depth pores

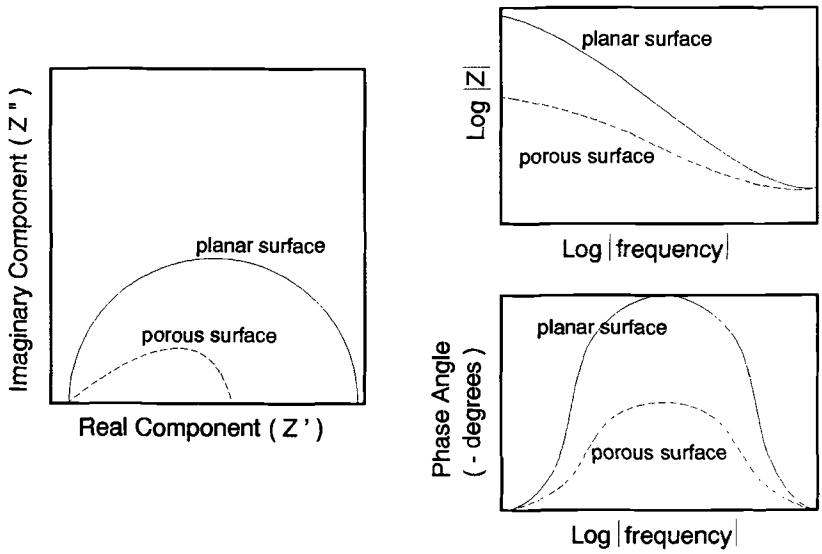

FIG. 3—*Comparison of the impedance responses of an electrode material in planar and porous configurations.*

exhibit "porous" behavior at high frequency and "planar" behavior at low frequency. The transition frequency between the two types of impedance responses is called the "critical frequency" and can be obtained from the impedance spectrum and related physical parameters such as the average pore depth and radius [*22,23*]. Factors such as a distribution of pore sizes and a nonnegligible external surface may be accounted for by vector addition of the impedances of the different sized pores and flat external surface at each frequency.

Adaptation of Porous Electrode Theory to Crevice Geometries—Porous electrode impedance theory was adapted for analysis of the crevice geometries associated with adhesive failure of laminate structures and metal/polymer bonds by assuming defects to be rectangular parallelepipeds with dimensions d, w, and t, as shown in Fig. 4. The circuit model proposed for electrolyte-filled defects in laminates is similar to Fig. 2, except in this case, dZ and dR_s, defined as the surface impedance and solution resistance per unit depth of defect, are calculated by the equations

$$R\,dx = dR_s = \frac{\rho_s\,dx}{wt} \quad \text{and} \quad \frac{Z}{dx} = dZ = \frac{Z_p}{w\,dx} \tag{6}$$

Most assumptions involved in this model are the same as those in the porous electrode model. Specifically, a simple constricted geometry is assumed in both models and the circuit components corresponding to the incremental surface impedance and solution resistance are assumed constant through the defect depth and directly calculable from bulk values.

Experimental Methods

The development of the impedance response of a crevice geometry has been confined thus far to the general case of a planar impedance, $Z(\omega)$, thereby allowing application of this model to any system with a known planar impedance response. For the present investigation of aluminum structures, the impedance response of planar aluminum must be incorporated in the model.

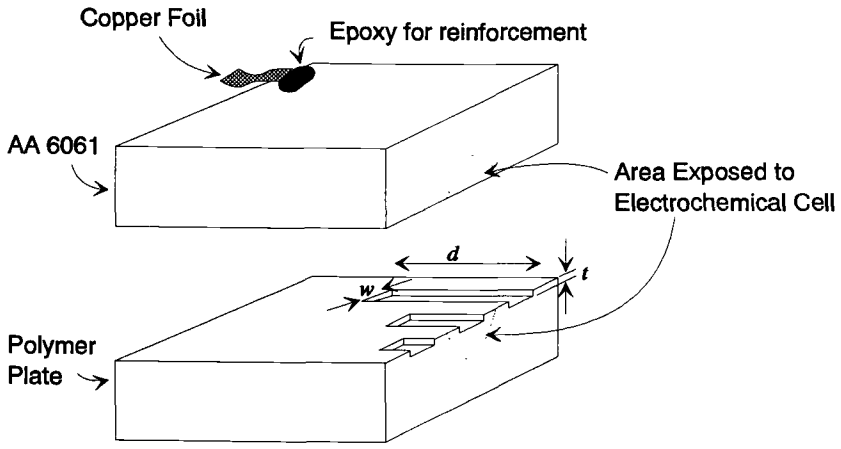

FIG. 4—*Schematic of simulated laminate specimens used for laminate modeling.*

Investigation of Planar Aluminum Specimens

The specimens used for flat sample investigation were typically high-purity aluminum (99.999%) polished to a mirror finish using Mastermet™ (Buehler) and degreased with hexane. These conditions were selected to obtain a baseline understanding of the impedance response of aluminum before introducing practical complications such as chemical heterogeneity caused by alloying elements and increased surface roughness, both of which can lead to a distribution of electrochemical time constants. Once these impedance spectra were documented, more realistic systems were investigated including aluminum alloys 1100, 6061, and 3003 with surface finishes ranging from Mastermet to 180 grit. While the more practical alloys and surface finishes resulted in impedance spectra with increased frequency dispersion, the general behavior was the same and one circuit model was deemed representative of all but the roughest surface finishes. Aluminum alloy 6061 was chosen as a representative alloy for the laminate investigations.

Investigation of Aluminum Laminate Specimens

As shown in Fig. 4, laminate specimens consisted of two 2 in. by 2 in. by 3/4 in. (5 cm by 5 cm by 2 cm) blocks, one of aluminum alloy 6061, and one of polymethylmethacrylate (PMMA), sandwiched together with a thin layer of silicone vacuum grease to provide a watertight seal. The aluminum blocks were polished to a 600 grit finish, spot-welded to copper foil for electrical connection, then degreased with hexane. The polymer blocks were polished to 600 grit on all sides, then machined on one of the large faces to create "defects" with known, rectangular dimensions. Typical defect dimensions were depths of 0.3 to 3 cm, widths of 0.4 to 1.0 cm, and thicknesses of 0.01 to 0.1 cm. A thin layer of silicone vacuum grease was applied to the "nondefective" region of the machined surface and the two blocks were then carefully pressed together to simulate a defective laminate of known defect dimensions.

Electrolyte

The electrolyte chosen for both planar and laminate studies was an aerated 0.1 molar solution of sodium borate ($Na_2B_4O_7$) buffered to pH 7 by addition of boric acid (H_3BO_4) to stabilize the oxide film. This particular solution was chosen for its nonaggressive effects on aluminum after long-term exposure [*33*]. In order to investigate the effects of various solution resistivities on defect detection, the $Na_2B_4O_7$ concentration was adjusted, but the pH was held constant in order to adjust the conductivity without compromising oxide stability.

Equipment

A Schlumberger 1250 frequency response analyzer and 1286 electrochemical interface were used to conduct impedance tests in the electrochemical cell shown schematically in Fig. 5. One endplate of the cylindrical cell contained a 1 cm^2 circular opening for the working electrode. A noncrevicing knife-edge Teflon® gasket was chosen for flat sample exposure; however, these gaskets leaked when used for laminate specimens, so nitrile o-rings were employed instead. The opposite endplate housed the counter electrode, a 6-cm^2 square of platinum clad niobium mesh. A saturated calomel reference electrode (SCE) was placed in a well having a Luggin capillary for accurate potential readings near the working electrode surface.

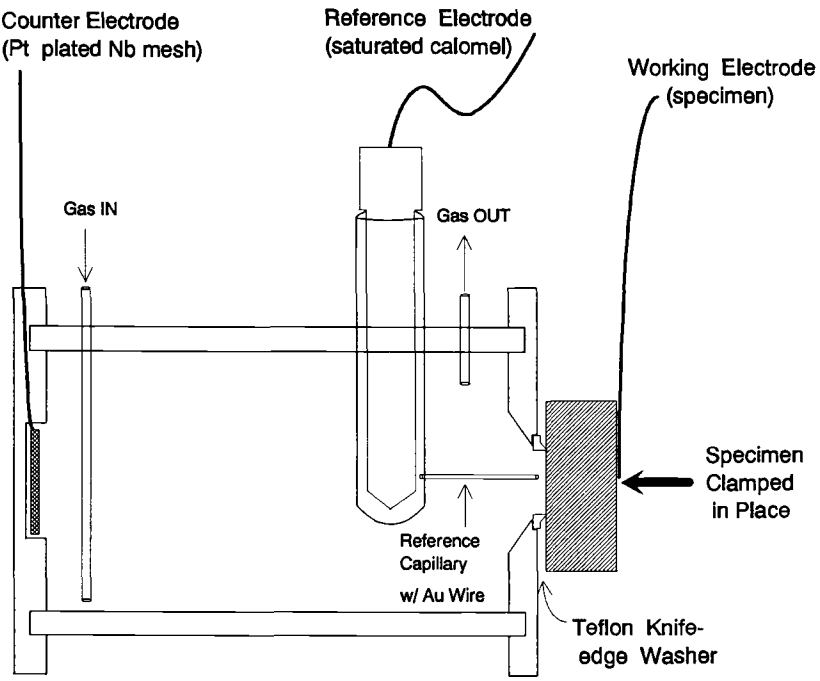

FIG. 5—*Flat sample electrochemical cell used in impedance experiments.*

Experimental Parameters

A dc potential of −0.60 V versus SCE with an applied ac signal of 10 to 20 mV rms was chosen for the impedance tests based upon results from polarization scans on various aluminum alloys. Data from potentiodynamic scanning experiments indicated that −0.6 V versus SCE was consistently within 100 mV of open circuit and resulted in currents below the sensitivity limit of available potentiostats (less than one nanoamp per square centimeter). The measured frequency range was typically between 65 kHz and 1 mHz. Some experiments were conducted outside this range; however, they provided additional information only in the case of extremely deep defects.

Experimental Results and Discussion

Planar Impedance Response of Aluminum

EIS has been employed to study aluminum in a variety of aqueous environments [*33–49*]. Figure 6 illustrates one of the more complete equivalent circuit models proposed for the aluminum/oxide/electrolyte interface. When using a nonaggressive borate electrolyte, this model can be simplified to the circuit model in Figure 7 [*33*]. Figure 8 compares the experimental impedance responses of 600 grit AA6061 and 99.999% aluminum with a Mastermet finish, both measured in aerated borate buffer, to the theoretical response of this circuit. While the spectra are quite similar, they are not in perfect agreement: the phase angle broadening and reduction in magnitude observed in the experimental spectra are commonly observed for solid electrodes. Possible explanations of this effect involve electrode inhomogeneities due to surface roughness, impurities, grain boundaries, and localized corrosion [*37,40–49*], however these effects are difficult to isolate and impossible

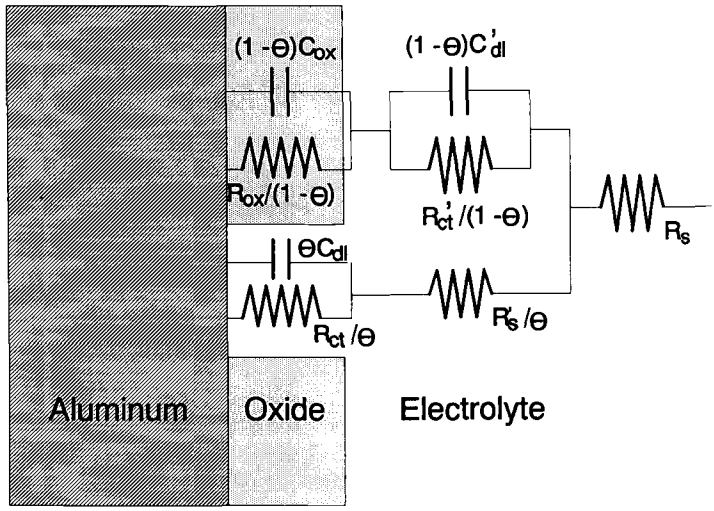

FIG. 6—*Circuit model for aluminum in electrolyte.*

to avoid in practice. Some investigators [*46,48*] insert additional circuit components such as the constant phase element to give experimental and theoretical data a better "fit." The physical interpretation of these additional components is not established and cannot be easily incorporated into the present modeling software. We have therefore not implemented such components at present, but are working on new software to accommodate these elements.

Incorporation of the Defect Geometry

The general circuit model for systems described by simple transmission line circuitry (Fig. 2) was applied to borate buffer exposed aluminum structures by replacing the general term, $Z(\omega)$, with the flat sample equivalent circuit model of this system (Fig. 7). The result

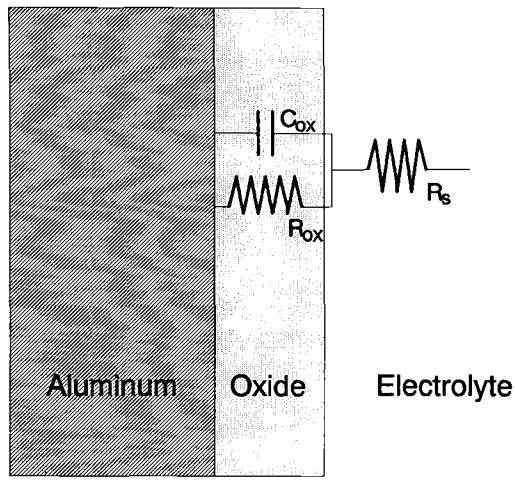

FIG. 7—*Simplified circuit model for aluminum in borate buffer.*

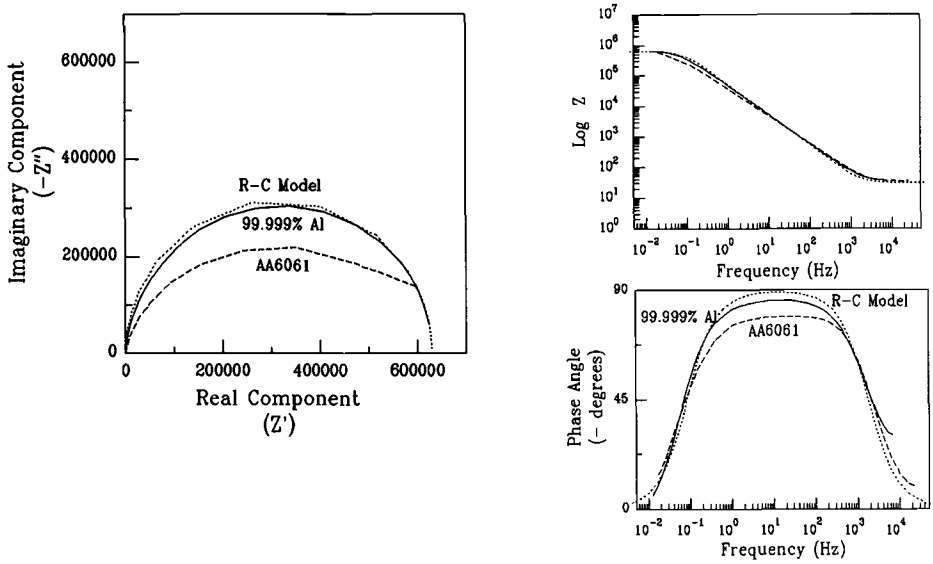

FIG. 8—*Comparison between experimental and theoretical data for planar aluminum specimens in borate buffer electrolyte.*

is the circuit depicted in Fig. 9. An incremental oxide resistance and capacitance are introduced to the model and are determined by

$$dR_{ox} = \frac{\rho_{ox} d_{ox}}{w\, dl} \quad \text{and} \quad dC_{ox} = \frac{\epsilon \kappa_{ox} w\, dl}{d_{ox}} \tag{7}$$

where ϵ is the permittivity of free space (8.85×10^{-12} F/m), w and dl are the defect width and incremental length (dl = (total defect depth)/(number of increments)), and d_{ox}, ρ_{ox}, and κ_{ox} are the oxide thickness, resistivity, and dielectric constant, respectively, determined from analysis of the flat sample impedance response [*33*].

The theoretical impedance response[3] of the circuit in Fig. 9 with defect dimensions w = 0.76 cm, d = 3.1 cm, t = 0.03 cm, and an exposed aluminum surface of 0.5 cm^2 is given by the solid line in Fig. 10. This combined impedance response includes the defect and boldly exposed surface, and can be understood by recognizing that the impedance associated with the defect (dashed line) is in parallel with the impedance of the exposed front surface (dotted line). Since current follows the path of least resistance, these spectra predict that the combined response would be described by the boldly exposed surface at high frequencies and the defect surface at low frequencies. All three plots indicate that the combined electrode impedance response is strikingly different from the flat sample impedance response. The magnitude response indicates two separate slopes as well as a distinct reduction in the low-frequency magnitude; the phase angle response reveals two phase angle peaks, compared to the single phase angle peak characteristic of planar samples; and the Nyquist plot indicates skewing in the combined spectrum. Both the impedance spectra of the defect with exposed planar surface and the defect alone exhibit critical transition frequencies. For the spectrum of the defect alone, this frequency marks the transition from

[3]Theoretical impedance data were generated using a *s*imulation *p*rogram for *i*ntegrated *c*ircuit *e*valuation called PSPICE Electrical Circuit Simulator Evaluation Version (January 1990). The production version is available from MicroSim Corporation, 20 Fairbanks, Irvine, CA 92718.

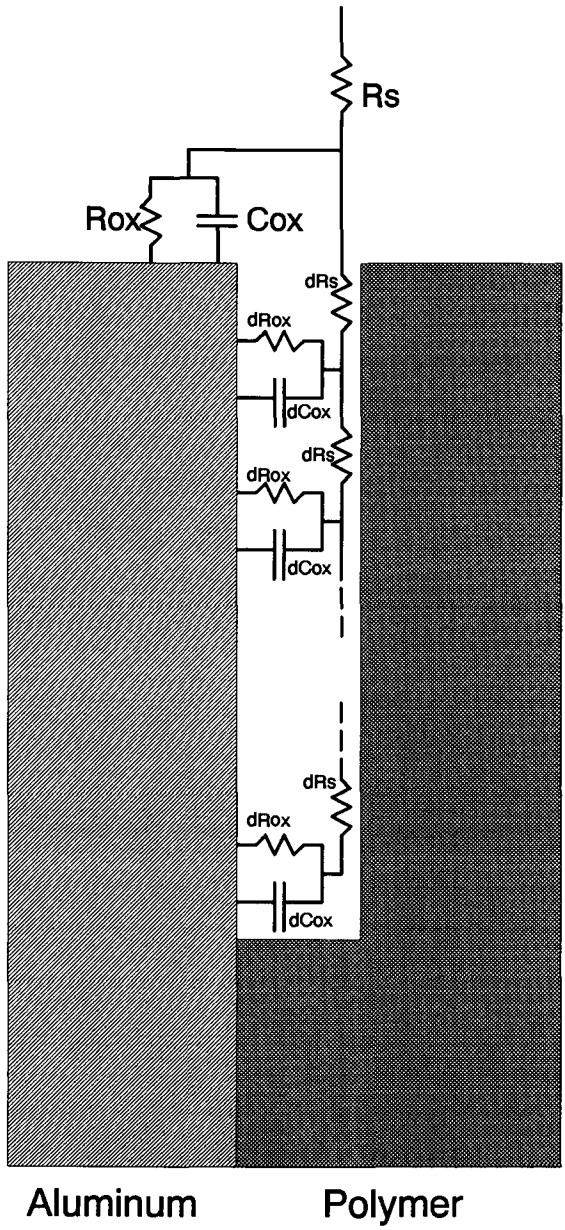

FIG. 9—*Equivalent circuit model for disbondment at an aluminum/polymer interface.*

high-frequency porous impedance behavior to lower-frequency planar behavior. For the defect with exposed planar surface, this frequency corresponds to the transition from the exposed planar surface response at high frequency to the defect response at low frequency. In both cases, the critical frequency depends on solution resistivity and defect dimensions [*22,23*]. The shifts in the impedance response of defective aluminum laminates (compared to planar specimens) demonstrate theoretical promise for the application of EIS

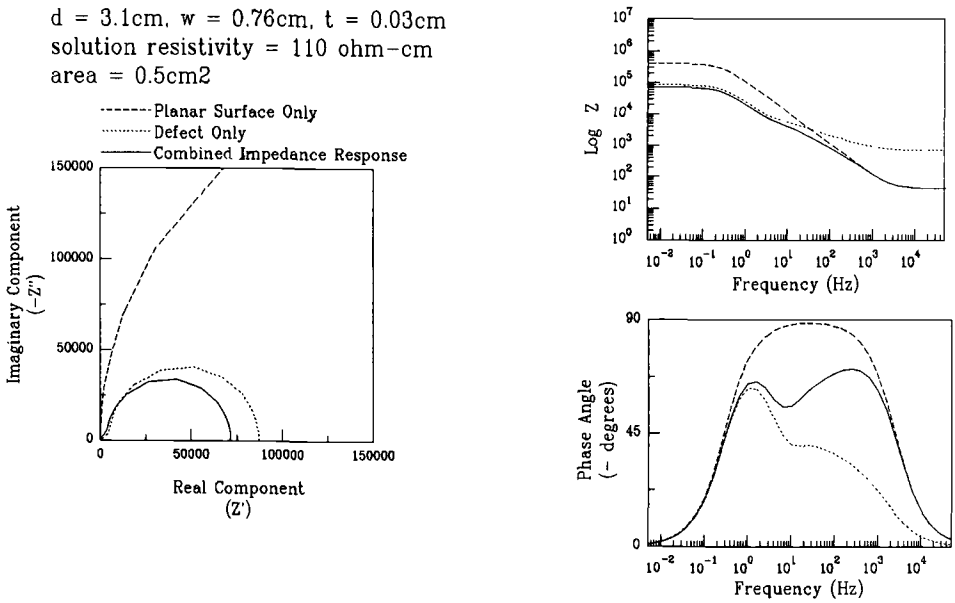

FIG. 10—*Theoretical impedance response of a laminate specimen illustrated in Fig. 4.*

as a crevice evaluation method. Given that the Bode plots illustrate the impedance shifts associated with this model more clearly than the Nyquist plots, subsequent data will be illustrated in the Bode format.

Impedance Trends Predicted by Variation of Physical Parameters

To assess practical defect evaluation by EIS, the theoretical capabilities and limitations must be determined. Towards this end, the impedance was calculated and experimentally verified with a range of physical parameters.

Boldly Exposed Area—A critical parameter in laminate investigations is the planar surface area of metal exposed at the surface. In porous electrodes, exposed planar surfaces are typically very small compared to interior pore surfaces and the front face is commonly neglected in impedance analyses. For adhesively bonded structures, boldly exposed surfaces can be similar in size to the surface exposed within a defect of catastrophic size, and such simplifications cannot be afforded. Figure 11 illustrates the calculated and experimental impedance for a range of exposed areas and their effect on the detectability of a 1.5 cm by 0.76 cm by 0.09 cm defect measured in a 110 Ω-cm solution. Under these conditions, all exposed surface areas evaluated allow distinction between the two phase angle peaks and clearly indicate the critical frequency between the high-frequency planar surface impedance response and the lower-frequency defect component. The key points are that the critical frequency does not change with the amount of planar area exposed and that areas significantly above 0.8 cm^2 allow poor distinction between the front area and defect responses even under ideal theoretical conditions. Experimentally, the area of exposed metal was controlled by shifting the specimen position relative to the cell opening. The corresponding impedance shifts reveal improved defect detection with decreased planar areas, as predicted by the model.

Solution Resistivity—Since solution resistivity is a controlled experimental parameter and not a value intrinsic to the defect, it is particularly important to understand its effects.

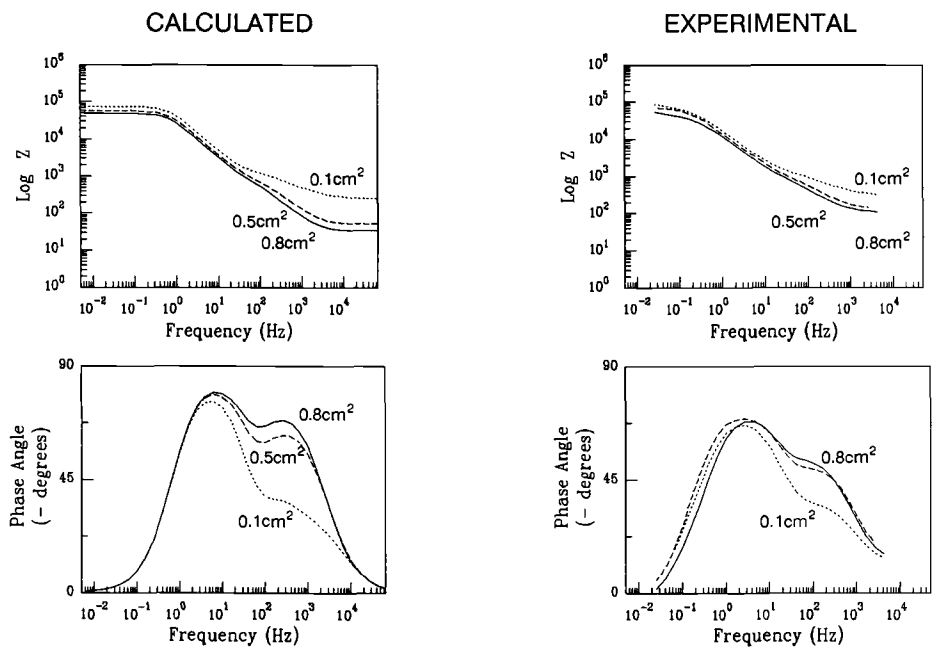

FIG. 11—*Theoretical and experimental impedance responses of a laminate specimen with various exposed planar surface areas.*

Figure 12 shows the calculated and experimental impedance response of a defect with d = 1.5 cm, w = 0.76 cm, and t = 0.09 cm, measured with a range of solution resistivities. The most obvious trend observed with variation in solution resistivity is the shift from complete defect penetration at low-solution resistivities (resulting in an almost completely planar impedance response), to porous electrode behavior at high resistivities. The porous behavior is evidenced in the impedance spectra by increased skewing of the Nyquist plot and a reduction of the width, magnitude, and frequency of the defect phase angle peak with increased solution resistance. The experimental impedance spectra confirm that increased solution conductivity increases the critical frequency and the magnitude and width of the phase angle peak associated with the defect impedance response.

Both calculated and experimental data emphasize that an appropriate solution resistivity is essential for good defect detection. If the solution resistivity is too high, the defect impedance signal may not be resolved from the low-frequency portion of the flat surface response. If it is too low, the current and potential distributions may not be sufficiently affected by the defect geometry to allow distinction from a flat sample response. The optimum solution resistivity for detection of a given defect is determined by its dimensions and the frequency range of the measuring equipment. In this example, the optimum solution resistivity is between 100 and 1000 Ω-cm.

Defect Depth—As the critical parameter in many failure analyses, there is great interest in the assessment of defect depth (defined by d in Fig. 4). Figure 13 illustrates the effect of defect depth on the calculated and experimental impedance response of three specimens in 110 Ω-cm electrolyte with defect widths and thicknesses of 0.76 cm and 0.09 cm, respectively, and depths ranging from 0.76 cm to 3.1 cm. As with solution resistivity. an optimum depth detectability range was observed. These data indicate that deeper defects shift the critical frequencies to lower values and decrease the low-frequency impedance limit. By appropriate choice of solution resistivity and minimization of the planar surface, shallow

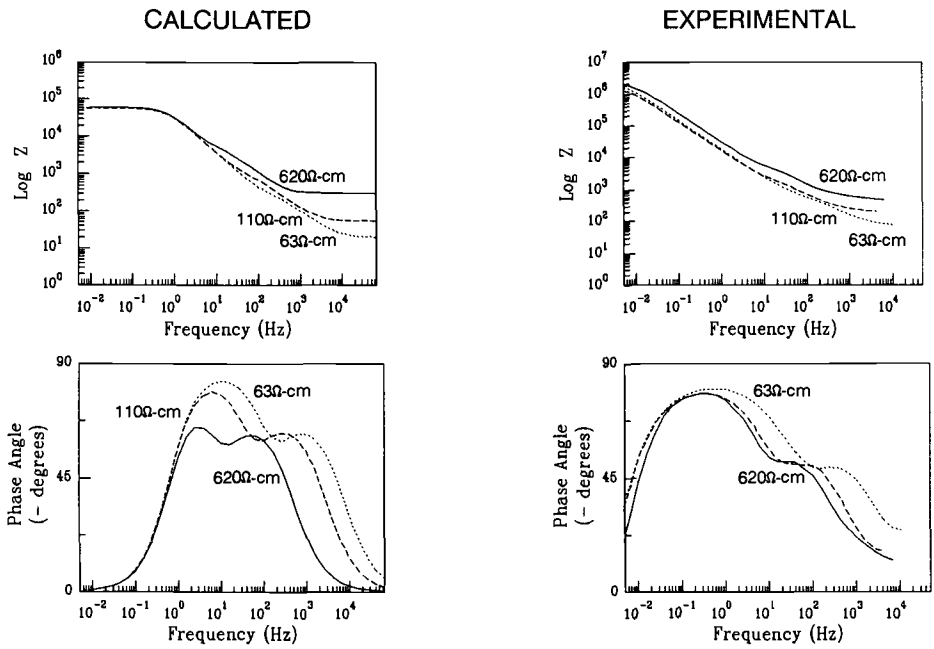

FIG. 12—*Calculated and experimental impedance responses of a laminate specimen evaluated in electrolytes with various solution conductivities.*

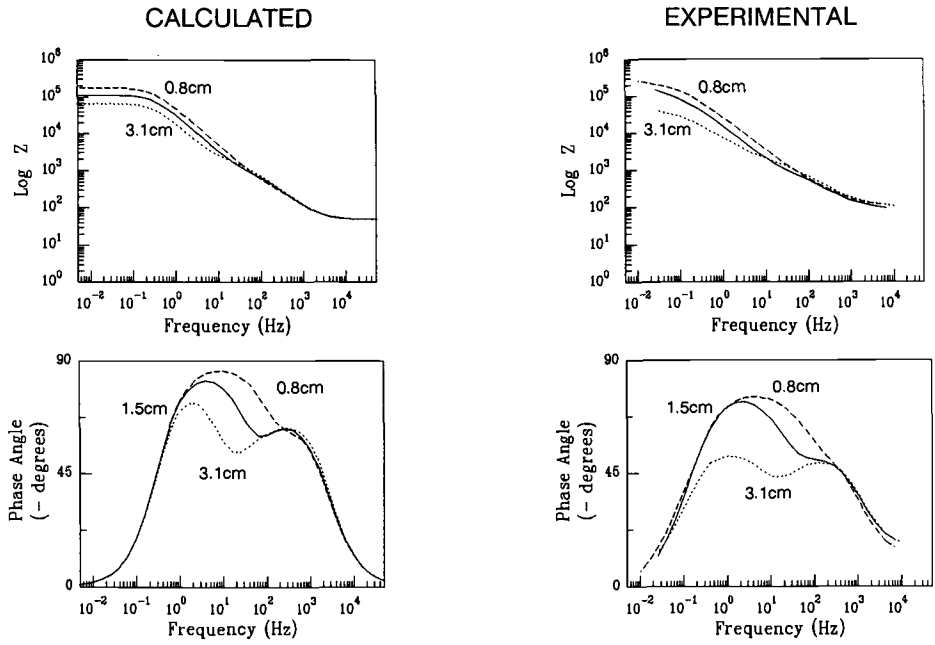

FIG. 13—*Calculated and experimental impedance spectra illustrating the effect of defect depth.*

defects or surface scratches are not confused with defects in the range of interest. Deeper defects translated to more constricted geometries, and resulted in impedance responses similar to porous electrodes with significant exposed planar surfaces. As with high-solution resistivities, deep defects risk being masked by the low-frequency portion of the flat sample impedance response. A decreased planar surface area or a different solution resistivity may be employed to assess defects whose dimensions are out of range.

Defect Thickness—Figure 14 shows the calculated and experimental impedance response as a function of defect thickness (defined by t in Fig. 4) for a defect 0.76 cm wide and 1.5 cm deep in a 110 Ω-cm solution. As with variations in solution resistance and defect depth, thickness differences also cause spectra to shift in frequency. These data confirm that tighter crevice geometries decrease the critical frequency and the low-frequency phase angle peak. As discussed previously, these effects can be compensated by selecting more conductive testing solutions and are most easily observed when the external area is minimized.

Conclusions

EIS has been shown to have theoretical promise for detection and evaluation of edge-exposed crevices including defects in aluminum/polymer laminates and adhesively bonded structures. Assuming rectangular defect geometries and uniform surface impedance and solution resistance within the defects, a circuit model has been proposed for creviced specimens based on the flat sample impedance response and physical parameters such as defect dimensions, solution resistivity, and boldly exposed electrode area. The impedance response of this circuit indicates that physical parameters directly affect the impedance response of a creviced specimen in predictable ways. This suggests the possibility of

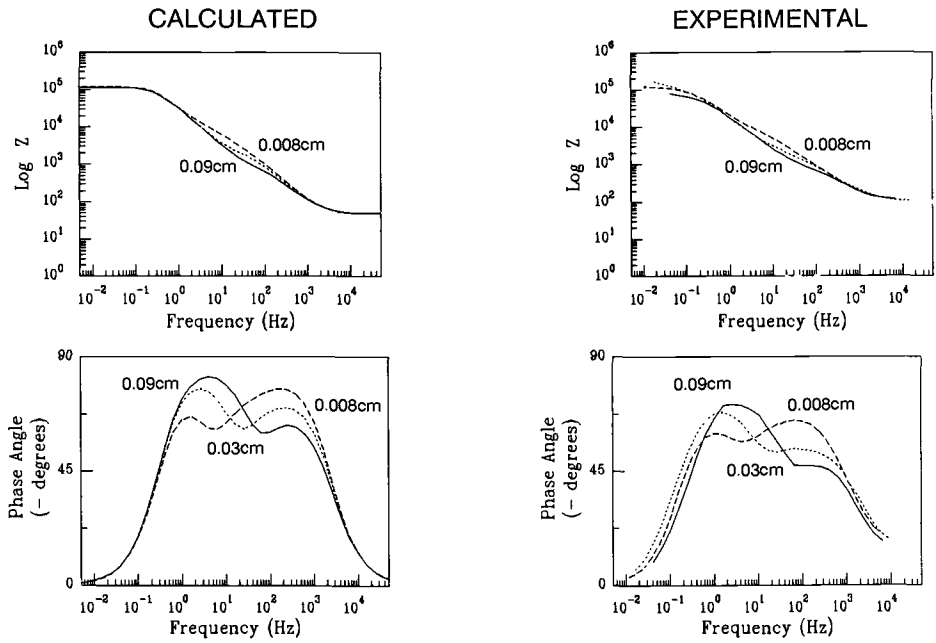

FIG. 14—*Theoretical and experimental spectra illustrating the effect of defect thickness variation on the overall impedance response of a machined laminate specimen.*

monitoring changes in defect geometry with time and even quantification of unknown defect geometries using impedance spectroscopy. Experimental studies on simulated aluminum laminates show that variations in physical parameters are detectable in specific shifts in the electrode impedance response and that impedance spectra can provide consistent indications of defect presence and relative size. The method and theoretical development indicate that any material whose flat sample impedance response is understood can be investigated in this manner, and that any penetrable crevice geometry could be detected and evaluated by the method, providing the appropriate testing solution resistivity is chosen and the planar metal surface is sufficiently small.

Acknowledgments

The authors gratefully acknowledge the support of this work by Alcan International, Limited and the Virginia Center for Innovative Technology.

References

[1] Chan, W. S., *Journal of Composites Technology and Research,* Vol. 16, No. 2, 1991, pp. 91–96.
[2] Donaldson, S. L., Mall, S., and Lingg, C., *Journal of Composites Technology and Research,* Vol. 13, No. 1, 1991, pp. 41–47.
[3] Ford, T., *Aircraft Engineering,* 1992, pp. 2–4, January.
[4] Gillespie, J. W. and Pipes, R. B., *Composite Structures,* Vol. 2, No. 1, 1984, pp. 46–49.
[5] Kachanov, L. M., *Polymer Mechanics,* Vol. 12, 1976, pp. 812–815.
[6] Sallam, S. and Simitses, G. J., *Composite Structures,* Vol. 4, 1985, pp. 361–381.
[7] Thompson, D. M., Griffin, O. H., Jr., and Vidussoni, M. A., *Journal of Composites Technology and Research,* Vol. 12, No. 4, 1990, pp. 209–216.
[8] Tiwari, A., Henneke, E. G., II, and Duke, J. C., *Journal of Adhesion,* Vol. 34, 1991, pp. 1–15.
[9] Witcomb, J. D., *Journal of Composites Technology and Research,* Vol. 13, No. 3, 1991, pp. 175–178.
[10] Zhou, S. G. and Sur, C. T., *Journal of Composites Technology and Research,* Vol. 12, No. 2, 1990, pp. 91–97.
[11] Baun, W. L., *Adhesive Joints: Formation, Characteristics, and Testing,* K. L. Mittal, Ed., Plenum Press, New York, 1982, pp. 3–16.
[12] Anderson, G. P., DeVries, K. L., and Sharon, G., *Adhesive Joints: Formation, Characteristics, and Testing,* K. L. Mittal, Ed., Plenum Press, New York, 1982, pp. 269–287.
[13] Romanko, J., Leichti, K. M., and Knauss, W. G., *Adhesive Joints: Formation, Characteristics, and Testing,* K. L. Mittal, Ed., Plenum Press, New York, 1982, pp. 567–86.
[14] *Adhesively Bonded Joints: Testing, Analysis, and Design, ASTM STP 981,* W. S. Johnson, Ed., American Society for Testing and Materials, Philadelphia, 1988.
[15] *Metals Handbook,* 8th ed., Vol. 2, H. E. Boyer, Ed., American Society for Metals, 1976, pp. 20–44.
[16] *Nondestructive Testing Handbook,* Vol. 2, R. McMaster, Ed., American Society for Nondestructive Testing, 1982.
[17] *Nondestructive Testing (Ultrasonic) Classroom Training Handbook,* General Dynamics, 1981.
[18] "Testing and Evaluation," *Material Evaluation,* December 1988, pp. 374–77.
[19] Rokhlin, S. I., *Adhesive Joints: Formation, Characteristics, and Testing,* K. L. Mittal, Ed., Plenum Press, New York, 1982, pp. 307–45.
[20] Lloyd, E. A. and Wadhwani, D. S., *Ultrasonic Materials Characterization,* National Bureau of Standards Special Technical Publication 596, H. Berger and M. Linzer, Eds., 1980.
[21] *Nondestructive Testing Handbook,*Vol. 3, P. McIntire, Ed., American Society for Nondestructive Testing, 1982.
[22] Armstrong, R. D. and Edmondson, K., *Journal of Electroanalytical Chemistry,* Vol. 63, 1975, pp. 287–302.
[23] Candy, J. P., Fouilloux, P., Keddam, M., and Takenouti, H., *Electrochimica Acta,* Vol. 26, No. 8, 1981, pp. 1029–1034.
[24] Lenhart, S. J., Chao, C. Y., and Macdonald, D. D., *Proceedings of the 16th Intersociety Conversion Engineering Conference,* August 9–14, 1981, pp. 663–666.
[25] Park, J. R. and Macdonald, D. D., *Corrosion Science,* Vol. 23, No. 4, 1983, pp. 295–315.
[26] Keddam, M., Rakotomavo, C., and Takenouti, H., *Journal of Applied Electrochemistry,* Vol. 14, 1984, pp. 437–448.

[27] Delnick, F. M., Jaeger, C. D., and Levy, S. C., *Chemical Engineering Communications*, Vol. 35, 1985, pp. 23–28.
[28] Marshall, S. L., *Journal of the Electrochemical Society*, Vol. 138, No. 4, 1991, pp. 1040–1047.
[29] DeLevie, R., *Electrochimica Acta*, Vol. 8, 1963, pp. 751–780.
[30] DeLevie, R., *Electrochimica Acta*, Vol. 9, 1964, pp. 1231–1245.
[31] DeLevie, R., *Electrochimica Acta*, Vol. 10, 1965, pp. 113–130.
[32] DeLevie, R., *Advances in Electrochemistry and Electrochemical Engineering*, Vol. 6, P. Delahay, Ed., Interscience Publishers, 1967, pp. 329–397.
[33] Schueller, G. R. T. and Taylor, S. R., "Evaluation of Natural Oxides on Aluminum in Neutral Borate Electrolyte," *The Journal of the Electrochemical Society*, Vol. 139, No. 10, 1992, pp. 2799–2805.
[34] Heine, M. A. and Pryor, M. J., *Journal of the Electrochemical Society*, Vol. 110, No. 12, 1963, pp. 1205–1214.
[35] Ikonopisov, S., Andreeva, L., and Vodenicharov, C., *Electrochimica Acta*, Vol. 15, 1970, pp. 421–429.
[36] Klein, I. E., Yaniv, A. E., and White, J. H., *Electrochimica Acta*, Vol. 17, 1972, pp. 2231–2237.
[37] Libsch, T. A. and Devereux, O. F., *Journal of the Electrochemical Society*, Vol. 121, No. 3, 1974, pp. 400–407.
[38] Mansfeld, F., Kendig, M. W., and Tsai, S., *Corrosion*, Vol. 38, No. 9, 1982, pp. 478–485.
[39] Bessone, J., Mayer, C., Juttner, K., and Lorenz, W. J., *Electrochimica Acta*, Vol. 28, No. 2, 1983, pp. 171–175.
[40] Bose, C. S. C. and Srinivasan, R., *Journal of Applied Electrochemistry*, Vol. 14, 1984, pp. 23–37.
[41] Hitzig, J., Juttner, K., Lorenz, W. J., and Paatsch, W., *Corrosion Science*, Vol. 24, No. 11/12, 1984, pp. 945–952.
[42] Hitzig, J., Juttner, K., Lorenz, W. J., and Paatsch, W., *Journal of the Electrochemical Society*, Vol. 133, No. 5, 1986, pp. 887–892,
[43] Barcia, O. E., Camara, J. L., and Mattos, O. R., *Journal of Applied Electrochemistry*, Vol. 17, 1987, pp. 641–647.
[44] Mansfeld, F. and Kendig, M. W., *Journal of the Electrochemical Society*, Vol. 135, No. 4, 1988, pp. 828–833.
[45] Mansfeld, F. and Shih, H., *Journal of the Electrochemical Society*, Vol. 135, No. 5, 1988, pp. 1171–1172.
[46] Juttner, K., Lorenz, W. J., and Paatsch, W., *Electrochimica Acta*, Vol. 29, No. 2/3, 1989, pp. 279–288.
[47] Shih, H. and Mansfeld, F., *Corrosion*, Vol. 45, No. 8, 1989, pp. 610–614.
[48] Fernandes, J. C. S., Ferreira, M. G. S., and Rangel, C. M., *Journal of Applied Electrochemistry*, Vol. 20, 1990, pp. 874–876.
[49] Scully, J. R., Peebles, D. E., Romig, A. D., Jr., Frear, D. R., and Hills, C. R., *Proceedings of the First International Symposium on the Corrosion of Electronic Materials and Devices*, J. D. Sinclair, Ed., The Electrochemical Society, Inc., 1991, pp. 14–21.

DISCUSSION

M. Kendig[1] *(written discussion)*—The existence of a characteristic frequency used by both the authors of this paper and the previous paper requires that the metallic surface be ideally polarized (passive in the case of this paper, noble in the case of the paper by Kelly and Newman). It must be pointed out that if a sufficiently rapid faradaic reaction occurs, then the impedance will not scale with surface area and the characteristic frequency related to complete signal penetration will not be observed.

G. R. T. Schueller and S. Ray Taylor (authors' closure)—It is the belief of the authors that low solution resistances (high electrolyte concentrations) can be used to evaluate metallic surfaces on which rapid faradaic reactions occur. (See section on solution resistivity.) This behavior has been sucessfully modeled by the methods described in this paper.

[1]Rockwell International Science Center, Thousand Oaks, CA 91360.

Corrosion of Steel in Soil and Concrete

Shirohi Sudo[1] *and Shiro Haruyama*[2]

Electrochemical Impedance of a Buried Large Structure

REFERENCE: Sudo, S. and Haruyama, S., "**Electrochemical Impedance of a Buried Large Structure,**" *Electrochemical Impedance: Analysis and Interpretation, ASTM STP 1188*, J. R. Scully, D. C. Silverman, and M. W. Kendig, Eds., American Society for Testing and Materials, Philadelphia, 1993, pp. 347–364.

ABSTRACT: The polarization resistance and electrochemical impedance for a two-electrode cell consisting of a buried metallic structure and a small nonpolarizable disk electrode has been discussed considering the distribution of the signal current. Since interfacial impedance decreases with increasing ac frequency, the electrochemical impedances at high and low frequencies correspond to those for the primary and secondary current distributions respectively. The complex plane plot of the electrochemical impedance of a buried structure measured with the probe exhibits a semicircle or semi-ellipse depending on the structure, the intercept of which is not proportional on the real axis to the polarization resistance. The impedance diagrams for a buried structure in the presence of local corrosion deviate from those in the absence of local corrosion below a certain frequency, which is determined by the distance between the local corrosion site and the probe electrode. This threshold frequency serves as a reliable tool for detecting the location of the local corrosion of a buried structure.

KEYWORDS: buried structure, polarization resistance, primary current distribution, secondary current distribution, corrosion monitoring, measuring area, local corrosion, distributed parameter system, electrochemical impedance

The electrochemical impedance method is finding increasing application in corrosion research, since the technique is one of the promising tools for obtaining mechanistic information as well as for monitoring the rate of corrosion. The correlation between the impedance and corrosion rate was first found experimentally by Epelboin et al. [*1*] and theoretically by Haruyama [*2*]. Based on the impedance theory, Haruyama and Tsuru [*3*] developed an automatic ac corrosion monitor that substantially measures the impedance data at two extreme frequencies. Although the corrosion monitoring based on electrochemical impedance has been successfully used in various service tests, there still remain many problems for understanding the impedance data, especially in much extended applications.

The corrosion of buried metallic structures, such as fuel tanks and pipelines, is becoming a serious problem around the world, and there is a plan for monitoring the uniform or local corrosion, or both, of the structures in service by measuring their polarization resistance or electrochemical impedance, or both. It is the electrochemical measurement of a two-electrode cell consisting of a large metallic structure and a probe electrode. The problems involved in this measurement are that the signal current is not uniform over the structure surface and the effective measuring area is not *a priori* known, being dependent

[1]Research manager, Electricity Technology Research and Development Center, Tohoku Electric Power Co., Inc., 7-2-1, Nakayama, Sendai, Miyagi 981, Japan.
[2]President, Tokyo National College of Technology, 1220-2, Kunugida, Hachioji, Tokyo 193, Japan.

on polarization resistance as well as frequency. It provides a problem on the impedance for a distributed parameter system. Corrosion of pipeline [*4–6*] was simulated by a cascade connection of finite simple electric circuits, but even the pipelines have not been strictly dealt with as a distributed parameter system.

The aim of this paper is to analyze the polarization resistance and the electrochemical impedance for the two-electrode cell consisting of a buried large metallic structure and a nonpolarizable disc electrode, considering the distribution of the signal current. The discussion is focused on the possibility of estimating the rate of uniform corrosion and the location of local corrosion sites on buried structures by the electrochemical impedance technique.

Polarization Resistance for a Buried Large Structure

Current Profile

The current profile (secondary current distribution) between a structure and a nonpolarizable probe electrode in a constant resistivity medium is obtained by solving the Laplace equation shown in Eq 1 with the boundary conditions regarding the geometry and configuration of the system and the electrochemical polarization at metal/electrolyte interface.

$$\nabla^2\phi = 0 \tag{1}$$

Analytical solution of Eq 1 is very complicated, even for a simple system, and the current profile is usually obtained by classical conformal mapping or modern finite element method. Since the boundary conditions of the present problem are relatively simple, the signal-current distribution is discussed in this paper by using the conformal mapping method that gives a relatively general solution.

The current profile between a large one- or two-dimensional object and a plate disk electrode of radius A is analyzed by the image method used in electromagnetism. Both the

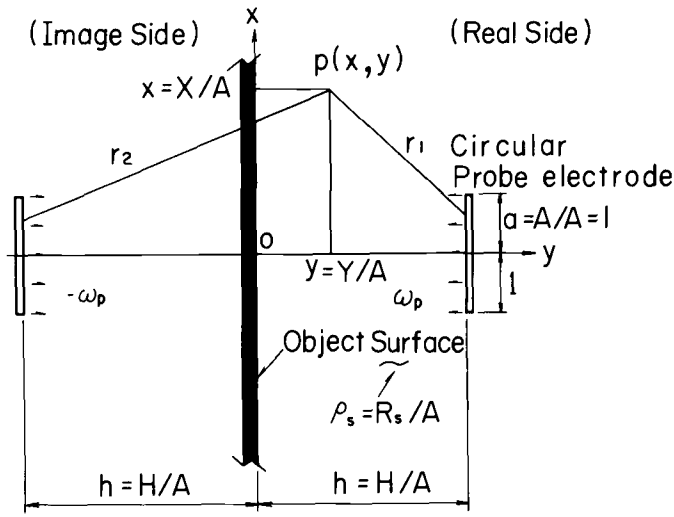

FIG. 1—*Image method for obtaining current profile.*

object and probe are assumed to be surrounded by a uniform electrolytic medium such as soil. Figure 1 shows the configuration for the image method on x-y coordinate, where H is the spacing between the two electrodes, ρ_s the specific resistance of the medium, and ω_p the signal-current density for both faces of the probe disk electrode. In order to generalize the discussion, all the parameters in this paper are normalized taking A as the unit, as summarized in Table 1. The assumptions and procedure for obtaining the current distribution at the object surface is as follows [7]: (1) In the absence of polarization, the potential v at $p(x,y)$ in Fig. 1 is obtained as the potential which is attributable to the sum of the respective currents from real and image probe electrodes, (2) The potential v' at $p(x,y)$ in the presence of polarization is assumed to be written as the sum $(u + v)$, where u is the potential attributed to the polarization and is written in a Fourier integral containing an unknown function $f(\lambda)$, (3) The potential $u_{y=0}$ due to low polarizations is proportional to the current density at the object surface, thus

$$u_{y=0} = \rho_c i(x) \tag{2}$$

where $i(x)$ represents a local current density and ρ_c, the polarization resistance, is known to be inversely proportional to the rate of corrosion [8,9] (it is assumed that the polarization resistance is uniform over the entire structure except otherwise noted), (4) The local current density $i(x)$ is written as

$$i(x) = i_{y=0}(x) = \frac{1}{\rho_s}\left|\frac{\partial v'}{\partial y}\right|_{y=0} \tag{3}$$

TABLE 1—*Symbols and definitions.*

Symbols				
Parameter	Unit	Normalized Parameter	Description	Relation
A	m	a	radius of probe	$a = A/A = 1$
H	m	h	gap between probe and structure	$h = X/A$
X	m	x	distance from probe center	$x = X/A$
W_p	A/m	ω_p	current density at probe	$\omega_p = W_p \cdot A^2$
$I(X)$	A/m	$i(x)$	current density at structure	$i = I \cdot A^2$
$V(X)$	V	$v(x)$	potential at structure	
R_s	Ω·m	ρ_s	specific resistance of medium	$\rho_s = R_s/A$
R_c	Ω·m^2	ρ_c	polarization resistance	$\rho_c = R_c/A^2$
		k	polarizability (ρ_c/ρ_s)	$k = R_c/R_s \cdot A$
C_{dl}	F/m^2	Γ_{dl}	double layer capacitance	$\Gamma_{dl} = C_{dl} \cdot A^2$

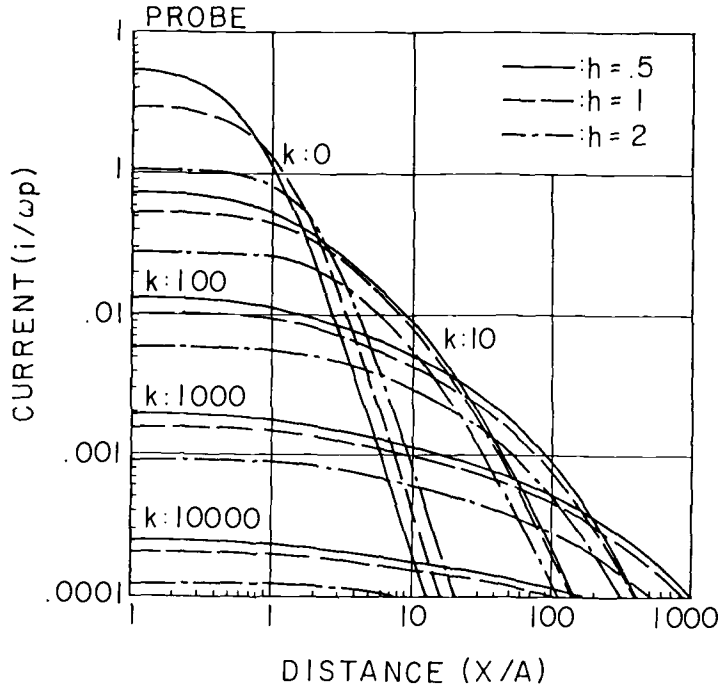

FIG. 2—*Distribution of signal current at object surface.*

After a conventional conformal mapping procedure [7], the current density on the object surface is expressed as

$$i(x) = \omega_p \Bigg[h((x^2 + h^2)^{-1/2} - (x^2 + h^2 + 1)^{-1/2}) - \frac{2hk}{\pi} \int_0^\infty \frac{\alpha \cos(\alpha x)}{1 + k\alpha} d\alpha \times \int_0^\infty ((\lambda^2 + h^2)^{-1/2} - (\lambda^2 + h^2 + 1)^{-1/2}) \cos(\alpha\lambda)\, d\alpha \Bigg] \tag{4}$$

where k represents the polarizability, ρ_c/ρ_s, and α and λ are the auxiliary parameters ($0 \sim \infty$) for the Fourier integral. The result of numerical calculation of Eq 4 is shown in Fig. 2, where the curves for $k = 0$ correspond to the current distribution in the absence of polarization (primary current distribution). It is seen in the figure that, with increasing polarization, the current profile becomes uniform over the object surface with the decrease of current density. This means that the effective measuring area for polarization measurement increases with increasing polarization resistance. The distance, where the current density decreases to the half value of the maximum current density, is named the nominal measuring distance x_m. On the current profile graph, the nominal measuring distance corresponds to the intercept of the current lines tangent to the probe surface at the structure surface.

Polarization Resistance

A similar analysis can be made for the probe electrode, the back face of which is sealed so as only the facing surface works as the electrode. From the results of the conformal

mapping analysis, it is found that the local current density on the object surface also obeys Eq 4 approximately in the case of the one-sided probe except in the vicinity of the nominal measuring distance, where the current decreases steeply to zero at x_m. This means that the effective distance for a polarization measurement is substantially limited to x_m in the case of the measurement by the one-sided probe electrode. As is expected from Fig. 2, the nominal measuring distance increases with increasing the polarization, as shown in Figs. 3 and 4 for two- and one-dimensional structures respectively.

Since the signal-current density on the object surface decreases with the distance from the probe electrode, the partial polarization resistance $R_c(x)$ apparently increases with the distance, although in fact it is originated from iR drop. Considering the linear current-potential relation, it is assumed that the apparent partial polarization resistance increases inversely proportional to the partial current density, thus

$$R_c(x) = \rho_c \frac{i(0)}{i(x)} = k\rho_s \frac{i(0)}{i(x)} = \frac{kR_s i(0)}{Ai(x)} \tag{5}$$

where the iR drop is assumed to be compensated at $x = 0$. Since the total polarization resistance measured, R_t, is the parallel combination of the infinite number of local polarization resistances over the surface, it is written as

$$R_t = \frac{R_c(0)}{\int_0^{x_m} i(x)\, ds} \tag{6}$$

where $R_c(0) = \rho_c = kR_s/A$, $ds = 2\pi x \cdot dx$ and $ds = 2w \cdot dx$ for two- and one-dimensional structures respectively, and w indicates the width of a long belt-like structure. The results of the numerical calculation of Eq 6 are also shown in Figs. 3 and 4 for two- and one-

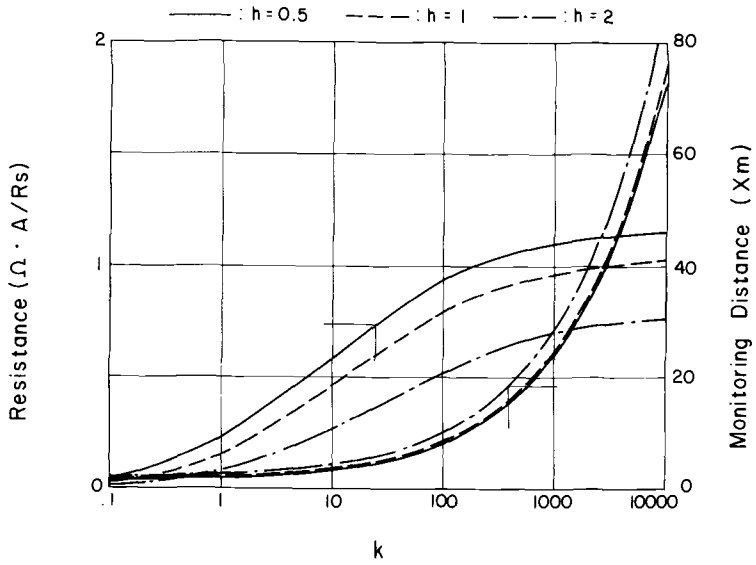

FIG. 3—*Dependency of apparent polarization resistance and nominal measuring distance on* k *value for a two-dimensional structure.*

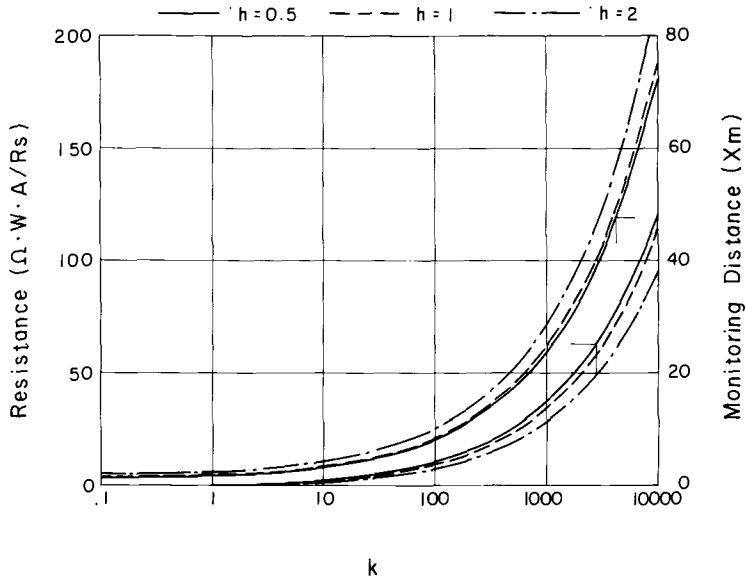

FIG. 4—*Dependency of apparent polarization resistance and nominal measuring distance on* k *value for a one-dimensional structure.*

dimensional structures respectively. Since an exact mathematical expression of $i(x)$ for a one-sided probe electrode is difficult to obtain, the calculation of Eq 6 was made using Eq 4 under the condition that $i(x) = 0$ at $x > x_m$.

Is is seen in Figs. 3 and 4 that, with increasing polarization, the nominal measuring area is greatly extended and the total polarization resistance increases, exhibiting a saturation for the two-dimensional structure. With the increase of the spacing H between the structure and the probe, the total polarization resistance decreases because of the increase in the nominal measuring area, as is also noted from the figures. It may be possible to limit the measuring area to the same size with the probe electrode by reducing the spacing, only when the polarization resistance is very low.

The (R_c/R_s) value (Eq 5) for buried steel structures is usually in the range between 10 and 1000 in service conditions, which corresponds to k values of 100 to 10 000 for a probe electrode 0.1 m in radius. Therefore, referring to Figs. 3 and 4, the nominal measuring distance is in the range of 1 to 10 m depending on the k value.

Although both $R_c(0)$ and $i(x)$ depend on the k value, it is possible to obtain the polarization resistance ρ_c ($=kR_sA$) from the measured R_t and R_s values by a trial and error procedure using Eqs 4 and 6. However, since the total polarization resistance is very low (especially for a two-dimensional structure because of a large measuring area), it is difficult to eliminate the contribution of the iR drop even at $x = 0$ in a service condition.

Electrochemical Impedance for a Buried Large Structure

It is well-known that the interfacial impedance decreases with increasing ac frequency because of the presence of the electrical double layer at interface. Therefore, it is likely that the decrease in frequency has the effect similar to the increase in polarization on the signal-current profile and nominal measuring area. Then, the impedance measurement of a

buried large structure is the measurement of an electrode, the surface area of which changes with frequency. It must be noted that the impedance at extreme high frequencies reduced to the medium resistance corresponding to the primary current distribution.

Electrochemical Impedance for Uniform Corrosion

Figure 5 shows schematically the arrangement and current profile for measuring the impedance of two- and one-dimensional structures buried in a medium of specific resistance R_s ($\rho_s = R_s/A$), where ω_p indicates the current density at the probe electrode. It is noted that the "current density" indicates that of an ac signal in the following discussion. (A scheme for a locally corroded structure is also drawn in Fig. 5 by the dotted lines, which will be discussed later.) The partial impedance at a point x on the object surface, $Z(x, j\omega)$, is represented by the equivalent circuit shown in Fig. 6 and written as

$$Z(x,j\omega) = Z_1(x) + Z_2(j\omega) \tag{7}$$

where ω represents the angular frequency, $Z_1(x)$ is the impedance determined by the medium resistance between the probe and the point x on the object, and $Z_2(j\omega)$ is the interfacial impedance, which is represented by parallel connection of the transfer resistance R_c and the double layer capacitance C. The transfer resistance is inversely proportional to the rate of corrosion [*1,2*]. The Warburg and the other complicated impedances are not considered.

Given that $j = (-1)^{1/2}$, $Z_2(j\omega)$ and $Z(x,j\omega)$ are written respectively as

$$\frac{1}{Z_2(j\omega)} = \frac{1}{R_c} + j\omega C \tag{8}$$

$$\frac{1}{Z(x,j\omega)} = RZ(x,\omega) + jIZ(x,\omega) \tag{9}$$

where

$$RZ(x,\omega) \equiv \frac{Z_1(x)[1 + \omega^2 R_c^2 C^2] + R_c}{[Z_1(x) + R_c]^2 + Z_1^2(x)\omega^2 R_c^2 C^2} \tag{10}$$

$$IZ(x,\omega) \equiv \frac{\omega R_c^2 C}{[Z_1(x) + R_c]^2 + Z_1^2(x)\omega^2 R_c^2 C^2} \tag{11}$$

The mathematical expression for $Z_1(x)$ in Eqs 10 and 11 is obtained by the following procedure. $Z_1(x)$ is given by applied voltage V divided by current density $J(x)$. Taking the center of the probe electrode as the origin of an angular coordinate r, Θ, the potential at a point distant t from a current source of infinitesimal area $2\pi r \cdot dr$ on the probe disk electrode is given by $(\rho_s \omega_p 2\pi r \cdot dr)/4\pi t$. Integrating over the entire disk surface, the potential at the object surface is written as

$$V(h) = -\frac{\rho_s \omega_p}{4\pi} \int_0^1 \frac{2\pi r\, dr}{(h^2 + r^2)^{1/2}} = -\frac{\rho_s \omega_p}{2} [(h^2 + 1)^{1/2} - h] \tag{12}$$

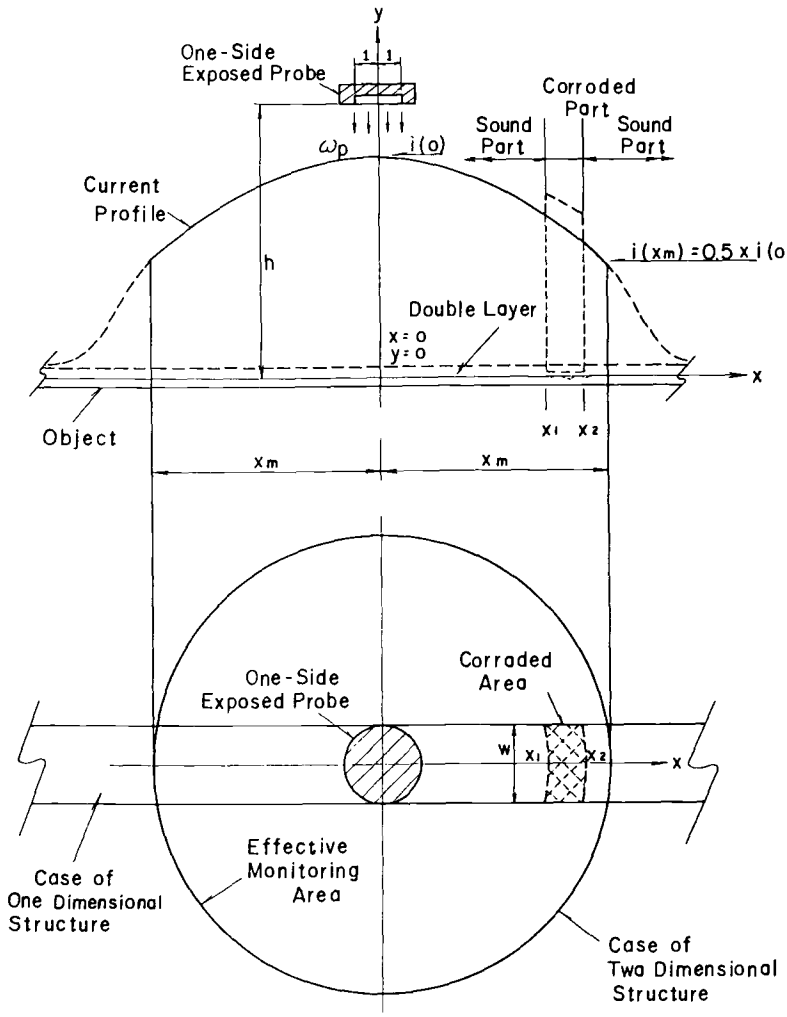

FIG. 5—*Schematic current profile between probe electrode and two- or one-dimensional structure, or both.*

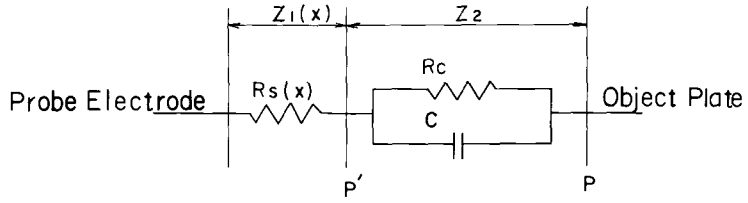

FIG. 6—*Equivalent circuit for partial impedance.*

The applied voltage is given by the difference in the potentials between the probe ($y = 0$) and the object ($y = h$) as

$$V = V(0) - V(h) = -\frac{\rho_s \omega_p}{2}[h + 1 - (h^2 + 1)^{1/2}] \tag{13}$$

Since the field strength $E(x)$ is given by $(\rho_s \omega_p\, dv)/4\pi t^2$ and the current density $J(x)$ at the point x is written as $E(x)/\rho_s$, the integration regarding dv over the entire disk surface yields

$$J(x) = -\frac{\omega_p}{4\pi}\int_0^1 \int_0^{2\pi} \frac{r\, dr\, d\Theta}{r^2 - 2xr\cos(\Theta) + x^2 + h^2} \tag{14}$$

A general solution of Eq 14 is difficult to obtain. Since $Z_1(x)$ plays an appreciable role in the total impedance only when the nominal measuring area becomes comparable to the surface area of the probe electrode, Θ in Eq 14 is approximated to be zero. Then,

$$J(x) \approx -\frac{\omega_p}{4}\ln\left[\frac{x^2 + h^2 + 1}{x^2 + h^2}\right] \tag{15}$$

From Eqs 13 and 15, $Z_1(x)$ is written as

$$Z_1(x) = \frac{V}{J(x)} = \frac{R_s[h + 1 - (h^2 + 1)^{1/2}]}{\frac{A}{2}\ln\left[\frac{x^2 + h^2 + 1}{x^2 + h^2}\right]} \left(\equiv \frac{Z_0}{Z(x)}\right) \tag{16}$$

Using Eq 16, Eqs 10 and 11 are rewritten as

$$RZ(x,\omega) = \frac{Z_0(1 + \omega^2 R_c^2 C^2)/Z(x) + R_c}{[Z_0/Z(x) + R_c]^2 + \omega^2 R_c^2 C^2 Z_0^2/Z^2(x)} \tag{17}$$

$$IZ(x,\omega) = \frac{\omega R_c^2 C}{[Z_0/Z(x) + R_c]^2 + \omega^2 R_c^2 C^2 Z_0^2/Z^2(x)} \tag{18}$$

where

$$Z_0 = R_s[h + 1 - (h^2 + 1)^{1/2}]/A \tag{19}$$

$$Z(x) \approx \left[1 - \frac{(x^2 + h^2)^{1/2}}{(x^2 + h^2 + 1)^{1/2}}\right] \tag{20}$$

On the other hand, the interfacial impedance $Z_2(j\omega)$ shown in Eq 8 decreases with increasing frequency and the increase in frequency yields an effect similar to the decrease in polarization resistance (k value) on the current profile and the nominal measuring distance x_m. In order to obtain quantitative information on the dependency of the current profile on frequency, a new parameter, the frequency-dependent polarizability, $k(\omega)$, is introduced, thus

$$k(\omega) = \frac{k|Z_2(\omega)|}{R_c} \tag{21}$$

where $|Z_2(\omega)|$ is the absolute value of the interfacial impedance $Z_2(j\omega)$ in Eq 8, and is written as

$$|Z_2(\omega)| = \frac{R_c}{(1 + \omega^2 C^2 R_c^2)^{1/2}} \tag{22}$$

$$k(\omega) = \frac{k}{(1 + \omega^2 R_c^2 C^2)^{1/2}} \tag{23}$$

It is noted from Eq 23 that $k(\omega) \rightarrow k$ for $\omega \rightarrow 0$ and $k(\omega) \rightarrow 0$ for $\omega \rightarrow \infty$, respectively, Now, $k(\omega)$ is used in place of k in Eq 4 for the calculation of $i(x)$. The nominal measuring distance x_m is obtained by taking the distance at $i(x) = 0.5 \cdot i(0)$ after calculating $i(x)$.

Now, the total impedance is written as

$$\frac{1}{Z(j\omega)} = RZ(\omega) + jIZ(\omega) \tag{24}$$

$$RZ(\omega) \equiv \int^{x_m} \int^{x_m} RZ(x,\omega)\, ds \tag{25}$$

$$IZ(\omega) \equiv \int^{x_m} \int^{x_m} IZ(x,\omega)\, ds \tag{26}$$

Namely, the real and imaginary parts of the total impedance are obtained by integrating Eqs 17 and 18 over the frequency-dependent nominal measuring area, respectively. Therefore, the Bode diagram and/or complex plane plot for the impedance are obtained by calculating and plotting $|Z|$ and Θ over a wide frequency range by using Eq 27.

$$|Z(j\omega)| = \frac{[RZ^2(\omega) + IZ^2(\omega)]^{1/2}}{RZ^2(\omega) + IZ^2(\omega)}, \qquad \Theta = \arctan\left(\frac{IZ(\omega)}{RZ(\omega)}\right) \tag{27}$$

The results of the calculation by this procedure will be shown in the following section.

Electrochemical Impedance for Local Corrosion

The dotted lines in Fig. 5 show the current profile for the case when a local corrosion region W in width occurs between x_1 and x_2 in the nominal measuring area for a two- or one-dimensional structure. The total impedance $Z(j\omega)$ for this case is represented by the parallel combination of the impedances for the locally corroded part $Z_c(j\omega)$ and for the

other relatively sound part $Z_f(j\omega)$. Given that $Z_t(j\omega)$ and $Z_{cf}(j\omega)$ are the impedances in the absence of local corrosion corresponding to the total area and the locally corroded area respectively, they are written as

$$\frac{1}{Z(j\omega)} = \frac{1}{Z_c(j\omega)} + \frac{1}{Z_f(j\omega)} \tag{28}$$

$$\frac{1}{Z_t(j\omega)} = RZ_t(\omega) + jIZ_t(\omega) \tag{29}$$

$$\frac{1}{Z_c(j\omega)} = RZ_c(\omega) + jIZ_c(\omega) \tag{30}$$

$$\frac{1}{Z_{cf}(j\omega)} = RZ_{cf}(\omega) + jIZ_{cf}(\omega) \tag{31}$$

where $RZ(\omega)$ and $IZ(\omega)$ indicate the real and imaginary parts of respective impedances. The following relations exist for these impedances.

$$Z_f(j\omega) = \frac{Z_{cf}(j\omega)\, Z_t(j\omega)}{Z_{cf}(j\omega) + Z_t(j\omega)} \tag{32}$$

$$RZ(\omega) = RZ_t(\omega) + RZ_c(\omega) - RZ_{cf}(\omega) \tag{33}$$

$$IZ(\omega) = IZ_t(\omega) + IZ_c(\omega) - IZ_{cf}(\omega) \tag{34}$$

The absolute value and phase shift of the total impedance are obtained from Eq 27 by using Eqs 33 and 34.

Since the current profiles for the locally corroded part and the other relatively sound part are interdependent upon each other, it is difficult to obtain the exact current profile for the locally corroded structure. Given that the partial current densities for $k = k_f$ and $k = k_c$ are $i(x,k_f)$ and $i(x,k_c)$, respectively (Eq 4) , the following assumptions are made to simplify the calculation: (1) The current distribution on the sound portion is not affected by the occurrence of local corrosion and is approximated by that in the absence of local corrosion, $i(x,k_f)$, (2) Given that the signal current density at $x = 0$ in the absence of local corrosion is $i(0,k_f)$ and that, in the case where local corrosion extends over the entire surface, is $i(0,k_c)$, it is assumed that

$$\frac{i(x,k_c)}{i(x,k_f)} = \frac{i(0,k_c)}{i(0,k_f)} = m \tag{35}$$

Then, using Eqs 17, 18, 25, and 26, the respective terms in Eqs 33 and 34 are written as

$$RZ_t(\omega) = \int_{x=0}^{x_m} RZ(x,\omega)\, ds_t: \qquad k = k_f, \quad i(x) = i(x,k_f) \tag{36}$$

$$RZ_c(\omega) = \int_{x=x_1}^{x_2} RZ(x,\omega)\, ds_c: \qquad k = k_c, \quad i(x) = mi(x,k_f) \tag{37}$$

$$RZ_{cf}(\omega) = \int_{x=x_1}^{x_2} RZ(x,\omega)\, ds_{cf}: \qquad k = k_f, \qquad i(x) = i(x,k_f) \tag{38}$$

$$IZ_t(\omega) = \int_{x=0}^{x_m} IZ(x,\omega)\, ds_t: \qquad k = k_f, \qquad i(x) = i(x,k_f) \tag{39}$$

$$IZ_c(\omega) = \int_{x=x_1}^{x_2} IZ(x,\omega)\, ds_c: \qquad k = k_c, \qquad i(x) = mi(x,k_f) \tag{40}$$

$$IZ_{cf}(\omega) = \int_{x=x_1}^{x_2} IZ(x,\omega)\, ds_{cf}: \qquad k = k_f, \qquad i(x) = i(x,k_f) \tag{41}$$

where $ds_t = 2\pi x \cdot dx$, $ds_c = w(dx)$ and $ds_{cf} = w(dx)$ for a two-dimensional structure and $ds_t = 2w(dx)$, $ds_c = w(dx)$ and $ds_{cf} = w\,(dx)$ for a one-dimensional structure, and $x_2 = x_m$ in the case of $x_1 < x_m < x_2$ and $RZ_{cf} = R_c = IZ_{cf} = IZ_c = 0$ for $x_m < x_1$.

The results of computer simulation based on Eqs 33 through 41 will be seen in the next section. The simulation utilized the parameter values approximating those for buried steel in service condition. Since buried metallic structures are usually covered with an oxide or organic film, a small capacitance value corresponding to the film is utilized in some of the calculation in place of the usual double layer capacitance.

Impedance Diagrams for a Buried Large Structure

Impedance Diagrams for a Two-Dimensional Structure

Uniform Corrosion—Figure 7 shows the examples of the Bode diagrams and the complex plane plots of the impedance for uniform corrosion of a large plate-like structure at different k values. The general feature of the Bode diagram is similar to that of a simple parallel resistance-capacitance circuit, except for a very slow decrease of the absolute value with the increase of frequency at intermediate frequencies. As distinct from the impedance for the simple circuit, however, the increase of the polarizability (k value) results in only a slight increase in the low-frequency impedance but an appreciable increase in the maximum phase shift. The complex plane plot of the impedance exhibits an inclined semi-ellipse. The size of the semi-ellipse increases with increasing polarizability but the intercept of the semi-ellipse on the real axis is not proportional to the polarizability, a behavior different from usual electrochemical impedance. As stated earlier, with increasing frequency the interfacial impedance decreases in a certain frequency region, which results in the decrease in the nominal monitoring area. The decrease in the monitoring area is accompanied by the decrease in the apparent double layer capacitance, which makes the slow impedance decrease at intermediate frequencies dull on the Bode diagram. Since the interfacial impedance diminishes at high frequencies, the net impedance at high frequencies is reduced to the electric resistance of the medium corresponding to the primary current distribution. On the other hand, the interfacial impedance increases at low frequencies, which results in the increase in the nominal measuring area. Therefore, the impedance at low frequencies is that which corresponds to the secondary current profile. With increasing the polarizability of the object, the nominal measuring area increases, which tends to reduce the apparent polarization resistance. The low-frequency impedance corresponds substantially to the apparent transfer resistance covering the nominal measur-

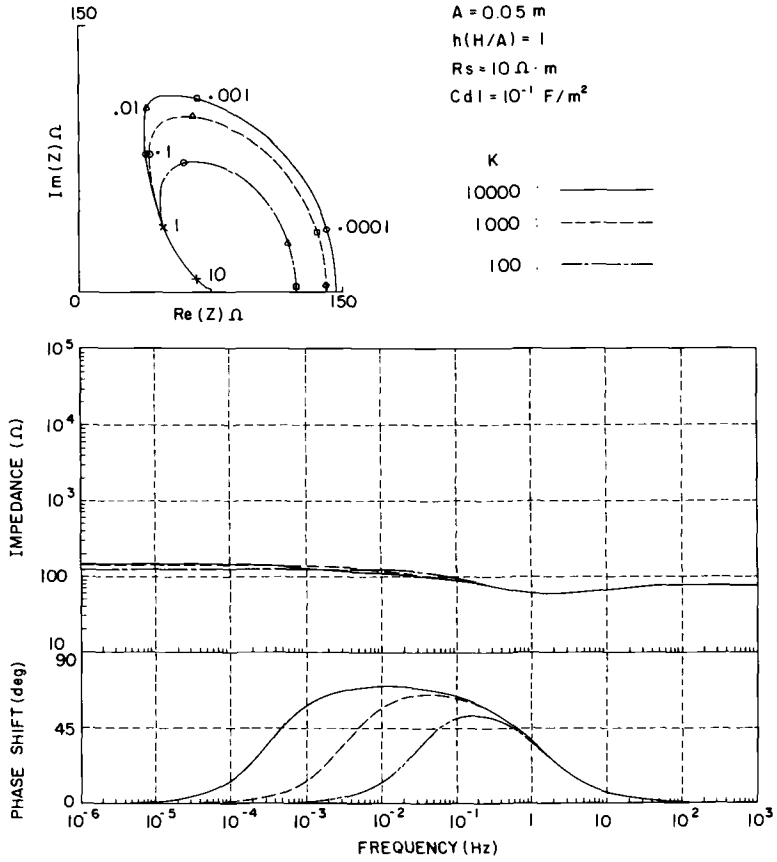

FIG. 7—*Impedance diagrams for two-dimensional structure at different* k *values.*

ing area. Thus, it is possible to estimate the net polarization resistance $R_c(0)$ for uniform corrosion of a buried plate-like structure by measuring the electrochemical impedance with a probe electrode, if the current distribution analysis described earlier is carefully made.

Local Corrosion—The effect of local corrosion on the impedance diagram is discussed in this section assuming that the rate of uniform corrosion, the specific resistance of the medium, and the arrangement of the probe are fixed. Figure 8 shows the impedance diagrams for a plate-like structure having a local corrosion at different distances. The solid lines in the figure indicate the diagrams in the absence of local corrosion, which are named the standard diagram. In the presence of local corrosion, the absolute value in the Bode diagram exhibits an extra arrest at intermediate frequencies, the magnitude of which increases with increasing distance from the probe electrode, eventually merging with the standard diagram. The standard phase shift graph shows a "volcano"-like curve. By introducing local corrosion, the low-frequency side of the volcano is deformed, exhibiting an extra volcano. The standard curve in the complex plane plot resembles an inclined semi-ellipse. By introducing local corrosion, the curve at low frequencies deviates from

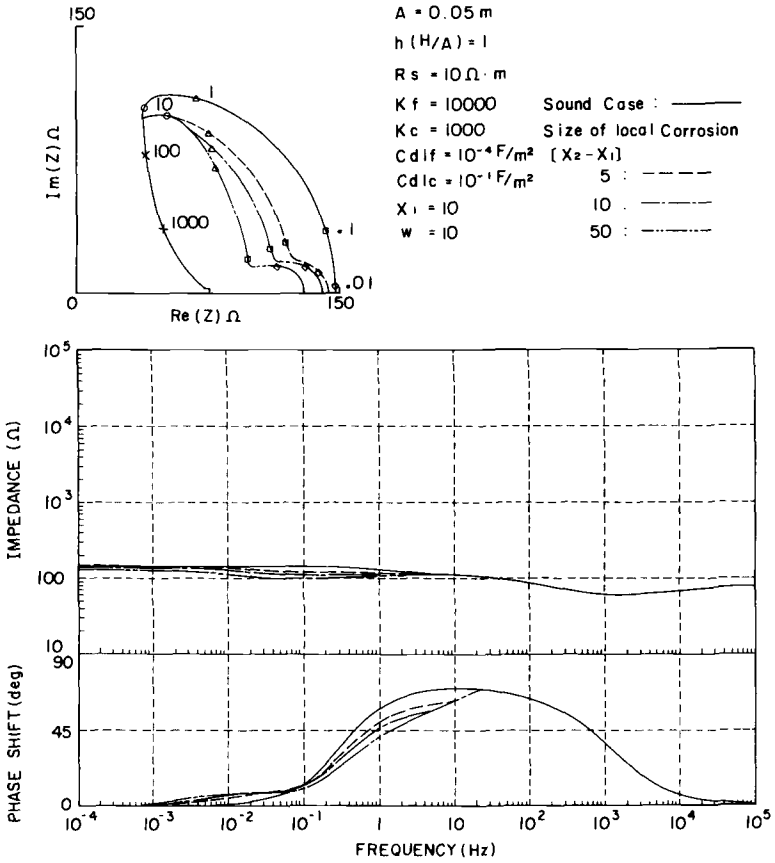

FIG. 8—*Impedance diagrams for a two-dimensional structure locally corroded at different positions.*

the standard, exhibiting an extra arc. The frequency where the deviation occurs decreases with increasing the distance of a local corrosion site from the probe. This is because the nominal measuring area increases with decreasing frequency and the deviation from the standard curve occurs in the frequency range where the local corrosion site is included in the nominal measuring area. The broken corner at the deviation frequency observed in the complex plane plots (Figs. 8, 9 and 10) is attributable to a sharp edge of the local corrosion and the approximation assumed for $i(x)$ in the vicinity of x_m.

The effect of the size of local corrosion of the impedance is shown in Fig. 9. When a local corrosion occurs in the nominal measuring area, the radius of the semi-ellipse on the complex plane plot decreases, exhibiting an extra arc at low frequencies. As is noted in Fig. 9, the radius of the arc increases with increasing the size of the local corrosion. Figure 10 shows the effect of the rate of local corrosion on the impedance diagram. The diameter of the low-frequency arc decreases with increasing the rate. As is seen in Bode diagrams in Figs. 9 and 10, the threshold frequency, where the deviation from the standard curve

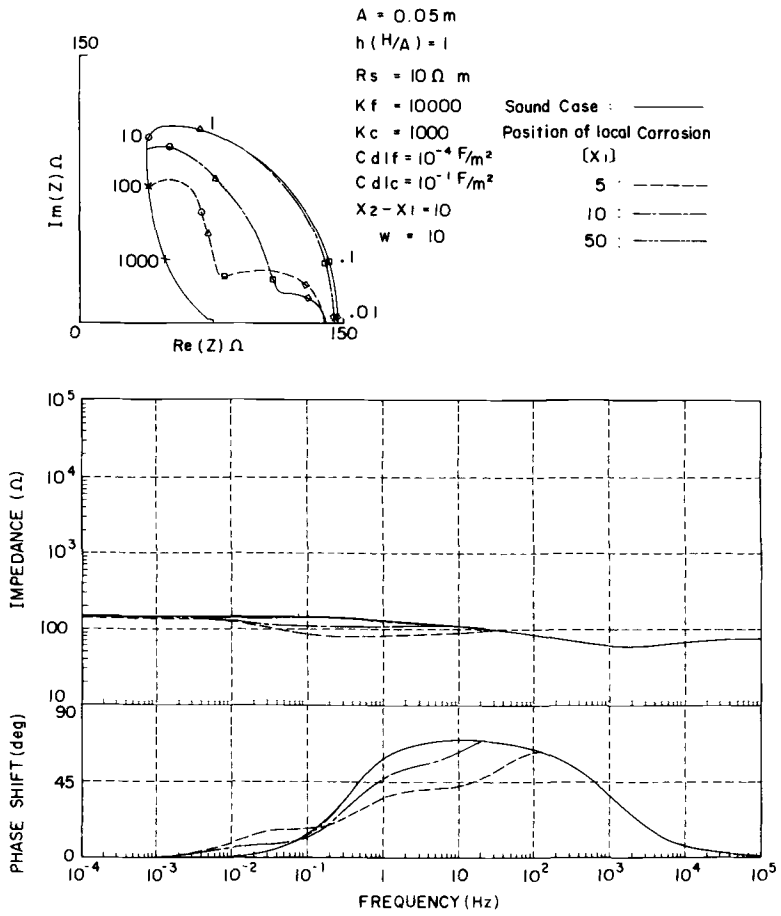

FIG. 9—*Impedance diagrams for two-dimensional structure locally corroded with different sizes.*

starts, is determined by the location of the local corrosion site, without depending on the rate and size of the local corrosion.

The nominal measuring area for a two-dimensional structure is usually a circle having the probe at its center. Therefore, it is possible to determine the location of a local corrosion site at a buried plate-like structure by measuring the impedance at three different probe positions. The distances of the local corrosion site from three different probe positions are determined from the three deviation frequencies on the impedance diagrams measured at the three different positions, respectively.

Impedance Diagrams for a One-Dimensional Structure

Uniform Corrosion—The procedure mentioned earlier is used for obtaining the impedance diagram for a one-dimensional structure. Figure 11 shows the simulated impedance

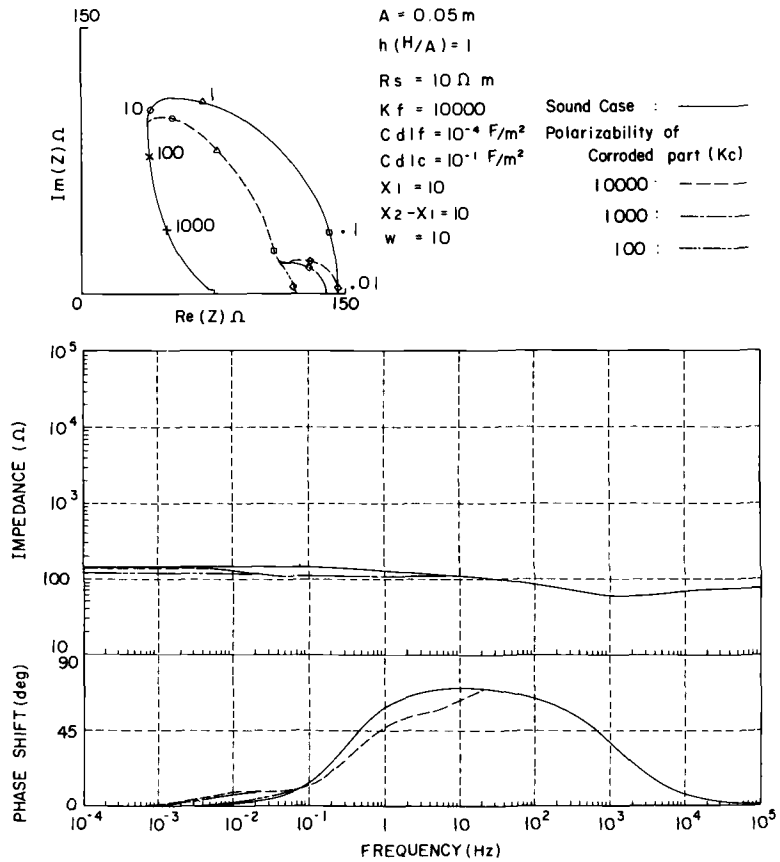

FIG. 10—*Impedance diagrams for two-dimensional structure locally corroded with different rates.*

diagrams for a belt-like structure with a different uniform corrosion rate. The complex plane plot exhibits a semicircle and the general feature of the Bode diagram is rather similar to that of a simple parallel resistance-capacitance circuit, except for a dull decrease of the absolute value with the increase of frequency at intermediate frequencies. It must be noted that the diameter of the semicircle is in proportion not to polarizability but approximately to the square root of k value.

Local Corrosion—The effect of local corrosion on the impedance diagrams is shown in Fig. 12. When a local corrosion occurs in the nominal measuring area, the diameter of the semicircle on the complex plane plot decreases, exhibiting an extra arc at low frequencies. With decreasing the distance of the local corrosion site from the probe electrode, the diameter of the semicircle decreases together with the increase of the arc diameter. The Bode diagram exhibits an extra arrest of the absolute value at intermediate frequencies and the breakpoint frequency increases with decreasing the distance approximately in inverse proportion to the distance. Therefore, as long as the other parameters are kept constant, the breakpoint frequency provides a powerful tool for determining the location of a local corrosion site of a one-dimensional structure.

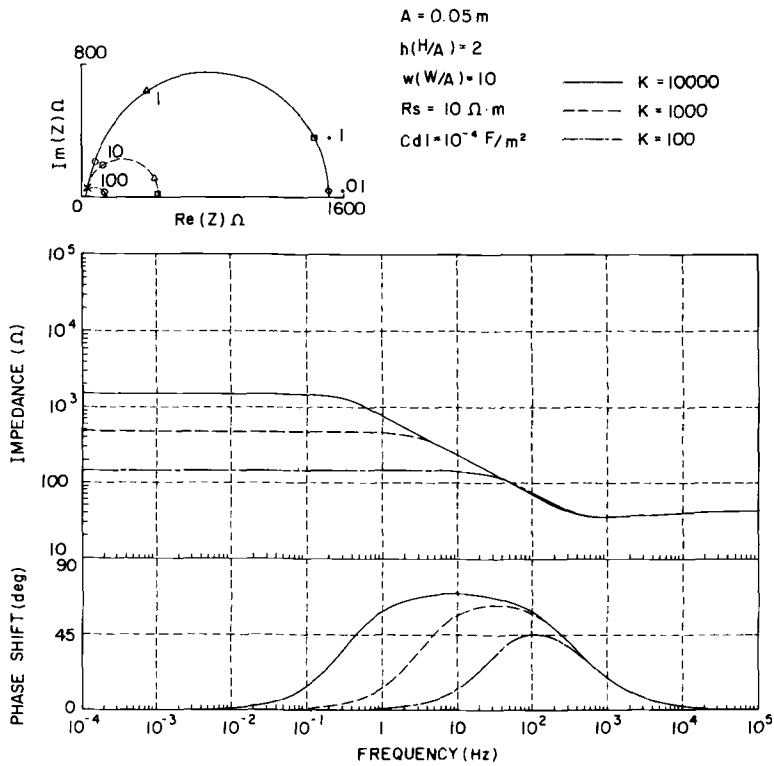

FIG. 11—*Impedance diagrams for one-dimensional structure at different* k *values.*

Summary

The polarization resistance and electrochemical impedance for a buried large structure has been discussed considering the distribution of the signal current. Since the current distribution, hence the effective measuring area, changes with the magnitude of polarization resistance, the apparent polarization resistance is not directly related to the true polarization resistance. A mathematical analysis considering the current distribution is necessary to obtain the true polarization resistance from the measured polarization resistance. The nominal measuring distance for a probe is usually in the range between 1 and 10 m depending on the polarizability and the other conditions.

In the measurement of the electrochemical impedance of a buried structure with a probe electrode, the distribution of the signal current, hence the measuring area, changes with the polarization resistance as well as frequency. The impedances at high and low frequencies correspond substantially to those for primary and secondary current distribution, respectively.

The complex plane plot of the electrochemical impedance thusly measured exhibits a semicircle or semi-ellipse depending on the structure, the intercept of which is not proportional on the real axis to polarization resistance as distinct from usual electrochemical impedance.

The impedance diagrams for a buried structure in the presence of local corrosion deviate from those in the absence of local corrosion below a threshold frequency which is deter-

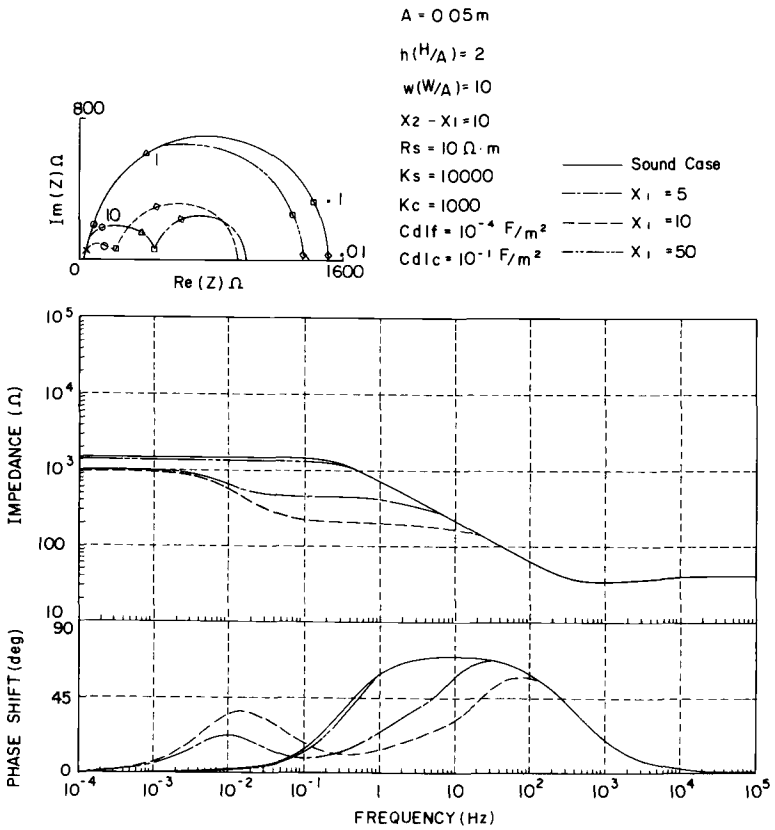

FIG. 12—*Impedance diagrams for one-dimensional structure locally corroded at different positions.*

mined by the distance of the local corrosion site from the probe without depending on the rate and size of the local corrosion. Therefore, this threshold frequency serves as a reliable tool for estimating the location of a local corrosion site on a large buried structure.

References

[1] Epelboin, I., Keddam, M., and Takenouchi, H., *Journal of Applied Electrochemistry*, Vol. 2, 1972, p. 71, in *Proceedings, 5th International Congress on Metallic Corrosion*, National Association of Corrosion Engineers, 1972, p. 90.

[2] Haruyama, S., in *Proceedings, 5th International Congress on Metallic Corrosion*, National Association of Corrosion Engineers, 1972, p. 82.

[3] Haruyama, S. and Tsuru, T., "A Corrosion Monitor Based on Impedance Method," *Electrochemical Corrosion Testing, ASTM STP 727*, F. Mansfeld and U. Bertocci, Eds., American Society for Testing and Materials, Philadelphia, 1981, p. 167.

[4] Macdonald, D. D., McKubre, M. C. H., and Urquidi-Macdonald, M., *Corrosion*, 44, 1988, p. 2.

[5] Zhang, J., Wenger, F., Jérome, M., and Galland, J., Paris, *301*, Série II, 14, 1985, p. 995.

[6] Zhang, J., Wenger, F., and Galland, J., Comptes rendu de l'Académie des Sciences, *304*, série II, 14, 1987, p. 797.

[7] Kasper, C., *Transaction of Electrochemical Society*, 78, 1940, pp. 131, 147.

[8] Wagner, C. and Traud, W., *Zeitschrift fur Elecktrochemie*, Vol. 44, 1938, pp. 7, 391.

[9] Stern, M. and Geary, A. L., *Journal of the Electrochemical Society*, Vol. 104, 1957, p. 56.

S. C. Kranc[1] *and A. A. Sagüés*[1]

Calculation of Extended Counter Electrode Polarization Effects on the Electrochemical Impedance Response of Steel in Concrete

REFERENCE: Kranc, S. C. and Sagüés, A. A., **"Calculation of Extended Counter Electrode Polarization Effects on the Electrochemical Impedance Response of Steel in Concrete,"** *Electrochemical Impedance: Analysis and Interpretation, ASTM STP 1188,* J. R. Scully, D. C. Silverman, and M. W. Kendig, Eds., American Society for Testing and Materials, Philadelphia, 1993, pp. 365–383.

ABSTRACT: Electrochemical impedance spectroscopy (EIS) measurements of corroding reinforcing steel in concrete are complicated by the formation of corrosion macrocells with associated potential gradients through the electrolyte. The measurements often require placing macroscopic counter electrodes in contact with the external concrete surface. This paper presents computations of the extent of current pattern changes and associated EIS response variations due to placement of counter electrodes. A model cylindrical reinforced concrete system was used, in which the rebar had a central active spot where both anodic and cathodic reactions took place. The rest of the bar surface was considered to be passive and supporting only cathodic reactions. The predicted impedance spectra yielded apparent polarization resistances that tended to underestimate the corrosion current. This was ascribed to nonuniformity of the excitation current distribution. Generally, current distribution effects overshadowed variations in the impedance response due to counter electrode placement or polarizability.

KEYWORDS: concrete, corrosion, electrochemical impedance, macrocells, measurement, counter electrode, polarizability, current distribution, computation

Nomenclature

a = rebar radius
A = active region length
b = cylinder radius
b_c = activation Tafel constant for oxygen reduction
b_a = activation Tafel constant for iron dissolution
C_s = effective oxygen concentration of concrete at the rebar surface
C_o = effective oxygen concentration of concrete in direct contact with air
C = effective oxygen concentration at any point in the concrete
C_{int} = interfacial capacitance of one rebar surface segment
$C_{int\ sp}$ = specific interfacial capacitance
CE = counter electrode length
D = effective diffusion coefficient of oxygen in concrete
E_o = equilibrium potential for the cathodic reaction

[1]Professors, Department of Civil Engineering and Mechanics, University of South Florida, Tampa, FL 33620.

E = polarized potential. The sign convention used in this paper is such that all potentials are with respect to the steel bar. Thus, the more positive E is at the bar surface, the faster the rate of the cathodic reaction tends to be.
E_{oa} = equilibrium potential for the anodic reaction
E^*_{CE} = dc potential at the electrolyte in immediate contact with the surface of the nonpolarizable electrode
E_{CE} = dc potential of the metal of a nonpolarizable counter electrode with respect to the rebar
E_{CP} = dc potential of the metal of a polarizable counter electrode with respect to the rebar
F = Farday's constant
i_c = cathodic current density
i_o = exchange current density for the cathodic reaction
i_a = anodic current density
i_{oa} = exchange current density for the anodic reaction
i_l = limiting current density
I_{mac} = total macrocell current
I_{corr} = total corrosion current
I_{app} = apparent total corrosion current
I_{cc} = ac excitation current flowing through the counter electrode of a guard electrode assembly
I_s = total ac excitation current flowing from the ac voltage source
I_a = anodic current of a surface element
I_c = cathodic current of a surface element
I_l = limiting current of a surface element
L = cylinder length
n = vector normal to a surface element
R_{app} = apparent polarization resistance
V_r = complex potential at the reference electrode location
V_s = ac potential of the voltage source
W_C = diffusional impedance
Z_{el} = impedance of a surface element of rebar or counter electrode (function of position and frequency)
σ = electrical conductivity of the concrete
ρ = electrical resistivity of the concrete
ω = angular frequency ($2\pi\cdot$ frequency of the test signal)

Reinforcing steel in concrete is initially passive, due to the high pH of the surrounding concrete pore solution. Passivity breakdown can take place because of chloride penetration from the external service environment (sea water, road deicing salts) or from atmospheric carbonation of the concrete [*1*]. Corrosion products formed after passivity breakdown create tensile stresses in the surrounding concrete, leading to cracks and eventual structural damage. Externally visible signs of corrosion may not develop until the deterioration has reached an advanced stage. As a result, a need exists for nondestructive forms of corrosion detection and rate measurement to diagnose condition and to specify corrective action in a timely fashion. Electrochemical polarization measurements are a natural choice for that purpose, and their application to steel in concrete has been the subject of many recent publications [*2–6*]. However, polarization measurements are complicated by factors which include the high resistivity of concrete, slow transport of

electroactive species, and macroscopically uneven electrical current distribution through the structure to be tested [*4*].

In a typical polarization measurement, an external counter electrode of finite dimensions is placed on the surface of the concrete. Excitation currents are driven by means of the external electrode through the concrete cover and into the underlying rebar. Changes in potential are measured by a reference electrode in contact with the concrete. Reinforced concrete structures are often of large proportions, and the severity of reinforcement corrosion can vary widely from point to point. Therefore, it is important to establish what portion of the structure is sampled by a polarization measurement. To that end, the counter electrode may be made with relatively large dimensions (in the hope of minimizing edge effects on current distribution) and the sample region corresponds roughly to the size of the counter electrode. Alternatively, a guard electrode may be placed around a smaller counter electrode, with both electrodes at the same potential by a voltage follower circuit [*7,8*]. Ideally, the current flowing through the central counter electrode will flow only to the rebar immediately below, thus sharply defining the sampling area.

The corrosion of steel in concrete normally results in the development of macrocells across characteristic distances which may be comparable to the size of the external electrodes previously discussed [*3,9,10*]. Thus, questions have been raised as to how the placement of a counter electrode on the concrete surface might alter the pre-existing corrosion macrocell pattern, and what will be the effect of that variation on the measured value of the corrosion rate. These questions are addressed in this paper for the case of a model system, computing the changes in the dc polarization distribution due to the external electrode placement. Since most polarization measurements for steel in concrete use small-signal techniques, the problem will be analyzed by computing the corresponding changes in the electrochemical impedance response of the system. The results are in principle applicable to other small-signal methods (polarization resistance, pulses) by considering the spectral composition of the signals used in each case [*6,11,12*].

A previous paper by the authors introduced an approach for the computation of corrosion macrocell current distribution and associated electrochemical impedance response in concrete [*13*]. The calculations presented here use a similar approach, expanded to include computation of oxygen distribution in the concrete and allowing for multiple electrode reactions at individual steel surface elements.

Procedure

dc Polarization Conditions, Initial System

The base system studied was a reinforced concrete cylinder with an axial rebar (see Fig. 1). A small active segment (corresponding to a region of chloride contamination) was introduced at the center of the bar; the rest of the bar surface was considered to be passive.

The concrete was treated as a homogeneous solid with a uniform effective oxygen diffusion coefficient and electrical conductivity. The effective oxygen concentration was considered to be constant along the lateral surface of the cylinder, equal to a value consistent with atmospheric exposure. No oxygen transport was allowed across the cylinder ends. The only cathodic reaction assumed was oxygen reduction

$$O_2 + 2H_2O + 4e \rightarrow 4OH^- \tag{1}$$

This reaction was assumed to take place at every point of the rebar surface at a rate given

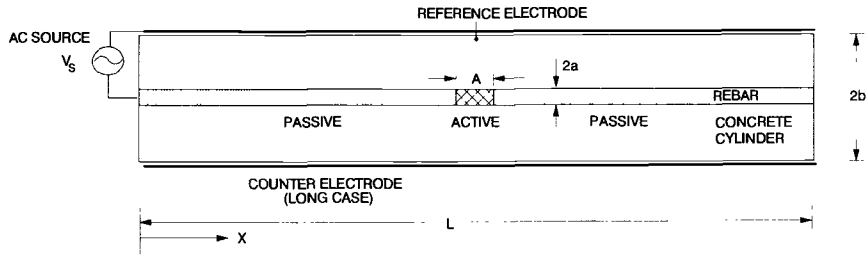

FIG. 1—*Longitudinal cross-section of the cylindrical reinforced concrete test system. The long counter electrode case is shown (CE = L).*

by the Butler-Volmer equation (concentration dependence included), with the additional assumption that the local potential is greatly removed from the equilibrium potential

$$i_c = i_o(C_s/C_o)\exp[(2.3/b_c)(E - E_o)] \tag{2}$$

(see the Nomenclature section for each symbol and appropriate sign convention). For simplicity, the parameters i_o and E_o were taken to be the same, regardless of whether the reaction was occurring on active or passive steel surface.

The only anodic reaction present was assumed to be iron dissolution, subject only to activation polarization. Unlike the cathodic reaction, iron dissolution was restricted only to the active portion of the bar. As in the case of oxygen reduction, the operating potential was assumed to be far enough removed from the equilibrium potential to neglect reverse reactions

$$Fe \rightarrow Fe^{++} + 2e^- \tag{3}$$

$$i_a = i_{oa}\exp[(2.3/b_a)(E_{oa} - E)] \tag{4}$$

Oxygen transport through the concrete was allowed to proceed by diffusion only. For the initial calculation, it was assumed that by the time the impedance measurements were started the system had achieved a steady state diffusional and electrochemical regime. Since the electrical conductivity was constant across the electrolyte, the electrical potential in the concrete satisfied Laplace's equation

$$\nabla^2 E = 0 \tag{5}$$

Likewise, because of steady state and uniform diffusivity, at every point of the concrete the oxygen concentration satisfied Laplace's equation

$$\nabla^2 C = 0 \tag{6}$$

At the steel surface the current supply across the electrolyte must match the net electrochemical action

$$i_a + i_c = \sigma\, dE/d\mathbf{n}|_{\text{metal}} \tag{7}$$

and the oxygen supply in turn needs to equal the amount consumed by the cathodic reaction

$$i_c = 4FD\, dC/d\mathbf{n}|_{\text{metal}} \tag{8}$$

The remaining boundary conditions were provided by the absence of oxygen transport at the cylinder ends and constant concentration at the sides

$$dC/d\mathbf{n}|_{\text{ends}} = 0 \tag{9}$$

$$C = C_o|_{\text{sides}} \tag{10}$$

The conditions expressed in Eqs 1 through 10 were formulated as difference equations based on nodes placed on a longitudinal section of the cylinder, representing the concrete cover over the bar. A matrix of 81 nodes on the axial direction by five nodes on the radial direction was used. The active central rebar region consisted of four nodes.

The difference equations were formulated to account for cylindrical symmetry along the main axis, thus obtaining full spacial simulation. The equations were solved by means of a Gauss-Seidel iterative method. For each internal node of the system and at each iteration step, the new value of C was obtained from the surrounding values of the previous iteration by Eq 6. The same procedure was used for E using Eq 5 in the same step. At the appropriate boundaries Eqs 2, 4, and 7–8 were applied consecutively at each node during the same step to obtain the new node values. Similar procedures were used for Eqs 9–10. The iteration process was stopped when the difference between consecutive steps fell below a preestablished error limit for E.

dc Polarization Conditions, System with External Electrode

A wrap-around counter electrode was considered to be placed around the central portion of the cylinder. The following variables were considered:

(1) Electrode size CE (Small, equal in length to the active region of the bar underneath, $CE = A$; and Large, the full length of the concrete cylinder, $CE = L$).
(2) Electrode polarizability (nonpolarizable electrode material; and polarizable electrode with various degrees of polarizability).

The **electrode size** was implemented by assigning additional boundary conditions to the appropriate number of nodes on the external concrete surface.

The **nonpolarizable** electrode condition was intended to approach the case where counter electrodes are made of materials (such as platinum mesh) that promote high exchange current densities of the operating electroactive species. The difference in potential between an ideal nonpolarizable electrode and the surrounding electrolyte is by definition not changed by currents sinking in or emerging from the electrode surface. Thus, the electrolyte region in direct contact with the electrode will be an equipotential surface where

$$E = E^*_{CE} \tag{11}$$

Note that E^*_{CE} is the potential *in the electrolyte* next to the counter electrode, measured with respect to the rebar. The material of the counter electrode will have a potential E_{CE}

with respect to the rebar which could be measured externally. However, it is the magnitude of E^*_{CE} that determines the polarization condition of the rebar surface.

The problem was solved for the case of open circuit EIS measurements, where the counter electrode does not introduce a net dc current in the rebar. The corresponding value of E^*_{CE} was calculated by proposing a seed value and computing the potential-concentration distribution satisfying Eqs 1 through 11 for the entire bar-counter electrode system. The computation used the same methods as for the initial system. From the solution, the resulting net current flowing in or out of the rebar was calculated, using Eq 7 and integrating the current over the rebar surface. The initial E^*_{CE} estimate was then changed in successive trials until a value was reached that resulted in a net bar current differing from zero by less than a preset target value.

The **polarizable electrode** condition was addressed as an approximation to a more general counter electrode behavior. Several degrees of electrode polarizability were considered. For convenience, the first set of counter electrode polarization characteristics were chosen to be equal to that of the bar material in the active condition.

To solve this problem, Eqs 6 through 8 and 10 were adapted to represent boundary conditions for the points corresponding to the counter electrode position. Eq 11 is no longer valid for a polarizable electrode, since the potential in the immediate liquid environment may vary from point to point. The polarization of the counter electrode may be described by equations such as Eqs 2 and 4 but those, as written, are for a metal that is at the same potential as the rebar. Since the counter electrode will develop its own potential E_{CP} with respect to the rebar, the polarization equations for the counter electrode must be modified accordingly

$$i_c = i_o(C_s/C_o)\exp[(2.3/b_c)(E - E_o - E_{CP})] \tag{12}$$

$$i_a = i_{oa}\exp[(2.3/b_a)(E_{oa} - E + E_{CP})] \tag{13}$$

The pertinent equations were solved as in the previous case, this time adjusting the value of E_{CP} in successive steps until a null in net bar current was obtained.

Two other polarizable counter electrode cases were considered, by replacing i_o and i_{oa} in Eqs 12 and 13 with $i_o/100$ and $i_{oa}/100$ in one case, and with $i_o/1000$ and $i_{oa}/1000$ in the other.

AC Polarization

For these calculations, an embedded reference electrode was assumed to be positioned at a point just below the counter electrode, at equal distance from both cylinder ends. The rebar acted as the working electrode. The excitation current for the impedance measurements was driven through the counter electrode.

The system's longitudinal cross-section was represented by an equivalent circuit grid as shown in Fig. 2. The grid corresponding to the bulk of the concrete was purely resistive, consisting of a matrix of 4 resistors in the radial direction by 80 in the longitudinal direction. The values of the resistors were scaled consistent with the system dimensions, the resistivity of the concrete, and the plane-to-cylindrical mapping requirement.

The bar surface was represented by discrete impedance elements that terminated the grid into the ground bus. The impedance of each surface element is a function of the dc polarization currents flowing to the element, the mass transport conditions at the element and their coupling with the rest of the system, and non-Faradaic terms such as interfacial capacitances. A full treatment of the system (cylindrical geometry, oxygen transport in both radial and longitudinal directions) cannot be addressed within the scope of this paper.

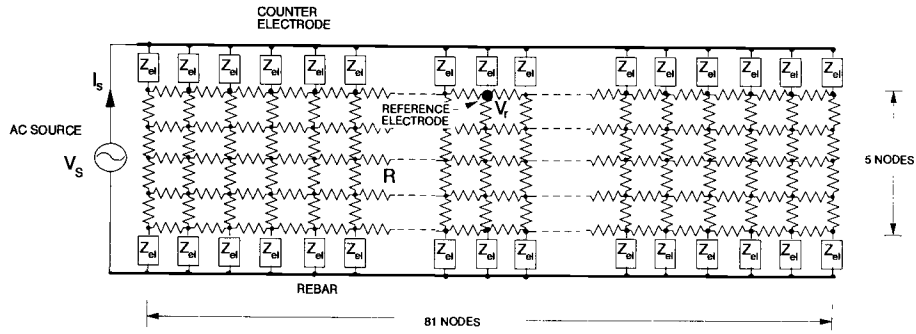

FIG. 2—*Equivalent circuit grid to calculate the impedance response of the system. The impedances Z_{el} of rebar or counter electrode surface elements are a function of the local dc current and of the test frequency. The resistances R are a function of position and concrete resistivity. The two-dimensional network is scaled for cylindrical symmetry.*

Instead, the impedance of individual elements was approximated by the available solution of the unidimensional problem for a discrete mixed-potential electrode. The approximation, detailed in Refs *14* through *16*, assumes an activation-limited anodic reaction and a combined activation-concentration controlled cathodic reaction. The reaction rates are I_a and I_c, respectively. I_l is the limiting current density for the cathodic reaction, which involves the diffusion of oxygen across a distance d. Under those conditions, the impedance of the element is given by the parallel combination of Faradaic impedances corresponding to the anodic and the cathodic reactions (Z_{fa} and Z_{fc}, respectively), and a non-Faradaic interfacial capacitance term (C_{int})

$$Z_{el} = (Z_{fa}^{-1} + Z_{fc}^{-1} + j\omega C_{\text{int}})^{-1} \tag{14}$$

where

$$Z_{fa} = R_a, \tag{15}$$

$$Z_{fc} = R_c + W_c, \tag{16}$$

and

$$R_a = b_a/2.3\, I_a, \tag{17}$$

$$R_c = b_c/2.3\, I_c, \tag{18}$$

$$W_c = [b_c/2.3(I_l - I_c]\tanh \sqrt{ju}/\sqrt{ju}, \tag{19}$$

with

$$u = \omega\, d^2/D \tag{20}$$

Following the treatment used in Ref *13*, the diffusion distance was approximated by the cylindrical equivalent

$$d = a \ln(b/a) \tag{21}$$

In the same manner [*13*],

$$i_l = 4FC_sD/d \tag{22}$$

From the values of i_a and i_c obtained in the dc calculations, the magnitudes I_a and I_c were evaluated for each surface element of the rebar. These magnitudes were used in turn to calculate, by means of Eqs 14 through 22, the impedance of each element at each frequency.

The counter electrode was joined to the nodes at the outer surface of the concrete, over the appropriate length, by suitable impedance elements. The polarizable counter electrode surface was modeled in a manner similar to that of the bar, except that no diffusional impedance term existed since the oxygen concentration was fixed at the counter electrode placement. The nonpolarizable electrode presents no impedance. That interface was represented by very small value resistors (1 Ω per element) to facilitate current computation.

The ac excitation signal was applied between the counter electrode and the bar by the ac voltage source V_s. The complex potential at the reference electrode node (V_r) was divided by the total complex current delivered by the voltage source (I_s), to obtain the complex impedance at each test frequency.

Node equations were written for each point of the network. This was done by establishing zero balance of current for the node, per the neighboring potential nodes and intervening impedance values. This produced a system of 405 equations, solved by a package matrix program (MATLAB) using a STARDENT computer. The resulting complex potentials at each node were used for impedance calculation as previously indicated.

TABLE 1—*System dimensions and calculation parameters.*

L (cm)	101.6
$2b$ (cm)	9.525
$2a$ (cm)	1.905
A (cm)	6.35
CE (cm)	
short	6.35
long	101.6
C_o (mol/cm^3 ($\times 10^{-7}$))	3
D (cm^2/s ($\times 10^{-4}$))	1
ρ (Ω-cm ($\times 10^4$))	1
E_{oa} (mV SCE)	780
E_o (mV SCE)	−160
i_o (A/cm^2)	1×10^{-9}
i_{oa} (A/cm^2)	3×10^{-8}
b_c (mV)	160
b_a (mV)	60
$C_{\text{int sp}}$ (μF/cm^2)	100

NOTE: Potentials are given with respect to the steel bar.

Results

System Configuration

Table 1 lists the system dimensions and polarization parameters used in the calculations. The bar dimensions and concrete cover are representative of those encountered in common construction practice. The concrete resistivity value assumed is consistent with that of concrete in contact with a humid environment [*17*]. The oxygen concentration at the external surface and the oxygen diffusion coefficient should be viewed as effective magnitudes, consistent with the general range of values reported in the literature [*18,19*]. In actuality, the heterogeneous nature of concrete and the geometry of its pore network pose a complex transport problem [*20*] that is only roughly approximated by the present treatment. The polarization parameters are representative of the range commonly observed for steel in concrete [*2,13*].

DC Calculations (see Table 2 for a summary of results)

Figure 3*a* shows the potential distribution at the bar surface for the initial (base) case where no external counter electrode is present. The active and passive regions are distinctly separated. As expected, the potential in the cathodic region decays with increasing distance from the anode. The same figure shows the potential distribution at the external surface of the concrete, where similar trends are observed but with less abrupt changes with position. Figure 4 shows the corresponding current (heretofore referred to as a macrocell current) density entering the electrolyte at the rebar surface. The active region behaves as a net anode, while the passive region is a net cathode. The macrocell current density has, as expected, its greatest magnitude at the junction of the cathodic with the anodic region, and magnitude minima at the center of the anodic region and at the ends of the cylinder.

Integration of the macrocell current density over the surface of the active region yielded a total macrocell current (I_{mac}) value of 320 μA. A very similar value (typically within 1%), but with opposite sign, was obtained for the passive zone. This match (a consequence of charge conservation implicit in Eq 5), was used as a secondary check of the calculation accuracy.

The corrosion rate at points of the active region can be obtained from the potential distribution and application of Eq 4. Integration of that current density over the active surface yielded a total corrosion current (I_{corr}) of 550 μA. A matching value was obtained

TABLE 2—*Summary of calculated results.*

Case	Counter Electrode		I_{corr} (μA)	I_{mac} (μA)	I_{mac}/I_{corr}	E^*_{CE} (mV)	E_{cp} (mV)	R_{app} (Ω)	I_{app} (μA)	I_{app}/I_{corr}
	Size	Polarizability								
Base	—	—	550	320	0.58	—	—	—	—	—
SNP	Short	nonpolarizable	560	320	0.57	514	—	62	420	0.75
SP	Short	same as active bar	560	320	0.57	—	−75	—	—	—
LNP	Long	nonpolarizable	860	620	0.72	356	—	80	325	0.38
LNPO*	Long	nonpolarizable	830	630	0.76	351	—	—	—	—
LP1	Long	same as active bar	860	620	0.72	—	−232	80	325	0.38
LP2	Long	1/100 as LP1	760	520	0.68	—	−248	70	370	0.49
LP3	Long	1/1000 as LP1	640	403	0.62	—	−279	80	325	0.38

*Using oxygen concentration distribution from the base case.

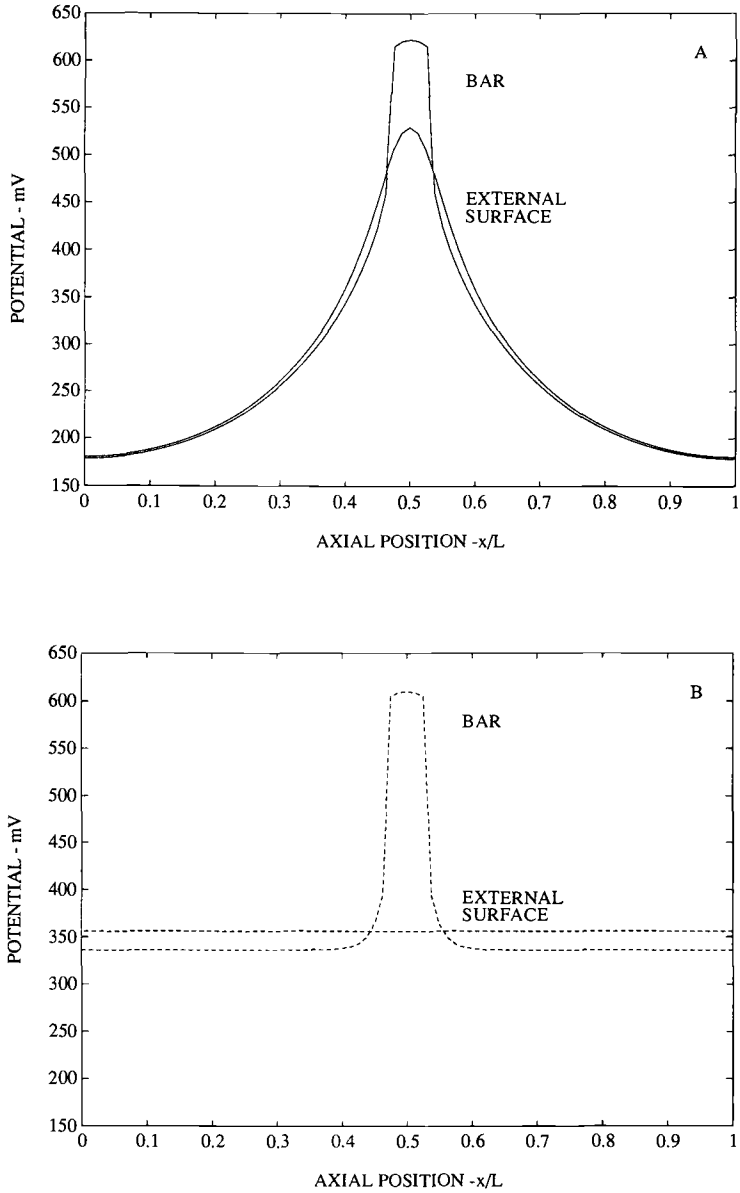

FIG. 3—(a) *DC potential in the concrete next to the bar and at the external surface in the absence of a counter electrode. The active bar region is at x/L values between approximately 0.47 and 0.53.* (b) *Same as* a *but with a nonpolarizable, long counter electrode in place.*

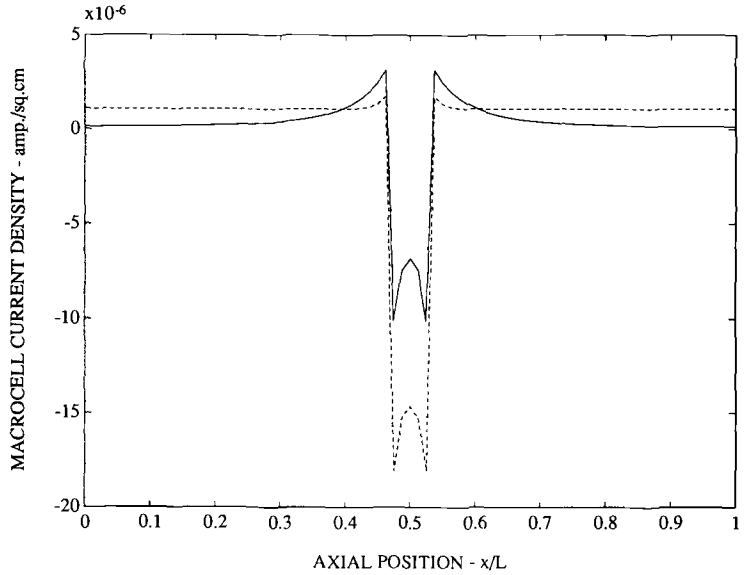

FIG. 4—*Macrocell current density at the rebar surface with (dashed line) and without (solid line) a nonpolarizable long counter electrode in place. Cathodic currents are positive; anodic currents are negative.*

by integrating the cathodic current density (Eq 2) over the entire bar surface. This agreement of anodic and cathodic overall rates provided an additional secondary check of computation accuracy. As expected, the corrosion current exceeded the macrocell current since the latter did not account for the local cell action at the active region.

Figure 5 shows the oxygen concentration profile in the concrete at the rebar surface. The oxygen demand at the active bar region is clearly evidenced by the lowering of the oxygen concentration there to about one tenth of the value at the concrete surface. Integration of the oxygen consumption rate per Eq 8 yielded a value coincident with the overall corrosion rate evaluated earlier. In addition, the computed oxygen flux across the external concrete surface matched that consumed at the bar surface. These checks further confirmed the solution as self-consistent.

Computation of the small, nonpolarizable electrode case resulted in potentials and currents at the bar surface that were almost identical to those obtained in the base case. The potential distribution at the concrete surface closely matched that of the base case, except for the counter electrode region. The potential there is constant, as per Eq 11. The condition of zero net current at the bar was reached for E^*_{CE} = 514 mV. The oxygen concentration distribution was virtually the same as that shown in Fig. 5 for the base case.

The long, nonpolarizable electrode problem produced results that differed significantly from the base case or the short nonpolarizable electrode case. The magnitude E^*_{CE} was 356 mV. As shown in Fig. 3*b*, the potential at the concrete in contact with most of the passive rebar region was dominated by the conditions near the counter electrode. The potential next to the active portion of the rebar was about 10 mV less in magnitude than that in the base or short electrode cases. This enhanced the overall extent of both the macrocell and corrosion currents, which were now 620 μA and 860 μA, respectively. Figure 4 shows the corresponding macrocell current distribution, allowing comparison with the base and short

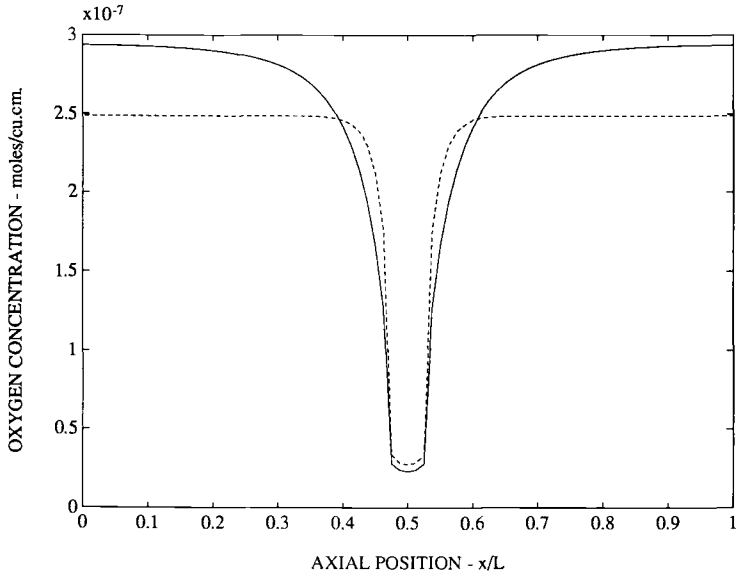

FIG. 5—*Effective oxygen concentration at the rebar surface with (dashed line) and without (solid line) a nonpolarizable long counter electrode in place.*

electrode cases. The macrocell current density has increased over the entire active region. On the passive region, the cathodic reaction rate actually decreased near the active portion but increased further away.

Figure 5 shows the oxygen concentration distribution for the long, nonpolarizable electrode case. Oxygen depletion was less than in the previous cases at or near the active region of the bar, but more pronounced than before over the rest of the bar surface.

In impedance measurements for diagnostic purposes of structures, the counter electrode is expected to be placed on the surface of the concrete for short times (minutes–hours). Characteristic relaxation times for the oxygen concentration patterns could be on the order of days–weeks because of the slow oxygen diffusivity and typical system dimensions. As a result, evaluation of the short-term effect of placing an external counter electrode on the polarization distribution of the system is of interest. This evaluation was approached by inspecting the case of a long, nonpolarizable electrode on the surface of the specimen, but keeping the oxygen concentration distribution equal to that of the base case. The resulting potentials and current distributions, as well as the integrated currents (Table 2), did not differ substantially from the steady state case.

Figure 6 summarizes the results of calculating I_{corr} and I_{mac} for long electrodes of various polarizabilities. The results for finite polarizability fall between the nonpolarizable limit (highest currents) and infinite polarizability (in effect, the base case with no counter electrode applied).

EIS Calculations

An example of the calculated magnitude of the specific impedance (Ω-cm^2) along the rebar surface is shown in Fig. 7 for the case of the long, nonpolarizable counter electrode. The results are shown at decade intervals for frequencies in the 10^{-4} to 1 Hz range. The

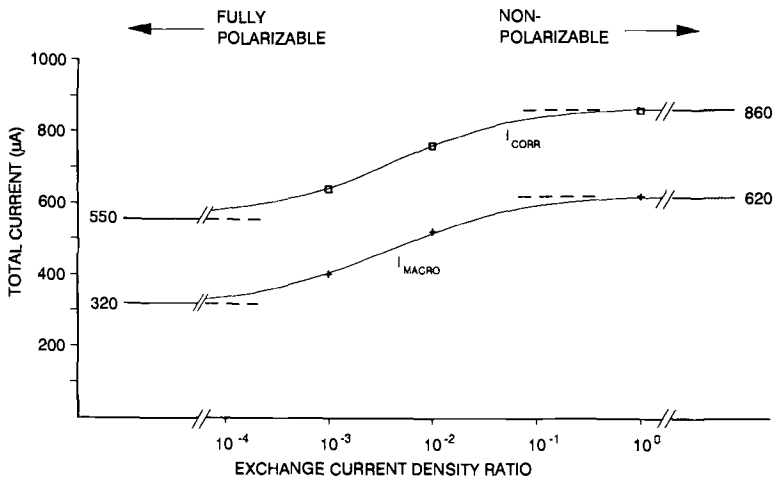

FIG. 6—*Total corrosion and total macrocell currents for long counter electrodes of various polarizabilities. The results are given as a ratio of exchange current densities (of both cathodic and anodic reactions) at the counter electrode to those of the same reactions at the rebar surface (active portion).*

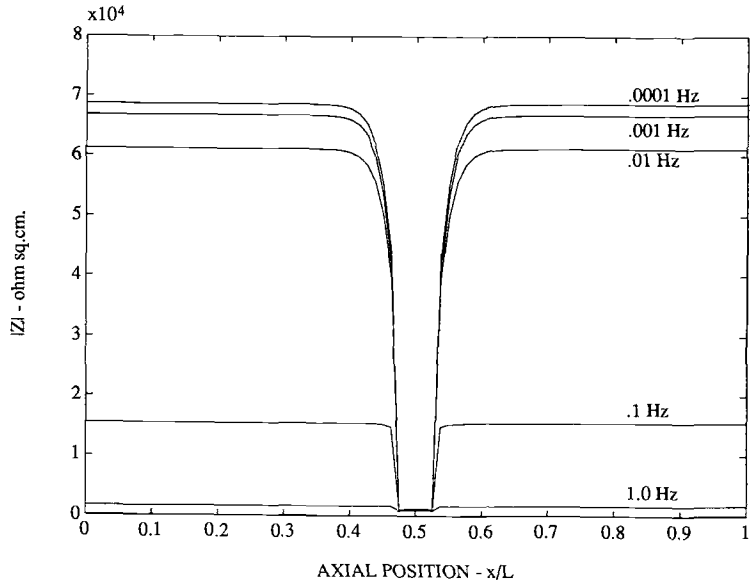

FIG. 7—*Specific impedance of the rebar surface at various test frequencies with a long, nonpolarizable counter electrode in place.*

impedance magnitude at the highest test frequency was small and relatively uniform along the bar surface. At progressively lower frequencies the impedance of the passive region became increasingly greater. This low-frequency impedance increased also with distance from the active portion of the rebar, reflecting the corresponding decrease in cathodic current density. This variation was more pronounced in the short counter electrode case, since there the cathodic current density changed more with axial position (see Fig. 4). The impedance of the active region remained small at all frequencies.

Incorporation of the specific impedance data in the system's equivalent circuit provided the results shown in Fig. 8.

The predicted impedance response for the short counter electrode cases was virtually the same regardless the degree of polarizability of the electrode. That result is shown in curve SNP in Fig. 8. Curve SNP is a noticeably depressed semicircle, with a small "tail" at the low frequency end corresponding to the diffusional impedance contribution in Eq 16. Disregarding that feature, the difference between the high- and low-frequency limits of the real impedance is ~62 Ω. This apparent polarization resistance R_{app} (not surface area-normalized) can be converted into a nominal total corrosion current I_{app} by using the common Stearn-Geary approximation [*21*]

$$I_{app} = B/R_{app} \tag{23}$$

with B = 26 mV, which is a value frequently used in evaluating corrosion rate from electrochemical measurements in concrete [*22*]. Application of Eq 23 to curve SNP yielded a value of I_{app} = 420 μA, which is listed in Table 2.

The impedance results for the long electrode cases are shown by curves LNP (nonpolarizable electrode), LP1, LP2 and LP3 (increasing degrees of polarizability) in Fig. 8. These curves, which approach ideal semicircles, had approximately the same high-frequency limit (~25 Ω). Curves LNP and LP1 were virtually overlapping, and are not shown separately. The apparent semicircle diameter and nominal corrosion current for each curve are listed in Table 2.

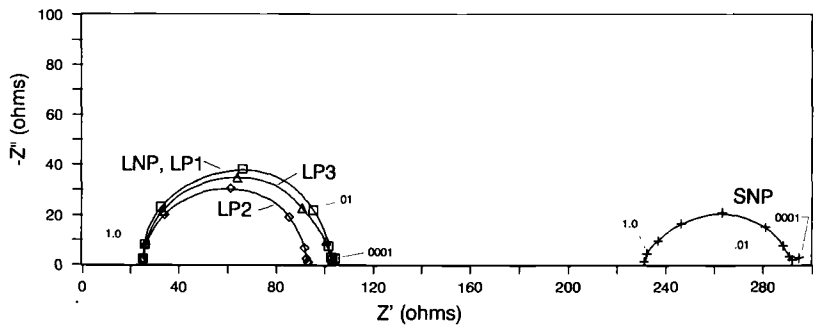

FIG. 8—*Calculated impedance for various test cases. The highest test frequency is 1 Hz. Frequency markers are in Hz. SNP: short, nonpolarizable counter electrode. LNP: long, nonpolarizable counter electrode. LP1-LP3: increasing long electrode polarizability.*

Discussion

The potential and current distributions observed for the base case followed expected trends that have been discussed elsewhere [*13*] (the reader is cautioned to keep in mind the potential sign convention used in this paper). The effect of the central anodic portion of the bar is to create there a potential extreme at the electrolyte in direct contact with the bar. As a result of the finite conductivity of the concrete, the associated macrocell current decays with distance from the anodic region, and the cathodic surface becomes consequently less polarized. The effect is still quite significant at the external concrete surface (Fig. 3*a*), illustrating the concept of corrosion detection by means of half-cell potential surveys of reinforced concrete structures (ASTM C 876, Test Method for Half-Cell Potentials of Uncoated Reinforcing Steel in Concrete). The magnitude of the macrocell and corrosion currents fell within the range expected for corroding reinforced concrete systems of comparable dimensions [*1,3,13*].

Application of the short counter electrode caused little change on the overall dc potential and current distribution. This is expected since the dimension of the electrode is small compared with the characteristic macrocell distance. Consequently, the polarizability of the short electrode is also of little effect.

As shown in Fig. 6, the presence of the counter electrode increased the corrosion and macrocell current magnitudes. The extent of the increment varied between the two extremes of infinite polarizability (effectively no counter electrode and therefore no effect), and the nonpolarizable electrode case which produced the greatest increase. The long counter electrode acted as a partial short circuit for the macrocell currents, reducing the effect of the intervening concrete resistance and allowing for greater oxygen consumption at the portions of the bar further away from the active region. This was manifested by a somewhat lower oxygen concentration at the surface of the bar than in the base or short counter electrode cases (Fig. 5).

Mathematically, the effect of placing a large, nonpolarizable electrode is not unexpected. The counter electrode represents a substantial change in the boundary conditions on the potential at the outer surface, i.e., instead of a condition of no current flow, the counter electrode forces a constant potential at the surface. As a result, the magnitudes of the macrocell currents change to adjust for the new conditions.

The high-frequency specific impedance of the bar surface (Fig. 7) was generally dominated by its interfacial capacitance. The assumed value of the specific interfacial capacitance $C_{\text{int sp}}$ (100 μF/cm^2 [*10*]), which was the same at all points of the bar surface, resulted in a capacitive impedance of about 1 kΩ-cm^2 at 1 Hz. The corresponding admittance overshadowed that of the Faradaic reactions at the same frequency in the passive region. At the active region the overall specific impedance was also on the order of 1 kΩ-cm^2, so that relatively little difference existed at high frequency between the active and passive portions of the bar. At lower frequencies the admittance of the interfacial capacitance became increasingly less important, and the impedance was determined by the Faradaic terms. At the lowest test frequency (0.1 mHz) the specific impedance over much of the passive region was almost two orders of magnitude greater than that of the active region. The impedance disparity between both regions was due primarily to differences in the dc current densities. The specific impedances were dominated by activation terms. Application of Eq 19 showed that, although there is significant oxygen depletion at points near the bar surface (see Fig. 5), the magnitude of W_c remains small compared with R_c in the frequency regime investigated.

The high-impedance limit in the long electrode curves in Fig. 8 was the same, regardless of electrode polarizability, because at that limit interfacial impedances are very small (see

Fig. 7). Therefore, the impedance of the system approached the resistance between the inner and outer walls of a homogeneous cylinder

$$R = \ln(b/a)/2\pi L\sigma \tag{24}$$

which for the parameters chosen in Table 1 results in $R = 25.21\ \Omega$, in close agreement with Fig. 8. For the short electrode the high-frequency limit was also nearly independent of the degree of polarizability for the same reason. However, the numeric value is not amenable to simple analytical prediction because of the more complicated current distribution. Nevertheless, the high-frequency limit was expected (and observed) to be higher than in the long electrode case because of the much reduced effective conductive path.

The relatively small magnitude of W_c permitted treating the low-frequency results as simply converging toward a real impedance limit. At this limit the current distribution was by no means uniform, since the specific impedance of the active region was much greater than that of the passive region (Fig. 7) and the overall interfacial impedance magnitude was comparable to the effective overall electrolyte resistance. This is illustrated by the calculations for the case of the long, nonpolarizable electrode in Fig. 9. The resulting low-frequency current constriction near the active zone causes its admittance to be underrepresented [*13,23*]. Since the effect was not present at the high-frequency end, then the R_{app} value (diameter of the apparent semicircle) was greater than that which would have been obtained with a mixed-potential electrode (of equal total corrosion current) uniformly distributed along the entire bar surface. This accounts for the consistent under-

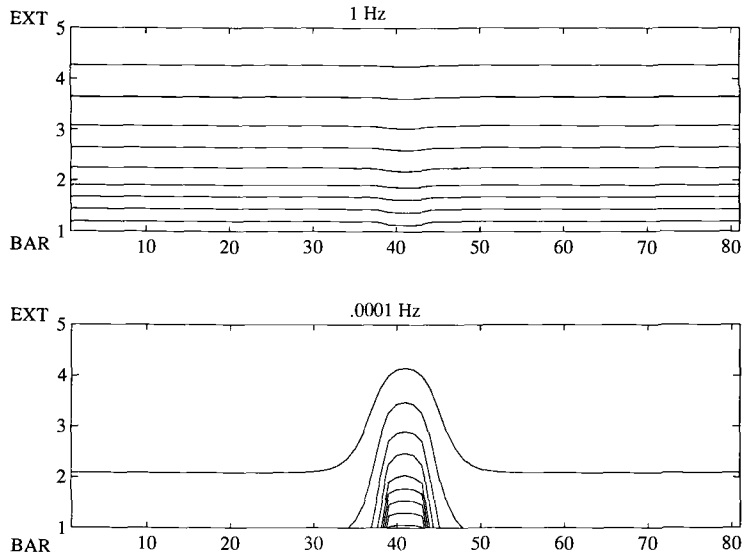

FIG. 9—*Differences between the ac signal distribution pattern at high and low frequencies, illustrated for the case of the long, nonpolarizable, counter electrode. The diagrams show equipotential (effective voltage) lines at 1 Hz (top) and 0.1 mHz (bottom). The lines are placed at 1 mV intervals; potential at the external surface was 10 mV. The top and bottom lines of each graph corresponds to the external (counter electrode) and rebar surfaces respectively. The vertical axis shows the position of radial nodes 1 to 5. The horizontal axis shows axial nodes 1 to 81. The aspect ratio has been modified for clarity.*

estimation of corrosion current for the cases listed in Table 2. It should be noted that while the value of B used here (26 mV) is primarily an empirical magnitude [*22*], it also may be viewed as representing a system where an anodic reaction with Tafel slope b_a = 26 × 2.3 mV = 60 mV is subject to activation control, while the matching cathodic reaction is under complete diffusional control [*21*]. For the system considered here, where oxygen diffusion exerts relatively little polarization control, a more appropriate nominal value for B should have been $b_a \times b_c/2.3(b_a + b_c)$ = 19 mV [*4,21*]. That would have led to even greater underestimation of the corrosion current.

Aside from an increase in effective electrolyte resistance, the short counter electrode impedance diagram shows greater distortion from an ideal semicircular shape than that observed when using a long electrode. This distortion stems from current distribution inequality along the bar, since the excitation signal needs to travel along increasing concrete distances to excite points at the bar which are remote from the center. At the high-frequency limit, this behavior resembles a transmission line with distributed resistance and capacitance. Simplified modeling of this type of system predicts that the high-frequency portion of the Nyquist diagram approaches the real axis at an angle of 45° [*5,24*]. This corresponded roughly to the observed behavior, accounting partially for the observed semicircular depression. The active-passive current distribution effect, prevalent at the low frequencies, caused additional distortion in both the short and long electrode cases.

The changes in the impedance response when varying the long electrode polarizability (curves LNP, LP1-3) were relatively small, and did not show a correlation with the corresponding changes in corrosion current. Examination of the spacial signal distribution in those cases revealed significant variation with counter electrode polarizability. This variation is linked to changes in the impedance distribution along the surface of the counter electrode. As shown in Fig. 10, the specific impedance along the counter electrode in case LP1 (low polarizability) was small and relatively uniform. As the polarizability increased (LP2, LP3), the specific impedance (at .0001 Hz) increased and its distribution

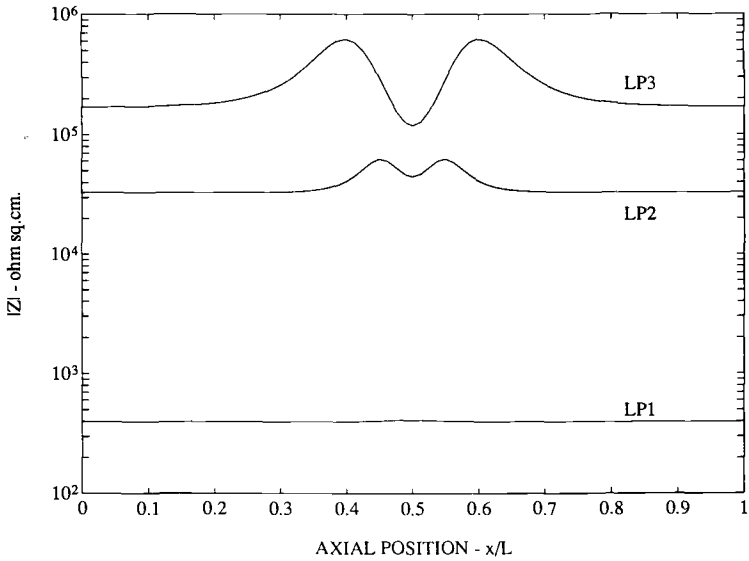

FIG. 10—*Specific impedance along the surface of counter electrodes of various polarizabilities at .0001 Hz.*

became more complicated. In case LP3, there is an absolute minimum of the counter electrode impedance at the point where the reference electrode is placed ($X/L = 0.5$). In case LP2 the minimum is local but not absolute. These conditions affected the overall current distribution (and thus the measured impedance response) in a manner that was not subject to prediction by simple trends.

The calculations presented in this paper predict that the placement of external counter electrodes can cause an increase in the overall rate of metal dissolution of steel in concrete. However, the calculated increase is moderate and the electrochemical impedance response is not expected to be excessively altered by the placement of the external electrode. This encouraging conclusion should be subjected to experimental confirmation.

The results did indicate the possibility of significantly underestimating corrosion rates due to frequency-dependent excitation current distribution. Calculations addressing in detail these effects in counter-guard electrode systems will be presented elsewhere.

Conclusions

(1) Counter electrode placement on the surface of a model reinforced concrete system resulted in moderate increases in the rate of corrosion and corrosion macrocell action. The increase results from an effective reduction in the net resistance between cathodic and anodic regions. Predictably, the effect became smaller with increasing counter electrode polarizability. Short counter electrodes, comparable in size with the active portion of the steel, had negligible effect on the corrosion distribution.

(2) The impedance spectrum obtained using a long external counter electrode showed smaller apparent electrolyte resistance values than when using a short electrode. The apparent polarization resistances were about the same for both types of electrodes, resulting in nominal corrosion currents insensitive to the electrode configuration.

(3) The nominal corrosion currents nevertheless consistently underestimated the values found in the dc model. AC current constriction around the actively corroding region of the rebar accounted for this effect.

References

[1] Slater, J. E., *Corrosion of Metals in Association with Concrete, ASTM STP 818*, American Society for Testing and Materials, Philadelphia, 1983.

[2] Naish, C., Harker, A., and Carney, R., "Concrete Inspection: Interpretation of Potential and Resistivity Measurements," in *Corrosion of Reinforcement in Concrete*, C. Page, K. Treadaway, and P. Bamforth, Eds., Elsevier Applied Science, London-New York, 1990, p. 314.

[3] Elsener, B. and Bohni, H. "Potential Mapping and Corrosion of Steel in Concrete," in *Corrosion Rates of Steel in Concrete, ASTM STP 1065*, N. S. Berke, V. Chaker, and D. Whiting, Eds., American Society for Testing and Materials, Philadelphia, 1990, p. 143.

[4] Sagüés, A., "Critical Issues in Electrochemical Corrosion Measurement Techniques for Steel in Concrete," Paper No. 141, *Corrosion/91*, National Association of Corrosion Engineers, Houston, TX, 1991.

[5] Macdonald, D., McKubre, M., and Urquidi-Macdonald, M., *Corrosion*, Vol. 44, 1988, p. 2.

[6] Macdonald, D., Urquidi-Macdonald, M., and El-Tantawy, Y., *Corrosion*, Vol. 47, 1991, p. 330.

[7] John, D., Eden, D., Dawson, J., and Langford, P., "Corrosion Measurements of Reinforcing Steel and Monitoring of Concrete Structures," Paper No. 136, *Corrosion/87*, National Association of Corrosion Engineers, Houston, TX, 1987.

[8] Feliu, S., Gonzalez, J., Andrade, C., and Rz-Maribona, I., "Errors Introduced by the Guard Ring Device in The On-Site Measurement of Rebar Corrosion Rates," in *Corrosion of Reinforcement in Concrete*, C. Page, K. Treadaway, and P. Bamforth, Eds., Elsevier Applied Science, London-New York, 1990, p. 293.

[9] Rendell, F. and Miller, W., "Macrocell Corrosion of Reinforcement in Marine Structures," in

Corrosion of Reinforcement in Concrete, C. Page, K. Treadaway, and P. Bamforth, Eds., Elsevier Applied Science, London-New York, 1990, pp. 167–177.
[*10*] Sagüés, A., "Electrochemical Impedance of Corrosion Macrocells on Reinforcing Steel in Concrete," Paper No. 132, *Corrosion/90,* National Association of Corrosion Engineers, Houston, TX, 1990.
[*11*] Gonzalez, J., Molina, A., Escudero, M., and Andrade, C., *Corrosion Science,* Vol. 25, 1985, p. 519.
[*12*] Gonzalez, J., Molina, A., Escudero, M., and Andrade, C., *Corrosion Science,* Vol. 25, 1985, p. 917.
[*13*] Kranc, S. C. and Sagüés, A. A., "Computation of Corrosion Macrocell Distribution and Electrochemical Impedance of Reinforcing Steel in Concrete," in *Computer Modeling in Corrosion, ASTM STP 1154,* R. S. Munn, Ed., American Society for Testing and Materials, Philadelphia, 1992, p. 95.
[*14*] Haruyama, S. "Faradic Impedance of Mixed Potential Electrode," *Proceedings of the Fifth International Congress on Metallic Corrosion,* National Association of Corrosion Engineers, Houston, TX, 1974, p. 82.
[*15*] Tsuru, T. "Treatment of Diffusion Impedance in AC Impedance Method," *61st Japan Society of Corrosion Engineers Symposium Report,* 1985, pp. 97–106.
[*16*] Sagüés, A. A. *Corrosion,* Vol. 44, 1988, p. 555.
[*17*] Millard, S. G., Ghassemi, M., Bungey, J., and Jafar, M., "Assessing the Electrical Resistivity of Concrete Structures for Corrosion Durability Studies," in *Corrosion of Reinforcement in Concrete,* C. Page, K. Treadaway, and P. Bamforth, Eds., Elsevier Applied Science, London-New York, 1990, p. 303.
[*18*] Tuutti, K., *Corrosion of Steel in Concrete,* Swedish Cement and Concrete Research Institute, 1982.
[*19*] Gjorv, O., Vennesland, O., and El-Busaidy, A., *Materials Performance,* Vol. 25, No. 12, 1986, p. 39.
[*20*] Garboczi, E. J., *Cement and Concrete Research,* Vol. 20, 1990, p. 591.
[*21*] Mansfeld, F., "The Polarization Resistance Technique," in *Advances in Corrosion Science and Technology,* Vol. 6, M. Fontana and R. Staehle, Eds., Plenum Press, New York, 1976.
[*22*] Andrade, C. and Gonzalez, J., *Werkstoffe und Korrosion,* Vol. 29, 1978, p. 515.
[*23*] Oltra, R. and Keddam, M. *Corrosion Science,* Vol. 28, 1988, p. 1.
[*24*] DeLevie, R. *Electrochimica Acta,* Vol. 9, 1964, p. 1231.

DISCUSSION

H. Takenouti[1] *(written discussion)*—The calculation of current and potential distribution seemed to be performed by a two-dimensional matrix according to your figure. However, if this calculation gives a good qualitative approach to the problem, it cannot draw a quantitative conclusion, because the local current density is quite different on two- and three-dimensional systems.

S. C. Kranc and A. A. Sagüés (authors' closure)—The computational grid is based on a two-dimensional axisymmetric radial coordinate system. The Laplace equations for the electric potential and the oxygen concentration, as well as the boundary conditions, are written in the appropriate polar form. Similar scaling criteria are used for the equivalent circuit grid. Thus, the quantitative aspects of a three-dimensional axisymmetric system are preserved. We have recently made some calculations, which include angular dependence, to further clarify the conditions surrounding very localized, asymmetric corrosion conditions.

[1]UPR15 DU CNRS, Physique des Liquides et Electrochimie, 75252 Paris Cedex 05, France.

Morph I. Jafar,[1] *John L. Dawson,*[1] *and D. Gareth John*[1]

Electrochemical Impedance and Harmonic Analysis Measurements on Steel in Concrete

REFERENCE: Jafar, M. I., Dawson, J. L., and John, D. G., **"Electrochemical Impedance and Harmonic Analysis Measurements on Steel in Concrete,"** *Electrochemical Impedance: Analysis and Interpretation, ASTM STP 1188*, J. R. Scully, D. C. Silverman, and M. W. Kendig, Eds., American Society for Testing and Materials, Philadelphia, 1993, pp. 384–403.

ABSTRACT The premature deterioration of concrete structures due to corrosion of the steel reinforcement is often a major problem in civil engineering. Polarization and electrochemical impedance spectroscopy can be used to study the development of passivity and corrosion mechanisms, and assess electrochemical kinetics on the steel reinforcement. However, *in-situ* corrosion rate measurements on reinforcing steel in laboratory test cubes, or structures on-site, are not always easy to obtain with either dc or ac techniques. This is because it is often virtually impossible to measure polarization resistance (R_p) at zero frequency or even measure the charge transfer resistance (R_{ct}) due to the large diffusion components associated with the overall mechanisms.

This paper discusses the implementation of harmonic analysis as a corrosion rate measurement technique on laboratory concrete specimens prepared with and without the addition of sodium chloride to the mix. The analysis technique, which is an extension of electrochemical impedance, is rapid to use. Harmonic analysis also has the advantage over other electrochemical measurements in that it enables the corrosion rate to be determined by simultaneous determination of the corrosion current and evaluation of Tafel constants. The data showed that there was a good agreement between the corrosion rates and the corresponding corrosion potentials.

KEYWORDS: concrete, corrosion potential, corrosion rate, chloride, Tafel slopes, Stern-Geary constant, electrochemical impedance spectroscopy (EIS), harmonic analysis

Steel in Concrete

It is well-known that steel embedded in concrete is normally protected because of the high alkaline environment (a pore solution of pH = 13) produced by the hydration (setting/curing) process, which induces the formation of a protective passive film of iron oxide (γ-Fe_2O_3) on the surface of the steel [*1*]. However, concrete is permeable; it contains not only aqueous filled pores, but also pores and cracks which permit the diffusion of atmospheric oxygen required to maintain passivity. The porous structure also enables depassivation and corrosion to occur due to carbonation or attack by aggressive ions such as chloride, or both [*2,3*]. The conjoint action of carbonation (the ingress of atmospheric carbon dioxide and conversion of calcium hydroxide to calcium carbonate with a decrease of pH) and the presence of chloride is particularly detrimental.

The quality of concrete, determined by parameters such as permeability, water/cement ratio, and electrical resistivity, affect the ability of concrete to resist depassivation of the

[1]Senior project officer, senior consultant, and technical developments manager, respectively, CAPCIS Ltd., Manchester M1 2PW, U.K.

oxide film. The chloride/hydroxyl ion ratio is often significant; also, the fact that concrete is permeable makes the depth of cover over the reinforcement an important factor in controlling chloride ingress and carbonation.

Once local depassivation occurs, a corrosion cell is formed with the passive areas acting as the cathode. The volumetric increase due to the formation of corrosion products eventually produces stresses in the concrete cover which ultimately leads to cracking, delamination, and spalling.

Electrochemical Measurements

Electrochemical techniques can provide information on the condition of the reinforcement (isopotential mapping to determine active or passive regions), the identification of pitting (electrochemical noise), and the corrosion rate at the time of the measurement. A number of reviews of these methods, including on-site applications and limitations, are available in the literature [*4–8*].

One of the main advantages of electrochemical measurements is that they they are nondestructive, which is important particularly on-site when structural integrity is of concern. These techniques are relatively easy and quick to perform and provide information on the evolution of corrosion with time; they are also less time consuming for laboratory work compared with traditional weight-loss measurements.

The earliest reported electrochemical impedance data on steel in concrete in 1979 showed the evaluation of the impedance from a typically aqueous corrosion system during setting and curing with distinct charge transfer and diffusion components, to an essentially passive system as the protective film develops and the hydration proceeds with development of the porous concrete structure [*9*]. It should be noted that although the electrochemical response for steel in concrete is comparable with measurements in other aqueous systems it also has some significant differences [*10*], in particular, the importance of slow diffusion of oxygen through the concrete matrix, the effect of the solid calcium hydroxide (portlandite) layer at the steel/concrete interface (which gives rise to a film dielectric component) and the concrete dielectric.

Figure 1 illustrates typical electrochemical impedance complex plane plots for steel in concrete and Fig. 2 shows equivalent circuits developed to describe experimental plots [*11,13–17*]. The electrochemical response of steel in concrete was first described [*11*] by a Randel's type equivalent circuit (charge transfer resistance, R_{ct}, double layer capacitance, C_{dl}, Warbung diffusion, W, and a solution resistance, R_s) but with the incorporation of a series/parellel combination R_f, C_f to represent the dielectric film effect. The high-frequency dielectric (R_f, C_f) increases as concrete dries and can be particularly pronounced in polymer-modified concrete or repair mortars [*13*]. This is presumed to be the result of a decrease in the dielectric constant of the "bound" water as the gel structure becomes more predominant due to the loss of "free" water. Wenger demonstrated that this high-frequency arc, which appears two or three months after curing, is independent of electrochemical reactions and is likely to be solid calcium hydroxide precipitated as a thin film on the steel [*14*].

Wenger considers that the charge transfer resistance (R_{ct}) is in series with an adsorbed reaction intermediate (R_f, C_f in Fig. 2*b*) but with passivation this adsorbed intermediate is not observed [*12*]. A circuit similar to Fig. 2*a* was used by Newton and Sykes [*15*] but with a second high-frequency relaxation from the concrete (R_c, C_c in Fig. 2*c*), and with the diffusion term not required during passivity. However, Andrade et al. [*16,17*] have employed a parallel combination (Fig. 2*d*) rather than a series combination, and they incorporate the dielectric effects in a high-frequency response (R_{HF}, C_{HF}). Noggerath and Bohni

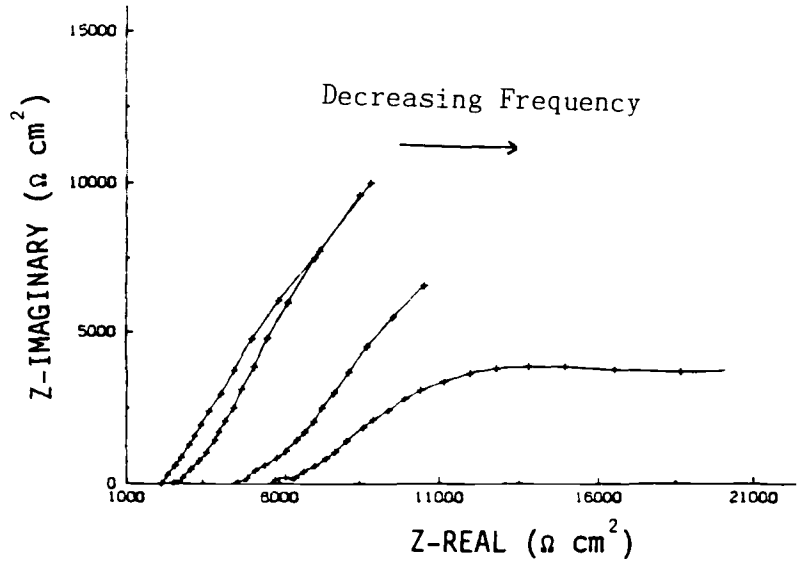

FIG. 1—*Typical impedance plots for steel in concrete.*

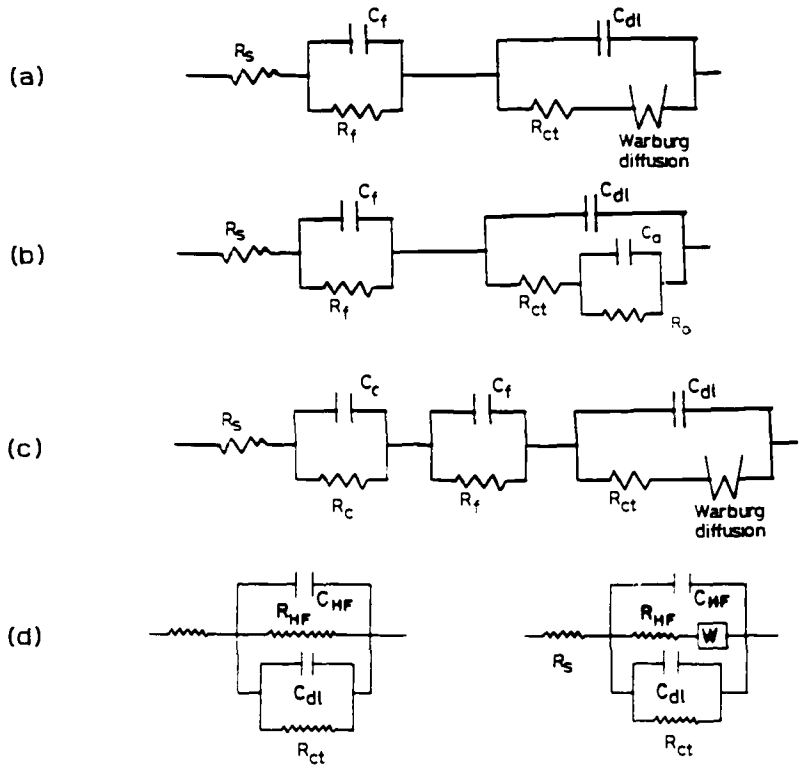

FIG. 2—*Equivalent circuits for steel in concrete.* (a) *Ref* 11. (b) *Ref* 13. (c) *Ref* 15. (d) *Refs* 16, 17.

[*18*] have simulated the development of macrocells which combine different areas of active pits in a passive surface with particular emphasis on the ohmic and geometric effects. A common theme is the measurement of the charge transfer resistance, R_{ct}, (sometimes referred to by some authors as the polarization resistance, R_p). A true polarization resistance (zero frequency measurement) would incorporate the charge transfer resistance, the lime-rich dielectric film resistance (R_f), concrete dielectric (R_c), plus any other relaxations that are present, possibly absorbed intermediates or diffusion in the case of active corrosion, or both.

Corrosion Rate Evaluations

A practical concern with steel in concrete is the determination of corrosion rates. Most techniques use the Stern-Geary relationship [*19*], which is based on the steady state, or zero frequency, measurement of the polarization resistance, R_p

$$i_{corr} = B/R_p \tag{1}$$

$$\text{where the Stern-Geary constant } B = \frac{b_a b_c}{2.303(b_a + b_c)} \tag{2}$$

b_a, b_c are the anodic and cathodic Tafel slopes, respectively. Practical R_p measurements may include diffusion (Warburg) and adsorption (pseudo-resistance) components as illustrated in Figs. 1 and 2; note that the impedance does not always return to the real axis, even at very low frequencies (few mHz). An alternative and standard method is to use the charge transfer resistance R_{ct} instead of R_p [*20,21*]. This not only allows measurements to be made at higher frequencies but, because any adsorption of intermediates and diffusion processes are coupled to the charge transfer, it enables the corrosion rate to be determined from

$$i_{corr} = B'/R_{ct} \tag{3}$$

Appropriate values of b'_a and b'_c, required to evaluate B' (in the form of Eq 2), may be obtained from the slope of graphs of log $1/R_{ct}$ versus E as analogous polarization curves; alternatively, b'_a and b'_c can be predicted by theoretical consideration of the electron transfer process, as developed by Bockris et al. [*22,23*].

Evaluation of R_{ct} can also be achieved by simulation and use of an appropriate equivalent circuit. Values of the components in the equivalent circuit are adjusted until the simulated curve fits the experimental plot [*11*]; the value of R_{ct} in the simulation is then used for the corrosion rate determination. Such a procedure is rather lengthy and not suitable for rapid evaluation of corrosion rates.

An alternative procedure to ac and dc techniques entails the use of a galvanostatic pulse to obtain a time domain measurement. The appropriate time constant, which is related to the corrosion rate, is obtained from the plot of change of measured parameters versus time [*7,15*]. For an applied current step I_{app} the potential, V_t at time t is $V_t = I_{app}[R_{ct}[1 - \exp(-t/(R_{ct}C_{dl}))] + R_s]$, subtracting the potential readings from the final steady state value gives $In(V_{max} - V_t) = In(I_{app}R_{ct}) - t(R_{ct}/C_{dl})$, from which R_{ct} can be obtained graphically.

In all cases of corrosion rate measurement, the means by which the data is obtained must be given. In particular, with linear polarization type instrumentation, the frequency

of measurement, or time interval used from the start of the perturbation, must be clearly stated; this indicates whether R_p or R_{ct} is being assessed.

A value of the Stern-Geary constant B is required for an estimate of the corrosion rate. The Concrete Society [*24*] recommends a B value of 50 mV regardless of the electrochemical state of the steel in concrete. Andrade et al. [*25,26*] have used values for B of 25 mV and 52 mV for steel in active and passive state, respectively, and these are based on weight-loss determinations used to calibrate their linear polarization measurements. Wenger obtained a B value of 35 mV from impedance and weight-loss calibrations [*27*].

Harmonic Analysis

The harmonic response of a system to a sinusoidal voltage or current perturbation has been of interest to electrochemists for a number of years [*28–30*]. It has been used to assess the effect of large amplitude perturbations on increased corrosion rates [*31,32*], as a means of corrosion monitoring [*33–37*], for determining corrosion rates in cathodically protected systems [*38*], and for measuring steel in concrete [*39*].

The harmonic response arises from the nonlinearality of the current/potential curve, the nonlinearality increasing as one moves further away from the corrosion potential. Electrochemical impedance spectroscopy (EIS) measurements and the Stern-Geary relationship assume that within a few millivolts of the corrosion potential, an approximately linear (*E-i*) relationship pertains. Impedance is concerned with the fundamental response while linear polarization neglects the higher terms in the series expansion used to derive the Stern-Geary relationship. Reflection of the sinusoidal perturbation, f, from the nonlinear curve results in faradaic distortion or harmonic responses at $2f$, $3f$, $4f$, etc., while any nonsymmetry of the E/i curve will produce a faradaic rectification response giving a dc offset or zeroth harmonic f_0. The harmonic responses contain sufficient information to describe the anodic and cathodic processes (Tafel slopes) and the corrosion current; essentially, the fundamental and the two harmonics ($2f$, $3f$) provide three equations, or data sets, which are solved to give the three unknowns, i_{corr}, b_a, and b_c.

Simple analysis based on Fourier series expansion [*34–36*] or Power series expansion [*30*] of the Butler-Volmer equation for the faradaic current, i_{farad}, can be employed, as below, although a more rigorous approach should use a Bessel function analysis [*36,38,39*], particularly if the data are to be developed into harmonic impedance spectroscopy.

A basic appreciation is obtained by considering the current response to a voltage perturbation for an activation process

$$i_{farad} = i_{corr}\,(\exp(\Delta E/b_a) - \exp(-\Delta E/b_c)) \tag{4}$$

A series expansion, neglecting $(\Delta E)^4$ and higher terms gives

$$\exp\left(\pm\frac{\Delta E}{b_{a/c}}\right) = 1 \pm \frac{\Delta E}{b_{a/c}} \pm \frac{1}{2!}\left(\frac{\Delta E}{b_{a/c}}\right)^2 \pm \frac{1}{3!}\left(\frac{\Delta E}{b_{a/c}}\right)^3 \tag{5}$$

and for a sinusoidal input of amplitude U_0

$$\Delta E = U_0 \sin \omega t; \qquad \Delta E^2 = U_0^2 \sin^2 \omega t; \qquad \Delta E^3 = U_0^3 \sin^3 \omega t$$

Substitution into Eq 5 gives

$$i_{\text{farad}} = \bar{i}_0 + i_f \sin \omega t + i_{2f} \sin (2\omega t - \pi/2) + i_{3f} \sin (3\omega t + \pi)$$

where

$$\bar{i}_0 = \frac{i_{\text{corr}}}{4}\left(\frac{1}{b_a^2} - \frac{1}{b_c^2}\right) U_0^2 \text{ the dc or zeroth component} \tag{6}$$

$$i_f = i_{\text{corr}}\left(\frac{1}{b_a} + \frac{1}{b_c}\right) U_0 \text{ amplitude of fundamental or first harmonic} \tag{7}$$

$$i_{2f} = \frac{i_{\text{corr}}}{4}\left(\frac{1}{b_a^2} - \frac{1}{b_c^2}\right) U_0^2 \text{ amplitude 2nd harmonic} \tag{8}$$

$$i_{3f} = \frac{i_{\text{corr}}}{24}\left(\frac{1}{b_a^3} + \frac{1}{b_c^3}\right) U_0^3 \text{ amplitude of 3rd harmonic} \tag{9}$$

Solving Eqs 7, 8, and 9 gives

$$i_{\text{corr}} = \frac{i_f^2}{(48)^{0.5}(2i_f i_{3f} - i_{2f}^2)^{0.5}} \tag{10}$$

A simple approach is used to calculate the anodic Tafel slope (b_a) and the cathodic Tafel slope (b_c) from the amplitude U_0 and the current i_f and i_{2f}.

If $b_a < b_c$

$$\frac{1}{b_a} = \frac{1}{2U_0}\left(\frac{i_f}{i_{\text{corr}}} + \frac{4i_{2f}}{i_f}\right) \tag{11}$$

$$\frac{1}{b_c} = \frac{1}{2U_0}\left(\frac{i_f}{i_{\text{corr}}} - \frac{4i_{2f}}{i_f}\right) \tag{12}$$

or if $b_a > b_c$

$$\frac{1}{b_a} = \frac{1}{2U_0}\left(\frac{i_f}{i_{\text{corr}}} - \frac{4i_{2f}}{i_f}\right) \tag{13}$$

$$\frac{1}{b_c} = \frac{1}{2U_0}\left(\frac{i_f}{i_{\text{corr}}} + \frac{4i_{2f}}{i_f}\right) \tag{14}$$

Practical harmonic measurements require instrumentation which produce negligible distortion in the harmonic currents either by use of a very high purity sine wave generator or a means of eliminating spurious signals or both. As with any electrochemical impedance technique, the amplitude of the perturbation U_0 should be small (less than 10 mV), and this is also required to minimize the error in the Taylor series expansion approximation; for U_0 between 5 to 10 mV this error is negligible [*35*]. However, the second and third harmonics

are of low amplitude and a detectable response typically requires U_0 to be between 10 to 20 mV. The effects of 10 to 100 mV perturbations on the response of steel in concrete have been reported which suggest that a U_0 of 10 to 15 mV is reasonable [39].

In summary, the present work is concerned with the application of harmonic analysis, an alternative technique to electrochemical impedance and linear polarization to measure the corrosion rate of steel in concrete obtained without the use of an assumed value for the Stern-Geary constant B. The data are presented in the context of EIS and establish agreement, if any, between measured corrosion potentials and the corresponding corrosion rates.

Experimental Procedure

Specimen Preparation

A batch of concrete blocks (150-mm cubes containing steel bars) was made by mixing cement, sand, aggregate, and water in the ratio 1:2:3 and 0.5, respectively. Two types of cement were used in this study, ordinary portland cement (OPC, ASTM Type 1) and sulphate resisting portland cement (SRPC, ASTM Type V). Two levels of sodium chloride additions (2% and 5%) were made by dissolving the required weight in the mixing water prior to mixing with other constituents. The mix design is given in Table 1.

Each block (150 mm by 150 mm by 150 mm) contained four rust-free "as received" mild steel rods used as rebars. The rods, 3-mm-diameter and 150-mm-long each, were cleaned using a detergent, rinsed with acetone, and dried with a blast of hot air. Then, an electrical wire was soldered to one end of the rod for electrical contact. Each rod and electrical connection was masked using heat shrinkage tubing to give an exposed surface area of 700 mm^2. In order to overcome any problem of crevice corrosion at the steel/masking interface, the gap between the rod and heat shrinkage tubing was filled with fresh cement powder prior to using a heat gun to shrink the tubing onto the rod. The steel rods were placed with 20 mm and 40 mm depths of cover and a depth of 40 mm at each end of exposed steel area.

Blank concrete blocks were prepared as before but without the addition of sodium chloride to the concrete mix in order to compare their performance against the chloride-containing specimens. All the blocks were cured in water for 28 days then placed in glass tanks containing 3% NaCl solution to a depth of approximately 100 mm.

Potential Measurements

Electrochemical potential measurements were carried out using a portable saturated calomel reference electrode (SCE) placed in the 3% NaCl solution, adjacent to the concrete block, and connected to the steel rod via a high impedance voltmeter. These corro-

TABLE 1—*Quantities of constituents per 1 m^3.*

Cement	400 kg/m^3
Fine aggregate	800 kg/m^3
Coarse aggregate (max. size 20 mm)	1200 kg/m^3
Water/cement ratio	0.5
NaCl (1)	0 kg/m^3 (0% the "blank")
(2)	8 kg/m^3 (2% NaCl)
(3)	20 kg/m^3 (5% NaCl)

sion potentials were obtained in conjunction with the electrochemical impedance and harmonic analysis measurements.

Electrochemical Impedance

Electrochemical impedance spectra were obtained from the rods embedded in the concrete using a Solartron Schlumberger 1250 frequency response analyzer in conjunction with a Thompson 251 ministat interface and a BBC microcomputer for data control, acquisition, and analysis, using CAPCIS CORRSOFT IMPED software. A three-electrode arrangement was used, using a working electrode, a counter electrode, and an SCE placed in the salt solution. The counter electrode was a piece of metal oxide activated titanium mesh. A small amplitude (10 mV rms) sinusoidal wave was applied via the working electrode (rod) and the response was measured over a range of frequencies, approximately 10 kHz to 10 mHz. The impedance data were plotted as a complex plane (Nyquist type) plot of real (resistive) component Z' against imaginary (capacitive) component $-jZ''$, with frequency as a parameter.

The plots enabled the estimation of the "solution" resistance (R_s); the charge transfer resistance (R_{ct}), polarization resistance (R_p), and the double layer capacitance C_{dl} could be evaluated in some cases by a simple extrapolation of the complex plane plots.

Harmonic Analysis

Harmonic analysis measurements were performed using a Solartron-Schlumberger 1250 frequency response analyzer as before and with a 10 mV amplitude (U_0) to perturbate the test electrode in a similar manner as EIS. The current response was measured in terms of the fundamental (i_f), second harmonic (i_{2f}), and third harmonic (i_{3f}). The harmonic values were used in the determination of the corrosion current (i_{corr}) by the simple calculation, previously described, as part of the microcomputer software.

The corrosion rates of the test electrodes were calculated using the following equation

$$\text{Corrosion rate } (\mu\text{m/yr}) = K\frac{ai_{corr}}{nD} \tag{15}$$

where

a = atomic weight of the metal,
i_{corr} = corrosion current density in $\mu A/cm^2$,
n = number of electrons,
D = density of the metal g/cm^3, and
K = constant depending on the penetration rate units desired; for μm/yr, $K = 3.27$.

For iron or steel: Corrosion Rate (μm/yr) = $11.6i_{corr}$.

Results

Curing Period

Evolution of electrochemical impedance spectra during curing of specimens of Type I (OPC) and Type V (SRPC) gave similar trends in that the initial and largely charge transfer process was converted over about a five-day period to that of passivated steel. There were

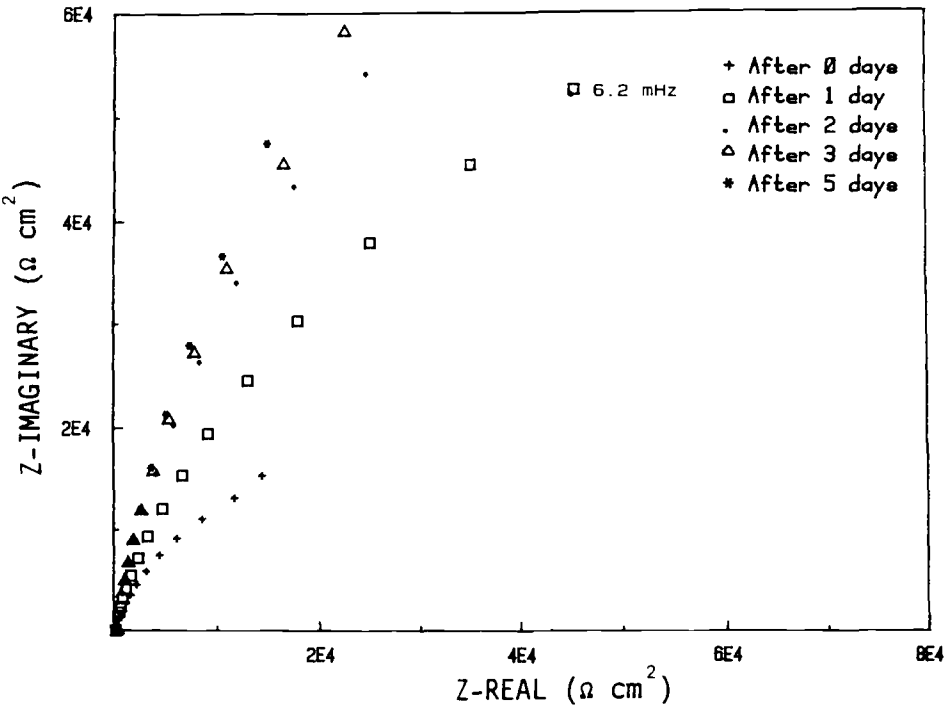

FIG. 3—*Electrochemical impedance of mild steel in OPC/concrete with no chloride.*

some minor observed differences between the two types of cement, but the major differences were between specimens with and without chloride addition. This can be seen in Figs. 3 and 4 which show typical impedance results from chloride-free OPC (Type I) and 5% NaCl addition to the mix, respectively. The data are summarized in Table 2.

The presence of chloride decreased the measured solution resistances, presumably by increasing the pore water conductivities. More significantly, the chloride decreased the charge transfer resistances as measured after fixed times of curing. Thus, although corrosion occurs initially in all cases, this slowly leads to the establishment of the passive film as the highly alkaline and porous structure develops during continuing hydration. The higher corrosion rates obtained in chloride-containing specimens are perhaps indicative of the competition between aggressive chloride ions and passivating hydroxyl ions. Corrosion rates were obtained from estimates of the charge transfer resistance, typically extrapolation of the semicircle plot to the real axis.

Immersion Tests

Exposure of the test blocks by partial immersion in 3% sodium chloride-containing solutions ensured availability of atmospheric oxygen by diffusion plus maintenance of a high pore solution conductivity and minimization of the film dielectric effect. The major experimental parameter of interest was the ingress of chloride ions from the immersion solution and the influence of depth of cover plus the presence of chloride in the original mix.

The results obtained from blank (chloride-free) concrete specimens made with ordinary

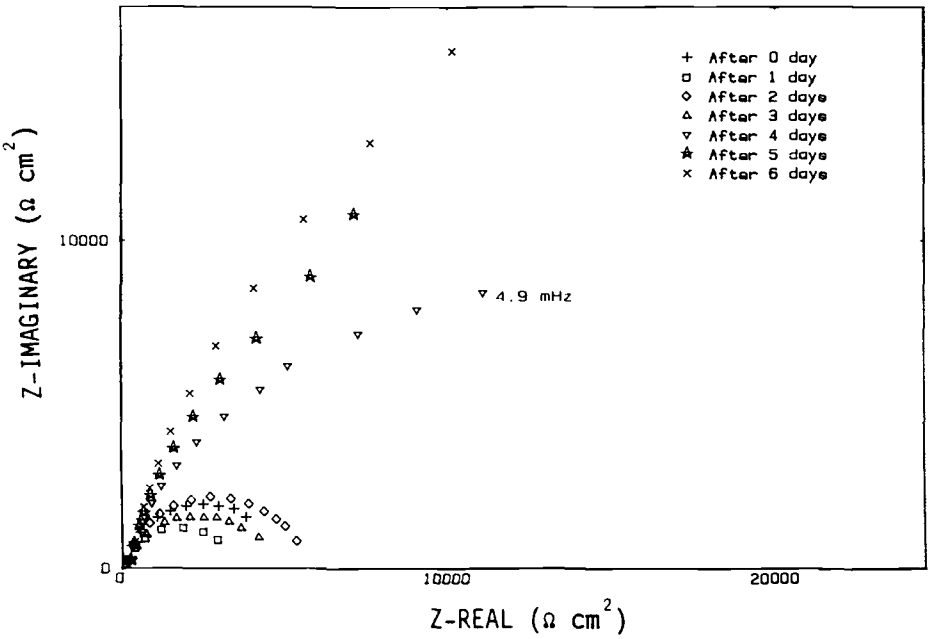

FIG. 4—*Electrochemical impedance of mild steel in OPC/concrete with 5% NaCl.*

portland cement (Type I) and sulphate resisting portland cement (Type V) showed that the corrosion potentials were more positive than −170 mV (versus SCE). There was no noticeable difference in the potentials between specimens with 20 mm and 40 mm depth of cover during the initial period of exposure. This was primarily due to the continuing presence of a passive film and the absence of agressive chloride ions at the steel interface to initiate corrosion. However, the ingress of chloride ions from the immersion solution

TABLE 2—*Impedance data over first few days of curing.*

	0% NaCl			2% NaCl			5% NaCl		
Days	R_s (Ω cm²)	R_{ct} (kΩ cm²)	CR (μm yr^{-1})	R_s (Ω cm²)	R_{ct} (kΩ cm²)	CR (μm yr^{-1})	R_s (Ω cm²)	R_{ct} (kΩ cm²)	CR (μm yr^{-1})
					Type 1 (OPC)				
0	53	60	1.4	23	5.8	14	17	5	16.4
5	335	>300	0.25	...	...	...	...	...	...
6	...	...	...	176	142	0.57	166	90	0.90
					Type V (SRPC)				
0	77	19	1.01	22	3.9	20.9	13	4.45	18.3
5	499	253	0.32	270	179	0.45	25	57	1.43

NOTE: with Cl^{-1} additions the R_{ct} decreased during the first day of cure showing an increase in corrosion rate of 20% with Type 1 and 25% to 50% with Type V.

(3% NaCl) led to a slight increase in corrosion activity of the low cover (20 mm) specimens with time. It was difficult to estimate the values of either the charge transfer resistance (R_{ct}) and corrosion rates from the electrochemical impedance data due to the passive and largely capacitive response obtained from these specimens. This is illustrated in Fig. 3, which shows a typical complex plane plot for steel in concrete without the presence of chloride. The response is mainly capacitive with a large time constant indicative of passive steel. The solution resistance (R_s) values were around 400 Ω cm^2.

However, using the harmonic analysis technique it was possible to obtain values for the Tafel slopes and the corrosion rates for these "blank" specimens (Table 3). The calculated Tafel slopes (b_a, b_c) from the "blank" Type I (OPC) and Type V (SRPC) specimens were (49 mV, 47 mV) and (54 mV, 51 mV), respectively. These values gave Stern-Geary constants or B values of 10.5 mV and 11.4 mV, respectively, which are significantly lower than the values quoted in other references.

Figures 5, 6, and 7 show typical complex plane plots for chloride-containing concrete specimens after twelve months' immersion in 3% NaCl solution. These plots include depressed semicircle relaxations and Warburg diffusion impedance. In all cases the "solution" resistance (R_s), charge transfer resistance (R_{ct}), and polarization resistance (R_p) were significantly lower than those of chloride-free specimens, thus indicating a nonpassive (active) behavior of the steel rods. However, detailed analysis or judgment, or both, based on evaluation of each data set or plot is required to obtain an estimate of the R_{ct} values and corrosion rates.

The addition of 2% NaCl to the concrete mix resulted in a much less capacitive behavior and a lower R_s between 200 and 300 Ω cm^2, due to an increase in the conductivity of the pore solution. Corrosion rates were significantly higher than those with no chloride addition, indicating some breakdown of the passive film. The high cover specimens exhibited corrosion rates below 14.5 μm/yr and potentials more positive than −345 mV (versus SCE) for OPC (Type I), compared with corrosion rates less than 15.2 μm/yr and potentials more positive than −370 mV for SRPC (Type V) specimens. The low cover specimens exhibited higher corrosion rates up to 270 μm/yr for OPC and 280 μm/yr for SRPC and more negative potentials down to −690 mV for OPC and −760 mV for SRPC.

Harmonic analysis results exhibited trends similar to those obtained from electrochemical impedance. The potentials obtained from OPC (Type I) specimens in the range −220

TABLE 3—*Examples of harmonic analysis results.*

Specimen	Concrete Cover, mm	Potential −mV (SCE)	Fundamental, V	Second, V	Third, V	Tafel Slopes (b_a,b_c)	B, mV
Blank OPC-1	20	81	1.9315	0.0038	0.0035	49,47	10.5
Blank SRPC-1	20	81	1.9473	0.0052	0.003	54,51	11.4
2% OPC-8	20	439	6.505	0.026	0.002	130,108	23.7
2% OPC-9	20	225	3.324	0.011	0.003	71,65	14.8
2% SRPC-2	20	275	3.239	0.009	0.002	86,79	17.9
2% SRPC-11	20	327	3.588	0.023	0.008	46,41	9.5
5% OPC-1	20	545	12.613	0.015	0.007	89,85	18.9
5% OPC-9	20	522	7.873	0.108	0.015	55,42	10.4
5% SRPC-1	40	479	3.781	0.049	0.004	79,56	32.8
5% SRPC-2	20	551	6.758	0.091	0.002	231,103	44.2

*NOTE: the voltages given in this table are recorded direct from the frequency response analyzer; these are then converted to harmonic currents using the relevant value of the counter resistor.

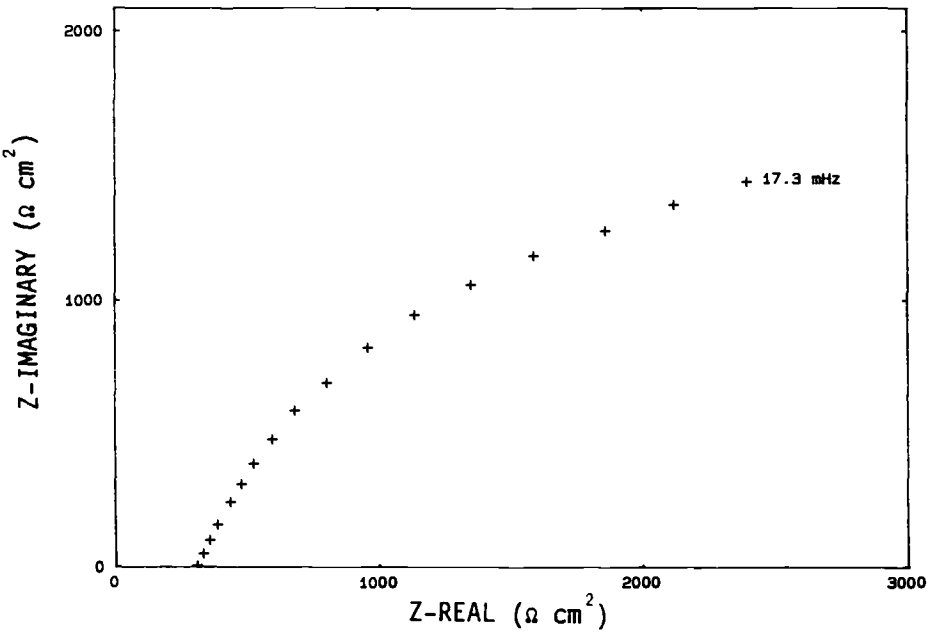

FIG. 5—*Complex plane plot for OPC specimen (5% NaCl, 40 mm cover), potential −408 mV.*

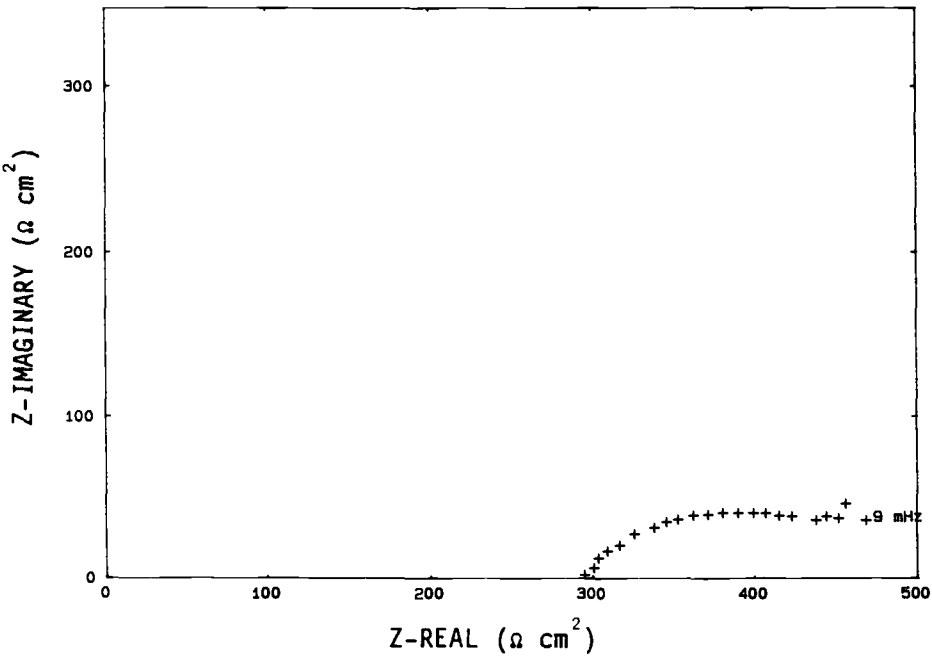

FIG. 6—*Complex plane plot for OPC specimen (5% NaCl, 20 mm cover), potential −560 mV.*

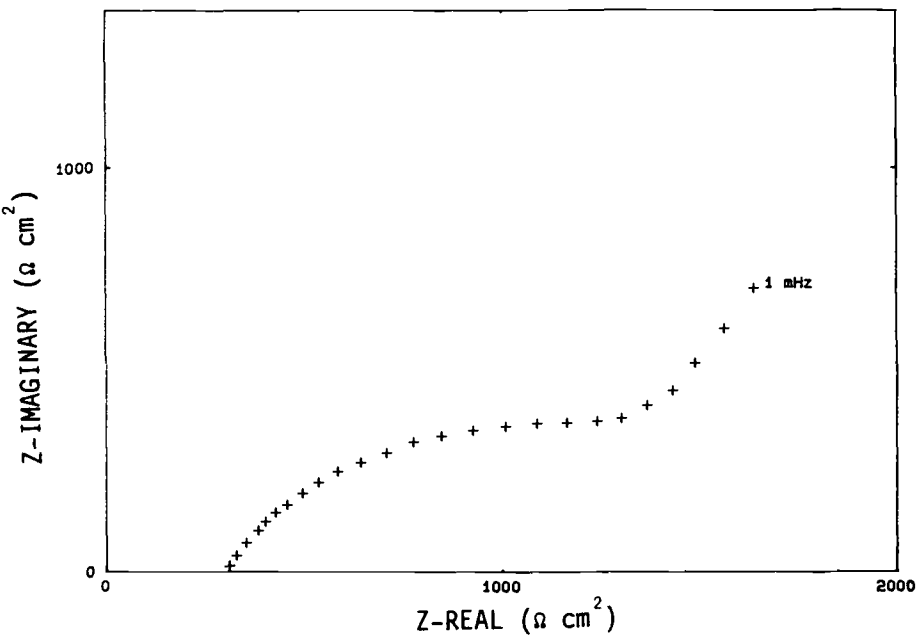

FIG. 7—*Complex plane plot for OPC specimen (5% NaCl, 20 mm cover).*

mV to −620 mV (versus SCE) had corresponding corrosion rates of up to 131 μm/yr for specimens with 20 mm depth of cover. However, for specimens with 40 mm cover, more noble potentials, −125 mV to −451 mV (versus SCE) and lower corrosion rates (up to 19.8 μm/yr) were observed. The results obtained from SRPC (Type V) specimens for the range −160 mV to −750 mV gave up to 172 μm/yr for lower cover specimens. But specimens with 40 mm cover exhibited slightly more positive potentials than −480 mV and lower corrosion rates (<22 μm/yr). The Stern-Geary constant B values for the OPC and SRPC specimens containing 2% NaCl are given in Table 3.

The results obtained from concrete specimens containing 5% NaCl in the mix were similar to those obtained from 2% NaCl specimens. The increase of salt content from 2% to 5% did not appear to make significant changes in the resistivity of the electrolyte and the corrosion behavior of the embedded steel. Electrochemical impedance results showed that for the OPC (Type I) specimens with 20 mm cover with corrosion potentials in the range −250 mV to −690 mV (verses SCE), the estimated corrosion rates ranged from 1.2 μm/yr to 270 μm/yr. The high cover (40-mm) specimens showed corrosion potentials and rates in the range −130 mV to −350 mV (versus SCE) and 1 μm/yr to 40 μm/yr, respectively. The SRPC (Type V) specimens showed lower corrosion rates than the OPC (Type I) specimens, up to 126 μm/yr and −580 mV for the low cover and up to 14.5 μm/yr and −325 mV for the high cover.

The harmonic analysis data showed that the low cover (20-mm) OPC (Type I) specimens exhibited active potentials, between −190 mV and −640 mV (versus SCE), and the estimated corrosion rates were in the range 1 μm/yr to 100 μm/yr. Whereas the high cover (40 mm) specimens showed potentials and corrosion rates in the range −150 mV to −490 mV and 1 μm/yr to 23 μm/yr, respectively. For SRPC (Type V) specimens the low cover specimens exhibited potentials in the range −190 mV to −550 mV and corrosion rates

between 1 μm/yr to 132 μm/yr, compared with potentials between −140 mV to −480 mV and corrosion rates of 1 μm/yr to 28 μm/yr for the high cover specimens. The values of Stern-Geary constant B for some OPC and SRPC specimens containing 5% NaCl are given in Table 3.

Regression Analysis

The corrosion rates obtained by electrochemical impedance and harmonic analysis and the corresponding corrosion potential were analyzed to determine if there was agreement between the two techniques. A regression analysis of the data was carried out; almost all data points falling within 95% confidence limits (large dashed lines) as shown in Figs. 8 to 11 and the resulting equations are summarized in Tables 4 and 5. Figures 8 to 11 show the corrosion rate data plotted on a logarithmic scale versus the corrosion potentials.

The ASTM criteria of half cell potential regions giving low probability, uncertain, and high probabilities of corrosion, are also shown in Figs. 8 to 11 (see ASTM C 876, Test Method for Half-Cell Potentials of Uncoated Reinforcing Steel in Concrete). The ASTM $Cu/CuSO_4$ potentials are converted to the SCE scale for comparison. This ASTM guideline was based on information from Californian bridge decks [*40*], but the present results show a linear relationship between the logarithmic values of each set of corrosion rate data and corresponding corrosion potentials, regardless of the type of cement, depth of cover, or the salt content. The ASTM criteria of a "high probability," "low probability," and "uncertain" region would therefore appear to be somewhat arbitrary.

Data obtained on different bridges by Swiss workers [*7*] suggest that plotting corrosion potentials against percent cumulative frequency can be used to distinguish "active" and "passive" regions; the actual potential regions vary from bridge to bridge depending on the exposure conditions.

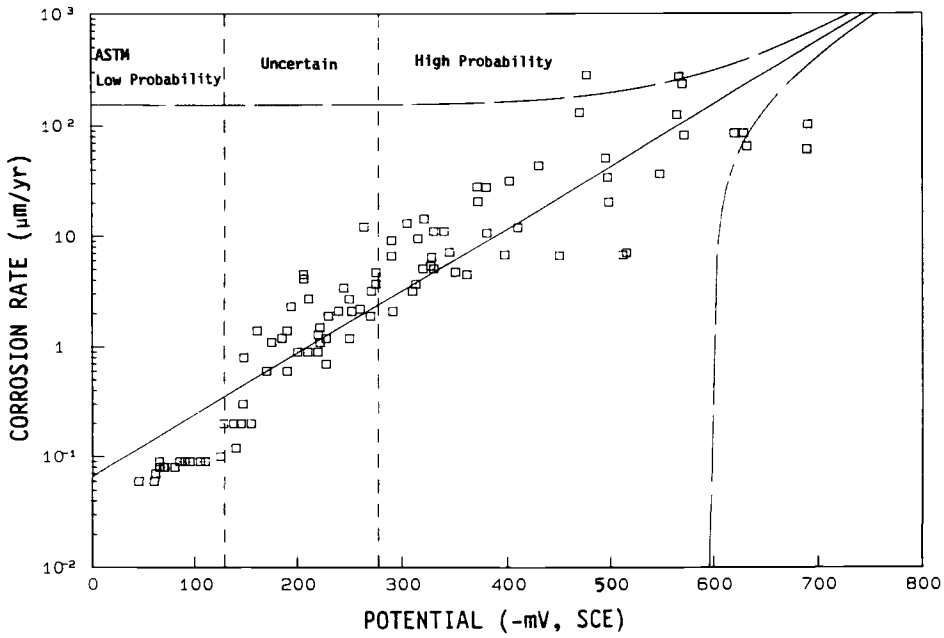

FIG. 8—*Electrochemical impedance data from all OPC specimens.*

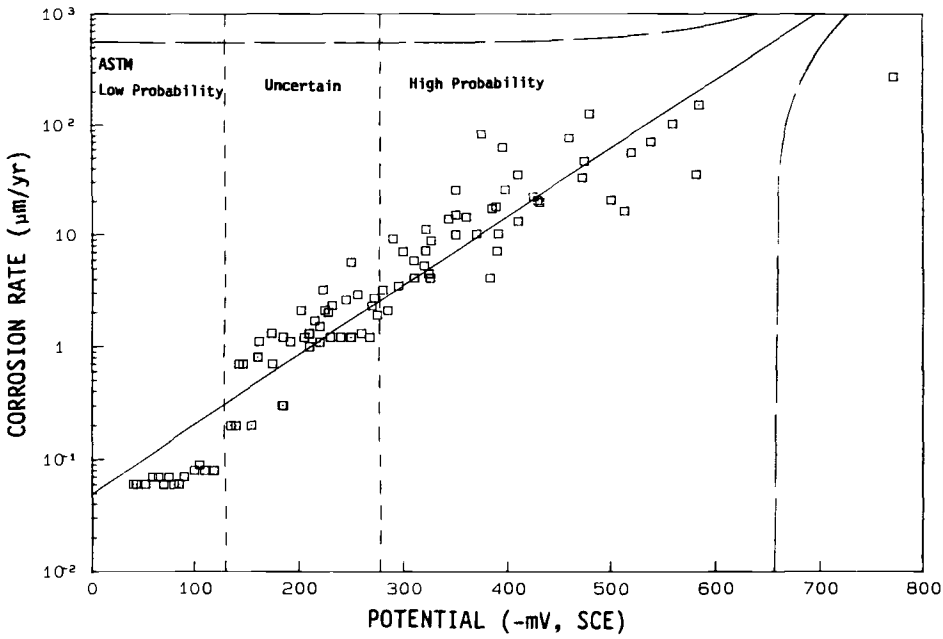

FIG. 9—*Electrochemical impedance data from all SRPC specimens.*

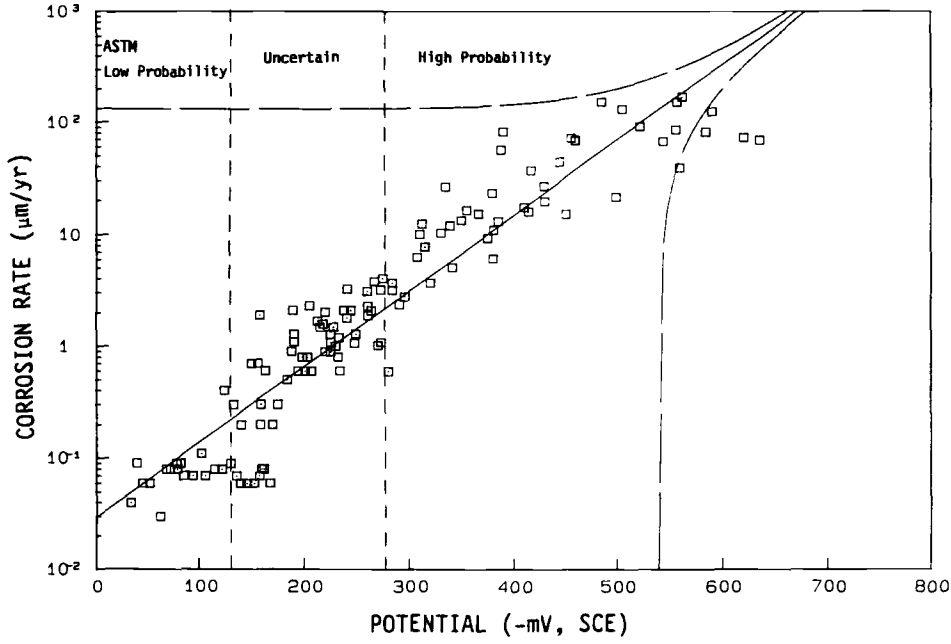

FIG. 10—*Harmonic analysis data from all OPC specimens.*

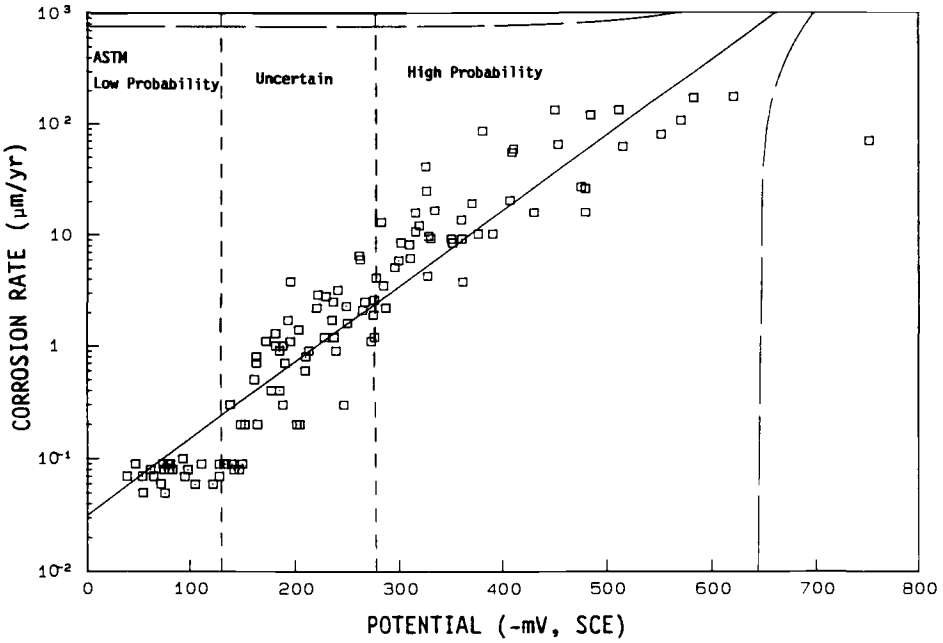

FIG. 11—*Harmonic analysis data from all SRPC specimens.*

Discussion

The results from this study demonstrate that EIS was able to discriminate between steel specimens that were essentially passive (largely capacitive with large charge transfer resistances and a large diffusion impedance), those with very active corrosion (relatively low charge transfer resistances and a low diffusion impedance), and those obvious intermediate situations. The evolution of the spectra during curing and the influence of increasing corrosion in the presence of high chloride additions and exposure diffusion illustrate

TABLE 4—*Exponential regression results from electrochemical impedance measurements.*

Specimen	Exponential Regression Equation	Correlation Coefficient
Blank-OPC	$x = 0.050e^{0.006E}$	0.78
Blank-SRPC	$x = 0.049e^{0.004E}$	0.77
2% NaCl-OPC-20 mm cover	$x = 0.028e^{0.010E}$	0.85
2% NaCl-OPC-40 mm cover	$x = 0.033e^{0.018E}$	0.88
5% NaCl-OPC-20 mm cover	$x = 0.100e^{0.011E}$	0.91
5% NaCl-OPC-40 mm cover	$x = 0.030e^{0.017E}$	0.89
2% NaCl-SRPC-20 mm cover	$x = 0.117e^{0.011E}$	0.94
2% NaCl-SRPC-40 mm cover	$x = 0.056e^{0.014E}$	0.92
5% NaCl-SRPC-20 mm cover	$x = 0.146e^{0.013E}$	0.92
5% NaCl-SRPC-40 mm cover	$x = 0.085e^{0.013E}$	0.91
All-OPC	$x = 0.066e^{0.013E}$	0.92
All-SRPC	$x = 0.049e^{0.014E}$	0.94

x = corrosion rate (μm/yr), E = corrosion potential (mV).

TABLE 5—*Exponential regression results from harmonic analysis measurements.*

Specimen	Exponential Regression Equation	Correlation Coefficient
Blank-OPC	$x = 0.063e^{0.011E}$	0.17
Blank-SRPC	$x = 0.065e^{0.002E}$	0.31
2% NaCl-OPC-20 mm cover	$x = 0.082e^{0.013E}$	0.91
2% NaCl-OPC-40 mm cover	$x = 0.050e^{0.014E}$	0.92
5% NaCl-OPC-20 mm cover	$x = 0.110e^{0.013E}$	0.91
5% NaCl-OPC-40 mm cover	$x = 0.092e^{0.013E}$	0.90
2% NaCl-SRPC-20 mm cover	$x = 0.072e^{0.012E}$	0.88
2% NaCl-SRPC-40 mm cover	$x = 0.053e^{0.014E}$	0.88
5% NaCl-SRPC-20 mm cover	$x = 0.058e^{0.015E}$	0.90
5% NaCl-SRPC-40 mm cover	$x = 0.096e^{0.013E}$	0.89
All-OPC	$x = 0.029e^{0.016E}$	0.92
All-SRPC	$x = 0.031e^{0.016E}$	0.94

x = corrosion rate (μm/yr), E = corrosion potential (mV).

this mechanistic approach. The basic corrosion model can be represented by a relatively simple equivalent circuit as shown in Fig. 2*a* or 2*c*. In some corrosion cases a clearly defined charge transfer and diffusion process was observed (Fig. 7). However, in other cases the plots were of a very flattened appearance (Fig. 6), indicating considerable time constant dispersion, probably as a result of the localized nature of the corrosion attack.

The results also highlight the major problem with the use of EIS in that evaluating the corrosion rate is often difficult and sometimes impossible, a point also made by Andrade et al. [*17*]. The use of harmonic analysis provides a simple and practical means of obtaining corrosion rate information [*39*]. The frequency range of measurement must be selected to correspond to the charge transfer region (in the present work this was 100 mHz, 200 mHz, and 300 mHz for the fundamental and harmonics). This is comparable to the time domain measurement of a few seconds used by Newton and Sykes [*15*] and up to eight seconds employed by Elsener et al. [*7*] in their galvanostatic pulse determinations. It is also the probable reason why so called "polarization resistance" measurements have been reasonably successful for corrosion monitoring of steel in concrete [*8,25,26*]; the linear polarization resistance instrumentation essentially takes the measurements over a few seconds and evaluates the charge transfer resistance.

A major advantage of harmonic analysis is the determination of both the Tafel constants and Stern-Geary B values. In the present work a mean B value of 20 mV was obtained from the harmonic analysis. This compares with 26 mV given by Andrade [*25,26*] for linear polarization type measurements on active specimens and 35 mV by Wenger from impedance [*27*], but is lower than the 52 mV [*25,26*] for passive steel or the 50 mV recommended by the Concrete Society [*24*]. Literature values of B [*41*] for steel in seawater and chloride solutions (neutral, acidic, and alkaline) are 20 ± 9 mV and 22 ± 10 mV, respectively, but increase to 38 ± 29 mV and 43 ± 19 mV for inhibited waters and tap water as the steel becomes passive.

The results from this study showed that the electrochemical response of the blank (chloride free) specimens that developed during curing was that of a passive surface. This is largely capacitive and the complex plane impedance does not return to the resistive (real) axis at low frequencies, i.e., the charge transfer resistance (R_{ct}) and diffusion is very large, hence the corrosion rate is extremely low even when exposed to chloride-containing environments. Concrete specimens containing chloride in the original mix exhibited a nonpassive behavior during continued exposure with lower charge transfer resistances and

higher corrosion rates. The corrosion rates obtained from specimens with 20 mm concrete cover were found to be significantly higher than those obtained from specimens with 40 mm cover. This was presumably due to the presence of higher concentrations of chloride ions at the steel from the immersion solution because of the low cover.

The sodium chloride added to the mix had an obvious effect on the corrosion process in that the observed potentials were more negative with increased chloride content. However, during the initial exposure period the corrosion rates were low, the system being virtually passive suggesting that the initiation of corrosion was a slow process. This may be due to the fact that most of the chloride added to the mix is "bound" into the solid cement structure and not free to cause film breakdown on the steel. Ingress of chloride from the immersion solution resulted in higher corrosion rates.

There was no significant difference in performance between SRPC (Type V) and OPC (Type I) specimens despite the difference in the tricalcium aluminate (C_3A) content, 3% C_3A, and 11% C_3A, respectively. Of course the lower the C_3A content, the lower the chloride binding capacity of the cement. The lack of difference in performance may be attributed to the high levels of chloride added to the concrete mix which were enough to react with most of the C_3A, if not all, to form a solid compound of tricalcium chloroaluminate.

Conclusions

(1) EIS of steel in concrete can demonstrate the presence of a passive type film on the steel by the capacitive response. Specimens exhibiting chloride-induced attack have distinct charge transfer resistances and in some cases adsorption or a diffusion component, or both, may also be observed.

(2) Electrochemical techniques can provide information on the corrosion rate at the time of the measurement. However, it is not always easy to obtain an estimate of the charge transfer resistance from electrochemical impedance data particularly when the system is essentially passive.

(3) Harmonic analysis was found to be a practical and rapid technique for corrosion rate determination. It had the advantage over electrochemical impedance in that it could measure the corrosion rate and the apparent Tafel slopes from each measurement.

(4) The Stern-Geary constant or B value obtained from harmonic analysis was 20 mV.

(5) A regression analysis showed that there is a logarithmic relationship between corrosion rates as measured by electrochemical impedance or harmonic analysis, or both, and the corrosion potential of steel embedded in the concrete.

(6) The research showed that distinct regions of probability of corrosion, as determined by potential measurements and given in ASTM C 876, could not be detected.

(7) The results obtained from all electrochemical measurements on steel electrodes embedded in concrete specimens made with ordinary portland cement (Type I) and sulphate resisting portland cement (Type V), with the addition of 2% and 5% NaCl to the mix, showed that increasing the depth of cover from 20 mm to 40 mm had a significant effect on reducing the corrosion rate of embedded electrodes within the test time interval used. This may be attributed to the later arrival of the chloride from the test solution.

References

[1] Kupfer, H., Hilsdore, J., and Rusch, H., *Journal of American Concrete Institute*, No. 66, August 1969.

[2] Slater, J. E., *Corrosion of Metals in Association with Concrete, ASTM STP 818*, American Society for Testing and Materials, Philadelphia, 1983.
[3] Page, C. L. and Treadaway, K. W. J., *Nature*, Vol. 297, 1982, p. 109.
[4] Cavalier, P. G. and Vassie, P. R., *Proceedings of Institution of Civil Engineers* U.K., Vol. 70, 1981, p. 461.
[5] Glass, G. K., Page, C. L., and Short, N. R., *UK Corrosion '88*, Brighton, U.K., October 3-5, 1988.
[6] *Corrosion Rates of Steel in Concrete, ASTM STP 1065*, N. S. Berke, V. Chaker, and D. Whiting, Eds., American Society for Testing and Materials, Philadelphia, 1990.
[7] Elsener, B., Muller, S., Suter, M., and Bohni, H., "Corrosion Monitoring of Steel in Concrete: Theory and Practice," *Corrosion of Reinforcement in Concrete*, C. L. Page, K. W. J. Treadaway, and P. B. Bamforth, Eds., Elsevier Applied Science, London, New York, 1990, p. 348.
[8] Dawson, J. L., John, D. G., Jafar, M. I., Hladky, K., and Sherwood, L., "Electrochemical Methods for the Inspection and Monitoring of Corrosion of Reinforcing Steel in Concrete," C. L. Page, K. W. J. Treadaway, and P. B. Bamforth, Eds., Elsevier Applied Science, London, New York, 1990, p. 358.
[9] Dawson, J. L., Callow, L. M., Hladky, K., and Richardson, J. A., *Corrosion '79*, Houston, TX, Paper No. 125, National Association of Corrosion Engineers, 1979.
[10] Dawson, J. L. and Langford, P. E., "The Electrochemistry of Steel Corrosion in Concrete Compared to Its Response in Pore Solution," *The Use of Synthetic Environments for Corrosion Testing, ASTM STP 970*, P. E. Francis and T. S. Lee, Eds., American Society for Testing and Materials, Philadelphia, 1988, pp. 264–273.
[11] John, D. G., Searson, P. C., and Dawson, J. L., *British Corrosion Journal*, Vol. 16, 1981, p. 102.
[12] Wenger, F. and Galland, J., "Application of Electrochemical Impedance Measurements to the Monitoring of Corrosion in Reinforced Concrete Structures in Marine Environments," *Proceedings of EUROCORR '87*, Karlsruhe, W. Germany, April 1987.
[13] John, D. G., Cooke, A. T., Treadaway, W. J., and Dawson, J. L., "Repairs of Concrete—A Laboratory and Exposure Site Investigation," *Corrosion of Reinforcement in Concrete Construction*, A. P. Crane, Ed., Ellis Horwood Ltd., Chichester, England, 1983, p. 263.
[14] Wenger, F., Thesis published in *Metaux, Corrosion, Industrie*, Vols. 742, 745, and 746 (1987).
[15] Newton, C. J. and Sykes, J. A., *Corrosion Science*, Vol. 28, 1988, p. 1051.
[16] Feleu, S., Gonzales, J. A., and Andrade, C., *Corrosion Science*, Vol. 26, 1986, pp. 961–970.
[17] Andrade, C., Alonso, C., and Gonzalez, J. A., *Materials Science Forum*, Vols. 44 and 45, 1989, pp. 329–336.
[18] Noggerath, J. and Bohni, H., *Materials Science Forum*, Vols. 44 and 45, 1989, pp. 357–374.
[19] Stern, M. and Geary, A. L., *Journal of Electrochemical Society*, Vol. 104, 1957, p. 56.
[20] Haruyama, S. and Tsuru, T., "A Corrosion Monitor Based on Impedance Method," *Electrochemical Corrosion Testing, ASTM STP 727*, F. Mansfeld and U. Bertocci, Eds., American Society for Testing and Materials, Philadelphia, 1981, p. 167.
[21] Epelboin, I., Gabrielli, C., Keddam, M., and Takenouti, H., "Alternating-Current Impedance Measurements Applied to Corrosion Studies and Corrosion Rate Determination," *Electrochemical Corrosion Testing, ASTM STP 727*, F. Mansfeld and U. Bertocci, Eds., American Society for Testing and Materials, Philadelphia 1981, p. 150.
[22] Bockris, J. O'M., Drazic, D., and Despic, A. R., *Electrochimica Acta*, Vol. 4, 1961, pp. 325–361.
[23] Bockris, J. O'M. and Reddy, A. K. N., *Modern Electrochemistry*, Vol. 2, Plenum Press, New York, 1970.
[24] Concrete Society Technical Report No. 36, U.K., 1989.
[25] Andrade, C. and Gonzalez, J. A., *Werkstoffe and Korrosion*, Vol. 29, 1978, p. 515.
[26] Gonzalez, J. A. and Andrade, C., *British Corrosion Journal*, Vol. 17, 1982, p. 21.
[27] Wenger, F. and Galland, J., *Materials Science Forum*, Vols. 44 and 45, 1989, pp. 375–386.
[28] Smith, D. C., *Electroanalytic Chemistry*, Vol. 1, M. Dekker, New York, 1969.
[29] Rangarajan, S. K., *Journal of Electroanalytical Chemistry*, Vol. 62, 1975, p. 31.
[30] Rao, G. P. and Mishra, A. K., *Journal of Electroanalytical Chemistry*, Vol. 77, 1977, p. 276.
[31] Bertocci, U., *Corrosion*, Vol. 35, 1979, p. 211.
[32] Bertocci, U. and Mullen, J. L., "Effect of Large Voltage Modulations on Electrodes Under Charge - Transfer Control," *Electrochemical Corrosion Testing, ASTM STP 727*, F. Mansfeld and U. Bertocci, Eds., American Society of Testing and Materials, Philadelphia, 1981, p. 365.
[33] Lawson, K., Ph.D. thesis, UMIST, Manchester, U.K., 1989.
[34] Meszaros, L., *Figyelo Korrosios*, Vol. 21, No. 2, 1981, p. 30.

[35] Devay, J. and Meszaros, L., *Acta Chimica Academy of Science Himary*, Vol. 104, No. 13, 1980, p. 311.
[36] Gill, J. S., Callow, L. M., and Scantlebury, J. D., *Corrosion*, No. 29, 1983, p. 31.
[37] Xu, N., Dawson, J. L., Thompson, G. E., and Wood, G. C., *Journal of Chinese Society of Corrosion and Protection*, Vol. 4, 1984, pp. 159–167.
[38] McKubre, M. C. H. and Syrett, B. C., "Harmonic Impedance Spectroscopy for the Determination of Corrosion Rates in Cathodically Protected Systems," *Corrosion Monitoring in Industrial Plants Using Nondestructive Testing and Electrochemical Methods, ASTM STP 908*, G. C. Moran and P. Labine, Eds., American Society for Testing and Materials, Philadelphia, 1986, p. 433.
[39] Lawson, K. and Scantlebury, J. D., *Materials Science Forum*, Vols. 44 and 45, 1989, pp. 387–402.
[40] Stratfull, R. F., *Corrosion*, Vol. 13, 1957, p. 173.
[41] Graner, R., Moreland, P. J., and Pini, G., *A Literature Review of Polarisation Resistance Constant (B) Values for the Measurement of Corrosion Rate*, National Association of Corrosion Engineers, Houston, TX, 1982.

Coatings on Metals

Martin W. Kendig,[1] *S. Jeanjaquet,*[1] *and J. Lumsden*[1]

Electrochemical Impedance of Coated Metal Undergoing Loss of Adhesion

REFERENCE: Kendig, M. W., Jeanjaquet, S., and Lumsden, J., **"Electrochemical Impedance of Coated Metal Undergoing Loss of Adhesion,"** *Electrochemical Impedance: Analysis and Interpretation, ASTM STP 1188,* J. R. Scully, D. C. Silverman, and M. W. Kendig, Eds., American Society for Testing and Materials, Philadelphia, 1993, pp. 407–427.

ABSTRACT: A critical analysis of the concepts used to correlate parameters determined from electrochemical impedance spectra to the evaluation of the loss of adhesion of an organic coating from steel is made. In particular, the breakpoint method is called into question based on a theoretical analysis of the double layer capacitance of the coating/metal interface. A model for a coating undergoing disbonding about a macroscopic defect is described. The impedance of a fusion-bonded epoxy (FBE) pipeline coating about a large defect is considered in light of this model. The observations approach characteristics predicted by the model.

KEYWORDS: organic coatings, polymer, fusion-bonded epoxy (FBE), pipeline, breakpoint frequency, capacitance, cathodic disbonding

Numerous authorities have stated that the corrosion protection of metal substrates by organic films may result less from the barrier properties of the coating and more with the maintenance of a good adhesive bond under the chemical and electrochemical conditions imposed by the environment. Mayne, for example, has pointed out that the transmission of water and oxygen through organic films far exceeds that required to maintain corrosion rates typically observed for bare metal [*1*]. Others have also attested to the concept that mass transport of corrodents through the coating is only secondary in defining the protective role of the coating [*2,3*]. Adhesion of the coating so as to block ionic paths between local cathodes and anodes most likely presents one of the most important roles of organic coatings in providing corrosion protection.

Background

Intuitively, electrochemical impedance spectroscopy (EIS) provides a measure of the resistance of the film to ionic and aqueous transport. There is quite general agreement on the equivalent circuit model for organic coatings. However, the interpretation of the meaning of the elements remains a subject of some debate. Much discussion has focused on the relationship of the coating resistance (often referred to as R_{po}) to the loss of adhesion [*4*]. This theory seems to rely on the assumption that the ohmic element representing the resistance to charge transport across the coating, R_{po}, contributes to the impedance of the test specimen only where disbonding has occurred, being nearly infinite elsewhere. A recent analysis [*5*] using data previously presented [*6*] suggests that this

[1]Technical staff member, senior technical specialist, and technical staff member, respectively, Rockwell International Science Center, Thousand Oaks, CA 91360.

model is generally not correct. This is illustrated in Fig. 1 which shows the time dependence of R_{po} for polybutadiene on steel pretreated in different ways, and for a free-film that represents by experimental design a 100% disbonded film. Extrapolating to zero time R_{po} for all of the coatings show values within a factor of three of 1 MΩ (ca 10^7 Ω cm^2) (see Fig. 1). This corresponds to an apparent bulk resistivity for the coating that is several orders of magnitude below that for a typical organic polymer. Hence, R_{po} is governed by defects in the film even at initial times. The coatings on the substrates show varying decreases in R_{po} while the completely disbonded or free-film shows no drop in R_{po}. R_{po} remains more or less constant and high for the 100% disbonded coating while R_{po} for the films on the steel substrates decreases with exposure time. It is very difficult then to attribute the decrease in R_{po} (or an increase in the frequency, f_b that is proportional to the inverse product of the nearly invariant coating capacitance, C_c, and R_{po}) to a loss in adhesion. A logical conclusion is that the polymeric coating on a substrate becomes more transparent to ionic transport either as a result of chemical degradation associated with corrosion, or more likely by expanding the pre-existing macroscopic defects due to tensile stresses produced by growing corrosion product. This mechanism is summarized by the schematic in Fig. 2 [7]. Of course, it must be recognized that the electrical properties of a free-film may or may not mimic a disbond on a coating where electro-osmosis, osmosis, and the buildup of corrosion products could locally alter R_{po} of the coating. Quantification of such effects on R_{po} is not available. Until such data become available, the free-film data in Fig. 1 cast doubt on, but do not disprove, the hypothesis embraced by many that R_{po} relates directly to disbonding.

The assumption that the impedance of the coating/metal interface is comparable to that of the coating capacitance except when disbonding occurs is also questionable in light of basic double layer theory and experimental permeation data from a paper by Ruggeri and Beck [8], which allow a rough estimation of the impedance of the coating/metal interface in the absence of disbonding or any interfacial charge transport reactions. Accordingly, the impedance of this interface would be that of the double layer at the coating/metal interface and is in series with the coating impedance as shown in Fig. 4*a*. According to an extension of the Debye-Huckel theory, the reciprocal length x of the diffuse double layer produced by the coating/metal interface relates to the concentration of ionic species, c_j of charge z_j and the relative dielectric constant of the medium ϵ according to the equation

$$x = \{(4\pi/(\epsilon\epsilon_0 RT))\Sigma[z_j c_j]\}^{1/2} \tag{1}$$

where ϵ_0 is the dielectric constant of free space. The capacitance of the diffuse double layer, C_d^o is then

$$C_d^o = \epsilon\epsilon_j x/4\pi \tag{2}$$

For the purposes of an estimation of C_d^o for the coating/metal interface, recognize that

$$C_d^o \propto (\epsilon C)^{1/2} \tag{3}$$

where ϵ and C are the dielectric constant of the coating and the ionic concentration in the coating, respectively. A typical estimate of the latter can be obtained from the work of Ruggeri and Beck [8] as 10^{-4} M for a polyurethane coating equilibrated with a 0.1 M NaCl and the dielectric constant for polymeric resins is quite near to 2.5 [9]. Assuming the double layer capacitance for metals in aqueous 0.5 M NaCl (ϵ = 80) is about 20 μF/cm^2,

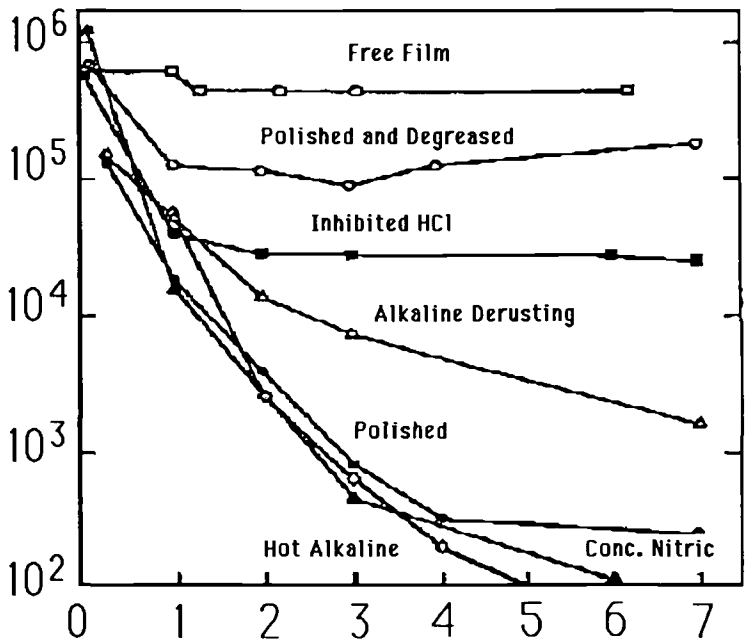

FIG. 1—*Time dependence for a polybutadiene coating on steel having different pretreatments, and for a free film. The specimens had an exposed area of 20 cm² and were exposed to 0.5 M NaCl.*

then C_d^o can be estimated as 0.050 μF/cm². Depending on the thickness of the coating, the impedance of this capacitive element would be one to two orders of magnitude below that for the coating (which is to say $C_d^o \gg C_c$). Note that there is no need to consider the Helmholz layer since the diffuse double layer is sufficiently large due to the low ionic concentration and dielectric constant of the coating.

The impedance magnitude and phase spectra presented in Figs. 3*a* and *b* were calculated using the value of 0.050 μF/cm² for the metal/coating capacitance, C_d^o and a value of 0.11 nF/cm² for the coating capacitance, C_c (the value for a 20-μm coating of a material with a relative dielectric constant, ϵ, of 2.5), and the model in Fig. 4*a*. Clearly, a breakpoint frequency f_b, where the negative phase equals 45°, exists without an assumption of disbonding. Only if the impedance of the interface becomes comparable or high relative to the coating, the case for $C_d^o <$ or comparable to C_c, does f_b disappear as shown in the spectra of Figs. 3*c* and *d*. This is usually not the case, and, therefore, f_b will in general be observed. However, f_b does not necessarily relate to disbonding, but rather its increase relates to a decrease in R_{po}. The important point of these considerations is that disbonding is not required for C_d^o to become much higher than C_c or for R_{po} to decrease, the result of which will be an increase in f_b. Hence, the dependence of R_{po} on disbonding is not general, and its persistent use as a measure of corrosion-induced disbonding may lead to erroneous conclusions. While a high f_b certainly provides a very useful measure of coating degradation, it must by no means be associated only with a loss of adhesion.

This paper proposes a general model for the impedance of a coating undergoing adhesion loss. However, the main experimental focus will be on a special case where disbond-

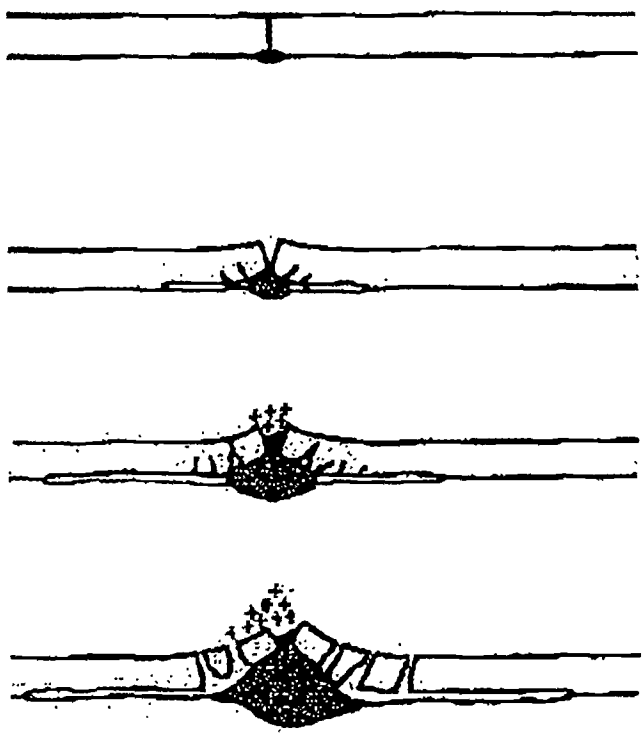

FIG. 2—*Schematic of the coating degradation process.*

ing propagates away from a large coating defect. For this case the breakpoint, f_b, is at a frequency well above that for which we have experimental access. We use here an extension of the general model to interpret our data.

Theoretical Model

The circuit schematics presented in Fig. 4 represent the evolution of the impedance of an organic film immersed in a corrosive environment and undergoing disbonding. For no disbonding the resistance associated with the coating (possibly associated with ionic transport at defects or regions of low cross-linking [*10*]) shorts the coating capacitance C_c. The $R_{po}C_c$ network defining the coating impedance is in series with the capacitance C_d^o representing the capacitance of the diffuse double layer at the coating/metal interface as described in the previous section. No resistor representing faradaic charge transport shorts C_d^o for this case (Fig. 4*a*).

Once disbonding commences, the interface undergoes hydration and corrosion starts. C_d^o increases to C_d, the double layer capacitance for an aqueous environment and corrosion initiates. The faradaic charge transfer reaction associated with corrosion gives rise to a finite corrosion resistance R_c in parallel with C_d (Fig. 4*b*). If this site is highly localized, which it most certainly is for most coatings, then cathodic disbonding will proceed away from the more anodic defect. The result may be modeled by a transmission line as shown in Fig. 4*c*. When that (the ohmic resistance under the film represented by $\{R_{si}\}$) becomes sufficiently small, the elements of the transmission line can be lumped to give the model

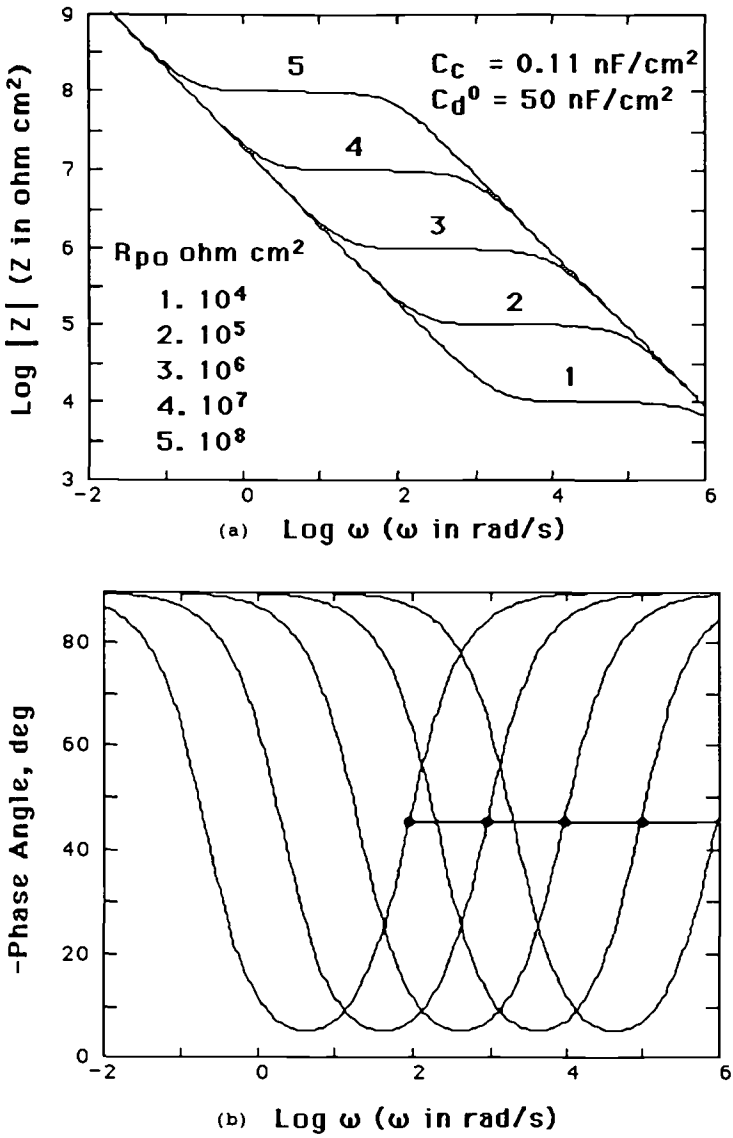

FIG. 3—*Calculated impedance spectra. I.* C_c = *0.11 nF/cm² and* C_d^o = *50 nF/cm², (a) magnitude and* (b) −*phase versus log of the frequency in radians/s. II.* C_c = *0.11 nF/cm² and* C_d^o = *0.11 nF/cm², (c) magnitude and* (d) −*phase versus log of the frequency in radians/s.*

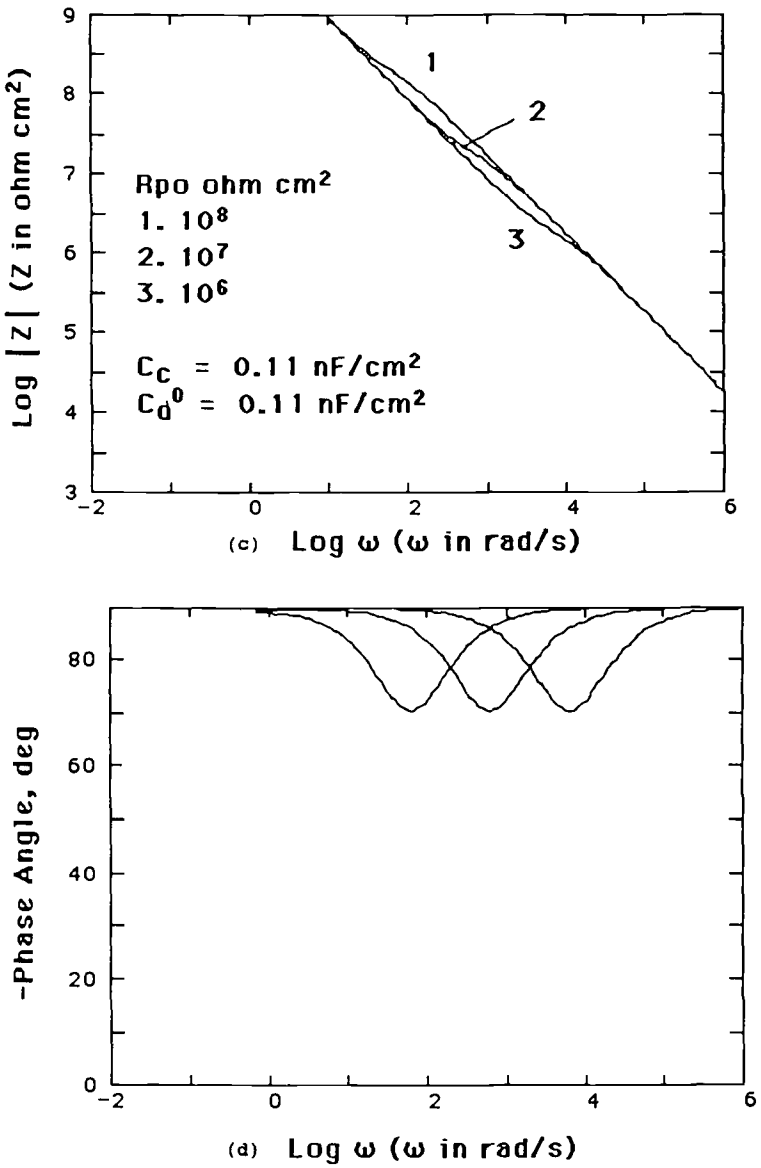

FIG. 3—(continued)

shown in Fig. 4*d*. The case of Fig. 4*d* was assumed by J. D. Kellner for his analysis of the cathodic disbonding of tape coatings from pipe line steel [*11*].

Two limiting cases can be considered. If $\{R_{si}\}$ remains high, then the impedance spectra at low frequencies reach a limiting value with increased disbonding (increased N of the model) and the maximum in the negative of the phase angle remains less than 45°. This is illustrated in Figs. 4*e* and *f*. On the other hand, the negative of the phase angle will remain

above 45° and close to 90° for sufficiently low values of $\{R_{si}\}$, and the impedance at low frequencies will scale with the area disbonded as shown in Figs. 4*g* and *h*.

This work will focus on the special case where R_{po} is relatively small, the case where a macroscopic defect exists in the coating. For this case only the impedance represented by the metal at the disbonding is considered. The two aforementioned important cases can be considered. In one case, $\{R_{si}\}$ is relatively small due to a large gap in the disbond zone. For the second case, $\{R_{si}\}$ is relatively large due to a small gap defining the disbond. These two cases have great significance for efficient cathodic protection of pipe around holidays undergoing disbonding. In the case where $\{R_{si}\}$ is large, the ohmic resistance can effectively shield the region in the disbond, whereas if $\{R_{si}\}$ is small, the cathodic potential sufficiently extends down the crevice formed by the disbond.

Experimental

Scotch Kote® 206N Slow FBE coatings on sand and grit-blasted (the standard surface preparation) carbon steel 1-cm by 2.7-cm billets of varying length were obtained from 3M (P.O. Box 2963, Austin, TX 45572). The coatings were nominally 350 μm thick as determined by a magnetic thickness tester (Checkline Coating Thickness Tester, Electromatic Equipment Co., Cedarhurst, NY). The coatings were cured at 450° F. A 0.6-cm-diameter hole was placed through the coating to the substrate by a flat mill to minimize damage to

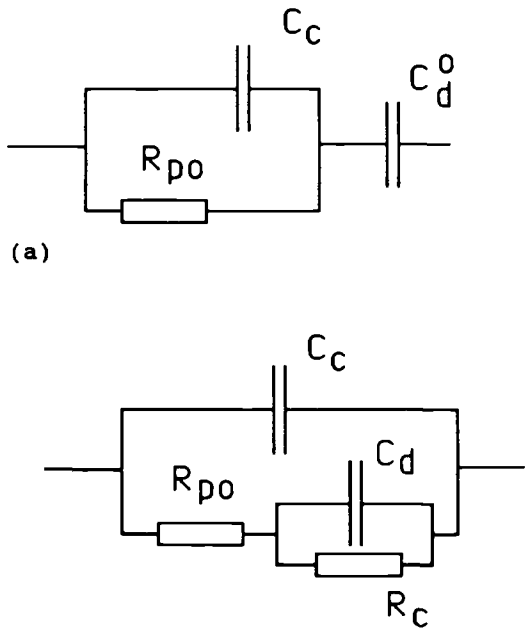

FIG. 4—*Equivalent circuit schematics for an organic coating:* (a) *Adhering coating before commencement of corrosion.* (b) *Adhering coating with the initiation of corrosion.* (c) *Coating with a disbond.* (d) *Coating with a disbond and virtually zero values for* $\{R_{si}\}$. (e) *Calculated magnitude and* (f) *phase spectra using the model of* 4c *for high* $\{R_{si}\}$. (g) *Calculated magnitude and* (h) *phase spectra for the model of* 4c *using low values of* $\{R_{si}\}$.

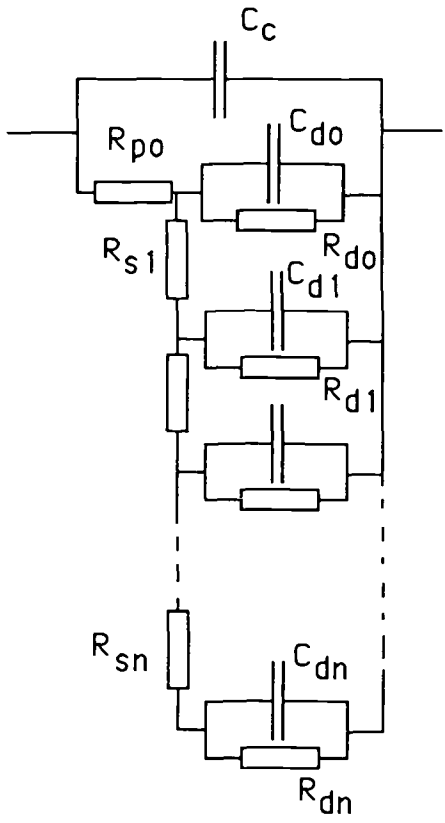

(c)

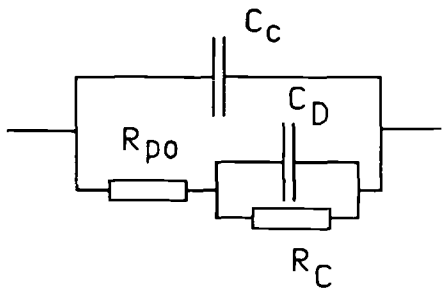

$C_D = \Sigma C_{di}$

$1/R_D = \Sigma 1/R_{di}$

(d)

FIG. 4—(continued)

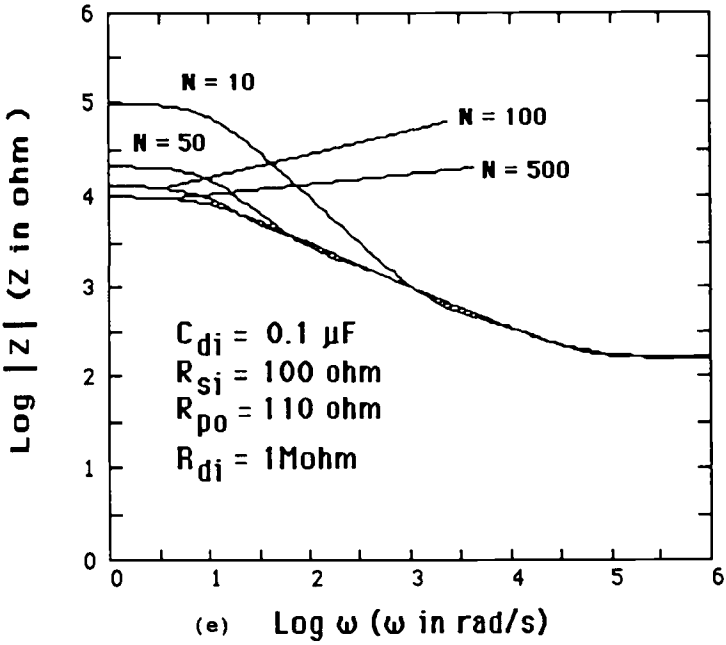

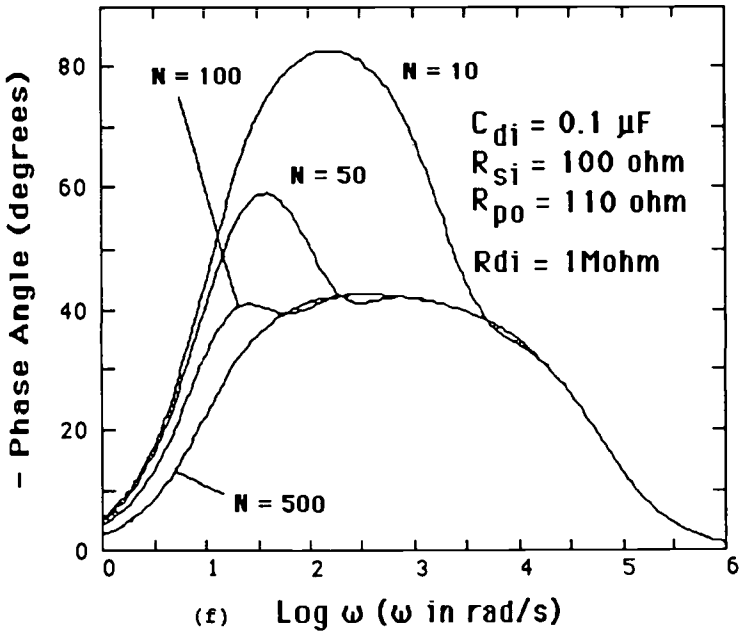

FIG. 4—(continued)

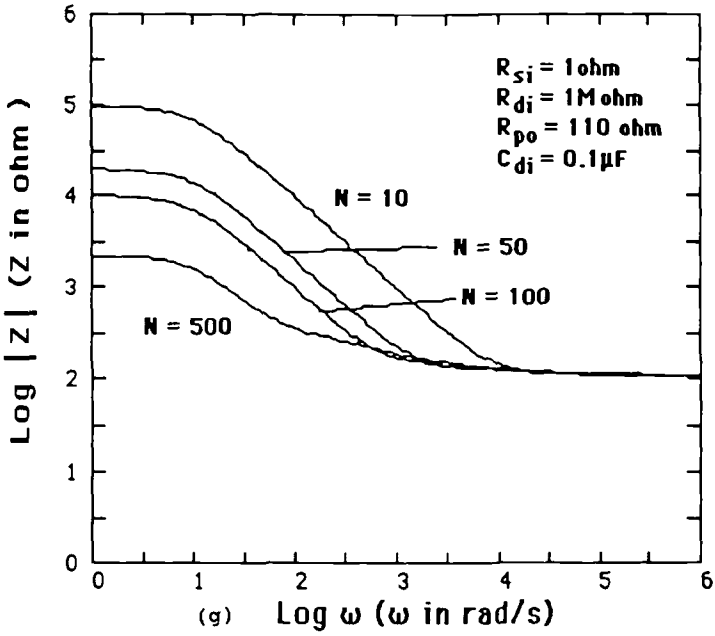

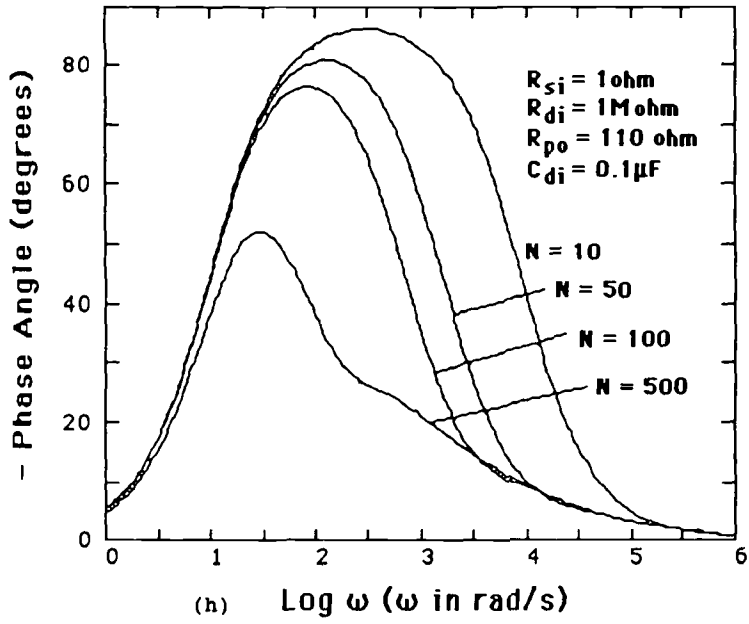

FIG. 4—(continued)

the substrate. One specimen was prepared using a substrate cleaned in a standard fashion while the second specimen was contaminated with a solution of 3% NaCl which was applied to the cleaned surface and allowed to dry before applying the FBE.

A 6-cm-length of each specimen was placed in a solution that remained open to the air. The solution contained 1% by weight of each of the following: Na_2SO_4, Na_2CO_3, and NaCl. The impedance of the defective coating was measured after a few minutes immersion and was then subjected to a cathodic polarization of -1.440 mV versus SCE using the PAR Model 173 Potentiostat. The impedance measurement used the potentiostat and a Solartron 1170 Frequency Response Analyzer controlled by a HP 9825 desktop computer. The impedance was measured using a ± 10 mV peak to peak sign wave modulation between 10^4 and 30 mHz. The apparatus and approach for making the measurement has been described elsewhere [*12*]. For subsequent evaluations of the impedance, the cathodic polarization was removed from the specimens momentarily before making the impedance measurement. The potential dropped rapidly to a more or less steady value within a minute of removing the cathodic polarization. This was the potential chosen for the impedance measurement which was then taken immediately. Following the impedance measurement the polarization at -1.440 V was reapplied immediately. After 72 to 96 h of this exposure, the specimens were disconnected from the potentiostat and removed from the solution. Radial scribes were made away from the defect and, where possible, the coating was pulled from the substrate; the substrate was then examined microscopically to evaluate the extent of cathodic disbonding.

Since the defect determined the impedance, there is no clear justification for normalizing the data to any particular area although the total area of the exposed specimen was 47 cm^2 and the defect was 0.3 cm^2.

Results

Figures 5*a* and *b* show the results of the log impedance magnitude spectra for the respective chloride-contaminated specimen and the specimen having the standard surface preparation. Some nonsteady state effects for the initial zero hour sample at the lower frequencies (below about 1 Hz or 6.28 rad/s) may occur. Above this frequency the data at zero hours have more meaning. For the contaminated specimen, the spectra revert to a constant pattern after about 1 h while the specimen treated with the standard surface preparation shows a somewhat more gradual decrease in impedance with cathodic polarization time. The important feature for both of these curves is the change from a -0.8 slope of log Z versus log ω slope to a slope approaching -0.5. This is more easily seen in the negative phase angle dependence (Figs. 6*a* and *b*) which decreases with exposure and cathodic polarization from a maximum of about 75° to between 50 and 55° for the specimen with a standard preparation, and between 40 and 55° for the contaminated specimen. Note that, as expected, no change in the high-frequency impedance occurs. R_{po} for this case remains at about 18 to 20 Ω and is not influenced by the treatment. Note that f_b for this coating is well above those frequencies for which there is experimental access and, hence, is consistent with the very large defect.

The data in Figs. 5 through 6 fit a very simple single time constant model

$$Z = R_{po} + R_{\text{corr}}/(1 + (j\omega\tau)^{\alpha}) \tag{4}$$

where $\tau = R_{\text{corr}} * C_{\text{eff}}$. C_{eff} is not necessarily a double layer capacitance, but rather an effective capacitance as defined by the equation. Alpha (α) is a parameter that ranges between approximately 0.5 and 1. The results of the experimental fit of the data in Figs. 5

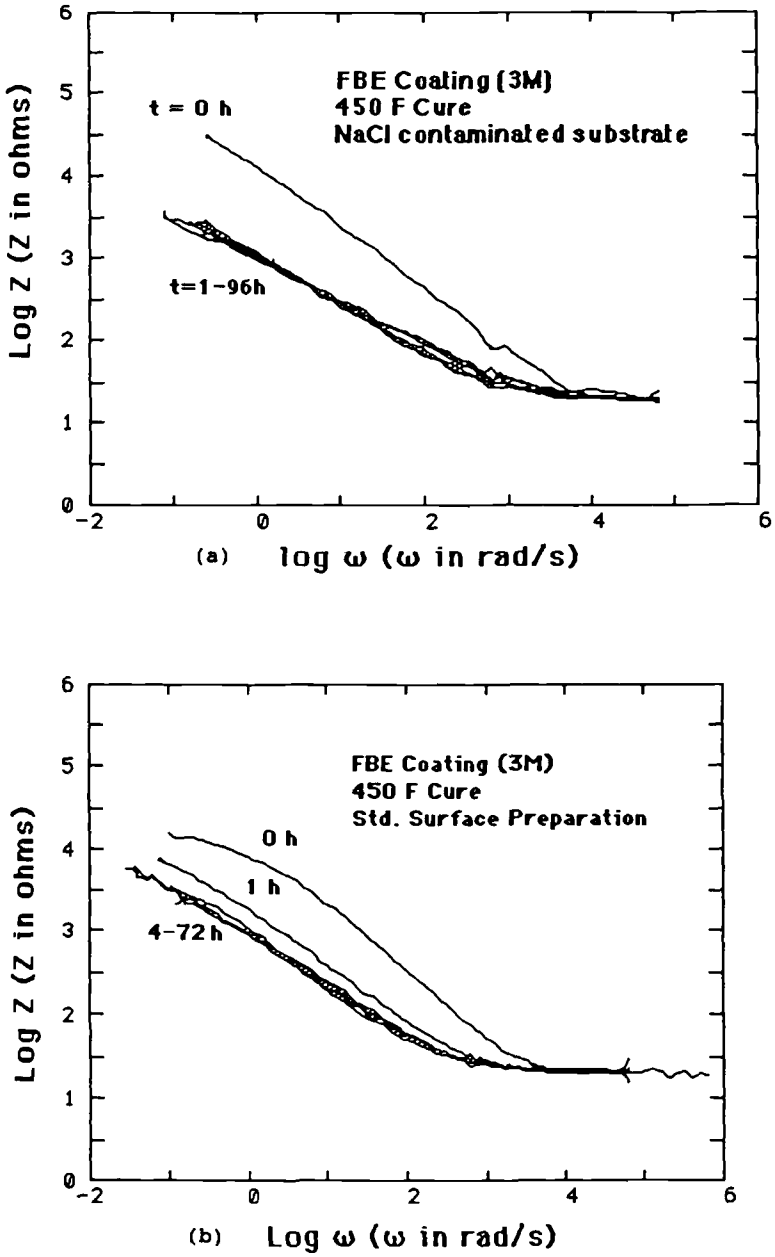

FIG. 5—*Log impedance magnitude versus log of the frequency in radians/s for an FBE coating on* (a) *an NaCl-contaminated surface, and on* (b) *a surface prepared by standard methods. Specimens were exposed to an aqueous solution 1% by weight in each of sodium chloride, sodium carbonate, and sodium sulfate at a potential of −1.440 V versus SCE. The cathodic polarization was removed for the impedance measurement.*

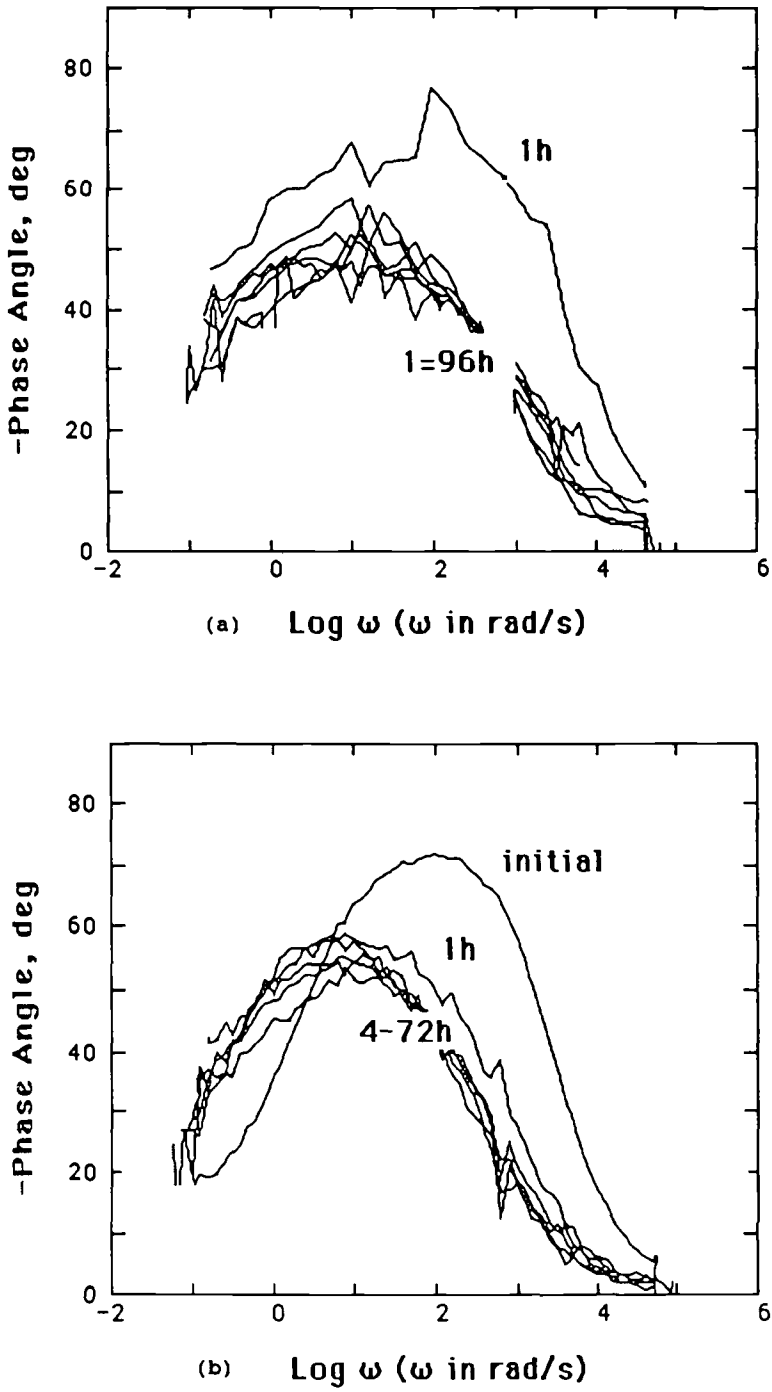

FIG. 6—*Phase angle spectra for the specimens if Figs.* 5a *and* b, *respectively.*

through 6 appear in Figs. 7*a* through *c*. As can be seen, the corrosion resistance drops from initial values above 1 kΩ to below 1 kΩ with the NaCl-contaminated surface being slightly less than that for the standard surface preparation (Fig. 7*a*). The effective capacitances for the two surface treatments also show a relatively similar behavior as seen in Fig. 7*b*. Initial rapid rise from about 100 μF to values well over 2000 μF suggests that the effective capacitance cannot be attributed to double layer charging. After long times (70 h for the standard preparation and over 90 h for the NaCl-contaminated specimen) a decrease in the capacitance occurs.

The value of the exponent α appears in Fig. 7*c*. Here there is a very strong difference between the two specimens. The contaminated specimen shows a α that becomes much closer to 0.5, the theoretical value for a transmission line comprised of identical elements, as compared to the surface that was not contaminated. In both cases there is a precipitous drop in α after exposure to the cathodic disbonding polarization in the test environment.

The potentials for the specimens are initially at open circuit, which is above −500 mV versus SCE as shown in Fig. 7*d*. During the off-time between cathodic polarizations, the open circuit potential drops to a steady value of about −850 mV versus SCE (Fig. 7*d*).

These data represent a sum of both the impedances for the base of the defect and the impedance of the cathodically disbonding crevice. To estimate the impedance of the disbonding crevice, the initial impedance is assumed to represent that for the base of the defect and can be subtracted from the observed impedance

$$1/Z_{\text{crevice}} = 1/Z_{\text{observed}} - 1/Z_{\text{initial}} \tag{5}$$

The resulting Z_{crevice} also fits the simple model represented by Eq 4. The apparent parameters obtained for the crevice alone appear in Figs. 8*a* through *c*.

R_{corr} for the crevice is initially more than an order of magnitude lower for the NaCl-contaminated specimen as compared to the standard preparation as shown in Fig. 8*a*, but varies somewhat erratically with time which may be attributed to the considerable error inherent to performing the subtraction of Eq 5.

The contaminated specimen shows an initially low R_{corr} which increases with time to become comparable with the uncontaminated surface. C_{eff} for both specimens generally increases with time (Fig. 8*b*). After 70 h C_{eff} for the noncontaminated surface increases rapidly and then decreases while C_{eff} increases uniformly over the test period to reach a value of 4000 μF. As is the case for the R_{corr}, the high variation in the time dependence for these parameters may result more from the error in the subtraction.

The α value for the crevice impedance appears in Fig. 8*c*. The value for the NaCl-contaminated specimen decreases from 0.7 to near 0.5, the theoretical value for a transmission line of identical elements; whereas the noncontaminated standard preparation gives a value that levels out and then increases at about 0.6.

The actual extent of disbonding for the coating was evaluated by microscopic analysis (Figs. 9*a*, *b*). Note that the disbond zone is characterized by a black magnetite layer and is distinguished from the lighter region containing light-colored debris resulting from cohesive fracture of the polymer as it was pulled from well-bonded regions of the surface (see Fig. 9*b*). The NaCl-contaminated specimen was completely disbonded from the specimen. No cohesive failure of the coating occurred as it was pulled from the surface anywhere on the NaCl-contaminated specimen. On the other hand, the specimen with no contamination disbonded only to a distance of about 0.2 mm away from the hole as indicated in Fig. 9*b*. Pulling the coating from the surface elsewhere required cohesive failure of the coating.

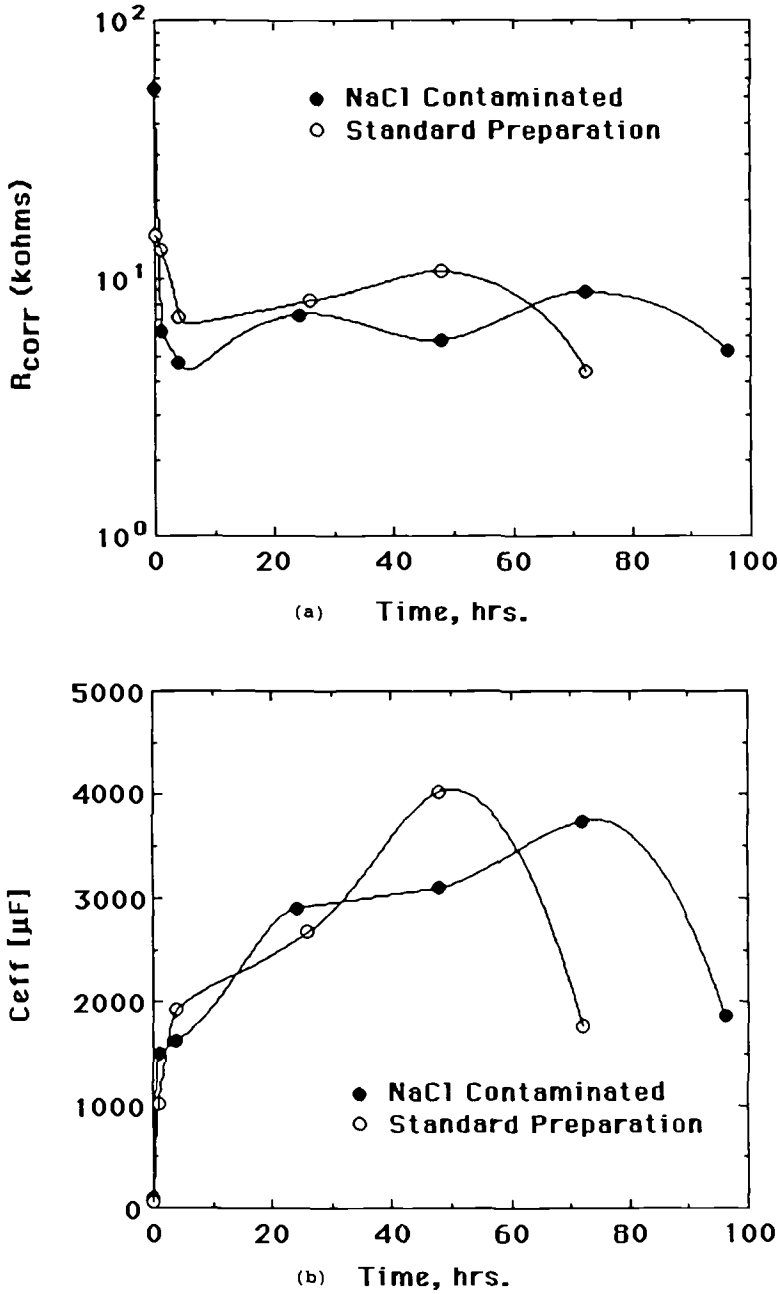

FIG. 7—*Time dependence for* (a) R_{corr}, (b) C_{eff}, (c) α, *and* (d) *the corrosion potential determined for a 0.3 cm² defect in an FBE-coated steel evaluated from the data of Figs. 5 and 6.*

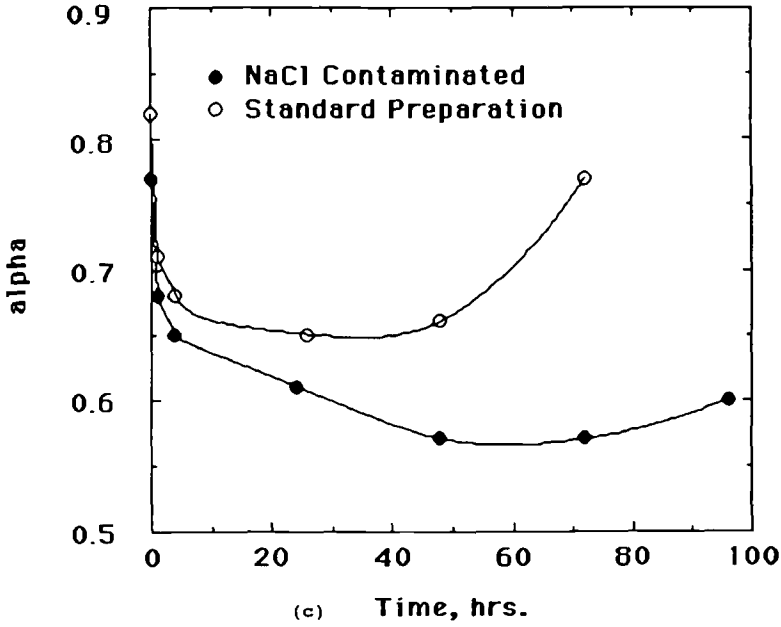

(c)

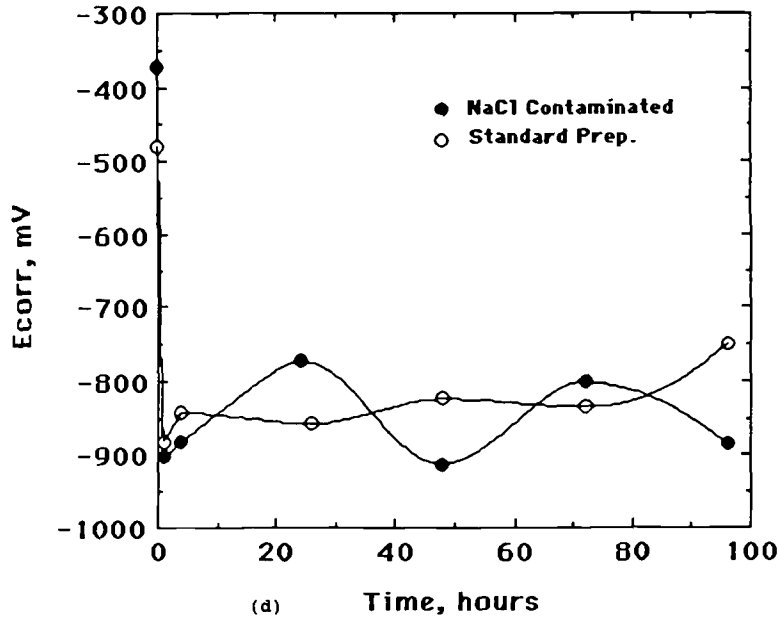

(d)

FIG. 7—(continued)

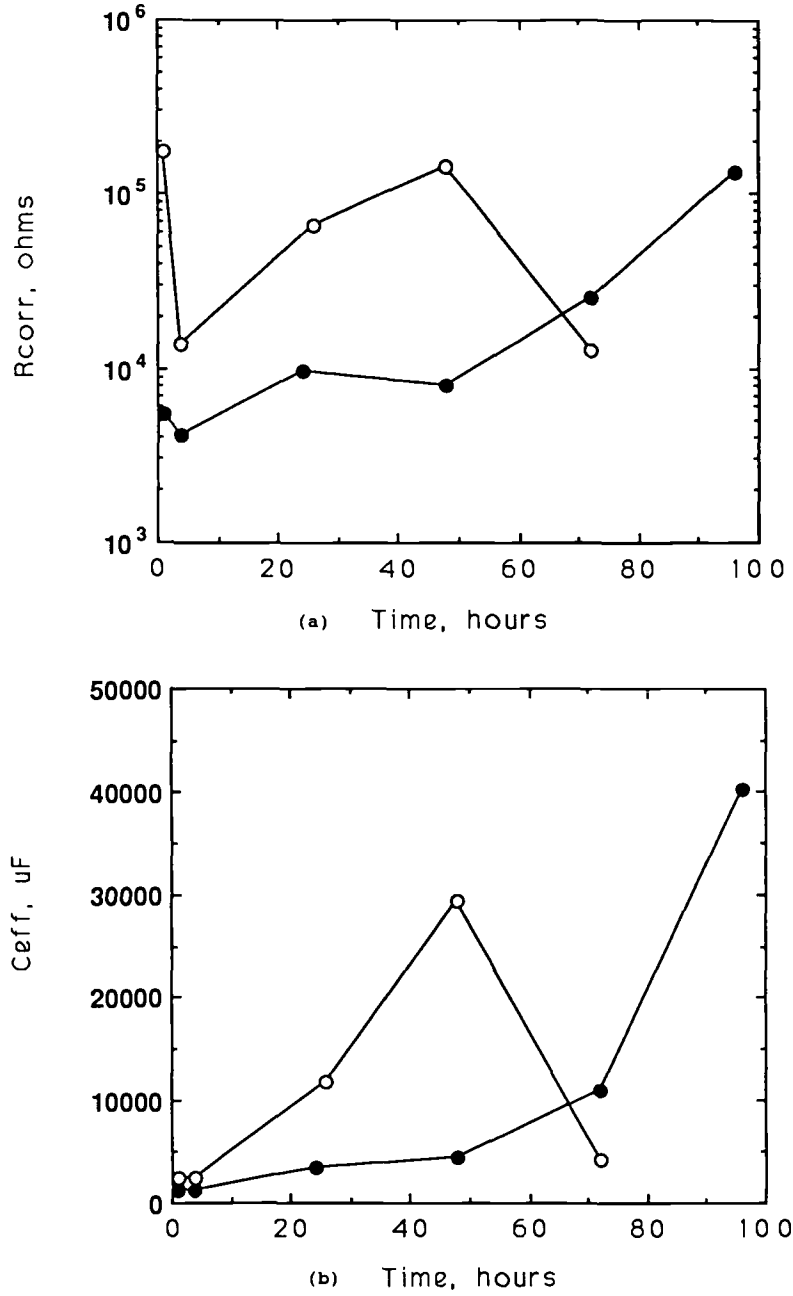

FIG. 8—*Time dependence for* (a) R_{corr}, (b) C_{eff}, *and* (c) α *determined for the crevice produced by cathodic polarization after subtracting the defect admittance from the data of Figs. 5 and 6.* (●) *contaminated,* (○) *standard preparation.*

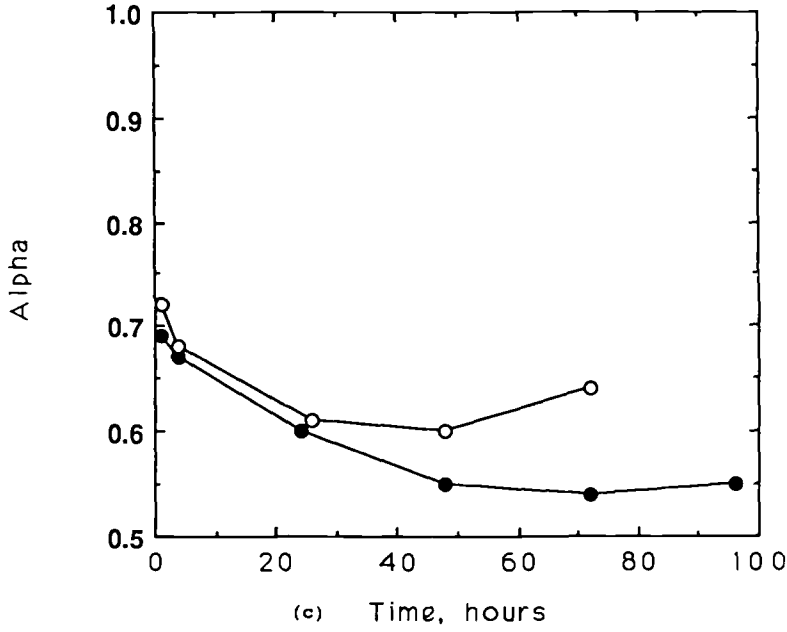

FIG. 8—(continued)

Discussion of Experimental Results

The actual disbonding observed by the post-test removal of a portion of the film suggests a factor on the order of (1 cm/0.02 cm)^2 or 63 000 for the ratio of area disbonded between the two specimens (chloride-contaminated and standard preparation). Despite the differences in the impedance parameters (see Figs. 7 and 8), the differences are not sufficiently large to be attributed directly to the area disbonded. More likely, the apparent impedance of the crevice is that of a distributed network like the transmission line model proposed in Fig. 4. That α for the highly disbonded specimen does not reach 0.5 may reflect a nonuniform distribution of values for the individual elements as presented in Fig. 4. The more disbonded specimen (NaCl-contaminated) gives a α that more nearly approaches the theoretical value. The erratic behavior of the noncontaminated specimen, as demonstrated by the variation in the values of C_{eff} and R_{corr} (Figs. 8*a* and *b*, respectively) is attributed to intermittent initiation of corrosion within regions of the cathodic crevice.

The model of Fig. 4 appears to predict some aspects of the behavior of the impedance as a result of disbonding for the system under consideration. Specifically, the impedance approaches the transmission line behavior and does not appear to be directly related to the extent of disbonding after sufficient disbonding has initiated (which may be as low as a fraction of a mm away from the crevice).

Despite the scatter, R_{corr} for the more extensively disbonded crevice is generally lower as compared to the blank (standard preparation) although R_{corr} for the standard specimen did drop after 60 h exposure to a value comparable to that for the contaminated specimen. Clearly there is not a strong relationship of R_{corr} or C_{eff} to the area disbonded for this system. This certainly is predicted by the high ohmic resistance (R_{si}) case of the proposed model in Fig. 4.

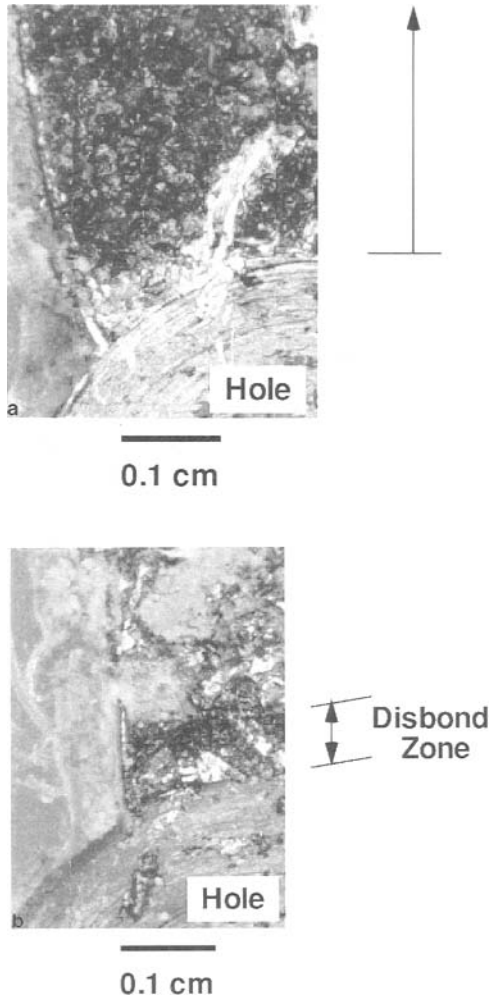

FIG. 9—*Micrographs of the cathodically disbonded coating:* (a) *NaCl contaminated specimen, and* (b) *no contamination. The dark regions adjacent to the milled hole represent magnetite substrates where no adhesion exists. The well-bonded regions contain debris from cohesively failed coating after it was pulled from the substrate.*

The FBE coatings evaluated here differ from the tape coatings considered by Kellner. For the tape coatings, the ohmic resistance R_{si} of Fig. 4 may very well be sufficiently low that the effective capacitance does indeed scale with the area disbonded as assumed by Kellner [*11*]. This certainly does not appear to be the case for the the FBE-coated specimens, and suggests that the ohmic resistance in the crevice of the FBE is relatively high, which can contribute to shielding of the cathodic protection once disbonding commences.

Summary and Conclusions

The impedance of an organic coating on a steel surface seems to depend primarily on the transport of ionic species across the coating. To consider that disbonding plays a direct role in the observed impedance for all cases remains questionable. Only in as much as disbonding promotes corrosion, which in turn degrades the coating through mechanical and chemical processes, does the decrease in R_{po} and increase in f_b correlate with disbonding. In this sense the breakpoint frequency is a measure of the integrity of the transport properties of the coating. Indeed, as shown by Scully, f_b provides a very good predictor of coating performance [*13*]. Nevertheless, variation of the breakpoint has been shown on the basis of a simple theoretical analysis not to necessarily require coating disbonding (see Figs. 3*a*, *b*). The observation of a breakpoint does require that the coating/metal interface have a sufficiently low impedance (resistive or capacitive) which will be the case under all reasonable assumptions.

We and others have theoretically and experimentally considered the impedance of an organic coating on steel for the special case that a large macroscopic defect exists in the coating and disbonding occurs away from the defect. A transmission line model is required for the case of a sufficiently high ohmic resistance in the crevice formed between the disbonded polymer and the substrate, and predicts two important behaviors: (1) the impedance will develop a constant phase element with a α value of 0.5 which gives rise to a phase angle that does not fall below $-45°$, and (2) the impedance will not scale with the area disbonded. The observation for the disbonding of an FBE coating about a large hole suggests that both these conditions are at least approached if not entirely met for this particular system.

Acknowledgments

We acknowledge valuable discussions with Prof. Florian Mansfeld between 1980 and 1986 during which time the concepts for this work were first developed. The theoretical aspects of this work was supported by the Office of Naval Research under contracts N00014-79-C-0437. The recent work presented in this paper has been supported by ONR contract N00014-90-C-0010 and the experimental evaluation of the pipeline coating was made with the support of the Gas Research Institute. We also acknowledge useful discussions with J. N. Murray of The David Taylor Research Center during the final revision of this manuscript.

References

[*1*] Mayne, J. E. O., "The Mechanism of Protective Action of Paints." *Corrosion*, L. L. Shreir, Ed., Vol. 2, 1976, p. 15:34.

[*2*] Walter, G. W., *Corrosion Science*, Vol. 26, No. 1, 1986, p. 27.

[*3*] Mansfeld, F. and Kendig, M., "Lifetime Prediction of Organic Coating/Metal Systems," Final Report for the period July 1, 1979–October 31, 1985, N00014-79-C-0437, NR036-(471), SC5222.FR, 1986.

[*4*] Haruyama, S., Asari, M., and Tsuru, T., "Impedance Characteristics During Degradation of Coated Steel," *Corrosion Protection by Organic Coatings*, M. Kendig and H. Leidheiser, Eds., Proceedings Vol. 87-2, The Electrochemical Society, 1987, p. 197.

[*5*] Kendig, M., Mansfeld, F., and Tsai, C. H., *Corrosion*, Vol. 47, No. 12, 1991, p. 964.

[*6*] Mansfeld, F. and Kendig, M., "Electrochemical Impedance Tests for Protective Coatings," *Laboratory Corrosion Tests and Standards, ASTM STP 866*, G. S. Haynes and R. Baboian, Eds., American Society for Testing and Materials, Philadelphia, 1985, pp. 122–142.

[*7*] Kendig, M., Mansfeld, F., and Arora, A., "Evaluation of Protective Coatings with Acoustic

Emission and Impedance Measurements," in *9th International Congress on Metallic Corrosion*, National Research Council of Canada, 1984, p. 73.

[8] Ruggeri, R. T. and Beck, T. R., "The Transport Properties of Polyurethane Paint," *Corrosion Control by Organic Coatings*, H. Leidheiser, Jr., Ed., National Association of Corrosion Engineers, 1981, p. 62.

[9] Hill, N., Vaughan, W., Price, A., and Davies, M., "Dielectric Properties and Molecular Behaviour," Van Nostrand, London, 1969, p. 411.

[10] Mayne, J. E. O., *British Corrosion Journal*, 1970, p. 106.

[11] Kellner, J. D., "Computer-Controlled AC Impedance Measurements for Evaluation of Anti-Corrosion Pipeline Coatings," *Electrochemical Techniques for Corrosion Engineering*, R. Baboian, Ed., National Association of Corrosion Engineers, 1986, p. 161.

[12] Kendig, M., Allen, A., and Mansfeld, F., *Journal of the Electrochemical Society*, Vol. 131, 1984, p. 935.

[13] Scully, J., *Journal of the Electrochemical Society*, Vol. 136, 1989, p. 979.

William Stephen Tait,[1] *Kristy A. Handrich,*[1] *Susan W. Tait,*[2] *and Jonathan W. Martin*[3]

Analyzing and Interpreting Electrochemical Impedance Spectroscopy Data from Internally Coated Steel Aerosol Containers

REFERENCE: Tait, W. S., Handrich, K. A., Tait, S. W., and Martin, J. W., "**Analyzing and Interpreting Electrochemical Impedance Spectroscopy Data from Internally Coated Steel Aerosol Containers,**" *Electrochemical Impedance: Analysis and Interpretation, ASTM STP 1188,* J. R. Scully, D. C. Silverman, and M. W. Kendig, Eds., American Society for Testing and Materials, Philadelphia, 1993, pp. 428–437.

ABSTRACT: Internally coated steel aerosol container corrosion and coating parameters derived from electrochemical impedance spectroscopy (EIS) data can have a range of values, requiring collection of data from multiple samples on a given coated container/electrolyte system. Multiple specimens enable estimation of distribution curve shape, and thus estimation of the fraction of the entire container population that will experience failure at a given time. Three types of EIS curves, (1) Bode magnitude, (2) Bode phase, and (3) Nyquist, should be used to determine how many responses (time constants) are present in an EIS data set. Capacitances are used to determine what type of process is being observed for each responses. Low Chi-square values lead to the conclusion that more accurate estimates of capacitances are obtained from analysis of individual responses, instead of from analyzing an entire data set with a single equivalent electrical circuit.

KEYWORDS: electrochemical impedance spectroscopy (EIS), Bode magnitude, Bode phase, Nyquist, Chi-square (X^2), corrosion resistance extremes

Previous publications have discussed the use of electrochemical impedance spectroscopy (EIS) data for predicting container service lifetime (CSL) of internally coated steel aerosol containers [*1–6*]. In these publications, two extremes in coating and corrosion parameters were found to correspond to:

(1) CSLs of >2 years when coated containers exhibited capacitive dielectric behavior, in which coating capacitance was approximately 1 nF/cm^2 and pore resistance was $>10^9$ Ω·cm^2 after 100 days of exposure;
(2) CSL of <1 year when corrosion resistance decreased to $<10^7$ Ω·cm^2 within 100 days of exposure. Coating parameters were not monitored for this type of corrosion behavior because metallic corrosion resulted in container perforation.

CSL is defined as the time at which >1% of the entire container population has perforated due to metallic corrosion.

[1]Research associate and scientist, respectively, S. C. Johnson and Son, Racine, WI 53403.
[2]Educational consultant, Tait & Associates, Racine, WI 53402.
[3]Senior materials research engineer, National Institute of Standards and Technology, Gaithersburg, MD 20899.

However, predicting long-term container corrosion behavior from coating and corrosion parameters derived from EIS data is not always straightforward. A range of values for these parameters is typically observed for a given container/electrolyte system and extremes in this range must be considered in order to make accurate predictions on CSL and to estimate what fraction of the entire container population will fail after a specified time.

It is the intention of this paper to discuss some of the techniques used to analyze and account for the broad range of coating and corrosion parameter values and some of the errors that can arise from using various analysis techniques.

Experimental

Experimental test cells, electrodes, and determination of CSL values were discussed in a previous publication [*5*]. A 100 kHz to 5 mHz frequency range was used to collect EIS data with an 11 points per decade sampling. Data were gathered at room temperature using a Solartron model 1255 HF Frequency Response Analyzer with an EG&G Princeton Applied Research model 273 Potentiostat.* Corrosion and coating parameters were derived from either Nyquist plots using software developed by Boukamp [*7*], or from Bode plots using linear regression analysis.

Data presented in this paper were gathered from several studies consisting of EIS measurements on specimen sizes ranging from 95 to 100 containers, using deionized water (18 MΩ·cm resistance) or 0.4 M potassium chloride solution as test electrolytes. Test electrodes were fabricated from commercial epoxy-coated steel aerosol containers [*1*].

Discussion of Data and Analysis Techniques

It was previously mentioned that corrosion and coating parameters obtained from EIS data can have a range of values, even when specimens are prepared by the same process [*1,8–10*]. Parameter values can range from 3 orders of magnitude, after 20 days exposure, to 1 order of magnitude, after 100 days exposure [*1*]. It was demonstrated in a previous publication that the range of values is due to coating variations and not measurement protocol [*6*]. However, the questions still remained as to what types of statistical analyses should be used to analyze parameters derived from EIS data in order to make meaningful CSL predictions, and how to estimate the number of failures that would occur during a specified period of time.

Statistical Treatment of EIS Data

A 3 order of magnitude range for corrosion resistance values can make the difference between predicting whether CSL will be >2 years or <1 year. Extreme values for coating and corrosion parameters, such as low corrosion resistances ($<10^7$ Ω·cm^2) or high coating capacitances (much >1 nF/cm^2), result in coated container failure from metallic corrosion and coating delamination, respectively.

It is necessary to know, or be able to accurately estimate, distribution curve shape for coating and corrosion parameters in order to estimate the number of containers having extreme values (on either end of the distribution) [*11*] and that will thus fail within a given time. The distribution curve shape could be estimated by calculating the mean and standard deviation from repetitive specimens if parameter values were normally distributed, because a normal distribution curve is symmetrical about its mean.

*Mention of equipment is given solely to define experimental details and does not constitute an endorsement.

Unfortunately, coating and corrosion parameters are not normally distributed. This can be seen from the curves in Fig. 1 which contain two probability plots used to test the validity of applying a given distribution (probability density function, or pdf) to a population (coating and corrosion parameters) [*12*]. These curves are generated by: (a) calculating the differences (residuals) between individual parameters and the population (parameter) mean, (b) rank ordering the residuals, (c) calculating the probability for each using the pdf being considered, and (d) plotting the calculated probabilities as a function of the residuals. The solid line indicates the trend the data (circles) would follow if the appropriate pdf was chosen.

One can see from the top graph that the parameters are not normally distributed because the probabilities for their residuals do not follow the straight line. It can be seen from the bottom graph that the parameters are log-normally distributed, thus the distribution for corrosion and coating parameters from coated containers are not symmetrical about the mean. Consequently, normal statistics (simple means and standard deviations) cannot be used to estimate distribution curve shape. It can only be estimated by a histogram generated from EIS measurements on repetitive specimens.

Variations in multiple replicates have been observed by others on a variety of coated metal systems [*8,10,13–15*]. Consequently, it is hypothesized that observations of parameter variations reported in this paper (and the need to account for parameter variations) most likely apply also to other coated metal systems, particularly when service lifetime predictions are being developed from coating or corrosion parameters.

Figure 2 illustrates how parameters derived from EIS data are used to estimate the fraction of containers that will fail from corrosion. This figure contains a typical histogram (boxes) for coating pore resistance values. A normal distribution curve for these parameters, represented by the solid curve, is included for purpose of illustration. Figure 2 is also typical for coating and double layer capacitances and corrosion resistance values.

When extreme values (e.g., corrosion resistance $<10^7$ $\Omega \cdot cm^2$) for a parameter are known, the number of units having parameter values exceeding or less than the extremes (and will fail) can be estimated by calculating the area under the high or low tail of the distribution curve or histogram. This concept is illustrated in Fig. 2 where hypothetical high and low extremum for pore resistance are identified as vertical lines. Figure 2 also illustrates how normal statistics (solid line) can lead to over-estimation of extremes in the left tail and under-estimation of extremes in the right tail when applied to non-normally distributed parameters. Under- and over-estimation of the number of containers having extreme values leads to erroneous estimations of CSL.

High and low extremum for corrosion resistance, high extremum for pore resistance, and low extremum for coating capacitance were identified at the beginning of this paper and in a previous publications [*1,2*]. Work is proceeding at this time to determine extreme value magnitudes for pore resistance, coating and double layer capacitances, and the minimum number of repetitions needed for estimating distribution curve shape.

Graphical Analysis of EIS Data

Nyquist plots are commonly used to present and analyze EIS data. However, Mansfeld presented example Nyquist plots where the coating response was obscured by the faradaic response, but readily observed in the corresponding Bode magnitude plots [*16*]. There are also cases where the differences between responses from different processes are difficult to distinguish on a Bode magnitude plot. One such example, obtained from studies using deionized water, is contained in Fig. 3. This curve is typical of the Bode magnitude plots obtained from studies on coated containers exposed to 18 $M\Omega \cdot cm$ deionized water. Exam-

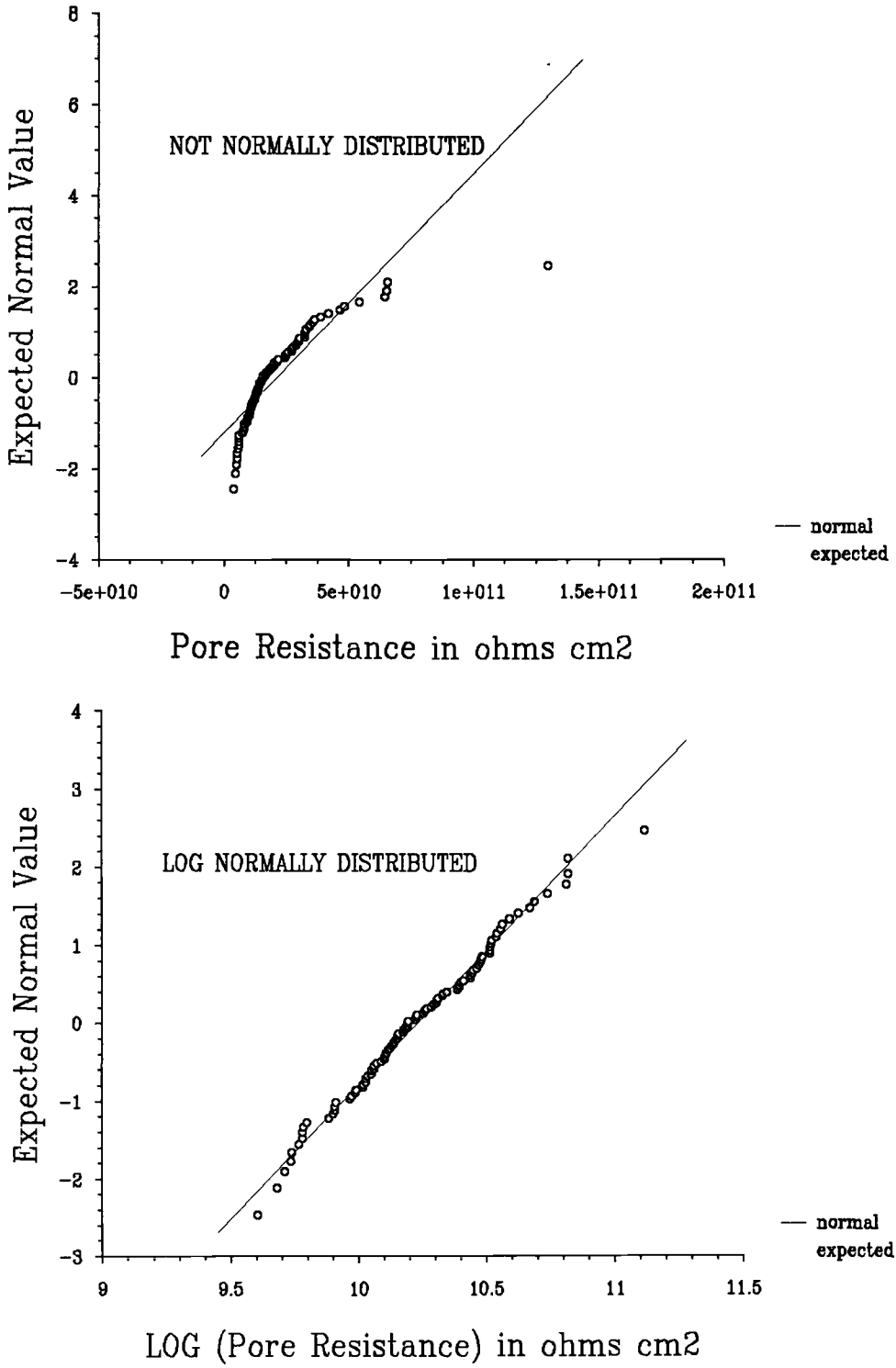

FIG. 1—*Testing for the type of distribution: normal and log-normal distributions.*

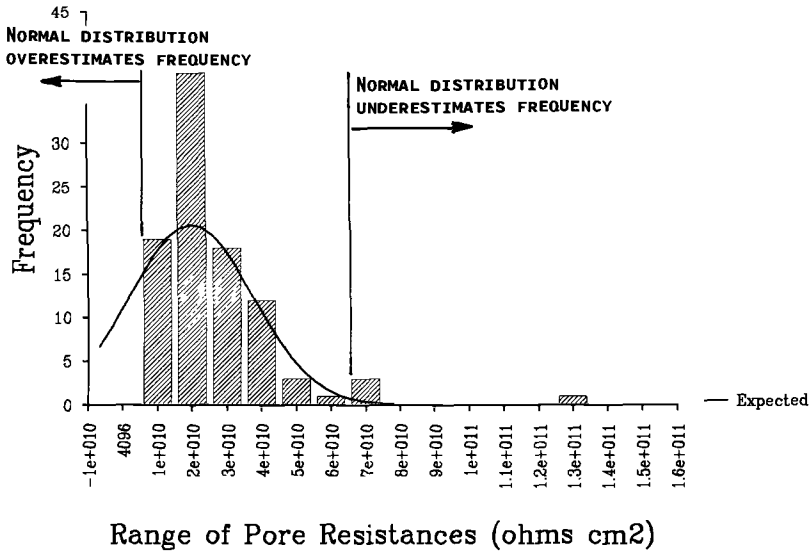

FIG. 2—*Typical histogram for coating pore resistance, corrosion resistance, double layer, and corrosion capacitance values.*

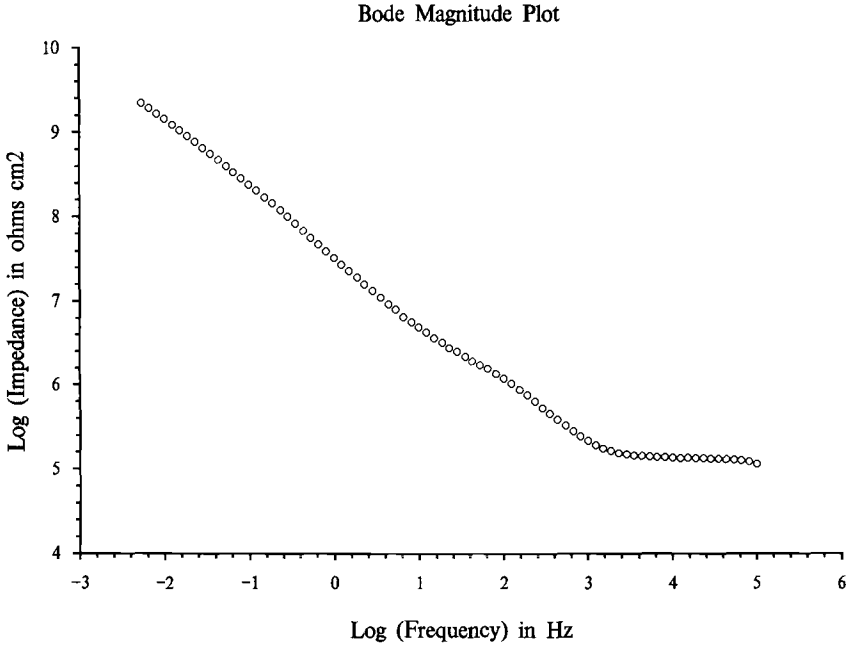

FIG. 3—*Bode magnitude plot.*

ining the corresponding Bode phase plot in Fig. 4 reveals three distinct responses: the first at high frequencies, the second at approximately 100 Hz, and the third at lower frequencies. Figure 5 contains a summary Bode magnitude plot in which the location of the responses are indicated along with their values for resistance and capacitance. It is interesting to note that all three of the responses (time constants) in Fig. 5 have capacitances that are typical for organic coatings.

It is suggested that three types of plots, (1) Bode phase, (2) Bode magnitude, and (3) Nyquist, should be examined to determine how many responses are contained in a given EIS data set.

Potential Errors Arising from Modeling EIS Data

A common technique for analyzing EIS data is to obtain coating and corrosion parameters by mathematically modeling all of the data with an equivalent electrical circuit. However, ambiguities can arise from this modeling technique. For example, Silverman discussed how several different equivalent circuits can be used to model the same EIS data set [*17*]. Multiple equivalent circuit models can cause confusion about the physical significance of each component in the equivalent circuit.

Boukamp's software uses the Chi-square (X^2) statistic to test how well a model fits a data set. The X^2 test is used to assess the degree of correspondence between a model (expected value) and the corresponding experimental data [*18*]. We have often observed that the X^2 statistic ranges from 10^4 to 10^8 when data are modeled with a single equivalent circuit. The right column of Table 1 contains typical X^2 values obtained when equivalent circuits were used to model EIS data. An ideal fit of a model to a data set would result in a

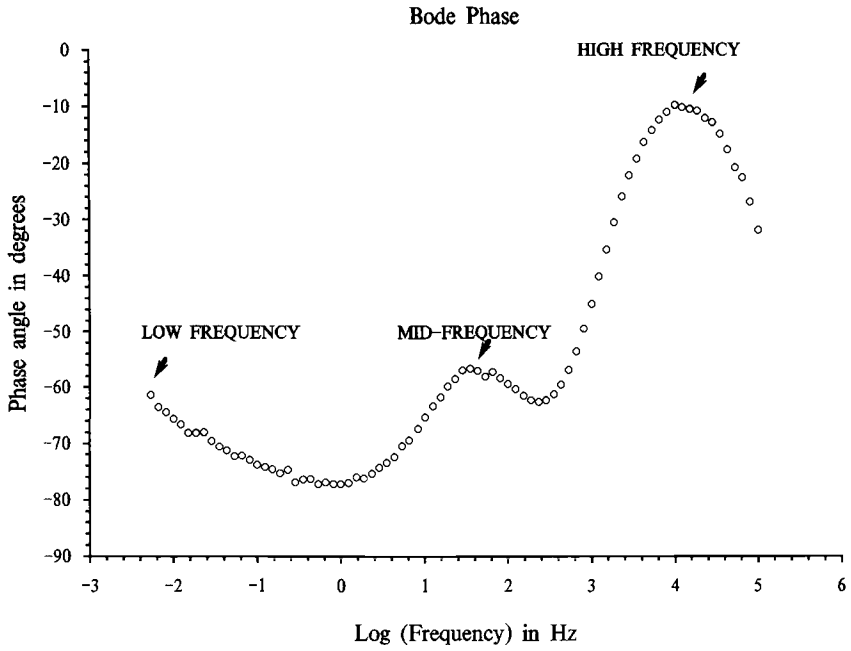

FIG. 4—*Corresponding Bode phase plot for Fig. 3.*

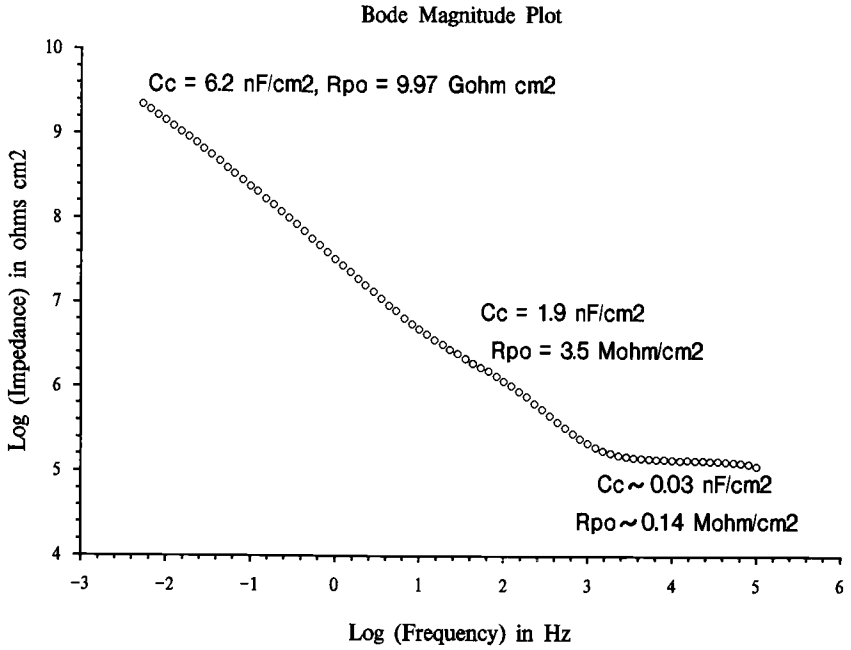

FIG. 5—*Bode magnitude plot with coating parameters for each response identified in Fig. 4.*

X^2 statistic equal to 0. Consequently, the high X^2 values in Table 1 suggest that the assumed equivalent circuit is not a good fit to the data.

Conversely, when data associated with each response are analyzed separately using a modified Randles circuit (constant phase element [*19*] is substituted for the capacitor), X^2 values typically range from 10^{-3} to 10^{-5}—in other words, nearly an ideal fit. Typical X^2 values obtained from this technique are contained in the left column of Table 1. The results in Table 1 suggest that more accurate estimates of coating and corrosion parameters can be obtained by analyzing data for individual responses in the EIS data set, as opposed to using a single circuit to model the entire data set.

TABLE 1—*Comparison of X^2 values for different analysis techniques.*

Analyzing Individual Responses (Time Constants)	Using Equivalent Electrical Circuit Models
1.66×10^{-3}	2.48×10^{6}
1.12×10^{-3}	2.08×10^{7}
6.02×10^{-4}	6.82×10^{5}
6.36×10^{-4}	6.99×10^{4}
4.55×10^{-3}	2.20×10^{6}
1.74×10^{-3}	1.52×10^{7}
1.19×10^{-3}	1.68×10^{6}
9.15×10^{-5}	2.07×10^{6}
4.25×10^{-3}	1.69×10^{8}
1.00×10^{-3}	2.68×10^{8}

TABLE 2—*Partial listing of percent differences between parameters obtained from different EIS analysis techniques (mean values are for 95 repetitions).*

Coating Capacitance	Pore Resistance	Double Layer Capacitance	Corrosion Resistance
77.2%	2.0%	1436.5%	0.72%
1327	46.9	519.1	3.53
44.3	32.1	186.0	45.6
301	40.9	14.2	45.6
274	44.9	3773.6	16.8
51	1.4	10.0	48.8
3758	57.3	137.9	108.7
15.9	2.1	795.7	46.1
31.6	1.2	7.9	16.0
439	13.0	12.6	2.0
18.2	16.0	2.27	49.7
37.1	6.3	1129.4	7.0
26.7	8.0	11.7	12.1
29.2	3.7	8.35	89.4
2963	8.3	4.93	2.47
852	80.5	2.3	13.1
264	96.5	11.3	6.77
Mean = 609%	Mean = 27%	Mean = 613%	Mean = 72%

The percent difference between parameters obtained from the two analysis method were calculated for 0.4 M KCl data in order to identify which parameters caused high X^2 values observed for single circuit models. Table 2 contains examples of percent differences between the two methods for corrosion and pore resistances, coating and double layer capacitances. Most of the differences in resistance values are <100% and the average difference for 95 repetitions was <100% for both types of resistances. Many of the capacitance differences are >100% and several were >1000%. The average difference for both capacitances was approximately 600%. This observation leads to the conclusion that high X^2 values are caused by errors in capacitance values arising from use of a single equivalent circuit model.

Using Capacitance Values to Guide Interpretation of Results from Analyses

Table 2 also illustrates that if resistances were the only parameters needed for data interpretation and prediction of CSL, then the method used to analyze data would not be important.

However, we have found it useful to use capacitance values to interpret what type of processes are being observed with each individual response. Table 3 contains capacitance

TABLE 3—*Capacitance values used to determine what types of processes are associated with a given electrochemical event.*

Capacitance	Value
Coating	on the order of 1 nF/cm^2
Double layer (corrosion)	10 to 100 μF/cm^2
Oxide	several hundred to thousands μF/cm^2

magnitudes typically associated with faradaic processes (corrosion) [*20*], coatings [*21,22*], and oxides [*23*].

Percentage differences in capacitance values of 1000%, such as those seen in Table 2, can make the difference between determining whether an observed resistance is for the coating or a faradaic process, and thus the difference between predicting one- or two-year CSL.

For example, if the middle frequency resistance value in Fig. 5 was interpreted to be a corrosion resistance, the conclusion would be that this coated container would fail within one year. However, the corresponding capacitance has a magnitude typical for a coating; thus, the conclusion is that this resistance is a pore resistance and the coated metal is exhibiting capacitive dielectric behavior. No corrosion or coating degradation were observed after 100 days exposure on the specimen from which Fig. 5 data were gathered, confirming that the middle frequency resistance was indeed a pore resistance.

Conclusions

Coating and corrosion parameters derived from EIS data (from coated steel aerosol containers) typically have a range of values that can be several orders of magnitude. The range of parameter values leads to the need for collecting multiple repetitions on each container/electrolyte variable. Multiple repetitions enable estimation of the distribution curve shape, which is needed to estimate the number of containers that will have extreme values. Estimation of the number of extreme values is important because extremum in the distribution (e.g., low resistances and high capacitances) result in container failure.

Examination of three types of EIS curves, (1) Bode magnitude, (2) Bode phase and (3) Nyquist, is needed to determine how many responses (time constants) are contained in an EIS data set.

Capacitance values are useful for determining what type of process is being observed for each response in an EIS data set.

Chi-square (X^2) values indicate that more accurate estimates for capacitance values can be obtained from analysis of individual responses, using a modified Randles circuit, instead of analyzing the entire data set with one equivalent electrical circuit.

References

[*1*] Tait, W. S. and Maier, J. A., *Journal of Coating Technology,* Vol. 62, No. 781, 1990, pp. 41–44.
[*2*] Tait, W. S., *Journal of Coating Technology,* Vol. 61, No. 768, 1989, pp. 57–61.
[*3*] Tait, W. S. and Maier, J. A., *Advances in Corrosion Protection by Organic Coatings, 89-13,* pp. 251–258, The Electrochemical Society, Pennington, NJ, 1989.
[*4*] Tait, W. S., *Proceedings of the ACS Division of Polymeric Materials: Science and Engineering,* Vol. 58, 1988, pp. 322–328.
[*5*] Tait, W. S., *Corrosion Protection by Organic Coatings,* Vol. 87-2, The Electrochemical Society, Pennington, NJ, 1987.
[*6*] Tait, W. S., Handrich, K. A., and Maier, J. A., *Proceedings of the Steel Structures Painting Council Evaluation and Durability Conference,* SSPC 91-15, April 29–May 3, 1991, Pittsburgh, PA, 1991.
[*7*] Boukamp, B. A., *Solid State Ionics,* Vols. 18&19, 1986, pp. 136–140.
[*8*] Feliu, S., Morcillo, M., and Galvan, J. C., *Advances in Corrosion Protection by Organic Coatings,* Vol. 89-13, The Electrochemical Society, Pennington, NJ, 1989, pp. 280–290.
[*9*] Jun, T. Y., *Progress in Organic Coatings,* Vol. 19, 1991, pp. 88–94.
[*10*] Martin, J. W., McKnight, M. E., Nguyen, T., and Embree, E., *Journal of Coating Technology,* Vol. 61, No. 772, 1989, pp. 39–48.
[*11*] Nelson, W., *Accelerated Testing: Statistical Models, Test Plans and Data Analyses,* John Wiley & Sons, NY, 1990.
[*12*] CSS: Statistical Software Manual, Statsoft Inc., Tulsa, OK, 1991, p. GRA-306.
[*13*] Murray, J. N. and Hack, H. P., *CORROSION/91,* Paper 131, Cincinnati, OH, March 1991.

[*14*] Martin, J. W., Embree, E., and Tsao, W., *Journal of Coating Technology,* Vol. 62, No. 790, 1990, p. 25.
[*15*] Hospandaruk, V., Huff, J., Zurilla, R. W., and Greenwood, H. T., *Society of Automotive Engineers,* Paper No. 780186, Detroit, MI, February 27–March 3, 1978.
[*16*] Mansfeld, F., *Corrosion,* Vol. 44, No. 8, 1988, pp. 558–559.
[*17*] Silverman, D. C., *Corrosion,* Vol. 47, No. 2, 1990, pp. 87–89.
[*18*] Siegel, S. and Castellan, Jr., N. J., *Nonparametric Statistics,* McGraw-Hill Book Company, NY, 1988, p. 45.
[*19*] Ross Macdonald, J., *Impedance Spectroscopy: Emphasizing Solid Materials and Systems,* John Wiley & Sons, NY, 1987, p. 13.
[*20*] Bard, A. J. and Faulkner, L. R., *Electrochemical Methods: Fundamentals and Applications,* John Wiley & Sons, NY, 1980, p. 8.
[*21*] Pebere, N., Picaud, T., Duprat, M., and Dabosi, F., *Corrosion Science,* Vol. 29, No. 9, 1989, pp. 1073–1086.
[*22*] Scully, J. R., Report No. DTNSRDC/SME-86/006, David W. Taylor Naval Ship Research and Development Center, Annapolis, MD, 1986, p. 105.
[*23*] Eggers, W. J., Private communication with author, May 1989.

Sebastián Feliu, Jr.,[1] *Rosa Barajas,*[1] *José M. Bastidas,*[1] *Manuel Morcillo,*[1] *and Sebastián Feliu*[1]

Study of Protection Mechanisms of Zinc-Rich Paints by Electrochemical Impedance Spectroscopy

REFERENCE: Feliu, S. Jr., Barajas, R., Bastidas, J. M., Morcillo, M., and Feliu, S., **"Study of Protection Mechanisms of Zinc-Rich Paints by Electrochemical Impedance Spectroscopy,"** *Electrochemical Impedance: Analysis and Interpretation, ASTM STP 1188,* J. R. Scully, D. C. Silverman, and M. W. Kendig, Eds., American Society for Testing and Materials, Philadelphia, 1993, pp. 438–449.

ABSTRACT: The authors present a review of their research work in an endeavor to interpret the behavior of zinc-rich paints (ZRP) using electrochemical impedance spectroscopy (EIS). This technique can provide much useful information about the protection mechanisms of ZRP. The tendency of some of these coatings to act like an electrode with a very large accessible internal area (that of the interconnected zinc particles) is examined. This situation favors the cathodic protection of the steel substrate by the zinc particles. The higher frequency arc chord in the Nyquist diagrams and the Warburg coefficient calculated from the low-frequency diffusion tail enables the extent and evolution of the coating barrier effect to be determined.

KEYWORDS: electrochemical impedance spectroscopy (EIS), zinc-rich paints (ZRP), cathodic protection, barrier stages

For a long time, paints with a high content of zinc particles (Fig. 1) have been successfully employed for steel protection. It seems to be clearly established that in the early stages of coating performance there is a period of intense electrochemical activity, in which the preferential attack of zinc particles provokes cathodic protection of the steel base [*1*]. The extent and duration of this period of cathodic protection is considered to be limited by the contact between the zinc particles, which is lost with time. This effect is illustrated in Fig. 2, obtained with panels immersed in a saline solution of 3% NaCl. As can be seen, the potential moves in the noble direction with increasing time [*2*]. In this example, negative potentials of over −0.80 V/SCE (usually specified as necessary for protection of steel) are not maintained for more than 80 days in the most favorable case of the 84% zinc ethyl silicate type coating. It might be thought that the useful life of zinc-rich paint (ZRP) coatings is limited to the life of the electronic contact between the zinc particles, which is a function of the paint type and composition. However, this is not completely correct, since a subsequent long-term protection develops through the formation of zinc compounds [*3,4*]. In this case, the protective behavior is assigned to the secondary effect of zinc corrosion products in blocking the pores in the coating and rendering it compact and adherent.

[1]Research assistant, research assistant, scientific researcher, research professor, and research professor, respectively, CENIM, Ciudad Universitaria, 28040-Madrid, Spain.

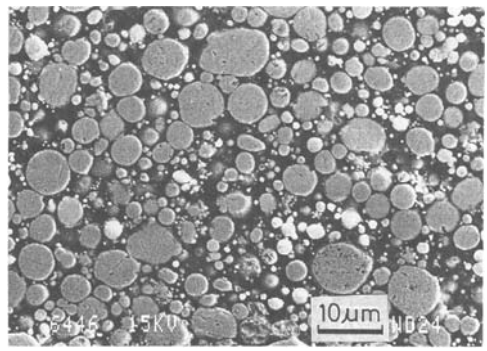

FIG. 1—*Cross-section SEM picture of a ZRP coating before exposure, showing the interconnected spherical zinc particles.*

The electrochemical nature of most of the phenomena involved in the protective action of paint coatings justifies the convenience of applying electrochemical techniques for their study. The electrochemical impedance spectroscopy (EIS) has the advantage of scarcely disturbing the system, since the ac signal applied is very small, and of offering a detailed analysis of the different processes that influence its behavior. There have been several attempts to apply impedance techniques to the study of ZRP coatings on steel [*5–8*]. Some of these studies are based on data obtained at a fixed frequency (e.g., 1 kHz); other times, despite the use of a wide range of frequencies, the measurements do not include the lowest frequencies (1 to 10 mHz). However, a detailed analysis of the relaxation phenomena involved in corrosion reactions (e.g., mass transfer processes) requires in most cases impedance measurements at frequencies as low as 1 mHz [*9*]. For this reason the information obtained in these studies is only partial.

In this paper the authors present a review of their research work over the last ten years, concerning the application of EIS technique in order to clarify how different parameters affect the mechanisms by which steel protection is attained with ZRP coatings. Most of the experimental information and results given have been taken from published works by the

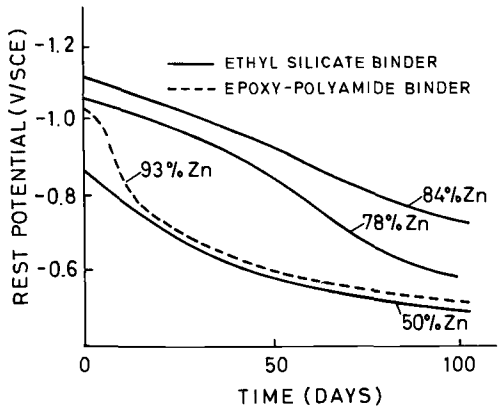

FIG. 2—*Evolution of rest potential with time of steel panels coated with different ZRP paints immersed in 3% NaCl solution.*

authors [*2,10–14*]. In the subsequent paragraphs, using this technique, information will be obtained about the following points:

(a) The corrosion rate of zinc particles acting as sacrificial anodes. This rate shows the tendency of zinc to sacrifice itself in favor of the steel substrate. Low zinc corrosion rates point to a poor capacity of this metal to provide cathodic protection.
(b) The quantity of zinc particles connected between each other and with the steel substrate that participate in the cathodic protection mechanism. It is of major interest to know the evolution of the quantity of interconnected particles.
(c) The electrical resistance of the coating itself, which is closely related to the resistance by the ZRP coating to the electrical flow and to the operation of corrosion microcells.
(d) The diffusion resistance of the reacting species through the coating, which considerably influence the development of electrochemical reactions in the metal/coating/electrolyte system. A very strong hindrance to diffusion favors the stability of the system.

Impedance Measurements

A simple method of measuring impedance with ZRP coatings is to use the technique described in Ref *2*. Here, the electrolyte, reference electrode, and auxiliary electrode are placed in a small plastic cylinder attached to the surface of the ZRP coating. The surface exposed to the electrolyte (3% NaCl solution) was 3.14 cm^2.

Table 1 summarizes the ZRP compositions used in the experiments. The paints were formulated with different percentages of zinc and Fe_2P particles and two types of vehicles: ethyl silicate and epoxy-polyamide. The higher levels of zinc tested correspond to the usual ZRP composition. The lower levels of zinc were expressly chosen with the purpose of obtaining more complete information about the influence of this variable. Considering the vehicles ethyl silicate and epoxy-polyamide, the effects of two binders of radically different characteristics and representative of typical families of ZRPs are compared. The relatively high cost of zinc and the desire to avoid some interferences with the welding process was the reason for the inclusion of the conductive extender Fe_2P in this study. The

TABLE 1—*Zinc dust and conductive Fe_2P particles contents (% by weight) in the coatings tested* [2,11].

Vehicle	Zinc Dust	Fe_2P Particles
Ethyl Silicate	84	0
	78	0
	50	0
	84	12
	77	12
	59	24
Epoxy-polyamide	97	0
	93	0
	78	0
	68	0
	85	11
	82	11
	72	21

replacement of part of the zinc particles with Fe_2P particles may obviously produce a substantial change in the behavior of the coating.

As a general rule, the Nyquist diagrams of the series of ZRP tested show one or two arcs. In the case of the diagrams of one arc, this may or may not be accompanied by a straight line diffusion tail. The single arc may appear in the zone of high or medium frequencies. Depending on the frequency zone where the arc is placed, it might be interpreted as being due to the combined effect of the ionic resistance and capacitance of the insulating layer (high frequencies), or to the charge transfer resistance and capacitance of the double layer on the metal (intermediate frequencies). When two arcs appear, the arc of the lower frequencies probably corresponds to a mass transport process in a layer of finite thickness (curved diffusion tail) [*2,10,11*].

Nyquist diagrams representative of those obtained with the ZRP coatings are shown in Fig. 3. Diagrams of Type A often appear with the ethyl silicate vehicle and short exposure times, whereas diagrams of Type B tend to appear after long exposure times and with the epoxy-polyamide vehicle.

Information Regarding the Cathodic Protection Mechanism

The possibilities of cathodic protection of the steel by the zinc particles depend on the continuity of the electric contact of these particles between themselves and with the steel base. Initially, it is reasonable to assume that the response to the electrical signal of the ZRP-coated steel is due almost exclusively to the interconnected zinc particles, because the whole effective surface area of these numerous particles (Fig. 1) is considerably larger than the accessible surface area of the steel. For this reason, the arc in the high- or medium-frequency range is assumed to be chiefly related to the corrosion reaction of the zinc particles. This arc can be simulated, to a first approximation, by a semicircle, and its diameter will correspond to the polarization resistance (R_p) of the reaction. The R_p values (thus estimates) are shown in Fig. 4. On the assumption that an analogous relation to the Stern-Geary equation [*15*] is applicable, the rate of the metallic attack (of the zinc particles that are electrically interconnected between themselves and the steel base) will be inversely related to R_p. A small R_p value and hence a high corrosion rate will indicate the

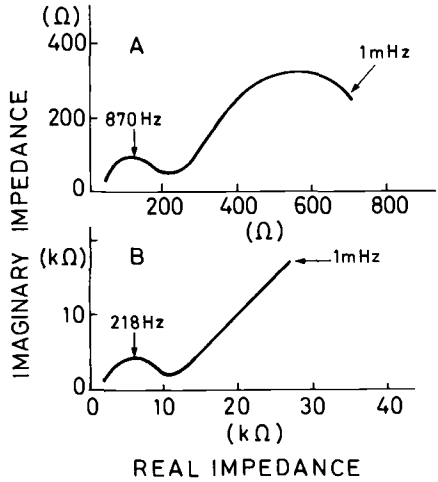

FIG. 3—*Typical examples of Nyquist diagrams obtained with the ZRP coatings.*

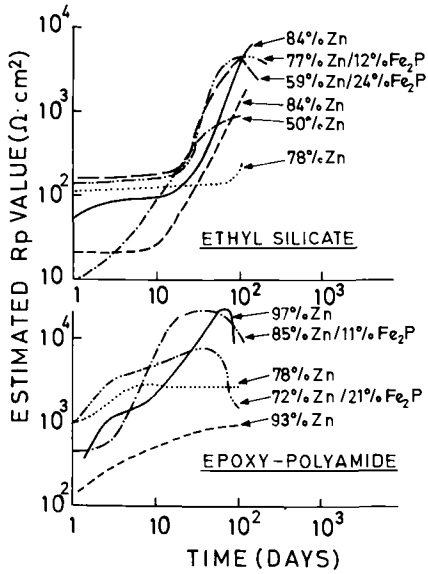

FIG. 4—*Polarization resistance versus time.*

existence of a large mass of zinc in contact with the steel base, and probably a very effective cathodic protection. As will be discussed later, the increase of the R_p value with time in Fig. 4 can be interpreted as a result of: (1) electrical disconnection of the zinc particles, and (2) the buildup around them of an insulating barrier of corrosion products (Fig. 5). In both cases, the effective surface area of zinc decreases and one would expect an increase in the apparent polarization resistance.

It is interesting to check whether the response of the ZRP coating to the application of an electrical signal affects the majority or only a small part of zinc particles. The first case will indicate the existence of a high degree of electrical interconnection of the conductive particles, which surely favors the galvanic action and cathodic protection of steel. The

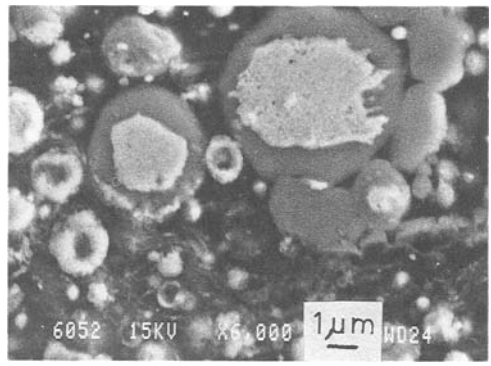

FIG. 5—*Cross-section SEM micrographs of 78% zinc epoxy-polyamide ZRP coating after a 30-day immersion period in 3% NaCl solution, showing a thick layer of corrosion products on the zinc surface.*

second case will indicate a low number of conductive particles in electrical contact and thus less availability of zinc anodic surface (greater polarization of the zinc) for the cathodic protection of the steel substrate.

The proportion of zinc particles in electrical contact can be determined by comparing the electrochemically estimated zinc corrosion values with those directly determined by the hydrogen evolution method [*2,11*]. In the early stages of exposure, the R_p values obtained from the impedance diagrams is expected to correspond essentially to the zinc particles electrically connected between each other and with the steel substrate, which are the only ones that respond to the applied signal. The corrosion of these particles can be estimated by integration with respect to time of the Stern-Geary equation [*15*].

On the other hand, the real value of corroded zinc is obtained by means of the hydrogen evolution method [*16*], by which the weight of metallic zinc remaining in the coating is deduced from the volume of hydrogen gas evolved in the reaction between the ZRP coating (previously scraped from the steel substrate) and the HCl. It must be stressed that in contrast to the electrochemical measurements, in this case the corrosion values refer to the whole amount of zinc particles whether they are interconnected or not. It is evident that if both values are approximately the same, the greater part of zinc particles will be in electrical contact. On the contrary, if the estimated corrosion value from the electrochemical measurement is much lower than the one directly determined by the hydrogen evolution method, many of these particles will be electrically insulated.

In Fig. 6, the estimated values from the impedance measurements are compared with the real corrosion values obtained by the direct method of hydrogen evolution. With this purpose, corrosion currents given by Stern-Geary's equation were integrated over five- and ten-day periods, during which frequent measurements were made. The corrosion values estimated electrochemically for ethyl silicate ZRP coatings are somewhat greater than the real values, regardless of the zinc and of Fe_2P particles percentages used. The differences (twice as much) can be attributed to the lack of precision in the value of constant B and to the possibility of the ZRP coating acting somewhat as a porous electrode [*2,11*]. The conclusion is that the greater part of the zinc and Fe_2P particles in these coatings maintain electrical contact between each other and with the steel base. On the contrary, the epoxy-polyamide ZRP coatings behave as if a few conductive particles were only in electrical contact.

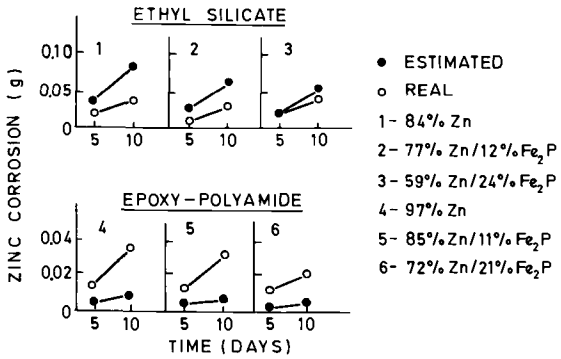

FIG. 6—*Comparison of electrochemically estimated zinc corrosion values with the real ones.*

Information Based on Capacitance Values

The impedance measurement permits capacitance estimations of the double layer on the zinc particles or on the steel surface directly exposed to the saline solution, as well as of the insulating films on the electrode.

Figure 7 shows the variation with time of the capacitance values of the series of ZRP tested coatings [*2,11*]. Values of the same order or higher than the typical values of capacitance for the double layer on a flat electrode are determined at the beginning of exposure to the saline medium. Quite remarkably, the initial capacitances of some of the ethyl silicate coatings are around one hundred times greater than the typical capacitances for a flat metal surface, which suggests an electrode with very large accessible internal surface, i.e., a great number of zinc and Fe_2P particles electrically connected between each other and with the steel substrate. The lower capacitance values of the epoxy-polyamide coatings are explained by a lower number of interconnected particles and a smaller surface area exposed to the electrolyte, possibly due to the better wetting properties of this vehicle [*13*].

Later, during the prolonged exposure to the saline solution and due to the accumulation of corrosion products over the zinc particles, these tend to become electrically insulated. It is possible that the corrosion first affects the more external zinc particles. A gradual passivation of these particles is also possible, starting with the outermost particles (the surface covered first by corrosion products). The result is equivalent to an increase in the average thickness of the insulating film on the conductive metallic particles. The capacitance value will therefore diminish.

In general, capacitance tends to decrease when the zinc content of ZRP also decreases. This behavior is less evident with paints in which part of the zinc has been replaced by Fe_2P. The difference is that now the addition of Fe_2P compensates for the reduction in zinc, thus ensuring the electrical contact between a larger number of conductive particles (of zinc and of Fe_2P) [*2,10,11*].

Information Based on the Ohmic Resistance of the Coating

It should be understandable from the foregoing that after some time (days) of action of the agressive medium, the high- or medium-frequency arc of the impedance diagrams may no longer be principally linked with the charge transfer resistance of the zinc particles

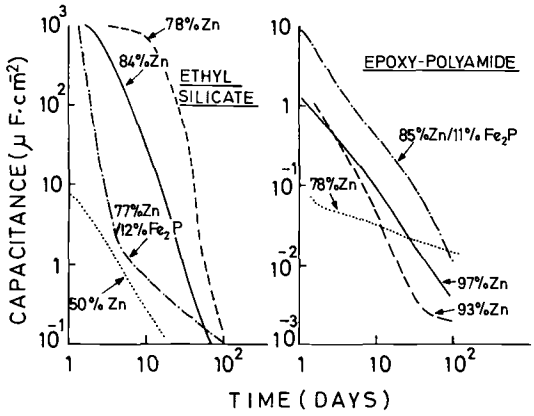

FIG. 7—*ZRP coating capacitance value versus time.*

reaction, but rather with the ohmic resistance of the zinc corrosion products accumulated within the coating (Fig. 5). In this way, the increase with time of the apparent R_p values after a period of about ten days (Fig. 4) has been attributed to the incorporation into the coating of insoluble zinc corrosion products [*2,10,11*], and is in line with the aforementioned drop in the value of the electric capacitance of the coating. The tendency to increase the value of R_p with time is more evident with the ethyl silicate vehicle coatings and with higher zinc contents. This tendency is reversed after sufficiently long periods of exposure (e.g., 100 days) due to the perforation of the paint coating. The latter phenomenon appears sooner in the epoxy-polyamide vehicle coatings and with a lower zinc content. It is as if the effect of progressive deterioration of the coating (opening and widening of channels through the coating) eventually prevailed over the blocking effect of the steel base and zinc particles by the corrosion products.

Information Supplied by the Diffusion Tail

Besides considering the arc of high or medium-frequencies, as referred to previously, we also have the possibility of considering the diffusion tail or diffusion arc shown by the diagram at low frequencies to analyze the barrier effect of the coating.

The accumulation of corrosion products in the pores of paint coatings generally favors the appearance of diffusion tails [*17*]. In the case of ZRP coatings, it is reasonable to assume that the progressive formation and accumulation of insoluble zinc corrosion products inside the porous coating also affects the diffusion of the reacting species.

At low frequency, a trend towards the formation of straight line tails, of about 45° slope, has been observed in the case of epoxy-polyamide coatings [*2,10,11*]. With ethyl silicate coatings the trend is towards the formation of low-frequency arcs that also transform with time into straight lines (Fig. 8).

These low-frequency tails and arcs might be expected to bear a close relation with the

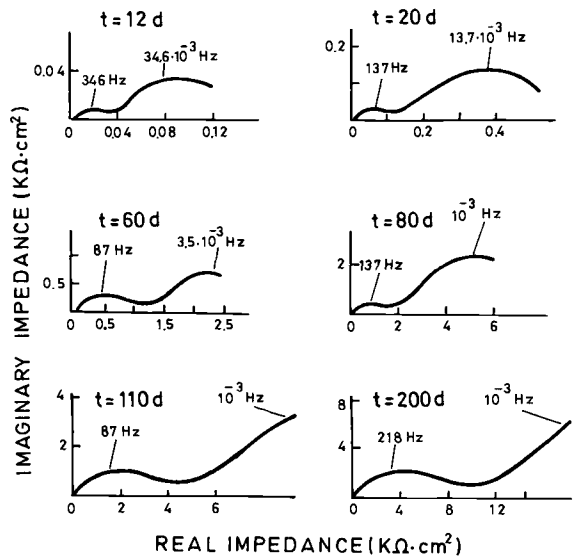

FIG. 8—*Evolution of Nyquist diagrams as a function of immersion time in 3% NaCl solution, for the 84% zinc ethyl silicate ZRP coating.*

diffusion coefficient of the electroactive species D. Theoretically [*18*], the diffusion impedance (Z_D) is given by the equation

$$Z_D = (1 - j)\sigma w^{-1/2} \times \tanh [\delta(jw/D)^{1/2}] \quad (1)$$

where σ is the Warburg coefficient, w is the angular frequency, δ is the Nernst diffusion-layer thickness, and $j = (-1)^{1/2}$. If the numerical value of $\delta/D^{1/2}$ is high, the hyperbolic tangent term tends towards unity, and the impedance plot shows a straight line of slope 45°. As the value of $\delta/D^{1/2}$ decreases, the diffusion tail tends to curve over towards the real axis which is intersected at a sufficiently low frequency. Thus, the small value of D will favor the semi-infinite diffusion (inclined straight line tail), while the high values of D will favor the finite diffusion. The arc transformation in a straight line with the ethyl silicate paints may be attributed to the increasing blocking of the coating pores by the zinc corrosion products. The initial lower porosity of the epoxy-polyamide paints explains the formation of straight line tails from the first moments of exposure to the saline solution.

Warburg Coefficient

When the electrode includes a porous coating, the Warburg coefficient σ is expressed in terms of the diffusion coefficient D for the species through the pores in the coating (i.e., through only a fraction of the coating surface) and a concentration C, which depends on the concentration gradient through the pores. This coefficient is known to follow a dependence on D and C of the form [*19,20*]

$$\sigma = RT/2^{1/2}n^2F^2 \times 1/CD^{1/2}$$

where R, T, F, and n stand for the usual electrochemical parameters.

If C remains roughly constant, which is likely to occur when the maximum concentration gradient is reached (diffusion controlled reaction), then σ becomes an exclusive function of D. Thus, it is not unreasonable to expect that the greater the value of σ, the more hindered the diffusion process (smaller values of D) and therefore the greater the barrier effect of the ZRP coating.

In the case of straight line diffusion tails (semi-infinite diffusion), one finds from Eq 1 without the hyperbolic term

$$\sigma = Z'_D \times w^{1/2} \quad \text{or} \quad \sigma = Z''_D \times w^{1/2}$$

Therefore, the value of σ can be obtained from the values of the real or imaginary components of the impedance vector, Z'_D or Z''_D, which are determined experimentally. In the case of diffusion tails which bend towards the real axis, the value of σ may be derived from the equations given by Ref *20*. In this case

$$\sigma = 1.06\, Z''_{D(\max)} \times (w_{\max})^{1/2}$$

where the maximum value for the impedance component, $Z''_{D(\max)}$, and the frequency at this point, $w_{\max}$, are also determined experimentally.

Applying either of these equations according to the particular type of diffusion tail, approximate values of σ are obtained for each ZRP coating, zinc and Fe_2P contents, type of vehicle, and time of exposure to the saline solution (Fig. 9).

There is an enormous increase in σ during the first 50 to 100 days in the case of the ethyl

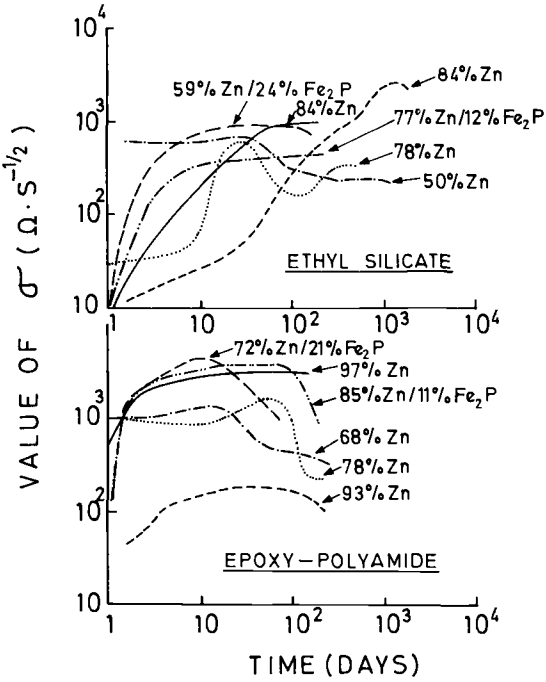

FIG. 9—*Warburg coefficient (σ) versus time.*

silicate vehicle paints with the higher zinc contents, which clearly demonstrates the important role played by the barrier effect in the protection mechanisms of these paints. Figure 9 also shows the enormous increase of σ in the paints formulated with the Fe_2P extender. The conclusion is that the conductive extender does not damage the development of the barrier effect in the ethyl silicate ZRP coatings.

The value of σ in the epoxy-polyamide vehicle paints is initially very high (Fig. 9). The evolution of σ also shows an increase in the barrier effect. Nevertheless, the relative increase of σ is now less significant than in the paints with an ethyl silicate vehicle. With the epoxy-polyamide coatings, the variation curve of σ with time passes through a maximum. The subsequent decline is due to the perforation of the coating, as confirmed by the appearance of rust points.

Finally, it is interesting to note the close relationship between the value of σ and the R_p value estimated from the length of the arc chord drawn at high or medium frequencies (Fig. 10), which corroborates the idea that both parameters depend similarly on the accumulation of zinc corrosion products within the coating.

Conclusions

(1) The measurements using the EIS technique provide a very valuable tool for the study of the anticorrosive protection mechanisms of ZRPs. These measurements obtained in a very wide range of frequencies allow us to examine the different processes that determine the behavior of these paints, from the faster processes, generally of charge transfer, to the slower ones, generally of mass transport.

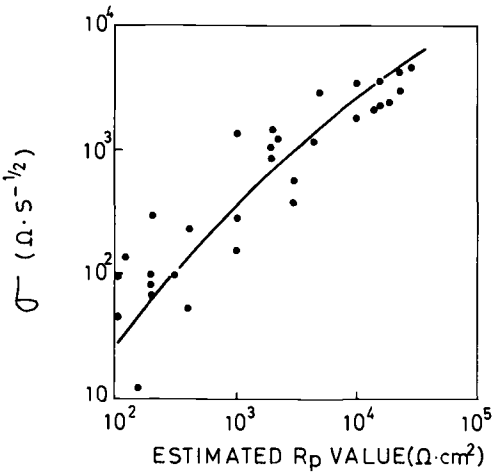

FIG. 10—*Relation between σ and the estimated value of polarization resistance.*

(2) The impedance diagrams permit monitoring of the evolution of the fundamental anticorrosive mechanisms of ZRP coatings, which mainly operate in two stages: the first one cathodic in nature, followed by the second of a barrier type. Specifically, such diagrams provide quantitative information about the dependence of these two stages on the following variables: (a) exposure time to the agressive medium, (b) percentage of zinc and conductive extender (Fe_2P) particles in the coating, and (c) type of vehicle used.

(3) It is shown that significant parameters for the interpretation of the behavior of ZRP coatings are: (a) the value of R_p determined from the arc of the high- or medium-frequency range in the Nyquist diagram, (b) the electrical capacitance that is calculated from the impedance data, and (c) the Warburg coefficient which is calculated from the diffusion tails at low frequencies.

References

[1] Evans, U. R. and Mayne, J. E. O., "Protection by Paints Richly Pigmented with Zinc Dust," *Society of Chemical Industry Journal*, Vol. 22, 1944, pp. 109–110.

[2] Feliu, S., Barajas, R., Bastidas, J. M., and Morcillo, M., "Mechanism of Cathodic Protection of Zinc-Rich Paints by Electrochemical Impedance Spectroscopy. I Galvanic Stage," *Journal of Coatings Technology*, Vol. 61, No. 775, 1989, pp. 63–69.

[3] Ross, T. K. and Lingard, J., "The Electrochemical Properties of Zinc-Rich Paints," *Transactions of the Institute of Metal Finishing*, Vol. 40, 1963, pp. 186–190.

[4] Theiler, F., "The Rust Preventing Mechanism of Zinc Dust Paints," *Corrosion Science*, Vol. 14, No. 7, 1974, pp. 405–414.

[5] Meszaros, L. and Lindqvist, S. A., "Study of the Performance of Zinc-Rich Paints Coatings," *Proceedings EUROCORR'82*, Budapest, Sec. 2, 1982, pp. 147–156.

[6] Szauer, T. and Brandt, A., "Impedance Measurements of Zinc-Rich Paints," *Journal of the Oil and Colour Chemists' Association*, Vol. 67, No. 1, 1984, pp. 13–15.

[7] Forsén, O., Yläsaari, S., and Fabritius, J., "Evaluating the Possibilities for the Development of Testing Zinc Rich Paints by Electrochemical Methods," *Proceedings of the 9th International Congress on Metallic Corrosion*, Toronto, 1984, pp. 477–480.

[8] Pereira, D., Scantlebury, J. D., Ferreira, M. G. S., and Almeida, M. E., "The Application of Electrochemical Measurements to the Study and Behaviour of Zinc-Rich Coatings," *Corrosion Science*, Vol. 30, 1990, pp. 1135–1147.

[9] Macdonald, D. D. and Mckubre, M. C. H., "Electrochemical Impedance Techniques in

Corrosion Science," *Electrochemical Corrosion Testing, ASTM STP 727*, F. Mansfeld and U. Bertocci, Eds., American Society for Testing and Materials, Philadelphia, 1981, pp. 110–149.

[*10*] Feliu, S., Barajas, R., Bastidas, J. M., and Morcillo, M., "Mechanism of Cathodic Protection of Zinc-Rich Paints by Electrochemical Impedance Spectroscopy. II Barrier Stage," *Journal of Coatings Technology*, Vol. 61, No. 775, 1989, pp. 71–76.

[*11*] Feliu, S., Jr., Bastidas, J. M., Morcillo, M., and Feliu, S., "Effect of the Di-Iron Phosphide Conductive Extender on the Protective Mechanisms of Zinc-Rich Coatings," *Journal of Coatings Technology*, Vol. 63, No. 794, 1991, pp. 67–72.

[*12*] Feliu, S., Jr., Morcillo, M., Bastidas, J. M., and Feliu, S., "Zinc Reactivity in Zinc-Rich Coatings Co-Pigmented with Di-Iron Phosphide," *Journal of Coatings Technology*, Vol. 63, No. 793, 1991, pp. 31–34.

[*13*] Morcillo, M., Barajas, R., Feliu, S., and Bastidas, J. M., "A SEM Study on the Galvanic Protection of Zinc-Rich Paints," *Journal of Materials Science*, Vol. 25, No. 5, 1990, pp. 2441–2446.

[*14*] Bastidas, J. M., Feliu, S., Jr., Morcillo, M., and Feliu, S., "Study of the Electrochemical Noise Generated by the Mild Steel/Zinc-Rich Paint/NaCl Solution System," *Progress in Organic Coatings*, Vol. 18, No. 3, 1990, pp. 265–273.

[*15*] Stern, M. and Geary, A. L., "Electrochemical Polarization I. A Theoretical Analysis of the Shape of Polarization Curves," *Journal of the Electrochemical Society*, Vol. 104, 1957, pp. 56–62.

[*16*] International Standard ISO 3549-1976: Zinc dust pigment for paints.

[*17*] Hepburn, B. J., Gowers, K. R., and Scantlebury, J. D., "Interpretation of Low Frequency AC Impedance Data for Organic Coatings on Mild Steel," *British Corrosion Journal*, Vol. 21, 1986, pp. 105–108.

[*18*] Llopis, J. and Colom, F., "Study of the Impedance of a Platinum Electrode Acting as Anode," *Proceedings of the 8th Meeting CITCE*, 1956, Butterworths, London, 1958, pp. 414–427.

[*19*] Armstrong, R. D. and Edmondson, K., "The Impedance of Cadmium in Alkaline Solution," *Electroanalytical Chemistry and Interfacial Electrochemistry*, Vol. 53, 1974, pp. 371–384.

[*20*] Dawson, J. L. and John, D. G., "Diffusion Impedance. An Extended General Analysis," *Journal of Electroanalytical Chemistry*, Vol. 110, 1980, pp. 37–47.

Richard D. Granata[1] *and Kevin J. Kovaleski*[1]

Evaluation of High-Performance Protective Coatings by Electrochemical Impedance and Chronoamperometry

REFERENCE: Granata, R. D. and Kovaleski, K. J., **"Evaluation of High-Performance Protective Coatings by Electrochemical Impedance and Chronoamperometry,"** *Electrochemical Impedance: Analysis and Interpretation, ASTM STP 1188,* J. R. Scully, D. C. Silverman, and M. W. Kendig, Eds., American Society for Testing and Materials, Philadelphia, 1993, pp. 450–462.

ABSTRACT: Coatings evaluation methodologies using electrochemical impedance spectroscopy (EIS) and chronoamperometry are described for high-performance corrosion protective coating systems. Three types of coating systems were studied: (1) fusion-bonded epoxy, (2) a marine-service epoxy, and (3) a polyimide used in electronics applications. The coating systems were monitored as a function of exposure to water, elevated temperature, and time. The data obtained were characterized by a high impedance at low frequency under ambient laboratory conditions that decreased with exposure time or temperature. The long-term, low-frequency decreases were irreversible; short-term, temperature-dependent decreases were reversible. Measurements are described which extended the limits of low-frequency measurements by use of a chronoamperometry technique. This low-current technique was a useful ancillary method for coating systems and enabled the estimation of low-frequency impedance and capacitance values not conveniently measurable by frequency response analyzers or fast-Fourier transform methods.

KEYWORDS: electrochemical impedance, polymer coatings, chronoamperometry, protective coatings, corrosion control

The objectives of this paper are to discuss some limitations of electrochemical impedance measurements in protective polymer coatings' assessment and to describe ways to surmount these limitations. Electrical and electrochemical methods provide useful information on protective polymer coating systems for metal substrates. Care must be exercised in selection and application of specific techniques so that erroneous information is not obtained and the test method does not measure self-induced damage. Surveys of electrical and electrochemical measurements as they have been applied to protective polymer coatings have identified techniques and reported data/results [*1,2*]. Representative work [*1–21*], including several meetings and symposia, indicates strong interest in development of electrochemical impedance and electrical methods for protective coatings assessment.

Coating evaluations by the described electrochemical methods were intended for high-performance protective systems. The coating systems studied were for long-term protection or resistance to highly aggressive exposure conditions. Useful impedance measurements are difficult to acquire on such systems due to the high resistance and slow response

[1]Senior research scientist and research assistant, respectively, Lehigh University, Zettlemoyer Center for Surface Studies and Department of Chemistry, respectively, Bethlehem, PA 18015.

time to environmental exposure. Specific experimental techniques have been developed for these types of protective coatings.

Three types of coating systems were studied: (1) fusion-bonded epoxy (FBE), (2) marine-service epoxy, and (3) polyimide used in electronics applications. The coating systems were evaluated as a function of exposure to water at elevated temperature or as a function of exposure time.

High-performance coating systems have been characterized by a high impedance ($|Z| > 10^9\ \Omega \cdot cm^2$) at low frequency ($f < 10^{-2}$ Hz) under ambient laboratory conditions (20 to 25°C, 50% relative humidity (RH)), which decreased with exposure time to aggressive electrolytes [*22*] or elevated temperature [*23*]. These long-term, low-frequency impedance decreases corresponded to underfilm corrosion processes and coating degradation and were irreversible: The initial protective properties could not be regained by drying, cleaning, or equilibration. Determinations of electrochemical and electrical properties using either dc or low-frequency ac methods under ambient laboratory conditions require techniques capable of high sensitivity, often necessitating operation of commercial instrumentation in the lowest current range with low signal-to-noise ratio. Data obtained at low frequencies with impedance have been very useful for coatings performance predictions [*2–10*]. Significant difficulties can be encountered acquiring data near equipment sensitivity limits. Guidelines for accommodating these difficulties may be extracted from the work of many researchers [*2,3,6,8,11,14,22–24*]; these include recommendations for specimen preparation, preconditions for measurements including bias potential and equilibration, and definition of appropriate test parameters such as voltage amplitude and low-frequency limit and validation of instrumentation measurement range. In this paper, we describe additional measurements that extend the limits of low-frequency measurements by use of chronoamperometric techniques. Low-current methods are useful ancillary methods, not intended to replace frequency-based measurements, which enable estimation of low-frequency impedance and capacitance values for coating systems not conveniently measurable by frequency response analyzers, lock-in analyzers, or FFT methods.

Experimental

Measurement Systems

The two measurement systems were: (1) an electrochemical impedance spectrometer based upon a frequency response analyzer connected to a computer with a potentiostat/current-follower, and (2) a computer-controlled electrometer.

Electrochemical Impedance—Data were obtained from a system consisting of an EG&G Princeton Applied Research Corp., Model 173/179 potentiostat with computer-controlled Solartron 1250 frequency response analyzer. The impedance spectra were determined from 65.5 kHz to 3.1 mHz. The input amplitude was 15 mV above 100 mHz and 50 mV below 100 mHz. The impedance limits for the measurement systems were $10^{10}\ \Omega \cdot V^{-1}$ and 150 pF (a 0.01 V applied voltage enabled measurement of $10^8\ \Omega$ for system capacitance greater that 150 pF). A diagram of the impedance measurement system is shown in Fig. 1. In one experiment, a final impedance spectrum was obtained using a 500 mV input amplitude for the fusion-bonded epoxy (FBE) specimen.

The electrochemical cell was a glass cylinder clamped and o-ring sealed to the specimen surface. The seal exposed 8.8 cm^2 of specimen surface to the distilled water test medium. The reference electrode was Ag/AgCl, and a carbon rod served as the counter electrode.

Studies were conducted on separate sets of specimens, each at room temperature (RT)

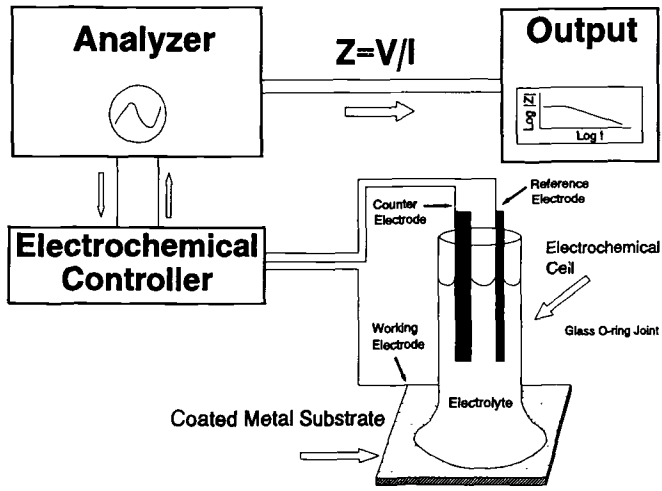

FIG. 1—*Electrochemical impedance system.*

and at one of three elevated temperature excursions (40, 60, or 80°C). The FBE was evaluated at RT and only one elevated temperature, 80°C. The typical sequence consisted of: (1) the impedance spectrum taken at RT (this procedural step was designated RT1.); (2) the specimen incubated at the test temperature for 1.5 h and the impedance spectrum taken at the elevated temperature (this step was designated by the temperature used, e.g., 80°C); (3) the specimen equilibrated at RT for 1.5 h and a spectrum recorded (this step was designated RT2); and (4) specimens equilibrated at ambient laboratory conditions (22°C and 50% RH) for 1 week and a final spectrum recorded (this final step was designated RT3).

Additional impedance measurements were made using powdered graphite as the conductive phase between the specimen and counter electrodes to determine the response without an electrolyte or water.

Chronoamperometry—A diagram of the chronoamperometry system is shown in Fig. 2. The cell configuration was two-electrode with the reference electrode (<10 kΩ) serving also as the counter electrode. A small amplitude (0.3 to 2.0 V) direct voltage was applied to the specimen while monitoring the current with a sensitive current measuring device, a Keithley Model 617 electrometer with 10^{-16} A sensitivity, 2 pF input capacitance and 0.33 to 2.0 s measurement time (range dependent). The current versus time curve obtained was analyzed for resistive and capacitive components. A simple model circuit was assumed for preliminary data analyses (Fig. 3 and Eq 1).

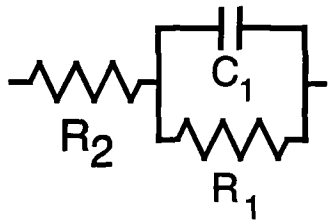

FIG. 2—*Chronoamperometry system.*

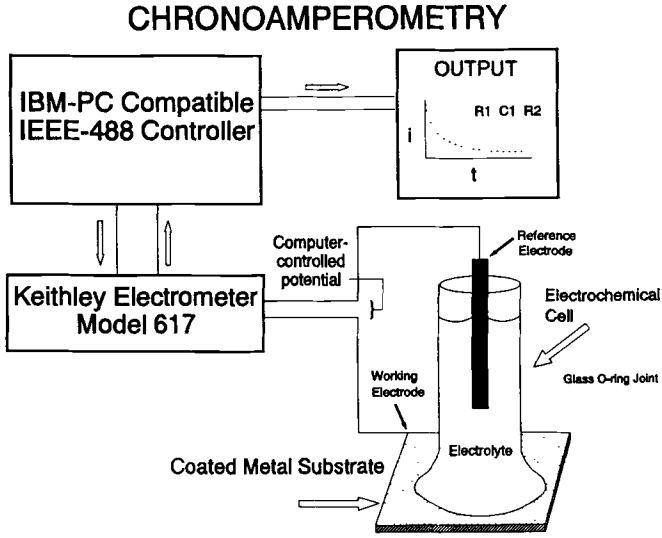

FIG. 3—*Simple equivalent circuit.*

$$I(t) = V\left(\frac{1}{R_2} - \frac{1}{R_1 + R_2}\right)e^{\frac{-(R_1 + R_2)t}{R_1R_2C_1}} + \frac{V}{R_1 + R_2} \quad (1)$$

A minimization procedure was used to determine the bias potential for the system before beginning the current versus time measurements. The procedure consisted of applying a potential (initially 0 V versus Ag/AgCl), measuring the coulombs for a set time of 10 s, adjusting the applied potential, and repeating until a minimum coulomb measurement was obtained. The bias potential obtained corresponded well with the expected corrosion potential or with the corrosion potential obtained by direct measurement of an equilibrated specimen.

Specimen Preparation

Solvent-Based Epoxy—Specimens were prepared from 10 by 20 by 0.05 cm SAE-1010 steel panels. The panels were wet ground with 240 grit SiC paper and rinsed with ethanol. Epoxy primer MIL-P-24441/1 was applied by draw bar at a thickness of 0.015 cm wet. Some panels were allowed to air-cure overnight; the remaining panels were oven-cured at 85°C for 1 h. Two coats of epoxy topcoat MIL-P-24441/5 were applied by draw bar at 0.018 cm wet thickness. The first topcoat was allowed to air-cure overnight for those specimens with air-cured primer. The final coat for the air-cured specimens was allowed to air-cure 1 week. The two additional topcoats of oven-heated primer specimens were each cured at 85°C for 1 h. The panels were cut into 5 cm squares. Final dry thicknesses ranged from 0.017 to 0.024 cm, ±2%, measured with an Elcometer Model 150 electronic magnetic thickness gage.

Polyimide—Substrates for polyimide specimens were also prepared in the same manner as the solvent-based epoxy, but were cut into 5 cm squares before applying the coatings. The polyimide was applied by spin-coating, followed by a cure of 12 min at 85°C and 20 min at 200°C. Cured film thicknesses were 0.001 cm measured with a magnetic thickness gage.

FBE—The precoated specimens were obtained from a commercial coatings supplier and prepared by the supplier following the recommended specifications. Materials were those typically used for pipeline and concrete reinforcing bar coatings applications. The coatings application process generally consisted of heating the specimen above the cure temperature of the epoxy system, electrostatically spraying the powdered coating material onto the heated metal substrate followed by additional heat-cure at 230°C for approximately 10 min. Cured film thicknesses ranged from 0.035 to 0.040 cm as determined by the supplier and verified with a magnetic thickness gage.

Results

Electrochemical Impedance

Data generated from impedance measurements are summarized in Figs. 4 through 8 for each of the coating systems. The sets of data for each coating are given as Bode magnitude plots, where the logarithm of the absolute value of the impedance (log $|Z|$) was plotted versus the logarithm of the frequency. Figure 8 shows the Bode phase data corresponding to the Bode magnitude information in Fig. 7. The plot labeled RT1 was the first measurement at RT. The plots labeled with elevated temperature (40, 60, or 80) were for spectra obtained at the indicated temperature. The plot labeled RT2 was the impedance spectrum after the specimen returned to RT. The plot labeled RT3 was the impedance spectrum after the coating was exposed to air for 7 days at RT. In the case of the FBE, the ambient air exposure was not performed because the RT2 data were identical to the RT1 data and the immersion tests were continued for longer duration.

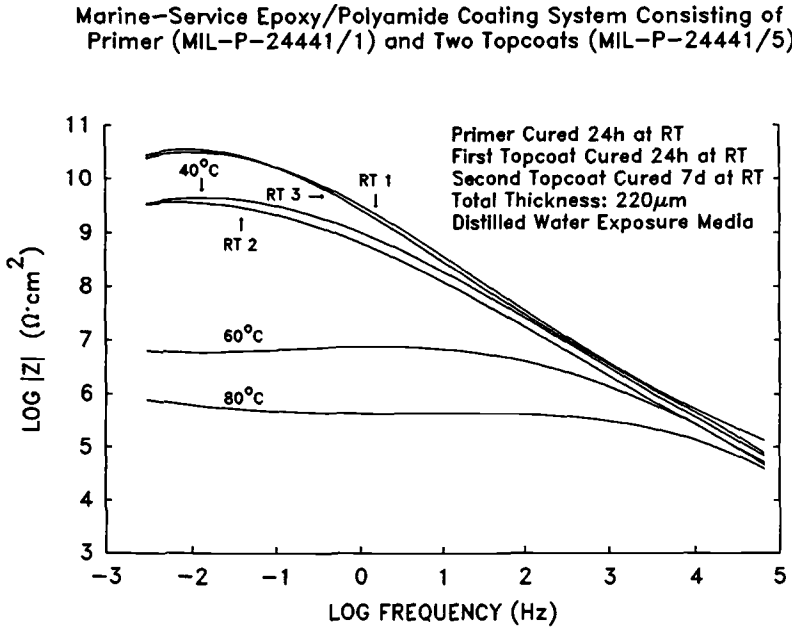

FIG. 4—*Impedance data for air-dried marine-service epoxy.*

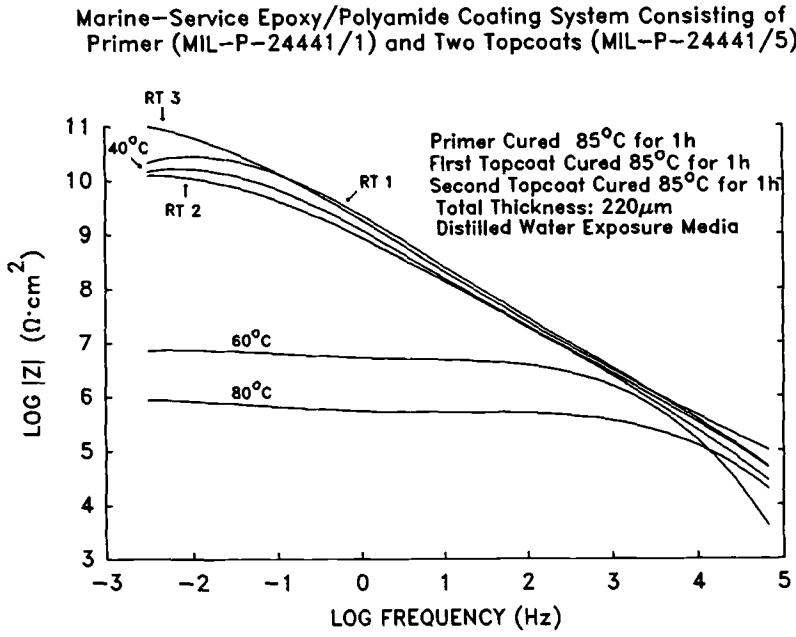

FIG. 5—*Impedance data for oven-cured marine-service epoxy.*

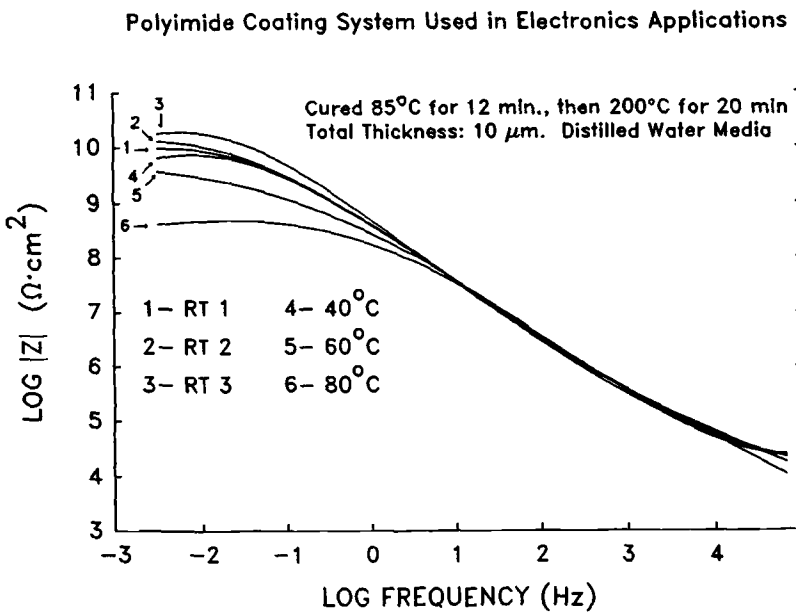

FIG. 6—*Impedance data for polyimide.*

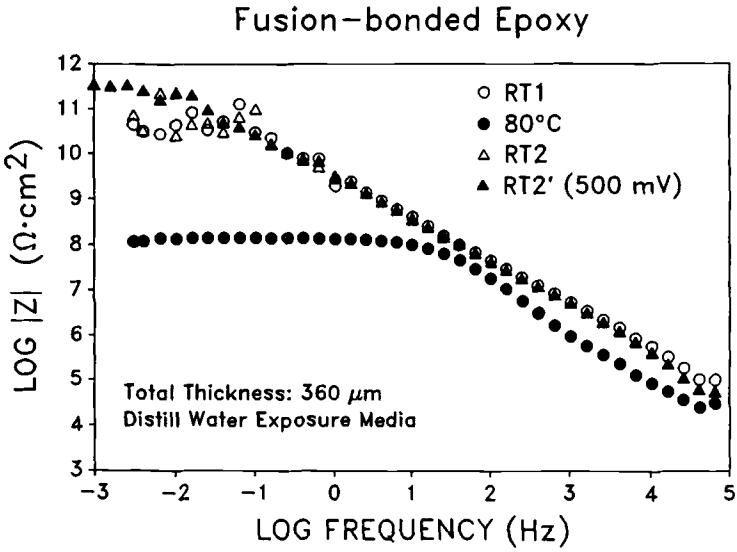

FIG. 7—*Impedance data for fusion-bonded epoxy.*

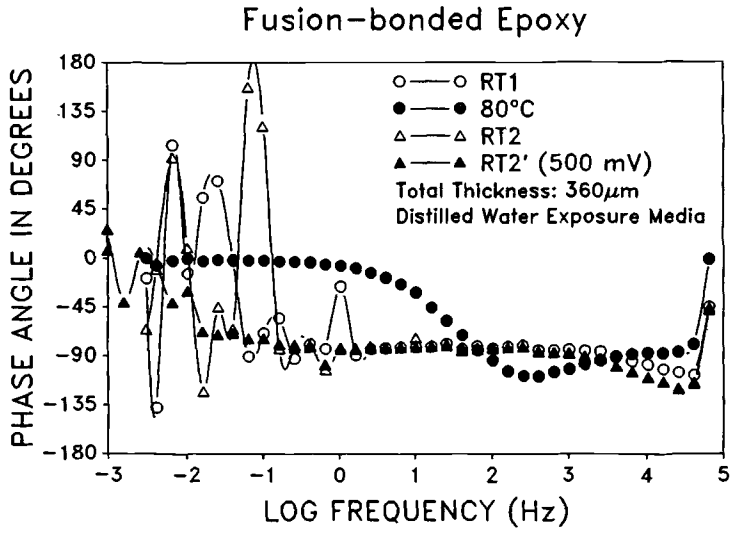

FIG. 8—*Impedance data (phase angle) for fusion-bonded epoxy.*

Chronoamperometry

Typical data obtained with the amperometric technique are shown in Fig. 9 for the FBE specimen. Additional results are given in Table 1 showing values for repetitive measurements and after further immersion times.

A set of measurements was obtained using a standard cell consisting of $R_1 = 2.5 \times 10^{11}$ Ω, $C_1 = 22$, 33, or 55 pF and $R_2 = 10^{11}$ Ω (Fig. 2 notation), and 0.5, 1, or 2 V applied

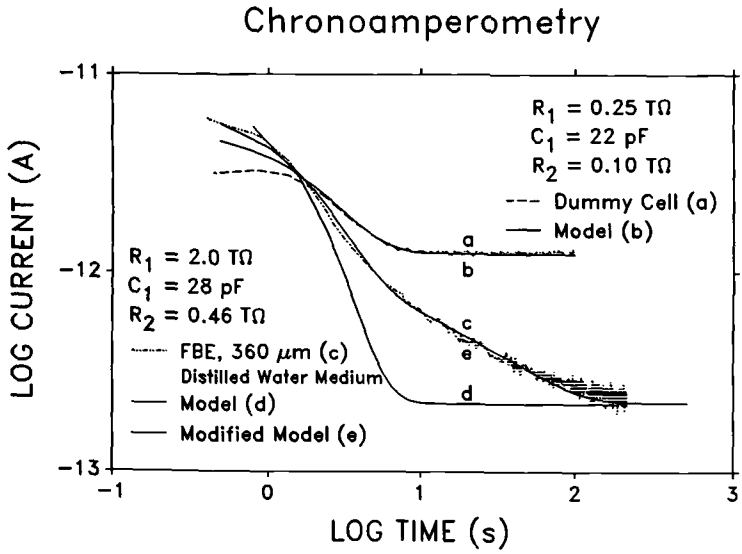

FIG. 9—*Chronoamperometric data for fusion-bonded epoxy.*

TABLE 1—*Chronoamperometry results for 0.035 cm fusion-bonded epoxy coating on steel.*

Time, d	Trial	C_1, pF	R_1, TΩ	R_2, TΩ
0	1	342	0.19	0.0078
	2	99	0.33	0.18
	3	83	0.36	0.22
	4	83	0.36	0.21
1	1	30	3.8	0.45
	2	29	3.9	0.47
	3	28	2.0	0.46
	4	27	1.8	0.50
4	1	33	4.7	0.53
	2	34	2.6	0.52
	3	34	3.2	0.51
	4	33	2.2	0.49
5	1	33	1.7	0.56
	2	31	1.7	0.62
	3	31	1.6	0.61
	4	31	1.8	0.65

NOTE: TΩ = 10^{15} Ω

TABLE 2—*Standard circuit results.*

	Step Voltage, V		
C_1, pF	0.50	1.0	2.0
22	25	25	25
33	34	35	35
55	58	55	56

NOTE: Measured resistances were ±10% of rated values. Experimental conditions are being modified to minimize noise and to establish stable initial conditions.

voltages. Results are listed in Table 2. Representative plots of measured data (curve a) and modeled data (curve b) are shown in Fig. 9.

Discussion

The impedance data for each coating system showed consistent results. During the relatively short duration (4.5 h) required for obtaining a measurement set including the elevated temperature, the decrease in low-frequency impedance was *reversible*. Typical behavior of impedance at various times (isothermal) is shown in Fig. 10, where a polybutadiene coating system degraded irreversibly and yielded lower impedance values in the low-frequency range. The short-term, reversible impedance behavior as a function of temperature shown in Figs. 4 through 8 is the "hydrothermal impedance response." The detailed properties for this phenomenon have long been under investigation in our laboratory. Generally, the hydrothermal impedance response required the presence of water (graphite experiments discussed in the following paragraphs) and was not apparently related to the coating glass transition temperature or thermal expansion coefficient. Some additional details are given later in this paper.

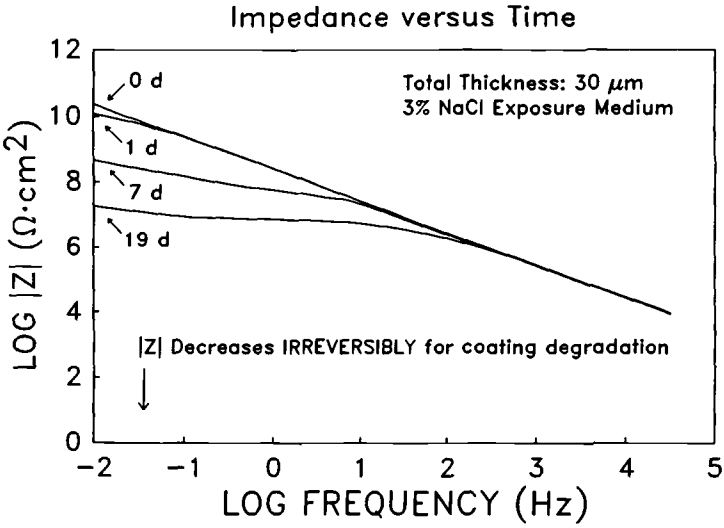

FIG. 10—*Impedance data for polybutadiene at increasing exposure times.*

Impedance data for the coating systems showed that the coatings fell into two classes: The marine-service epoxy specimens (Figs. 4 and 5) showed a large (10^5) change in the low-frequency impedance when the temperature of the test cell was increased, and the polyimide (Fig. 6) and FBE (Figs. 7 and 8) showed relatively small changes ($<10^3$) under the same conditions. The significance of these observations to appraising the protective properties of coatings using EIS in terms of polymer/water interactions has not yet been fully determined. However, for an initial test, a set of four epoxies coated on steel to the same film thicknesses were exposed to 100% RH for 24 h. The epoxies were formulated with different crosslink/hydrophobe starting material combinations. Impedance measurements were made with specimens from the same batch but were not used for the humidity test. Two epoxies yielded low-frequency impedance values at 60°C, $>10^9$ $\Omega \cdot cm^2$ versus $<10^6$ $\Omega \cdot cm^2$ for the remaining two epoxies. The data are presented in Table 3. Those specimens coated with materials having the lower values showed extensive underfilm rust spots whereas those with higher values revealed no evidence of corrosion. Additional tests are underway. These observations are likely to have a strong relationship to the effects of exposing polymer-coated metal to the natural environment and investigation of the phenomenon should provide a better understanding of long-term protection mechanisms by organic coatings subjected to cyclic exposure or ambient conditions.

Experiments with the epoxy/polyamide and with polyimide coatings, in which temperature-dependent impedance measurements were made using a dry conductive phase of powdered graphite between the coated metal and the counter electrode, have shown that part of the observed impedance behavior was due to water adsorbed by the coating under non-immersed conditions (22°C, 50% RH), and that most of the large impedance change versus temperature at low frequency was due to the presence of water.

The examples provided imply that correlation of hydrothermal properties with coatings performance would enable more detailed mechanism determination of the role water plays in protective coating degradation. This approach is particularly useful when high resistivity/measurement sensitivity considerations cause difficulties at ambient laboratory temperatures. Elevation of coated specimen temperature to reasonable service temperature values (± 10°C) accelerates or enhances water uptake and increases system conductivity to more easily measured ranges.

Another aspect of electrochemical impedance experiments should be considered with respect to data shown in Fig. 7. The data scatter observed for RT measurements at low frequencies and high-impedance values was characteristic of low signal-to-noise ratio.

TABLE 3—*Hydrothermal response and corrosion properties.*

Epoxy/Cure Agent	Log R_f^* (60°C) 3.1×10^{-3} Hz	Rust observed 24 h, 100% RH
DER 332/TETA	9.3	No
DER 332/UNIREZ 2140	9.5	No
DER 736/TETA	4.6	Yes
DER 736/UNIREZ 2140	5.2	Yes

*See Fig. 3.

NOTE: DER = DOW epoxy resin (Dow Chemical Corporation). DER 332 = diglycidylether of bisphenol A. DER 736 = aliphatic diepoxy. UNIREZ = polyamide (Union Camp Company). TETA = triethylenetetramine.

There was no clear separation of signal-from-noise. This difficulty is more evident in the phase angle data for the FBE specimen (Fig. 8). Note the large scatter at low frequencies, particularly for RT1 and RT2. The spectrum labeled RT2 was obtained using an input amplitude of 500 mV. The data scatter due to noise is much reduced. However, the use of such high amplitudes for general evaluation of coating systems should be approached cautiously. Figure 11 shows the damaging effect of repetitive cathodic polarization scans on an epoxy-coated specimen having a small uncoated defect [*18*]. A coating system can be damaged by large polarization potentials or controlled current techniques in which the potential is not limited to small values [*9,25*]. Applied potentials above 100 mV should be used cautiously. Controlled current techniques require more caution since the applied potential may easily exceed 100 mV unless potential limits are imposed. The damage is caused by cathodic processes under coatings and has been extensively studied [*25–27*]. In a specific study involving cathodic polarization and impedance measurements, the degradation was distinctively evident [*9*]. The cathodic portion of an applied waveform generates hydroxide beneath the coating at small polarizations from the equilibrium potential. The cathodic charge participating in the cathodic reaction, the flux of reactants and the hydrolytic stability of the organic bonds contribute to the probability of coating damage.

Chronoamperometry represents an alternative to increasing the applied potential for impedance measurements. The results for the FBE can be obtained at polarization potentials not likely to cause coating system damage. In addition, measurements can be made quickly for estimation of very high impedances. For example, Fig. 9 shows the data and calculated values of resistances and capacitance for the same FBE system whose impedance data were shown in Figs. 7 and 8. The calculation was based upon the 3-component

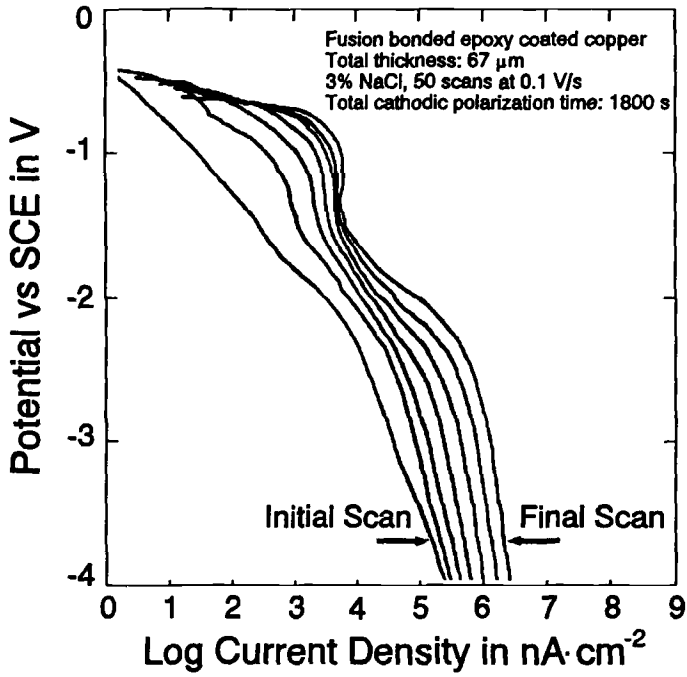

FIG. 11—*Potentiodynamic scans (dc) inducing coating damage in epoxy-coated copper* [18].

equivalent circuit shown in Fig. 2. The equivalent circuit was a reasonable model for the specimen based upon the electrochemical impedance data for the specimen. Note that after the initial portion of the current decreased, appreciable deviation was observed (Fig. 9, curve c versus curve d). An additional model using a transmission line component provided an apparent better correlation (Fig. 9, curve e). Other models may also provide useful correlations. Discussions of appropriate methods for modeling chronoamperometric data and detailed comparison to impedance data are beyond the scope of this paper and will be the subject of future work. The most interesting comparison of the impedance and chronoamperometric results was the value for the low-frequency impedance, 0.2 TΩ (T = 10^{15}). Figures 7 and 8 are sensitivity limited, versus the value for R_1, 2.0 TΩ (Fig. 9 and Table 1). Also, the impedance spectroscopy method yielded approximately 45 pF after correction for the measurement system impedance versus 30 pF for amperometry. The chronoamperometric approach provided greater sensitivity than the impedance method. In this comparison, the sensitivity limit for the chronoamperometric measurements permitted the determinations of approximately 10^3 to 10^5 greater impedance values than electrochemical impedances at low frequencies using currently available measuring equipment. Most recent commercial impedance systems are capable of providing an increase in sensitivity by factors of 10 to 500 over the system used in this study. Special specifications for highly resistive materials may be required to enhance commercial impedance systems beyond current standards and would result in less useful systems. Also, data acquisition time needed for frequency response analyzer and lock-in analyzer methods would likely be long for high-resistance specimens. Therefore, alternatives to the commercial systems should be considered. The chronoamperometry method development and comparison to electrochemical impedance methods are being pursued with the intent of examining complementary applications [*28*].

Summary

Electrochemical impedance and electrical measurement technique limitations based upon sensitivity or measurement period considerations and possible coating damage due to excessive applied voltage have been presented. An experimental approach for complementary use of electrochemical impedance and chronoamperometry in the evaluation of high-performance protective organic coatings has been described. Hydrothermal effects have been described and provide a useful approach to coating characterization.

Acknowledgment

The authors are grateful for support of the Office of Naval Research, Grant N00014-90-J-1229.

References

[*1*] Leidheiser, H., Jr., *Progress in Organic Coatings*, Vol. 7, 1979, p. 79.
[*2*] Leidheiser, H., Jr., *Journal of Coatings Technology*, Vol. 63, No. 802, 1991, p. 20.
[*3*] Kendig, M. W. and Scully, J., *Corrosion*, Vol. 46, No. 1, 1990, pp. 22–29.
[*4*] Walter, G. W., *Corrosion Science*, Vol. 26, 1986, p. 681.
[*5*] Walter, G. W., *Journal of Electroanalytical Chemistry*, Vol. 118, 1981, pp. 259–273.
[*6*] Walter, G. W., *Corrosion Science*, Vol. 32, No. 10, 1991, p. 1085.
[*7*] Walter, G. W., *Corrosion Science*, Vol. 32, No. 10, 1991, p. 1059.
[*8*] Hack, H. P. and Scully, J. R., *Journal of the Electrochemical Society*, Vol. 138, No. 1, 1991, pp. 33–40.
[*9*] Haruyama, S., Asari, M., and Tsuru, T., "Impedance Characteristics During Degradation of

Coated Steel," *Corrosion Protection by Organic Coatings*, M. W. Kendig and H. Leidheiser, Jr., Eds., The Electrochemical Society, Proceedings Volume 87-2, 1987, pp. 197-207.
[*10*] Scully, J. R., *Journal of the Electrochemical Society*, Vol. 136, No. 4, 1989, pp. 979-990.
[*11*] Titz, J., Wagner, G. H., Spähn, H., Ebert, M., Jüttner, K., and Lorenz, W. J., *Corrosion*, Vol. 46, No. 3, 1990, p. 221.
[*12*] Silverman, D. C., *Corrosion*, Vol. 47, No. 2, 1991, p. 87.
[*13*] Greenen, F. M., DeWit, J. H. W., and VanWesting, E. P. M., *Progress in Organic Coatings*, Vol. 18, No. 3, 1990, pp. 299-312.
[*14*] Tait, W. S. and Maier, M. A., *Journal of Coatings Technology*, Vol. 62, No. 781, 1990, pp. 41-44.
[*15*] Skerry, B. S., *Journal of Coatings Technology*, Vol. 60, No. 765, 1988, p. 97.
[*16*] Isaacs, H. S. and Kendig, M. W., *Corrosion*, Vol. 36, No. 6, 1980, p. 6.
[*17*] Mayne, J. E. O. and Mills, D. J., *Journal of the Oil and Colour Chemists' Association*, Vol. 58, 1975, p. 155.
[*18*] Granata, R. D., Deck, P., and Leidheiser, H., Jr., *Journal of Coatings Technology*, Vol. 60, No. 763, 1988, pp. 41-51.
[*19*] Kendig, M. W., *Corrosion Science*, Vol. 23, No. 4, 1983, pp. 317-329.
[*20*] Mansfeld, F., Kendig, M. W., and Tsai, S., *Corrosion*, Vol. 38, No. 9, 1982, pp. 478-485.
[*21*] Kendig, M. W., Tsai, S., and Mansfeld, F., *Materials Performance*, Vol. 23, No. 6, 1984, pp. 37-40.
[*22*] Leidheiser, H., Jr., Granata, R. D., and Turoscy, R., *Corrosion*, Vol. 43, No. 5, 1987, pp. 296-297.
[*23*] White, M. L. and Leidheiser, H., Jr., and Koch, G. H., *Materials Performance*, Vol. 25, No. 12, 1986, pp. 9-12.
[*24*] Mansfeld, F., Jeanjaquet, S. L., and Kendig, M. W., "An Electrochemical Impedance Study of Reactions at the Metal/Coating Interface," *Corrosion Protection by Organic Coatings*, M. W. Kendig and H. Leidheiser, Jr., Eds., The Electrochemical Society, Proceedings Vol. 87-2, 1987, pp. 217-228.
[*25*] Leidheiser, H., Jr. and Wang, W., *Journal of Coatings Technology*, Vol. 53, No. 672, 1981, pp. 77-84.
[*26*] Leidheiser, H., Jr., Wang, W., Granata, R. D., Vedage, H., and White, M. L., *Journal of Coatings Technology*, Vol. 56, No. 717, 1984, pp. 55-56.
[*27*] Leidheiser, H., Jr. and Kendig, M. W., *Corrosion*, Vol. 32, 1976, p. 69.
[*28*] Granata, R. D. and Tiedge, K. W., in *CORROSION 92*, 1992, NACE paper 92469.

DISCUSSION

M. Kendig[1] *(written discussion)*—In trying to improve the sensitivity of the impedance analysis to high impedance system, the authors should consider the following alternatives:

(1) Use a higher surface area sample.
(2) Apply LaPlace Analysis to the data to back out an impedance spectrum.

[1]Rockwell International Science Center, Thousand Oaks, CA 91360.

Peter Kamarchik[1]

Improved Coatings Testing and Evaluation Using Electrochemical Impedance Spectroscopy

REFERENCE: Kamarchik, P., **"Improved Coatings Testing and Evaluation Using Electrochemical Impedance Spectroscopy,"** *Electrochemical Impedance: Analysis and Interpretation, ASTM STP 1188,* J. R. Scully, D. C. Silverman, and M. W. Kendig, Eds., American Society for Testing and Materials, Philadelphia, 1993, pp. 463–474.

ABSTRACT: Electrochemical impedance spectroscopy (EIS) of automotive and general industrial electrodeposited coatings and of container interior coatings for beverage and food end-uses is described. We have correlated the electrochemical impedance data with traditional test data from exposure testing ranging from continuous salt fog to cyclic scab corrosion, artificial sauerkraut exposure, canned pet food exposure, and food processing conditions. Changes in the impedance spectra after exposures of only a fraction of the usual exposure time were generally well-correlated with visual examination of the test panels after completion of the usual length of test. The impedance spectra permitted an early observation of film deterioration even though no visually observable changes had occurred.

KEYWORDS: electrochemical impedance spectroscopy (EIS), coatings, paint, corrosion, cure, crosslinking, pretreatment

The traditional method for evaluating the ability of a coating to protect a substrate from a corrosive environment is to expose coated test panels to either the actual service conditions or to an environment that is chemically designed to model the actual service environment yet accelerate its effects. After exposure times, which can be considerable (even the major portion of the overall product development time), the panels are visually examined for signs of deterioration of the coating and attack on the substrate. In the case of container interior coatings, foods or other products are packed in the cans and stored for up to two years before the coatings can be evaluated. The obvious drawback to this kind of testing is the time required and the possibility that modes of failure entirely different from those seen in the service life may result from the use of aggressive test conditions. In addition, this kind of evaluation procedure gives little or no information on the chemical processes taking place which affect the type and rate of failure. Electrochemical impedance spectroscopy (EIS) offers an approach that promises to reduce the time needed to evaluate formulations and gives insight into the chemical nature of the failure mechanism.

Virtually all coating product types use some kind of accelerated testing in which the coating is subjected to a corrosive environment. Our current work includes electrodeposited automotive primers and industrial one-coat finishes, coil coatings, and container interior formulations for beverage and food cans. We have correlated the electrochemical impedance data with traditional test data from exposure testing ranging from continuous

[1]Senior research associate, PPG Industries, Inc., Allison Park, PA 15101.

salt fog to cyclic scab corrosion, artificial sauerkraut, canned pet food exposure, and food processing conditions. In this paper, three coating projects where EIS played an important role in the coating formulation development or problem resolution will be discussed in some detail. This paper is meant to provide a survey of the utility of EIS in our laboratory.

Of particular interest to the automotive and industrial electrodeposition product lines is the effect that the electrodeposition process has on the phosphate pretreatment previously applied to the metal and the subsequent influence on coating system performance [*1–3*]. In this case, the EIS data not only allowed an early evaluation of the corrosion resistance of the overall coating system, but helped suggest mechanisms that may explain the observed improvement in performance for low levels of pretreatment dissolution.

Another project concerned a concept involving almost all coatings product lines, that is, extent of cure. The idea of complete cure, as used by a coatings chemist, is not synonymous with exhaustion of all chemically reactive functional groups. In fact, some systems, when at optimum performance level, called "full-cure," have more than half of the potential reactive functionality remaining. What is important is the ability to measure degrees of cure relative to that of a coating cured to a desired level of performance properties. For a particular coating system using mixed epoxy and acrylic backbone polymer types, the low-frequency limit impedance observed after the coating was exposed to a boiling solution of 3% aqueous NaCl acidified with lactic and acetic acids correlated well with a theoretical relative degree of cure based on an approximate kinetic model and knowledge of the temperature profile during the curing bake. These impedance values also correlated well with T_g data as obtained from thermomechanical analysis [*4*].

In the third project to be discussed, we made use of EIS to get an early evaluation of container interior coating quality. In some cases, this has been correlated to long-term packed can evaluations. It has been demonstrated that, under shelf storage conditions, the rate of decrease of the low-frequency impedance can be correlated to shelf life [*5*]. An accurate determination of the rate, however, can take weeks or even months. Our evaluation, though not yet verified by many long-term tests, suggests that accelerated aging conditions coupled with EIS measurements can effectively differentiate formulations in tests of less than one day duration.

Experimental

The equipment used for all the experiments described in this paper is an EG&G PAR model 273 potentiostat/galvanostat and a Solartron 1255 frequency response analyzer. These components are interfaced to an IBM PS/2 model 30 computer. Most experiments involved single-frequency measurements from 100 000 Hz to 5 Hz combined with a multi-frequency technique that gave data in the 10 Hz to 0.1 Hz range. The multi-frequency Fourier transform technique was used at low frequencies to shorten the analysis time. Occasionally, experiments were done to frequencies as low as 0.01 Hz, but, in the system under study, little additional information was obtained. The signal amplitude was usually 10 mV in both the high-frequency and low-frequency ranges, but for the initial measurements on good coatings and for those that showed little deterioration, the low currents obtained made it necessary to use 20 mV in the low-frequency region. The most useful data presentation style was the Bode log impedance versus log frequency plot. The corresponding phase angle plot was not usually found to be of additional value and has not been included in this paper.

Coated test panels were prepared by applying the coating by electrodeposition or by "draw-down." Electrodeposition is described elsewhere [*6*]. Draw-down application simply refers to manually spreading a uniform layer of a coating over a substrate.

For experiments carried out on panels, a circular section of 1 cm^2 was exposed to the electrolyte in the PAR Instruments model K0235 flat cell. The electrolyte used was 5% aqueous NaCl in equilibrium with air. For experiments on container liners, the container was filled with either a 5% aqueous NaCl solution, as previously described, or with the material that will be commercially packed in these cans. Examples of these test solutions include soft drinks, diet soft drinks, sauerkraut, and various pet foods. The use of these types of test electrolytes is important, as we are currently attempting to seal counter electrodes into the packed food can so that measurements can be carried out without opening the can and terminating the pack test. In these experiments the can was filled with electrolyte with the counter electrode immersed in it. In this way the entire inner surface of the can became the working electrode. A Ag/AgCl reference electrode was also immersed in the electrolyte.

Results and Discussion

Phosphate Pretreatment Evaluation

In the cationic electrodeposition coating process, the metal to be coated is made the cathode in an electrolytic cell, with the electrolyte supporting an aqueous dispersion of cationically charged polymer micelles [*6*]. Electrolysis of water raises the pH at the cathode to a level where the dispersion is destabilized and therefore coagulates onto the metal workpiece [*6*]. The high pH boundary layer at the metal surface has been found to be damaging to the crystalline phosphate pretreatment previously precipitated onto the metal surface [*1–3*]. The purpose of this work was to determine what electrodeposition process variables affect phosphate dissolution and to determine how coating service performance would be affected.

The experimental procedure involved controlling the applied voltage and electrolysis time for electrolyzing buffer solutions or electrocoat baths to give phosphate dissolutions varying from negligible levels to 80% of the initial weight deposited. These changes in phosphate were monitored by X-ray fluorescence. The coated panels were then subjected to either salt spray or cyclic scab corrosion conditions [*7*]. Failure was monitored by ordinary visual inspection and compared to EIS results.

For a system of cold rolled steel/zinc phosphate/acrylic one-coat electrocoat, a phosphate loss of 8 to 10% was observed for coating conditions typical of a properly functioning commercial electrocoat line. Salt spray and cyclic scab corrosion testing indicate improved performance for the electrocoated panel over the same coating spray-applied as a control, even though the electrocoated panel experienced as much as a 10% loss of its phosphate pretreatment. The rapid decrease in low-frequency impedance of the salt spray panels for this acrylic one-coat electrocoated system is indicative of poorer corrosion resistance for the spray-applied coating than for the electrodeposited coating. A comparison of the impedance spectra show superimposable curves for the initial run through Day 3 for the electrocoated panel (Fig. 1). The sprayed panel shows a significant drop in impedance after only one day and a drop of a factor of 100 by the third day (Fig. 2). This drop continues to the conclusion of the experiment, with the coating resistance at this time reduced to 0.2×10^6 Ω-cm^2. In contrast, although the electrocoated panel drops in impedance during the test, this drop is less rapid than that for the spray-applied coating.

In addition, the EIS curve for the 22nd day for the electrocoated panel shows that, by this time, a diffusion controlled process has become an important part of the overall impedance. This is shown by the spectral region with a slope of about ¼, which occurs from a log frequency of 2.5 to a log frequency of 1.0 and by the spectral region with slope

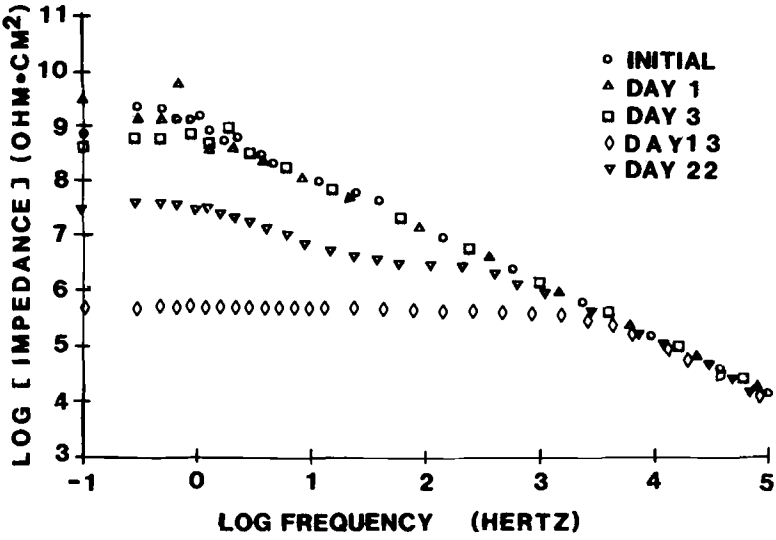

FIG. 1—*Acrylic one-coat, electrocoated, salt-spray.*

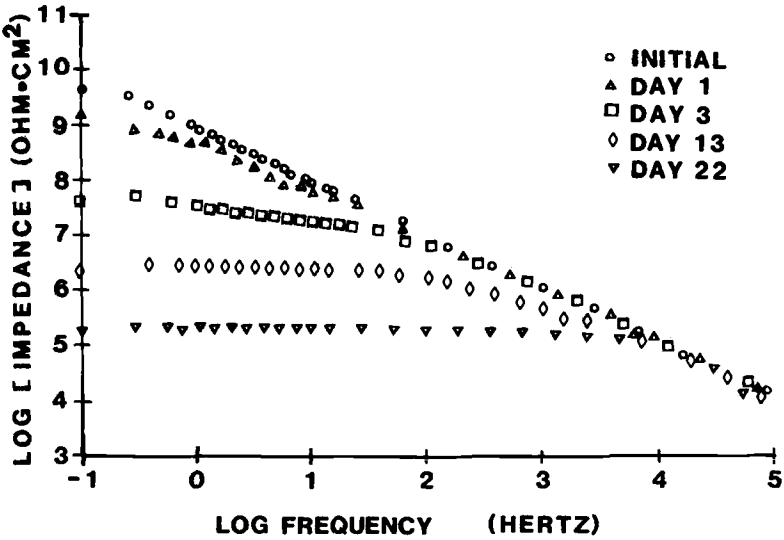

FIG. 2—*Acrylic one-coat, spray-applied, salt-spray.*

of ½ which occurs from log frequency of 1.0 to 0. This is not seen with the spray-applied coating. These data suggest that superior adhesion of the electrocoated paint creates resistance to the advancing front of corrosion products under the paint film. This type of under-film corrosion process has been shown to exhibit diffusion-controlled ionic conductivity [*8*]. The data also suggest that poorer adhesion of the spray-applied film causes the corrosion products and film to be spalled from the panel allowing the impedance to be dominated by transfer resistance rather than coating resistance. This difference in per-

formance may be attributed to the electrical driving force associated with the electrocoat process that causes the filling of pores in the pretreatment layer. There is no such driving force for a spray-applied coating. In fact, surface tension may act to keep the paint out of these pores. Additionally, the phosphate dissolution process being described may increase the number of these pores or increase their accessibility by removal of impurities or an amorphous or microcrystalline surface layer.

This hypothesis was tested on a second system, Hot Dipped Galvanized (HDG)/zinc phosphate/epoxy-based cationic primer. All phosphate loss in this experiment was due to the electrocoat process alone and was either 0% for the panels coated at 200 V or 7 to 8% for the panels coated at 280 V. The control was a draw-down on virgin phosphated substrate. For this coating, after 33 days, the scab corrosion panels were evaluated for extent of corrosion and were ranked with the 280 V panel best and the 200 V panel slightly better than the draw-down but much worse than the 280 V panel.

The salt-spray panels (also after 33 days) showed failure confined to the scribe area with blisters over the scribe separated by little or no scribe creep. The 280 V panel was best and showed a few blisters up to 5 mm diameter and at least some creep over 60% of the scribe. The 200 V panel had several blisters up to 7 mm diameter and at least some creep over 75% of the scribe. The draw-down panel had a few blisters up to 6 mm diameter and at least some creep over 70% of the scribe. The 200 V panel and the draw-down panel were therefore very similar in both tests with the 280 V panel being substantially better.

Electrochemical impedance spectra were run on the electrocoated panels referred to earlier that had been subjected to cyclic scab corrosion. Even the initial values of the low-frequency impedance indicated differences among these panels. The values obtained at 0.1 Hz were 3.31×10^9 Ω-cm^2, 1.10×10^9 Ω-cm^2, and 1.38×10^9 Ω-cm^2 for the 280 V, 200 V, and draw-down panel, respectively (Figs. 3–8). Several authors [*7,9,10*] have associated the impedance of the low-frequency plateau with inherent film quality. This low-frequency plateau represents the sum of the coating resistance, the transfer resistance, and the resistance of the electrolyte. Since the latter two resistances change little from coating to coating, changes in the low-frequency plateau represent changes in the

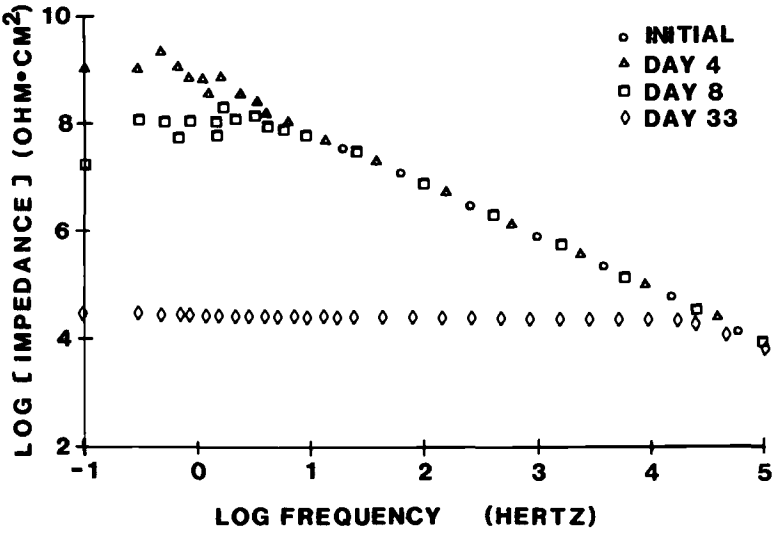

FIG. 3—*Epoxy-primer, draw-down, cyclic scab corrosion.*

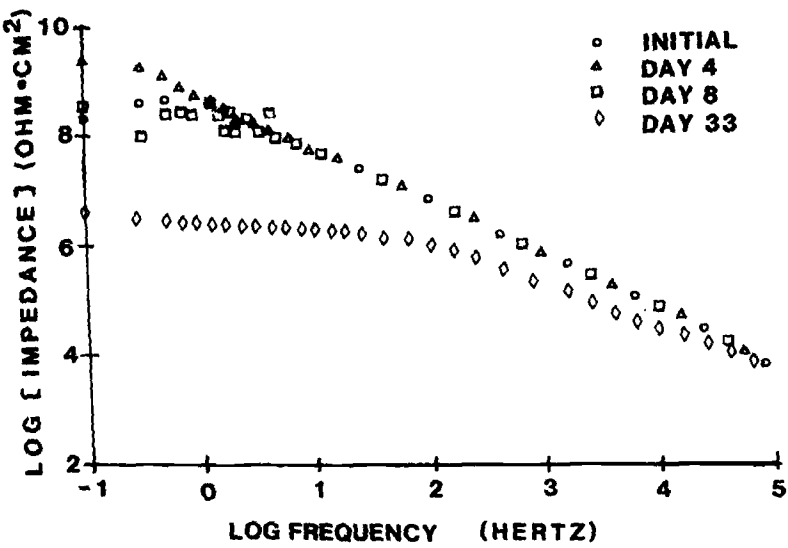

FIG. 4—*Epoxy-primer, E-coat 200 V, cyclic scab corrosion.*

coatings. A higher initial impedance value and its maintenance over exposure time is indicative of few conductive paths through the film and hence improved corrosion resistance [*7,11,12*]. A comparison of the rate of decrease of impedance, seen in the EIS curves of Figs. 3 through 8, to the visual observation of corrosion described earlier shows EIS capable of early indication of failure. The visual observations showed difference in performance only after about 25 days of testing. The EIS spectra showed significant differences in the degree of impedance decrease in only about three days. Those panels that

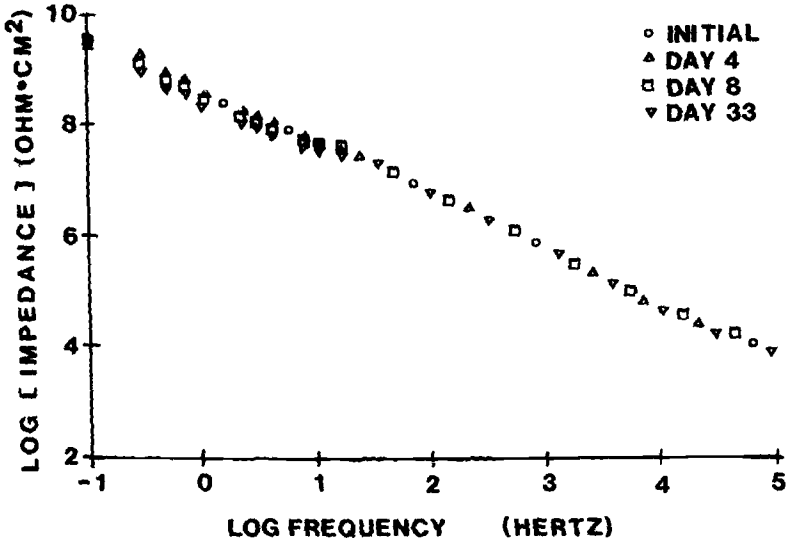

FIG. 5—*Epoxy-primer, E-coat 280 V, cyclic scab corrosion.*

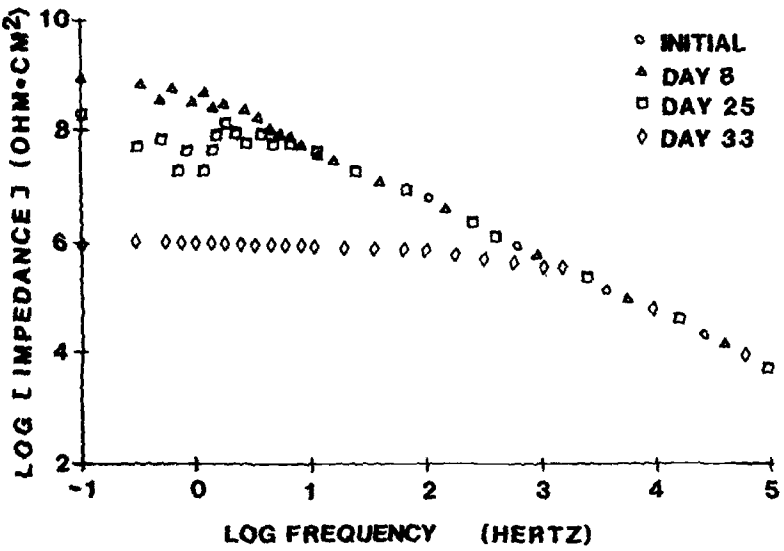

FIG. 6—*Epoxy-primer, E-coat 200 V, salt-spray.*

showed order of magnitude decreases in the first three test days ultimately failed by visual observation at 33 days of testing. At the same time, those panels that maintained their initial impedance for a week or more did not fail after 33 days as judged by visual observation.

Besides the initial low-frequency limit impedance, the change from a largely capacitive to a resistive film is also a measure of film integrity and, hence, corrosion resistance. For all three panel types coated with the epoxy based primer, the impedance spectra in Figs. 3

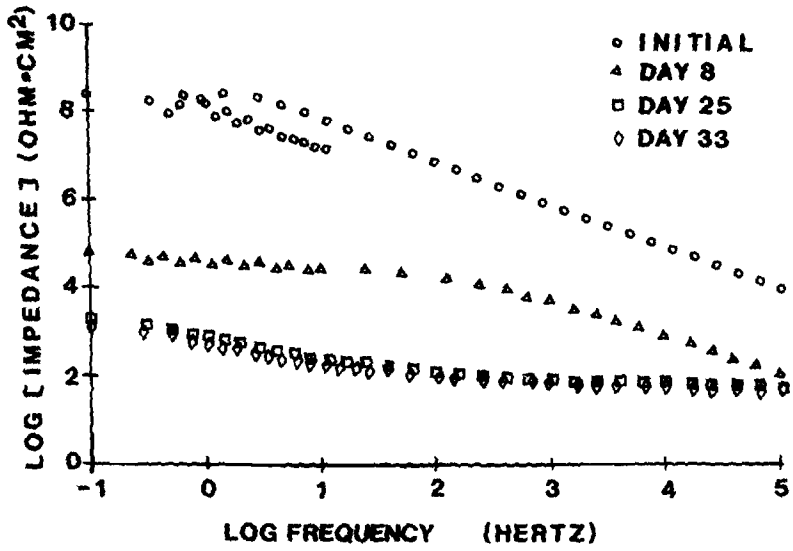

FIG. 7—*Epoxy-primer, draw-down, salt-spray.*

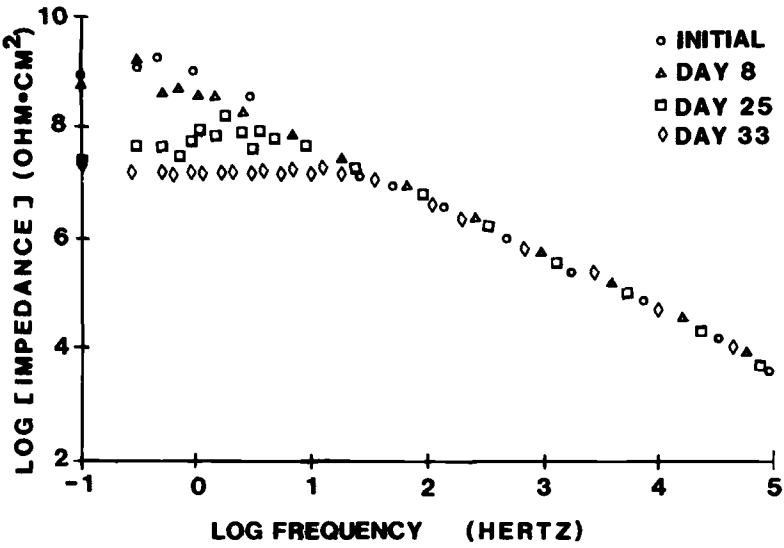

FIG. 8—*Epoxy-primer, E-coat 280 V, salt-spray.*

through 5 are superimposable except at the lowest frequencies for the initial run through Day 25. By Day 33, however, a significant portion of the spectrum, for the panel coated at 200 V, shows resistive behavior. The coating resistance was measured as 4.72×10^6 Ω-cm^2, a significant drop from the initial value of 1.10×10^9 Ω-cm^2. The panel prepared as a draw-down showed resistive behavior, by Day 33 over almost the entire spectrum, with a value which dropped from an initial 1.38×10^9 Ω-cm^2 to 3.0×10^4 Ω-cm^2. The breakdown of the film, which opens ion conductive channels, results in the vast changes in impedance noted earlier and accounts for the rapid acceleration of corrosion after an induction period [*13,14*].

There are two comparisons of interest in these data. The first is the similarity of the corrosion results, both visual observation and EIS spectra, for the draw-down and the 200 V panels. Even though the coating application methods were different, the degree of phosphate dissolution was zero in both cases. The second comparison is between the two electrocoated panels. Here, even though the application method was the same and the film thicknesses were controlled to be equal, their performances were very different. It appears that the method of application is not important but rather that the difference in performance is controlled by the amount of phosphate dissolution. Although it is possible that a change in the character of the coated film between 200 and 280 V specimens could account for the performance difference, these results suggest that an important role is played by the "etching" of the phosphate during electrocoating.

Degree of Cure Measured by EIS

Hybrid coating systems using both epoxy/blocked isocyanate and acrylic/melamine cure mechanisms were evaluated for degree of cure by observing the decrease in the low-frequency limit impedance after the coating had received four days exposure to an aqueous 3% NaCl solution acidified with lactic and acetic acids. The coating was electrocoated onto aluminum sheet stock and then cured, with a thermocouple attached to the metal to give the cure temperature profiles shown in Fig. 9. These measured profiles correspond to

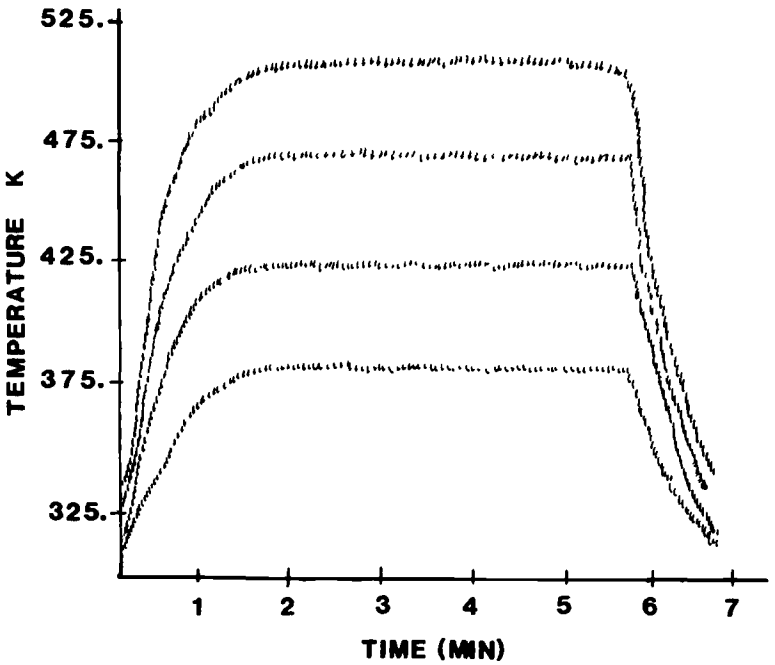

FIG. 9—*Cure temperature profile for epoxy/acrylic.*

oven set points of 120°C, 165°C, 205°C, and 230°C. Assuming that first-order kinetics apply to the cure reaction, and using literature values for activation energies of these reactions [*15*], integrated theoretical extents of reaction could be calculated. With the cure obtained at the 205°C bake defined as full cure and assigned a relative extent of reaction of 1.0, then the other values become 0.76, 0.90, and 1.10 for the bakes at 120°C, 165°C, and 230°C, respectively.

EIS spectra were run with the conditions given in the previous experimental section. All four bake conditions gave a low frequency (0.1 Hz) impedance of about 6×10^8 Ω-cm^2 as an initial measurement before exposure to the test solution. After exposure, the panels were rerun and the ratio of the log of the observed low-frequency impedance to its initial value was calculated. This number versus the integrated extent of reaction previously discussed is plotted in Fig. 10. The approximately linear relationship can be used to calculate relative degrees of cure of test panels by nondestructively measuring the low-frequency impedance before and after exposure to a test solution.

A more traditional method of assessing the cure of a coating is to measure the softening temperature by thermomechanical analysis. Figure 11 shows a plot of TMA softening temperature versus theoretical extent of reaction that confirms the varying extent of cure seen in the EIS result versus theoretical extent of reaction plot.

Container Liner Evaluations

In these experiments, we are attempting to get a rapid evaluation of container interior coatings by accelerating the deterioration of the coating by exposure to food packing conditions, boiling foodstuffs, or other aggressive conditions. One example is pack testing containers with pet foods consisting of gravies of meat by-products. (Pack testing refers to

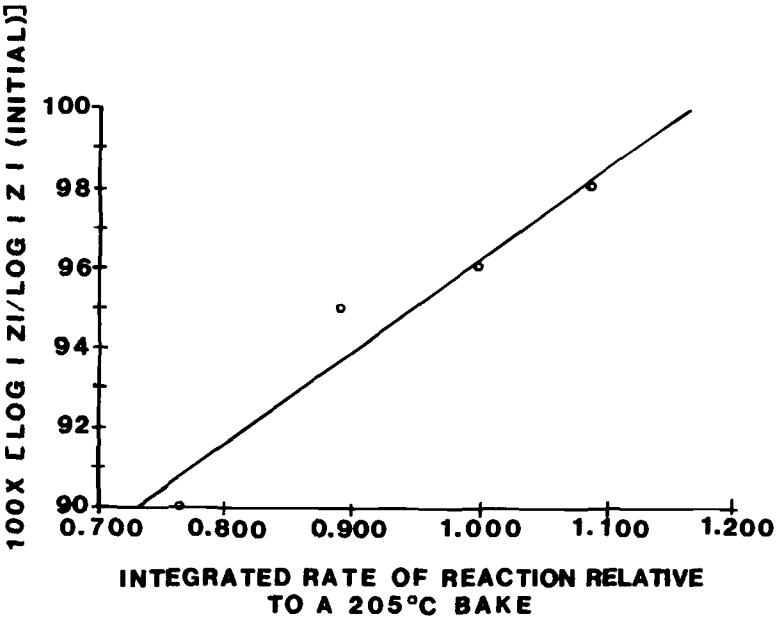

FIG. 10—*AC impedance as a function of cure (four days exposure to acidified salt solution).*

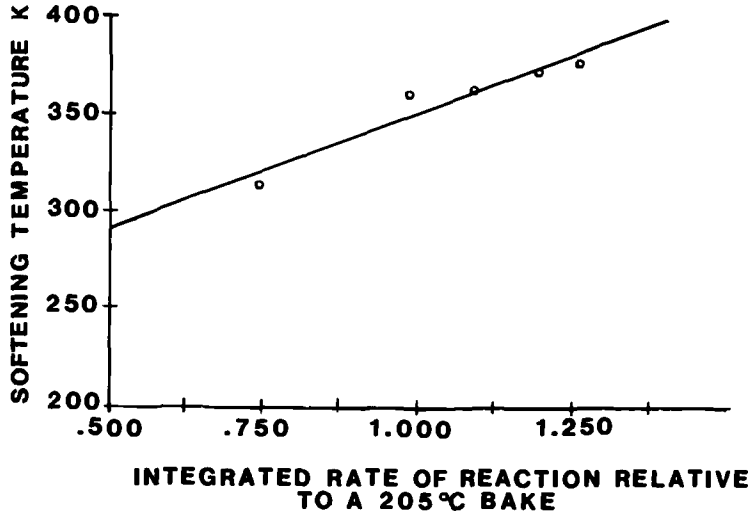

FIG. 11—*TMA transition temperature versus bake temperature.*

sealing the material of test into the cans using the conditions of temperature and pressure encountered in normal can filling, commercial food processing lines.) These are generally very high in fats and salt content. In the packing cycle, temperatures as high as 120°C are obtained. A control can, with the standard coating, not exposed to the pet food packing, was run with 5% aqueous NaCl as the electrolyte. The EIS curve is shown in Fig. 12. This

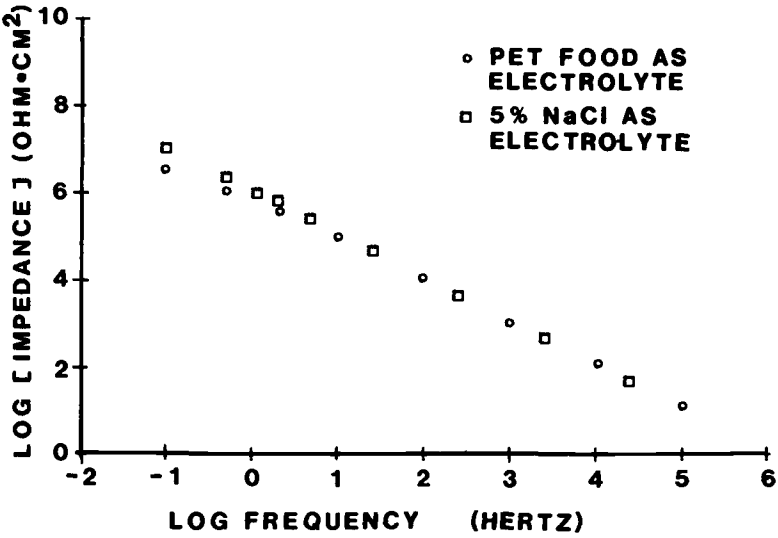

FIG. 12—*Initial spectra before pack testing.*

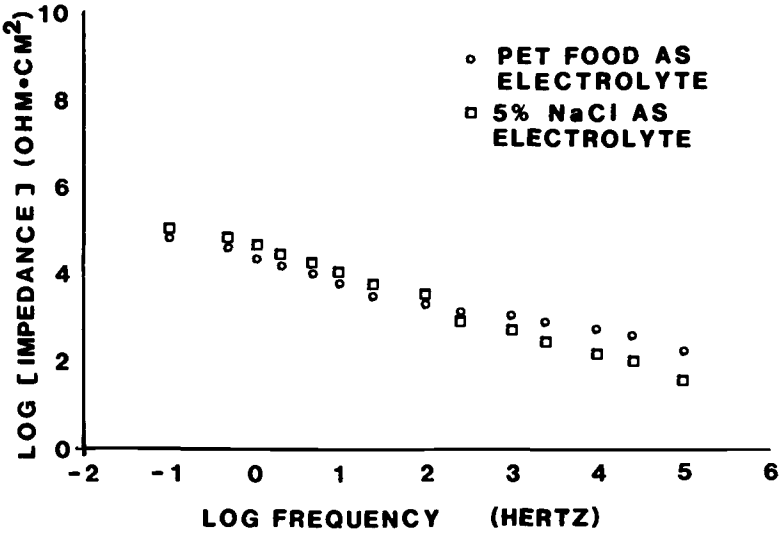

FIG. 13—*Spectra taken after pack testing with pet food.*

figure also shows the result for the same can run with the pet food as the EIS electrolyte. For this can, the log low-frequency impedance is 7.0 (Ω-cm^2). When pack tested with the pet food, this can gives the response shown in Fig. 13. Curves for both 5% NaCl and the packed pet food used as the electrolyte are shown. The agreement between the EIS spectra of these two electrolytes has led us to pack cans with an electrode sealed inside so that progress of the test can be monitored without destroying the can. These tests are currently in development. The log low-frequency impedance of the standard product, after pack testing, was 5.0 (Ω-cm^2), a substantial decrease from the control. By comparison,

experimental products, in low- and high-film thickness versions, gave log values of the low-frequency impedances of 5.3 and 6.5 (Ω-cm^2), respectively. These results correlated well with nine-month shelf tests that were done on these products.

Similar testing is being done using a boiling solution of a diet cola product. This test solution has been found to be very aggressive to many types of can liner formulations. Again, it is interesting that the standard product and four experimental container liner formulations gave very similar initial values of low-frequency impedance. Log impedance values ranged from 7.0 to 7.3 (Ω-cm^2), with the standard product control giving a value of 7.1 (Ω-cm^2). After one hour exposure to the boiling diet cola however, the control had dropped to 6.8 (Ω-cm^2), while the experimental formulations had reached values of 6.6, 5.7, 4.9, and 5.9 (Ω-cm^2). Thus a one hour accelerating procedure allows the EIS testing to discriminate among formulations where no visual difference or other measurement techniques discern a difference. Shelf testing is in progress on these coatings but these results have allowed the shifting of research emphasis to the most promising formulation variations. Thus far we have no long-term storage test results to correlate to the electrochemical impedance results.

Summary

The purpose of this paper was to provide a broad survey of the kinds of problems that have been addressed by EIS. The easy adaptability of measurement techniques allows for a wide variety of specimen types to be run. It has improved our understanding of the corrosion control mechanism of automotive electrocoat primers, provided a convenient means of measuring cure, and has greatly shortened the development time of several coatings systems by providing valuable feedback on the quality of a coating in very short testing times.

References

[1] Kamarchik, P., "The Effect of Pretreatment Dissolution on Electrocoat Corrosion Resistance," Paper No. 912298 presented at 1991 SAE Automotive Corrosion Conference, Dearborn, MI, October 1991.
[2] Schoff, C. K., *Proceedings, XXth FATIPEC Congress*, Nice, France, September 1990.
[3] Cape, T., *Proceedings, Electrocoat 88*, Gardner Publications, Cincinnati, OH, March 1988.
[4] Schoff, C. K. and Kamarchik, P., "Application of Thermal Mechanical Analysis to Organic Coatings," *Materials Characterization by Thermomechanical Analysis, ASTM STP 1136*, A. Riga and M. Neag, Eds., 1990.
[5] Tait, W. S., *Journal of Coatings Technology*, Vol. 61, No. 768, January 1989, p. 57.
[6] Pierce, P. E., *Journal of Coatings Technology*, Vol. 53, No. 672, January 1981, p. 52.
[7] Christman, T. K., Stropki, J. T., and Schoff, C. K., "Evaluation of Accelerated Corrosion Test Procedures," *Proceedings of the SAE Automotive Corrosion and Prevention Conference*, Paper No. 892583, Dearborn, MI, December 1989.
[8] Macdonald, J. R., *Impedance Spectroscopy*, John Wiley & Sons, New York, 1987.
[9] Leidheiser, H. and Granata, R. D., *IBM Journal of Research and Development*, Vol. 32, No. 5, September 1988, p. 582.
[10] Leidheiser, H., *Progress in Organic Coatings*, Vol. 7, 1979, p. 79.
[11] Pebere, N., Picaud, T., Duprat, M., and Dabosi, F., *Corrosion Science*, Vol. 29, No. 9, 1989, p. 1073.
[12] Miskovic-Stankovic, V. B. and Drazic, D. M., *Journal of Coatings Technology*, Vol. 63, No. 793, February 1991, p. 25.
[13] Homma, K., Kihira, H., and Ito, S., "Application of Alternating Current Impedance Method to Evaluation of Coating Deterioration," Paper No. 483, *Proceedings, CORROSION91*, NACE Annual Conference, Cincinnati, OH, March 1991.
[14] Scantlebury, J. D. and Sussex, G. A. M., *Corrosion Control by Organic Coatings*, H. Leidheiser, Ed., NACE, Houston, TX, 1981.
[15] Bauer, D. R., *Progress in Organic Coatings*, Vol. 14, 1986, p. 193.

Author Index

A–B

Agarwal, Pankaj, 115
Ahmadun, M. B. H., 255
Barajas, Rosa, 438
Bastidas, José M., 438
Bertocci, Ugo, 9

C–F

Chechirlian, Serge, 23
Cottis, R. A., 173
Dawson, John L., 237, 255, 384
Dougherty, Brian J., 154
Eden, David A., 237
Feliu, Sebastián, 438
Feliu, Sebastián, Jr., 438

G

Gabrielli, Claude, 140
Garcia-Rubio, Luis H., 115
Granata, Richard D., 450
Greene, Harold, 37

H

Hack, Harvey, 220
Halliop, E., 313
Handrich, Kristy A., 428
Haruyama, Shiro, 347
Hirozawa, Stanley T., 205

J

Jafar, Morph I., 384
Jeanjaquet, S., 407
John, D., Gareth, 384

K

Kamarchik, Peter, 463
Keddam, Michel, 23, 140
Kelly, Robert G., 94
Kendig, Martin W., 1, 343, 407, 462
Kolman, David G., 73
Kovaleski, Kevin J., 450
Kranc, S. C., 365

L–M

Lin, S. H., 297
Lumsden, J., 407
Mansfeld, Florian, 37, 236, 251, 275, 297
Martin, Jonathan W., 428
Morcillo, Manuel, 438

N–R

Newman, Roger C., 94
Orazem, Mark E., 115
Palmer, James W., 237
Pickering, Howard, 220
Ricker, Richard E., 9
Roberge, Pierre R., 54, 313
Rothwell, A. Neil, 237

S

Sagüés, A. A., 365
Schueller, Gayle R. T., 328
Scully, John R., 1, 276
Shih, Hong, 37, 297
Silverman, David C., 1, 192
Smedley, Stuart I., 154
Stewart, Kevin C., 73
Sudo, Shirohi, 347

T

Tait, Susan W., 428
Tait, William Stephen, 428
Takenouti, Hisasi, 22, 23, 140, 383
Tsai, C. H. (Raymond), 37
Taylor, S. Ray, 73, 328
Thompson, G. E., 255
Turcotte, David E., 205
Turgoose, S., 173

W–Y

Wang, Y., 297
Xiao, H., 297
Young, Alison J., 94
Yousri, Sid, 313

Subject Index

A

Acetic acid, conductivity, 23
Adhesive bond, 328
Aerosol containers, internally coated, 428
Aluminum
  amphoterism, 205
  anodized
    impedance, 37
    statistical process control, 313
  corrosion, 1
  EIS evolution during porous anodic film sealing, 255
  inhibition, silicate polymerization effect, 205
  thin films, corrosion, 276
Aluminum alloys, localized corrosion, detection and monitoring, 297
Aluminum/methanol systems, impedance data, 154
Aluminum/methanol/water systems, impedance data, 154
Aluminum oxide film, 276
Aluminum/polymer laminates, equivalent circuit modeling, 328
Amino-trimethyl phosphonic acid, 192
ANALEIS, 37
Anodic reactions, 9
Anodizing, process control, 313
Artifacts, 73

B

Barrier stages, zinc-rich paints, 438
Bode magnitude, 428
Bode phase, 428
Bode plots, 255
Breakpoint method, 407
Buried structure, electrochemical impedance, 347

C

Capacitance, double layer, 407
Carbon steels, differential corrosion, 237
Cathodic disbonding, 407
Cathodic protection, zinc-rich paints, 438
Cathodic reactions, 9
Charge transfer control, 37
Charge transfer kinetics, 9
Chi-square, 428
Chronoamperometry, 450
Circuit models, 23
  aluminum/polymer laminates, 328
  corroding film-covered metal, 173
  corrosion prediction, 192
  parasitic conduction pathways, 73
  RC model, 54
Coatings
  accelerated testing, 463
  improved testing and evaluation, 463
  internally coated steel aerosol containers, 428
  loss of adhesion, 407
  see also Paints
CO_2 corrosion, 237
Concrete, steel in, 1
  counter electrode polarization effects, 365
  electrochemical impedance and harmonic analysis, 384
Container service lifetime, 428
Copper-nickel alloys, corrosion resistance, 220
Corrosion, 1
  aluminum, 1
    thin films, 276
  differential, carbon steels, 237
  electrochemical impedance spectroscopy, data analysis, 37
  film-covered metals, 173
  high impedance systems, 154
  local
    buried structure, 347
    detection and monitoring, 297
  model polarization curves, 9
  monitoring, 54, 347
  potential
    electrochemical noise, 205
    steel in concrete, 384
  prediction from circuit models, 192

Corrosion (*cont.*)
rate, steel in concrete, 384
resistance
copper-nickel alloys, 220
extremes, 428
steel in concrete or soil, 1
Corrosion inhibitors, 1
carbon steel in seawater, 237
high-performance protective coatings, 450
silicate polymerization, 205
testing and evaluation, 192, 463
Corrosion-product film, corrosion resistance, 220
Counter electrode, polarization effects, 365
Cracking, stress-corrosion, 94
Crosslinking, 463
Cure, coatings, 463
Current
distribution, 365
primary and secondary distribution, 347

D

Dealloyed layers, coarsening characterization, 94
Deconvolution, Kramers-Kronig transformation, 115
Diffusional impedance, aluminum thin film corrosion, 276
Distributed parameter system, 347

E

Electrochemical impedance spectroscopy
aluminum anodizing statistical process control, 313
aluminum/polymer laminate equivalent circuit modeling, 328
aluminum thin film corrosion characterization, 276
analysis by systematic permutation of data points, 54
counter electrode polarization effects of steel in concrete, 365
data analysis, corrosion, 37
electrochemical noise, 205
evolution during porous anodic film sealing on aluminum, 255
high-performance protective coatings, 450
improved testing and evaluation of coatings, 463
internally coated steel aerosol containers, 428
interpreting from segmented electrode arrangements, 237
Kramers-Kronig relations application, 115
localized corrosion, detection and monitoring, 297
loss of adhesion of organic coatings, 407
parasitic conduction pathways, 73
steel in concrete, 384
validation by Kramers-Kronig transformation, 140
zinc-rich paint protection mechanisms, 438
Electrochemical noise, inhibitor system study, 205
Electrodes
impedance, low conductivity media, 23
kinetics, polarization curves, 9
porous, coarsening of dealloyed layers, 94
segmented arrangements
EIS interpretation, 237
Electrolyte resistance, 23
Equivalent circuits, *see* Circuit models
Error structure, frequency-dependent, 115

F

Faradaic relaxation phenomena, 23
Film-covered metals, impedance, 173
Film-induced cleavage, coarsening of dealloyed layers, 94
Films
corrosion-product, 220
hydration, 255
porous anodic sealing, EIS evolution during, 255
surface, corrosion, 173
unstable, electrochemical noise, 205
Fusion-bonded epoxy
evaluation, 450
loss of adhesion, 407

G

Galvanic effects, 237

H

Harmonic analysis, steel in concrete, 384
High impedance systems, data validation using Kramers-Kronig transformation, 154
Hydration, open circuit potential, 276
Hydrothermal sealing, porous anodic films on aluminum, 255

I

Impedance spectra, calculated from polarization curve, 9
Interface modeling, 54
Interface regulating device, Kramers-Kronig transformation relation, 140
Iron, corrosion inhibitor evaluation, 192

K

Kramers-Kronig transformation, 1
  application in EIS, 115
  high impedance system data validation, 154
  relation to interface regulating device, 140

L

Laminates, equivalent circuit modeling, 328
Low conductivity media
  artifacts, 73
  electrode impedance, 23
  parasitic conduction pathways and EIS measurements, 73
Luggin capillary, 23

M

Marine-service epoxy, evaluation, 450
Mass transfer control, 37
Measurement models, Kramers-Kronig transformation, 115
Measuring area, 347
Metal coatings, 1
Metal matrix composites, localized corrosion, detection and monitoring, 297
Metals, film-covered, impedance, 173
Metastable pitting, 276

N

Nitrate, aluminum inhibition, 205
Nyquist plots, 428
Nyquist representation, 54

O

Organic coatings, loss of adhesion, impedance, 407
Oxide capacitance and resistance, 276

P

Paints
  improved testing and evaluation, 463
  zinc-rich, protection mechanisms, 438
Palladium sputter-coating, corrosion product, 220
Parasitic conduction pathways, electrochemical impedance spectroscopy, 73
Passivation, Kramers-Kronig transformation, 140
Passivity, 276
Permutation technique, 54
Phase angle, 297
Pipelines
  electrochemical impedance, 347
  loss of adhesion of organic coatings, 407
Pit capacitance, 276
Pitting, 37, 297
Polarizability, 365
Polarization curve, impedance spectra calculated from, 9
Polarization resistance, 347
  corrosion prediction, 192
Polyimide, evaluation, 450
Polymer coatings
  high-performance, 450
  impedance behavior, 37
  loss of adhesion, impedance, 407
Pore electrolyte, corrosion-product film, 220
Potential distribution, impedance measurements, 23
Potentiodynamic polarization, aluminum anodizing statistical process control, 313
Pretreatment, coatings, 463

R

Repassivation, 276
Rotating cylinder electrode, 192

S

Salt spray test, 313
Silicate polymerization, aluminum inhibition, 205
Simulation, ANALEIS, 37
Sodium chloride, concrete effects, harmonic analysis, 384
Software, ANALEIS, 37
Stability, Kramers-Kronig transformation, 140
Steel
  cathodic protection, zinc-rich paints, 438
  in concrete
    corrosion, 1
    counter electrode polarization effects, 365
    electrochemical impedance and harmonic analysis, 384
  in soil, corrosion, 1
  corrosion inhibitor evaluation, 192
  internally coated aerosol containers, 428
  loss of adhesion of organic coatings, 407
  in water, artifacts, 73
Stern-Geary constant, 384
Stress-corrosion cracking, correlation with coarsening of dealloyed layers, 94
Surface diffusion, coarsening of dealloyed layers, 94
Surface films, corrosion, 173

T

Tafel slopes, 384
Theta phase precipitates, 276
Transmission line theory, 328
Transpassive dissolution, Kramers-Kronig transformation, 140

V

Validation criterion, Kramers-Kronig transformation, 140

W

Weld corrosion, 237
Welded joints, differential corrosion, 237

Z

Zinc-rich paints, protection mechanisms, 438

ISBN 0-8031-1861-9